Finite Element Simulation of Additive Manufacturing with Enhanced Accuracy

July 2022

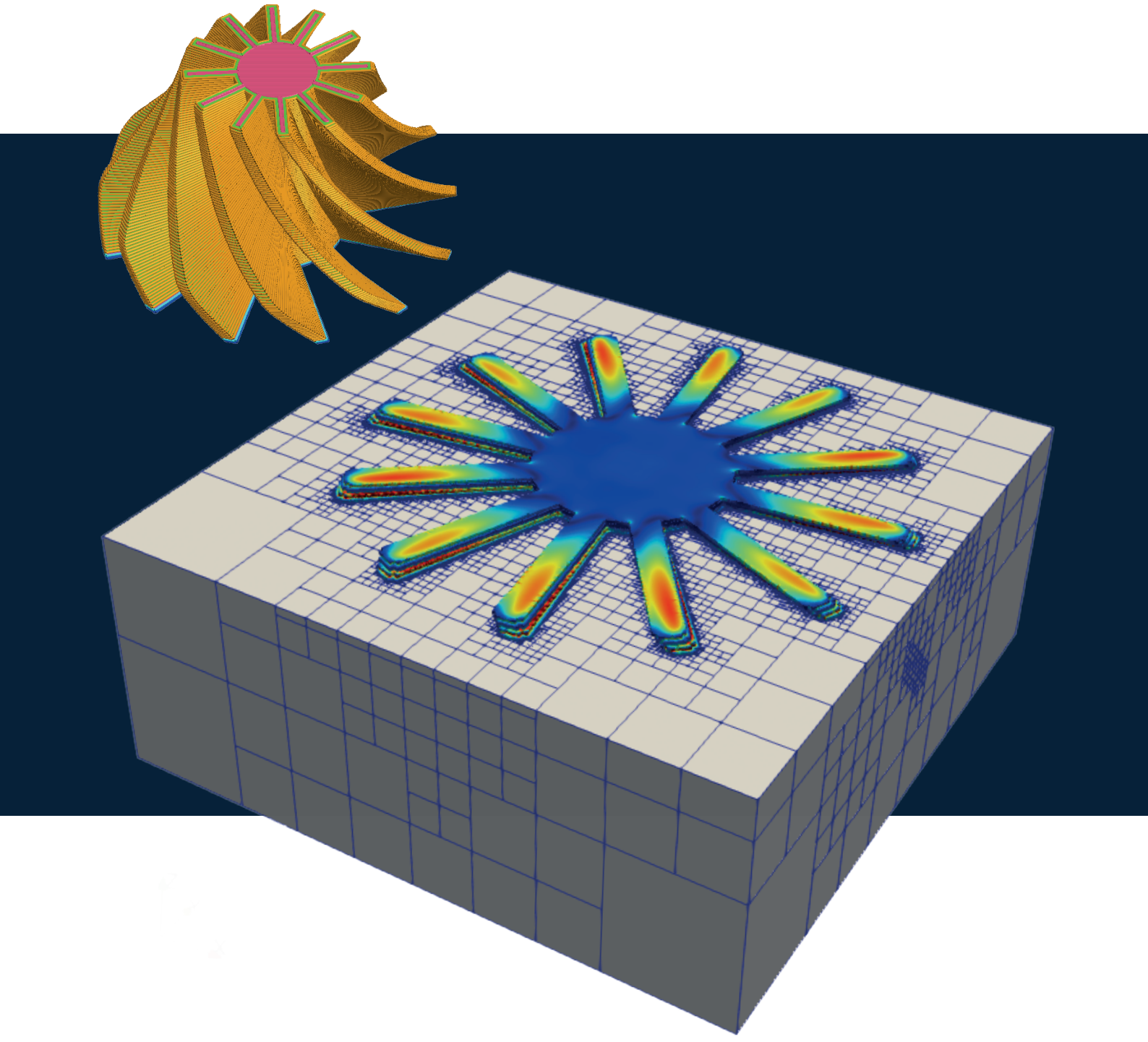

PhD. thesis by **Carlos Augusto Moreira Filho**

Supervisors Prof. Miguel Cervera
Prof. Michele Chiumenti

FINITE ELEMENT SIMULATION OF ADDITIVE MANUFACTURING WITH ENHANCED ACCURACY

Carlos Augusto Moreira Filho

Doctoral Degree in Civil Engineering

Thesis submitted as a compendium of publications

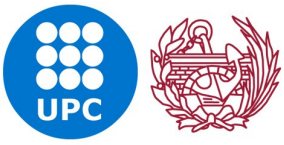

Technical University of Catalonia

Department of Civil and Environmental Engineering

Supervisors:

Prof. Miguel Cervera
Prof. Michele Chiumenti

Barcelona, July 2022

Carlos Augusto Moreira Filho: *Finite element simulation of additive manufacturing with enhanced accuracy*,
A Thesis submited in partial fulfillment of the requirements for the degree of Doctor of Philosophy. ©
July 2022

ACTA DE CALIFICACIÓN DE LA TESIS DOCTORAL

Reunido el tribunal integrado por los abajo firmantes para juzgar la tesis doctoral:

Título de la tesis: *Finite element simulation of additive manufacturing with enhanced accuracy*
Autor de la tesis: *Carlos Augusto Moreira Filho*

Acuerda otorgar la calificación de:

☐ No apto
☐ Aprobado
☐ Notable
☐ Sobresaliente
☐ Excelente
☐ Excelente Cum Laude

Barcelona, ... de ..... de .....

El Presidente

.....
(nombre y apellidos)

El Secretario

.....
(nombre y apellidos)

El vocal

.....
(nombre y apellidos)

ACKNOWLEDGMENTS

I was very lucky to find people willing to offer their help and support in many different ways during this period.

I am deeply grateful to my supervisors, Prof. Miguel Cervera and Prof. Michele Chiumenti for their trust in me and for their kind welcome when I got to Barcelona. Aside from the personal aspect, they are the ones who helped me with their brilliant scientific advices, assistance and guidance to overcome the complexity of the work. Their experience is a very valuable and intangible asset that I was able to count on.

I am also truly indebted and thankful to Prof. Joan Baiges for his guidance and support.

I am extremely thankful for the friendship of Gabriel and Kim, from the COMET group, and Prof. Manuel, Henning, Ino, Samuel and Laura, from the FEMUSS group. They were a source of inspiration and mutual understanding of what each other was going through.

I would like to thank all my officemates who provided me a friendly work ambient.

I would like to thank Prof. José Elias Laier, Prof. Rodrigo Ribeiro Paccola and Prof. Edson Denner Leonel, from the University of São Paulo, for their encouragement and assistance in pursuing a doctoral degree.

Here I thank my parents, Ana and Carlos, for giving me everything that I needed and that was necessary to pursue this path so far away from home, I cannot put into words the gratitude that their support means to me. Mané, my brother, I am also extremely grateful to you for throwing an unexpected visit in the middle of the pandemic, it is always good to have a piece of home brought here.

Thank to my family, especially in the memory of my beloved grand-parents, Lula, Manoel and Flora, whom their presence was felt closely travelling this path along-side me. To my grand-mother, Lucinha, for the warm support from Brazil.

I would have never completed this work without the support of my dear wife, Natália, who was always there at the most difficult and, also, at the most joyful times. She is the source of inspiration and motivation that I need.

Finally, I would like to express my appreciation to all those who provided me the possibility to complete this thesis.

ABSTRACT

This thesis develops numerical methods to improve the accuracy and computational efficiency of the part-scale simulation of Additive Manufacturing (AM) (or 3D printing) metal processes. AM is characterized by multiple scales in space and time, as well as multiple complex physics that occur in three-dimensional growing-in-time geometries, making its simulation a remarkable computational challenge.

To this end, the computational framework is built by addressing four key topics: (1) a Finite Element technology with enhanced stress/strain accuracy including the incompressible limit; (2) an Adaptive Mesh Refinement (AMR) strategy accounting for geometric and solution accuracies; (3) a coarsening correction strategy to avoid loss of information in the coarsening AMR procedure, and (4) a GCode-based simulation tool that uses the exact geometric and process parameters data provided to the actual AM machinery.

In this context, the mixed displacement/deviatoric-strain/pressure $\boldsymbol{u}/\boldsymbol{e}/p$ FE formulation in (1) is adopted to solve incompressible problems resulting from the isochoric plastic flow in the Von Mises criterion typical of metals. The enhanced stress/strain accuracy of the $\boldsymbol{u}/\boldsymbol{e}/p$ over the standard and $\boldsymbol{u}/p$ FE formulations is verified in a set of numerical benchmarks in iso-thermal and non-isothermal conditions. A multi-criteria AMR strategy in (2) is used to improve computational efficiency while keeping the number of FEs controlled and without the strictness of imposing the commonly adopted 2:1 balance scheme. Avoiding this enables to use high jumps on the refinement level between adjacent FEs; this improves the mesh resolution on the region of interest and keeps the mesh coarse elsewhere. Moving the FE solution from a fine mesh to a coarse mesh introduces loss of information. To prevent this, a coarsening correction strategy presented in (3) restores the fine solution in the coarse mesh, providing computational cost reduction and keeping the accuracy of the fine mesh solution accuracy.

Lastly, design flexibility is one of the main advantages of AM over traditional manufacturing processes. This flexibility is observed in the design of complex components and the possibility to change the process parameters, i.e. power input, speed, waiting pauses, among others, throughout the process. In (4) a GCode-based simulation tool that replicates the exact path travelled and process parameters delivered to the AM machiney is developed. Furthermore, the GCode-based tool together with the AMR strategy allows to automatically generate an embedded fitted cartesian FE mesh for the evolving domain and removes the challenging task of mesh manipulation by the end-user.

The FE framework is built on a high-performance computing environment. This framework enables to accelerate the process-to-performance understanding and to minimize the number of trial-and-error experiments, two key aspects to exploit the technology in the industrial environment.

RESUMEN

Esta tesis tiene como objetivo desarrollar métodos numéricos para mejorar la precisión y eficiencia computacionales en simulaciones de piezas fabricadas mediante Manufactura Aditiva (MA), también conocida como Impresión $3D$. La manufactura aditiva es un problema complejo que involucra múltiples fenómenos físicos, que se desarolla en múltiples escalas, y cuya geometría evoluciona en el tiempo.

Para tal fin, se plantean cuatro objetivos: (1) Desarrollo de una tecnología de elementos finitos para capturar con mayor precisión tanto tensiones como deformaciones en casos en el que el material tiene comportamiento isocórico; (2) Una estrategia de adaptividad de malla (AMR), que busca modificar la malla teniendo en cuenta la geometría y los errores en la solución numérica; (3) Una estrategia para minimizar la aproximación numérica durante el engrosamiento (*coarsening*) de la malla, crucial en la reducción de tiempos de cómputo en casos de piezas de grandes dimensiones; y (4) Un marco de simulación basado en la lectura de ficheros GCode, ampliamente usado por maquinaria de impresión en procesos de manufactura aditiva, un formato que no sólo proporciona los datos asociados a la geometría, sino también los parámetros de proceso.

Con respecto a (1), esta tesis propone el uso de una formulación mixta en desplazamientos / deformación-desviadora / presión ($\boldsymbol{u}/\boldsymbol{e}/p$), para simular la deposición de materiales con deformación inelástica isocórica, como ocurre en los metales. En cuanto a la medición de la precisión en el cálculo de las tensiones y las deformaciones, en esta tesis se realiza un amplio número de experimentos tanto en condiciones isotérmicas como no isotérmicas para establecer una comparativa entre las dos formulaciones mixtas, $\boldsymbol{u}/\boldsymbol{e}/p$ y $\boldsymbol{u}/p$. Con respecto a (2), para mejorar la eficiencia computacional manteniendo acotado el número total de elementos finitos, se desarrolla una novedosa estrategia multicriterio de refinamiento adaptativo. Esta estrategia no se restringe a mallas con balance 2:1, permitiendo así tener saltos de nivel mayores entre elementos adyacentes. Por otra parte, para evitar la pérdida de información al proyectar la solución a mallas más gruesas, se plantea una corrección en (3), que tiene como objetivo recuperar la solución de la malla fina, garantizando así que la malla gruesa conserve la precisión obtenida en la malla fina. El proceso de manufactura aditiva se distingue por su gran flexibilidad comparándolo con otros métodos tradicionales de manufactura. Esta flexibilidad se observa en la posibilidad de construir piezas de gran complejidad geométrica, optimizando propiedades mecánicas durante el proceso de deposición. Por ese motivo, (4) se propone la lectura de ficheros en formato GCode que replica la ruta exacta del recorrido del láser que realiza la deposición del material.

Los ingredientes lectura de comandos escritos en lenguaje Gcode, multicriterio de adaptividad de malla y el uso de mallas estructuradas basadas en octrees, permiten capturar con gran precisión el dominio discreto eliminando así la engorrosa tarea de generar un dominio discreto ad-hoc para la pieza a modelar.

Los desarrollos de esta tesis se realizan en un entorno de computación de altas prestaciones (HPC) que permite acelerar el estudio de la ejecución del proceso de impresión y por ende reducir el número de experimentos destructivos, dos aspectos clave que permiten explorar y desarrollar nuevas técnicas en manufactura aditiva de piezas industriales.

CONTENTS

LIST OF FIGURES

ACRONYMS

FE Finite Element
FEM Finite Element Method
HF High Fidelity
ROM Reduced Order Model
AM Additive Manufacturing
SRI Selective Reduced Integration
VMS Variational Multi-Scale
OSS Orthogonal Subgrid Stabilization
GLS Galerkin Least-square method
DOF Degrees of Freedom
AMR Adaptive Mesh Refinement
PDE Partial Differential Equation
SPR Super-convergent Patch Recovery
GPU Graphical Processing Units
HAZ Heat Affected Zone
SLM Selective Laser Melting
SLS Selective Laser Sintering
MLS Metal Laser Sintering
EBM Electron Beam Melting
APDL ANSYS Parametric Design Language
FCM Finite Cell Method
SAT Separating Axis Theorem
IGA IsoGeometric Analysis
TMAZ Thermo-Mechanically Affected Zone
PBF Powder Bed Fusion
DED Direct Energy Deposition
FDM Fused Deposition Modelling
XRD X-Ray Diffraction
EBW Electron Beam Welding
LENS Laser Engineered Net Shaping
WAAM Wire Arc Additive Manufacturing
FSW Friction Stir Welding
ALE Arbitrary Lagrangian-Eulerian
CAD Computer Aided Design
CLI Common Layer Interface
STL STereoLithography
HTC Heat Transfer Coefficient
RP Rapid Prototyping

CWM Computational Welding Mechanics
LPB Laser Powder-Bed Fusion
CSR Compressed Sparse Row
SAT Separating Axis Theorem
LMP Laser Melting Processes
CM Conventional Manufacturing
SM Subtractive Manufacturing

Part I

SUMMARY DOCUMENT

This part is dedicated to present the numerical models developed in this Thesis. The details, proofs and numerical results, are referenced to the corresponding scientific article.

1

INTRODUCTION

1.1 Motivation

Additive Manufacturing (AM), also known as 3D printing, or free-form fabrication, is quickly gaining traction in the industry as a way to increase design flexibility, save energy, and shorten the time-to-market of new components. AM differs from Conventional Manufacturing (CM) or Subtractive Manufacturing (SM) processes, because it is based on the layer-by-layer deposition of new material, resulting in monolithic components, rather than assembling several parts together or removing material from a starting work piece. This innovative process draws attention from industry of many fields, such as the aeronautical industry (jet engine parts, aircraft stiffeners, micro-turbines), medical applications (dental bridges, medical tools, prosthetics), the automotive industry (cooling systems, heat shields), among others.

Traditional manufacturing (CM/SM) processes frequently fail to meet design requirements when complex geometries are generated via shape optimization or when micro-scale design is used to fulfill certain desired functionalities (e.g., weight reduction, thermal conductivity, or noise isolation). As a result, fabricating such geometries using AM processes is preferred.

The flexibility of AM also enables the creation of new tools/components with spatially-varying material distributions, e.g. lattice structures or multi-material; tailor-made solutions, e.g. medical bio-implants, and the use of embedded components, e.g. inter-layer circuit used for digital monitoring.

The advantages of AM over traditional manufacturing are innovation, part consolidation, lower energy consumption, waste reduction, reduced time-to-market, light weighting, agility of manufacturing operations (U. S. Department of Energy, 2012). Innovation is brought up in a way that difficult/novel geometries are only feasible with AM processes. Part consolidation relates to the creation of components with fewer and more complex parts, resulting in more optimized products built with more flexible manufacturability requirements. Lower energy consumption through the AM ability to eliminate production steps, use less material and producing lighter products. The layer-by-layer production can reduce materials and costs, generating less waste production. The required time for a component to reach the market is also reduced, due to the elimination of the part tooling and prototype fabrication from the production chain. The use of topological optimized shapes reduces the weight and keeps the functionality specifications of the product. Last, the manufacturing operations gain agility with the AM capability of rapidly responding to market changes.

On the one hand, AM is a novel technology that requires more research to properly comprehend its usefulness, constraints, and limits. Experimental analysis is being vastly used to better understand the structural behavior of AM components. These experiments are expensive, time-consuming, based on trial-and-error and demand the fabrication of several demonstrators before its actual manufacturing.

On the other hand, accurate computer-aided simulations are extremely useful in resolving these bottlenecks. Numerical simulations have the ability to accelerate the understanding of the process-structure-property-performance relationship, allowing AM applications to reach their full potential. Furthermore, numerical simulations may enable a change to a digital design and certification paradigm, allowing for engineers to certify designs before they are built, resulting in faster and less expensive AM product design.

In this regard, numerical methods for assessing AM simulations with enhanced accuracy and computational efficiency are a valuable tool for the adoption of the AM as industrial-scale manufacturing process.

1.2 Objectives

The main objective of the present doctoral thesis is to develop, validate and apply an accurate and computationally efficient Finite Element (FE) framework for the simulation of AM processes.

To achieve this primary objective, the following major objectives are addressed, organized in the following topics:

- **State-of-the-art review**. To perform an exhaustive investigation of the existing publications on the challenges and numerical solutions adopted to address the simulation of AM processes focusing on the part-scale analysis of metallic components.
- **FE technology**. To address the isochoric constraint of plastic deformations using a novel FE technology with enhanced stress/strain suitable for strain-driven constitutive laws.
- **Numerical accuracy**. To improve the numerical solution accuracy of the thermo-mechanical problem providing new numerical strategies in the field of the FE technology and Adaptive Mesh Refinement (AMR) strategies.
- **Computational efficiency**. To reduce the computational cost of the AM simulation using AMR strategies and parallelization.
- **Complex geometries**. To reduce the modelling difficulties that arise when complex geometries are generated for the AM, and at the same time the input data complexity is minimized.
- **Validation**. To validate the numerical strategies comparing the results with numerical benchmarks, experimental tests, analytical solutions, well-known formulations/strategies and fine meshes as reference.

1.3 Thesis outline

This thesis addresses numerical methods to improve the accuracy and computational efficiency of the part-scale simulation of AM metal processes. For that purpose, the thesis covers the topics of FE technology, AMR strategies and AM machinery.

The thesis outline is as follows: Chapter 2 provides a comprehensive overview of the current state-of-the-art in the numerical simulation of the part-scale AM components. Chapter 3 presents the FE technologies suitable to tackle the isochoric behavior found in metals. Chapter 4 introduces the thermo-mechanical modelling, including the heat source model, time-integration considerations and the thermo-visco-plastic/visco-elastic constitutive model used for the solid/liquid phases, respectively. Chapter 5 describes the multi-criteria strategy and the coarsening correction procedure. Chapter 6 introduces some additional remarks required for the automatic mesh generation when introducing the coarsening/refinement geometric criterion described in Chapter 5. Chapter 7 presents the conclusions and lines of future research. Finally, the articles included in this doctoral thesis by a compendium of publications are provided in the Appendix.

1.4 Research dissemination

1.4.1 *Publications in peer-reviewed international journals*

The doctoral Thesis is presented as a compendium of the following publications:

- J. Baiges, M. Chiumenti, C. A. Moreira, M. Cervera and R. Codina **An Adaptive Finite Element strategy for the numerical simulation of Additive Manufacturing processes**, Additive Manufacturing, 37 (2021) 101650. https://doi.org/10.1016/j.addma.2020.101650

  Impact Factor: 10.998 (Q1)

- M. Chiumenti, M. Cervera, C. A. Moreira and G. B. Barbat **Stress, Strain and dissipation accurate 3-field formulation for non-linear isochoric deformation**, Finite Elements in Analysis and Design, 192 (2021) 103534. https://doi.org/10.1016/j.finel.2021.103534

  Impact Factor: 2.972 (Q1)

- C. A. Moreira, G. B. Barbat, M. Cervera, and M. Chiumenti **Accurate thermal-induced structural failure analysis under incompressible conditions**, Engineering Structures (2022), 261:114213, ISSN 0141-0296. https://doi.org/10.1016/j.engstruct.2022.114213

  Impact Factor: 4.471 (Q1)

- C. A. Moreira, M. A. Caicedo, M. Cervera, M. Chiumenti and J. Baiges **A Multi-criteria h-Adaptive Finite Element Framework for Industrial Part-Scale Thermal Analysis in Additive Manufacturing Processes**, Engineering with Computers, (2022). https://doi.org/10.1007/s00366-022-01655-0

  Impact Factor: 7.963 (Q1)

1.4.2 *Presentations in international conferences*

During the development of this thesis, the ongoing work and results were presented in the following international conferences:

- G. B. Barbat, C. A. Moreira, M. Cervera and M. Chiumenti **Modelling of incompressible damage with an enhanced-accuracy mixed thermo-mechanical formulation**, VIII International Conference on Coupled Problems in Science and Engineering, Sitges, Spain. June 2019.

- C. A. Moreira, G. B. Barbat, M. Chiumenti and M. Cervera **Mixed FE formulation for modelling incompressible damage with thermo-mechanical coupling**, XV International Conference on Computational Plasticity. Fundamentals and Applications, Barcelona, Spain. September 2019.

- M. Chiumenti, M. Cervera, C. A. Moreira and G. B. Barbat **On the mixed three-field formulation for strain localization problems encompassing the incompressible limit**, International Conference on Plasticity, Damage and Fracture 2020 (ICPDF 20), Rivera Maya, Mexico. January 2020.

- M. Chiumenti, J. Baiges, M. Cervera, R. Codina, M. A. Caicedo, C. A. Moreira and J. M. Martinez **HPC framework for the thermo-mechanical simulation of DED Additive Manufacturing processes**, Simulation for Additive Manufacturing (SimAM-2021), Glasgow, United Kingdom. September 2021.

- C. A. Moreira, J. Baiges, M. Cervera, M. A. Caicedo and M. Chiumenti **An automatic octree mesh generation based on laser activation path for the metal deposition process in Additive Manufacturing**, XVI International Conference on Computational Plasticity. Fundamentals and Applications, Barcelona, Spain. September 2021.

- J. Baiges, M. Chiumenti, C. A. Moreira, M. Cervera and R. Codina **An adaptive finite element strategy for numerical simulation of Additive Manufacturing processes**, XVI International Conference on Computational Plasticity. Fundamentals and Applications, Barcelona, Spain. September 2021.

2

STATE OF THE ART

This chapter addresses the recent developments and challenges encountered in the simulation of Additive Manufacturing (AM) of metal processes. The difficulties that arise from the AM simulation of metals with enhanced accuracy are: 1) the material incompressibility; 2) the appropriate choice on the thermo-mechanical modelling to achieve accurate solutions; 3) the high computational cost demanded by such processes involving growing domains and 4) the handling of the data associated to AM processes.

In this context, this chapter is outlined as follows: Section 2.1 discusses the use of several FE technologies developed to tackle the isochoric plastic flow behavior of the metals. Section 2.2 summarizes the simplified and more refined constitutive models adopted for the simulation of manufacturing processes, as well as the advantages and disadvantges of each one of them. Section 2.3 presents the main ingredients of the Adaptive Mesh Refinement (AMR) techniques to reduce computational cost. Finally, Section 2.4 deals with the data acquisition from an input file in addition to the activation strategies commonly used in the FE simulation of growing domains.

2.1 Finite element technology

The Finite Element Method (FEM) has been developed to approximate the behavior of a continous domain by its discritized approximation to solve complex mathematical models (Hrennikoff, 1941; Courant, 1943). In practice, the continuous domain is divided into small finite portions, namely the finite elements (FE), and the unknowns are approximated using interpolation functions to solve a weak form of the Partial Differential Equations (PDEs) that describe the phenomenon of interest. This method has been widely applied in the engineering field to solve fluid dynamics, solid mechanics, fluid-structure interaction, heat transfer, among other problems.

The first FEM developed was the displacement-based formulation, also known as the irreducible/standard formulation. The standard/irreducible formulation is vastly employed in commercial software and uses the displacement field at the nodes as primal variable. Nevertheless, it was observed that the standard FEM has some limitations depending on the choice of discretization, geometry and material. In the case of incompressible materials, the displacement-based formulation fails, due to volumetric locking, specially when low-order elements are adopted (Prathap, 1985; Bathe, 1996; Crisfield, 1993; Zienkiewicz, 1965; Belytschko et al., 2000).

2.1.1 *The early attempts to address the incompressibility problem*

Material incompressibility means that the material deforms under stress without volumetric change, i.e. the volumetric strain, that is, the strain ($\boldsymbol{\varepsilon}$) first invariant is $tr(\boldsymbol{\varepsilon}) = (\varepsilon_x + \varepsilon_y + \varepsilon_z) = 0$. Isotropic elastic materials are incompressible if the Poisson ratio is equal to $\nu = 0.5$. In this case, the bulk-modulus of the material $K \to \infty$. This behavior is typically found in rubber-like materials. In the nonlinear regime, in Von Mises materials such as metals, the plastic flow is isochoric (constant volume), so that when material flows it results in the incompressibility constraint ($tr(\boldsymbol{\varepsilon}) \simeq tr(\boldsymbol{\varepsilon}^p) = 0$).

The earliest attempt to tackle the incompressibility constraint was derived from a reduced form of the Hellinger-Reissner principle (Hellinger, 1907; Reissner, 1950). The strong form from this principle corresponds to the constitutive and kinematic equations, and the solution of the variational form is rewritten in terms of the displacements and the mean-stress (Hermann, 1965; Fraeijs de Veubeke, 1965)

to solve incompressible/near-incompressible elasticity problems. The multi-field approach, where the stresses/strains are taken as additional primal fields, is called assumed stresses/strains or mixed FEs.

The work of Hermann (1965) was extended to orthotropic (Taylor et al., 1968) and anisotropic (Key, 1969) incompressible elasticity problems. Although the use of mixed methods was becoming popular to solve constrained problems, its naive application reproduced results as bad as the standard formulation (Hughes, 1977).

A mathematical theory for mixed formulations was developed by Babuska (1971); Brezzi (1974); Babuska et al. (1975). The reason behind the failure of some mixed formulations is the incompatibility of the interpolations adopted for each field, causing element instabilities. The choice of the interpolation used in each field in the mixed FE method should pass the $inf - sup$ condition, also known as the Babuska-Brezzi (B-B) condition. At that time, the computational cost of mixed methods was a major drawback.

Hence, in the search for solutions to the unstable behavior of the primitive mixed FE formulations, Fried (1974) introduced gradually the incompressibility constraint upon mesh refinement to balance the discretization error and to avoid the ill-conditioning of the system. In this work, the underintegration of the volumetric part of the strain energy is suggested to prevent the volumetric locking.

The works of Naylor (1974); Nagtegaal et al. (1974) corroborated the findings made by Fried (1974) and applied the underintegration to standard elements, resulting in accurate displacements and stresses results. This extended the first use of reduced integration of the 8-node serendipity element with the 2×2 Gauss quadrature proposed by (Zienkiewicz et al., 1971) for plate/shell problems demonstrating improvement over the full 3×3 Gauss quadrature.

Doherty applied the concept of selective integration for the first time in 1968 (Doherty et al., 1969), where the shear contribution was exactly integrated and the volumetric part was underintegrated. The equivalence of the mixed formulations and the reduced/selective integration was explained by Hughes (1977); Malkus and Hughes (1978).

Zienkiewicz et al. (1978) studied two approaches to solve metal forming and extrusion processes. In this work, the mixed $\boldsymbol{u}/p$ with a Lagrangian constraint and the penalty function approach are used to deal with the incompressibility, resulting from the Von Mises flow. Both approaches are very similar and differ in the manner that the constraint is imposed. The element used are a nine and eight node element using reduced 2×2 Gauss integration.

Next, the concept of Selective Reduced Integration (SRI) element was introduced by Hughes to address anisotropic elastic materials (Hughes et al., 1978; Malkus and Hughes, 1978). Thereafter, the authors extended this approach to create the $\bar{\boldsymbol{B}}$-element (Hughes, 1980, 1987). Subsequently, Zienkiewicz and coworkers developed the $\bar{\boldsymbol{B}}$-method for nearly-incompressible solids (Zienkiewicz and Taylor, 2000). The pressure of the SRI is computed at the centroid of the element, while the $\bar{\boldsymbol{B}}$-element computes the constant mean-stress from the averaging of the volumetric strain. The advantage of the $\bar{\boldsymbol{B}}$-element over the SRI is that it is easily extended to large strain kinematics. Simo and coworkers extended the $\bar{\boldsymbol{B}}$-element in large strain elasto-plasticity (Simo et al., 1985).

Sloan and Randolph (1982) investigated the ability of displacement-based FE to predict collapse loads in the fully plastic regime in soil mechanics problems, extending the work presented by Nagtegaal et al. (1974).

The Hu-Washizu principle (Hu, 1954; Washizu, 1975) is an extension of the Hellinger-Ressner principle (Stolarski and Belytschko, 1987). The strong form from the Hu-Washizu principle corresponds to the constitutive equation, strain-displacement equation and kinematic equations (conservation of momentum, Neumann boundary conditions and interior continuity conditions) (Belytschko et al., 2000). Simo and Hughes (1986) showed that the assumed strain method falls into the class of variational methods based on the Hu-Washizu principle and that the appropriate stress recovery needs be compatible with this principle.

Following the ideas of Simo and Hughes (1986) and Stolarski and Belytschko (1987) that the assumed strain methods derive from the Hu-Washizu principle, Simo and Riffai (1990); Simo and Armero (1992) proposed an enhanced strain method of incompatible modes for nonlinear analysis. The basis of the method of incompatible modes lies in the enrichment of the standard FE subspace of displacement fields with a discontinuous interelement basis functions. The works of Simo and Riffai (1990); Simo and Armero (1992) also gave a set of instructions on how to choose the assumed strain interpolation properly, otherwise difficulties to achieve stability and convergence may arise.

Simo et al. (1993) made improvements to the elements presented in Simo and Riffai (1990); Simo and Armero (1992) to address the volumetric locking and the spurious hourglass modes. Nevertheless, in their work instabilities were observed in the deformed meshes. This observation gave rise to the question on how to design stable FEs.

To properly design a stable FE that satisfies the strictness of the B-B conditions (Brezzi and Fortin, 1991; Brezzi et al., 1993) is not easy. The stability of the FEs can be tested using the methodology presented by Fortin (1977). This allowed to find several stable *displacement − pressure* ($\boldsymbol{u}/p$) FE formulations using discontinuous (Crouzeix and Raviart, 1973; Fortin, 1977, 1981; Oden and Jacquotte, 1984) and continuous (Taylor and Hood, 1973; Bercovier and Pironneau, 1979) pressure approximations.

However, achieving stability may require the adoption of unusual interpolations. Fig. 1 shows some unusual combinition of interpolations of stable FEs. Fig. 1(a)-(b) are used for elasticity problems, where the arrows represent the tractions and the inner triangle is the stress tensor (Johnson and Mercier, 1978; Arnold et al., 1984b); Fig. 1(c)-(d) are used for second order elliptic problems, where the arrows correspond to the normal component of the flux (Raviart and Thomas, 1975; Brezzi et al., 1984); and Fig. 1(e) is used to plate bending problems, where the arrows are the moment tensor (Arnold, 1990). Arnold (1990) states that stable low order FEs are less usual than achieving stability with high order elements, thus unconditionally stable elements may introduce additional computational cost.

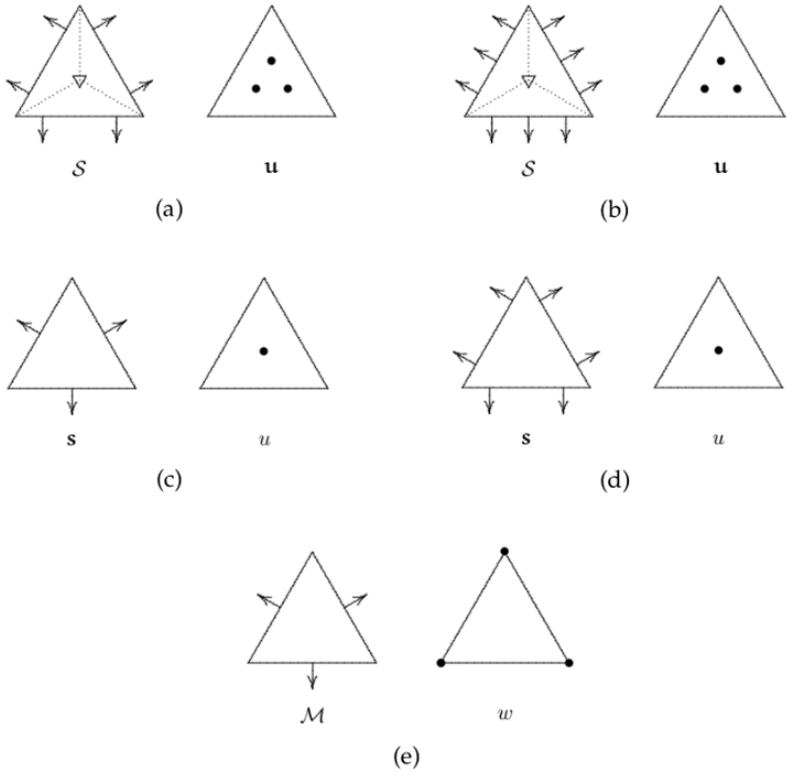

Figure 1: Unusual stable mixed FEs. (a)-(b) Elasticity elements from Johnson-Mercier (a); and Arnold-Douglas-Gupta (b). (c)-(d) Elements for scalar second order elliptic problems from Raviart-Thomas (c); and Brezzi-Douglas-Marini (d). (e) The plate bending element from Hellan-Herman-Johnson. (Arnold, 1990).

2.1.2 *The use of stabilized FEs to address the incompressibility problem with enhanced accuracy*

Instead of pursuing the difficult task of creating stable FEs it was found that adding appropriate extra terms to the Galerkin approximation may result in circumventing the strictness of the B-B conditions. The introduction of such terms opens the field of stabilization methods.

In this sense, a new class of stable FE was developed using the Petrov-Galerkin method, where the solution and the test function FE spaces are different. In this methodology, arbitrary combinations of continuous displacement and pressure interpolations may be adopted (Hughes et al., 1985). This

approach was applied to solve nearly incompressible elasticity (Hughes and Franca, 1987; Franca et al., 1988) and visco-plastic flows (Maniatty et al., 2001; Maniatty and Liu, 2003).

Hughes et al. (1989) developed another stabilization technique named Galerkin Least-square method (GLS) were the least-square form of the residuals are added to the Galerkin method. As a breakthrough, this approach allows for the use of the Galerkin method with equal order interpolations for the unknown fields. The use of stabilization techniques to circumvent the B-B conditions had imediate impact to help popularize the use of mixed methods with equal order interpolation.

Later, Hughes and coworkers proposed a Variational Multi-Scale (VMS) approach based on a coarser scale, solved by the FEs, and a finer scale that helps to stabilize the solution (Hughes, 1995; Hughes et al., 1998). The ideas behind the VMS were present in the previous attempts, which consisted in enriching the FE solution, but this time in a finer scale called sub-grid.

The VMS method was adopted in computational incompressible fluid dynamics and produced an enhanced stabilization procedure, namely the Orthogonal Subgrid Stabilization (OSS) (Codina, 2000; Codina and Blasco, 2000). The analysis of this stabilization technique has been made for the linearized incompressible Navier-Stokes problem (Codina, 2008a), the linear elastic incompressible problem using the three-field (displacements/stresses/pressure) formulation (Codina, 2008b) and for Darcy's equations (Badia and Codina, 2009).

The GLS, VMS and OSS stabilization methods have been sucessfully applied to a large variety of problems, such as incompressible elasticity (Franca et al., 1988; Hughes and Franca, 1987; Chiumenti et al., 2002), elasto-dynamics (Scovazzi et al., 2015; Rossi et al., 2016; Scovazzi et al., 2017; Zeng et al., 2017; Liu and Marsden, 2018), hyper-elasticity (Maniatty et al., 2002; Masud and Truster, 2013; Bonet et al., 2015; Schröder et al., 2011) and elasto-plasticity and damage, (Maniatty et al., 2001; Maniatty and Liu, 2003; Cervera et al., 2003, 2004a,b; Chiumenti et al., 2004; Agelet de Saracibar et al., 2006; Cervera and Chiumenti, 2009; Cervera et al., 2010b).

The stabilization techniques helped spreading the use of the mixed FE formulations, which usually adopt stresses/strains as additional fields. The use of such mixed FEs shows improvements in the convergence rate of the stress/strain fields compared to the standard FE formulation (Badia and Codina, 2009; Cervera et al., 2010a). The global and local stress/strain convergence rate for the standard formulation are h_e^k and h_e^{k-1}, respectively, where h_e is the FE size and k is the degree of the interpolation adopted. For standard elements with linear interpolation the local convergence of the stresses is not guaranteed (h_e^0).

The use of stress/strains as additional nodal variables enhances the stress/strain results, and this has been demonstrated in problems of crack propagation in $2D$ and $3D$ (Benedetti et al., 2016, 2017; Cervera et al., 2017; Barbat et al., 2018; Vlachakis et al., 2019; Cervera et al., 2020), structural size-effect (Barbat et al., 2020), compressible and incompressible plasticity (Puso and Solberg, 2006; Cervera et al., 2010a; Benedetti et al., 2015; Cervera et al., 2015), nearly incompressibility in finite strains (Puso and Solberg, 2006; Gee et al., 2009).

Badia and Baiges (2013) developed a stabilized hybrid continuous-discontinuous Galerkin method to solve incompressible flow problems. The authors state that the equal order interpolation is the optimal choice in the trade-off between accuracy and efficiency.

Recently, a new mixed strain/displacement FE including the $\bar{\boldsymbol{B}}$ approximation has been presented as the $\boldsymbol{\varepsilon}/\bar{\boldsymbol{B}}$ element to tackle nearly incompressible conditions with enhanced stress/strain accuracy (Saloustros et al., 2021) for beams, plates and shells problems.

In the context of incompressible problems, to achieve stress/strain accuracy, the stress tensor is split into the deviatoric stress ($\boldsymbol{s}$) and pressure (p), giving rise to the 3-field displacement/deviatoric stress/pressure formulation ($\boldsymbol{u}/\boldsymbol{s}/p$) (Codina, 2008b; Chiumenti et al., 2015). As most of the nonlinear constitutive models are defined in a strain-driven format, a natural choice is to split the $\boldsymbol{\varepsilon}/\boldsymbol{u}$ formulation into the deviatoric strain and pressure ($\boldsymbol{u}/\boldsymbol{e}/p$) (Chiumenti et al., 2021).

The 3-field formulation has proven to be accurate in terms of stress/strain and dissipation, although the number of Degrees of Freedom (DOF) per node increases substantially. However, Chiumenti et al. (2021) show that the $\boldsymbol{u}/\boldsymbol{e}/p$ requires a much lower number of DOF and elements to achieve the same level of accuracy than the standard and ($\boldsymbol{u}/p$) formulations, reflecting in less computational time.

Fig. 2-(a) compares the local stress error for the standard, $\boldsymbol{u}/p$ and $\boldsymbol{u}/\boldsymbol{e}/p$ formulations using the same mesh, while Fig. 2-(b) presents the results for similar number of DOF among the FE formulations. Lastly, Fig. 2-(c) presents the rate of convergence of the stress field upon mesh refinement; the $\boldsymbol{u}/\boldsymbol{e}/p$

formulation achieves a global error of 1% employing a much coarser mesh than the standard and the mixed $\boldsymbol{u}/\boldsymbol{e}/p$ formulations.

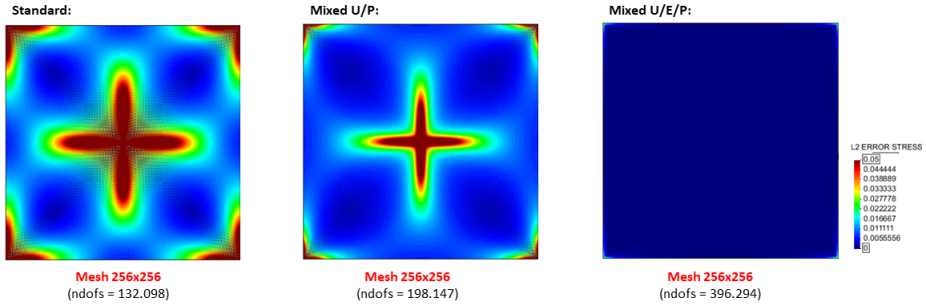

(a)

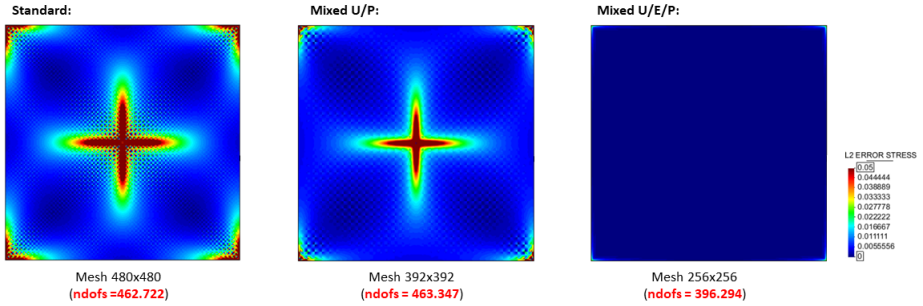

(b)

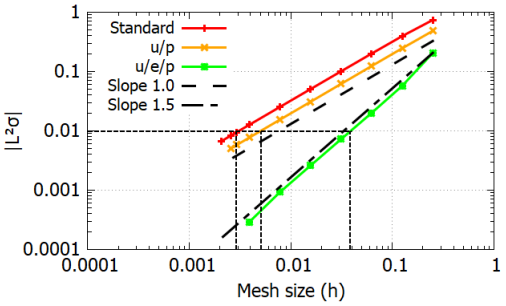

(c)

Figure 2: Comparison between the standard FE formulation and the mixed $\boldsymbol{u}/p$ and $\boldsymbol{u}/\boldsymbol{e}/p$ formulations. (a) L_2-norm of the local stress error using the same mesh. (b) L_2-norm of the local stress error for similar number of DOF. (c) Convergence rate for the stress field for all the three formulations upon mesh refinement.

Moreira et al. (2022a) extended the work of Chiumenti et al. (2021) to coupled thermo-mechanical applications. The improvement in the strain field and the computed dissipation of the the mixed 3-field formulation over the $\boldsymbol{u}/p$ was demonstrated in several incompressible problems of thermal-induced failure.

This motivated a comparison between the $\boldsymbol{u}/p$ and $\boldsymbol{u}/\boldsymbol{e}/p$ formulations in a topology optimization setting of linear elasticity for incompressible materials (Castañar et al., 2022). The topological derivatives inherit the benefits of the higher accuracy of the $\boldsymbol{u}/\boldsymbol{e}/p$ because its computation depends directly on the strains and stresses.

Stabilized mixed formulations provide enhanced accuracy in the additional fields compared to the standard FE formulation. Nevertheless, the FE technology adopted depends on which type of analysis is required by the AM simulation, i.e., simplified strategies using the inherent strains method do not require the FE technology to solve for incompressible conditions; contrarily, high-fidelity thermo-

mechanical analysis needs to address the isochoric flow. The proper choice of the FE technology is key towards the development of reliable and cost-efficient AM simulation frameworks.

2.2 Thermo-mechanical modelling

The choice of the proper thermo-mechanical modelling is deeply connected to the AM process to be simulated. For AM processes where very fast cooling rates are observed, i.e. the deposition of thin-layers that reaches room temperature rapidly, as in Powder Bed Fusion (PBF) processes, the use of simplified elastic models is possible without comprising the accuracy of the predicted results. For low temperature gradients, an elasto-plastic constitutive law with temperature-dependent properties is preferred as the yield stress may be considered temperature-independent. Finally, for high temperature gradients induced by the AM process, the more adequate constitutive model is the thermo-elasto-plastic or thermo-elasto-visco-plastic.

Next, the common strategies used in the AM simulation for structural assessment are divided in two categories: 1) The simplified uncoupled approach; 2) Thermo-mechanical coupled modelling.

2.2.1 *Simplified Elastic approach for AM processes*

Linear elasticity is the most simple constitutive model used in the uncoupled simplified models for AM processes. A common technique that makes use of the linear elastic law is the *inherent strains* approach; it assumes that the Thermo-Mechanically Affected Zone (TMAZ) is very thin and the heat dissipates rapidly.

This assumption is especially used in AM processes with very thin layers, i.e. powder-bed processes. The TMAZ varies from 100-150 μm and the heat affects only a few layers. In this case, powder-bed processes generally assume that the evolution of plastic strains and temperature gradients only occurs in those few layers. Thus, a purely elastic stress analysis can be adopted with a suitable *inherent strains* tensor that represents the combined contributions of the plastic and thermal strains in the AM process. This way, the elastic strains $\boldsymbol{\varepsilon}^e$ are simply computed as $\boldsymbol{\varepsilon}^e = \boldsymbol{\varepsilon} - \boldsymbol{\varepsilon}_{inh}$, where $\boldsymbol{\varepsilon}$ are the total strains and $\boldsymbol{\varepsilon}_{inh}$ is the *inherent strains* tensor.

The *inherent strains* tensor can be obtained from experimental data or from small-scale, nonlinear, numerical simulations (Bugatti and Semeraro, 2018). The method was proposed by Ueda et al. (1975) and was first applied to large structures in the context of welding simulation by Deng et al. (2007).

Keller and Ploshikhin (2014) propose a thermo-mechanical model to simulate the scanning of a hatching-scale region and define the *inherent strains* tensor. Next, the authors apply the computed *inherent strains* tensor in a purely mechanical analysis to predict the residual distortion of the component, obtaining a very good agreement with experimental results.

Li et al. (2015a) use the *inherent strains* method in four different scanning strategies and validate their numerical results with experimental data. In their work, the thermal and thermo-mechanical models employed to extract the *inherent strains*, have temperature independent properties, which is usually a source of numerical inaccuracy in AM processes.

Alvarez et al. (2016) apply the *inherent strains* method to define the macro-layer (activation of several layers at once) size with best accuracy and computational cost for the Selective Laser Melting (SLM) process. The actual AM printing layer thickness is 30 μm and the macro-layer corresponding to the best accuracy and computational cost is composed of 8 layers (240 μm).

Liang et al. (2018) and Liang et al. (2019) present a modified version of the *inherent strains* method for the Direct Energy Deposition (DED) process. The authors validate the numerical results with distortion measurements of a single wall and a rectangular contour components. Later, Liang et al. (2020) extended the modified *inherent strains* approach to lattice structures.

Fig. 3 shows the computed distoritions of the original and modified methods, compared to the measured values along two sample lines. The computed distortions from the modified *inherent strains* method result in much better values and the maximum distortion is very close to the measured value (Liang et al., 2019).

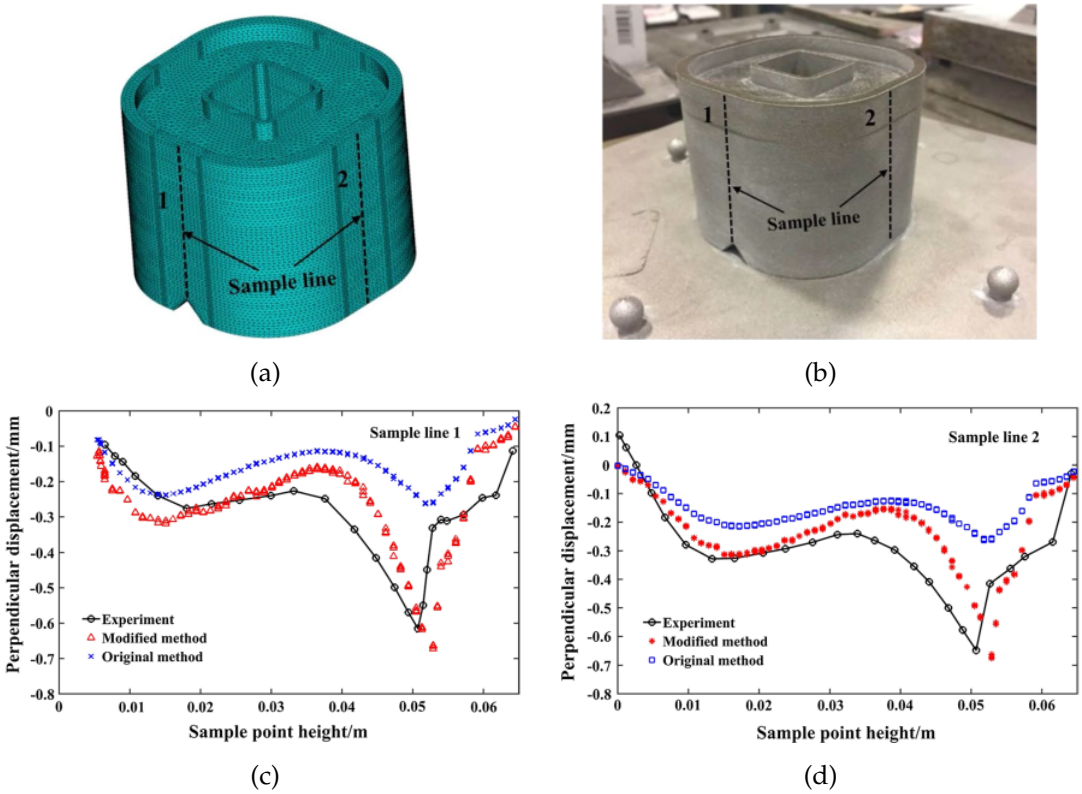

Figure 3: Complex canonical part: (a) The FE mesh and the position of the sample lines. (b) The printed part and the position of the sample lines. (c)-(d) Computed and measured distortions for the sample line 1 and 2, respectively. (Liang et al., 2019).

Setien et al. (2019) define an empirical methodology to determine the *inherent strains* and apply it to a bridge benchmark. In their findings for the periodic scanning strategy, the equivalent *inherent strains* lead to in-plane isotropy. Furthermore, the longitudinal and transversal values of the *inherent strains* tensor can be assumed as orthogonal due to the nature of the hatches of the tested specimen, but this should be checked for more complex geometries.

2.2.2 *Thermo-Mechanical Coupled Modelling*

A more realistic approach to the simulation of AM processes is to consider the temperature-dependency of the mechanical properties. In several manufacturing processes the high temperatures change dramatically the mechanical properties, which affect the mechanical response. In this sense, the constitutive laws are also affected by the thermal field, resulting in a coupling between the thermal and mechanical analyses.

The thermo-mechanical behavior of AM processes can be considered as weakly or strongly coupled. The weak coupling enables a *staggered* scheme, which is the most adopted solution (Cheng et al., 2016; ul Abdein et al., 2009; Kong and Kovacevic, 2010), but monolithic and adiabatic schemes are also found in literature (Armero and Simo, 1992; Riedlbauer et al., 2014; Schoinochoritis et al., 2017). The staggered scheme decouples the temperature and mechanical problems, thus solving for the temperature field, the corresponding mechanical temperature-dependent properties can be adopted.

Regarding the thermo-mechanical constitutive modelling, the AM technology is relatively recent and the constitutive models used are similar to the ones adopted in previous manufacturing processes, such as: 1) Welding; 2) Casting; 3) Friction Stir Welding; 4) Forming; 5) Moulding; 6) Machining.

Agelet de Saracibar et al. (1999) employ the isentropic split (Armero and Simo, 1992) to solve the coupled thermo-mechanical solidification problem using a thermo-elasto-plastic constitutive model accounting for the multi-phase change contribuition.

Cervera et al. (1999) extend the constitutive law presented in Agelet de Saracibar et al. (1999) considering the continuous transition between liquid-solid phases by assuming that both phases work in a series arrangement as a visco-elastic-visco-plastic Maxwell element.

Bellet et al. (2003) propose a visco-elasto-plastic model for the thermo-mechanical analyses of casting processes to predict the macroshrinkage phenomenon. The idea is to avoid a unique elasto-visco-plastic constitutive law from liquid-phase to room temperature. In this way, the authors separate the behavior of the liquid and solid phases. The temperature that switches the liquid-to-solid model is called the transition temperature. For the liquid-phase, a thermo-viscoplastic model is used and for the solid-phase a thermo-elasto-viscoplastic model is adopted. Fig. 4-(a) shows the computed pipe shrinkage phenomenon in different times. Fig. 4-(b) presents the computed and measured shapes for the part geometry, resulting from the shrinkage phenomenon in the casting process.

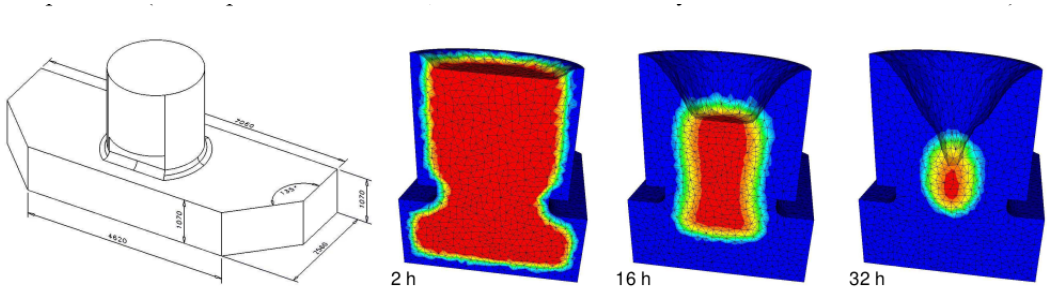

(a)

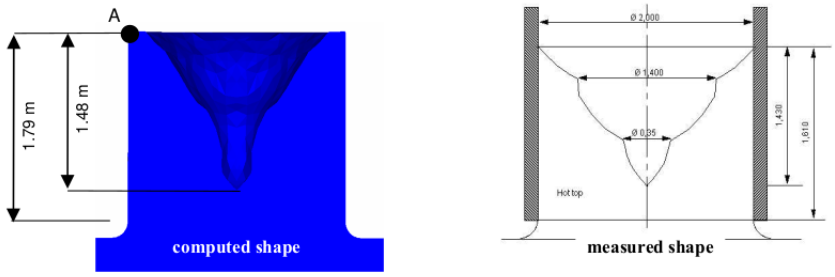

(b)

Figure 4: Casting process: (a) Evolution of the pipe shrinkage in different times. (b)Final computed shape (*left*) and the measured shape (*right*). (Bellet et al., 2003).

Zhu and Chao (2004) use a thermo-elasto-plastic model assuming the von Mises yield criterion and the associated flow rule to study the variation of transient temperature and residual stresses in friction stir welded plates made of 304L stainless steel.

Chiumenti et al. (2010) adopt the J_2-thermo-elasto-visco-plastic model including the phase-change presented in Agelet de Saracibar et al. (1999); Cervera et al. (1999) to the simulation of welding processes. The pure-visco model (Norton-Hoff) presents an incompressible characteristic and, therefore, the authors consider the mixed $\boldsymbol{u}/p$ formulation to deal with the isochoric constraint.

Ding et al. (2011) make use of a thermo-elastic-plastic model and a model based on an advanced steady-state thermal analysis to assess the thermo-mechanical analysis of the Wire Arc Additive Manufacturing (WAAM) process. The first model uses a Lagrangian reference frame for the transient analysis and the second uses an Eulerian reference frame for the steady-state analysis. The steady-state approach saved up-to 80% computational time compared to the transient approach, but is restricted to cases where long weld paths and constant welding speed are used.

Fu and Guo (2014) indicate that for simulations composed of heating and cooling cycles, the material temperature-dependent properties must be considered to achieve an accurate prediction of distortions and residual stresses.

Denlinger et al. (2015) perform a validation of the built of a wall structure using the DED process. In the simulation, the thermo-elasto-plastic constitutive model is employed and several relaxation temperatures are tested. When the temperature goes above the relaxation temperature, henceforth named as annealing temperature, the stresses and plastic strains are reset to 0. Making use of the annealing temperature provides very good correlations, conversely, when no annealing temperature is adopted overestimation of up to 500% is observed in the distortions. For the titanium-alloy *Ti-6Al-4V*, the annealing temperature found is 690^0C.

Dialami et al. (2016) adopt an Arbitrary Lagrangian-Eulerian (ALE) approach to simulate the Friction Stir Welding (FSW) process. The authors adopt a double approach for the constitutive model, one for the Global level where a thermo-elasto-visco-plastic model covers the full temperature range, leading to accurate temperature, distortions and residual stresses evolution. Additionally, at the Local level model, thermo-rigid-visco-plastic constitutive models, such as Norton-Hoff, Carreau or Sheppard-Wright may be used (Chiumenti et al., 2013; Dialami et al., 2013; Bussetta et al., 2014). The local model neglects both the elastic and thermal strains and the global-local model approach is intended to solve problems dominated by high strain-rates. In FSW process, high mechanical dissipation takes place as a result of the friction of the tool tip and the welded part, the result is that 90% of the plastic dissipation is converted into heat.

Chiumenti et al. (2016) apply the J_2-thermo-visco-elasto-plastic law with small strains kinematics to the Electron Beam Welding (EBW) process. The material reproduce either an elato-plastic behavior, at room temperature, or a pure-visco behavior, at temperatures above the melting point. In addition, the constitutive law takes into account the phase-change by computing the solid/liquid fraction. The authors use the mixed $\boldsymbol{u}/p$ formulation and the appropriate split in the constitutive model. The thermal-shrinkage is caused by the density variation in the solidification process. The numerical model is calibrated and validated through an experimental campaign with remarkably good results in terms of the measured and predicted temperature and distortions.

Denlinger and Michaleris (2016) compare the predicted distortions with experimental data applying the annealing temperature for the *Ti-6Al-4V* and *Inconel625* materials, using the same constitutive model as in Denlinger et al. (2015). The *Inconel625*, in opposition to the *Ti-6Al-4V*, provide good predictions without the need to consider the annealing temperature.

Chiumenti et al. (2017a) calibrate and validate the Laser Engineered Net Shaping (LENS) process for the thermal analysis considering the phase-change process. The global effect of the latent heat to the liquid-solid phase-change can be neglected saving 60% of the computational time of the simulation.

Denlinger et al. (2017) validate a thermo-mechanical model with *in-situ* experiments of a 91 $[mm^3]$ specimen using an elasto-plastic finite strain constitutive model.

Lu et al. (2018) provide a numerical simulation callibrated with experimental data for the simulation of laser solid forming processes using the Ti-6Al-4V alloy and two scanning patterns (longitudinal and transversal). The thermo-elasto-visco-plastic model includes the thermal shrinkage, visco-plastic behavior, thermal softening, creep behavior and strain-hardning according to the references Chiumenti et al. (2010, 2016). In this work, the analysis of a thin-walled structure showed that the cooling phase was responsible for the development of 70% of the residual stresses and 60% of the total distortions. Fig. 5 presents the residual J_2-stresses of the thin-wall for the two different scanning patterns.

Zhang et al. (2018a) present a framework for the thermo-mechanical simulation of the PBF process to single-track and part-scale analyses. The constitutive model adopted is the thermo-elasto-visco-plastic model. For the part-scale analysis, the interface between the part under construction and powder is considered through a level-set function and the fluid-flow in the fusion zone is ignored, as well as the inertial terms.

Fig. 6 presents the cross-section of a single-track evolution of the melt-pool of two different cases of the Marangoni effect, where $\frac{\partial \gamma}{\partial T}$ is the temperature-dependecy coefficient of the surface tension. The red line represents the melt-pool geometry, the black-line corresponds to the initial position of the powder and the arrows are the velocity field of the liquid (Zhang et al., 2018a).

Cattenone et al. (2018) investigate the influence of 4 constitutive models to predict distortions and residual stresses in the Fused Deposition Modelling (FDM). The constitutive laws have temperature-dependent physical properties (density, heat coefficient, specific heat and thermal expansion coefficient) and vary the mechanical properties (the Young modulus and Yield stress) between temperature-dependent or independent. The models investidated are: 1) Linear Elastic

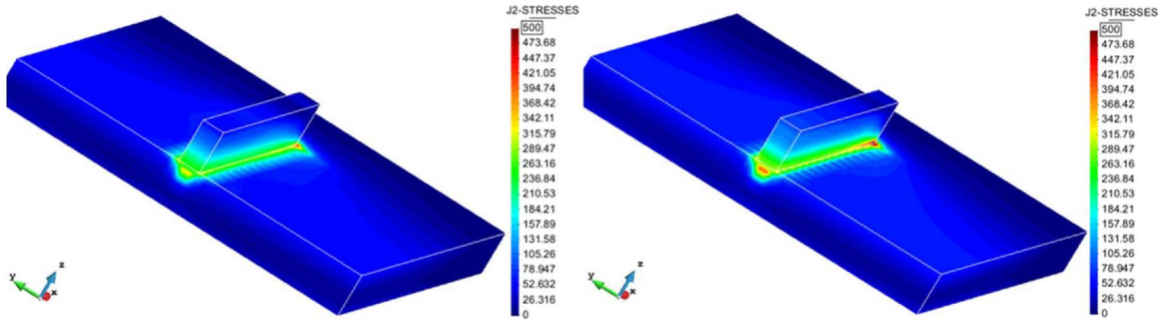

(a) (b)

Figure 5: Thin-wall residual J_2-stresses: (a) Longitudinal scanning pattern. (b) Transversal scanning pattern. (Lu et al., 2018).

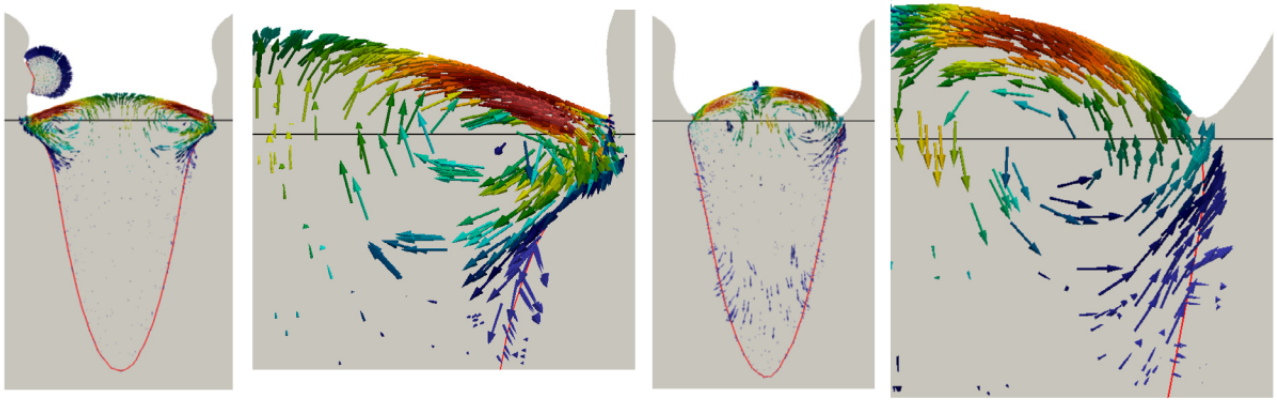

$\frac{\partial \gamma}{\partial T} = -4.8 \times 10^{-4}\ \mathrm{N \cdot m^{-1} \cdot K^{-1}}$ $\frac{\partial \gamma}{\partial T} = +4.8 \times 10^{-4}\ \mathrm{N \cdot m^{-1} \cdot K^{-1}})$

Figure 6: Melt-pool geometry in a cross section of a single-track simulation for the extreme value cases of $\partial \gamma / \partial T$ found on the literature. (Zhang et al., 2018a).

with temperature-independent mechanical properties; 2) Linear Elastic with temperature-dependent Young's modulus; 3) Elasto-plastic with temperature-dependent Young's modulus and temperature-independent yield stress; 4) Elasto-plastic with temperature-dependent mechanical properties. In models $1-3$, no physically acceptable results of the residual stresses are obtained, being the only acceptable constitutive law for FDM the thermo-elasto-plastic (model 4).

Lu et al. (2019) presents a simplified activation procedure to speed-up the thermo-mechanical analysis. In the work, the J_2-thermo-elasto-visco-plastic model to asses the residual stresses and distortions of a box-shaped and a S-shaped components. The speed-up in the activation process is a result of activating 4 layers at each time step. This provides a 77% CPU-time reduction. This strategy compromises the local accuracy, but the average values of the temperature and distortions are preserved.

Yang et al. (2019) undergo a blind challenge for the prediction of residual stresses and distortions, namely AM-Benchmark 2018 - challenge 1, where experimental results are obtained by X-Ray Diffraction (XRD). The authors adopt a thermo-mechanical model with temperature-independent and dependent properties. The temperature-dependent properties being the thermal conductivity, specific heat capacitance, the Young modulus, the Poisson ratio and the thermal expansion coefficient. The authors justify the use of temperature-independent plasticity because the range of temperatures observed induce a small temperature-dependency in the plastic behavior.

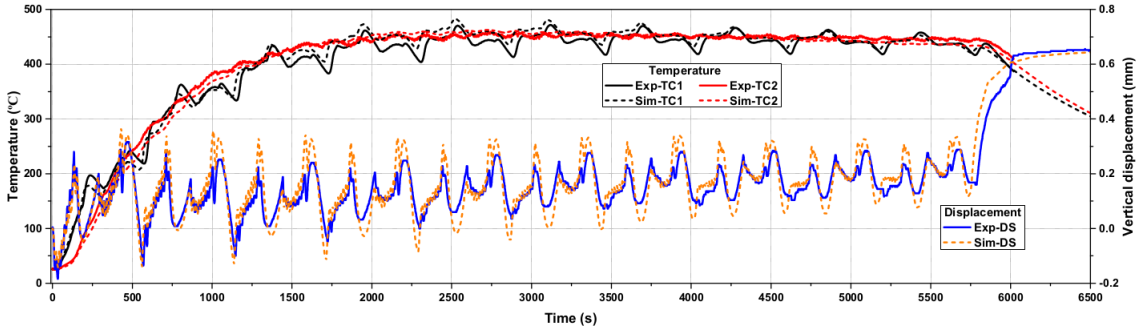

Figure 7: Validation of the thermo-mechanical model for a 40-layer thin-wall. (Lu et al., 2021a).

Carraturo et al. (2020a) use the same temperature-dependent properties as Yang et al. (2019) after the good results obtained using the temperature-independent yield stress model. The authors perform an immersed thermo-mechanical simulation using the elasto-plastic model for infinitesimal strains obtaining very good correlation with experimental results for the deflection measurements (less than 5% error).

Carraturo et al. (2020b) compare different laser scanning strategies to minimize residual stresses. To simulate the influence of the scanning strategies, the authors adopt a elasto-plastic with infinitesimal strains kinematics, where the temperature-dependent properties are the Young modulus, the Poisson ration, the thermal expansion coefficient and the Yield stress. The authors conclude that the best scanning strategy is to keep the power density constant.

Levine et al. (2020) analyze the outcomes and conclusions of the blind submissions of the AM-Benchmark 2018 series, where the experimental results are reported in Phan et al. (2019). Overall, the simulations that included substantial underlying physics produced more accurate results than those that used empirical methods. All the submitted results had substantial deviations with respect to residual elastic strains and distortions. However qualitatively correct results can be matched when the laser path effects are included.

Lu et al. (2021a) callibrate the thermo-mechanical model from the experimental data of a 40 layer block from in-situ measurements to mitigate the residual stress in DED processes. The FE model adopts the mixed $\boldsymbol{u}/p$ formulation and the J_2-thermo-elasto-visco-plastic, where part of the thermal-strain is resulting from a shrinkage coefficient. Prior to conducting the sensitivity study on the parameters that affect the residual stresses, the authors perform a callibration of the thermo-mechanical model with experimental data, providing remarkable agreement, see Fig. 7. Next, the authors create a three-bar AM model to help understand the key factors of the development of residual stresses. This model is used to compute the yielding temperature, described as the temperature that causes the material to yield in the three-bar model. The key causes of the residual stresses are attributed to the maximum gradient temperature and the yield temperature, that causes the mechanical restraint during the thermal deformation.

Lu et al. (2021b) adopt the J_2-thermo-elasto-visco-plastic with a non-Newtonian beahavior of the pure-visco law for the mushy phase (from the annealing temperature to the liquid temperature). The authors evaluate the substrate design that leads to minimal residual stress in the DED process, using a thin-wall as an industrial demonstrator and evaluating several substrate designs. Fig. 8 shows the geometry of the proposed substrates and the mechanical responses for the substrate demonstrators.

Patil et al. (2021) present a benchmark of multi-layer simulations for residual stresses in small AM metal parts. In their work, the finite strain plasticity model is adopted using multi-mechanics iterations, instead of a staggered approach. The thermo-mechanical response was practically insensitive to the number of the multi-mechanics iterations, which shows that the staggered approach is sufficient to deal with the thermo-mechanical coupling.

Lu et al. (2021c) study the warpage of several thin-walled structures produced from the Laser Powder-Bed Fusion (LPB) process. The warpage can significantly reduce by using vertical stiffners; the warpage effect is more prone to occur in open sections, because of their lower stiffness; the wall

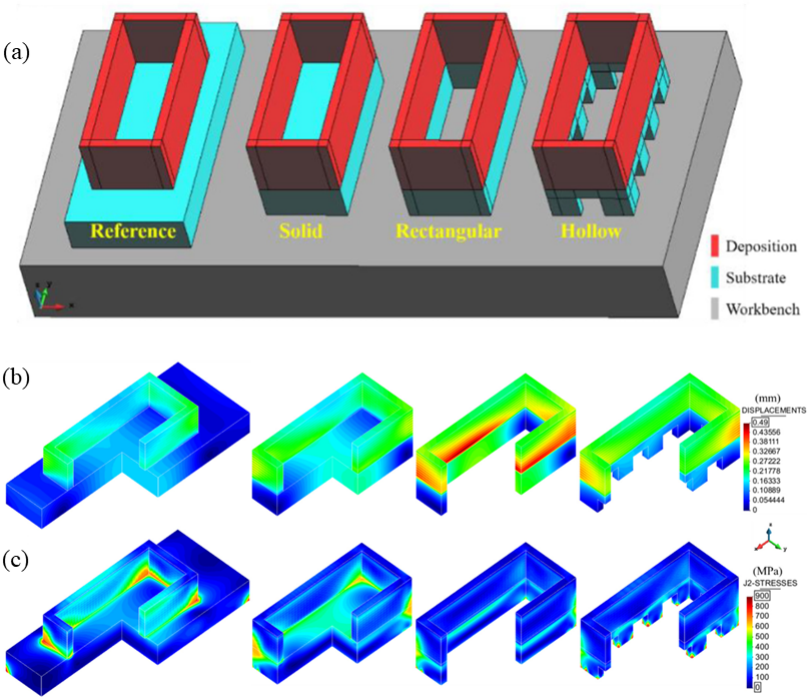

Figure 8: Box-shaped component with thin-walls: (a) Geometries of the different substrates analyzed. (b) Final distortions. (c) Final residual J_2-stresses. (Lu et al., 2021b).

thickness plays an important role on the development of warpage. Fig. 9 shows the warpage on a semi-cylindrical and a L-shaped thin-walled parts with and without the vertical stiffners.

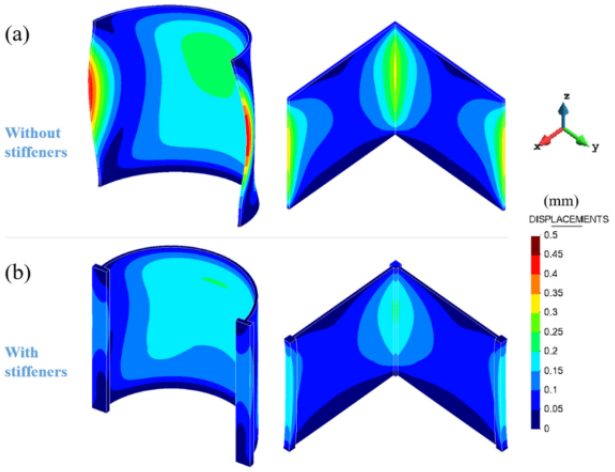

Figure 9: Open thin-walled structures warpage: (a)-(b) without and with vertical stiffners, respectively. (Lu et al., 2021c).

2.3 Adaptive Mesh Refinement

Adaptive Mesh Refinement (AMR) is an important tool when numerically solving problems where the relevant physical phenomena are localized in small portions of the computational domain. This

technique enables to adaptively modify the characteristics of the FE discretization close to the region of interest.

This section discusses the AMR techniques and the common error-estimators used to adpat the FE mesh. In addition, the data-structures used to handle the mesh information are discussed, and the applications of AMR to AM problems are presented.

2.3.1 *Adaptive Mesh Refinement techniques*

The most common refinements techniques are: 1) h-refinement, where the size of the FE in the region of interest is changed; 2) p-refinement, where the interpolation function used in the FE is enriched; 3) r-refinement or *recolocation*, searches for the optimal position of the nodes without changing the total number of DOF and 4) hp-refinement, which combines techniques 1 and 2.

Babuska et al. (1981) compare the rate of convergence in terms of DOF for fix meshes employing p and h-refinement in $1D$ and $2D$ elasticity problems. The p-version results converge twice as fast as the h-version.

One of the earliest use of AMR is the work of Berger and Oliger (1984) where hyperbolic PDE in $1D$ and $2D$ were solved using finite differences for uniform fine and coarse meshes and compared to the AMR results. The algorithm starts with a rectangular coarse grid and, as the solution progresses, points of the mesh with high truncation errors are marked. The marked points are clustered and fine rectangular grids are created in a way that all marked points are interior to the fine grids.

Peraire et al. (1987) adapt triangular meshes of FEs based on the computed solution to determine the optimal nodal values for the mesh parameters (directional spacing, stretching parameter and stretching direction). This is the first attempt of anisotropic AMR. The anisotropy is evaluated using directional error estimates along the principal directions of the Hessian (second derivatives) matrix. Later, this method has been generalized for $3D$ (Peraire et al., 1992).

Demkowicz et al. (1989) offer guidelines for implementing hp-refinement to accomodate the different required data structures (connectivity, shape functions degrees, node locations, element neighbors, etc), choosing local mesh sizes and polynomial degrees of freedom aiming at reducing element-wise errors.

Zienkiewicz et al. (1989) extend the h-refinement procedures to hp-refinement to obtain optimal mesh and accuracy. In the proposed problems, the desired accuracy of 1% is achieved for $p = 4$ requiring less DOF; however, the effective computational cost was not assessed.

Babuska and Suri (1990) note that the higher the FE polynomial order of the p-version, the less sparse is the system of equations. This represents that there is a trade-off between a more costly solution and faster rate of convergence. A detailed analysis is provided in Babuska and Elman (1989); Babsuka and Scapolla (1987). In order to describe complex geometries, the p-version requires curvilinear elements with high distortions. The number of necessary quadrature points depends on the distortions observed in the mesh, which may pose drawbacks in the use of p-refinement to describe complex geometries.

Ortiz and Quigley (1991) develop a r-adaptivity strategy for strain-localization problems in $J2$-plasticity. The approach handles the history variables on the evolving mesh by adopting a consistent mesh transfer operator according to the Hu-Washizu principle. The method is based on the discontinuous distribution of history dependent parameters employing local interpolation functions. The local interpolation functions are chosen in a way that unit values are obtained at the Gauss points.

Pastor et al. (1991) extend the work of Peraire et al. (1987) to soil mechanics using a refinement function based on the bifurcation for non-homogeneous stress fields.

Lee and Bathe (1994) use h-refinement and mixed $\boldsymbol{u}/p$ FE formulations to solve elastic and elasto-plastic problems using all-quadrilateral meshes. The authors create a series of procedures to guarantee stress accuracy including: 1) a pointwise indicator for the stress error; 2) a pointwise indicator of the plastic strain increment error; 3) a quadrilateral element mesh generator to build a new mesh on the deformed configuration and 4) data transfer across models by mapping the state and history-dependent variables. Fig. 10 shows a perforated plate in plane-strain conditions where the localization phenomenon appears in the adaptively refined mesh.

Szabo et al. (1995) and Holzer and Yosibash (1996) sucessfully use p-refinement in elasto-plastic $2D$ problems including cycles of loading and unloading, achieving good results with respect to the h-refined and exact solutions.

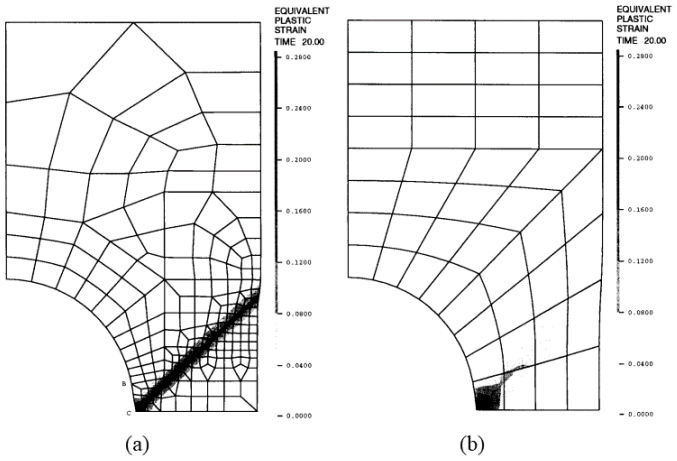

(a) (b)

Figure 10: Shear-band localization in a perforated plate: (a) Adaptive mesh. (b) Coarse mesh. (Lee and Bathe, 1994).

Deb et al. (1996) develop a mesh enrichment to identify shear-bands in strain-localization problems in elasto-visco-plasticity. The mesh adaptivity criterion combines three localization characteristics (velocity variations, equivalent plastic strain and the ratio between the elastic and elasto-plastic tensor) to predict individual element behavior. Furthermore, a modified L_2 projection is proposed to transfer the state variables between two sucessive refined meshes. The approach prevents the diffusion of internal variables of localized elements into non-localized portions of the domain.

Boroomand and Zienkiewicz (1999) introduce a direct Gauss point-to-point transfer operator to solve elasto-plasticity problems. The authors employ appropriate weight functions, based on the least-squares procedure, to pass polynomials over the integration points. The weight functions are defined element-wise according to the weight of the Gauss points in the numerical integration process. This method prevents the spread of the local information over a large area when several adaptive steps are performed.

Perić et al. (1999) adopt a *h*-refinement strategy to solve the elasto-plastic thermo-mechanical coupled problem in finite strains for metal forming, high-speed machining and blanking, and projectile impact modelling.

Duster and Rank (2001) compare the *p*-refinement and *h*-refinement in a elasto-plastic benchmark to assess the accuracy of both methodologies. On the one hand, the authors recommend the *p*-refinement because of its higher accuracy. On the other hand, the *h*-refinement is preferred in cases when complex geometries are involved, because they require finer meshes to discretize the domain. Additionally, the error on the energy norm is proportional to $h^{min(r-1,p)}$ (Zienkiewicz et al., 1989), where r is the regularity of the PDE. Discontinuities in the boundary conditions, loading/source and geometry lead the solution to be non-smooth, thus r may be as low as $3/2$; therefore, refining the polynomial order and refining the mesh will lead to similar errors.

Zhou and Randolph (2007) apply *h*-refinement to simulate cylindrical and spherical penetrometers in strain-softening clay using large-deformation kinematics. In their work, the remeshing and interpolation technique with small strain proposed by Hu and Randolph (1998) is used. This is an ALE technique (Ghosh and Kikuchi, 1991) in which a series of small-strain increments are performed and followed by a remeshing. The stresses and material properties are interpolated between the new Gauss points and the Gauss points from the previous mesh.

Khoei et al. (2007, 2008) provide a *h*-refinement scheme with error-estimator and an efficient data-transfer operator for shear-band development in elasto-plasticity and crack propagation in $2D$ problems. The data-transfer operator computes the nodal value gradients using the Super-convergent Patch Recovery (SPR) (Zienkiewicz and Zhu, 1992a) and then transfers the nodal value gradients to the nodes on the new mesh. The new mesh gradient values at the Gauss points are evaluated using the shape functions of the new mesh and the transferred nodal value of the gradients. Later, Khoei et al. (2013) extended the approach using a modified version of the SPR to simulate the crack growth in $3D$

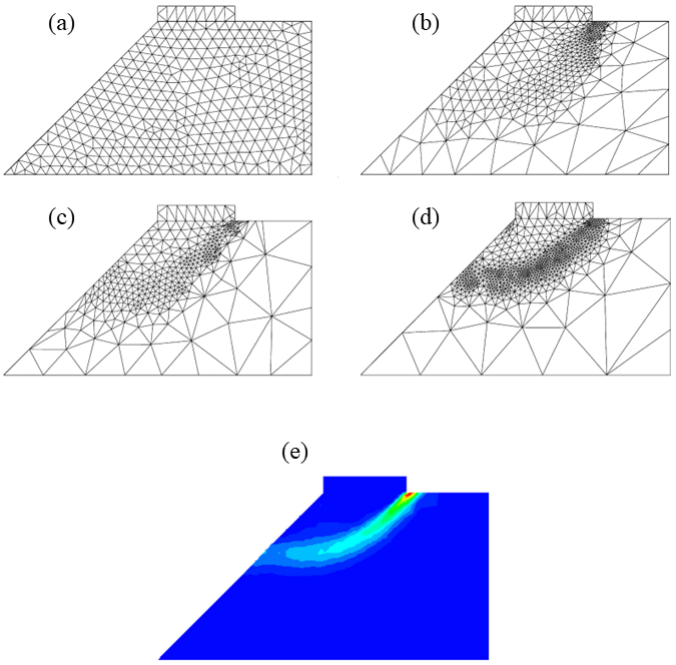

Figure 11: Shear-band localization in a slope: (a) Initial mesh. (b) first AMR at $\delta = 50\,mm$. (c) second AMR at $\delta = 80\,mm$. (d) third AMR at $\delta = 80\,mm$. (e) plastic strains contour for the final AMR mesh. (Khoei et al., 2007).

problems. Fig. 11 shows the evolution of the AMR mesh in a slope and the numerical solution for the shear-band localization problem (Khoei et al., 2007).

Badia and Baiges (2013) applied *h*-adaptivity combined with a continuous-discontinuous Galerkin method to solve incompressible flow problems. AMR together with the discontinuous Galerkin enables the use of non-conforming meshes to accurately describe the sharp solutions typical of the incompressible flows. Fig. 12-(a) shows the velocity and pressure solutions for an incompressible flow. Fig. 12-(b) presents the adaptively refined mesh and the sharp pressure singularity at the corner.

Zander et al. (2016b) attribute the lack of dissemination of the *hp*-adaptivity to its high implementation complexity. The difficulty lies in the non-correspondence between the shape functions of the fine-scale elements and their coarse neighbours.

Alhadeff et al. (2016) developed a *h*-adapvitity scheme suitable for Graphical Processing Units (GPU) for dynamic fracutre mechanics including the inter-element cohesive zone model.

Salazar de Troya and Tortorelli (2018) use *h*-adaptivity to topology optimization problem subjected to stress-constrains. The authors solve the stress singularity problem combining a fraction filter to impose a minimum volume together with the RAMP penalization and a RAMP-like stress definition.

Jomo et al. (2021) present a hierarchical multi-grid approach employing the Finite Cell Method (FCM) and *hp*-refinement for large-scale computation of the Poisson and elasticity problems. The small cut-element issue is addressed by using Additive Schwarz smoothing techniques.

2.3.2 *Error-estimators*

The question on how and where to perform the mesh refinement/coarsening brought interest to the development of a posteriori error estimators to answer this question in an efficient and automatic manner.

The mathematical ground of the AMR to minimize mesh error was set by Babuska and Rheinboldt (1978). It consists in defining an element-wise value for the error of an energy norm.

Diaz et al. (1983) create an error-estimate for *r*-refinement by associating the node position that minimizes the error associated with the interpolation of the exact solution using a finite element

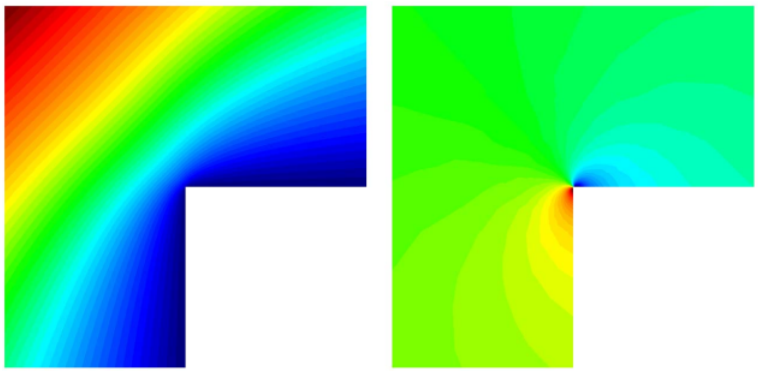

(a)

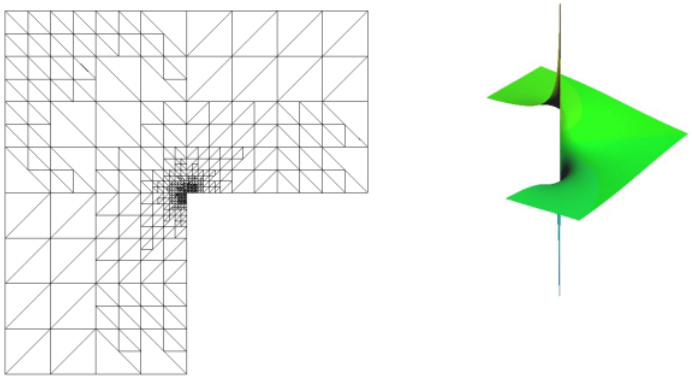

(b)

Figure 12: AMR used to solve the incompressible flow. (a) Computed solution for the velocity (*left*) and pressure (*right*). (b) The non-conforming mesh at a intermediate time-step (*left*) and the pressure singularity at the corner (*right*). (Badia and Baiges, 2013).

function space. After the new mesh is found and changed, computations restart to obtain the new error of the mesh.

Rank (1986) proposes an error estimator to evaluate the residual at sampling points of the FEs, which for linear elements were the element midpoint, and uses this information to optimize the mesh.

A simple and efficient error-estimate for mesh adaptivity is the flux projection estimate, known as the Zienkiewicz-Zhu (ZZ) estimator (Zienkiewicz and Zhu, 1987; Ainsworth et al., 1989). The error-estimator compares the projected flux from the Gauss points to the nodal points with the flux at the element super-convergent point (Zienkiewicz and Zhu, 1992a,b). For the cases where linear interpolation is used, the element super-convergent point coincides with the centroid of the element, coinciding with the sampling points of Rank (1986).

Babuska and Miller (1987) propose an equivalent estimator for the H^1 finite element error. The method is a posteriori error-estimate for the energy norm. The estimator is composed of element-wise error *indicators* and the mesh adaptivity is based on the mesh distribution of these indicators.

Rencis and Kwo-Yih (1989) coupled a posteriori error-estimation with h-refinement for the boundary element method in $2D$ and $3D$ axisymmetric problems to solve the Laplace equation. The self-adaptive mesh starts from an initial coarse boundary mesh and uses the boundary L_2 error norm to automatically adapt the mesh.

Belytschko and Tabbara (1993) use h-refinement to solve transient problems with plastic response and localization phenomena using various error estimation criteria. The authors conclude that an error-estimator based on the L_2-projection of strains is the most effective for the constant strain elements.

Later, Perić et al. (1994) tackle the strain-localization problem using an h-refinement AMR coupled with a modified version of the the ZZ estimator, adopting the rate of plastic work as the error measure. In Perić et al. (1999) an error estimator for the h-refinement strategy in a finite strain setting for elasto-

plastic problem of the thermo-mechanical coupled problem of metal forming, high-speed machining and blanking, and projectile impact modelling is designed.

Hughes et al. (1998) suggest the use of the fine scales in the VMS as a measure of the error on the coarse FE scale. Hauke et al. (2006b) used an element error norm for the one dimensional convection-diffusion equation in the VMS framework for the first time.

Hauke et al. (2006a,c) extended the approach using high-order elements. These ideas were applied in the context of Navier-Stokes, linear elasticity and higher order ordinary differential equations (Rossi et al., 2013; Hauke et al., 2015; Hauke and Irisarri, 2015; Irisarri and Hauke, 2015).

Masud et al. (2011) derives an error-estimator based on the algebraic multi-grid approach for linear elasticity where the contribution on the boundaries of the elements are neglected.

Barbié et al. (2015) use *h*-adaptivity associated with the local defect correction and the ZZ error estimator applied to meshes with refinement ratio greater than 2 in nonlinear solid mechanics problems. The ZZ estimator efficiency is related to the regularity of the mesh.

Baiges and Codina (2017) apply the subgrid scales to nonlinear solid mechanics problems considering the subscales also on the elements boundaries and using the stabilized mixed $\boldsymbol{u}/p$ formulation.

2.3.3 *Handling Data-Structures*

Apart from properly chosing an error-estimator, the success of the AMR also lies in handling mesh information during refinement and coarsening. In this sense, two main approaches are commonly used, block-structured and unstructured.

On the one hand, the Block-structured data utilizes unions of mapped regular grids. This method is cheap and enables the re-use of uniform-mesh codes (Berger and Oliger, 1984; Calder et al., 2000; Colella et al., 2007; Luitjens et al., 2007; Burstedde et al., 2011), but is not indicated in the case of complex geometries or unstructured meshes. On the other hand, tree-data structures, i.e. *quadtrees* ($2D$) and *octrees* ($3D$), make use of a hierarchical data structure to take advantage of the block-structure features of mapping and storing regular grids (Benzley et al., 1995; Biswas and Strawn, 1998). This hierarchical nature reduces the complexity of searching procedures and enhances the efficiency of mesh partitioning (Campbell et al., 2003).

Therefore, the idea of *quadtrees* ($2D$) (Finkel and Bentley, 1974) and *octrees* ($3D$) (Meagher, 1982) becomes appealing to handle data-structures. *Quadtrees* and *octrees* divide the initial element, henceforth called *parent element*, in halves for each direction of the element. This refinement rule is called *isotropic* refinement, as all directions are split in the same number of divisions.

In terms of topological efficiency, AMR meshes using simplicial (triangular and tetrahedral) elements and tree-based (quadrilateral and hexahedral) elements have been studied (Burstedde et al., 2011; Holke, 2018) and the tree-based structure results in better performance in terms of storage and hierarchy computation.

The completely unstructured data provides greater geometric flexibility, at the cost of storing all the neighbor relations between mesh elements, which reduces the efficiency of storage and hierarchy computation (Flaherty et al., 1997; Norton et al., 2001; Lawlor et al., 2006). In AM, the fast access to data and low memory consumption is key due to the frequent data access necessary during the simulation.

Kirk et al. (2006) use unstructured data and store all the mesh information in each processor, which compromises the scalability of the algorithm. Jansson et al. (2012) uses a tetrahedral unstructured framework without hanging nodes, presenting strong scalability up to $1,000$ processors for the incompressible flow problem.

In the development of efficient handling of isotropic AMR, Baiges and Bayona (2016) presented an algorithm for computational physics meshes in a distributed memory environment. The library is developed for nodally based parallel partitions, which means that the node belongs to a single processor, but the element can belong to several processors at the same time. Furthermore, the algorithm enables multilevel refinement jumps between neighbor elements, efficiently handles data-structures for $2D$ and $3D$ meshes, with low memory consumption and scaling up-to thousands of processors.

Fig. 13 presents the domain for a heat transfer problem with the inital and AMR mesh (with both quadrilateral and triangular elements) and the processor distribution after the load rebalancing using the algorithm presented in Baiges and Bayona (2016).

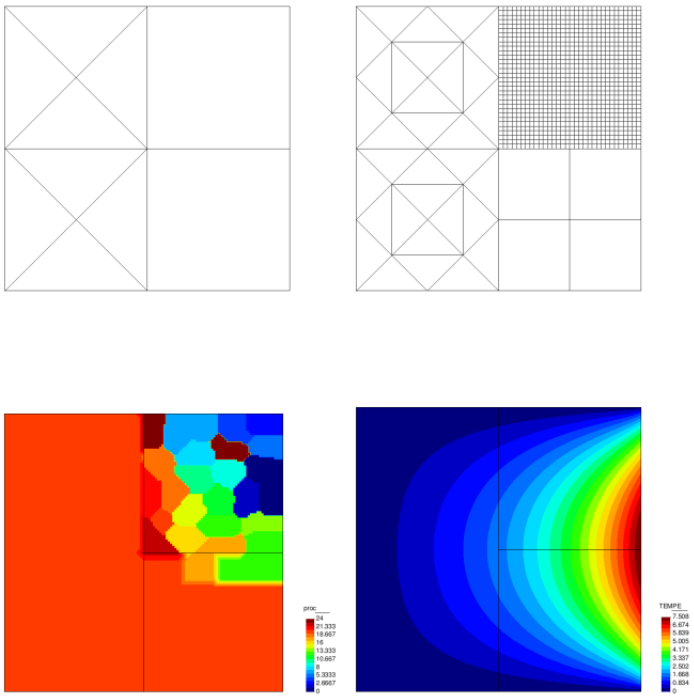

Figure 13: Evolution of the temperature field and the DOF for the moving heat load, where the gray area represent the solidified structure.(Baiges and Bayona, 2016).

2.3.4 *AMR applied to Additive Manufacturing*

In the context of AM simulations, different scales (microstructural, melt-pool and part-scale) might be involved and each one of them demands different simulation strategies to be adopted. In this sense, the common AM simulation approaches are:

a) The High Fidelity approach, when the advancement of the heat source per time step, Δl, is approximately the size of the FE (h_e) and h_e is approximately the size of the heat source spot radius.

b) The Hatch-by-Hatch approach, when greater portions of the scanning path defined by consecutive straight lines, each straight line of the scanning path is named *hatch*. In this approach the requirement of the advance of the heat source is less strict than the High Fidelity (HF).

c) The Layer-by-Layer approach, when the whole layer is deposited at once with an average heat input.

d) The Multi-Layer approach, when a group of layers is deposited at once with an average heat input equivalent as the heat input for the group of layers, including the re-coating time between layers.

Chiumenti et al. (2017b) provide guide-lines to choose the appropriate approach of the AM simulation for the desired application, as well as the required mesh resolution.

For thermo-mechanical applications, HF or the Hatch-by-hatch approach should be selected and the appropriate representative FE size used. In this case, the use of *uniform* fix meshes requires a high number of FEs to discretize the geometry and meet the mesh resolution requirements for thermo-mechanical applications. Some researchers adopt *uniform* fixed fine meshes (Matsumoto et al., 2002; Dai

and Shaw, 2002; Patil and Yadava, 2007; Ma and Bin, 2007; Antony et al., 2014; Chiumenti et al., 2017a,b), but the high computational cost makes this approach prohibitive for industrial-sized components.

Luo and Zhao (2018) categorizes the AMR adopted to simulate AM processes into two schemes: static AMR (Ren et al., 2010; Contuzzi et al., 2011; Hussein et al., 2013; Cheng et al., 2014; Li et al., 2015b) and dynamic AMR (Michaleris, 2014; Pal et al., 2014; Zeng et al., 2015; Denlinger et al., 2014; Dunbar et al., 2016; Denlinger et al., 2017). This depends on whether the mesh is updated or not during the simulation. The former has relatively low computational cost and high simulation accuracy, but is suitable for single-layer components only and the mesh cannot change with the advancement of the melt-pool. The latter is suitable for multi-layered components, achieves high simulation accuracy at low computational costs, but it demands a more complex implementation and requires data-transfer from the old to the new mesh.

Ren et al. (2010) adopts a static *h*-refinement strategy and use the ANSYS Parametric Design Language (APDL) to simulate a dynamically moving Gaussian heat source for the Selective Laser Sintering (SLS) process.

Contuzzi et al. (2011) use the static AMR to build a *h*-refined mesh at the depositing region and the substrate portions away from the depositing region is filled with coarse FEs. The work simulates the powder-liquid-solid change by checking the nodal temperatures for the SLM process.

Hussein et al. (2013) study the evolution of the thermal and stress fields in a static *h*-refined mesh when the layer is deposited over loose powder without support structures instead of a solid substrate.

Michaleris (2014) use *h*-refinement for the heat transfer analysis of a thin wall component built using metal deposition employing a hybrid element activation strategy.

Pal et al. (2014) use dynamic AMR to *h*-refine the area where the moving heat source is and analyze the travelling thermo-mechanical wave caused by the localized heat source.

Cheng et al. (2014) use dynamic AMR to refine the area close to the Heat Affected Zone (HAZ) and coarsen the region far away. The FE model incorporates temperature-dependent properties and a Gaussian volumetric distribution for the heat input. Numerical and experimental results achieve good agreement.

Denlinger et al. (2014) perform a thermo-mechanical simulation of a large part for the Electron Beam Melting (EBM) process simulation adopting dynamic AMR. The authors use an isoparametric mapping to interpolate the Gauss point values to the new mesh and divide the simulation process in three stages, allowing mesh coarsening after each stage. The first stage corresponds to the deposition of the first layer, stage two goes from the second through the ninth layer and stage three from the tenth to the 80^{th} layer. The numerical comparison with the experimental setting obtained a maximum error in the distortion measurements of 29%.

Riedlbauer et al. (2014) use dynamic AMR to refine and coarsen structured meshes. The work compares the performance of the monilithic and adiabatic split approaches (Armero and Simo, 1992) to assess evolution of the temperature field and Von Mises stresses within the melt pool for the EBM process. The performance comparison between methodologies is done for a thermo-elastic constitutive model.

Li et al. (2015b) use the static AMR approach and develop a multiscale thermal model to predict the component distortions for the SLM process. The thermal information is transferred from the micro-scale laser scanning to the meso-scale layer hatching and to the macro-scale part build-up. The transfer is done with an equivalent heat source developed from the thermal history of the melt pool in the micro-scale laser scanning model and applied to the meso-scale hatch layer and incorporated in the macro-scale to predict distortions.

Zeng et al. (2015) compare the thermal model using the dynamic AMR approach with the *uniform* fix fine mesh model and also with experimental results. The dynamic AMR compared to the fix fine mesh model saves up to 80 % in computational time and 99.95 % physical memory required for the postprocess files due to the reduced number of FEs.

Dunbar et al. (2016) study the post-building distortion of different scanning patterns using dynamic AMR to discretize the cylindrical component. The maximum numerical and experimental distortion difference is 12 %. For thin-walled cylindrical geometries, the distortions and stress accumulation are caused by the compression of solidifying material of the current layer acting on the previous layers.

Patil et al. (2015) and Pal et al. (2015) use a dynamic AMR to predict the thermal and microstructural development of the α and β phases in the Metal Laser Sintering (MLS) process based on a multi-scale spatio-temporal discretization of the moving heat source.

Denlinger et al. (2017) validate a thermo-mechanical model using *in-situ* experiments of a 91 $[mm^3]$ specimen adopting an elasto-plastic finite strain constitutive model. In their work, dynamic AMR is used to keep the mesh refined in the latest set of layers close to the deposition area, while the region below is coarsened; this strategy is treated henceforth as the layer-wise AMR. The authors use the same isoparametric mapping described in Denlinger et al. (2014) to interpolate the Gauss point variables.

Gouge et al. (2019) apply dynamic AMR based on a multi-scale approach to reduce the mesh density according to a pre-activation re-meshing scheme. The authors perform thermo-mechanical analyses to part-scale models and compare numerical and experimental results. The authors claim that the mesh adaptivity is one of the source of errors observed in the numerical-experimental comparison.

Khan and De (2019) use dynamic AMR to refine the region close to the heat source and gradually coarsen elements away from the heat source. A mapping of the temperature field is performed from the fine to the coarse mesh. The authors investigate the development of the melt pool and compare the numerical results of the AMR model with the fixed fine mesh model and experimental results.

Kollmannsberger et al. (2018) combine a hierarchical *hp*-refinement strategy with the FCM to reduce the number of DOFs for moving thermal loads and phase-change simulations. Fig. 14 shows the FE mesh and the moving thermal load in different times and the evolution of the DOF during the simulation, where the gray area represents the solidified structure.

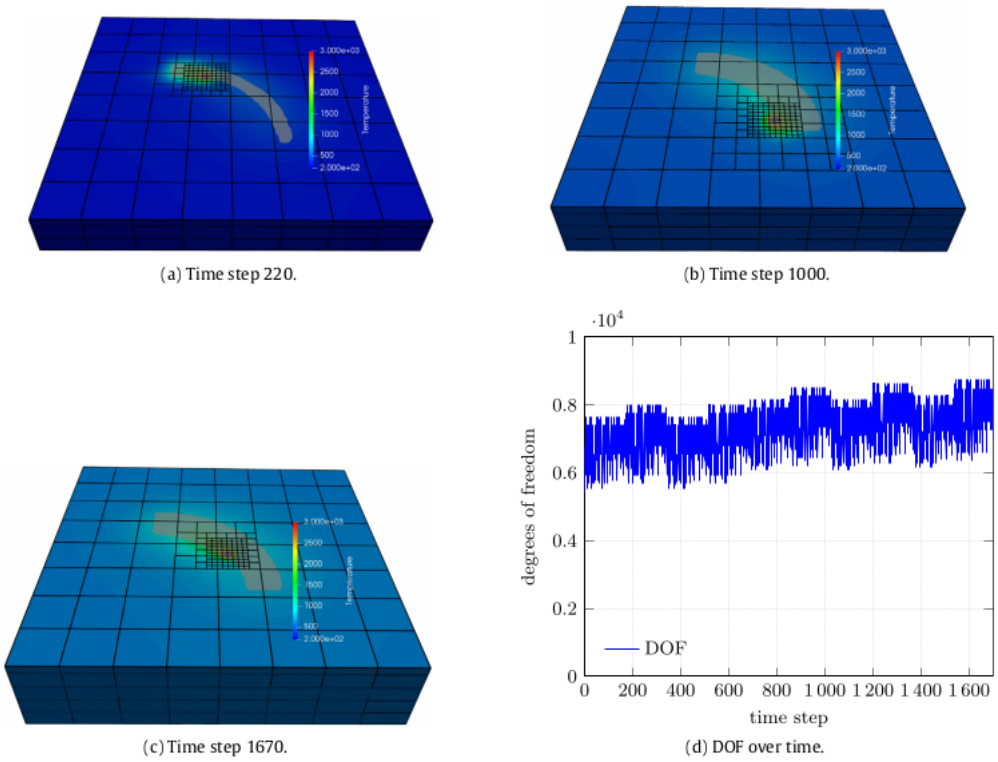

Figure 14: Evolution of the temperature field and the DOF for the moving heat load, where the gray area represent the solidified structure.(Kollmannsberger et al., 2018).

Li et al. (2019) analyze layer-wise AMR strategies with variable number of refined layers (2, 4, and 8 layers) and different transition jumps from the fine to the coarse meshes (2, 3 and 4 isotropic refinement level jumps). The authors obtain the thermo-mechanical response of a thin-wall structure and compare the AMR results with the solution from the fixed fine mesh model. The more the number of refined layers and the smoother the transition, the more accurate the solution. Nevertheless, the number of refined layers plays a minor role compared to the fine-coarse refinement level jumps. The computational speed-up gained with the 2 fine layer model pays-out the difference in the numerical accuracy (50 % speed-up and less than 5 % difference with respect to the 8 fine layer model).

Carraturo et al. (2019) apply truncated hierarchical B-splines in an IsoGeometric Analysis (IGA) setting for the linear heat transfer problem. The authors define a set of algorithms to provide admissible refinement and coarsening of the mesh using B-splines for moving heat sources.

Kollmannsberger et al. (2019) validate a thermal model, including the latent heat contribution, with the experimental set from the AMB2018-02c omparing isotropic and anisotropic conductivity models to accurately predict the melt-pool shape.

Neiva et al. (2019) present a highly scalable FE framework based on dynamic AMR for growing domains combined with the FCM. The work dynamically adapts the mesh following a geometric criterion. The HAZ is transformed into a cuboid and the background FE mesh is checked wether is inside or outside the HAZ by means of the Separating Axis Theorem (SAT). The accuracy outside the refined HAZ is achieved by the imposition of a $2:1$ balance scheme; i.e., the coarsening scheme should fullfil the following relation between neighbour FEs: $h_c = 2 \times h_f$, where h_c and h_f are the coarse and fine FEs, respectively.

Olleak and Xi (2020) combine the layer-wise AMR with high-order tetrahehdral FEs to simulate the thermo-mechanical response of a bridge benchmark (NIST benchmark test AMB2018-01). In their work, the number of refined layers considered are $N = 5$ and $N = 10$, but no significant improvements in the predicted distortions are obtained from $N = 5$ to $N = 10$.

Baiges et al. (2021) apply the layer-wise AMR with large jumps between the refined and coarse areas to compute the mechanical response based on the inherent strains method. To compensate the loss of accuracy during the coarsening step, the authors compute coarsening correction terms that aim to keep the previous solution, provided by the fine mesh, in the updated coarse mesh. From this work, Fig. 15 presents, at the top, a cantilever beam with an initial fine mesh that is used to solve the mechanical problem and, in a second time-step, the solution is derefined to the coarse mesh presented. Fig. 15 shows, at the bottom, the displacement field at the final step of the analysis (coarsened mesh) for the reference solution in Fig. 15-(a), the AMR solution *without* and *with* the coarsening correction terms in Fig. 15-(b)-(c), respectively.

Carraturo et al. (2021a) apply the dynamic AMR presented in Carraturo et al. (2019) to the topology optimization problem for AM applications using a phase-field approach (Auricchio et al., 2019). The authors evaluate the influence of the problem parameters using four stopping criteria. Additionaly, a workflow to convert the smooth isogeometric solution into $3D$ printed components is presented.

Kollmannsberger and Kopp (2021) compare the convergence rate of the first-order and the second-order time-stepping schemes using a temporal-spatial discretization employing hp-refinement for the moving heat source. Although the second-order method presents a better convergence rate, numerical oscillations are observed. The expected convergence rate is only achieved when strongly graded time-steps are used for the initial discontinuous solution.

Carraturo et al. (2021b) use hp-refinement and FCM to capture the solidification process and residual stress evolution in the SLM process. The authors use the same integration grids for the thermal and mechanical problems, but a finer FCM grid is applied for the thermal problem to correctly capture the melt pool shape.

Moreira et al. (2022b) employ h-refinement based on a multi-criteria approach to enhance the numerical accuracy and reduce the computational cost. The multi-criteria is based on a geometric criteria to obtain the refined mesh in the HAZ region and a ZZ error-estimator with the SPR approach to guarantee the solution accuracy outside the HAZ. The approach is combined with a GCode reader that provides the process parameter information as well as the geometric definition of the domain. The user neither needs to model the component geometry nor spend time in creating a FE mesh. The FE framework is well suited for the AM process simulation of complex geometries. From this work, Fig.16 show the building process of a component at two different time instants, where the red box represents the current position of the HAZ bounding-box. Note that the remain refined area, not contained by the HAZ, has been refined according to the ZZ error-estimator.

The computational simulation of AM processes requires a large number of time steps and the tracking of large amounts of information. The h-adaptivity is efficient for all class of problems (smooth and non-smooth solutions) and is preferred when complex geometries are analyzed; furthermore, it requires less data storage than other adaptivity approaches, saving computational resources, and the transferring between meshes complexity is lower than other adaptivity schemes.

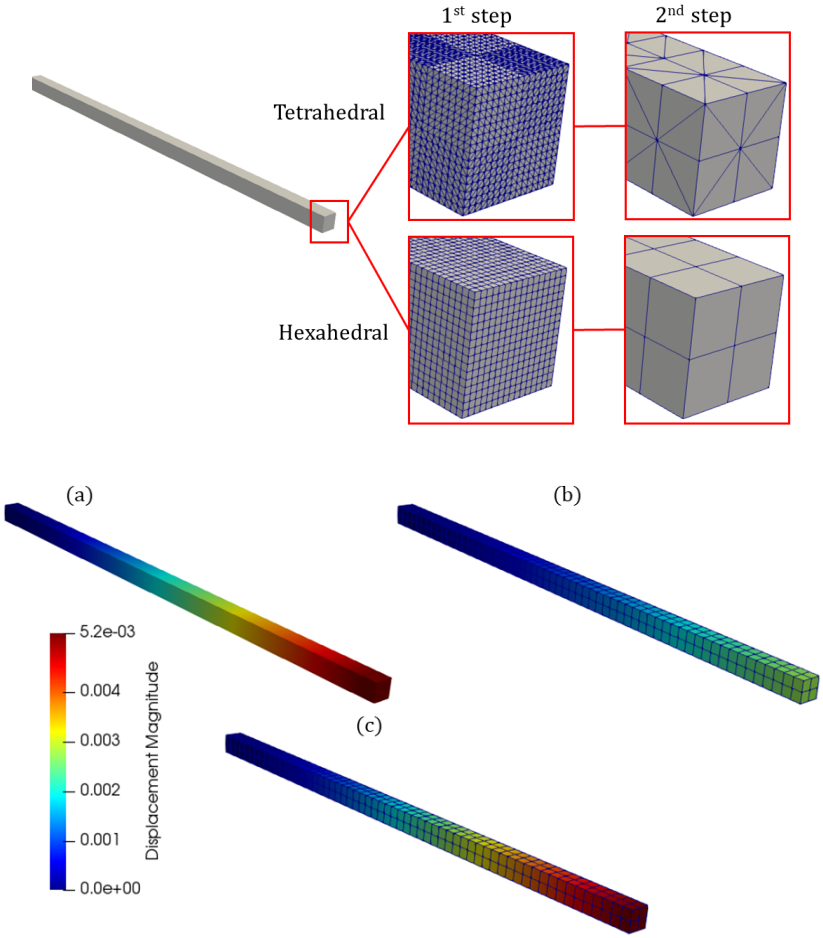

Figure 15: Cantilever beam: At the top, the FE discretizations adopted. At the bottom, the displacement results at the final step of the analysis. (a) Fine fixed mesh. (b) AMR mesh *without* the coarsening correction terms. (c) AMR mesh *with* the coarsening correction terms.

2.4 AM Machinery

The AM process relies on Computer Aided Design (CAD) tools to provide the AM printer with the necessary data to produce the component. The component designers must supply the AM printer with the geometry and the process parameters, such as power input, and intermediate pauses to be used. When addressing the computational simulation of the AM process, the information obtained from the pre-processing and used in the simulation must be the same as the data provided to the AM printer.

In the pre-processing stage, the component designers prepare the CAD geometry of the component, convert the geometry to a STereoLithography (STL) mesh, and slice the STL mesh to obtain a Common Layer Interface (CLI) or GCode file. The handling of these geometric data and process parameters from the pre-processing stage is discussed in Section 2.4.1.

After this, the pre-process data is translated into computational information to simulate the growing domain. The most common approaches used in the simulation of growing domains are examined in Section 2.4.2.

2.4.1 *Geometry and process parameters data acquisition*

Information to be transferred to the AM printer and used for the simulation of the AM process can be delivered in two standard formats: the CLI (Commission of the European Communities & Bayerische Motoren Werke, 1994) and the GCode (RS-274). Both formats are obtained after slicing the CAD

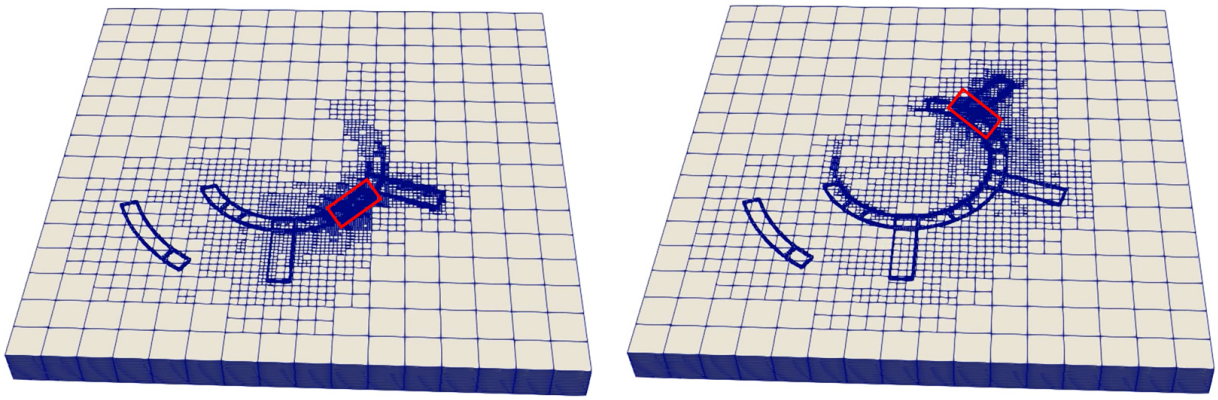

(a) (b)

Figure 16: Spatial discretization obtained by the multi-criteria approach. (a)-(b) Evolution of the FE mesh at two different times with the red box representing the current position of the HAZ.

geometry prepared in STL format by the designers. The scanning sequence is defined for each layer obtained by the slicing process (Wong and Hernandez, 2012; Singh et al., 2017).

The slicing process consists in intersecting the STL mesh by two parallel planes, separated by the layer thickness. The volume contained in-between these two planes is later converted in a sequence of straight lines, namely hatches, in an specific order, also known as the scanning/path sequence. The scanning sequence can be stored in a CLI or GCode formats by softwares called 3*D slicers*, such as *Cura* (Braam, 2017–2022), *Netfabb* (Autodesk, 2016–2022), *Slic3r* (Ranellucci, 2011–2022), *Simplify3D* (Webster, 2013–2022), etc.

Choi and Kwok (1999, 2002) present a memory efficient slicing algorithm for Rapid Prototyping (RP) that converts a STL mesh into a CLI file. The memory constraint to convert the STL to a CLI is overcomed by reading only the facets of the current layer, minimizing the number of searching operations and memory requirements.

Brown and de Beer (2013) develop an algorithm to convert the STL mesh into a simple GCode format capable of being interpreted by entry-level 3*D* printers. The algorithm efficiency is assessed by analyzing 3 case studies specimens printed from the converted GCode in a BFB 3000 3*D* printer.

Neiva et al. (2019) manage the geometrical information for the AM simulation using a CLI parser that aggregates an array of layer entities. Each layer of the CLI file generates a layer instance and stores the information of the layer height. Likewise, instances of the polylines and hatches, associated to each layer in the CLI file, are also created. This object-oriented structure enables the extension to other file formats.

Livesu et al. (2019) present a tool to be used in the AM process simulation that reads a group of 2*D* slices from a CLI file and converts into a tetrahehdral mesh using *TetWild* (Hu et al., 2018).

On the one hand, the interpretation of the CLI file is easy and requires only the reading of a sequence of straight lines. On the other hand, the process parameters need be provided by the analyst separately, remaining unchanged during the simulation, which may not be the case in the actual AM printing of the component.

Contrariwise, the GCode standard (Association et al., 1980) enables to set process parameters directly inside the file, permitting the flexibility to change the design of process parameters during the course of the printing/simulation.

Yeung et al. (2018) implement a modified version of the GCode, namely the AM GCode, that bound the simulated velocities/accelerations to match the capabilities of the machinery movements. The authors demonstrate that the step velocities assume infinite acceleration, which in practice are impossible to achieve. In this way, the authors limit the jerk (time derivative of the acceleration) and the result is a modified version of the initial GCode, leading to a more accurate geometry-time description of the AM process. Fig. 17 shows the difference in the simulated GCode command and the actual measurements for the machine displacement, speed and acceleration.

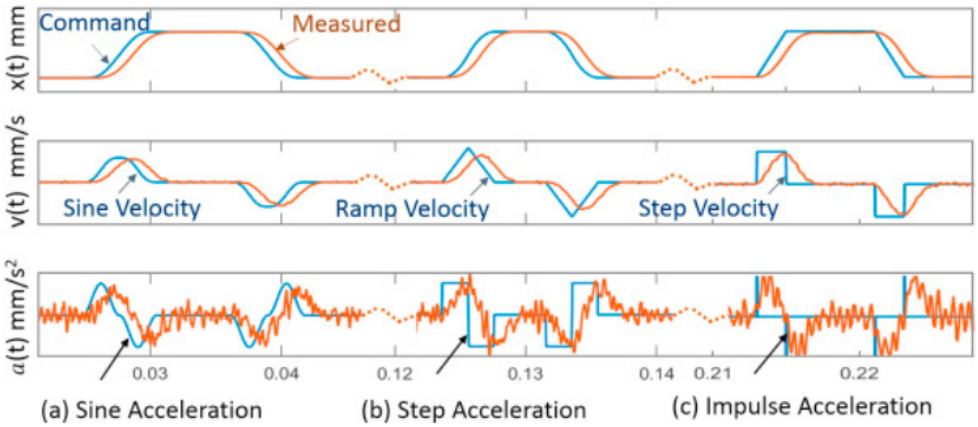

Figure 17: Comparison in the simulated GCode command and the measurements for the displacement, speed and acceleration (Yeung et al., 2018).

Cattenone et al. (2018) employ *ABAQUS* software (Smith, 2009) in the analysis of FDM technology. The STL is converted into a GCode file using a slicer. Later, a *MATLAB* (MATLAB, 2018) script retrieves the information about the nozzle position, nozzle velocity and cross-section to be used in the element activation strategy.

Carraturo et al. (2020b) make use of the work of Yeung et al. (2018) to obtain the required information directly from a GCode file to perform a study on the influence of the laser control strategy on the development of residual stresses.

Moreira et al. (2022b) present an easy-to-use AM FE framework using *fitted* AMR meshes where the required information about the geometry and process parameters (hatches, power input, depositing and recoating speeds, time-pauses) for the AM simulation comes directly from the GCode file. The analyst is entitled to provide information about the desired size of the FEs in the HAZ, the power input efficiency, the inital conditions, the HAZ bounding-box parameters and the temperature-dependent material data.

Erturk et al. (2022) present a study of the microstructure and the mechanical characteristics of lattice structures produced by the PBF process. The lattice structures parameters used in the study are obtained using the STL and CLI formats. Two types of structures are analyzed, bending-dominant and stress-dominant. The results shows that increasing the relative density of the lattice structures increases the global strength in either type of structures. Nevertheless, the stress-dominant structures present better mechanical properties than the bending-dominant structures for the same relative density.

2.4.2 *Element activation strategies*

In the matter of simulating evolving physical domains, the main strategies to deal with the growing of computational domains are the *quiet-element* and the *element birth-death* approaches.

In the former, the FE domain is composed of active and quiet-elements, in the sense that they are included into the system of equations, but the material properties are chosen in a way that the analysis is not affected by their presence. In the latter, the inactive elements are not considered in the system of equations until the corresponding material is deposited.

2.4.2.1 *Quiet-element approach*

Michaleris (2014) presents the advantages and disadvantges of the quiet-element approach. The strong points are: it is easy to implement and to be used with commercial FE softwares through user-created routines, the constant number of equations throughout the simulation does not require equation renumbering and the solver is initialized only at the beginning of the simulation.

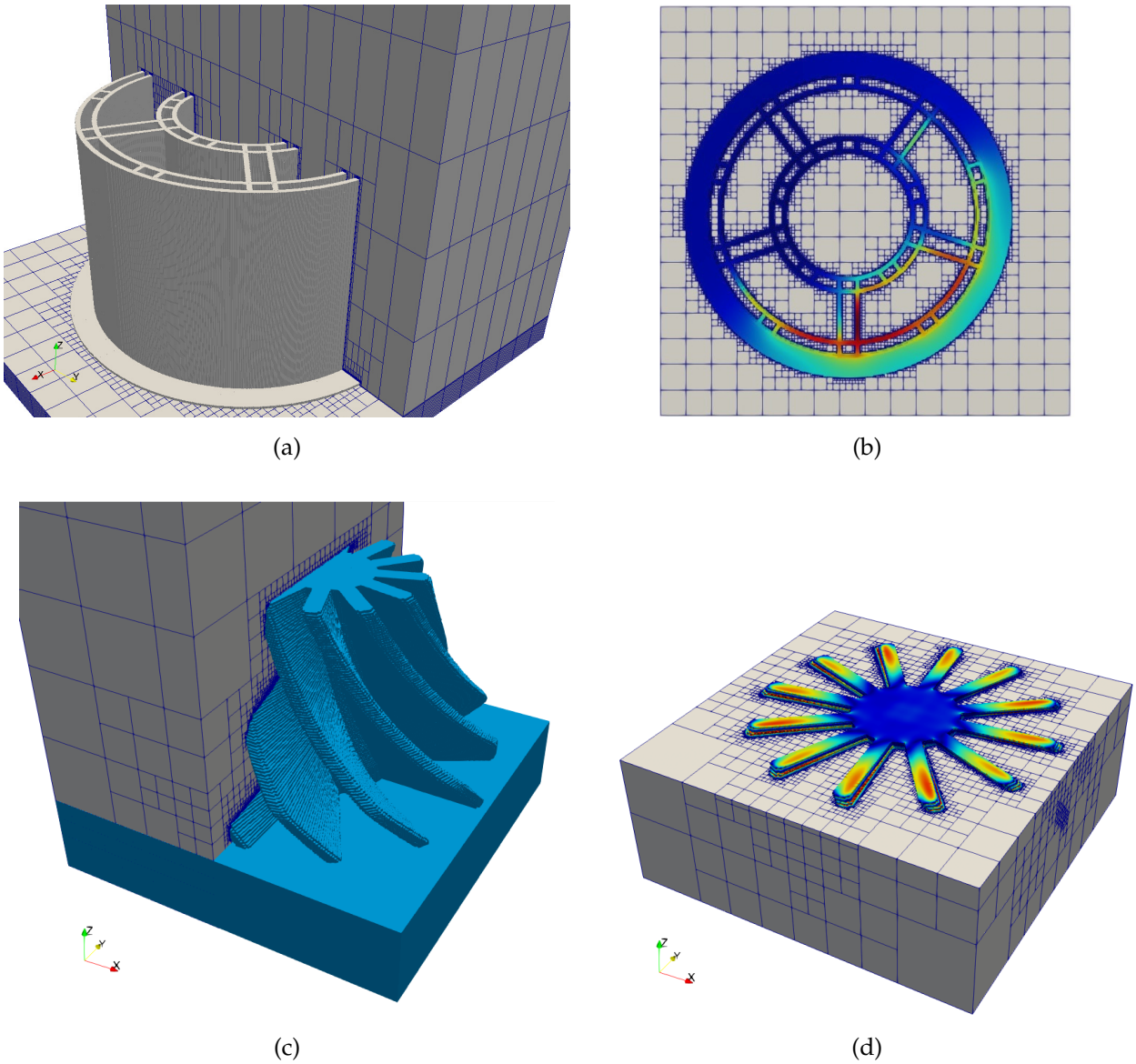

(a) (b)

(c) (d)

Figure 18: Complex geometries obtained directly from a GCode file using octree mesh generation. (a)-(b) Background mesh of the printing of a ball bearing. (c)-(d) Background mesh of the printing of a propeler.

On the down side, Michaleris (2014) shows that the scale factors used to artificially remove the contribution of the inactive element need be carefully chosen. In this sense, the scale factors are applied to the thermal conductivity (s_k) and to the specific heat (s_{C_p}). On the one hand, when the scale factors are too small, this causes the system of equations to be ill-conditioned. On the other hand, if the scale factors are not sufficiently small, the heat transfer through the quiet-elements, leads to an erroneous solution. Additionally, Michaleris (2014) observed long run times when the simulation has a majority of the elements as quiet-elements.

Denlinger et al. (2014) adopts a hybrid method using both the quiet-element and the element birth-death approaches to assess the thermo-mechanical behavior of the AM of large parts. The hybrid method initializes all the elements that correspond to the component to be manufactured as inactive, not contributing to the global system of equations. Next, the depositing layer is identified and all the elements belonging to the current deposition layer are added to the analysis as quiet-elements.

Denlinger et al. (2015) present the residual stress and distortion analyses of a DED manufactured wall structure using the quiet-element method. In this study, the authors adopt the thermal conductivity and specific heat scale factors as $s_k = 10^{-6}$ and $s_{C_p} = 10^{-2}$, respectively, to avoid the issues addressed in the work of Michaleris (2014).

The hybrid approach is again employed by Denlinger and Michaleris (2016) to compare the effect of stress relaxation when using different materials for the deposition process of DED.

Denlinger et al. (2017) use the hybrid approach to the thermo-mechanical analysis of LPB process and experimental validation of the manufacturing process of 8 layer cube in a HF setting.

2.4.2.2 *Element birth-death approach*

Michaleris (2014) also presents the advantages and disadvantges of the element birth-death approach. On the positive side, the element birth-death does not suffer neither from ill-conditioning nor errors introduced by scaling factors. The system of equations contains only active elements and the number of required element computations are very much reduced.

On the negative side, the birth-death is not easily implemented into commercial softwares from user routines. The constant addition of new active elements require renumbering and reinitialization of the solver. Inactive elements sharing nodes with active elements may introduce artificial thermal energy. This may be corrected at the moment of the element activation by resetting the activation temperature to the initial temperature, instead of using an interpolation value. In this way, the temperature is forced to be discontinuous.

Lindgren et al. (1999) use the quiet-element and the element birth-death approaches to compare the transient temperatures and residual stresses of a multipass welding of a thick plate. Good agreement between both methods is observed; also, computational cost reduction is achieved by the element birth-death.

Lindgren and Hedblom (2001) also employ both methods to compare the analysis of multipass welding in a large deformation analysis. In the quiet-element approach, although the properties are scaled to not contribute in the thermal analysis, the inactive quiet-elements present accumulated plastic strains, that must be reset. This procedure is not required in the element birth-death approach.

Roberts (2012) employed the element birth-death using *ANSYS* (ANSYS10 Inc, 2007) to investigate the effect of material and process parameters on the residual stress distribution of Laser Melting Processes (LMP). The author identifies that the residual stresses develop through two mechanisms: 1) the steep temperature gradient observed in the cooling phase of the melted powder; 2) the shrinkage and consolidation of the molten material interacting with previous layers.

Lindgren et al. (2016) evaluate the changes in the microstructure in the process zone and the solid material using the element birth-death approach. The authors apply techniques developed in the Computational Welding Mechanics (CWM) field to obtain the overall behavior of the macro-scale model. The simulation of the AM process of DED is treated similarly to the multi-pass welding approach.

3

FE TECHNOLOGIES WITH ENHANCED STRESS/STRAIN ACCURACY

This chapter presents the FE technologies to tackle the material incompressibility constraint, due to the J_2 plastic isochoric flow.

In this sense, the chapter is outlined as: Section 3.1 presents the strong, weak and discrete FE forms of the standard irreducible FE formulation. Section 3.2 introduces the $\bar{\boldsymbol{B}}$ and the mixed $\boldsymbol{u}/p$ FE formulations. Section 3.3 derives the mixed $\boldsymbol{u}/\boldsymbol{e}/p$ formulation with enhanced accuracy for the stress/strain fields.

The FE technologies are described for the general $3D$ case in Voigt's notation. Therefore, the displacement $\boldsymbol{u} = (u, v, w)^T$ is a vector of 3 components and the stress $\boldsymbol{\sigma} = (\sigma_x, \sigma_y, \sigma_z, \tau_{xy}, \tau_{yz}, \tau_{xz})^T$ and the strain $\boldsymbol{\varepsilon} = (\varepsilon_x, \varepsilon_y, \varepsilon_z, \varepsilon_{xy}, \varepsilon_{yz}, \varepsilon_{xz})^T$ are vectors of 6 components.

3.1 The standard irreducible *u* formulation

Although the standard $\boldsymbol{u}$ formulation does not fit into the FE technologies with enhanced accuracy, it is the base for the forthcoming formulations.

3.1.1 *Strong form*

The strong form of the nonlinear solid mechanics problem is written in terms of the displacement $\boldsymbol{u}$ for the standard irreducible FE formulation. Under the hypothesis of small strains, linear kinematics, the displacement $\boldsymbol{u}$ and the total strains $\boldsymbol{\varepsilon}$ are related through the compatibility equation

$$\boldsymbol{\varepsilon} = \boldsymbol{S}\boldsymbol{u} \tag{3.1}$$

where $\boldsymbol{S}$ is the differential symmetric gradient operator

$$\boldsymbol{S} = \begin{bmatrix} \partial_x & 0 & 0 & \partial_y & 0 & \partial_z \\ 0 & \partial_y & 0 & \partial_x & \partial_z & 0 \\ 0 & 0 & \partial_z & 0 & \partial_y & \partial_x \end{bmatrix}^T \tag{3.2}$$

Correspondingly, equilibrium between the stress vector $\boldsymbol{\sigma}$ and the body forces $\boldsymbol{f} = (f_x, f_y, f_z)^T$ is defined by the Cauchy equation

$$\boldsymbol{S}^T\boldsymbol{\sigma} + \boldsymbol{f} = \boldsymbol{0} \tag{3.3}$$

where $\boldsymbol{S}^T$ is the differential divergence operator, adjoint to the $\boldsymbol{S}$ in Eq. (3.1).

The constitutive equation relates the stress vector $\boldsymbol{\sigma}$ and the strain vector $\boldsymbol{\varepsilon}$

$$\boldsymbol{\sigma} = \boldsymbol{C}\boldsymbol{\varepsilon} \tag{3.4}$$

where $\boldsymbol{C}$ is the fourth-order secant constitutive tensor which can be expressed in Voigt's notation as a 6×6 matrix.

Substituting Eqs. (3.1) and (3.4) into the Cauchy equation (3.3), leads to the Navier equation written in terms of displacements, $\boldsymbol{u}$:

$$\boldsymbol{S}^T\boldsymbol{C}\boldsymbol{S}\boldsymbol{u} + \boldsymbol{f} = \boldsymbol{0} \tag{3.5}$$

together with the prescribed Dirichlet's and Neumann's conditions imposed in the boundary Γ. The boundary Γ can be split accordingly to the Dirichlet or the Neumann conditions, respectively as Γ_u and Γ_t, such that $\Gamma = \Gamma_u \cup \Gamma_t$ and $\Gamma_u \cap \Gamma_t = \varnothing$.

It is assumed herein that the prescribed displacements vanish on the boundary Γ_u

$$\boldsymbol{u} = \boldsymbol{0} \text{ in } \Gamma_u \tag{3.6}$$

In addition, the prescribed traction on the boundary Γ_t are

$$\boldsymbol{t} = \bar{\boldsymbol{t}} \text{ in } \Gamma_t \tag{3.7}$$

3.1.2 *Weak form*

The weak form of the problem is obtained as follows. First, Eq. (3.5) is premultiplied by an arbitrary virtual displacement $\delta\boldsymbol{u}$ and integrated over the spatial domain, Ω:

$$\int_\Omega \delta\boldsymbol{u}^T[\boldsymbol{S}^T\boldsymbol{C}\boldsymbol{S}\boldsymbol{u}]d\Omega + \int_\Omega \delta\boldsymbol{u}^T\boldsymbol{f}d\Omega = \boldsymbol{0} \qquad \forall\delta\boldsymbol{u} \tag{3.8}$$

The virtual displacement $\delta\boldsymbol{u}$ also conforms with the boundary conditions, so that $\delta\boldsymbol{u} = \boldsymbol{0}$ in Γ_u. Next, the Divergence Theorem is applied to the first term of Eq. (3.8) and the boundary is split $\Gamma = \Gamma_u \cup \Gamma_t$. The Dirichlet boundary terms vanish on Γ_u ($\delta\boldsymbol{u} = \boldsymbol{0}$), the weak form of Eq. (3.8) becomes

$$\int_\Omega (\delta\boldsymbol{u}\boldsymbol{S})^T(\boldsymbol{C}\boldsymbol{S}\boldsymbol{u})d\Omega = \int_\Omega \delta\boldsymbol{u}^T\boldsymbol{f}d\Omega + \int_{\Gamma_t} \delta\boldsymbol{u}^T\bar{\boldsymbol{t}}d\Gamma \qquad \forall\delta\boldsymbol{u} \tag{3.9}$$

with the right hand side being the virtual work of the external forces, written as

$$W(\delta\boldsymbol{u}) = \int_\Omega \delta\boldsymbol{u}^T\boldsymbol{f}d\Omega + \int_{\Gamma_t} \delta\boldsymbol{u}^T\bar{\boldsymbol{t}}d\Gamma \qquad \forall\delta\boldsymbol{u} \tag{3.10}$$

The solution to the solid mechanics problem is to find the displacements $\boldsymbol{u}$ that verify the system of Eq. (3.9) in compliance with the boundary condition $\boldsymbol{u} = \boldsymbol{0}$ on Γ_u, given an arbitrary virtual displacement $\delta\boldsymbol{u}$, which vanishes on Γ_u.

3.1.3 *FE approximation*

Firstly, the continuous domain Ω is discretized into FEs partitions such that $\Omega = \cup\Omega_e$, and the discrete FE approximations of the displacements $\boldsymbol{u}$ is taken such that

$$\boldsymbol{u} \doteq \hat{\boldsymbol{u}} = \boldsymbol{N}_u\mathbf{U} \tag{3.11}$$

where $\mathbf{U}$ is the vector comprising the values of the nodal displacements of the FE mesh. $\boldsymbol{N}_u$ is the matrix containing the interpolation functions of the FE approximation.

Secondly, the Galerkin method is applied, where the discrete virtual displacement field takes the same approxiamtion as in Eq. (3.11), so that

$$\delta\boldsymbol{u} \doteq \delta\hat{\boldsymbol{u}} = \boldsymbol{N}_u\delta\mathbf{U} \tag{3.12}$$

Introducing Eqs. (3.11) and (3.12), the system of equations defined in Eq. (3.9) becomes

$$\int_\Omega \underbrace{(\boldsymbol{S}\boldsymbol{N}_u\delta\mathbf{U})^T}_{=\delta\mathbf{U}^T\boldsymbol{B}_u^T}\boldsymbol{C}\underbrace{(\boldsymbol{S}\boldsymbol{N}_u\mathbf{U})}_{=\boldsymbol{B}_u\mathbf{U}}d\Omega = \hat{W}(\delta\mathbf{U}) \qquad \forall\delta\mathbf{U} \tag{3.13}$$

where $\boldsymbol{B}_u$ is the discrete strain-displacement matrix, defined as

$$\boldsymbol{B}_u = \boldsymbol{S}\boldsymbol{N}_u \tag{3.14}$$

and $\hat{W}(\delta\mathbf{U})$ is the virtual work done by the traction $\bar{\boldsymbol{t}}$ and the body forces $\boldsymbol{f}$, defined as

$$\hat{W}(\delta\mathbf{U}) = \int_\Omega (\boldsymbol{N}_u \delta\mathbf{U})^T \boldsymbol{f} d\Omega + \int_{\Gamma_t} (\boldsymbol{N}_u \delta\mathbf{U})^T \bar{\boldsymbol{t}} d\Gamma \qquad \forall \delta\mathbf{U} \tag{3.15}$$

The discrete virtual displacement $\delta\mathbf{U}$ is an arbitrary nodal vector, thus the system of Eq. (3.13) can be written in matrix format as

$$\left[\begin{array}{c} \mathbf{K}_{UU} \end{array} \right] \left[\begin{array}{c} \mathbf{U} \end{array} \right] = \left[\begin{array}{c} \boldsymbol{F} \end{array} \right] \tag{3.16}$$

where $[\mathbf{U}]^T$ is the array of nodal values of displacements and

$$\mathbf{K}_{UU} = \int_\Omega \boldsymbol{B}_u^T \boldsymbol{C} \boldsymbol{B}_u d\Omega \tag{3.17}$$

and

$$\boldsymbol{F} = \int_\Omega \boldsymbol{N}_u^T \boldsymbol{f} d\Omega + \int_{\Gamma_t} \boldsymbol{N}_u^T \bar{\boldsymbol{t}} d\Gamma \tag{3.18}$$

Furthermore, the integrals over the domain are understood as the sum of the integrals over the FEs of the mesh

$$\int_\Omega (\cdot)\, d\Omega = \sum_e \int_{\Omega_e} (\cdot)\, d\Omega_e \tag{3.19}$$

and, for the sake of simplicity, $\mathbf{U}$ is to be considered the nodal values of the whole FE mesh.

3.2 Isochoric formulations

In this Section, the split of the strains into the volumetric and deviatoric-strains is introduced to address the volumetric-locking presented by the standard irreducible FE formulation when the material presents an incompressible behavior.

The strains can be written in terms of its volumetric and deviatoric components as

$$\boldsymbol{\varepsilon} = \frac{1}{3} e_{vol} \boldsymbol{I} + \boldsymbol{e} \tag{3.20}$$

with e_{vol} the volumetric strain (scalar), and $\boldsymbol{e}$ is the deviatoric-strain vector, defined as

$$e_{vol} = tr(\boldsymbol{\varepsilon}) = (\varepsilon_x + \varepsilon_y + \varepsilon_z) = \boldsymbol{G}^T \boldsymbol{u} \tag{3.21}$$

$$\boldsymbol{e} = (\varepsilon_x - \frac{1}{3} e_{vol}, \varepsilon_y - \frac{1}{3} e_{vol}, \varepsilon_z - \frac{1}{3} e_{vol}, \varepsilon_{xy}, \varepsilon_{yz}, \varepsilon_{xz})^T \tag{3.22}$$

e_{vol} can be computed as the divergence of the displacements $\boldsymbol{u}$ where $\boldsymbol{G} = (\partial_x, \partial_y, \partial_z)^T$ is the gradient operator and $\boldsymbol{G}^{\mathrm{T}}$ is the adjoint divergence operator. Introducing Eq. (3.21) and Eq. (3.20) into Eq. (3.1), the deviatoric-strains $\boldsymbol{e}$ can be computed in terms of the displacements $\boldsymbol{u}$ as

$$\boldsymbol{e} = \boldsymbol{S}\boldsymbol{u} - \underbrace{\frac{1}{3} \boldsymbol{I} (\boldsymbol{G}^{\mathrm{T}} \boldsymbol{u})}_{e_{vol}} = \boldsymbol{W}\boldsymbol{u} \tag{3.23}$$

where $\boldsymbol{S}$ is presented in Eq. (3.2) and $\boldsymbol{W}$ is the operator defined as

$$\boldsymbol{W} = \boldsymbol{S} - \frac{1}{3} \boldsymbol{I} \boldsymbol{G}^{\mathrm{T}} = \frac{1}{3} \begin{bmatrix} 2\partial_x & -\partial_x & -\partial_x & 3\partial_y & 0 & 3\partial_z \\ -\partial_y & 2\partial_y & -\partial_y & 3\partial_x & 3\partial_z & 0 \\ -\partial_z & -\partial_z & 2\partial_z & 0 & 3\partial_y & 3\partial_x \end{bmatrix}^T \tag{3.24}$$

3.2.1 *The $\bar{\boldsymbol{B}}$ formulation*

The $\bar{\boldsymbol{B}}$ formulation can be understood as an extension of the standard FE formulation or a particular case of the $\boldsymbol{u}/p$ formulation adopting the SRI approach. This FE technology is only applicable for quadrilateral and hexahedra elements, in $2D$ and $3D$, respectively in the near-incompressible limit.

The strong and weak forms are identical to the ones presented in Sections 3.1.1 and 3.1.2, since there are no additional fields.

3.2.1.1 *FE approximation*

The difference between the standard and the $\bar{\boldsymbol{B}}$ formulations arises because a split of the strain-displacement operator into the deviatoric and volumetric parts is performed as follows

$$\boldsymbol{B}_u = \boldsymbol{B}_u^{dev} + \boldsymbol{B}_u^{vol} \tag{3.25}$$

where $\boldsymbol{B}_u^{dev}$ and $\boldsymbol{B}_u^{vol}$ are the deviatoric and volumetric parts of the strain-displacement operator, respectively. Eq. (3.25) can be rewritten using the definitions in Eqs. (3.14) and (3.23) as

$$\boldsymbol{B}_u = \boldsymbol{S}\boldsymbol{N}_u = \underbrace{\boldsymbol{W}\boldsymbol{N}_u}_{=\boldsymbol{B}_u^{dev}} + \underbrace{\frac{1}{3}\boldsymbol{I}\boldsymbol{G}^T\boldsymbol{N}_u}_{=\boldsymbol{B}_u^{vol}} \tag{3.26}$$

In the classical $\bar{\boldsymbol{B}}$ method presented in Hughes (1980, 1987), the $\bar{\boldsymbol{B}}_u$ is defined as

$$\bar{\boldsymbol{B}}_u = \boldsymbol{B}_u^{dev} + \bar{\boldsymbol{B}}_u^{vol} \tag{3.27}$$

where $\bar{\boldsymbol{B}}_u^{vol}$ is the mean volumetric sub-matrix of the strain-displacement operator defined as

$$\bar{\boldsymbol{B}}_u^{vol} = \frac{1}{n_g}\sum_{i=1}^{n_g}(\boldsymbol{B}_u^{vol})_i \tag{3.28}$$

where n_g is number of integration points in the element.

Therefore, the system of equations presented in Eq. (3.16) for the standard irreducible FE can be rewritten using the new definition of the $\bar{\boldsymbol{B}}_u$ strain-displacement operator in Eq. (3.27) as

$$\left[\begin{array}{c} \bar{\mathbf{K}}_{UU} \end{array}\right]\left[\begin{array}{c} \mathbf{U} \end{array}\right] = \left[\begin{array}{c} \boldsymbol{F} \end{array}\right] \tag{3.29}$$

with

$$\bar{\mathbf{K}}_{UU} = \int_\Omega \bar{\boldsymbol{B}}_u^T \boldsymbol{C}\bar{\boldsymbol{B}}_u d\Omega \tag{3.30}$$

3.2.2 *The $\boldsymbol{u}/p$ formulation*

The stress is split now into the deviatoric and pressure components as

$$\boldsymbol{\sigma} = p\mathbf{I} + \boldsymbol{s} \tag{3.31}$$

where $\boldsymbol{I} = (1,1,1,0,0,)^T$ is the second-order identity tensor in Voigt's notation, the scalar p is the pressure and $\boldsymbol{s}$ is the deviatoric-stress vector defined as

$$p = \frac{1}{3}(\sigma_x + \sigma_y + \sigma_z) \tag{3.32}$$

$$\boldsymbol{s} = (\sigma_x - p, \sigma_y - p, \sigma_z - p, \tau_{xy}, \tau_{yz}, \tau_{xz})^T \tag{3.33}$$

Next, the volumetric/deviatoric split of the constitutive law is written as

$$p = Ke^{vol} \tag{3.34}$$

$$\boldsymbol{s} = \boldsymbol{C}^{dev}\boldsymbol{\varepsilon} = \boldsymbol{C}^{dev}\boldsymbol{e} \tag{3.35}$$

with K and $\boldsymbol{C}^{dev}$ being the secant bulk modulus and the secant deviatoric constitutive matrix, respectively.

3.2.2.1 *Strong form*

The strong form of the nonlinear solid mechanics problem is written in terms of the displacement $\boldsymbol{u}$ and pressure p fields.

Introducing the Eq. (3.31) into the Cauchy equation presented in Eq.(3.3) yields

$$\boldsymbol{S}^T\boldsymbol{s} + \boldsymbol{G}p + \boldsymbol{f} = \boldsymbol{0} \tag{3.36}$$

Note that $\boldsymbol{G} = \boldsymbol{S}^T\boldsymbol{I}$, and employing the compatibility relation between displacements and strains and Eq. (3.35) into Eq. (3.36) results in

$$\boldsymbol{S}^T\boldsymbol{C}^{dev}\boldsymbol{S}\boldsymbol{u} + \boldsymbol{G}p + \boldsymbol{f} = \boldsymbol{0} \tag{3.37}$$

Finally, the volumetric constraint is rewritten by introducing Eq. (3.21) into Eq.(3.34), leading to the strong form written in terms of displacements $\boldsymbol{u}$ and pressures p as

$$\begin{aligned} \boldsymbol{S}^T\boldsymbol{C}^{dev}\boldsymbol{S}\boldsymbol{u} + \boldsymbol{G}p + \boldsymbol{f} &= \boldsymbol{0} \\ \boldsymbol{G}^T\boldsymbol{u} - \frac{p}{K} &= 0 \end{aligned} \tag{3.38}$$

3.2.2.2 *Weak form*

The variational form of the problem defined in Eq. (3.38) follows the same procedure described in Section 3.1.2.

First, the first equation of the strong form is premultiplied by a virtual displacement $\delta\boldsymbol{u}$ and integrated over the spatial domain, applying the divergence theorem in the two first terms. The boundary term is split in the Dirichlet and Neumann boundaries, $\Gamma = \Gamma_u \cup \Gamma_t$. The Dirichlet boundary terms vanish ($\delta\boldsymbol{u} = \boldsymbol{0}$) such that

$$\int_\Omega (\delta\boldsymbol{u}\boldsymbol{S})^T(\boldsymbol{C}^{dev}\boldsymbol{S}\boldsymbol{u})d\Omega + \int_\Omega \delta\boldsymbol{u}^T\boldsymbol{G}pd\Omega = \int_\Omega \delta\boldsymbol{u}^T\boldsymbol{f}d\Omega + \int_{\Gamma_t} \delta\boldsymbol{u}^T\bar{\boldsymbol{t}}d\Gamma \qquad \forall\delta\boldsymbol{u} \tag{3.39}$$

Next, the second equation of the strong form is premultiplied by an arbitrary virtual pressure δp and integrated over the spatial domain

$$\int_\Omega (\delta p\boldsymbol{G})^T\boldsymbol{u}d\Omega - \int_\Omega \delta p^T\frac{p}{K}d\Omega = 0 \qquad \forall\delta p \tag{3.40}$$

The resulting weak form of the $\boldsymbol{u}/p$ formulation is

$$\begin{aligned} \textstyle\int_\Omega(\delta\boldsymbol{u}\boldsymbol{S})^T(\boldsymbol{C}^{dev}\boldsymbol{S}\boldsymbol{u})d\Omega + \int_\Omega \delta\boldsymbol{u}^T\boldsymbol{G}pd\Omega = W(\delta\boldsymbol{u}) \qquad \forall\delta\boldsymbol{u} \\ \textstyle\int_\Omega(\delta p\boldsymbol{G})^T\boldsymbol{u}d\Omega - \int_\Omega \delta p^T\frac{p}{K}d\Omega = 0 \qquad \forall\delta p \end{aligned} \tag{3.41}$$

Note that the system of equations (3.41) is symmetric. The solution to the solid mechanics problem is to find the displacements $\boldsymbol{u}$ and pressure p that verify the system of Eq. (3.41) in compliance with the boundary condition $\boldsymbol{u} = \boldsymbol{0}$ on Γ_u, given an arbitrary virtual displacement $\delta\boldsymbol{u}$, which vanishes on Γ_u and an arbitrary virtual pressure δp.

3.2.2.3 *FE approximation*

The continuous domain of the problem needs to be discretized in a FE partition in a way that $\Omega = \cup\Omega_e$. Additionally, the FE approximations of the displacement $\boldsymbol{u}$ and the pressure p are taken as

$$\begin{aligned} \boldsymbol{u} &\doteq \hat{\boldsymbol{u}} = \boldsymbol{N}_u\mathbf{U} \\ p &\doteq \hat{p} = \boldsymbol{N}_p\mathbf{P} \end{aligned} \tag{3.42}$$

where $\mathbf{U}$ and $\mathbf{P}$ are the vectors containing the nodal displacements and pressures of the FE mesh, respectively. Furthermore, the matrices $\boldsymbol{N}_u$ and $\boldsymbol{N}_p$ are the FE interpolation functions adopted.

Similarly, applying the Galerkin method, the discrete virtual displacements $\delta\mathbf{U}$ and discrete virtual pressure $\delta\mathbf{P}$ approximations are given as

$$\begin{aligned}\delta\boldsymbol{u} \doteq \delta\hat{\boldsymbol{u}} &= \boldsymbol{N}_u\delta\mathbf{U}\\ \delta p \doteq \delta\hat{p} &= \boldsymbol{N}_p\delta\mathbf{P}\end{aligned} \tag{3.43}$$

Now, introducing the FE approximations defined in Eqs. (3.42) and (3.43) into the weak form of the $\boldsymbol{u}/p$ formulation in Eq. (3.41), the system of equations becomes

$$\begin{aligned}&\int_\Omega(\boldsymbol{N}_u\delta\mathbf{U}\boldsymbol{S})^T(\boldsymbol{C}^{dev}\boldsymbol{S}\boldsymbol{N}_u\mathbf{U})d\Omega + \int_\Omega(\boldsymbol{N}_u\delta\mathbf{U})^T\boldsymbol{G}\boldsymbol{N}_p\mathbf{P}d\Omega = \hat{W}(\delta\mathbf{U}) \qquad \forall\delta\mathbf{U}\\ &\int_\Omega(\boldsymbol{N}_p\delta\mathbf{P}\boldsymbol{G})^T\boldsymbol{N}_u\mathbf{U}d\Omega - \int_\Omega(\boldsymbol{N}_p\delta\mathbf{P})^T\tfrac{\boldsymbol{N}_p\mathbf{P}}{K}d\Omega = 0 \qquad \forall\delta\mathbf{P}\end{aligned} \tag{3.44}$$

Eq. (3.44) can be simplified by taking into account the equality $\boldsymbol{B}_u = \boldsymbol{N}_u\boldsymbol{S}$; therefore, the FE approximation can be written as

$$\begin{aligned}&\int_\Omega(\boldsymbol{B}_u\delta\mathbf{U})^T(\boldsymbol{C}^{dev}\boldsymbol{B}_u\mathbf{U})d\Omega + \int_\Omega(\boldsymbol{N}_u\delta\mathbf{U})^T\boldsymbol{G}\boldsymbol{N}_p\mathbf{P}d\Omega = \int_\Omega(\boldsymbol{N}_u\delta\mathbf{U})^T\boldsymbol{f}d\Omega + \int_{\Gamma_t}(\boldsymbol{N}_u\delta\mathbf{U})^T\bar{\boldsymbol{t}}d\Gamma \qquad \forall\delta\mathbf{U}\\ &\int_\Omega(\boldsymbol{N}_p\delta\mathbf{P}\boldsymbol{G})^T\boldsymbol{N}_u\mathbf{U}d\Omega - \int_\Omega(\boldsymbol{N}_p\delta\mathbf{P})^T\tfrac{\boldsymbol{N}_p\mathbf{P}}{K}d\Omega = 0 \qquad \forall\delta\mathbf{P}\end{aligned} \tag{3.45}$$

The virtual displacements $\delta\mathbf{U}$ and virtual pressure $\delta\mathbf{P}$ are arbitrary, thus the system of equations in Eq. (3.45) can be written in matrix format as

$$\begin{bmatrix}\boldsymbol{K}_{UU}^{dev} & \boldsymbol{K}_{UP}\\ (\boldsymbol{K}_{UP})^T & -\boldsymbol{M}_{PP}\end{bmatrix}\begin{bmatrix}\mathbf{U}\\ \mathbf{P}\end{bmatrix} = \begin{bmatrix}\mathbf{F}\\ \mathbf{0}\end{bmatrix} \tag{3.46}$$

where $[\mathbf{U}\ \mathbf{P}]^T$ is the array of nodal values of displacements and pressure and the terms given in Eq. (3.46) are defined as

$$\boldsymbol{K}_{UU}^{dev} = \int_\Omega \boldsymbol{B}_u^T\boldsymbol{C}^{dev}\boldsymbol{B}_u d\Omega \tag{3.47}$$

$$\boldsymbol{K}_{UP} = \int_\Omega \boldsymbol{N}_u^T\boldsymbol{G}\boldsymbol{N}_p d\Omega \tag{3.48}$$

$$\boldsymbol{M}_{PP} = \int_\Omega \boldsymbol{N}_p^T\frac{1}{K}\boldsymbol{N}_p d\Omega \tag{3.49}$$

and

$$\mathbf{F} = \int_\Omega \boldsymbol{N}_u^T\boldsymbol{f}d\Omega + \int_{\Gamma_t}\boldsymbol{N}_u^T\bar{\boldsymbol{t}}d\Gamma \tag{3.50}$$

3.2.2.4 *Variational Multi-Scale Stabilization*

In this thesis, the mixed approximation adopts linear FE interpolation for all the fields involved, which does not comply with the stability conditions (Babuska, 1971; Brezzi, 1974; Babuska et al., 1975).

On the one hand, this approach is preferrable due to its simplicity in the implementation and formulation of the FE, rather than adopting exotic interpolations or introducing additional difficulties in the implementation (Arnold et al., 1984a; Lewis and Schrefler, 1987; Jha and Juanes, 2007; White and Borja, 2008; Gavagnin et al., 2020). On the other hand, it requires stabilization to circumvent the Inf-Sup conditions and the VMS method is employed.

In this context, the VMS stabilization (Hughes, 1995; Hughes et al., 1998; Codina, 2000; Codina and Blasco, 2000) is chosen. The method consists in enriching the FE approxiamtion with a fine scale $\tilde{\boldsymbol{u}}$, namely the sub-grid scale. The new components introduced in the FE approximations are not solved by the original FE coarse scale $\boldsymbol{u}_h$. The sub-grid scale terms are computed from the residuals of the discrete solution. In this way, the continuous displacements $\boldsymbol{u}$ and pressure p are approximated by the new enhanced displacements $\hat{\boldsymbol{u}}$ and pressure $\hat{p}$ approximations, such that

$$\begin{aligned} \boldsymbol{u} \doteq \hat{\boldsymbol{u}} &= \boldsymbol{u}_h + \tilde{\boldsymbol{u}} \\ p \doteq \hat{p} &= p_h + \tilde{p} \end{aligned} \tag{3.51}$$

where $\tilde{\boldsymbol{u}}$ and $\tilde{p}$ are the sub-grid scales of the displacements and the pressure, respectively.

The residual-based nature of the VMS approach defines the sub-grid terms, as

$$\begin{aligned} \tilde{\boldsymbol{u}} &= \tau_u [\boldsymbol{S}^T \boldsymbol{C}^{dev} \boldsymbol{S} \boldsymbol{u}_h + \boldsymbol{G} p_h + \boldsymbol{f}] \\ \tilde{p} &= \tau_p [\boldsymbol{G}^T \boldsymbol{u}_h - \frac{p_h}{K}] \end{aligned} \tag{3.52}$$

where τ_u and τ_p are the stabilization parameters.

Optimal convergence rates can be achieved by choosing the stabilization parameters (Cervera et al., 2010a; Chiumenti et al., 2021) as

$$\begin{aligned} \tau_u &= c_u \frac{h_e^2}{2\tilde{G}} \\ \tau_p &= \frac{2c_p}{3} \tilde{G} (\frac{1+\nu}{1-\nu}) \frac{h_e}{L_0} \end{aligned} \tag{3.53}$$

with c_u and c_p being arbitrary stabilization constants, such that $0 \leqslant c_u \leqslant 1$ and $0 \leqslant c_p \leqslant 1$, $\tilde{G}$ is the effective secant shear modulus, ν is the Poisson ratio, h_e is the size of the FE and L_0 is the characteristic length of the problem. Note that, upon mesh refinement, the contribution of the sub-grid scales vanish ($\tilde{\boldsymbol{u}} \to 0$ and $\tilde{p} \to 0$).

Likewise, the virtual displacements $\delta\boldsymbol{u}$ and pressure δp are enriched by the sub-grid finer scales, yielding the following

$$\begin{aligned} \delta\boldsymbol{u} \doteq \delta\hat{\boldsymbol{u}} &= \delta\boldsymbol{u}_h + \delta\tilde{\boldsymbol{u}} \\ \delta p \doteq \delta\hat{p} &= \delta p_h + \delta\tilde{p} \end{aligned} \tag{3.54}$$

Subsequently, the discrete stabilized FE approximation are obtained by using Eqs. (3.51 - 3.53) and the FE interpolation to Eq. (3.41), such that

$$\begin{aligned} \int_\Omega (\boldsymbol{B}_u \delta\mathbf{U})^T (\boldsymbol{C}^{dev} \boldsymbol{B}_u \mathbf{U}) d\Omega + \tau_p \int_\Omega \boldsymbol{N}_u \boldsymbol{G} (\boldsymbol{G}\boldsymbol{N}_u)^T \mathbf{U} d\Omega + (1 - \tfrac{\tau_p}{K}) \int_\Omega (\boldsymbol{N}_u \delta\mathbf{U})^T \boldsymbol{G}\boldsymbol{N}_p \mathbf{P} d\Omega = \\ \hat{W}(\delta\mathbf{U}) \qquad \forall \delta\mathbf{U} \end{aligned}$$

$$\begin{aligned} (1 - \tfrac{\tau_p}{K}) \int_\Omega (\boldsymbol{N}_p \delta\mathbf{P} \boldsymbol{G})^T \boldsymbol{N}_u \mathbf{U} d\Omega - (1 - \tfrac{p}{K}) \int_\Omega \boldsymbol{N}_p \delta\mathbf{P} \frac{\boldsymbol{N}_p \mathbf{P}}{K} d\Omega + \\ -\tau_u \int_\Omega (\boldsymbol{N}_p \boldsymbol{G})^T \boldsymbol{G}\boldsymbol{N}_p \mathbf{P} d\Omega = 0 \qquad \forall \delta\mathbf{P} \end{aligned} \tag{3.55}$$

and $\delta\mathbf{U}$ and $\delta\mathbf{P}$ are arbitrary, thus the discrete stabilized FE system is written in matrix form as

$$\begin{bmatrix} \boldsymbol{K}_{UU}^{dev} + \tau_p \boldsymbol{K}_{UGG} & (1 - \tfrac{\tau_p}{K}) \boldsymbol{K}_{UP} \\ (1 - \tfrac{\tau_p}{K}) (\boldsymbol{K}_{UP})^T & -(1 - \tfrac{\tau_p}{K}) \boldsymbol{M}_{PP} - \tau_u \boldsymbol{K}_{PGG} \end{bmatrix} \begin{bmatrix} \mathbf{U} \\ \mathbf{P} \end{bmatrix} = \begin{bmatrix} \mathbf{F} \\ \mathbf{0} \end{bmatrix} \tag{3.56}$$

where $[\mathbf{U}\ \mathbf{P}]^T$ is the array of nodal values of displacements and pressure and the additional terms given in Eq. (3.56) are defined as

$$\boldsymbol{K}_{UGG} = \int_\Omega \boldsymbol{N}_u \boldsymbol{G} (\boldsymbol{G}\boldsymbol{N}_u)^T d\Omega \tag{3.57}$$

$$\boldsymbol{K}_{PGG} = \int_\Omega (\boldsymbol{N}_p \boldsymbol{G})^T \boldsymbol{G}\boldsymbol{N}_p d\Omega \tag{3.58}$$

3.3 Enhanced stress/strain accuracy

The $\boldsymbol{u}/p$ formulation shows an enhanced solution of the pressure field, nevertheless the total strains are still piece-wise constant and discontinuous among elements. The following step is to design a FE formulation with enhanced stress/strain accuracy for nonlinear solid mechanics problems.

3.3.1 *The $\boldsymbol{u}/\boldsymbol{e}/p$ formulation*

The forthcoming development is an extension of the $\boldsymbol{u}/\boldsymbol{s}/p$ (Chiumenti et al., 2015) suitable for strain-driven nonlinear constitutive laws.

3.3.1.1 *Strong form*

The Cauchy equation is written in terms of displacements, deviatoric-strains and pressure introducing Eq.(3.35) into Eq. (3.36), such that

$$\boldsymbol{S}^T\boldsymbol{C}^{dev}\boldsymbol{e} + \boldsymbol{G}p + \boldsymbol{f} = \boldsymbol{0} \tag{3.59}$$

The mixed $\boldsymbol{u}/\boldsymbol{e}/p$ strong form of the solid mechanics problem is then obtained by adding the constitutive relation in Eq. (3.38-b) and the displacement/deviatoric-strain kinematic relation in Eq. (3.23)

$$\begin{aligned} \boldsymbol{S}^T\boldsymbol{C}^{dev}\boldsymbol{e} + \boldsymbol{G}p + \boldsymbol{f} &= \boldsymbol{0} \\ \boldsymbol{W}\boldsymbol{u} - \boldsymbol{e} &= \boldsymbol{0} \\ \boldsymbol{G}^T\boldsymbol{u} - \frac{p}{K} &= 0 \end{aligned} \tag{3.60}$$

to be solved with the appropriate Dirichlet's and Neumann's boundary conditions.

3.3.1.2 *Weak form*

The variational form of the mixed $\boldsymbol{u}/\boldsymbol{e}/p$ problem is obtained as follows.

Firstly, Eq. (3.60-a) is premultiplied by a virtual displacement $\delta\boldsymbol{u}$ that is also conforming to the boundary conditions ($\delta\boldsymbol{u} = \boldsymbol{0}$ on Γ), integrated over the domain Ω:

$$\int_\Omega \delta\boldsymbol{u}^T\boldsymbol{S}^T\boldsymbol{C}^{dev}\boldsymbol{e}d\Omega + \int_\Omega \delta\boldsymbol{u}^T\boldsymbol{G}pd\Omega + \int_\Omega \delta\boldsymbol{u}^T\boldsymbol{f}d\Omega = \boldsymbol{0} \qquad \forall\delta\boldsymbol{u} \tag{3.61}$$

Secondly, the divergence theorem is used to the left-hand side in Eq. (3.61) and the boundary is split into the Neumann and Dirichlet boundaries, recalling that the Dirichlet boundary terms are null. Therefore, the Principle of Virtual Work is derived as follows

$$\int_\Omega \delta\boldsymbol{u}^T\boldsymbol{S}^T\boldsymbol{C}^{dev}\boldsymbol{e}d\Omega + \int_\Omega \delta\boldsymbol{u}^T\boldsymbol{G}pd\Omega = \underbrace{\int_\Omega \delta\boldsymbol{u}^T\boldsymbol{f}d\Omega + \int_{\Gamma_t} \delta\boldsymbol{u}^T\bar{\boldsymbol{t}}d\Gamma}_{W(\delta\boldsymbol{u})} \qquad \forall\delta\boldsymbol{u} \tag{3.62}$$

where $W(\delta\boldsymbol{u})$ is the virtual work performed by the body forces $\boldsymbol{f}$ and traction $\bar{\boldsymbol{t}}$ and the left-hand side is the virtual work done by the internal forces.

Thirdly, Eq. (3.60-b) is premultiplied by an arbitrary virtual deviatoric-strain $\delta\boldsymbol{e}$ and integrated over the domain, resulting in

$$\int_\Omega \delta\boldsymbol{e}^T\boldsymbol{W}\boldsymbol{u}\,d\Omega - \int_\Omega \delta\boldsymbol{e}^T\boldsymbol{e}\,d\Omega = \boldsymbol{0} \qquad \forall\delta\boldsymbol{e} \tag{3.63}$$

The fourth-order operators identity ($\boldsymbol{I}_4$), volumetric ($\boldsymbol{V}$), deviatoric ($\boldsymbol{D}$) are introduced in Voigt's notation

$$\boldsymbol{I}_4 = \begin{bmatrix} 1 & 0 & 0 & 0 & 0 & 0 \\ 0 & 1 & 0 & 0 & 0 & 0 \\ 0 & 0 & 1 & 0 & 0 & 0 \\ 0 & 0 & 0 & 1 & 0 & 0 \\ 0 & 0 & 0 & 0 & 1 & 0 \\ 0 & 0 & 0 & 0 & 0 & 1 \end{bmatrix} \tag{3.64}$$

$$\boldsymbol{V} = \frac{1}{3}\boldsymbol{I}\boldsymbol{I}^T = \frac{1}{3}\begin{bmatrix} 1 & 1 & 1 & 0 & 0 & 0 \\ 1 & 1 & 1 & 0 & 0 & 0 \\ 1 & 1 & 1 & 0 & 0 & 0 \\ 0 & 0 & 0 & 0 & 0 & 0 \\ 0 & 0 & 0 & 0 & 0 & 0 \\ 0 & 0 & 0 & 0 & 0 & 0 \end{bmatrix} \tag{3.65}$$

$$\boldsymbol{D} = \boldsymbol{I_4} - \boldsymbol{V} = \frac{1}{3}\begin{bmatrix} 2 & -1 & -1 & 0 & 0 & 0 \\ -1 & 2 & -1 & 0 & 0 & 0 \\ -1 & -1 & 2 & 0 & 0 & 0 \\ 0 & 0 & 0 & 3 & 0 & 0 \\ 0 & 0 & 0 & 0 & 3 & 0 \\ 0 & 0 & 0 & 0 & 0 & 3 \end{bmatrix} \tag{3.66}$$

Eq. (3.35) can now be rewritten using the fourth-order deviatoric operator $\boldsymbol{D}$ as

$$\boldsymbol{s} = \boldsymbol{C}^{dev}\boldsymbol{e} = \boldsymbol{D}\boldsymbol{C}\boldsymbol{e} = 2G\boldsymbol{D}\boldsymbol{e} = 2G\boldsymbol{e} \tag{3.67}$$

where G is the secant shear modulus. The following relations are satisfied using the fourth-order deviatoric operator $\boldsymbol{D}$

$$\boldsymbol{C}^{dev}\boldsymbol{D} = \boldsymbol{C}^{dev} \tag{3.68}$$

$$\boldsymbol{W} = \boldsymbol{D}\boldsymbol{S} \tag{3.69}$$

$$\boldsymbol{D}\boldsymbol{e} = \boldsymbol{e} \tag{3.70}$$

In the following, Eq. (3.63) is premultiplied by $\boldsymbol{C}^{dev}$

$$\int_\Omega \delta\boldsymbol{e}^T\boldsymbol{C}^{dev}\boldsymbol{W}\boldsymbol{u}\, d\Omega - \int_\Omega \delta\boldsymbol{e}^T\boldsymbol{C}^{dev}\boldsymbol{e}\, d\Omega = \boldsymbol{0} \qquad \forall\delta\boldsymbol{e} \tag{3.71}$$

Now, applying the relations in Eqs. (3.68)-(3.70), the weak form of the deviatoric constitutive equation becomes

$$\int_\Omega \delta\boldsymbol{e}^T[\boldsymbol{C}^{dev}(\boldsymbol{S}\boldsymbol{u})]d\Omega - \int_\Omega \delta\boldsymbol{e}^T(\boldsymbol{C}^{dev}\boldsymbol{e})d\Omega = \boldsymbol{0} \qquad \forall\delta\boldsymbol{e} \tag{3.72}$$

Finally, Eq. (3.60-c) is premultiplied by an arbitrary virtual pressure δp and integrate over the spatial domain:

$$\int_\Omega (\delta p\boldsymbol{G})^T\boldsymbol{u}d\Omega - \int_\Omega \delta p^T\frac{p}{K}d\Omega = 0 \qquad \forall\delta p \tag{3.73}$$

Hence, the resulting weak form of the mixed $\boldsymbol{u}/\boldsymbol{e}/p$ problem is given by:

$$\begin{aligned} &\textstyle\int_\Omega(\delta\boldsymbol{u}\boldsymbol{S})^T\boldsymbol{C}^{dev}\boldsymbol{e}d\Omega + \int_\Omega \delta\boldsymbol{u}^T\boldsymbol{G}pd\Omega = W(\delta\boldsymbol{u}) \quad \forall\delta\boldsymbol{u} \\ &\textstyle\int_\Omega \delta\boldsymbol{e}^T[\boldsymbol{C}^{dev}(\boldsymbol{S}\boldsymbol{u})]d\Omega - \int_\Omega \delta\boldsymbol{e}^T(\boldsymbol{C}^{dev}\boldsymbol{e})d\Omega = \boldsymbol{0} \quad \forall\delta\boldsymbol{e} \\ &\textstyle\int_\Omega(\delta p\boldsymbol{G})^T\boldsymbol{u}d\Omega - \int_\Omega \delta p^T\frac{p}{K}d\Omega = 0 \qquad \forall\delta p \end{aligned} \tag{3.74}$$

Note that the system of equations (3.74) is symmetric. The solution to the mixed $\boldsymbol{u}/\boldsymbol{e}/p$ problem is to find the displacements $\boldsymbol{u}$, the deviatoric-strains $\boldsymbol{e}$ and pressure p that verify the system of Eq. (3.74) in compliance with the boundary condition $\boldsymbol{u} = \boldsymbol{0}$ on Γ_u, given an arbitrary virtual displacement $\delta\boldsymbol{u}$, which vanishes on Γ_u, an arbitrary virtual deviatoric-strain $\delta\boldsymbol{e}$ and an arbitrary virtual pressure δp.

3.3.1.3 *FE approximation*

The discretezed version of the problem is obtained by dividing the continuous domain into FE partitions, such that $\Omega = \cup\Omega_e$. The continuous displacements $\boldsymbol{u}$, deviatoric-strains $\boldsymbol{e}$ and pressure p are replaced by the discrete FE approximations

$$\begin{aligned} \boldsymbol{u} &\doteq \hat{\boldsymbol{u}} = \boldsymbol{N}_u \mathbf{U} \\ \boldsymbol{e} &\doteq \hat{\boldsymbol{e}} = \boldsymbol{N}_e \mathbf{E} \\ p &\doteq \hat{p} = \boldsymbol{N}_p \mathbf{P} \end{aligned} \tag{3.75}$$

$\mathbf{U}$, $\mathbf{E}$ and $\mathbf{P}$ are the vectors of nodal values of the displacements, deviatoric-strains and pressure, respectively, and their corresponding matrices containing the FE interpolation functions are $\boldsymbol{N}_u$, $\boldsymbol{N}_e$ and $\boldsymbol{N}_p$.

Applying the Galerkin method, the discrete virtual displacements $\delta\boldsymbol{u}$, virtual deviatoric-strains $\delta\boldsymbol{e}$ and virtual pressure δp approximations are taken as

$$\begin{aligned} \delta\boldsymbol{u} &\doteq \delta\hat{\boldsymbol{u}} = \boldsymbol{N}_u \delta\mathbf{U} \\ \delta\boldsymbol{e} &\doteq \delta\hat{\boldsymbol{e}} = \boldsymbol{N}_e \delta\mathbf{E} \\ \delta p &\doteq \delta\hat{p} = \boldsymbol{N}_p \delta\mathbf{P} \end{aligned} \tag{3.76}$$

Introducing the approximations in Eqs. (3.75) - (3.76) into the variational form of the $\boldsymbol{u}/\boldsymbol{e}/p$ in Eq. (3.74) and integrating over the spatial domain, results in

$$\begin{aligned} &\int_\Omega (\boldsymbol{S}\boldsymbol{N}_u \delta\mathbf{U})^T \boldsymbol{C}^{dev} \boldsymbol{N}_e \mathbf{E} d\Omega + \int_\Omega (\boldsymbol{N}_u \delta\mathbf{U})^T \boldsymbol{G} \boldsymbol{N}_p \mathbf{P} d\Omega = \hat{W}(\delta\mathbf{U}) \quad \forall \delta\mathbf{U} \\ &\int_\Omega (\boldsymbol{N}_e \delta\mathbf{E})^T [\boldsymbol{C}^{dev} (\boldsymbol{S}\boldsymbol{N}_u \mathbf{U})] d\Omega - \int_\Omega (\boldsymbol{N}_e \delta\mathbf{E})^T (\boldsymbol{C}^{dev} \boldsymbol{N}_e \mathbf{E}) d\Omega = \mathbf{0} \quad \forall \delta\mathbf{E} \\ &\int_\Omega (\boldsymbol{N}_p \boldsymbol{G} \delta\mathbf{P})^T \boldsymbol{N}_u \mathbf{U} d\Omega - \int_\Omega (\boldsymbol{N}_p \delta\mathbf{P})^T \tfrac{\boldsymbol{N}_p \mathbf{P}}{K} d\Omega = 0 \quad \forall \delta\mathbf{P} \end{aligned} \tag{3.77}$$

The virtual displacements $\delta\mathbf{U}$, virtual deviatoric-strains $\delta\mathbf{E}$ and virtual pressure $\delta\mathbf{P}$ are arbitrary and $\boldsymbol{S}\boldsymbol{N}_u = \boldsymbol{B}_u$, thus the Eq. (3.77) is rewritten as

$$\begin{aligned} &\int_\Omega \boldsymbol{B}_u^T \boldsymbol{C}^{dev} \boldsymbol{N}_e \mathbf{E} d\Omega + \int_\Omega \boldsymbol{N}_u^T \boldsymbol{G} \boldsymbol{N}_p \mathbf{P} d\Omega = \mathbf{F} \\ &\int_\Omega \boldsymbol{N}_e^T [\boldsymbol{C}^{dev} \boldsymbol{B}_u \mathbf{U}] d\Omega - \int_\Omega \boldsymbol{N}_e^T (\boldsymbol{C}^{dev} \boldsymbol{N}_e \mathbf{E}) d\Omega = \mathbf{0} \\ &\int_\Omega (\boldsymbol{N}_p \boldsymbol{G})^T \boldsymbol{N}_u \mathbf{U} d\Omega - \int_\Omega \boldsymbol{N}_p^T \tfrac{\boldsymbol{N}_p \mathbf{P}}{K} d\Omega = 0 \end{aligned} \tag{3.78}$$

The algebraic system of Eq. (3.78) can be rewritten in matrix format as

$$\begin{bmatrix} \mathbf{0} & \boldsymbol{K}_{UE} & \boldsymbol{K}_{UP} \\ (\boldsymbol{K}_{UE})^T & -\boldsymbol{M}_{EE} & \mathbf{0} \\ (\boldsymbol{K}_{UP})^T & \mathbf{0} & -\boldsymbol{M}_{PP} \end{bmatrix} \begin{bmatrix} \mathbf{U} \\ \mathbf{E} \\ \mathbf{P} \end{bmatrix} = \begin{bmatrix} \mathbf{F} \\ \mathbf{0} \\ \mathbf{0} \end{bmatrix} \tag{3.79}$$

where $[\mathbf{U}\ \mathbf{E}\ \mathbf{P}]^T$ is the array of nodal values of displacements, deviatoric-strains and pressure and the new terms are

$$\boldsymbol{M}_{EE} = \int_\Omega \boldsymbol{N}_e^T \boldsymbol{C}^{dev} \mathbf{N}_e d\Omega \tag{3.80}$$

$$\boldsymbol{K}_{UE} = \int_\Omega \boldsymbol{B}_u^T \boldsymbol{C}^{dev} \boldsymbol{N}_e d\Omega \tag{3.81}$$

3.3.1.4 *Variational Multi-Scale Stabilization*

Using now the VMS method, the continuous fields are approximated by

$$\begin{aligned} \boldsymbol{u} \doteq \hat{\boldsymbol{u}} &= \boldsymbol{u}_h + \tilde{\boldsymbol{u}} \\ \boldsymbol{e} \doteq \hat{\boldsymbol{e}} &= \boldsymbol{e}_h + \tilde{\boldsymbol{e}} \\ p \doteq \hat{p} &= p_h + \tilde{p} \end{aligned} \tag{3.82}$$

The same procedure is applied to the discrete virtual displacements $\delta\boldsymbol{u}$, virtual deviatoric-strains $\delta\boldsymbol{e}$ and virtual pressure δp as follows

$$\begin{aligned} \delta\boldsymbol{u} \doteq \delta\hat{\boldsymbol{u}} &= \delta\boldsymbol{u}_h + \delta\tilde{\boldsymbol{u}} \\ \delta\boldsymbol{e} \doteq \delta\hat{\boldsymbol{e}} &= \delta\boldsymbol{e}_h + \delta\tilde{\boldsymbol{e}} \\ \delta p \doteq \delta\hat{p} &= \delta p_h + \delta\tilde{p} \end{aligned} \tag{3.83}$$

The variational form in Eq. (3.74) is rewritten including the subg-grid scale terms, such that the resulting weak form of the mixed $\boldsymbol{u}/\boldsymbol{e}/p$ problem is given by

$$\begin{aligned}
&\int_\Omega [\boldsymbol{S}\delta\boldsymbol{u}_h]^T(\boldsymbol{C}^{dev}\boldsymbol{e}_h)d\Omega + \int_\Omega [\boldsymbol{S}\delta\boldsymbol{u}_h]^T(\boldsymbol{C}^{dev}\tilde{\boldsymbol{e}})d\Omega + \int_\Omega \delta\boldsymbol{u}_h{}^T(\boldsymbol{G}p_h)d\Omega + \\
&\quad + \int_\Omega \delta\boldsymbol{u}_h^T(\boldsymbol{G}\tilde{p})d\Omega = W(\delta\boldsymbol{u}_h) && \forall\delta\boldsymbol{u}_h \quad (a) \\
&\int_\Omega \delta\boldsymbol{e}_h^T[\boldsymbol{C}^{dev}\boldsymbol{S}\boldsymbol{u}_h]d\Omega + \int_\Omega \delta\boldsymbol{e}_h^T[\boldsymbol{C}^{dev}\boldsymbol{S}\tilde{\boldsymbol{u}}]d\Omega + \\
&\quad - \int_\Omega \delta\boldsymbol{e}_h^T\boldsymbol{C}^{dev}\boldsymbol{e}_h d\Omega - \int_\Omega \delta\boldsymbol{e}_h^T\boldsymbol{C}^{dev}\tilde{\boldsymbol{e}}d\Omega = \boldsymbol{0} && \forall\delta\boldsymbol{e}_h \quad (b) \\
&\int_\Omega \delta p_h^T(\boldsymbol{G}^T\boldsymbol{u}_h)d\Omega + \int_\Omega \delta p_h^T(\boldsymbol{G}^T\tilde{\boldsymbol{u}})d\Omega - \int_\Omega \delta p_h^T\frac{p_h}{K}d\Omega - \int_\Omega \delta p_h^T\frac{\tilde{p}}{K}d\Omega = 0 && \forall\delta p_h \quad (c) \\
&\int_\Omega [\boldsymbol{S}\delta\tilde{\boldsymbol{u}}]^T(\boldsymbol{C}^{dev}\boldsymbol{e}_h)d\Omega + \int_\Omega [\boldsymbol{S}\delta\tilde{\boldsymbol{u}}]^T(\boldsymbol{C}^{dev}\tilde{\boldsymbol{e}})d\Omega + \int_\Omega \delta\tilde{\boldsymbol{u}}^T(\boldsymbol{G}p_h)d\Omega + \\
&\quad + \int_\Omega \delta\tilde{\boldsymbol{u}}^T(\boldsymbol{G}\tilde{p})d\Omega = W(\delta\tilde{\boldsymbol{u}}) && \forall\delta\tilde{\boldsymbol{u}} \quad (d) \\
&\int_\Omega \delta\tilde{\boldsymbol{e}}^T[\boldsymbol{C}^{dev}\boldsymbol{S}\boldsymbol{u}_h]d\Omega + \int_\Omega \delta\tilde{\boldsymbol{e}}^T[\boldsymbol{C}^{dev}\boldsymbol{S}\tilde{\boldsymbol{u}}]d\Omega + \\
&\quad - \int_\Omega \delta\tilde{\boldsymbol{e}}^T\boldsymbol{C}^{dev}\boldsymbol{e}_h d\Omega - \int_\Omega^T \delta\tilde{\boldsymbol{e}}^T\boldsymbol{C}^{dev}\tilde{\boldsymbol{e}}d\Omega = \boldsymbol{0} && \forall\delta\tilde{\boldsymbol{e}} \quad (e) \\
&\int_\Omega \delta\tilde{p}^T(\boldsymbol{G}^T\boldsymbol{u}_h)d\Omega + \int_\Omega \delta\tilde{p}^T(\boldsymbol{G}^T\tilde{\boldsymbol{u}})d\Omega - \int_\Omega \delta\tilde{p}^T\frac{p_h}{K}d\Omega - \int_\Omega \delta\tilde{p}^T\frac{\tilde{p}}{K}d\Omega = 0 && \forall\delta\tilde{p} \quad (f)
\end{aligned} \tag{3.84}$$

The residual-based sub-grid solution in the variational form, presented in the system of equations Eq. [3.84(d)-3.84(f)], are assumed as

$$\begin{aligned} \tilde{\mathbf{u}} &= \tau_u[\mathbf{S}^T(\mathbf{C}^{dev}\mathbf{e}_h) + \mathbf{G}p_h + \mathbf{f}] \\ \tilde{\mathbf{e}} &= \tau_e[\mathbf{W}\mathbf{u}_h - \mathbf{e}_h] \\ \tilde{p} &= \tau_p[\mathbf{G}^T\mathbf{u}_h - \frac{p_h}{K}] \end{aligned} \tag{3.85}$$

τ_u, τ_e and τ_p are the stabilization parameters.

In order to obtain optimum convergence rates upon mesh refinement, the stabilization parameters need to be chosen as (Badia and Codina, 2009; Castillo and Codina, 2014):

$$\begin{aligned} \tau_u &= \frac{c_u h_e L_0}{2\tilde{C}^{dev}} \\ \tau_e &= c_e\frac{h_e}{L_0} \\ \tau_p &= c_p C^{vol}\frac{h_e}{L_0} \end{aligned} \tag{3.86}$$

where L_0 is a characteristic length of the problem, c_u, c_e and c_p are arbitrary stabilization constants, h_e is the FE size and $\tilde{C}^{dev}$ is the secant shear modulus defined as

$$\tilde{C}^{dev} = \frac{\|\mathbf{s}_h\|}{2\,\|\mathbf{e}_h\|} \tag{3.87}$$

and $\tilde{K}$ is the compressibility modulus computed from the Fourier analysis (Badia and Codina (2009)), such that:

$$C^{vol} = \left(\frac{c_1}{2\tilde{G}} + \frac{c_2}{\tilde{K}} \right)^{-1} \tag{3.88}$$

where $\tilde{G}$ and $\tilde{K}$ are the *effective secant shear modulus* and *effective bulk modulus*, respectively. The constants c_1 and c_2 are arbitrary, but $\mathcal{O}(1)$; thus choosing them conveniently as $c_1 = 1$ and $c_2 = \frac{2}{3}$, C^{vol} can be written in terms of $\tilde{G}$ as

$$C^{vol} = \frac{2}{3}\tilde{G}\left(\frac{1+\nu}{1-\nu} \right) \tag{3.89}$$

Note that, upon mesh refinement ($h_e \to 0$), the stabilization terms in Eq. (3.86) tend to zero.

Next, the residual-based solution presented in Eqs. (3.86) is introduced to the discrete variational form of Eqs. [3.84(a)-3.84(c)] together with the FE approximations in Eqs. (3.75 - 3.76), resulting in

$$\begin{aligned}
&(1-\tau_e)\int_\Omega (\delta\mathbf{U}^T \underbrace{\boldsymbol{N}_u^T \boldsymbol{S}^T}_{=\boldsymbol{B}_u^T})(\boldsymbol{C}^{dev}\boldsymbol{N}_e\mathbf{E})d\Omega + \tau_e \int_\Omega (\delta\mathbf{U}^T \underbrace{\boldsymbol{N}_u^T \boldsymbol{S}^T}_{=\boldsymbol{B}_u^T})(\boldsymbol{C}^{dev}\underbrace{\boldsymbol{S}\boldsymbol{N}_u}_{=\boldsymbol{B}_u}\mathbf{U})d\Omega + \\
&+(1-\tfrac{\tau_p}{K})\int_\Omega \delta\mathbf{U}^T\boldsymbol{N}_u^T\boldsymbol{G}\boldsymbol{N}_p\mathbf{P}d\Omega + \tau_p\int_\Omega \delta\mathbf{U}^T\boldsymbol{N}_u^T\boldsymbol{G}\boldsymbol{G}^T\boldsymbol{N}_u\mathbf{U}d\Omega = \hat{W}(\delta\mathbf{U}) \qquad \forall\delta\mathbf{U} \\
&(1-\tau_e)\int_\Omega \delta\mathbf{E}^T\boldsymbol{N}_e^T[\boldsymbol{C}^{dev}(\underbrace{\boldsymbol{S}\boldsymbol{N}_u}_{=\boldsymbol{B}_u}\mathbf{U})]d\Omega - \tau_u\int_\Omega(\delta\mathbf{E}^T\boldsymbol{N}_e^T\boldsymbol{S}\boldsymbol{C}^{dev})(\boldsymbol{C}^{dev}\boldsymbol{S}^T\boldsymbol{N}_e\boldsymbol{E})d\Omega \qquad \forall\delta\mathbf{E} \\
&-\tau_u\int_\Omega(\delta\mathbf{E}^T\boldsymbol{N}_e^T\boldsymbol{S})[\boldsymbol{C}^{dev}(\boldsymbol{G}\boldsymbol{N}_p\mathbf{P})]d\Omega - (1-\tau_e)\int_\Omega \delta\mathbf{E}^T\boldsymbol{N}_e^T\boldsymbol{C}^{dev}\boldsymbol{N}_e\mathbf{E}d\Omega = \mathbf{0} \\
&(1-\tfrac{\tau_p}{K})\int_\Omega \delta\mathbf{P}^T\boldsymbol{N}_p^T(\boldsymbol{G}^T\boldsymbol{N}_u\boldsymbol{U})d\Omega - \tau_u\int_\Omega(\delta\mathbf{P}^T\boldsymbol{N}_p^T\boldsymbol{G}^T)(\boldsymbol{C}^{dev}\boldsymbol{S}^T\boldsymbol{N}_e\mathbf{E})d\Omega + \\
&-\tau_u\int_\Omega(\delta\mathbf{P}^T\boldsymbol{N}_p^T\boldsymbol{G}^T)(\boldsymbol{G}\boldsymbol{N}_p\mathbf{P})d\Omega - (1-\tfrac{\tau_p}{K})\int_\Omega \delta\mathbf{P}^T\boldsymbol{N}_p^T\tfrac{\boldsymbol{N}_p\mathbf{P}}{K}d\Omega = 0 \qquad \forall\delta\mathbf{P}
\end{aligned} \tag{3.90}$$

The virtual displacements, virtual deviatoric-strains and virtual pressure are arbitrary; this leads to the stabilized FE system of equations:

$$\begin{bmatrix}
\tau_e\boldsymbol{K}_{UU}^{dev} + \tau_p\bar{\boldsymbol{K}}_{UGG} & (1-\tau_e)\boldsymbol{K}_{UE} & (1-\tfrac{\tau_p}{K})\boldsymbol{K}_{UP} \\
(1-\tau_e)(\boldsymbol{K}_{UE})^T & -(1-\tau_e)\boldsymbol{M}_{EE} - \tau_u\boldsymbol{K}_{EE} & -\tau_u\boldsymbol{K}_{EP} \\
(1-\tfrac{\tau_p}{K})(\boldsymbol{K}_{UP})^T & -\tau_u(\boldsymbol{K}_{EP})^T & -(1-\tfrac{\tau_p}{K})\boldsymbol{M}_{PP} - \tau_u\boldsymbol{K}_{PGG}
\end{bmatrix}
\begin{bmatrix} \mathbf{U} \\ \mathbf{E} \\ \mathbf{P} \end{bmatrix} =
\begin{bmatrix} \mathbf{F} \\ \mathbf{0} \\ \mathbf{0} \end{bmatrix} \tag{3.91}$$

where $[\mathbf{U}\ \mathbf{E}\ \mathbf{P}]^T$ is the array of nodal values of the displacements, deviatoric-strains and pressure and the new terms displayed in Eq. (3.91) are

$$\bar{\boldsymbol{K}}_{UGG} = \int_\Omega \boldsymbol{N}_u^T\boldsymbol{G}\boldsymbol{G}^T\boldsymbol{N}_u d\Omega \tag{3.92}$$

$$\boldsymbol{K}_{EE} = \int_\Omega (\boldsymbol{N}_e^T\boldsymbol{S}\boldsymbol{C}^{dev})(\boldsymbol{C}^{dev}\boldsymbol{S}^T\boldsymbol{N}_e)d\Omega \tag{3.93}$$

$$\boldsymbol{K}_{EP} = \int_\Omega (\boldsymbol{N}_e^T\boldsymbol{S}\boldsymbol{C}^{dev})(\boldsymbol{G}\boldsymbol{N}_p)d\Omega \tag{3.94}$$

4

THERMO-MECHANICAL MODELLING

In this chapter, thermo-mechanical modelling is addressed, aiming to the accurate description of the physical phenomena that occur during the AM process.

The thermo-mechanical coupling is performed in a staggered manner (Agelet de Saracibar et al., 1999, 2001; Chiumenti et al., 2013; Dialami et al., 2016, 2017), considering temperature-dependent properties in both the thermal and mechanical analyses.

The thermo-visco-plastic-elasto-plastic model is considered. An annealing temperature is used as a threshold between the visco-plastic model and the elasto-plastic model. (Bellet et al., 2003; Agelet de Saracibar et al., 1999; Cervera et al., 1999; Chiumenti et al., 2010, 2016; Zhang et al., 2018a).

The outline of the chapter is as follows. Section 4.1, the thermal analysis is described considering a DED manufacturing process. The time integration aspects and thermo-mechanical coupling are presented in Section 4.2. In Section 4.3, the phase-change and the annealing mechanism are introduced. Lastly, Section 4.4 and Section 4.5 present the elasto-plastic and visco-plastic models provided for the solid and liquid-like phases, respectively.

4.1 Thermal analysis

In this section, the strong and weak form of the thermal problem are presented followed by the FE approximation, the external heat source definition and the boundary conditions involved in the DED process.

4.1.1 *Strong form*

The strong form of the thermal problem is described by the energy balance equation written in terms of the temperature T

$$\dot{H} = -\nabla \cdot \boldsymbol{q} + \dot{r} \; on \; \Omega \tag{4.1}$$

where $\dot{H}$ is the rate of enthalpy, $\dot{r}$ represents the rate of heat source and $\mathbf{q}$, is the heat-flux computed according to the Fourier law

$$\mathbf{q} = -k\nabla T \tag{4.2}$$

with $k = k(T)$ being the temperature-dependent thermal conductivity of the material.

The enthalpy rate $\dot{H}$ in Eq. (4.1) can be rewritten in terms of the temperature rate $\dot{T}$ as

$$\dot{H} = \rho c \dot{T} \tag{4.3}$$

where $\rho = \rho(T)$ is the temperature-dependent material density and $c = c(T)$ is the temperature-dependent specific heat capacity of the material.

Introducing Eqs. (4.2)-(4.3) into Eq. (4.1), the strong form of the thermal problem becomes

$$\rho c \dot{T} - \nabla \cdot (k \nabla T) = \dot{r} \quad on \; \Omega \tag{4.4}$$

to be solved with the appropriate Dirichlet's and Neumann's boundary conditions.

4.1.2 *Weak form*

Introducing the test function δT and applying the divergence theorem to the second term on the righ-hand side of Eq. (4.4), yields the weak form of the thermal problem

$$\int_{\Omega}[\delta T(\rho c\dot{T})]d\Omega+\int_{\Omega}[k\nabla\delta T\cdot\nabla T]d\Omega=\int_{\Omega}[\delta T\dot{r}]d\Omega-\int_{\Gamma}[\delta T\bar{q}]d\Gamma \tag{4.5}$$

where $\bar{q}$ are the prescribed heat flux. Note that $\bar{q}=\mathbf{q}\cdot\mathbf{n}$, $\mathbf{n}$ being the normal vector to the free surface and the prescribed temperatures vanish at the boundary Γ.

The solution to the AM thermal problem is to find the temperature $T(t)\in H^1(\Omega(t))$ in $(t_0,t_f]$, that satisfies Eq. (4.5) together with the appropriate boundary conditions, where t_0 and t_f are the initial and final instant of the AM process, respectively.

The thermal problem is subjected to the initial conditions at instant $t_0=0$, such that the initial temperature field is defined as $T(\boldsymbol{x},t_0)=T_0(\boldsymbol{x})$.

4.1.3 *FE approximation*

The domain Ω is discretized in a FE partition such that $\Omega=\cup\Omega_e$. Th Galerkin method is employed to approximate the temperature and virtual temperature fields as

$$\begin{aligned}T&\doteq\hat{T}=\boldsymbol{N}_T\boldsymbol{T}\\ \delta T&\doteq\delta\hat{T}=\boldsymbol{N}_T\delta\boldsymbol{T}\end{aligned} \tag{4.6}$$

where $\boldsymbol{T}$ and $\delta\boldsymbol{T}$ are the finite element nodal temperature and virtual temperature vectors, respectively, and $\boldsymbol{N}_T$ is the matrix containing the interpolation function adopted.

Introducing the FE discrete approximations into the continuous weak form of Eq. (4.5), we obtain

$$\int_{\Omega}\delta\boldsymbol{T}^T\boldsymbol{N}_T^T\rho c\boldsymbol{N}_T\dot{\boldsymbol{T}}d\Omega+\int_{\Omega}\delta\boldsymbol{T}^T\boldsymbol{N}_T^T\boldsymbol{G}^Tk\boldsymbol{G}\boldsymbol{N}_T\boldsymbol{T}d\Omega=\int_{\Omega}\delta\boldsymbol{T}^T\boldsymbol{N}_T^T\dot{r}d\Omega-\int_{\Gamma}(\delta\boldsymbol{T}^T\boldsymbol{N}_T^T\bar{q})d\Gamma\ \forall\delta\boldsymbol{T} \tag{4.7}$$

The choice of the virtual field is arbitrary, thus the Galerkin approximation of Eq. (4.7) is

$$\int_{\Omega}\boldsymbol{N}_T^T\rho c\boldsymbol{N}_Td\Omega\dot{\boldsymbol{T}}+\int_{\Omega}\boldsymbol{B}_T^Tk\boldsymbol{B}_Td\Omega\boldsymbol{T}=\int_{\Omega}\boldsymbol{N}_T^T\dot{r}d\Omega-\int_{\Gamma}\boldsymbol{N}_T^T\bar{q}d\Gamma \tag{4.8}$$

with $\boldsymbol{B}_T=\boldsymbol{G}\boldsymbol{N}_T$.

4.1.4 *Boundary Conditions*

In the DED process simulation, the most common heat loss mechanisms identified at the boundary Γ are two: 1) The heat transfer by conduction between the building component and the substrate; 2) The heat losses originated by the heat transfer by radiation and convection through the free surfaces in contact with the environment.

In this sense, the heat loss mechanisms $\bar{q}$, can be replaced by

$$\bar{q}=q_{cond}+q_{conv}+q_{rad} \tag{4.9}$$

with q_{cond} the heat loss by conduction, q_{conv} is the equivalent heat loss by convection and q_{rad} is the radiation flux through the environment (Chiumenti et al., 2017a; Lu et al., 2019).

The domain Ω is closed by the smooth boundary Γ, such that $\Gamma=\Gamma_s\cup\Gamma_e$, where Γ_s and Γ_e are the component-substrate boundary and the environment boundary, respectively.

The temperature at the interface of the substrate-component is given by:

$$T\mid_{\Gamma_s}=T_s \tag{4.10}$$

Heat Loss by Conduction. The heat loss by conduction between the substrate and component is given by Newton's law (Dialami et al., 2013) as

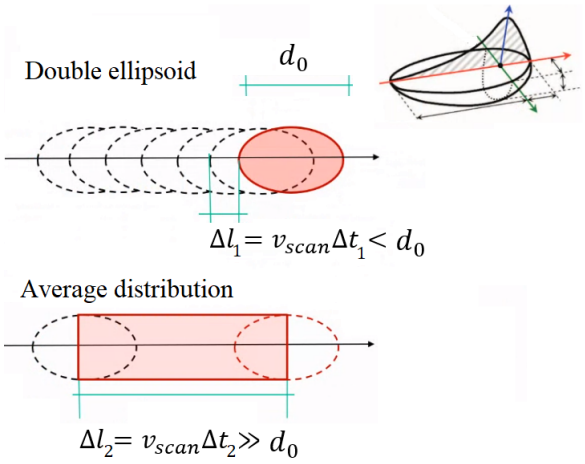

Figure 19: Power distributions and their corresponding HAZ.

$$q_{cond} = h_{cond}(T - T_s), \text{ on } \Gamma_s \tag{4.11}$$

where h_{cond} is the Heat Transfer Coefficient (HTC) by conduction on Γ and T_s is the temperature of the substrate.

Environmental Heat Loss. The heat loss through the environment is due to the convection and radiation heat transfers, expressed by Newton's law as

$$q_{conv} = h_{conv}(T - T_e), \text{ on } \Gamma_e \tag{4.12}$$

$$q_{rad} = h_{rad}(T - T_e), \text{ on } \Gamma_e \tag{4.13}$$

where h_{conv} and h_{rad} are the HTCs associated to the convection and radiation, respectively, and T_e is the environment temperature. The HTC for the radiation (Chiumenti et al., 2017b) can be expressed as

$$h_{rad} = \sigma\epsilon(T^3 + T^2T_e + TT_e^2 + T_e^3) \tag{4.14}$$

where σ is the Stefan-Boltzmann constant and ϵ is the emissivity parameter of the radiating surface.

4.1.5 *External Heat Source*

For AM processes, there are several forms to provide the power input (e.g., electric arc, laser beam or electron beam). In computational simulations, two methodologies are widely used. The first one represents the power input as a Gaussian/Double ellipsoid density distribution (Goldak et al., 1984; Ren et al., 2010; Chiumenti et al., 2016; Gouge et al., 2019) and the second one computes an uniformly distributed average value of the power (Ma and Bin, 2007; Li et al., 2016; Lu et al., 2018) applied to the HAZ.

The former approach is used for the study of the melt-pool, where the time-scale involved is small. The latter approach is employed for part-scale analyses and validated with several numerical and experimental tests by Chiumenti et al. (2017a,b) and is adopted herein.

Fig.19 shows the power distribution as a function of the length-scale, Δl_1, for the double-ellipsoid distribution, and for length-scale for the average distribution, Δl_2, where v_{scan} is the laser scanning speed, Δt_1 and Δt_2 are the time increment for the double-ellipsoid and the average distribution approaches, respectively and d_0 the spot size of the power input.

The average heat density distribution per unit volume at the instant t^{n+1} is computed as

$$\dot{r} = \frac{\eta W}{V_{\text{HAZ}}^{n+1}}, \tag{4.15}$$

where η is the efficiency of the heat absorption and W is the total power input and V_{HAZ}^{n+1} is the heat affected volume at the current time t^{n+1}, which is the bounding-box that corresponds to the average

distribution length-scale Δl_2 in Fig.19. The heat affected volume at the current time t^{n+1} is computed between the initial and final position during the current time-increment, $\Delta t = t^{n+1} - t^n$, as

$$V_{\text{HAZ}}^{n+1} = \sum_{e=1}^{n_e} V^{(e)}|_{e\,\epsilon\,\text{HAZ}}, \tag{4.16}$$

4.2 Time integration and thermo-mechanical coupling

Next, the time integration scheme and thermo-mechanical coupling are presented for the AM process.

4.2.1 *Time integration*

The AM process includes very different physics and very different time-scales characteristic of the micro-structure (micro-scale), melt-pool (meso-scale) and component (macro/part-scale) analyses.

The simulation of the melt-pool, for instance, is driven by physical phenomena that occur in a very small time-scale, which results in even smaller time-steps for their proper simulation, in the order of μs (Zhang et al., 2018a).

Contrarily, the time-step increment of a part-scale analysis is roughly estimated as $\Delta t = d/v$, where d is the size of the heat source spot and v is the speed (Zhang et al., 2018a), and this value may be scaled up-to 40 times without affecting the results (Zhang et al., 2018b). Thus, the time-stepping required for the part-scale is much larger than for the melt-pool analysis.

Kollmannsberger and Kopp (2021) investigate the convergence-rate of first and second-order time integration schemes, focusing on the backward Euler and the Crank-Nicholson methods for LPB processes. In their work, when large time-scales are to be solved, which is the case for the part-scale analysis, solution oscillations may appear in the Crank-Nicholson method, see Fig. 20-(a). Additonaly, the Crank-Nicholson method only achieves second-order convergence on the asymptotic regime for small time-increments (high number of time-steps), see Fig. 20-(b).

For this reasons, the implicit backward Euler method is used to advance in time (Agelet de Saracibar et al., 1999, 2001; Chiumenti et al., 2013; Dialami et al., 2017) to solve the discrete thermo-mechanical problem.

The time-increment $\Delta t = t^{n+1} - t^n$ is set automatically according to the deposition speed v_{dep} and the recoating speed v_{rec}, which may vary from hatch to hatch. Threfore, the time-increment Δt is not fix. The time-increment where the power input is *on* Δt_{on} is computed using the the deposition speed and a constant (user-defined) length Δl. When the power input is *off*, the time-increment Δt_{off} is calculated with the recoating speed (v_{rec}). The Δt_{off} enables the component-substrate to experience cooling. Thus, the Δt_{on} and Δt_{off} are computed as

$$\Delta t_{\text{on}} = \frac{\Delta l}{v_{dep}} \tag{4.17}$$

$$\Delta t_{\text{off}} = \frac{\Delta l}{v_{rec}} \tag{4.18}$$

In the event of an undesired over-heating of the component-substrate, is possible to introduce a pause interval in the GCode file to cool down the AM built or wait the set to reach a desired maximum temperature. Then, the pause time t_{pause} is defined in the GCode and a user-defined number of divisions of the pause n_{pause} is used to compute the pause-increment Δt_{pause} as

$$\Delta t_{pause} = \frac{t_{pause}}{n_{pause}}, \tag{4.19}$$

4.2.2 *Thermo-mechanical coupling*

In AM problems, the mechanical dissipation is negligible and a staggered solution of the thermo-mechanical problem is preferred; adding iterative cycles among the thermal and mechanical partitions does not improve the thermo-mechanical response (Patil et al., 2021). The two sub-problems, the

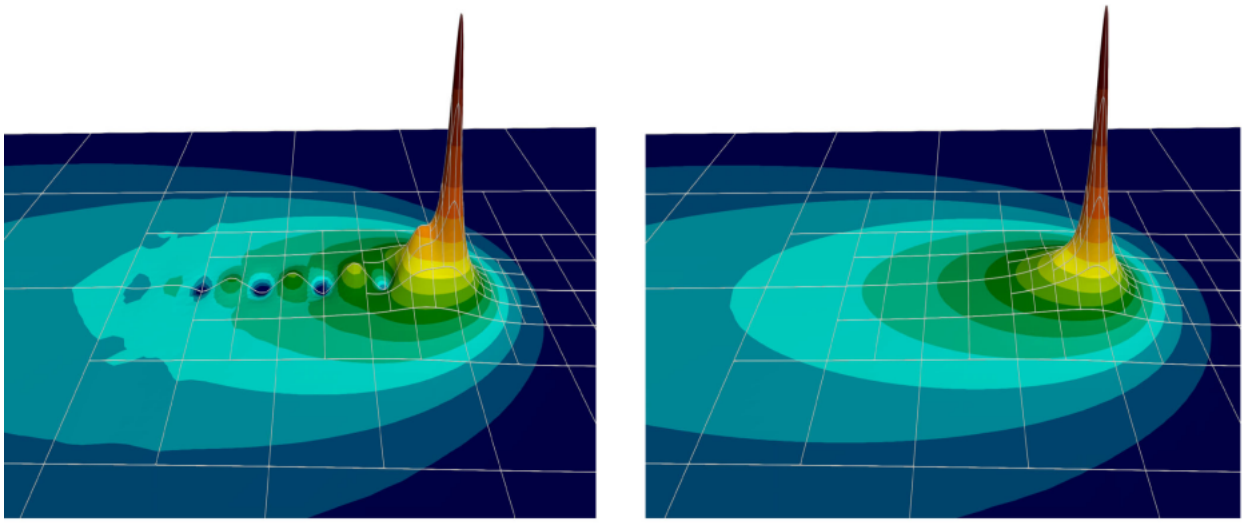

(A) Crank-Nicolson (B) Backward Euler

(a)

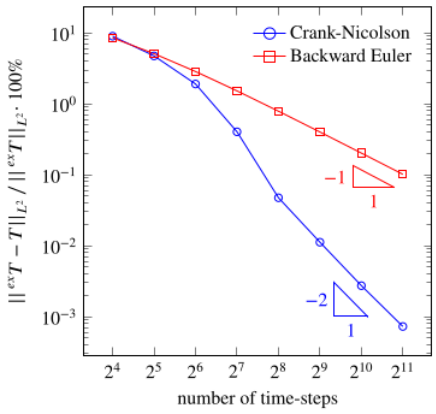

(b)

Figure 20: Comparative results between the backward Euler and the Crank-Nicholson methods. (a) Solution oscillations in the Crank-Nicholson results. (b) Convergence-rate of the time integration methods. (Kollmannsberger and Kopp, 2021)

thermal and the mechanical, are solved separately and no iterative loops over the two sub-problems are needed to guarantee the convergence of the solution (Chiumenti et al., 2013; Patil et al., 2021).

First, the thermal problem is linearized assuming temperature-dependent properties computed at t^n, and solved to get the temperature-field at t^{n+1}. Next, the temperature-dependent properties of the mechanical problem are computed using the solution $T(\boldsymbol{x}, t^{n+1})$.

4.3 Phase change and annealing

The phase-change process is generally much faster than the thermal diffusion of the power input at the HAZ. Thus, the net influence of the phase-change in the thermo-mechanical problem can be neglected (Chiumenti et al., 2017a) because melting and solidification occur within the same time interval ($\Delta t = t^{n+1} - t^n$). This assumption removes the associated non-linearity originated in the thermal analysis. Nevertheless, the phase-change is considered for the choice of the appropriate constitutive model.

Denlinger et al. (2015) reset the plastic strains when the temperature rises above the annealing temperature T_{annel}. Thus, when the material is in liquid-like state.

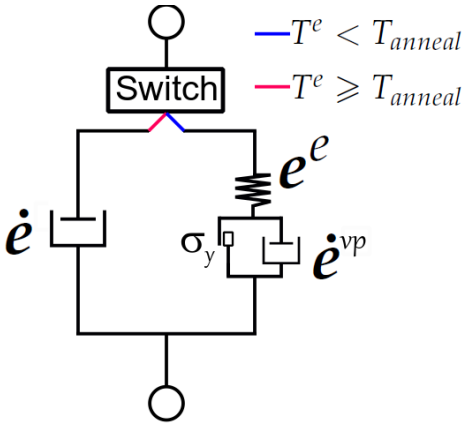

Figure 21: Phase-change model according to the FE temperature.

Bellet et al. (2003) adopt a transition temperature within the range of the solidification interval. Herein, the annealing temperature is used as the threshold to switch between the visco-plastic and the elasto-plastic constitutive models.

The solution of the thermal problem permits the computation of the thermal-strain ε^t as

$$\varepsilon^t = 3[\alpha(T^e)(T^e - T_{ref}) - \alpha(T_0)(T_0 - T_{ref})] \tag{4.20}$$

where α is the temperature-dependent thermal-expansion coefficient, T_{ref} is the reference temperature, taken as $T_{ref} = 20\ [^oC]$, T_0 is the initial temperature of the material at $t = t_0$ and T^e is the average temperature of the FE at the current time $t = t^{n+1}$.

The FE temperature, T^e, used to compute the thermal-strains should be taken as

$$T^e = \begin{cases} T_{anneal} & \text{for } T^e \geqslant T_{anneal} \\ T^e & \text{for } T^e < T_{anneal} \end{cases} \tag{4.21}$$

Note that, whether the FE has a $T^e \geqslant T_{anneal}$, Eq. (4.20) results in no thermal-strains ε^t. This corresponds to the deposition of the melted material in a liquid-like phase. The thermal-strains start to develop when the stiffening of the material occurs ($T^e < T_{anneal}$).

The annealing temperature is also employed to set the material constitutive model. Introducing the additive split of the total strains into their elastic, visco-plastic and elasto-plastic counterparts, and together with the annealing temperature threshold, the elastic strain is defined as

$$\boldsymbol{\varepsilon}^e = \begin{cases} \boldsymbol{\varepsilon} - \boldsymbol{\varepsilon}^{vp} & \text{for } T^e \geqslant T_{anneal} \quad \text{(Liquid-like phase)} \\ \boldsymbol{\varepsilon} - \boldsymbol{\varepsilon}^{vp} - \boldsymbol{\varepsilon}^p - \boldsymbol{\varepsilon}^t & \text{for } T^e < T_{anneal} \quad \text{(Solid phase)} \end{cases} \tag{4.22}$$

where $\boldsymbol{\varepsilon}^{vp}$ and $\boldsymbol{\varepsilon}^p$ are the visco-plastic and elasto-plastic strains, respectively.

Fig. 21 presents a scheme of the constitutive model including the phase-change assumption through the annealing temperature threshold.

4.4 Solid phase: elasto-plastic model

Herein, the elasto-plastic model is presented. Eq. (4.22)-(b) is rewritten in terms of the deviatoric-strains as

$$\boldsymbol{e}^e = \boldsymbol{e} - \boldsymbol{e}^{vp} - \boldsymbol{e}^p \tag{4.23}$$

Applying the additive split of the deviatoric-strains, presented in Eq. (4.23), the deviatoric-stresses results in

$$\boldsymbol{s} = \boldsymbol{C}_0^{dev}\boldsymbol{e}^e = \boldsymbol{C}_0^{dev}(\boldsymbol{e} - \boldsymbol{e}^{vp} - \boldsymbol{e}^p) \tag{4.24}$$

where $\boldsymbol{C}_0^{dev}$ is the deviatoric part of the elastic constitutive matrix. Introducing Eqs. (4.23)-(4.24) and the thermal-strains into the constitutive equations in Eqs. (3.34)-(3.35) results in the elasto-plastic constitutive model:

$$p = K(\nabla \cdot \boldsymbol{u} - \varepsilon^t)$$
$$\boldsymbol{s} = \boldsymbol{C}_0^{dev}(\boldsymbol{e} - \boldsymbol{e}^{vp} - \boldsymbol{e}^p) \tag{4.25}$$

The corresponding equivalent deviatoric-stress τ is given by

$$\tau = \sqrt{\frac{3}{2}}\,\|\boldsymbol{s}\| = \sqrt{\frac{3}{2}[\boldsymbol{s}^T\boldsymbol{s}]} \tag{4.26}$$

The J_2 plastic yield criterion, $\Phi(T, q)$, is defined as

$$\Phi(\boldsymbol{s}, T, q) = \tau(\boldsymbol{s}) - r_p(T, q) \leqslant 0 \tag{4.27}$$

where $r_p(T, q)$ is the temperature-dependent yield surface radius

$$r_p(T, q) = \sigma_y(T) - q(T, \xi) \tag{4.28}$$

where $\sigma_y(T)$ is the temperature-dependent elastic uniaxial stress threshold, ξ is the equivalent plastic strain and q is a stress-like internal variable that controls the *isotropic hardening* of the model

$$q(T, \xi) = -[\sigma_\infty(T) - \sigma_y(T)][1 - \exp(\delta\xi)] - H\xi \qquad \text{for } 0 \leqslant \xi \leqslant \infty \tag{4.29}$$

$$\xi = \sqrt{\frac{2}{3}}\,\|\boldsymbol{e}^p\| \tag{4.30}$$

where $\sigma_\infty(T)$ is the temperature-dependent ultimate stress, H is the linear hardening parameter and δ is the coefficient that controls the exponential hardening law.

The plastic evolution laws are

$$\dot{\boldsymbol{e}}^p = \dot{\lambda}\mathbf{n} \tag{4.31}$$

$$\dot{\xi} = \dot{\lambda}\sqrt{\frac{2}{3}} \tag{4.32}$$

where $\dot{\lambda}$ is the visco-plastic multiplier determined by the Kuhn-Tucker and consistency conditions and $\mathbf{n}$ is the normal to the yield surface, defined by

$$\mathbf{n} = \frac{\partial\Phi(\boldsymbol{s}, T, q)}{\partial\boldsymbol{s}} = \frac{\boldsymbol{s}}{\|\boldsymbol{s}\|} \tag{4.33}$$

The Kuhn-Tucker conditions, related to the loading and unloading, hold:

$$\dot{\lambda} = 0 \quad \Phi < 0 \quad \text{(Elastic unloading)} \tag{4.34}$$

$$\dot{\lambda} > 0 \quad \Phi = 0 \quad \text{(Plastic loading)} \tag{4.35}$$

$$\dot{\lambda}\Phi = 0 \tag{4.36}$$

In addition, the visco-plastic multiplier assumes the following rate-dependent evolution law

$$\dot{\lambda} = \left\langle \frac{\Phi(\boldsymbol{s}, T, q)}{\eta} \right\rangle^{\frac{1}{m}} \tag{4.37}$$

where $\langle\cdot\rangle$ are the Macauly brackets. Therefore, the stress is allowed to exceed the yield surface, with a viscous overstress $\eta(\dot{\lambda})^m$, being $\eta(T)$ and $m(T)$are the temperature-dependent plastic viscosity and rate sensitivity, respectively (Chiumenti et al., 2016).

4.5 Liquid-like phase: visco-plastic model

The liquid-like behavior of the material implies that the incompressibility constraint ($K \to \infty$) applies to the melted material. Additionaly, in the liquid-phase the elastic component of the strain tensor vanishes (Chiumenti et al., 2016), yielding the following:

$$\begin{cases} \nabla \cdot \boldsymbol{u} = \varepsilon^t \\ \\ \boldsymbol{e} = \boldsymbol{e}^{vp} \end{cases} \tag{4.38}$$

In this sense, only volumetric thermal and viscous shear deformations take place. The yield surface radius defined in Eq. (4.28) vanishes above the annealing temperature $r_p = 0$. Thus, the consequence of this behavior is a pure viscous model.

Furthermore, above the melting point, the liquid-phase behaves as a Newtonian fluid. For this reason, the rate sensitivity of the viscous law is taken as $m = 1$. Therefore,

$$\boldsymbol{s} = \eta(T)\dot{\boldsymbol{e}}^{vp} \tag{4.39}$$

5

ADAPTIVE MESH REFINEMENT

In this chapter, the aspects related to the Adaptive Mesh Refinement (AMR) are addressed. A multi-criteria hierarchical octree-based AMR strategy is described for the AM simulation. This strategy aims to reduce geometry and mesh manipulation, while providing an efficient environment to tackle complex geometries. The approach enables to eliminate both the user interaction and the need for initial fine meshes to describe those geometries.

This chapter is divided as follows. In Section 5.1, the octree meshing is detailed including the treatment of the hanging nodes and mesh projections. In the sequence, the refinement/coarsening criteria adopted are discussed in Section 5.2, followed by the coarsening correction strategy in Section 5.3. Complementary aspects to fully accomplish the automatic mesh generation are addressed in chapter 6. Lastly, the coarsening correction strategy is considered.

5.1 Octree meshing

The tree-data structures, *quadtrees* and *octrees*, are easy to parallelize and provide better performance when working with block-structure methods. *Octrees/quadtrees* are capable of refining parallel meshes using a single mapping sequence due to its organized structure (Baiges and Bayona, 2016).

The octree mesh partitioner divides the element isotropicaly, i.e. the element is divided in halves in all directions, creating 8 new elements. The newly created elements are called *child* elements and the original element is the *parent* element. This introduces a hierarchical relation between *parent* and *child* elements.

The FE partition Ω_e at the time instant $t = t_0$ defines the base of the octree hierarchy $\Omega_e(t_0) = \Omega_{e_0}$. All the FEs $\cup\Omega_e(t_0)$ are named as level *zero* FEs. The FEs created from the octree division of the level *zero* FEs are named sequentialy as level *one* elements. The level *one* elements are the corresponding *branch* to the level *zero* elements. Additionaly, the level *one* elements are concurrently child elements to the level *zero* elements and also parent elements to the level *two* elements.

Fig. 22 presents a color scheme of the octree hierarchy structure. Fig. 22-(a) presents the level zero FE partition and the resulting FE partition after 4 adaptivity cycles have been applied. Fig. 22-(b) shows a color scheme to represent the parent-child relation among the several existing refinement levels.

5.1.1 *Hanging nodes*

If a hanging node is introduced in an edge between two or more FEs and no additional measure is taken this results in a non-conforming interpolation of the displacements (and other interpolated unknowns) for the affected FEs. Note that derived fields are discontinuous anyway.

To restore the inter-element conformity of the nodal solution when hanging nodes are used, several techniques have been developed. Amidst the popular hanging node treatments, there are: 1) the hanging node constraint (Rheinboldt and Mesztenyi, 1980; Shephard, 1984; Badia et al., 2020, 2021; Neiva and Badia, 2021), detailed next; 2) the use of the discontinuous-Galerkin approach to treat the hanging nodes as a discontinuous field (Cockburn and Shu, 1998); 3) the hybrid continuous-discontinuous Galerkin that introduces the low computational cost of the continuous Galerkin approach (Badia and Baiges, 2013); and 4) the multi-level *hp* formulation for high-order mesh adaptivity (Zander et al., 2015; Di Stolfo et al., 2016; Zander et al., 2016a).

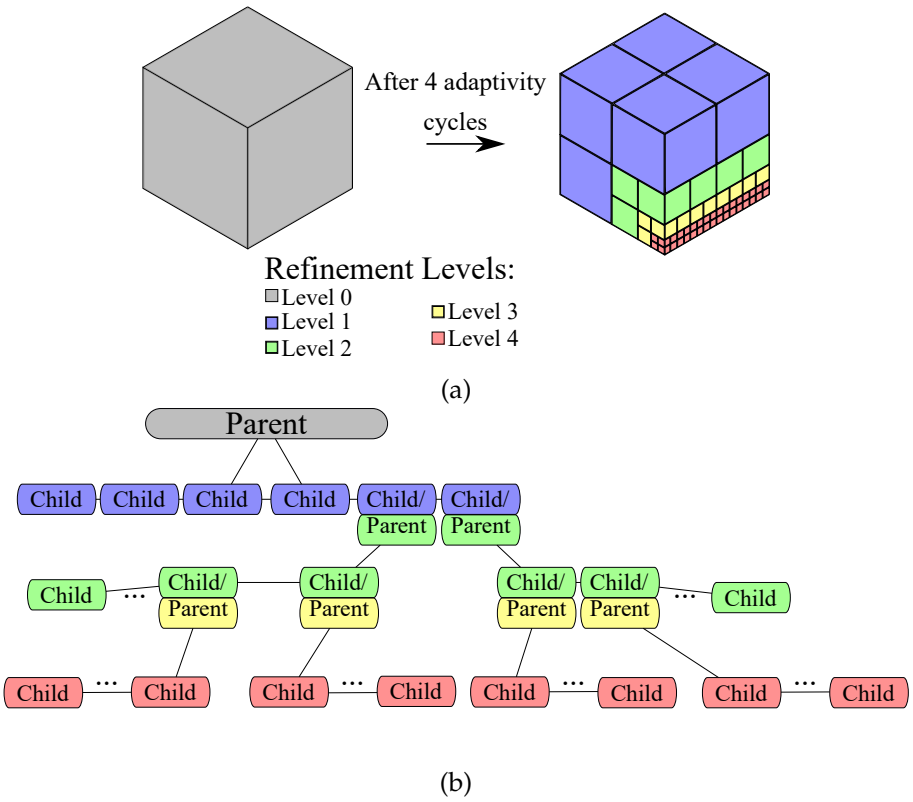

Figure 22: Color scheme of the octree hierarchy.

The relations between the hanging nodes and their parent nodes is established from an elemental loop that checks the node matching of faces and edges which connect to the higher elements. The hanging nodes are the nodes that are neither present in both sides of the face, nor in all elements concurring to the same edge.

In most tree-based algorithms, the hanging node treatment follows a $2:1$ balance condition that must be satisfied. This condition imposes that there exists only one hanging node on the interface of two adjacents FEs. This enforces that the refinement level difference between the coarsest and finest adjacent FE is $Lev(\mathrm{FE}_f) - Lev(\mathrm{FE}_c) = 1$, where $Lev(\cdot)$ is the refinement level, FE_f and FE_c are the finest and coarsest FE of a patch of adjacent FEs, respectively.

Contrariwise, the $2:1$ balance condition is not imposed in the following. The treatment of the hanging nodes consists in constraining the values of the hanging nodes according to the values of the parent nodes (Baiges et al., 2017). This is achieved from a hanging node list with the recursive dependency structure stored in a Compressed Sparse Row (CSR) format. Since there is no $2:1$ balance condition that must be satisfied, the number of parent nodes that contributes to the value of the hanging node may be arbirtrarily large and the CSR format provides good efficiency to handle such volume of data.

Fig. 23 presents the hanging node constraint treatment for the nodes unknowns $\boldsymbol{u}_3$, $\boldsymbol{u}_4$ and $\boldsymbol{u}_5$ computed from the unknowns of the standard parent nodes $\boldsymbol{u}_1$ and $\boldsymbol{u}_2$. This is achieved by modifying the test/shape functions as

$$\phi^*(\boldsymbol{x}) = \phi(\boldsymbol{x}) + \sum_{i=1}^{n_{hanging}} (\phi(\boldsymbol{x}_i)\phi_{h_i}(\boldsymbol{x})) \tag{5.1}$$

where ϕ^* is the modified test/shape function, written in terms of the original shape/test function ϕ and ϕ_{h_i} is the hanging shape/test function, computed according to the spatial location of the hanging node, where $\boldsymbol{x}_i$ is the i-th hanging node position, and $n_{hanging}$ is the number of hanging nodes.

The straight-forward application of the parent-child hanging node constraint may lead to scenarios where a hanging node is active and contributes to an inactive parent, causing a *singular* system. To

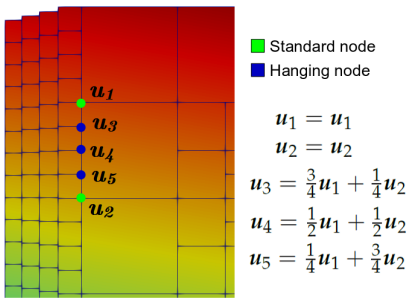

Figure 23: Hanging node unknown computation values from parent nodes.

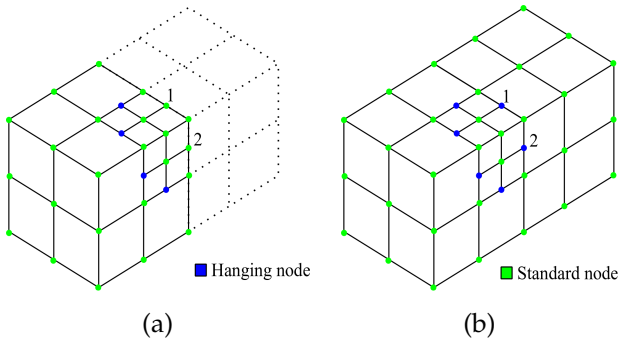

Figure 24: Node classification between standard and hanging at two time instants. (a) $t = t^n$. (b) $t = t^{n+1}$.

avoid this situation, the algorithm checks if the parent node is active or inactive, and, if required, modifies the status of the hanging node to a *standard* node.

Fig. 24 illustrates the change on the classification of the nodes 1 and 2 from the standard status to hanging node in two subsequent time instants; Fig. 24-(a) standard nodes at $t = t^n$ and Fig. 24-(b) hanging nodes at $t = t^{n+1}$, respectively.

5.1.2 *Mesh projections*

In the AM process, the FE space evolves over time, representing the deposition of new material. This requires the building of a new finite element space and the data-transfer from the mesh at the previous instant t^n to the current instant t^{n+1}.

The data-transfer process occurs at the same time refinement and/or coarsening of the mesh takes place. The data-transfer is performed through mesh projections from the the solution at the instant t^n to the computed mesh at the instant t^{n+1}.

The data-transfer is done through mesh projections procedures of the nodal and gaussian variables. For nodal variables, such as the displacement $\boldsymbol{u}$ (and deviatoric-strain $\boldsymbol{e}$ and pressure p, if is the case of the mixed $\boldsymbol{u}/\boldsymbol{e}/p$ formulation) and temperature, a point-to-point projection is used. Let the nodal variable, herein, be called as $\boldsymbol{u}_h$, representing the nodal variables involved in the thermo-mechanical problem.

Therefore, the point-to-point projection from the mesh Ω_e^n at the previous time instant t^n, onto the new mesh Ω_e^{n+1} at the current time instant t^{n+1} is given by:

$$P^{n+1}(\boldsymbol{u}_h^n) \tag{5.2}$$

where $P^{n+1}(\cdot)$ is the point-to-point projection onto the new mesh Ω_e^{n+1}, computed from the nodal unknowns at the time instant t^n, $\boldsymbol{u}_h^n$.

This procedure is computationally cheap and straightforward for nested octree-based meshes; the nodal values at the hanging nodes are interpolated from the corresponding parent elements, following

the procedure described in Section 5.1.1 and the nodal solution of pre-existing nodes in the Ω_e^n are kept.

The historic variables stored at the quadrature points, such as the strains, are transferred through a element by element L_2 projection, such that:

$$\Pi^{n+1}(\boldsymbol{\varepsilon}^n) \tag{5.3}$$

where $\Pi^{n+1}(\cdot)$ is the element-wise L_2 projection.

The projection is computed for each element FE^{n+1} of the new mesh according to

$$\int_{FE^{n+1}} \delta\boldsymbol{u}\Pi^{n+1}(\boldsymbol{\varepsilon}^n)d\Omega = \int_{FE^{n+1}} \delta\boldsymbol{u}\boldsymbol{\varepsilon}^n d\Omega \qquad \forall\delta\boldsymbol{u} \in W_{h,FE^{n+1}} \tag{5.4}$$

with $\delta\boldsymbol{u}$ being the weight function and $W_{h,FE^{n+1}}$ is the finite element space of the new mesh restricted to the considered FE. The projection $\Pi^{n+1}(\boldsymbol{\varepsilon}^n)$ is computed, interpolated and stored at the quadrature points of the new FE.

5.2 Refinement/coarsening criteria

The framework developed for the thesis starts from a single FE in the initial partition Ω_{e_0}. To create the FE mesh, it is required to build a coarsening/refinement array $\mathbf{f}$, that contains the information on the action that the octree mesh partitioner RefficientLib (Baiges and Bayona, 2016) should take for each i-th FE, that is: 1) Refine ($f_i = 1$); 2) Coarsen ($f_i = -1$); 3) No action required ($f_i = 0$).

Furthermore, the minimum and maximum refinement levels (Lev_{min}, Lev_{max}, respectively) need be set as the refinement thresholds to avoid the mesh to reach undesired FE sizes. The refinement level threshold should be checked in all the refinement criteria and are written as:

$$Lev(\text{FE}) < Lev_{min} \;\rightarrow f_i = 1 \tag{5.5}$$

$$Lev(\text{FE}) > Lev_{max} \rightarrow f_i = -1 \tag{5.6}$$

5.2.1 *Geometric criteria*

The accuracy of the AM process simulation lies on the fine discretization of the domain close to the HAZ. The computational cost of the simulation can be saved by coarsening the regions away from the HAZ. The procedure that classifies whether a region is close or away from the HAZ is defined as a geometric criterion. In this thesis, two geometric criteria are presented.

5.2.1.1 *Layer-wise strategy*

The layer-wise strategy is a purely geometric criterion where the set of the latest layers is kept refined from a fix distance of the current deposition layer. The fix distance from the depositionlayer is called the refinement height h_{ref}.

The refinement height h_{ref} is computed on the opposite direction of the built of the component (in the z-coordinate). The fix distance is chosen considering the influence of the HAZ in the latest set of layers. The FEs contained inside the refinement height are kept refined and coarsened, otherwise. Therefore, the finest mesh size is preserved for the latest layers and the elements below the refinement height are coarsened.

The layer-wise AMR strategy compares the maximum z-coordinate of the FE, $max_z(\text{FE})$, with the maximum and minimum coordinates of the volume defined by the current deposition plane, z_{dep}, and the parallel plane defined using the refinement height h_{ref} (downward the building direction), namely the refinement height plane, $z_{ref} = z_{dep} - h_{ref}$.

In the case where the maximum z-coordinate of the FE does not belong to this volume, the value of the coarsening/refinement array for this FE is set as $f_i = -1$ and $f_i = 1$, otherwise. The FEs with at least one node inside the fix distance between the current deposition plane and the refinement height

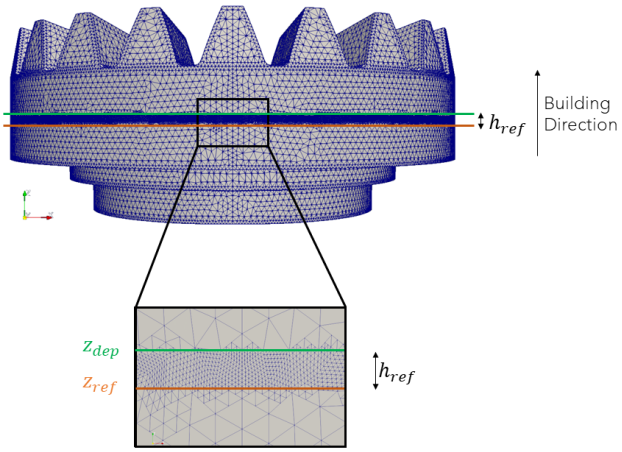

Figure 25: Layer-wise strategy. The FEs outside the volume defined by the refinement height plane z_{ref} and the current deposition plane z_{dep} are coarsened ($f_i = -1$) to the minimum refinement level Lev_{min}. On the other hand, the FEs contained in-between those planes are refined ($f_i = 1$) up to the maximum refinement level Lev_{max}.

plane are refined until they reach the maximum refinement level threshold. Contrarily, the FEs outside this volume are coarsened until the minimum refinement level threshold is achieved.

Fig. 25 presents a gear with an initial FE mesh and the refined area in-between the current deposition plane z_{dep} and the refinement height plane z_{ref}. Notice that, when the current deposition height z_{dep} is updated to a new layer, the new refinement plane z_{ref} is computed and the FE mesh is updated from the new set of coarsening/refinement array $\mathbf{f}$.

$$max_z(\text{FE}) > z_{ref} \wedge max_z(\text{FE}) < z_{dep} \rightarrow f_i = 1 \tag{5.7}$$

$$max_z(\text{FE}) < z_{ref} \rightarrow f_i = -1 \tag{5.8}$$

$$max_z(\text{FE}) > z_{dep} \rightarrow f_i = -1 \tag{5.9}$$

Note that Eqs. (5.7)-(5.9) are complemented with the thresholds Lev_{min} and Lev_{max} provided in Eqs. (5.5)-(5.6). Furthermore, Eq. (5.7) defines the refine status ($f_i = 1$) to the FE contained by the current deposition and refinement height planes. Eq. (5.8) performs the coarsening of the FE away from the refinement height plane (HAZ) and Eq. (5.9) coarsens the FE that remains inactive during the deposition of the current layer.

5.2.1.2 *Bounding box strategy*

This Section presents the geometric AMR criterion based on the HAZ bounding box position. The additional details on the necessary input data, the generation of the bounding box and the collision detection are presented in Chapter 6.

The bounding box geometric criterion consists in a search algorithm where an oriented reference volume intersects the FEs of the background mesh Ω_h^b. At the initial instant $t = t_0$, the background mesh Ω_h^b coincides with the initial FE partition Ω_{e0}.

The oriented volume (OV) is a fictitious prism, containing the HAZ at the current instant t^{n+1}, being immersed in Ω_h^b. The OV prism is constructed using the process parameters of: 1) the hatch length, which determines the OV length; the melt-pool width, b_{pool}, that generates an in-plane width of the OV which is perpendicular to the hatch length direction and 3) the height of the OV, in the z-direction, composed by the layer thickness, h_{layer}, and the power input penetration height, z_{power}, resulting in the melt-pool height, h_{pool}. These process parameters and the construction of the HAZ bounding box (OV) from a GCode input file are detailed in Chapter 6.

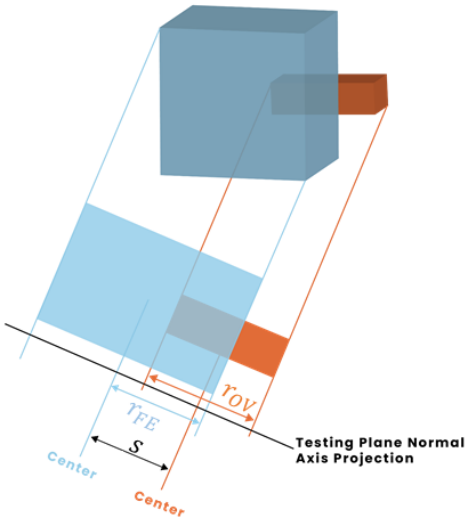

Figure 26: The visual interpretation of the SAT: The projection of the distance between the polytopes geometrical centers, defined by s, is compared to the sum of the projected half-sides of the OV, r_{OV}, and the FE, r_{FE}, respectively.

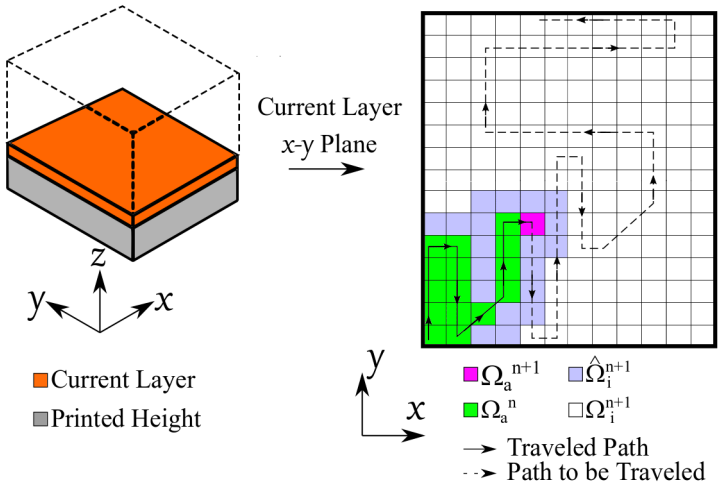

Figure 27: Classification of the active and inactive FEs at the current time instant t^{n+1} for the evolving domain.

In practice, the bounding box criterion compares the projected distance between the pair of polytopes centers, s, with the OV and FE projected half-sides, r_{OV} and r_{FE}, onto the normal direction of the test plane, $\mathbf{n}_{\text{tp}}$.

If $s > r_{\text{OV}} + r_{\text{FE}}$, the plane is a *separating plane*, which means the OV and the tested FE do not overlap. If the test finds a separating plane, no further checks are required, and both OV and FE do not intersect; otherwise a new test plane should be verified. Fig. 26 presents a visual description of this method.

In addition to the SAT, the bounding box geometric criterion considers that the AM process is an evolving domain problem. This creates, in the FE partition, elements that are either active or inactive for the current instant of the analysis t^{n+1}.

In this context, the evolving AM domain can be represented by four groups of FEs: 1) active FEs that intersect the current HAZ bounding box (OV), Ω_a^{n+1}; 2) the previously activated FE that do not intersect the current HAZ bounding box (OV), Ω_a^{n}; 3) inactive FEs that share nodes with active FEs, $\hat{\Omega}_i^{n+1}$ and 4) inactive FEs that do not share nodes with active FEs, Ω_i^{n+1}. Fig. 27 shows the FE classification for an arbitrary time instant of an AM process, where the current HAZ bounding box represents the Ω_a^{n+1} domain in purple.

If the OV, representing the HAZ, and the FE intersect, then the tested FE belongs to Ω_a^{n+1}, and is marked as *to be refined* ($f_i = 1$). If a separating plane is detected, and the tested FE does not belong to $\hat{\Omega}_i^{n+1}$, this FE $\in (\Omega_a^n \cup \Omega_i^{n+1})$ is marked as *to be coarsened* ($f_i = -1$). Finally, the FE $\in \hat{\Omega}_i^{n+1}$, is as an inactive FE that is a neighbor to an active FE. This FE is marked as *to do nothing* ($f_i = 0$), to prevent an active FE from Ω_a^n, that do not intersect the HAZ, from being coarsened; this preserves the geometry of the evolving domain.

Thus, the corresponding coarsening and refinement flag for the i-th FE, f_i, is determined as follows

$$\text{FE} \in (\Omega_a^{n+1}) \ \rightarrow f_i = 1 \tag{5.10}$$

$$\text{FE} \in (\Omega_a^n \cup \Omega_i^{n+1}) \rightarrow f_i = -1 \tag{5.11}$$

$$\text{FE} \in \hat{\Omega}_i^{n+1} \ \rightarrow f_i = 0 \tag{5.12}$$

Additionaly, Eq. (5.10)-(5.12) need be complemented with the general check of the minimum and the maximum desired refinement level, presented in Eq. (5.5)-(5.6). As a consequence, the difference between the maximum (Lev_{max}) and minimum (Lev_{min}) refinement levels provide a upper bound condition in the required number of mesh computations (Neiva et al., 2019).

5.2.2 *Accuracy-based criterion*

This section presents the gradient-based approach adopted in this thesis to prevent the coarsening process near the HAZ to affect the solution accuracy. In this context, an a-posteriori error-estimator is used (Zienkiewicz and Zhu, 1987) and described next.

Let $\mathbf{e}$ be the discretization error for a given discrete solution computed as:

$$\mathbf{e} = \nabla \boldsymbol{u} - \nabla \boldsymbol{u}_h, \tag{5.13}$$

where $\nabla \boldsymbol{u}$ and $\nabla \boldsymbol{u}_h$ are the analytical (exact) gradient of the unknown field and the discrete gradient computed from the FE solution, respectively.

Exact solutions are rarely found, and are, in general, only possible in very simple cases. To circumvent this issue, Zienkiewicz and Zhu (1992a,b) propose an accurate error-estimate to be used when the exact solution is not available. The authors show that exist a set of super-convergent points within the FE discretization where the solution can be used as a reference value when computing the error estimator. These values are a-posteriori computed at the FE super-convergent points and projected to the FE nodes. Thus, Eq. (5.13) becomes

$$\bar{\mathbf{e}} = P(\nabla \bar{\boldsymbol{u}}) - \nabla \boldsymbol{u}_h, \tag{5.14}$$

where $\bar{\mathbf{e}}$ is the discrete error estimator for the gradient of the unknowns, $\nabla \bar{\boldsymbol{u}}$ is the gradient of the unknowns computed at the super-convergent point, $P(\cdot)$ is a projection operator that projects $\nabla \bar{\boldsymbol{u}}$ onto the nodes of the FE mesh, and $\nabla \boldsymbol{u}_h$ is the gradient of unknowns computed from the FE solution. For the standard hexahedra tri-linear FE, adopted in the octree meshing, the super-convergent point is at the barycenter of the element.

Finally, the L_2-norm of the $\bar{\mathbf{e}}$ for the i-th FE, $|\bar{\mathbf{e}}_i|$, is computed and compared with the minimum and maximum admissible errors, as follows

$$|\bar{\mathbf{e}}_i| < \mathbf{e}_{\text{min}} \rightarrow f_i = -1 \tag{5.15}$$

$$|\bar{\mathbf{e}}_i| \geq \mathbf{e}_{\text{max}} \ \rightarrow f_i = 1 \tag{5.16}$$

$$\mathbf{e}_{\text{min}} \leq |\bar{\mathbf{e}}_i| < \mathbf{e}_{\text{max}} \ \rightarrow f_i = 0$$

5.3 Coarsening correction strategy

The effect of the information loss in the thermal analysis of the AM process is less significative than the loss of information in the mechanical analysis due to the dissipative nature of the heat transfer problem. For this reason, the coarsening correction strategy is presented for the mechanical problem.

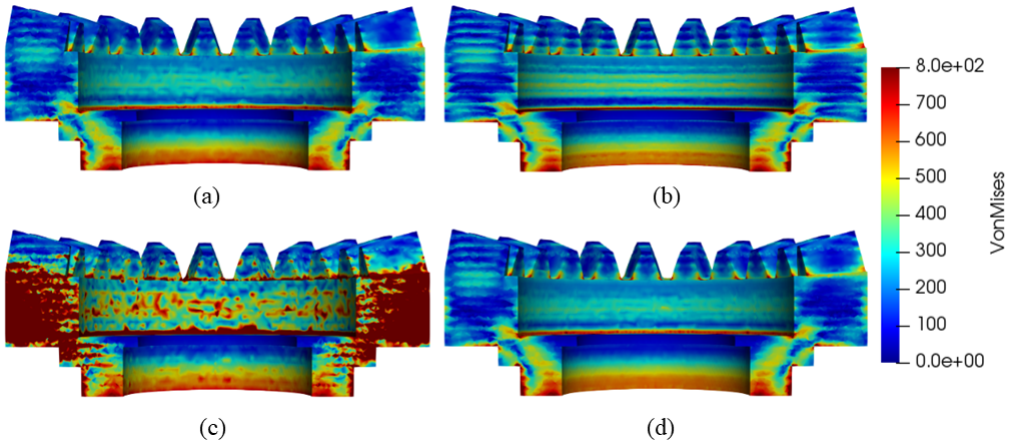

Figure 28: Von Mises stress at a section cut of a gear component. (a) Fixed coarse mesh. (b) Fixed fine mesh. (c) AMR strategy *without* the correction terms. (d) AMR strategy *with* the correction terms)

When coarsening is performed, the accuracy of the information stored in the fine mesh at the instant t^n is lost as a result of projection errors associated to $P^{n+1}(\cdot)$ and $\Pi^{n+1}(\cdot)$, when transferring the information to the new mesh at the instant t^{n+1}. Additionaly, the FE solution computed for Ω^n_{act} now has evolved to a new FE domain Ω^{n+1}_e at $t = t^{n+1}$, which also introduces errors. Note that Ω^{n+1}_e corresponds to the new mesh of the current time instant prior to the FE activation ($\Omega^{n+1}_e \neq \Omega^{n+1}_{act}$).

There are mainly two reasons for this. First, the solution in the fine mesh can present high jumps of the gradient of the unknowns (strains), which is L_2 averaged in the coarsening procedure, resulting in an averaged field where the characteristics of the fine solution are lost. Second, the mesh evolution may convert standard nodes into hanging nodes. In this case, the nodal unknowns are now interpolated from the parent nodes, which also affects the computation of the strain values, resulting in modified local stress/strain values.

Fig. 28 shows the *Von Mises* stress for a gear component using (a) a fixed coarse mesh; (b) a fixed fine mesh; (c) AMR strategy *without* correction terms and (d) AMR strategy *with* correction terms. Fig. 28 demonstrates the important changes in the local stress field resulting from the information loss from the coarsening procedure.

The correction strategy proposed may be interpreted as a VMS enrichment of the subscales for the nodal displacements. For an evolving domain, the solution at the time instant t^n is projected onto the new FE Ω^{n+1}_e, prior to the solution of the time instant t^{n+1}. The solution at t^n needs be preserved; therefore, the solution subscale component is added to compensate the information loss in the projection from Ω^n_{act} to Ω^{n+1}_e, resulting in:

$$\hat{\boldsymbol{u}}^n_h = P^{n+1}(\boldsymbol{u}^n_h) + \tilde{\boldsymbol{u}}^n_h \tag{5.17}$$

where $\hat{\boldsymbol{u}}^n_h$ is the corrected solution from the mesh projected at t^n to the current mesh Ω^{n+1}_e, $\tilde{\boldsymbol{u}}^n_h$ is the subscale associated to the information loss of the nodal displacements due to the mesh projection from Ω^n_{act} to Ω^{n+1}_e and $P^{n+1}(\boldsymbol{u}^n_h)$ is the point-to-point projection of $\boldsymbol{u}^n$ to the new mesh at t^{n+1}. Note that if the mesh does not change, $P^{n+1}(\boldsymbol{u}^n_h) = \boldsymbol{u}^n_h \rightarrow \hat{\boldsymbol{u}}^n_h = \boldsymbol{u}^n_h$ and the subscales contributions are null.

The solution of the current time instant t^{n+1} results in the corrected solution from the previous step and the increment of the solution, derived from the evolving mechanical problem. Thus, the solution of the nodal displacements are written in terms of the solution increment as

$$\boldsymbol{u}^{n+1}_h = \hat{\boldsymbol{u}}^n_h + \Delta\boldsymbol{u}^{n+1}_h \tag{5.18}$$

where $\Delta\boldsymbol{u}^{n+1}_h$ is the solution increment for the nodal displacements.

Introducing Eq. (5.17) into Eq. (5.18), the current time instant solution can be written using the mesh projections P^{n+1} and Π^{n+1}, as well as the subscales $\tilde{\boldsymbol{u}}^n_h$ and $\tilde{\boldsymbol{u}}^n_g$ as:

$$\boldsymbol{u}^{n+1}_h = P^{n+1}(\boldsymbol{u}^n_h) + \tilde{\boldsymbol{u}}^n_h + \Delta\boldsymbol{u}^{n+1}_h \tag{5.19}$$

In this format, the solution of the current time instant t^{n+1} corresponds to the point-to-point projection of the solution from the previous step, the displacement increment resulting from the evolving AM process and the subscales contribution that accounts for the loss of information.

5.3.1 *Stress correction terms*

The stresses shown in Fig. 28-(c) represent the stress field resulting from the coarsening procedure. This solution is polluted from projection errors. Therefore, it is required to correct the stress values to avoid these errors associated to the projections. For the current instant t^{n+1}, the stress field is defined in the current active mesh Ω_{act}^{n+1} as

$$\boldsymbol{\sigma}_h^{n+1} = \boldsymbol{C}(\boldsymbol{S}\boldsymbol{u}_h^{n+1} - \boldsymbol{\varepsilon}^{vp^{n+1}} - \boldsymbol{\varepsilon}^{p^{n+1}} - \boldsymbol{\varepsilon}^{t^{n+1}}) \tag{5.20}$$

where $\boldsymbol{\sigma}_h^{n+1}$ are the stresses for the current time instant t^{n+1}, computed from the solution $\boldsymbol{u}_h^{n+1}$, $\boldsymbol{\varepsilon}^{vp}$ are the visco-plastic strains, $\boldsymbol{\varepsilon}^{p}$ are the elasto-plastic strains and $\boldsymbol{\varepsilon}^{t}$ are the thermal-strains.

In order to simplify the notation, the visco-plastic strains, elasto-plastic strains and thermal-strains are written as the inherent strain, defined as

$$\boldsymbol{\varepsilon}_{inh} = \boldsymbol{\varepsilon}^{vp} + \boldsymbol{\varepsilon}^{p} + \boldsymbol{\varepsilon}^{t} \tag{5.21}$$

Thus, Eq. (5.20) is rewritten as

$$\boldsymbol{\sigma}_h^{n+1} = \boldsymbol{C}(\boldsymbol{S}\boldsymbol{u}_h^{n+1} - \boldsymbol{\varepsilon}_{inh}^{n+1}) \tag{5.22}$$

and the inherent strains computed in the current time instant ($\boldsymbol{\varepsilon}_{inh}^{n+1}$) are defined as

$$\boldsymbol{\varepsilon}_{inh}^{n+1} = \Pi^{n+1}(\varepsilon_{inh}^{n}) + \Delta\boldsymbol{\varepsilon}_{inh}^{n+1} \tag{5.23}$$

Note that the current-time instant inherent strains $\boldsymbol{\varepsilon}_{inh}^{n+1}$ are computed from the L_2-projection from the previous step plus the inherent strains increment from step t^n to t^{n+1}.

The stresses from the previous time instant t^n projected onto the current mesh Ω_e^{n+1} result in:

$$\hat{\boldsymbol{\sigma}}_h^{n} = \boldsymbol{C}[\boldsymbol{S}P^{n+1}(\boldsymbol{u}_h^{n}) - \Pi^{n+1}(\varepsilon_{inh}^{n})] \tag{5.24}$$

where $\hat{\boldsymbol{\sigma}}_h^{n}$ are the previous step stresses computed using the projected previous step variable $\boldsymbol{u}_h^{n}$ to the new mesh.

The proposed stress correction term, computed at t^{n+1} from the variables projected from the previous step, is introduced as

$$\tilde{\boldsymbol{\sigma}}^{n+1} = \Pi^{n+1}(\boldsymbol{\sigma}_c^{n}) - \hat{\boldsymbol{\sigma}}_h^{n} \tag{5.25}$$

where $\tilde{\boldsymbol{\sigma}}^{n+1}$ is the stress correction term, $\boldsymbol{\sigma}_c^{n}$ are the total corrected stresses from the time instant t^n and $\hat{\boldsymbol{\sigma}}^{n}$ are the stresses from the previous step computed from the point-to-point projection operator in the current mesh Ω_e^{n+1}.

Introducing Eq. (5.24) into Eq. (5.25), the stress correction term results in

$$\tilde{\boldsymbol{\sigma}}^{n+1} = \Pi^{n+1}(\boldsymbol{\sigma}_c^{n}) - \boldsymbol{C}[\boldsymbol{S}P^{n+1}(\boldsymbol{u}_h^{n}) - \Pi^{n+1}(\varepsilon_{inh}^{n})] \tag{5.26}$$

Finally, the total corrected stress field for the current time instant t^{n+1} is

$$\boldsymbol{\sigma}_c^{n+1} = \boldsymbol{\sigma}_h^{n+1} + \tilde{\boldsymbol{\sigma}}_h^{n+1} \tag{5.27}$$

Eq. (5.27) can be rewritten introducing Eqs. (5.22) and (5.26), resulting in

$$\boldsymbol{\sigma}_c^{n+1} = \Pi^{n+1}(\boldsymbol{\sigma}_c^{n}) + \boldsymbol{C}(\boldsymbol{S}\boldsymbol{u}_h^{n+1} - \boldsymbol{\varepsilon}_{inh}^{n+1}) - \boldsymbol{C}[\boldsymbol{S}P^{n+1}(\boldsymbol{u}_h^{n}) - \Pi^{n+1}(\varepsilon_{inh}^{n})] \tag{5.28}$$

where the first term is the projected corrected stress from the previous mesh at t^n with minimal loss of information, the second term are the stresses computed with the current time instant using the current

active mesh Ω_{act}^{n+1} and the last term are the stresses computed for the solution in Ω_{act}^{n} projected to Ω_{e}^{n+1}.

Note that the following definitions may be adopted for the stress increments:

$$\begin{aligned}\Delta\boldsymbol{\sigma}_h^{n+1} &= \boldsymbol{C}\boldsymbol{S}[\boldsymbol{u}_h^{n+1} - P^{n+1}(\boldsymbol{u}_h^n)] \\ \Delta\boldsymbol{\sigma}_{inh}^{n+1} &= \boldsymbol{C}[\boldsymbol{\varepsilon}_{inh}^{n+1} - \Pi^{n+1}(\varepsilon_{inh}^n)]\end{aligned} \tag{5.29}$$

such that the stress increment caused by the increment of the loads in the evolving solution is defined as

$$\Delta\boldsymbol{\sigma}^{n+1} = \Delta\boldsymbol{\sigma}_h^{n+1} - \Delta\boldsymbol{\sigma}_{inh}^{n+1} \tag{5.30}$$

Therefore, the total corrected stresses in Eq. (5.28) may be rewritten as

$$\boldsymbol{\sigma}_c^{n+1} = \Pi^{n+1}(\boldsymbol{\sigma}_c^n) + \Delta\boldsymbol{\sigma}^{n+1} \tag{5.31}$$

with the first term being the projected corrected stress from the previous mesh at t^n with minimal loss of information and $\Delta\boldsymbol{\sigma}^{n+1}$ is the increment of the stresses caused by the increment of the loads in the evolving solution.

For the initial step ($n = 1$) the stress correction term is set to $\tilde{\boldsymbol{\sigma}}^1 = \boldsymbol{0}$. This implies that the corrected stresses, for the first step, are simply the computed FE stresses $\boldsymbol{\sigma}_c^1 = \boldsymbol{\sigma}_h^1$. For the second step ($n = 2$), the stress correction term corresponds to the difference between the L_2-projection of the stresses and the stresses computed from the point-to-point projection of the nodal solution $\tilde{\boldsymbol{\sigma}}^2 = \Pi^2(\boldsymbol{\sigma}_h^1) - \hat{\boldsymbol{\sigma}}_h^1$ from the previous step ($n = 1$), such that:

$$\tilde{\boldsymbol{\sigma}}^2 = \Pi^2(\boldsymbol{C}\boldsymbol{S}\boldsymbol{u}_h^1 - \boldsymbol{C}\boldsymbol{\varepsilon}_{inh}^1) - \boldsymbol{C}[\boldsymbol{S}P^2(\boldsymbol{u}_h^1) - \Pi^2(\boldsymbol{\varepsilon}_{inh}^1)] \tag{5.32}$$

Additionaly, $\Pi^{n+1}(\boldsymbol{\sigma}_c^n)$ depends recursively on the previous solution $\boldsymbol{\sigma}_h^n$, see Eqs. (5.25) and (5.27). This can be interpreted as the recursive information transfer from the fine solution from the previous step to the current coarse mesh, preventing the loss of information.

5.3.2 *Force correction terms*

The discrete weak form of the mechanical problem, presented in Eq. (3.9), is introduced for the evolving domain at the time instant t^n considering the inherent strains $\boldsymbol{\varepsilon}_{inh}$, such that

$$\int_{\Omega_{act}^n} (\delta\boldsymbol{u}\boldsymbol{S})^T[\boldsymbol{C}(\boldsymbol{S}\boldsymbol{u}_h^n - \boldsymbol{\varepsilon}_{inh}^n)]d\Omega = \int_{\Omega_{act}^n} \delta\boldsymbol{u}^T\boldsymbol{f}^n d\Omega + \int_{\Gamma_t^n} \delta\boldsymbol{u}^T\bar{\boldsymbol{t}}^n d\Gamma \qquad \forall\delta\boldsymbol{u} \tag{5.33}$$

where the right hand side presented in Eq. (3.10) is rewritten for an evolving domain at the time instant t^n as

$$F^n(\delta\boldsymbol{u}) = \int_{\Omega_{act}^n} \delta\boldsymbol{u}^T\boldsymbol{f}^n d\Omega + \int_{\Gamma_t^n} \delta\boldsymbol{u}^T\bar{\boldsymbol{t}}^n d\Gamma \qquad \forall\delta\boldsymbol{u} \tag{5.34}$$

Ideally, the mesh projection from the solution at t^n, computed on the FE mesh at t^n (Ω_{act}^n), onto the new mesh at the time instant t^{n+1} (Ω_e^{n+1}) should preserve the equilibrium of the forces at the nodes of the mesh. In practice, this is not guaranteed, even when the stress correction term is employed.

The L_2-projection of the corrected stress from time instant t^n ($\Pi^{n+1}(\boldsymbol{\sigma}_c^n)$) onto the updated mesh at time instant t^{n+1} is

$$\int_{\Omega_e^{n+1}} (\delta\boldsymbol{u}\boldsymbol{S})^T\Pi^{n+1}(\boldsymbol{\sigma}_c^n)d\Omega = \int_{\Omega_e^{n+1}} (\delta\boldsymbol{u}\boldsymbol{S})^T(\hat{\boldsymbol{\sigma}}_h^n + \tilde{\boldsymbol{\sigma}}^{n+1})d\Omega \neq F^n(\delta\boldsymbol{u}) \qquad \forall\delta\boldsymbol{u} \tag{5.35}$$

The computed solution is in equilibrium of forces for the nodes in the Ω_{act}^n domain. Now, the domain has evolved to Ω_e^{n+1} and the solution $\boldsymbol{u}_h^n$ is projected $P^{n+1}(\boldsymbol{u}_h^n)$, but the equilibrium of the forces in the new mesh is not achieved for $P^{n+1}(\boldsymbol{u}_h^n)$. Instead, the equilibrium in the new mesh configuration Ω_e^{n+1} is given by $\hat{\boldsymbol{u}}_h^n$, such that

$$\int_{\Omega_e^{n+1}} (\delta \boldsymbol{u}\boldsymbol{S})^T \underbrace{[\boldsymbol{C}(\boldsymbol{S}\hat{\boldsymbol{u}}_h^n - \Pi^{n+1}(\boldsymbol{\varepsilon}_{inh}^n))]}_{=\hat{\boldsymbol{\sigma}}_h^n} d\Omega + \int_{\Omega_e^{n+1}} (\delta \boldsymbol{u}\boldsymbol{S})^T \underbrace{[\boldsymbol{C}(\boldsymbol{S}\hat{\boldsymbol{u}}_h^n - \Pi^{n+1}(\boldsymbol{\varepsilon}_{inh}^n))]}_{=\tilde{\boldsymbol{\sigma}}^{n+1}} d\Omega = F^n(\delta \boldsymbol{u}) \qquad \forall \delta \boldsymbol{u} \tag{5.36}$$

where the solution $\hat{\boldsymbol{u}}_h^n$ contains the contribution of the stress correction term $\tilde{\boldsymbol{\sigma}}_h^{n+1}$ and the projected stresses from the previous solution to the new mesh $\hat{\boldsymbol{\sigma}}_h^n$.

To solve the inequality shown in Eq. (5.35), correction forces are introduced to guarantee that the nodal solution obtained from the previous mesh Ω_{act}^n is in equilibrium in the new mesh Ω_e^{n+1}, prior to the activation of new elements. The correction force term is defined at the time instant t^{n+1} and computed using the projected solution from the previous time t^n as:

$$C^{n+1}(\delta \boldsymbol{u}) = \int_{\Omega_e^{n+1}} (\delta \boldsymbol{u}\boldsymbol{S})^T [\Pi^{n+1}(\boldsymbol{\sigma}_c^n)] d\Omega - F^n(\delta \boldsymbol{u}) \qquad \forall \delta \boldsymbol{u} \tag{5.37}$$

The correction force term is the residual force computed by projecting the corrected stress solution $\boldsymbol{\sigma}_c^n$ onto the new FE mesh Ω_e^{n+1}, while considering the stress correction terms $\tilde{\boldsymbol{\sigma}}_h^{n+1}$ in the equilibrium equation.

Therefore, the weak form of the evolving AM mechanical problem can be written for the active domain at the current time instant Ω_{act}^{n+1} as follows

$$\int_{\Omega_{act}^{n+1}} (\delta \boldsymbol{u}\boldsymbol{S})^T (\boldsymbol{C}[\boldsymbol{S}\boldsymbol{u}_h^{n+1} - \boldsymbol{\varepsilon}_{inh}^{n+1}]) d\Omega + \int_{\Omega_{act}^{n+1}} (\delta \boldsymbol{u}\boldsymbol{S})^T (\Pi^{n+1}(\boldsymbol{\sigma}_c^n) - \boldsymbol{C}[\boldsymbol{S}P^{n+1}(\boldsymbol{u}_h^n) - \Pi^{n+1}(\boldsymbol{\varepsilon}_{inh}^n)]) d\Omega =$$

$$\underbrace{\int_{\Omega_{act}^{n+1}} \delta \boldsymbol{u}^T \boldsymbol{f}^{n+1} d\Omega + \int_{\Gamma_t^{n+1}} \delta \boldsymbol{u}^T \bar{\boldsymbol{t}}^{n+1} d\Gamma}_{= F^{n+1}(\delta \boldsymbol{u})} + C^{n+1}(\delta \boldsymbol{u}) \qquad \forall \delta \boldsymbol{u} \tag{5.38}$$

and, introducing the correction forces terms of Eq. (5.37) into Eq. (5.38), results in

$$\int_{\Omega_{act}^{n+1}} (\delta \boldsymbol{u}\boldsymbol{S})^T (\boldsymbol{C}[\boldsymbol{S}\boldsymbol{u}_h^{n+1} - \boldsymbol{\varepsilon}_{inh}^{n+1}]) d\Omega + \int_{\Omega_{act}^{n+1}} (\delta \boldsymbol{u}\boldsymbol{S})^T (\Pi^{n+1}(\boldsymbol{\sigma}_c^n) - \boldsymbol{C}[\boldsymbol{S}P^{n+1}(\boldsymbol{u}_h^n) - \Pi^{n+1}(\boldsymbol{\varepsilon}_{inh}^n)]) d\Omega =$$

$$= \int_{\Omega_{act}^{n+1}} (\delta \boldsymbol{u}\boldsymbol{S})^T \Pi^{n+1}(\boldsymbol{\sigma}_c^n) d\Omega + F^{n+1}(\delta \boldsymbol{u}) - F^n(\delta \boldsymbol{u}) \qquad \forall \delta \boldsymbol{u} \tag{5.39}$$

$$\int_{\Omega_{act}^{n+1}} (\delta \boldsymbol{u}\boldsymbol{S})^T (\boldsymbol{C}[\boldsymbol{S}\boldsymbol{u}_h^{n+1} - \boldsymbol{\varepsilon}_{inh}^{n+1}]) d\Omega - \int_{\Omega_{act}^{n+1}} (\delta \boldsymbol{u}\boldsymbol{S})^T (\boldsymbol{C}[\boldsymbol{S}P^{n+1}(\boldsymbol{u}_h^n) - \Pi^{n+1}(\boldsymbol{\varepsilon}_{inh}^n)]) d\Omega = \tag{5.40}$$

$$= F^{n+1}(\delta \boldsymbol{u}) - F^n(\delta \boldsymbol{u}) \qquad \forall \delta \boldsymbol{u}$$

The correction terms (stresses and forces) account for the contribution of the subscales, otherwise lost during the mesh projection procedure.

This procedure requires additional computations, but the correction is computationally inexpensive. Fig. 29-(a)-(b) demonstrates the enhancement in the solution accuracy using the correction terms strategy for the AM process of a gear component. Fig. 29-(c)-(d) presents the computational cost (CPU-time and memory consumption, respectively) of the correction terms results in very similar run times of the standard AMR simulation without the correction terms.

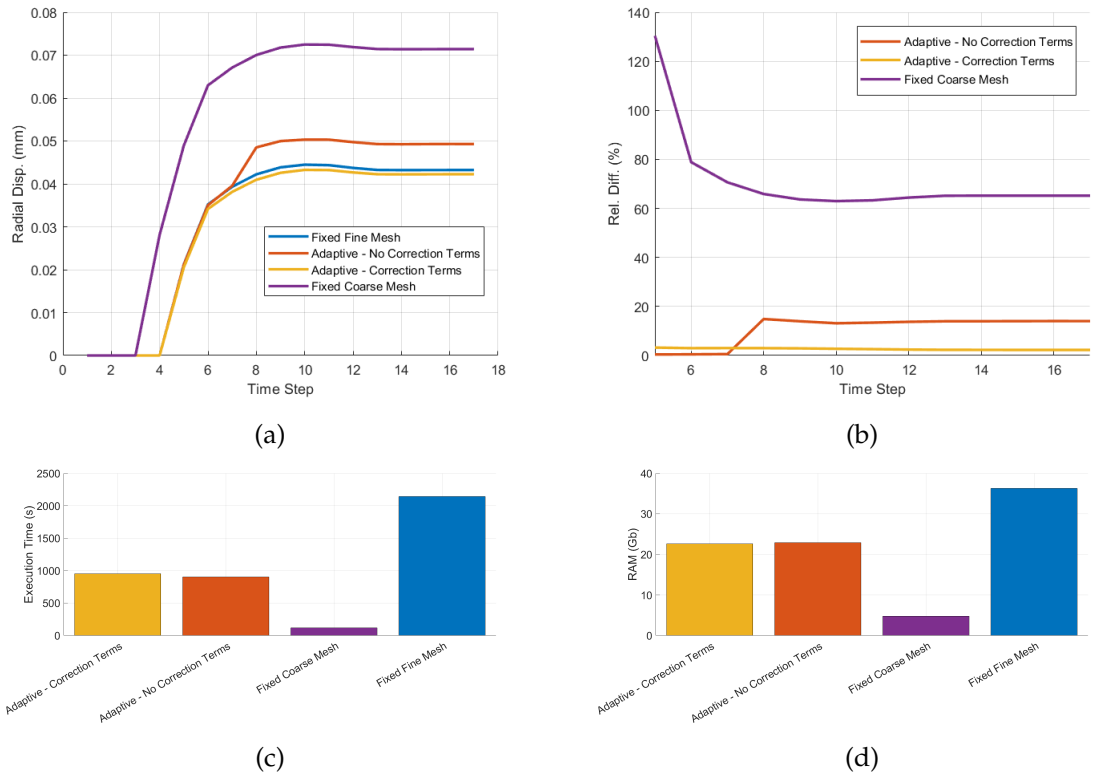

Figure 29: Coarsening correction terms influence on: (a) the displacement solution; (b) the relative percentual difference with respect to the reference solution; (c) simulation run times and (d) memory consumption.

6

AM MACHINERY

This chapter describes some aspects involved in the design of an automatic AM simulation framework and the outlook on the FE activation procedure for evolving domains.

In Section 6.1, the geometry and the process parameters from the GCode input file are presented, as well as providing the additional features required for the automatic mesh generation.

Section 6.2 addresses the searching technology used to generate the mesh automatically and to activate the FEs according to the evolving domain. Additionaly, some considerations are made for the FE activation procedure.

6.1 GCode reader and automatic meshing

The GCode is a format broadly used in industrial machine tooling. The advantage of using the GCode format relies on the fact that it can include additional data related to the *processing* parameters, such as the power input, time pauses, depositing and re-coating speeds.

This flexibility of the GCode format, to enable the change of the process parameters at any point of the printing, permits the design of better AM components. This is because the process parameters can be tunned to fulfill specific criteria, instead of remaining them constant during the manufacturing of the component. For instance, This makes possible to construct GCodes where the process parameters can be designed to minimize residual stresses by controling the temperature gradient between adjacent layers.

Therefore, an input format that contains not only the geometric shape of the component, but can also be molded according to specific criteria is important for the dissemination of the AM as an industrial-scale technology capable to produce quality components.

The simulation of the AM process also needs to account for all the changes provided to the actual machine tool. Thus, the GCode format is ideal for the accurate simulation of AM processes. Fig. 30 shows a comparison between a GCode, Fig. 30-(a), and a CLI format, Fig. 30-(a), in terms of a color scheme for the process parameters. Both file formats deliver the correct geometry, nevertheless, the process parameters for the CLI format are kept constant throughout the simulation process.

Regarding the GCode commands: `G1/G0` correspond to movement commands, where `G0` is a fast straight movement (with no deposition), and `G1` is a straight line movement with material feeding. Command `E` provides the information of the deposition process, where the attached value corresponds to the material feeding; if this value is different from zero, the machine is depositing new material in this segment, otherwise the machine is moving without deposition. Command `F` refers to the power source speed (in $[mm/min]$). The coordinates defined in a given command line corresponds to the final (x, y) coordinates of the hatch; while the initial coordinate of the hatch is defined in the previous command line.

The power source can be varied during along the process by using the command `G108` and introducing the P (power source) followed by `S` (of set) and the value of the new power source in $[W]$, e.g. `G108 P S2000`. In some cases, pauses are required during the printing process and the time interval can be set by `G4` followed by `S` and the value of the pause in $[s]$. In this format, the layer thickness is defined by the difference between two consecutive z-coordinates.

As an example, Fig. 31 shows a code snippet describing the scanning path in a GCode format considering variable process parameters. Table 1 shows the list of representative properties that are stored in each hatch.

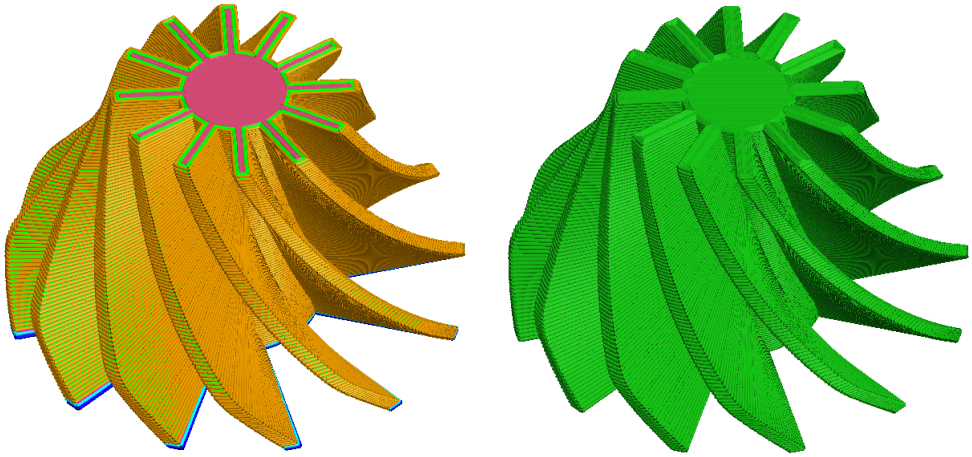

(a) (b)

Figure 30: Process parameter color scheme, where each color represents a different combination of power input and deposition speed. (a) Process parameters from the GCode format. (b) Process parameters from the CLI format.

Code	Command	Units
G0/G1	Hatch movement	mm
F	Update speed	mm/min
G4	Introduce time pause	seconds
G108	Update laser power	Watts
E	Extruding material	mm

Table 1: List of the process parameters provided by the GCode.

```
;Generated with Cura_SteamEngine 4.4.1
;LAYER_COUNT:247
;LAYER:0
G108 P S2000 ;Set laser power
G0 F3600 X163.281 Y128.413 Z0.2 ;Repositioning hatch speed 3600 mm/min
G1 F1800 X163.542 Y125.695 E0.03424 ;Depositing hatch 1800 mm/min
G1 X163.967 Y122.663 E0.07264 ;Depositing hatch 1800 mm/min
G1 X164.643 Y119.722 E0.11048 ;Depositing hatch 1800 mm/min
G108 P S1000 ;Set laser power
G1 X165.578 Y116.833 E0.14856 ;Depositing hatch 1800 mm/min
G1 X166.736 Y114.088 ;Recoating hatch 1800 mm/min
G1 X168.169 Y111.382 E0.22432 ;Depositing hatch 1800 mm/min
G1 X169.785 Y108.875 ;Recoating hatch 1800 mm/min
G1 X171.621 Y106.508 E0.29929 ;Depositing hatch 1800 mm/min
G1 X173.702 Y104.26 ;Recoating hatch 1800 mm/min
G4 S90 ;Set pause 90s
G1 X175.924 Y102.243 Z0.4 ;Repositioning hatch 1800 mm/min
G1 F2000 X178.3 Y100.436 E0.41277 ;Depositing hatch 2000 mm/min
```

Figure 31: Sample of a GCode format containing the power input path and some process parameters.

6.1.1 *Automatic mesh generation*

In the following, the aspects required for the generation of the automatic mesh procedure are considered to complement the geometric criteria for refinement and coarsening (Section 5.2). The time-step computation and the bounding box construction are detailed.

The GCode contains the total path L that the machine will travel during the manufacturing process. The total path L is the sum of the length of individual hatches l. The total time interval considered in the AM process is defined in the interval $t \in (0, T]$. The number of time-steps N of the AM simulation is computed from a user-defined parameter, the length increment per time-step Δl, such that $N = L/\Delta l$.

To define a time-step, the hatches that will be activated according to the length increment per time-step Δl need to be identified. To do so, all the hatches that are not yet activated are added together until the summation reaches the path-length increment Δl, such that

$$\Delta l = \sum_{i=1}^{n_h^{n+1}} l_i \tag{6.1}$$

where, l_i is the i-th hatch-length and n_h^{n+1} is the number of adjacent hatches that the total length is equal to the path-length increment Δl for the current time-step. The hatches included in the path-length increment Δl defines the domain Ω_a^{n+1} (see Fig. 32).

Next, after selecting the hatches l_i that are included in the path-length increment Δl, the time t_i to travel each hatch l_i is computed using the hatch deposition speed, read from the GCode, such that

$$t_i = \frac{l_i}{v_i} \tag{6.2}$$

where t_i is the time required to travel the i-th hatch-length l_i according to the i-th hatch deposition speed v_i.

For a given path-length increment Δl, the time-step is defined as $\Delta t = t^{n+1} - t^n$, such that t^n is the accumulated time from the previous time-step, at the beginning of the deposition of the current group of hatches, and t^{n+1} is given by

$$t^{n+1} = t^n + \sum_{i=1}^{n_h^{n+1}} t_i \tag{6.3}$$

Fig. 32 presents the hatches that belong to the total active domain Ω_{act}^{n+1}. The green bounding boxes represent the hacthes activated in previous time-steps Ω_a^n and the purple boxes are the hatches activated in the current time-step Ω_a^{n+1} with $n_h^{n+1} = 4$.

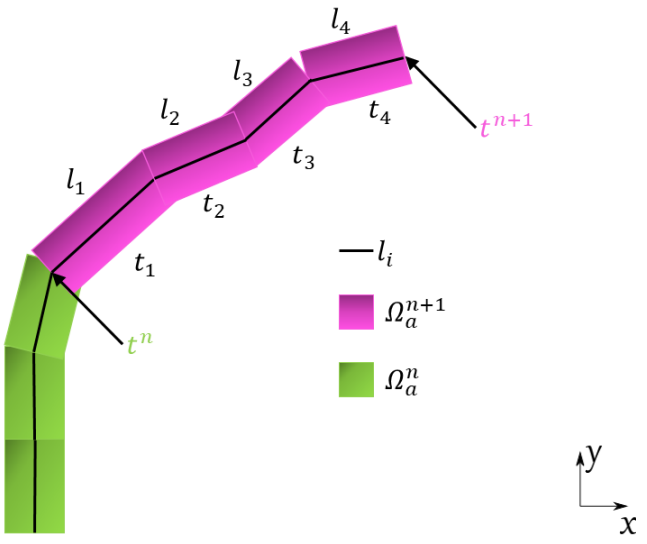

Figure 32: Definition of the active domain Ω_{act}^{n+1} and the information stored in the hatches about its length l_i and the required time t_i to travel the hatch length.

The hatches are unidimensional while the bounding box geometric criterion requires $3D$ polytopes. The bounding box volume is defined by the hatch length, l, the layer-thickness, h_{layer}, the heat source penetration, z_{power}, the melt-pool width, b_{pool} and the total height in which the power is distributed, namely the melt-pool height h_{pool}, computed as $h_{pool} = h_{layer} + z_{power}$.

Fig. 33 shows the initial and final nodal coordinates of the i-th hatch that define the current HAZ bounding box (OV). The bounding box is built by extruding the hatch initial and final position according to the the process parameters (b_{pool}, h_{layer} and z_{power}). Note that for each time-step the number of bounding boxes to be tested to generate the automatic mesh depend on n_h^{n+1}.

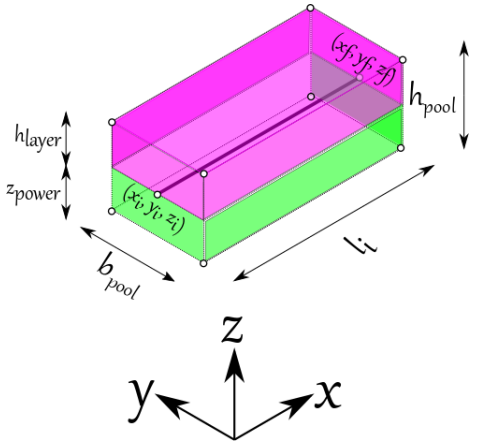

Figure 33: The HAZ bounding box (OV) construction using the process parameters and the hatch coordinates.

6.2 Growing computational domains

6.2.1 *Searching technology*

In this thesis, the searching algorithm for the automatic mesh generation and element activation looks for the collision between two prismatic polytopes, one representing the current position of the HAZ (OV), built from the GCode information (Section 6.1), and one being the FE to be tested using the *separating axis theorem* (SAT) (Eberly, 2002; Gottschalk et al., 2000; Neiva et al., 2019; Moreira et al., 2022b). For a pair of convex polytopes, formed by E edges and F faces each, the SAT states that the polytopes overlap if they intersect in at least one of their projections onto their $E^2 + 2F$ planes.

When both polytopes are box-shaped (prismatic), the number of planes to be tested is considerably reduced because parallel planes only need to be tested once. This results in $E = 3$ and $F = 3$, in a total of only 15 testing planes. In the case of using tetrahedra FEs, the number of testing planes increases to 44 ($E = 6$ and $F = 4$). The presence of a separating plane ($s > r_{OV} + r_{FE}$, see Fig. 26) returns the *non-intersection* between the HAZ and the FE, and the FE is not refined and no additional planes are required to be tested. Fig. 34 shows a $2D$ example of the AMR mesh after 5 adaptive cycles using the SAT searching algorithm with and without the $2:1$ balance scheme restriction.

In a cartesian mesh, the 3 FE testing planes are simply the unit vectors representing the system of coordinates (x, y, z). Therefore, the group of the FE testing planes $\boldsymbol{n}_{FE}$ is given by the 3×3 matrix:

$$\boldsymbol{n}_{FE} = \begin{bmatrix} 1 & 0 & 0 \\ 0 & 1 & 0 \\ 0 & 0 & 1 \end{bmatrix} \tag{6.4}$$

where the columns of the $\boldsymbol{n}_{FE}$ represents the $\boldsymbol{x}$-plane, $\boldsymbol{y}$-plane and $\boldsymbol{z}$-plane, respectively.

On the other hand, the HAZ bounding box testing planes are variable and need to be computed for all the n_h^{n+1} hatches that defines Ω_a^{n+1}, see Fig. 32. The layer-by-layer nature of the AM process also simplifies the computation of the HAZ bounding box testing planes, because the deposition direction is on the z-direction. Therefore, the HAZ bounding box top and bottom faces are parallel to the z-plane

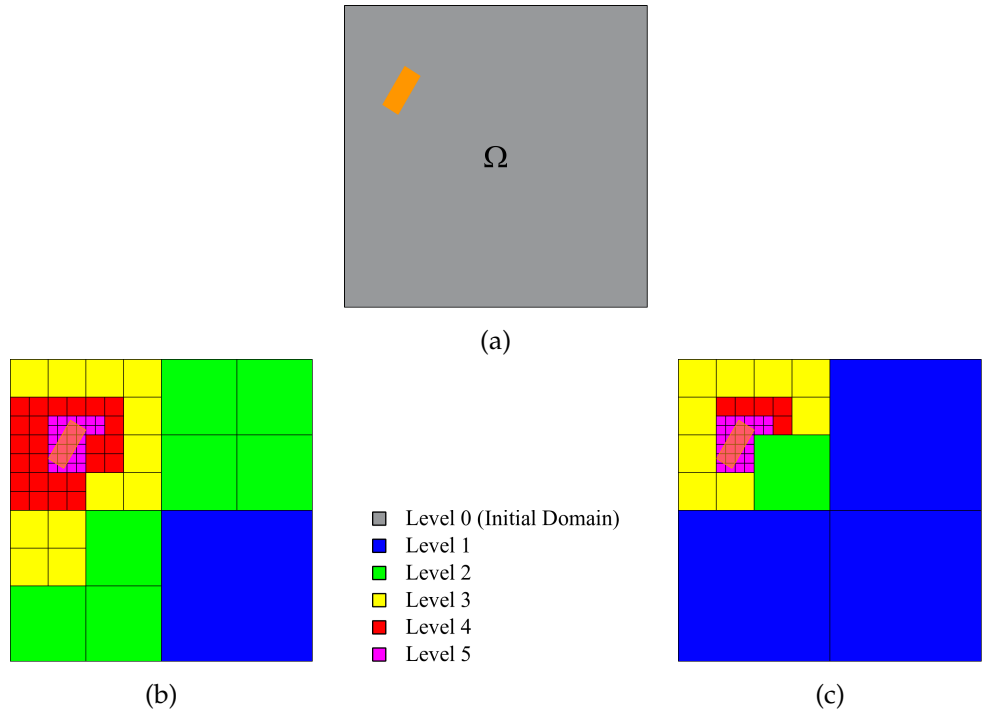

Figure 34: (a) *OV* embedded into the initial domain; Final mesh after 5 adaptivity cycles (b) with 2:1 balance; (c) without 2:1 balance.

defined from the unit vector $\boldsymbol{n}_z = (0,0,1)^T$; similarly, the $\boldsymbol{x}$ and $\boldsymbol{y}$-planes are parallel to the unit vectors $\boldsymbol{n}_x = (1,0,0)^T$ and $\boldsymbol{n}_y = (0,1,0)^T$, respectively. The hatch direction defines another testing plane, $\boldsymbol{n}_l$, such that:

$$\boldsymbol{n}_l = \frac{(\boldsymbol{x}_f - \boldsymbol{x}_i)}{l_i} \tag{6.5}$$

where $\boldsymbol{x}_i$ and $\boldsymbol{x}_f$ are the initial and final cartesian coordinates of the hatch, respectively, and l_i is the hatch length. Lastly, the third HAZ bounding box testing plane is orthogonal to the pair $\boldsymbol{n}_l$ and $\boldsymbol{z} - plane$ ($\boldsymbol{n}_z$), thus, computed as:

$$\boldsymbol{n}_b = \boldsymbol{n}_z \times \boldsymbol{n}_l \tag{6.6}$$

with $\boldsymbol{n}_b$ being the testing plane defined in the melt-pool width, b_{pool}. Therefore, the group of the testing planes defined by the HAZ bounding box is $\boldsymbol{n}_{HAZ} = [\boldsymbol{n}_l, \boldsymbol{n}_b, \boldsymbol{n}_z]$. Fig. 35 shows the testing planes of the FE and the HAZ bounding box.

Finaly, the remaining 9 testing planes are created from the the cross-product of the existing testing planes from the HAZ and the FE. Table 2 shows all the 15 testing planes necessary to verify the collision of two prismatic polytopes.

6.2.2 *FE activation*

For time t of the AM process, the domain is decomposed into its *active* and *inactive* parts. The current active part is defined as a FE partition $\Omega_{\text{act}}^{n+1} \subseteq (\Omega_a^{n+1} \cup \Omega_a^n)$, where Ω_a^{n+1} and Ω_a^n are FEs activated at t^{n+1} and the set of FEs activated previously, respectively. The inactive domain is defined as $\Omega_{\text{ina}}^{n+1} \subseteq (\Omega_i^{n+1} \cup \hat{\Omega}_i^{n+1})$, where Ω_i^{n+1} is the domain of inactive FEs and $\hat{\Omega}_i^{n+1}$ the domain of inactive FEs that share nodes with $\Omega_{\text{act}^{n+1}}$.

The nodes of the FE mesh are labelled according to three sets: 1) the common nodes of the active ($\Omega_{\text{act}}^{n+1}$) and inactive ($\Omega_{\text{ina}}^{n+1}$), defined as ξ^{skin}, 2) ξ^{int} is the set of nodes where all the adjacent FEs belong to $\Omega_{\text{act}}^{n+1}$ and 3) ξ^{ina} is the set of nodes belonging where all the adjacent FEs belong to the inactive domain (Ω_{ina}^{n+1}). Fig. 36 shows the domain and the nodal classifications of an arbitrary $x - y$ plane of the AM process.

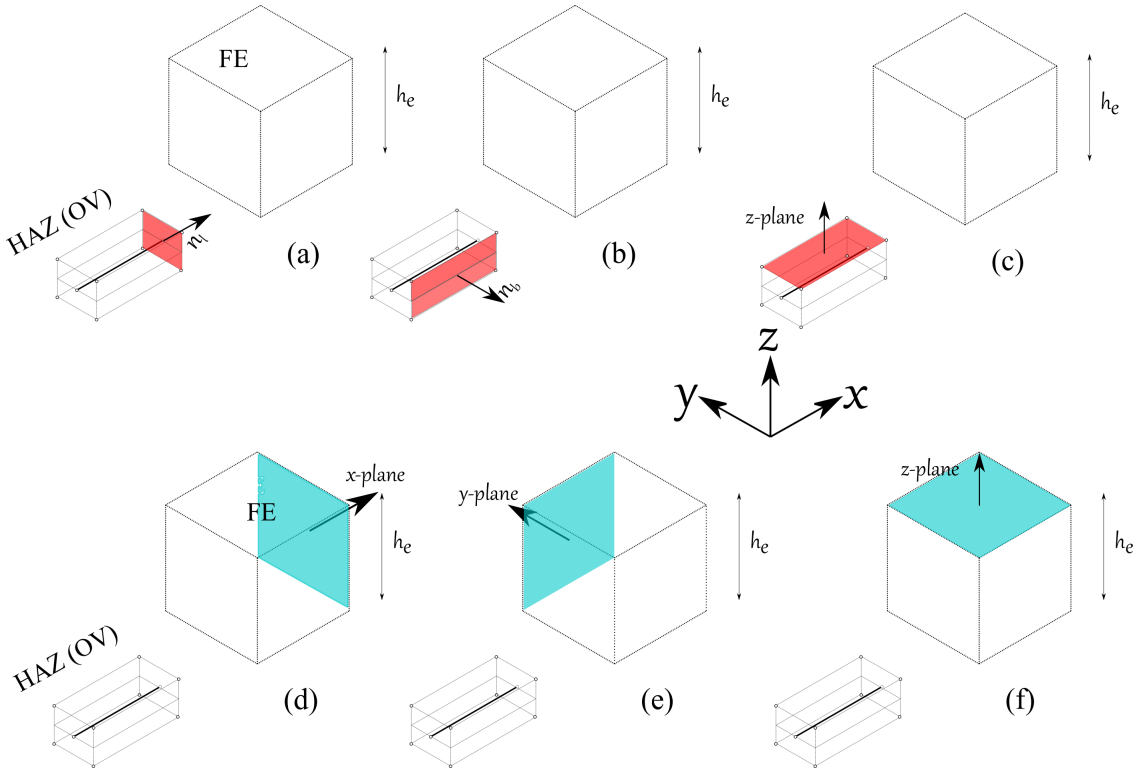

Figure 35: Testing planes for the HAZ bounding box (a)-(c) and for the FE (d)-(f).

Test Plane #	Polytope	Test Plane
1	HAZ	$\boldsymbol{n}_l$
2	HAZ	$\boldsymbol{n}_b$
3	HAZ	$\boldsymbol{n}_z$
4	FE	$\boldsymbol{n}_x$
5	FE	$\boldsymbol{n}_y$
6	FE	$\boldsymbol{n}_z$
7	HAZ × HAZ	$\boldsymbol{n}_l \times \boldsymbol{n}_l$
8	HAZ × HAZ	$\boldsymbol{n}_l \times \boldsymbol{n}_b$
9	HAZ × HAZ	$\boldsymbol{n}_l \times \boldsymbol{n}_z$
10	HAZ × HAZ	$\boldsymbol{n}_b \times \boldsymbol{n}_b$
11	HAZ × HAZ	$\boldsymbol{n}_b \times \boldsymbol{n}_z$
12	HAZ × FE	$\boldsymbol{n}_l \times \boldsymbol{n}_x$
13	HAZ × FE	$\boldsymbol{n}_l \times \boldsymbol{n}_y$
14	HAZ × FE	$\boldsymbol{n}_b \times \boldsymbol{n}_x$
15	HAZ × FE	$\boldsymbol{n}_l \times \boldsymbol{n}_y$

Table 2: List of the required testing planes to verify the collision detection between prismatic polytopes.

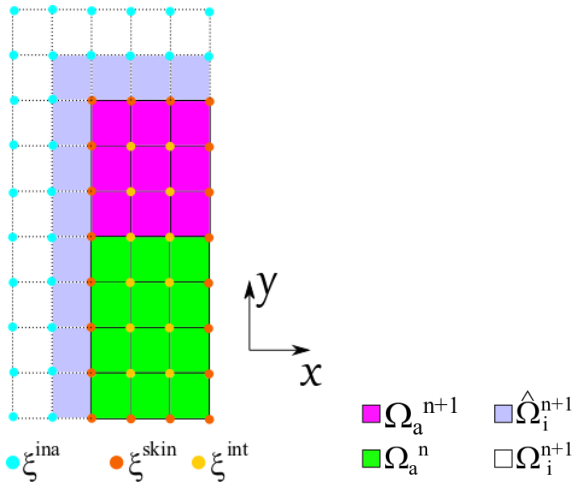

Figure 36: Definition of the evolving active domain ($\Omega_{\text{act}}^{n+1} \subseteq (\Omega_a^{n+1} \cup \Omega_a^n)$) and inactive domain ($\Omega_{\text{ina}}^{n+1} \subseteq (\Omega_i^{n+1} \cup \hat{\Omega}_i^{n+1})$) and the node classification.

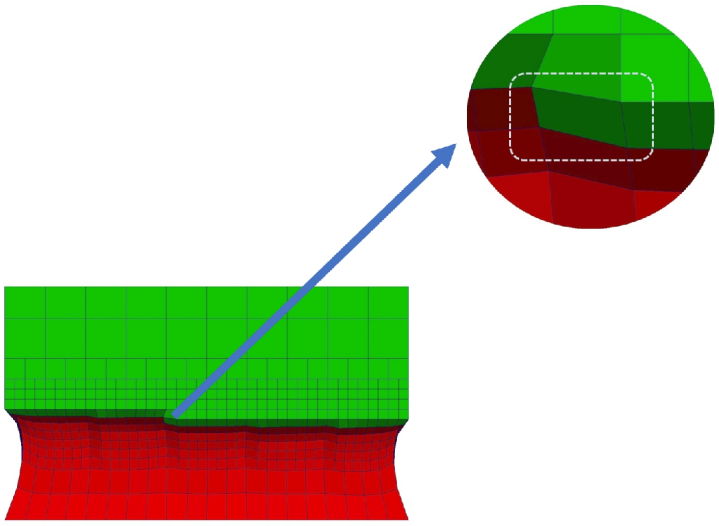

Figure 37: Displacement field induced by the FE activation process: red FEs are the elements activated in the previous time-steps. Green FEs elements are activated within the current time-step.

The element birth-death approach is used to add to the computational domain all the FEs that belongs to the corresponding domain of each time-step, that evolves according to the user-defined path-length increment, Δl. The inactive elements do not belong to the computational domain, therefore are not assembled to the global system of equations.

The activation procedure apply the search algorithm detailed in Section 6.2.1 to determine the FEs to be added to the discrete weak form. The problem is solved for the active domain at the current instant t^{n+1}, Ω_{act}^{n+1}, using an implicit approach for the time integration.

The activation process, i.e. adding new FEs to the system of equations, induces a movement of the nodes shared between the active and inactive domains, the set of ξ^{skin} nodes. Thus, when a FE is *born*, i.e. the FE is introduced in the system of equations, the effects of the initial displacements ($\boldsymbol{u}^0$), caused by the previous activation of adjacent FEs needs to be considered.

Fig. 37 shows the displacement fields in the Ω_{act}^{n+1} and Ω_{ina}^{n+1} FE partitions. The dark green FE in evidence is going to be activated in the next time instant. This FE presents a displacement field computed for the active domain, at the shared nodes between the Ω_{act}^{n+1} and Ω_{ina}^{n+1}, which, if not removed, generates spurious pre-stress and pollutes the solution.

The strains caused by the initial displacement, in the row of dark green FEs (Fig. 37), should not introduce any stress in the newly activated FE; thus, the total strain is computed as

$$\boldsymbol{\varepsilon}^* = \boldsymbol{\varepsilon} - \boldsymbol{\varepsilon}_{act} = \boldsymbol{S}(\boldsymbol{u} - \boldsymbol{u}^0) \tag{6.7}$$

where $\boldsymbol{\varepsilon}$ are the total strains, $\boldsymbol{\varepsilon}_{act}$ are the activation strains, $\boldsymbol{u}^0$ are the initial displacement field and $\boldsymbol{\varepsilon}^*$ are the compensated total strains, which removes the spurious effect of the activation strains for the FE activation.

This given, the general discrete weak form of the mechanical problem, presented in Eq. (3.9), can be rewritten for AM processes using the element birth-death approach for the current time instant t^{n+1} as:

$$\int_{\Omega_{act}^{n+1}} (\delta \boldsymbol{u} \boldsymbol{S})^T [\boldsymbol{C} \boldsymbol{S} (\boldsymbol{u}_h^{n+1} - \boldsymbol{u}_h^0)] d\Omega = \int_{\Omega_{act}^{n+1}} \delta \boldsymbol{u}^T \boldsymbol{f}^{n+1} d\Omega + \int_{\Gamma_t^{n+1}} \delta \boldsymbol{u}^T \bar{\boldsymbol{t}}^{n+1} d\Gamma \qquad \forall \delta \boldsymbol{u} \tag{6.8}$$

where the solution to the AM mechanical problem is to find $\boldsymbol{u}_h^{n+1}$ for the current instant t^{n+1}, subjected to the evolving boundary conditions in the evolving domain.

For a fix mesh, after the FE is activated, the initial displacements $\boldsymbol{u}^0$ of the FE do not change, as well as the corresponding activation strains $\boldsymbol{\varepsilon}_{act}$. On the one hand, if the layer height coincides with the size of the FE h_e, all the activated FEs will be activated with activation strains. On the other hand, if the HAZ is activated with several elements defining the layer thickness, only the elements on the interface between the previous and current layers will be activated with non-zero values for the activation strains.

In the context of the correction procedure presented in Section 5.3, the activation strains must be introduced in the correction terms similarly to the inherent strains $\boldsymbol{\varepsilon}_{inh}$.

7

CONCLUSIONS

The outline of this Chapter is as follows. Section 7.1 summarizes this doctoral thesis. Section 7.2 presents a list of conclusions. Section 7.3 provides the main contributions of this work. Section 7.4 suggests the lines of future research.

7.1 Summary

This doctoral thesis focuses on the development of numerical solutions to reduce the computational cost of AM simulations while delivering results of enhanced accuracy. For this purpose, a parallel FE framework for the simulation of AM with enhanced accuracy is developed, validated and employed in industrial applications.

Chapter 2 presents a detailed state-of-the-art on the main challenges regarding the numerical simulation of AM processes. The incompressibility problem arising from the Von Mises materials, such as metals, is addressed from the FE technology perspective. Numerical approaches for the thermo-mechanical modelling to obtain accurate thermal and mechanical responses is presented. Next, the high-demanding computational cost required by the AM simulation is tackled presenting several AMR strategies used in computational mechanics and also applied to AM problems. Lastly, the importance of delivering the same input data to both the actual machinery and the computational simulation is assessed.

Chapter 3 presents the FE technologies used to address the volumetric locking including the novel mixed $\boldsymbol{u}/\boldsymbol{e}/p$ formulation. The enhanced accuracy of the proposed FE formulation in the computation of the mechanical dissipation, stress/strain and computational cost reduction is assessed in Paper 2, where a series of benchmarks and proposed numerical examples are used.

Chapter 4 introduces the thermo-mechanical modelling aspects for the simulation of part-scale components in AM processes. The thermo-mechanical extension of the mixed $\boldsymbol{u}/\boldsymbol{e}/p$ formulation is used for the assessment of thermal-induced failure in Paper 3. Several benchmarks and numerical examples are used to compare the mixed $\boldsymbol{u}/p$ and $\boldsymbol{u}/\boldsymbol{e}/p$ with respect to the capability of reproducing failure mechanisms, load capacity and numerical stability. Additionaly, the heat source model presented is applied in Paper 4 in the AM context, obtaining good agreement with the experimental results.

Chapter 5 details the multi-criteria strategy used to generate the automatic mesh from the GCode while providing numerical accuracy. Additionaly, the coarsening correction strategy is presented to avoid the loss of information resulting from the mesh coarsening procedure. The improvement resulting from the coarsening correction strategy is presented in Paper 1, while the accuracy of the multi-criteria and automatic mesh generation from the GCode is presented in Paper 4. Several numerical analyses for the heat transfer problem of the DED process are used to assess the accuracy and computational cost efficiency of the multi-criteria approach.

Chapter 6 details the additional features required for the automatic mesh generation, including the data acquisition for the AM simulation from a GCode file, presented in Paper 4. The FE activation procedure adopted in Paper 1 is presented; the searching algorithm used to build the automatic mesh and activate the corresponding FEs is also described.

In this thesis, the ability of the proposed strategies in the field of the FE technology, the AMR technique and the AM machinery to reduce computational cost without compromising the solution accuracy is demonstrated.

7.2 Conclusions

The following conclusions can be drawn from the work presented in this thesis:

7.2.1 *Conclusions on the enhanced accuracy of the stress/strain mixed formulation*

- The mixed $\boldsymbol{u}/\boldsymbol{e}/p$ formulation can be used with a wide range of constitutive models, such as $J2$-plasticity, $J2$-damage, Drucker-Prager plasticity or damage models, etc, in the solid mechanics field and also in the fluid dynamics, for instance in non-newtonian rigid-viscoplastic flows.
- The mixed $\boldsymbol{u}/\boldsymbol{e}/p$ formulation presents a faster convergence rate for the stress/strain fields than the $\boldsymbol{u}/p$ upon mesh refinement, resulting in the desired accuracy with a much coarser mesh and less cpu-time.
- The better performance of the mixed $\boldsymbol{u}/\boldsymbol{e}/p$ formulation has been demonstrated with respect to mechanical dissipation accuracy and failure mechanisms.
- The 3-field formulation accomodates any FE approximation and has been applied to triangles, quadrilaterals, tetrahedras and hexahedras.
- The 3-field formulation addresses incompressible conditions in the elastic and inelastic regimes without presenting stress-locking, including when softening behavior is considered.
- As evidenced by this work, the mixed $\boldsymbol{u}/\boldsymbol{e}/p$ reproduces theoretical load capacity in the numerical benchmarks.
- The thermo-mechanical coupling of the 3-field formulation has been successfully implemented and the strong points observed in the mechanical applications are also observed in the thermo-mechanical numerical examples.
- The enhanced accuracy observed in the mixed 3-field formulation in the mechanical and thermo-mechanical scenarios make it a very appealing FE technology to be considered in industrial manufacturing problems, i.e. Friction Stir-Welding, Forging, Extrusion, AM, etc.
- In AM, mesh discretization is often determined by geometrical requirements rather than accuracy considerations. In those instances, using a FE technology with enhanced accuracy may not be necessary.

7.2.2 *Conclusions on the AMR applied to AM*

- The use of AMR is paramount to save computational resources and to reduce cpu-time in AM simulations.
- Not employing the 2 : 1 balance scheme provides coarser meshes, improving computational speed. On the other hand, large jumps on the refinement level of adjacent FEs may pollute the previously fine solution with errors associated with the mesh projections used.
- The coarsening correction strategy minimizes the effects of the projection errors in the mechanical solution by introducing a correction stress term and guaranteeing the equilibrium of forces at the nodes with the residual-based correction forces. The former corrects the information loss in the stress field resulting from the coarsening procedure, and the later is introduced in the weak form of the problem to prevent the information loss in the displacement field.
- The coarsening correction strategy has been successfully applied to hexahedra and tetrahedra meshes and different AM processes. The strategy enables cpu-time reduction, as a consequence of the unrestricted coarsening possibility (in opposition to the 2 : 1 balance scheme), while the solution accuracy is preserved.

- The use of a purely geometric criterion, i.e. layer-wise, without an associated error-estimator requires the calibration of the number of refined layers necessary to balance accuracy and efficiency.
- It is important to consider the use of an error-estimator for the AMR strategy in the simulation of AM processes that induce high temperature gradients in the manufactured component.
- The multi-criteria approach is used to avoid the 2 : 1 balance restriction without loosing numerical solution accuracy while the number of FEs is kept controlled. The balance between efficiency and accuracy is found with less effort than using a purely geometric criterion, where the coarsening criterion needs calibration.

7.2.3 *Conclusions on the numerical simulations of industrial components*

- The major competitive advantage of AM is the free-form design, resulting in very optimized and complex geometries. The use of the GCode to model the geometry, at the same time that it defines the process parameters, increases the simulation accuracy with respect to the actual manufacturing process.
- The proposed AM framework is able to avoid the CAD cleaning and meshing operations, giving agility to the AM simulation process, especially when complex geometries are involved.
- The *separating axis theorem* (SAT) is used to access the mesh building according to the evolving domain. The searching algorithm is highly scalable and efficient to identify the collision between the HAZ and the background FE mesh.
- Thin-walls are frequent in optimized AM components. This provides a coarsening geometrical constraint to preserve the component boundaries, which reduces the AMR advantages. In those cases, the number of active FEs increases, instead of reaching a stable value. Even so, the use of the AMR strategy still pays-off when the 2 : 1 balance constraint is avoided.
- The bottleneck to reduce the computational time in the HF simulation of AM components is in the required number of time steps necessary to obtain HF responses.

7.3 Main contributions

The research developed in this doctoral thesis includes the following original contributions:

- **Enhanced stress/strain FE formulation**. The development of a mixed 3-field FE formulation to tackle the incompressibility problem including thermo-mechanical applcations. This FE technology demonstrates superior performance compared to the widely used $\boldsymbol{u}/p$ formulation in terms of stress/strain accuracy in a wide variety of proposed problems and benchmarks. The mixed 3-field FE formulation may be a powerful tool in the simulation of industrial manufacturing processes.
- **Automatic mesh generation from GCode**. One of the primary sources of inaccuracies between the simulation and the actual component manufacturing lies in the different data provided to the machinery and the numerical simulation. The development of a GCode reader that stores the exact process parameters and geometrical data provided to the actual AM machinery reduces the user-interference in the modelling step. The SAT used to construct the evolving FE domain permits the simulation of very complex geometry starting from a single hexahedron FE describing the embedding domain.
- **Parallelized AM framework**. The feasability of HF simulations of AM processes demands high computational power and the parallelization of the AM framework is mandatory. The original AM framework has been initially developed in the in-house software COMET (COupled Mechanical and Thermal analysis) (Cervera et al., 2002) and moved to the FEMUSS (Finite Element Method Using Sub-grid Scales) platform, that uses a objected-oriented paradigm in a Fortran environment.

This has made it possible to increase the degree of complexity of the AM parts simulated and enabled the use of adaptive meshes *without* the 2 : 1 balance constraint. The implementation has been validated throughout an extensive campaign including thermal, mechanical and thermo-mechanical analyses.

- **Coarsening correction strategy**. The use of the coarsening correction strategy developed is key for the solution of the mechanical problem, especially when the 2 : 1 balance scheme is avoided. The large jumps on the gradients of the mechanical solution, when homogenized and projected to a much coarser mesh, introduces stress errors behavior that need to be corrected. This strategy enables the use of several refinement levels between adjacent FEs preserving the accuracy of the fine mesh solution at a very low computational cost.
- **Multi-criteria approach for AMR**. The use of a geometric criterion is very common for fast cooling-rate AM processes, such as the PBF. On lower cooling-rate AM technologies, the use of a geometric criterion without an error-estimator induces approximation errors from the coarser FEs. The incorporation of an extra criterion based on an a posteriori error-estimator, such as the ZZ-error estimator, reduces significantly the computed global error at almost no additional computational cost.

7.4 Lines of future research

In this thesis, the FE simulation of AM processes with enhanced accuracy is investigated. In order to advance in this field of research, the following lines of investigation need to be pursued:

- **Formulation Adaptivity**. Although the performance of the mixed $\boldsymbol{u}/\boldsymbol{e}/p$ has demonstrated to be less costly for a desired level of accuracy, the number of existing FEs in an AM component is driven by the complexity of the geometry. Therefore, a solution to make the use of the mixed 3-field formulation feasible is to combine it with the $\boldsymbol{u}/p$ formulation on the same geometric model. The development of an error-estimator to provide the automatic choice between both FE formulation is required, reducing the number of 3-field elements on less relevant portions of the domain and, in consequence, reducing the computational cost.
- **Reduced Order Model (ROM)**. The major bottleneck in the HF part-scale simulation of the AM process is the required number of time-steps, especially when industrial components are of interest. In this sense, the development and training of a ROM enables the reduction of the number of time-steps without compromising the quality of the obtained solution.
- **Multi-laser AM Simulation**. The possibility of introducing several GCodes, each one belonging to a different printer, permits the decrease in the both fabrication and simulation times required by the AM process. The number of time-steps is reduced by the increase in the number of activated FEs for each time-step, due to the use of several GCodes concurrently.
- **Shrinkage**. In the constitutive model presented, the shrinkage effect is not considered. This effect depends on the evolution of the rate of the liquid/solid fraction and may introduce large values for the thermal-strains. Inclusion of this effect may be of interest for massive components.
- **Nonlinear Kinematics**. The growing demands of the industry towards weight reduction translates into slender components. In this sense, the use of nonlinear kinematics may be required when high temperature gradients are observed in thin-walled manufactured components.

BIBLIOGRAPHY

C. Agelet de Saracibar, M. Cervera, and M. Chiumenti. On the formulation of coupled thermoplastic problems with phase-change. *International Journal of Plasticity*, 15(1):1–34, 1999. ISSN 0749-6419. doi: https://doi.org/10.1016/S0749-6419(98)00055-2. URL https://www.sciencedirect.com/science/article/pii/S0749641998000552.

C. Agelet de Saracibar, M. Cervera, and M. Chiumenti. On the constitutive modeling of coupled thermomechanical phase-change problems. *International Journal of Plasticity*, 17(12):1565–1622, 2001.

C. Agelet de Saracibar, M. Chiumenti, Q. Valverde, and M. Cervera. On the orthogonal subgrid scale pressure stabilization of finite deformation j2 plasticity. *Computer Methods in Applied Mechanics and Engineering*, 195(9):1224–1251, 2006. ISSN 0045-7825. doi: https://doi.org/10.1016/j.cma.2005.04.007. URL https://www.sciencedirect.com/science/article/pii/S004578250500160X.

M. Ainsworth, J. Z. Zhu, A. W. Craig, and O. C. Zienkiewicz. Analysis of the zienkiewiczâzhu aâposteriori error estimator in the finite element method. *International Journal for Numerical Methods in Engineering*, 28:2161–2174, 1989.

A. Alhadeff, S. Leon, W. Celes, and G. Paulino. Massively parallel adaptive mesh refinement and coarsening for dynamic fracture simulations. *Engineering with Computers*, 32:1–20, 07 2016. doi: 10.1007/s00366-015-0431-0.

P. Alvarez, J. Ecenarro, I. Setien, M. S. Sebastian, A. Echeverría, and L. Eciolaza. Computationally efficient distortion prediction in powder bed fusion additive manufacturing. *International Journal of Engineering Research & Science*, 2:39–46, 2016.

ANSYS10 Inc. Ansys release 10.0 documentation. https://www.ansys.com/products/structures/ansys-mechanical, 2007.

K. Antony, N. Arivazhagan, and K. Senthilkumaran. Numerical and experimental investigations on laser melting of stainless steel 316l metal powders. *Journal of Manufacturing Processes*, 16(3):345–355, 2014. ISSN 1526-6125. doi: https://doi.org/10.1016/j.jmapro.2014.04.001. URL https://www.sciencedirect.com/science/article/pii/S1526612514000383.

F. Armero and J. C. Simo. A new unconditionally stable fractional step method for non-linear coupled thermomechanical problems. *International Journal for Numerical Methods in Engineering*, 35(4):737–766, 1992. doi: https://doi.org/10.1002/nme.1620350408. URL https://onlinelibrary.wiley.com/doi/abs/10.1002/nme.1620350408.

D. N. Arnold. Mixed finite element methods for elliptic problems. *Computer Methods in Applied Mechanics and Engineering*, 82(1):281–300, 1990. ISSN 0045-7825. doi: https://doi.org/10.1016/0045-7825(90)90168-L. URL https://www.sciencedirect.com/science/article/pii/004578259090168L. Proceedings of the Workshop on Reliability in Computational Mechanics.

D. N. Arnold, F. Brezzi, and M. Fortin. A stable finite element for the stokes equations. *Calcolo*, 21(4):337–344, 1984a.

D. N. Arnold, J. Douglas, and C. P. Gupta. A family of higher order mixed finite element methods for plane elasticity. *Numerische Mathematik*, 45(1):1–22, 1984b.

Electronic Industries Association et al. *Interchangeable variable block data format for positioning, contouring, and contouring/positioning numerically controlled machines*. Electronic Industries Association, 1980.

Ferdinando Auricchio, Elena Bonetti, Massimo Carraturo, Dietmar Hömberg, Alessandro Reali, and Elisabetta Rocca. Structural multiscale topology optimization with stress constraint for additive manufacturing. *arXiv preprint arXiv:1907.06355*, 2019.

Autodesk. Autodesk netfabb. https://www.autodesk.com/products/netfabb/, 2016–2022.

I. Babsuka and T. Scapolla. Computational aspects of the h, p and h-p versions of the finite element method. *Advances in Computer Methods in Partial Differential Equations â Vol VI*, pages 233–240, 01 1987.

I. Babuska. Error-bounds for finite element method. *Numerische Mathematik*, 16:322–333, 1971. doi: 10.1007/BF02165003. URL https://doi.org/10.1007/BF02165003.

I. Babuska and H. Elman. Some aspects of parallel implementation of the finite-element method on message-passing architectures. *Journal of Computational and Applied Mathematics*, 27, 09 1989. doi: 10.1016/0377-0427(89)90365-8.

I. Babuska and A. D. Miller. A feedback element method with a posteriori error estimation: Part i. the finite element method and some basic properties of the a posteriori error estimator. *Applied Mechanics and Engineering*, 61:1–40, 1987.

I. Babuska and W. C. Rheinboldt. A-posteriori error estimates for the finite element method. *International Journal for Numerical Methods in Engineering*, 12(10):1597–1615, 1978. doi: https://doi.org/10.1002/nme.1620121010. URL https://onlinelibrary.wiley.com/doi/abs/10.1002/nme.1620121010.

I. Babuska and M. Suri. The p- and h-p versions of the finite element method, an overview. *Computer Methods in Applied Mechanics and Engineering*, 80(1):5–26, 1990. ISSN 0045-7825. doi: https://doi.org/10.1016/0045-7825(90)90011-A. URL https://www.sciencedirect.com/science/article/pii/004578259090011A.

I. Babuska, J. T. Oden, and J. Lee. Mixed-hybrid finite element approximations of second-order elliptic boundary-value problems. interim report. 1975.

I. Babuska, B. A. Szabo, and I. N. Katz. The p-version of the finite element method. *SIAM Journal on Numerical Analysis*, 18(3):515–545, 1981. doi: 10.1137/0718033. URL https://doi.org/10.1137/0718033.

S. Badia and J. Baiges. Adaptive finite element simulation of incompressible flows by hybrid continuous-discontinuous galerkin formulations. *SIAM Journal on Scientific Computing*, 35, 01 2013. doi: 10.1137/120880732.

S. Badia and R. Codina. Unified stabilized finite element formulations for the stokes and the darcy problems. *SIAM Journal on Numerical Analysis*, 47(3):1971–2000, 2009. doi: 10.1137/08072632X. URL https://doi.org/10.1137/08072632X.

S. Badia, A. F. Martín, E. Neiva, and F. Verdugo. A generic finite element framework on parallel tree-based adaptive meshes. *SIAM Journal on Scientific Computing*, 42(6):C436–C468, 2020. doi: 10.1137/20M1328786.

S. Badia, A. F. Martín, E. Neiva, and F. Verdugo. The aggregated unfitted finite element method on parallel tree-based adaptive meshes. *SIAM Journal on Scientific Computing*, 43(3):C203–C234, 2021. doi: 10.1137/20M1344512. URL https://doi.org/10.1137/20M1344512.

J. Baiges and C. Bayona. Refficientlib: An efficient load-rebalanced adaptive mesh refinement algorithm for high-performance computational physics meshes. *SIAM Journal on Scientific Computing*, 39, 01 2016. doi: 10.1137/15M105330X.

J. Baiges and R. Codina. Variational multiscale error estimators for solid mechanics adaptive simulations: An orthogonal subgrid scale approach. *Computer Methods in Applied Mechanics and Engineering*, 325:37–55, 2017. ISSN 0045-7825. doi: https://doi.org/10.1016/j.cma.2017.07.008. URL https://www.sciencedirect.com/science/article/pii/S0045782517305601.

J. Baiges, R. Codina, A. Pont, and E. Castillo. An adaptive fixed-mesh ale method for free surface flows. *Computer Methods in Applied Mechanics and Engineering*, 313:159 – 188, 2017. ISSN 0045-7825. doi: http://dx.doi.org/10.1016/j.cma.2016.09.041. URL http://www.sciencedirect.com/science/article/pii/S0045782516312567.

J. Baiges, M. Chiumenti, C. A. Moreira, M. Cervera, and R. Codina. An adaptive finite element strategy for the numerical simulation of additive manufacturing processes. *Additive Manufacturing*, 37:101650, 2021. ISSN 2214-8604. doi: https://doi.org/10.1016/j.addma.2020.101650. URL https://www.sciencedirect.com/science/article/pii/S2214860420310228.

G. Barbat, M. Cervera, and M. Chiumenti. Appraisement of planar, bending and twisting cracks in 3d with isotropic and orthotropic damage models. *International Journal of Fracture*, 210:1–35, 03 2018. doi: 10.1007/s10704-018-0261-3.

G. B. Barbat, M. Cervera, M. Chiumenti, and E. Espinoza. Structural size effect: Experimental, theoretical and accurate computational assessment. *Engineering Structures*, 213:110555, 2020. ISSN 0141-0296. doi: https://doi.org/10.1016/j.engstruct.2020.110555. URL https://www.sciencedirect.com/science/article/pii/S0141029619350801.

L. Barbié, I. Ramière, and F. Lebon. An automatic multilevel refinement technique based on nested local meshes for nonlinear mechanics. *Computers & Structures*, 147:14–25, 2015.

K. J. Bathe. *Finite element procedures*. Englewood Cliffs, New Jersey, United States, 1996.

M. Bellet, V. Fachinotti, O. Jaouen, S. Chapelle, I. Poitrault, and B. Lusson. Application of the arbitrary eulerian lagrangian finite element formulation to the thermomechanical simulation of casting processes, with focus on pipe shrinkage prediction. 05 2003.

T. Belytschko and M. Tabbara. H-adaptive finite element methods for dynamic problems, with emphasis on localization. *International Journal for Numerical Methods in Engineering*, 36(24):4245–4265, 1993. doi: https://doi.org/10.1002/nme.1620362409. URL https://onlinelibrary.wiley.com/doi/abs/10.1002/nme.1620362409.

T. Belytschko, W. K. Liu, and B. Moran. *Nonlinear Finite Elements for Continua and Structures*. John Wiley & Sons, Ltd, 2000.

L. Benedetti, M. Cervera, and M. Chiumenti. Stress-accurate mixed fem for soil failure under shallow foundations involving strain localization in plasticity. *Computers and Geotechnics*, 64:32–47, 2015. ISSN 0266-352X. doi: https://doi.org/10.1016/j.compgeo.2014.10.004. URL https://www.sciencedirect.com/science/article/pii/S0266352X14001876.

L. Benedetti, M. Cervera, and M. Chiumenti. High-fidelity prediction of crack formation in 2d and 3d pullout tests. *Computers & Structures*, 172:93–109, 08 2016. doi: 10.1016/j.compstruc.2016.05.001.

L. Benedetti, M. Cervera, and M. Chiumenti. 3d numerical modelling of twisting cracks under bending and torsion of skew notched beams. *Engineering Fracture Mechanics*, 176:235–256, 2017. ISSN 0013-7944. doi: https://doi.org/10.1016/j.engfracmech.2017.03.025. URL https://www.sciencedirect.com/science/article/pii/S0013794417300607.

S. E. Benzley, E. Perry, K. Merkley, B. Clark, and G. Sjaardema. A comparison of all hexagonal and all tetrahedral finite element meshes for elastic and elasto-plastic analysis. In *In Proceedings, 4th International Meshing Roundtable*, pages 179–191, 1995.

M. Bercovier and O. Pironneau. Error estimates for finite element method solution of the stokes problem in the primitive variables. *Numerische Mathematik*, 33:211–224, 1979.

M. J. Berger and J. Oliger. Adaptive mesh refinement for hyperbolic partial differential equations. *Journal of Computational Physics*, 53(3):484–512, 1984. ISSN 0021-9991. doi: https://doi.org/10.1016/0021-9991(84)90073-1. URL https://www.sciencedirect.com/science/article/pii/0021999184900731.

R. Biswas and R. C. Strawn. Tetrahedral and hexahedral mesh adaptation for cfd problems. *Applied Numerical Mathematics*, 26(1):135–151, 1998. ISSN 0168-9274. doi: https://doi.org/10.1016/S0168-9274(97)00092-5. URL https://www.sciencedirect.com/science/article/pii/S0168927497000925.

J. Bonet, A. J. Gil, and R. Ortigosa. A computational framework for polyconvex large strain elasticity. *Computer Methods in Applied Mechanics and Engineering*, 283:1061–1094, 2015. ISSN 0045-7825. doi: https://doi.org/10.1016/j.cma.2014.10.002. URL https://www.sciencedirect.com/science/article/pii/S0045782514003636.

B. Boroomand and O.C. Zienkiewicz. Recovery procedures in error estimation and adaptivity. part ii: Adaptivity in nonlinear problems of elasto-plasticity behaviour. *Computer Methods in Applied Mechanics and Engineering*, 176(1):127–146, 1999. ISSN 0045-7825. doi: https://doi.org/10.1016/S0045-7825(98)00333-8. URL https://www.sciencedirect.com/science/article/pii/S0045782598003338.

D. Braam. Cura ultimaker. https://github.com/Ultimaker/Cura, 2017–2022.

F. Brezzi. On the existence, uniqueness and aproximation of saddle point problems arising from lagrangian multipliers. *RAIRO*, 8-R2:129–151, 1974.

F. Brezzi and M. Fortin. *Mixed and hybrid finite element methods*. Springer, Berlin, Heidelberg, New York, 1991.

F. Brezzi, J. Douglas, and L. D. Marini. *Recent results on mixed finite element methods for second order elliptic problems*. Ist., Consiglio, 1984.

F. Brezzi, M. Fortin, and L. D. Marini. Mixed finite element methods with continuous stresses. *Mathematical Models and Methods in Applied Sciences*, 03(02):275–287, 1993. doi: 10.1142/S0218202593000151. URL https://doi.org/10.1142/S0218202593000151.

A. C. Brown and D. de Beer. Development of a stereolithography (stl) slicing and g-code generation algorithm for an entry level 3-d printer. In *2013 Africon*, pages 1–5, 2013. doi: 10.1109/AFRCON.2013.6757836.

M. Bugatti and Q. Semeraro. Limitations of the inherent strain method in simulating powder bed fusion processes. *Additive Manufacturing*, 23:329–346, 2018. ISSN 2214-8604. doi: https://doi.org/10.1016/j.addma.2018.05.041. URL https://www.sciencedirect.com/science/article/pii/S2214860417302877.

C. Burstedde, L. Wilcox, and O. Ghattas. p4est : Scalable algorithms for parallel adaptive mesh refinement on forests of octrees. *SIAM J. Scientific Computing*, 33:1103–1133, 01 2011. doi: 10.1137/100791634.

P. Bussetta, N. Dialami, R. Boman, M. Chiumenti, C. Agelet de Saracibar, M. Cervera, and J.-P. Ponthot. Comparison of a fluid and a solid approach for the numerical simulation of friction stir welding with a non-cylindrical pin. *steel research international*, 85(6):968–979, 2014. doi: https://doi.org/10.1002/srin.201300182. URL https://onlinelibrary.wiley.com/doi/abs/10.1002/srin.201300182.

A. C. Calder, B. C. Curts, L. J. Dursi, B. Fryxell, G. Henry, P. MacNece, K. Olson, P. Ricker, R. Rosner, F. X. Timmes, H. M. Tufo, J. W. Truran, and M. Zingale. High-performance reactive fluid flow simulations using adaptive mesh refinement on thousands of processors. In *SC '00: Proceedings of the 2000 ACM/IEEE Conference on Supercomputing*, pages 56–56, 2000. doi: 10.1109/SC.2000.10010.

Paul M Campbell, Karen D Devine, Joseph E Flaherty, Luis G Gervasio, and James D Teresco. Dynamic octree load balancing using space-filling curves. Technical report, Technical Report CS-03-01, Williams College Department of Computer Science, 2003.

M. Carraturo, C. Giannelli, A. Reali, and R. Vázquez. Suitably graded thb-spline refinement and coarsening: Towards an adaptive isogeometric analysis of additive manufacturing processes. *Computer Methods in Applied Mechanics and Engineering*, 348, 02 2019. doi: 10.1016/j.cma.2019.01.044.

M. Carraturo, J. Jomo, S. Kollmannsberger, A. Reali, F. Auricchio, and E. Rank. Modeling and experimental validation of an immersed thermo-mechanical part-scale analysis for laser powder bed fusion processes. *Additive Manufacturing*, 36:101498, 08 2020a. doi: 10.1016/j.addma.2020.101498.

M. Carraturo, B. Lane, H. Yeung, S. Kollmannsberger, A. Reali, and F. Auricchio. Numerical evaluation of advanced laser control strategies influence on residual stresses for laser powder bed fusion systems. *Integrating Materials and Manufacturing Innovation*, 9, 11 2020b. doi: 10.1007/s40192-020-00191-3.

M. Carraturo, P. Hennig, G. Alaimo, L. Heindel, F. Auricchio, M. Kastner, and A. Reali. Additive manufacturing applications of phaseâfieldâbased topology optimization using adaptive isogeometric analysis. *GAMM-Mitteilungen*, 44, 08 2021a. doi: 10.1002/gamm.202100013.

M. Carraturo, S. Kollmannsberger, A. Reali, F. Auricchio, and E. Rank. An immersed boundary approach for residual stress evaluation in selective laser melting processes. *Additive Manufacturing*, 46:102077, 06 2021b. doi: 10.1016/j.addma.2021.102077.

I. Castañar, J. Baiges, R. Codina, and H. Venghaus. Topological derivative-based topology optimization of incompressible structures using mixed formulations. *Computer Methods in Applied Mechanics and Engineering*, 390:114438, 2022. ISSN 0045-7825. doi: https://doi.org/10.1016/j.cma.2021.114438. URL https://www.sciencedirect.com/science/article/pii/S0045782521006757.

E. Castillo and R. Codina. Variational multi-scale stabilized formulations for the stationary three-field incompressible viscoelastic flow problem. *Computer Methods in Applied Mechanics and Engineering*, 279:579–605, 2014. ISSN 0045-7825. doi: https://doi.org/10.1016/j.cma.2014.07.006. URL https://www.sciencedirect.com/science/article/pii/S004578251400228X.

A. Cattenone, S. Morganti, G. Alaimo, and F. Auricchio. Finite element analysis of additive manufacturing based on fused deposition modeling (fdm): distortion prediction and comparison with experimental data. *Journal of Manufacturing Science and Engineering*, 141, 10 2018. doi: 10.1115/1.4041626.

M. Cervera and M. Chiumenti. Size effect and localization in j2 plasticity. *International Journal of Solids and Structures*, 46(17):3301–3312, 2009. ISSN 0020-7683. doi: https://doi.org/10.1016/j.ijsolstr.2009.04.025. URL https://www.sciencedirect.com/science/article/pii/S0020768309001930.

M. Cervera, C. Agelet de Saracibar, and M. Chiumenti. Thermo-mechanical analysis of industrial solidification processes. *International Journal for Numerical Methods in Engineering*, 46(9):1575–1591, 1999. doi: https://doi.org/10.1002/(SICI)1097-0207(19991130)46:9<1575::AID-NME713>3.0.CO;2-D. URL https://onlinelibrary.wiley.com/doi/abs/10.1002/%28SICI%291097-0207%2819991130%2946%3A9%3C1575%3A%3AAID-NME713%3E3.0.CO%3B2-D.

M. Cervera, C. Agelet de Saracibar, and M. Chiumenti. Comet: Coupled mechanical and thermal analysis. data input manual, version 5.0, 2002. URL http://www.cimne.upc.edu.

M. Cervera, M. Chiumenti, Q. Valverde, and C. Agelet de Saracibar. Mixed linear/linear simplicial elements for incompressible elasticity and plasticity. *Comput. Meth. App. Mech. Eng.*, 192:5249–5263, 2003.

M. Cervera, M. Chiumenti, and C. Agelet de Saracibar. Softening, localization and stabilization: Capture of discontinuous solutions in j2 plasticity. *International Journal for Numerical and Analytical Methods in Geomechanics*, 28:373 – 393, 04 2004a. doi: 10.1002/nag.341.

M. Cervera, M. Chiumenti, and C. Agelet de Saracibar. Shear band localization via local J2 continuum damage mechanics. *Comput. Meth. App. Mech. Eng.*, 193:849–880, 2004b.

M. Cervera, M. Chiumenti, and R. Codina. Mixed stabilized finite element methods in nonlinear solid mechanics: Part i: Formulation. *Computer Methods in Applied Mechanics and Engineering*, 199(37):2559–2570, 2010a. ISSN 0045-7825. doi: https://doi.org/10.1016/j.cma.2010.04.006. URL https://www.sciencedirect.com/science/article/pii/S0045782510001234.

M. Cervera, M. Chiumenti, and R. Codina. Mixed stabilized finite element methods in nonlinear solid mechanics: Part ii: Strain localization. *Computer Methods in Applied Mechanics and Engineering*, 199(37):2571–2589, 2010b. ISSN 0045-7825. doi: https://doi.org/10.1016/j.cma.2010.04.005. URL https://www.sciencedirect.com/science/article/pii/S0045782510001222.

M. Cervera, M. Chiumenti, L. Benedetti, and R. Codina. Mixed stabilized finite element methods in nonlinear solid mechanics. part iii: Compressible and incompressible plasticity. *Computer Methods in Applied Mechanics and Engineering*, 285, 03 2015. doi: 10.1016/j.cma.2014.11.040.

M. Cervera, G.B. Barbat, and M. Chiumenti. Finite element modeling of quasi-brittle cracks in 2d and 3d with enhanced strain accuracy. *Comput Mech*, 60:767 – 796, 2017. doi: https://doi.org/10.1007/s00466-017-1438-8.

M. Cervera, G. B. Barbat, and M. Chiumenti. Architecture of a multi-crack model with full closing, reopening and sliding capabilities. *Computational Mechanics*, 65:1593–1620, 2020.

B. Cheng, S. Price, J. Lydon, K. Cooper, and K. Chou. On process temperature in powder-bed electron beam additive manufacturing: Model development and validation. *Journal of Manufacturing Science and Engineering*, 136:061018, 12 2014. doi: 10.1115/1.4028484.

B. Cheng, S. Shrestha, and K. Chou. Stress and deformation evaluations of scanning strategy effect in selective laser melting. *Additive Manufacturing*, 12:240–251, 2016. ISSN 2214-8604. doi: https://doi.org/10.1016/j.addma.2016.05.007. URL https://www.sciencedirect.com/science/article/pii/S2214860416300914. Special Issue on Modeling & Simulation for Additive Manufacturing.

M. Chiumenti, Q. Valverde, C. Agelet de Saracibar, and M. Cervera. A stabilized formulation for incompressible elasticity using linear displacement and pressure interpolations. *Comput. Meth. App. Mech. Eng.*, 191:5253–5264, 2002.

M. Chiumenti, Q. Valverde, C. Agelet de Saracibar, and M. Cervera. A stabilized formulation for incompressible plasticity using linear triangles and tetrahedra. *International Journal of Plasticity*, 20 (8):1487–1504, 2004. ISSN 0749-6419. doi: https://doi.org/10.1016/j.ijplas.2003.11.009. URL https://www.sciencedirect.com/science/article/pii/S0749641903001608.

M. Chiumenti, M. Cervera, A. Salmi, C. Agelet de Saracibar, N. Dialami, and K. Matsui. Finite element modeling of multi-pass welding and shaped metal deposition processes. *Computer Methods in Applied Mechanics and Engineering*, 199(37):2343–2359, 2010. ISSN 0045-7825. doi: https://doi.org/10.1016/j.cma.2010.02.018. URL https://www.sciencedirect.com/science/article/pii/S0045782510000782.

M. Chiumenti, M. Cervera, C. Agelet de Saracibar, and N. Dialami. Numerical modeling of friction stir welding processes. *Computer methods in applied mechanics and engineering*, 254:353–369, 2013.

M. Chiumenti, M. Cervera, and R. Codina. A mixed three-field fe formulation for stress accurate analysis including the incompressible limit. *Computer Methods in Applied Mechanics and Engineering*, 283:1095–1116, 2015. ISSN 0045-7825. doi: https://doi.org/10.1016/j.cma.2014.08.004. URL https://www.sciencedirect.com/science/article/pii/S0045782514002667.

M. Chiumenti, M. Cervera, N. Dialami, B. Wu, L. Jinwei, and C. Agelet de Saracibar. Numerical modeling of the electron beam welding and its experimental validation. *Finite Elements in Analysis and Design*, 121:118–133, 2016. ISSN 0168-874X. doi: https://doi.org/10.1016/j.finel.2016.07.003. URL https://www.sciencedirect.com/science/article/pii/S0168874X16301378.

M. Chiumenti, X. Lin, M. Cervera, W. Lei, Y. Zheng, and W. Huang. Numerical simulation and experimental calibration of additive manufacturing by blown powder technology. part i: thermal analysis. *Rapid Prototyping Journal*, 23(2):448 – 463, 2017a. doi: https://doi.org/10.1108/RPJ-10-2015-0136.

M. Chiumenti, E. Neiva, E. Salsi, M. Cervera, S. Badia, J. Moya, Z. Chen, C. Lee, and C. Davies. Numerical modelling and experimental validation in selective laser melting. *Additive Manufacturing*, 18:171–185, 2017b. ISSN 2214-8604. doi: https://doi.org/10.1016/j.addma.2017.09.002. URL https://www.sciencedirect.com/science/article/pii/S2214860417302087.

M. Chiumenti, M. Cervera, C. A. Moreira, and G. B. Barbat. Stress, strain and dissipation accurate 3-field formulation for inelastic isochoric deformation. *Finite Elements in Analysis and Design*, 192:103534, 2021. ISSN 0168-874X. doi: https://doi.org/10.1016/j.finel.2021.103534. URL https://www.sciencedirect.com/science/article/pii/S0168874X21000184.

S. H. Choi and K. T. Kwok. A memory efficient slicing algorithm for large stl files. In *1999 International Solid Freeform Fabrication Symposium*, 1999.

S. H. Choi and K. T. Kwok. A tolerant slicing algorithm for layered manufacturing. *Rapid Prototyping Journal*, 2002.

Bernardo Cockburn and Chi-Wang Shu. The rungeâkutta discontinuous galerkin method for conservation laws v: Multidimensional systems. *Journal of Computational Physics*, 141(2):199–224, 1998. ISSN 0021-9991. doi: https://doi.org/10.1006/jcph.1998.5892. URL https://www.sciencedirect.com/science/article/pii/S0021999198958922.

R. Codina. Stabilization of incompressibility and convection through orthogonal sub-scales in finite element method. *Comput. Meth. App. Mech. Eng.*, 190:1579–1599, 2000.

R. Codina. Analysis of a stabilized finite element approximation of the oseen equations using orthogonal subscales. *Applied Numerical Mathematics*, 58(3):264–283, 2008a. ISSN 0168-9274. doi: https://doi.org/10.1016/j.apnum.2006.11.011. URL https://www.sciencedirect.com/science/article/pii/S0168927406002194.

R. Codina. Finite element approximation of the three-field formulation of the stokes problem using arbitrary interpolations. *SIAM J. Numerical Analysis*, 47:699–718, 07 2008b. doi: 10.1137/080712726.

R. Codina and J. Blasco. Stabilized finite element method for the transient Navier-Stokes equations based on a pressure gradient projection. *Comput. Meth. App. Mech. Eng.*, 182:277–300, 2000.

P. Colella, J. Bell, N. Keen, T. Ligocki, M. Lijewski, and B. Van Straalen. Performance and scaling of locally-structured grid methods for partial differential equations. In *Journal of Physics: Conference Series*, volume 78, page 012013. IOP Publishing, 2007.

Commission of the European Communities & Bayerische Motoren Werke. *Common Layer Interface (CLI): Version 2.0*. CEC, 1994. URL https://books.google.es/books?id=Op9-YgEACAAJ.

N. Contuzzi, S. Campanelli, and A. Ludovico. 3d finite element analysis in the selective laser melting process. *International Journal of Simulation Modelling*, 10:113–121, 09 2011. doi: 10.2507/IJSIMM10(3)1.169.

R. Courant. Variational methods for the solution of problems of equilibrium and vibrations. *Bulletin of the American Mathematical Society*, 49:1–23, 1943.

M. A. Crisfield. Non-linear finite element analysis of solids and structures, volume 1. *Journal of Engineering Mechanics*, 119(7):1504–1505, 1993. doi: 10.1061/(ASCE)0733-9399(1993)119:7(1504).

M. Crouzeix and P. A. Raviart. Conforming and nonconforming finite element methods for solving the stationary stokes equations i. *R.A.I.R.O.*, 7:33–75, 1973. doi: 10.1051/m2an/197307R300331. URL https://doi.org/10.1051/m2an/197307R300331.

L. Dai and L. Shaw. Distortion minimization of laser-processed components through control of laser scanning patterns. *Rapid Prototyping Journal*, 8:270–276, 12 2002. doi: 10.1108/13552540210451732.

A. Deb, J. H. Prevost, and B. Loret. Adaptive meshing for dynamic strain localization. *Computer Methods in Applied Mechanics and Engineering*, 137(3):285–306, 1996. ISSN 0045-7825. doi: https://doi.org/10.1016/S0045-7825(96)01068-7. URL https://www.sciencedirect.com/science/article/pii/S0045782596010687.

L. Demkowicz, J. T. Oden, W. Rachowicz, and O. Hardy. Toward a universal hp adaptive finite element strategy, part 1. constrained approximation and data structure. *Computer Methods in Applied Mechanics and Engineering*, 77(1-2):79–112, 1989.

D. Deng, H. Murakawa, and W. Liang. Numerical simulation of welding distortion in large structures. *Computer Methods in Applied Mechanics and Engineering*, 196(45):4613–4627, 2007. ISSN 0045-7825. doi: https://doi.org/10.1016/j.cma.2007.05.023. URL https://www.sciencedirect.com/science/article/pii/S0045782507002320.

E. R. Denlinger and P. Michaleris. Effect of stress relaxation on distortion in additive manufacturing process modeling. *Additive Manufacturing*, 12:51–59, 2016. ISSN 2214-8604. doi: https://doi.org/10.1016/j.addma.2016.06.011. URL https://www.sciencedirect.com/science/article/pii/S221486041630135X.

E. R. Denlinger, J. Irwin, and P. Michaleris. Thermomechanical modeling of additive manufacturing large parts. *Journal of Manufacturing Science and Engineering*, 136(6), 2014.

E. R. Denlinger, J. C. Heigel, and P. Michaleris. Residual stress and distortion modeling of electron beam direct manufacturing ti-6al-4v. *Proceedings of the Institution of Mechanical Engineers, Part B: Journal of Engineering Manufacture*, 229(10):1803–1813, 2015.

E. R. Denlinger, M. Gouge, J. Irwin, and P. Michaleris. Thermomechanical model development and in situ experimental validation of the laser powder-bed fusion process. *Additive Manufacturing*, 16: 73–80, 2017. ISSN 2214-8604. doi: https://doi.org/10.1016/j.addma.2017.05.001. URL https://www.sciencedirect.com/science/article/pii/S2214860417300441.

P. Di Stolfo, A. Schröder, N. Zander, and S. Kollmannsberger. An easy treatment of hanging nodes in hp-finite elements. *Finite Elements in Analysis and Design*, 121:101–117, 2016. ISSN 0168-874X. doi: https://doi.org/10.1016/j.finel.2016.07.001. URL https://www.sciencedirect.com/science/article/pii/S0168874X16301299.

N. Dialami, M. Chiumenti, M. Cervera, and C. Agelet de Saracibar. An apropos kinematic framework for the numerical modeling of friction stir welding. *Computers and Structures*, 117:48–57, 2013. ISSN 0045-7949. doi: https://doi.org/10.1016/j.compstruc.2012.12.006. URL https://www.sciencedirect.com/science/article/pii/S0045794912003069.

N. Dialami, M. Chiumenti, M. Cervera, and C. Agelet de Saracibar. Challenges in thermo-mechanical analysis of friction stir welding processes. *Archives of Computational Methods in Engineering*, 24, 01 2016. doi: 10.1007/s11831-015-9163-y.

N. Dialami, M. Cervera, M. Chiumenti, and C. A. de Saracibar. Local–global strategy for the prediction of residual stresses in fsw processes. *The International Journal of Advanced Manufacturing Technology*, 88(9):3099–3111, 2017.

A. R. Diaz, N. Klkuchl, P. Papalambros, and J. E. Taylor. Design of an optimal grid for finite element methods. *Journal of Structural Mechanics*, 11(2):215–230, 1983. doi: 10.1080/03601218308907442. URL https://doi.org/10.1080/03601218308907442.

J. Ding, P. Colegrove, J. Mehnen, S. Ganguly, P.M. Sequeira Almeida, F. Wang, and S. Williams. Thermo-mechanical analysis of wire and arc additive layer manufacturing process on large multi-layer parts. *Computational Materials Science*, 50(12):3315–3322, 2011. ISSN 0927-0256. doi: https://doi.org/10.1016/j.commatsci.2011.06.023. URL https://www.sciencedirect.com/science/article/pii/S092702561100365X.

W. P. Doherty, E. L. Wilson, and R. L. Taylor. *Stress analysis of axisymmetric solids utilizing higher-order quadrilateral finite elements*. Structural Engineering Laboratory, Berkeley, CA, USA, University of California, 1969.

A. J. Dunbar, E. R. Denlinger, M. F. Gouge, and P. Michaleris. Experimental validation of finite element modeling for laser powder bed fusion deformation. *Additive Manufacturing*, 12:108–120, 2016. ISSN 2214-8604. doi: https://doi.org/10.1016/j.addma.2016.08.003. URL https://www.sciencedirect.com/science/article/pii/S2214860416302032.

A. Duster and E. Rank. The p-version of the finite element method compared to an adaptive h-version for the deformation theory of plasticity. *Computer Methods in Applied Mechanics and Engineering*, 190: 1925–1935, 01 2001. doi: 10.1016/S0045-7825(00)00215-2.

D. Eberly. Dynamic collision detection using oriented bounding boxes. *Geometric tools, Inc.*, 2002.

A Tamer Erturk, M Bulduk, Gürkan Tarakçi, Gökhan Özer, and Eser Yarar. Investigation of the microstructure and mechanical characteristics of lattice structures produced by laser powder bed fusion method. *Metals and Materials International*, 28(1):155–167, 2022.

R. Finkel and J. Bentley. Quad trees: A data structure for retrieval on composite keys. *Acta Inf.*, 4:1–9, 03 1974. doi: 10.1007/BF00288933.

J. E. Flaherty, R. M. Loy, M. S. Shephard, B. K. Szymanski, J. D. Teresco, and L. H. Ziantz. Adaptive local refinement with octree load balancing for the parallel solution of three-dimensional conservation laws. *Journal of Parallel and Distributed Computing*, 47(2):139–152, 1997. ISSN 0743-7315. doi: https://doi.org/10.1006/jpdc.1997.1412. URL https://www.sciencedirect.com/science/article/pii/S074373159791412X.

M. Fortin. An analysis of the convergence of mixed finite element methods. *ESAIM: Mathematical Modelling and Numerical Analysis - Modélisation Mathématique et Analyse Numérique*, 11(4):341–354, 1977. URL http://www.numdam.org/item/M2AN_1977__11_4_341_0/.

M. Fortin. Old and new finite element methods for incompressible flows. *Int. J. Numer. Methods Fluids*, 1:347–364, 1981.

B. Fraeijs de Veubeke. Displacement and equilibrium models in the finite element method. In *Stress Analysis*. 1965.

L. P. Franca, T. J. R. Hughes, A. F. D. Loula, and I. Miranda. A new family of stable elements for nearly incompressible elasticity based on a mixed petrov-galerkin finite element formulation. *Numer. Math.*, 53:123–141, 1988. doi: https://doi.org/10.1007/BF01395881. URL https://doi.org/10.1007/BF01395881.

I. Fried. Finite element analysis of incompressible material by residual energy balancing. *International Journal of Solids and Structures*, 10:993–1002, 1974.

C. Fu and Y.B. Guo. Three-dimensional temperature gradient mechanism in selective laser melting of ti-6al-4v. *Journal of Manufacturing Science and Engineering*, 136, 12 2014. doi: 10.1115/1.4028539.

C. Gavagnin, L. Sanavia, and L. De Lorenzis. Stabilized mixed formulation for phase-field computation of deviatoric fracture in elastic and poroelastic materials. *Computational Mechanics*, 65(6):1447–1465, 2020.

M. W. Gee, C. R. Dohrmann, S. W. Key, and W. A. Wall. A uniform nodal strain tetrahedron with isochoric stabilization. *International Journal for Numerical Methods in Engineering*, 78(4):429–443, 2009. doi: https://doi.org/10.1002/nme.2493. URL https://onlinelibrary.wiley.com/doi/abs/10.1002/nme.2493.

S. Ghosh and N. Kikuchi. An arbitrary lagrangian-eulerian finite element method for large deformation analysis of elastic-viscoplastic solids. *Computer Methods in Applied Mechanics and Engineering*, 86(2):127–188, 1991.

J. Goldak, A. Chakravarti, and M.Bibby. A new finite element model for welding heat sources. *Metallurgical Transactions B*, 15:299 – 305, 1984. ISSN 0924-0136. doi: https://doi.org/10.1007/BF02667333.

S. Gottschalk, D. Manocha, and M. C. Lin. *Collision queries using oriented bounding boxes*. PhD thesis, University of North Carolina at Chapel Hill, 2000.

M. Gouge, E. Denlinger, J. Irwin, C. Li, and P. Michaleris. Experimental validation of thermo-mechanical part-scale modeling for laser powder bed fusion processes. *Additive Manufacturing*, 29:100771, 2019. ISSN 2214-8604. doi: https://doi.org/10.1016/j.addma.2019.06.022. URL https://www.sciencedirect.com/science/article/pii/S2214860418310340.

G. Hauke and D. Irisarri. Variational multiscale a posteriori error estimation for systems. application to linear elasticity. *Computer Methods in Applied Mechanics and Engineering*, 285:291–314, 2015. ISSN 0045-7825. doi: https://doi.org/10.1016/j.cma.2014.11.009. URL https://www.sciencedirect.com/science/article/pii/S0045782514004344.

G. Hauke, M. H. Doweidar, D. Fuster, A. Gómez, and J. Sayas. Application of variational a-posteriori multiscale error estimation to higher-order elements. *Computational Mechanics*, 38:382–389, 2006a. doi: https://doi.org/10.1007/s00466-006-0048-7.

G. Hauke, M. H. Doweidar, and M. Miana. The multiscale approach to error estimation and adaptivity. *Computer Methods in Applied Mechanics and Engineering*, 195(13):1573–1593, 2006b. ISSN 0045-7825. doi: https://doi.org/10.1016/j.cma.2005.05.029. URL https://www.sciencedirect.com/science/article/pii/S0045782505002963. A Tribute to Thomas J.R. Hughes on the Occasion of his 60th Birthday.

G. Hauke, M. H. Doweidar, and M. Miana. Proper intrinsic scales for a-posteriori multiscale error estimation. *Computer Methods in Applied Mechanics and Engineering*, 195(33):3983–4001, 2006c. ISSN 0045-7825. doi: https://doi.org/10.1016/j.cma.2005.07.012. URL https://www.sciencedirect.com/science/article/pii/S0045782505003452.

G. Hauke, D. Fuster, and F. Lizarraga. Variational multiscale a posteriori error estimation for systems: The euler and navier-stokes equations. *Computer Methods in Applied Mechanics and Engineering*, 283: 1493, 01 2015. doi: 10.1016/j.cma.2014.10.032.

E. Hellinger. Die allgemeinen ansätze der mechanik der kontinua. In *Mechanik*, pages 601–694. Springer, 1907.

L. R. Hermann. Elasticity equations for incompressible and nearly incompressible materials by a variational theorem. *AIAA Journal*, 3(10):1896–1900, 1965. doi: 10.2514/3.3277. URL https://doi.org/10.2514/3.3277.

J. Holke. Scalable algorithms for parallel tree-based adaptive mesh refinement with general element types, 2018.

S. Holzer and Z. Yosibash. The p-version of the finite element method in incremental elasto-plastic analysis. *International Journal of Numerical Methods in Engineering*, 39:1859–1878, 1996.

A. Hrennikoff. Solution of problems of elasticity by the framework method. *Journal of applied mechanics*, 8(4):169–175, 1941.

H. C. Hu. Some variational principles in elasticity and plasticity. *Acta Physica Sinica*, 10(3):259–290, 1954.

Y. Hu and M. F. Randolph. A practical numerical approach for large deformation problems in soil. *International Journal for Numerical and Analytical Methods in Geomechanics*, 22(5):327–350, 1998. doi: https://doi.org/10.1002/(SICI)1096-9853(199805)22:5<327::AID-NAG920>3.0.CO;2-X. URL https://onlinelibrary.wiley.com/doi/abs/10.1002/%28SICI%291096-9853%28199805%2922%3A5%3C327%3A%3AAID-NAG920%3E3.0.CO%3B2-X.

Y. Hu, Q. Zhou, X. Gao, A. Jacobson, D. Zorin, and D. Panozzo. Tetrahedral meshing in the wild. *ACM Trans. Graph.*, 37(4):60–1, 2018.

T. J. R. Hughes. Equivalence of finite elements for nearly incompressible elasticity. *J. Appl. Mech.*, 44(1): 181–183, 1977.

T. J. R. Hughes. Generalization of selective integration procedures to anisotropic and nonlinear media. *International Journal for Numerical Methods in Engineering*, 15(9):1413–1418, 1980. doi: https://doi.org/10.1002/nme.1620150914.

T. J. R. Hughes. *Finite Element Method: Linear Static and Dynamic Finite Element Analysis*. Prentice-Hall, Englewood Cliffs, New Jersey, 1987.

T. J. R. Hughes. Multiscale phenomena: Green's functions Dirichlet-to-Neumann formulation, sub-grid scale models, bubbles and the origins of stabilized formulations. *Comp. Meth. Appl. Mech. Eng.*, 127: 387–401, 1995.

T. J. R. Hughes and L. P. Franca. A new finite element formulation for computational fluid dynamics: Vii. the stokes problem with various well-posed boundary conditions: Symmetric formulations that converge for all velocity/pressure spaces. *Computer Methods in Applied Mechanics and Engineering*, 65 (1):85–96, 1987. ISSN 0045-7825. doi: https://doi.org/10.1016/0045-7825(87)90184-8. URL https://www.sciencedirect.com/science/article/pii/0045782587901848.

T. J. R. Hughes, M. Cohen, and M. Haroun. Reduced and selective integration techniques in the finite element analysis of plates. *Nuclear Engineering and Design*, 46(1):203–222, 1978. ISSN 0029-5493. doi: https://doi.org/10.1016/0029-5493(78)90184-X. URL https://www.sciencedirect.com/science/article/pii/002954937890184X. Special Issue Structural Mechanics in Reactor Technology-Smirt-4.

T. J. R. Hughes, L. P. Franca, and M. Balestra. A new finite element formulation for computational fluid dynamics: V. Circumventing the Babuska-Brezzi condition: A stable Petrov-Galerkin formulation of Stokes problem accommodating equal-order interpolation. *Comput. Meth. App. Mech. Eng.*, 59:85–99, 1985.

T. J. R. Hughes, G. R. Feijóo, L. Mazzei, and J.B. Quincy. The variational multiscale methodâa paradigm for computational mechanics. *Computer Methods in Applied Mechanics and Engineering*, 166(1):3–24, 1998. ISSN 0045-7825. doi: https://doi.org/10.1016/S0045-7825(98)00079-6. URL https://www.sciencedirect.com/science/article/pii/S0045782598000796. Advances in Stabilized Methods in Computational Mechanics.

T. J.R. Hughes, L. P. Franca, and G. M. Hulbert. A new finite element formulation for computational fluid dynamics: Viii. the galerkin/least-squares method for advective-diffusive equations. *Computer Methods in Applied Mechanics and Engineering*, 73(2):173–189, 1989. ISSN 0045-7825. doi: https://doi.org/10.1016/0045-7825(89)90111-4. URL https://www.sciencedirect.com/science/article/pii/0045782589901114.

A. Hussein, L. Hao, C. Yan, and R. Everson. Finite element simulation of the temperature and stress fields in single layers built without-support in selective laser melting. *Materials & Design (1980-2015)*, 52:638–647, 2013. ISSN 0261-3069. doi: https://doi.org/10.1016/j.matdes.2013.05.070. URL https://www.sciencedirect.com/science/article/pii/S0261306913005025.

D. Irisarri and G. Hauke. Variational multiscale a posteriori error estimation for 2nd and 4th-order odes. *International Journal of Numerical Analysis & Modeling*, 12(3), 2015.

N. Jansson, J. Hoffman, and J. Jansson. Framework for massively parallel adaptive finite element computational fluid dynamics on tetrahedral meshes. *SIAM Journal on Scientific Computing*, 34(1): C24–C41, 2012.

B. Jha and R. Juanes. A locally conservative finite element framework for the simulation of coupled flow and reservoir geomechanics. *Acta Geotechnica*, 2(3):139–153, 2007.

C. Johnson and B. Mercier. Some equilibrium finite element methods for two-dimensional elasticity problems. *Numerische Mathematik*, 30(1):103–116, 1978.

J. Jomo, O. Oztoprak, F. de Prenter, N. Zander, S. Kollmannsberger, and E. Rank. Hierarchical multigrid approaches for the finite cell method on uniform and multi-level h p -refined grids. *Computer Methods in Applied Mechanics and Engineering*, 386:114075, 12 2021. doi: 10.1016/j.cma.2021.114075.

N. Keller and V. Ploshikhin. New method for fast predictions on residual stress and distortion of am parts. In *2014 International Solid Freeform Fabrication Symposium*. University of Texas at Austin, 2014.

S. W. Key. A variational principle for incompressible and nearly-incompressible anisotropic elasticity. *International Journal of Solids and Structures*, 5:951–964, 1969.

K. Khan and A. De. Modelling of selective laser melting process with adaptive remeshing. *Science and Technology of Welding & Joining*, 02 2019. doi: 10.1080/13621718.2019.1575057.

A. R. Khoei, S. Asil Gharebaghi, A. Tabarraei, and A. Riahi. Error estimation, adaptivity and data transfer in enriched plasticity continua to analysis of shear band localization. *Applied Mathematical Modelling*, 31:983–1000, 06 2007. doi: 10.1016/j.apm.2006.03.021.

A. R. Khoei, H. Azadi, and H. Moslemi. Modeling of crack propagation via an automatic adaptive mesh refinement based on modified superconvergent patch recovery technique. *Engineering Fracture Mechanics*, 75(10):2921–2945, 2008. ISSN 0013-7944. doi: https://doi.org/10.1016/j.engfracmech.2008.01.006. URL https://www.sciencedirect.com/science/article/pii/S0013794408000155.

A. R. Khoei, M. Eghbalian, H. Moslemi, and H. Azadi. Crack growth modeling via 3d automatic adaptive mesh refinement based on modified-spr technique. *Applied Mathematical Modelling*, 37(1):357–383, 2013. ISSN 0307-904X. doi: https://doi.org/10.1016/j.apm.2012.02.040. URL https://www.sciencedirect.com/science/article/pii/S0307904X12001230.

B. S Kirk, J. W. Peterson, R. H. Stogner, and G. F. Carey. libmesh: a c++ library for parallel adaptive mesh refinement/coarsening simulations. *Engineering with Computers*, 22(3):237–254, 2006.

S. Kollmannsberger and P. Kopp. On accurate time integration for temperature evolutions in additive manufacturing. *GAMM-Mitteilungen*, 44(4):e202100019, 2021. doi: https://doi.org/10.1002/gamm.202100019. URL https://onlinelibrary.wiley.com/doi/abs/10.1002/gamm.202100019.

S. Kollmannsberger, A. Ãzcan, M. Carraturo, N. Zander, and E. Rank. A hierarchical computational model for moving thermal loads and phase changes with applications to selective laser melting. *Computers & Mathematics with Applications*, 75(5):1483–1497, 2018. ISSN 0898-1221. doi: https://doi.org/10.1016/j.camwa.2017.11.014. URL https://www.sciencedirect.com/science/article/pii/S0898122117307289.

S. Kollmannsberger, M. Carraturo, A. Reali, and F. Auricchio. Accurate prediction of melt pool shapes in laser powder bed fusion by the non-linear temperature equation including phase changes: Model validity: isotropic versus anisotropic conductivity to capture am benchmark test amb2018-02. *Integrating Materials and Manufacturing Innovation*, 8, 04 2019. doi: 10.1007/s40192-019-00132-9.

F. Kong and R. Kovacevic. 3d finite element modeling of the thermally induced residual stress in the hybrid laser/arc welding of lap joint. *Journal of Materials Processing Technology*, 210(6):941–950, 2010. ISSN 0924-0136. doi: https://doi.org/10.1016/j.jmatprotec.2010.02.006. URL https://www.sciencedirect.com/science/article/pii/S0924013610000476.

O. Lawlor, S. Chakravorty, T. Wilmarth, N. Choudhury, I. Dooley, G. Zheng, and L. KalÃ©. Parfum: a parallel framework for unstructured meshes for scalable dynamic physics applications. *Eng. Comput. (Lond.)*, 22:215–235, 12 2006. doi: 10.1007/s00366-006-0039-5.

N. S. Lee and K. J. Bathe. Error indicators and adaptive remeshing in large deformation finite element analysis. *Finite Elements in Analysis and Design*, 16(2):99–139, 1994. ISSN 0168-874X. doi: https://doi.org/10.1016/0168-874X(94)90044-2. URL https://www.sciencedirect.com/science/article/pii/0168874X94900442.

L. Levine, B. Lane, J. Heigel, K. Migler, M. Stoudt, T. Phan, R. Ricker, M. Strantza, M. Hill, F. Zhang, et al. Outcomes and conclusions from the 2018 am-bench measurements, challenge problems, modeling submissions, and conference. *Integrating Materials and Manufacturing Innovation*, 9(1):1–15, 2020.

R. Wynne Lewis and B. A. Schrefler. The finite element method in the deformation and consolidation of porous media. 1987.

C. Li, C. H. Fu, Y. B. Guo, and F. Z. Fang. Fast prediction and validation of part distortion in selective laser melting. *Procedia Manufacturing*, 1:355–365, 2015a. ISSN 2351-9789. doi: https://doi.org/10.1016/j.promfg.2015.09.042. URL https://www.sciencedirect.com/science/article/pii/S2351978915010422. 43rd North American Manufacturing Research Conference, NAMRC 43, 8-12 June 2015, UNC Charlotte, North Carolina, United States.

C. Li, J. F. Liu, Y. B. Guo, and Z. Y. Li. A temperature-thread multiscale modeling approach for efficient prediction of part distortion by selective laser melting. In *2015 International Solid Freeform Fabrication Symposium*. University of Texas at Austin, 2015b.

C. Li, C.H. Fu, Y.B. Guo, and F.Z. Fang. A multiscale modeling approach for fast prediction of part distortion in selective laser melting. *Journal of Materials Processing Technology*, 229:703 – 712, 2016. ISSN 0924-0136. doi: https://doi.org/10.1016/j.jmatprotec.2015.10.022. URL http://www.sciencedirect.com/science/article/pii/S0924013615301746.

C. Li, E. R. Denlinger, M. F. Gouge, J. E. Irwin, and P. Michaleris. Numerical verification of an octree mesh coarsening strategy for simulating additive manufacturing processes. *Additive Manufacturing*, 30:100903, 2019. ISSN 2214-8604. doi: https://doi.org/10.1016/j.addma.2019.100903. URL https://www.sciencedirect.com/science/article/pii/S2214860419303574.

X. Liang, L. Cheng, Q. Chen, Q. Yang, and A. C. To. A modified method for estimating inherent strains from detailed process simulation for fast residual distortion prediction of single-walled structures fabricated by directed energy deposition. *Additive Manufacturing*, 23:471–486, 2018. ISSN 2214-8604. doi: https://doi.org/10.1016/j.addma.2018.08.029. URL https://www.sciencedirect.com/science/article/pii/S2214860418304858.

X. Liang, Q. Chen, L. Cheng, D. Hayduke, and A. C. To. Modified inherent strain method for efficient prediction of residual deformation in direct metal laser sintered components. *Computational Mechanics*, 64(6):1719–1733, 2019.

X. Liang, W. Dong, S. Hinnebusch, Q. Chen, H. T. Tran, J. Lemon, L. Cheng, Z. Zhou, D. Hayduke, and A. C. To. Inherent strain homogenization for fast residual deformation simulation of thin-walled lattice support structures built by laser powder bed fusion additive manufacturing. *Additive Manufacturing*, 32:101091, 2020. ISSN 2214-8604. doi: https://doi.org/10.1016/j.addma.2020.101091. URL https://www.sciencedirect.com/science/article/pii/S2214860419317567.

L.-E. Lindgren and E. Hedblom. Modelling of addition of filler material in large deformation analysis of multipass welding. *Communications in Numerical Methods in Engineering*, 17(9):647–657, 2001. doi: https://doi.org/10.1002/cnm.414. URL https://onlinelibrary.wiley.com/doi/abs/10.1002/cnm.414.

L.-E. Lindgren, H. Runnemalm, and M. O. Näsström. Simulation of multipass welding of a thick plate. *International Journal for Numerical Methods in Engineering*, 44(9):1301–1316, 1999. doi: https://doi.org/10.1002/(SICI)1097-0207(19990330)44:9<1301::AID-NME479>3.0.CO;2-K. URL https://onlinelibrary.wiley.com/doi/abs/10.1002/%28SICI%291097-0207%2819990330%2944%3A9%3C1301%3A%3AAID-NME479%3E3.0.CO%3B2-K.

L.-E. Lindgren, A. Lundbäck, M. Fisk, R. Pederson, and J. Andersson. Simulation of additive manufacturing using coupled constitutive and microstructure models. *Additive Manufacturing*, 12:144–158, 2016. ISSN 2214-8604. doi: https://doi.org/10.1016/j.addma.2016.05.005. URL https://www.sciencedirect.com/science/article/pii/S2214860416300896. Special Issue on Modeling & Simulation for Additive Manufacturing.

J. Liu and A. L. Marsden. A unified continuum and variational multiscale formulation for fluids, solids, and fluidâstructure interaction. *Computer Methods in Applied Mechanics and Engineering*, 337:549–597, 2018. ISSN 0045-7825. doi: https://doi.org/10.1016/j.cma.2018.03.045. URL https://www.sciencedirect.com/science/article/pii/S0045782518301701.

M. Livesu, D. Cabiddu, and M. Attene. slice2mesh: A meshing tool for the simulation of additive manufacturing processes. *Computers & Graphics*, 80:73–84, 2019. ISSN 0097-8493. doi: https://doi.org/10.1016/j.cag.2019.03.004. URL https://www.sciencedirect.com/science/article/pii/S0097849319300275.

X. Lu, X. Lin, M. Chiumenti, M. Cervera, J. Li, L. Ma, L. Wei, Y. Hu, and W. Huang. Finite element analysis and experimental validation of the thermomechanical behavior in laser solid forming of ti-6al-4v. *Additive Manufacturing*, 21:30 – 40, 2018. ISSN 2214-8604. doi: https://doi.org/10.1016/j.addma.2018.02.003. URL http://www.sciencedirect.com/science/article/pii/S2214860417305997.

X. Lu, X. Lin, M. Chiumenti, M. Cervera, Y. Hu, X. Ji, L. Ma, H. Yang, and W. Huang. Residual stress and distortion of rectangular and s-shaped ti-6al-4v parts by directed energy deposition: Modelling and experimental calibration. *Additive Manufacturing*, 26:166–179, 2019. ISSN 2214-8604. doi: https://doi.org/10.1016/j.addma.2019.02.001. URL https://www.sciencedirect.com/science/article/pii/S2214860418305955.

X. Lu, M. Cervera, M. Chiumenti, and X. Lin. Residual stresses control in additive manufacturing. *Journal of Manufacturing and Materials Processing*, 5(4), 2021a. ISSN 2504-4494. doi: 10.3390/jmmp5040138. URL https://www.mdpi.com/2504-4494/5/4/138.

X. Lu, M. Chiumenti, M. Cervera, J. Li, X. Lin, L. Ma, G. Zhang, and E. Liang. Substrate design to minimize residual stresses in directed energy deposition am processes. *Materials & Design*, 202: 109525, 2021b. ISSN 0264-1275. doi: https://doi.org/10.1016/j.matdes.2021.109525. URL https://www.sciencedirect.com/science/article/pii/S0264127521000782.

X. Lu, M. Chiumenti, M. Cervera, H. Tan, X. Lin, and S. Wang. Warpage analysis and control of thin-walled structures manufactured by laser powder bed fusion. *Metals*, 11(5), 2021c. ISSN 2075-4701. doi: 10.3390/met11050686. URL https://www.mdpi.com/2075-4701/11/5/686.

J. Luitjens, B. Worthen, M. Berzins, and T. C. Hen. Scalable parallel amr for the uintah multi-physics code. 2007.

Z. Luo and Y. Zhao. A survey of finite element analysis of temperature and thermal stress fields in powder bed fusion additive manufacturing. *Additive Manufacturing*, 21:318–332, 05 2018. doi: 10.1016/j.addma.2018.03.022.

L. Ma and H. Bin. Temperature and stress analysis and simulation in fractal scanning-based laser sintering. *Int J Adv Manuf Technol*, 34:898–903, 2007. doi: https://doi.org/10.1007/s00170-006-0665-5.

D. S. Malkus and T. J. R. Hughes. Mixed finite element methods - reduced and selective integration techniques: A unification of concepts. *Comput. Methods Appl. Mech. Engrg.*, 15(1):68–81, 1978.

A. Maniatty and Y. Liu. Stabilized finite element method for viscoplastic flow: Formulation with state variable evolution. *International Journal for Numerical Methods in Engineering*, 56:185 – 209, 01 2003. doi: 10.1002/nme.554.

A. Maniatty, Y. Liu, O. Klaas, and M. S. Shephard. Stabilized finite element method for viscoplastic flow: formulation and a simple progressive solution strategy. *Computer Methods in Applied Mechanics and Engineering*, 190(35):4609–4625, 2001. ISSN 0045-7825. doi: https://doi.org/10.1016/S0045-7825(00)00346-7. URL https://www.sciencedirect.com/science/article/pii/S0045782500003467.

A. Maniatty, Y. Liu, O. Klaas, and M. Shephard. Higher order stabilized finite element method for hyperelastic finite deformation. *Computer Methods in Applied Mechanics and Engineering - COMPUT METHOD APPL MECH ENG*, 191:1491–1503, 01 2002. doi: 10.1016/S0045-7825(01)00335-8.

A. Masud and T. J. Truster. A framework for residual-based stabilization of incompressible finite elasticity: Stabilized formulations and fÂ¯ methods for linear triangles and tetrahedra. *Computer Methods in Applied Mechanics and Engineering*, 267:359–399, 2013. ISSN 0045-7825. doi: https://doi.org/10.1016/j.cma.2013.08.010. URL https://www.sciencedirect.com/science/article/pii/S0045782513002132.

A. Masud, T. J. Truster, and L. A. Bergman. A variational multiscale a posteriori error estimation method for mixed form of nearly incompressible elasticity. *Computer Methods in Applied Mechanics and Engineering*, 200(47):3453–3481, 2011. ISSN 0045-7825. doi: https://doi.org/10.1016/j.cma.2011.07.012. URL https://www.sciencedirect.com/science/article/pii/S0045782511002532.

MATLAB. *9.7.0.1190202 (R2019b)*. The MathWorks Inc., Natick, Massachusetts, 2018.

M. Matsumoto, M. Shiomi, K. Osakada, and F. Abe. Finite element analysis of single layer forming on metallic powder bed in rapid prototyping by selective laser processing. *International Journal of Machine Tools and Manufacture*, 42(1):61–67, 2002. ISSN 0890-6955. doi: https://doi.

org/10.1016/S0890-6955(01)00093-1. URL https://www.sciencedirect.com/science/article/pii/S0890695501000931.

D. Meagher. Geometric modeling using octree encoding. *Computer Graphics and Image Processing*, 19 (2):129–147, 1982. ISSN 0146-664X. doi: https://doi.org/10.1016/0146-664X(82)90104-6. URL https://www.sciencedirect.com/science/article/pii/0146664X82901046.

P. Michaleris. Modeling metal deposition in heat transfer analyses of additive manufacturing processes. *Finite Elements in Analysis and Design*, 86:51–60, 2014. ISSN 0168-874X. doi: https://doi.org/10.1016/j.finel.2014.04.003. URL https://www.sciencedirect.com/science/article/pii/S0168874X14000584.

C. A. Moreira, G. B. Barbat, M. Cervera, and M. Chiumenti. Accurate thermal-induced structural failure analysis under incompressible conditions. *Engineering Structures*, 261:114213, 2022a. ISSN 0141-0296. doi: https://doi.org/10.1016/j.engstruct.2022.114213. URL https://www.sciencedirect.com/science/article/pii/S0141029622003431.

C. A. Moreira, M. A. Caicedo, M. Cervera, M. Chiumenti, and J. Baiges. A multi-criteria h-adaptive finite-element framework for industrial part-scale thermal analysis in additive manufacturing processes. *Engineering with Computers*, 2022b. doi: https://doi.org/10.1007/s00366-022-01655-0.

J. C. Nagtegaal, D. M. Parks, and J. R. Rice. On numerically accurate finite element solutions in the fully plastic range. *Computer Methods in Applied Mechanics and Engineering*, 4(2):153–177, 1974. ISSN 0045-7825. doi: https://doi.org/10.1016/0045-7825(74)90032-2. URL https://www.sciencedirect.com/science/article/pii/0045782574900322.

D. J. Naylor. Stresses in nearly incompressible materials by finite elements with application to the calculation of excess pore pressures. *International Journal for Numerical Methods in Engineering*, 8(3): 443–460, 1974. doi: https://doi.org/10.1002/nme.1620080302. URL https://onlinelibrary.wiley.com/doi/abs/10.1002/nme.1620080302.

E. Neiva and S. Badia. Robust and scalable h-adaptive aggregated unfitted finite elements for interface elliptic problems. *Computer Methods in Applied Mechanics and Engineering*, 380:113769, 2021. ISSN 0045-7825. doi: https://doi.org/10.1016/j.cma.2021.113769. URL https://www.sciencedirect.com/science/article/pii/S0045782521001055.

E. Neiva, S. Badia, A. F. Martín, and M. Chiumenti. A scalable parallel finite element framework for growing geometries. application to metal additive manufacturing. *International Journal for Numerical Methods in Engineering*, 119(11):1098–1125, 2019. doi: https://doi.org/10.1002/nme.6085. URL https://onlinelibrary.wiley.com/doi/abs/10.1002/nme.6085.

C. D. Norton, J. Z. Lou, and T. A. Cwik. Status and directions for the pyramid parallel unstructured amr library. In *Proceedings 15th International Parallel and Distributed Processing Symposium. IPDPS 2001*, pages 1224–1231, 2001. doi: 10.1109/IPDPS.2001.925097.

J. T. Oden and O. P. Jacquotte. Stability of some mixed finite element methods for stokesian flows. *Computer Methods in Applied Mechanics and Engineering*, 43(2):231–247, 1984. ISSN 0045-7825. doi: https://doi.org/10.1016/0045-7825(84)90007-0. URL https://www.sciencedirect.com/science/article/pii/0045782584900070.

A. Olleak and Z. Xi. Efficient lpbf process simulation using finite element modeling with adaptive remeshing for distortions and residual stresses prediction. *Manufacturing Letters*, 24:140–144, 2020. ISSN 2213-8463. doi: https://doi.org/10.1016/j.mfglet.2020.05.002. URL https://www.sciencedirect.com/science/article/pii/S2213846320300055.

M. Ortiz and J. J. Quigley. Adaptive mesh refinement in strain localization problems. *Computer Methods in Applied Mechanics and Engineering*, 90(1):781–804, 1991. ISSN 0045-7825. doi: https://doi.org/10.1016/0045-7825(91)90184-8. URL https://www.sciencedirect.com/science/article/pii/0045782591901848.

D. Pal, N. Patil, K. Zeng, C. Teng, S. Xu, T. Sublette, and B. Stucker. Enhancing simulations of additive manufacturing processes using spatiotemporal multiscaling. 01 2014.

D. Pal, N. Patil, H. Rafi, K. Zeng, A. Moreland, A. Hicks, D. Beeler, and B. Stucker. A generalized feed forward dynamic adaptive mesh refinement and de-refinement finite element framework for metal laser sintering: Part ii (non-linear thermal simulations and validations). *Journal of Manufacturing Science and Engineering*, 138, 11 2015. doi: 10.1115/1.4032078.

M. Pastor, J. Peraire, and O. C. Zienkiewicz. Adaptive remeshing for shear band localization problems. *Arch. Appl. Mech.*, 61:30–39, 1991.

N. Patil, D. Pal, H. Khalid Rafi, K. Zeng, A. Moreland, A. Hicks, D. Beeler, and B. Stucker. A Generalized Feed Forward Dynamic Adaptive Mesh Refinement and Derefinement Finite Element Framework for Metal Laser SinteringâPart I: Formulation and Algorithm Development. *Journal of Manufacturing Science and Engineering*, 137(4), 08 2015. ISSN 1087-1357. doi: 10.1115/1.4030059. URL https://doi.org/10.1115/1.4030059. 041001.

N. Patil, R. Ganeriwala, J. M. Solberg, N. E. Hodge, and R. M. Ferencz. Benchmark multi-layer simulations for residual stresses and deformation in small additively manufactured metal parts. *Additive Manufacturing*, 45:102015, 2021.

R. B. Patil and V. Yadava. Finite element analysis of temperature distribution in single metallic powder layer during metal laser sintering. *International Journal of Machine Tools and Manufacture*, 47(7):1069–1080, 2007. ISSN 0890-6955. doi: https://doi.org/10.1016/j.ijmachtools.2006.09.025. URL https://www.sciencedirect.com/science/article/pii/S0890695506002598.

J. Peraire, M. Vahdati, K. Morgan, and O. C. Zienkiewicz. Adaptive remeshing for compressible flow computations. *Journal of Computational Physics*, 72(2):449–466, 1987. ISSN 0021-9991. doi: https://doi.org/10.1016/0021-9991(87)90093-3. URL https://www.sciencedirect.com/science/article/pii/0021999187900933.

J. Peraire, J. Peiró, and K. Morgan. Adaptive remeshing for three-dimensional compressible flow computations. *Journal of Computational Physics*, 103(2):269–285, 1992. ISSN 0021-9991. doi: https://doi.org/10.1016/0021-9991(92)90401-J. URL https://www.sciencedirect.com/science/article/pii/002199919290401J.

D. Perić, J. Yu, and D. R. J. Owen. On error estimates and adaptivity in elastoplastic solids: Applications to the numerical simulation of strain localization in classical and cosserat continua. *International Journal for Numerical Methods in Engineering*, 37(8):1351–1379, 1994. doi: https://doi.org/10.1002/nme.1620370806. URL https://onlinelibrary.wiley.com/doi/abs/10.1002/nme.1620370806.

D. Perić, M. Vaz, and D. R. J. Owen. On adaptive strategies for large deformations of elasto-plastic solids at finite strains: computational issues and industrial applications. *Computer Methods in Applied Mechanics and Engineering*, 176(1):279–312, 1999. ISSN 0045-7825. doi: https://doi.org/10.1016/S0045-7825(98)00342-9. URL https://www.sciencedirect.com/science/article/pii/S0045782598003429.

T. Q. Phan, M. Strantza, M. R. Hill, T. H. Gnaupel-Herold, J. Heigel, C. R. D'Elia, A. T. DeWald, B. Clausen, D. C. Pagan, J. Y. Peter Ko, et al. Elastic residual strain and stress measurements and corresponding part deflections of 3d additive manufacturing builds of in625 am-bench artifacts using neutron diffraction, synchrotron x-ray diffraction, and contour method. *Integrating Materials and Manufacturing Innovation*, 8(3):318–334, 2019.

G. Prathap. The poor bending response of the four-node plane stress quadrilateral. *International Journal for Numerical Methods in Engineering*, 21(5):825–835, 1985. doi: https://doi.org/10.1002/nme.1620210505.

M. A. Puso and J. Solberg. A stabilized nodally integrated tetrahedral. *International Journal for Numerical Methods in Engineering*, 67(6):841–867, 2006. doi: https://doi.org/10.1002/nme.1651. URL https://onlinelibrary.wiley.com/doi/abs/10.1002/nme.1651.

A. Ranellucci. Slic3r. github.com/alexrj/Slic3r, 2011–2022.

E. Rank. *Adaptivity and error estimation for finite element and boundary integral element method*. I. Babuska, O. C. Zienkiewicz, J. Gago & E. R. Arantes Oliveira. Wiley, Chichester, UK, 1986.

P. A. Raviart and J. M. Thomas. A mixed finite element method for second order elliptic problems. *Mathematical Aspects of the Finite Element Method, Rome*, 1975.

E. Reissner. On a variational theorem in elasticity. *Journal of Mathematics and Physics*, 29(1-4):90–95, 1950. doi: https://doi.org/10.1002/sapm195029190. URL https://onlinelibrary.wiley.com/doi/abs/10.1002/sapm195029190.

J. Ren, J. Liu, and J. Yin. Simulation of transient temperature field in the selective laser sintering process of w/ni powder mixture. volume 347, pages 494–503, 10 2010. ISBN 978-3-642-18368-3. doi: 10.1007/978-3-642-18369-0_59.

J. J. Rencis and J. Kwo-Yih. A self-adaptive h-refinement technique for the boundary element method. *Computer Methods in Applied Mechanics and Engineering*, 73(3):295–316, 1989. ISSN 0045-7825. doi: https://doi.org/10.1016/0045-7825(89)90070-4. URL https://www.sciencedirect.com/science/article/pii/0045782589900704.

W. C. Rheinboldt and C. K. Mesztenyi. On a data structure for adaptive finite element mesh refinements. *ACM Trans. Math. Softw.*, 6(2):166â187, jun 1980. ISSN 0098-3500. doi: 10.1145/355887.355891. URL https://doi.org/10.1145/355887.355891.

D. Riedlbauer, P. Steinmann, and J. Mergheim. Thermomechanical finite element simulations of selective electron beam melting processes: Performance considerations. *Computational Mechanics*, 54, 07 2014. doi: 10.1007/s00466-014-1026-0.

I. A. Roberts. Investigation of residual stresses in the laser melting of metal powders in additive layer manufacturing, 2012. URL http://hdl.handle.net/2436/254913.

R. Rossi, J. Cotela, N. M. Lafontaine, P. Dadvand, and S. R. Idelsohn. Parallel adaptive mesh refinement for incompressible flow problems. *Computers & Fluids*, 80:342–355, 2013. ISSN 0045-7930. doi: https://doi.org/10.1016/j.compfluid.2012.01.023. URL https://www.sciencedirect.com/science/article/pii/S0045793012000321.

S. Rossi, N. Abboud, and G. Scovazzi. Implicit finite incompressible elastodynamics with linear finite elements: A stabilized method in rate form. *Computer Methods in Applied Mechanics and Engineering*, 311, 11 2016. doi: 10.1016/j.cma.2016.07.015.

M. A. Salazar de Troya and D. A. Tortorelli. Adaptive mesh refinement in stress-constrained topology optimization. *Structural and Multidisciplinary Optimization*, 58(6):2369–2386, 2018.

S. Saloustros, M. Cervera, S. Kim, and M. Chiumenti. Accurate and locking-free analysis of beams, plates and shells using solid elements. *Computational Mechanics*, 67, 03 2021. doi: 10.1007/s00466-020-01969-0.

B. Schoinochoritis, D. Chantzis, and K. Salonitis. Simulation of metallic powder bed additive manufacturing processes with the finite element method: A critical review. *Proceedings of the Institution of Mechanical Engineers, Part B: Journal of Engineering Manufacture*, 231(1):96–117, 2017. doi: 10.1177/0954405414567522. URL https://doi.org/10.1177/0954405414567522.

J. Schröder, P. Wriggers, and D. Balzani. A new mixed finite element based on different approximations of the minors of deformation tensors. *Computer Methods in Applied Mechanics and Engineering*, 200:3583–3600, 12 2011. doi: 10.1016/j.cma.2011.08.009.

G. Scovazzi, B. Carnes, X. Zeng, and S. Rossi. A simple, stable, and accurate linear tetrahedral finite element for transient, nearly, and fully incompressible solid dynamics: A dynamic variational multiscale approach. *International Journal for Numerical Methods in Engineering*, 106(10), 11 2015. doi: 10.1002/nme.5138.

G. Scovazzi, T. Song, and X. Zeng. A velocity/stress mixed stabilized nodal finite element for elastodynamics: Analysis and computations with strongly and weakly enforced boundary conditions. *Computer Methods in Applied Mechanics and Engineering*, 325, 07 2017. doi: 10.1016/j.cma.2017.07.018.

I. Setien, M. Chiumenti, S. van der Veen, M. San Sebastian, F. Garciandía, and A. Echeverría. Empirical methodology to determine inherent strains in additive manufacturing. *Computers & Mathematics with Applications*, 78(7):2282–2295, 2019. ISSN 0898-1221. doi: https://doi.org/10.1016/j.camwa.2018.05.015. URL https://www.sciencedirect.com/science/article/pii/S0898122118302839. Simulation for Additive Manufacturing.

M. S. Shephard. Linear multipoint constraints applied via transformation as part of a direct stiffness assembly process. *International Journal for Numerical Methods in Engineering*, 20(11):2107–2112, 1984. doi: https://doi.org/10.1002/nme.1620201112. URL https://onlinelibrary.wiley.com/doi/abs/10.1002/nme.1620201112.

J. C. Simo and F. Armero. Geometrically non-linear enhanced strain mixed methods and the method of incompatible modes. *International Journal for Numerical Methods in Engineering*, 33(7):1413–1449, 1992. doi: https://doi.org/10.1002/nme.1620330705. URL https://onlinelibrary.wiley.com/doi/abs/10.1002/nme.1620330705.

J. C. Simo and T. J. R. Hughes. On the variational foundations of assumed strain methods. *Journal of Applied Mechanics, ASME*, 53:51–54, 1986.

J. C. Simo and M. Riffai. A class of mixed assumed strain methods and the method of incompatible modes. *Int. J. Numer. Methods eng.*, 29:1595–1638, 1990.

J. C. Simo, R. L. Taylor, and K. S. Pister. Variational and projection methods for the volume constraint in finite deformation elasto-plasticity. *Computer Methods in Applied Mechanics and Engineering*, 51(1):177–208, 1985. ISSN 0045-7825. doi: https://doi.org/10.1016/0045-7825(85)90033-7. URL https://www.sciencedirect.com/science/article/pii/0045782585900337.

J. C. Simo, F. Armero, and R. L. Taylor. Improved versions of assumed enhanced strain tri-linear elements for 3d finite deformation problems. *Computer Methods in Applied Mechanics and Engineering*, 110(3):359–386, 1993. ISSN 0045-7825. doi: https://doi.org/10.1016/0045-7825(93)90215-J. URL https://www.sciencedirect.com/science/article/pii/004578259390215J.

S. Singh, S. Ramakrishna, and R. Singh. Material issues in additive manufacturing: A review. *Journal of Manufacturing Processes*, 25:185 – 200, 2017. ISSN 1526-6125. doi: https://doi.org/10.1016/j.jmapro.2016.11.006. URL http://www.sciencedirect.com/science/article/pii/S152661251630161X.

S. W. Sloan and M. F. Randolph. Numerical prediction of collapse loads using finite element methods. *International Journal for Numerical and Analytical Methods in Geomechanics*, 6:47–76, 1982.

M. Smith. *ABAQUS/Standard User's Manual, Version 6.9*. Dassault Systèmes Simulia Corp, United States, 2009.

H. Stolarski and T. Belytschko. Limitation principles for mixed finite elements based on the hu-washizu variational formulation. *Computer Methods in Applied Mechanics and Engineering*, 60(2):195–216, 1987. ISSN 0045-7825. doi: https://doi.org/10.1016/0045-7825(87)90109-5. URL https://www.sciencedirect.com/science/article/pii/0045782587901095.

B. A. Szabo, S. M. Holzer, and R. L. Actis. Solution of elastic-plastic stress analysis problems by the p-version of the finite element method. 12 1995. URL https://www.osti.gov/biblio/198207.

C. Taylor and P. Hood. A numerical solution of the navier-stokes equations using the finite element technique. *Computers and Fluids*, 1(1):73–100, 1973. ISSN 0045-7930. doi: https://doi.org/10.1016/0045-7930(73)90027-3. URL https://www.sciencedirect.com/science/article/pii/0045793073900273.

R. L. Taylor, K. S. Pister, and L. R. Herrmann. On a variational theorem for incompressible and nearly-incompressible orthotropic elasticity. *International Journal of Solids and Structures*, 4(9):875–883, 1968. ISSN 0020-7683. doi: https://doi.org/10.1016/0020-7683(68)90084-X. URL https://www.sciencedirect.com/science/article/pii/002076836890084X.

U. S. Department of Energy. Additive manufacturing: Pursuing the promise. https://www1.eere.energy.gov/manufacturing/pdfs/additive_manufacturing.pdf, 2012.

Y. Ueda, K. Fukuda, K. Nakacho, and S. Endo. A new measuring method of residual stresses with the aid of finite element method and reliability of estimated values. *Journal of the Society of Naval Architects of Japan*, 1975:499–507, 1975.

M. Zain ul Abdein, D. Nelias, J. F. Jullien, and D. Deloison. Prediction of laser beam welding-induced distortions and residual stresses by numerical simulation for aeronautic application. *Journal of Materials Processing Technology*, 209(6):2907–2917, 2009. ISSN 0924-0136. doi: https://doi.org/10.1016/j.jmatprotec.2008.06.051. URL https://www.sciencedirect.com/science/article/pii/S0924013608005542.

G. Vlachakis, M. Cervera, G. Barbat, and S. Saloustros. Out-of-plane seismic response and failure mechanism of masonry structures using finite elements with enhanced strain accuracy. *Engineering Failure Analysis*, 01 2019. doi: 10.1016/j.engfailanal.2019.01.017.

K. Washizu. Variational methods in elasticity and plasticity, ed. ii, 1975.

C. Webster. Simplify3d. https://www.simplify3d.com/, 2013–2022.

J. A. White and R. I. Borja. Stabilized low-order finite elements for coupled solid-deformation/fluid-diffusion and their application to fault zone transients. *Computer Methods in Applied Mechanics and Engineering*, 197(49):4353–4366, 2008. ISSN 0045-7825. doi: https://doi.org/10.1016/j.cma.2008.05.015. URL https://www.sciencedirect.com/science/article/pii/S0045782508002016.

K. V. Wong and A. Hernandez. A review of additive manufacturing. *ISRN Mechanical Engineering*, 2012: 10 pages, 2012. doi: 10.5402/2012/208760. URL https://doi.org/10.5402/2012/208760.

Y. Yang, M. Allen, T. London, and V. Oancea. Residual strain predictions for a powder bed fusion inconel 625 single cantilever part. *Integrating Materials and Manufacturing Innovation*, 8, 07 2019. doi: 10.1007/s40192-019-00144-5.

H. Yeung, B. M. Lane, M. A. Donmez, J. C. Fox, and J. Neira. Implementation of advanced laser control strategies for powder bed fusion systems. *Procedia Manufacturing*, 26:871–879, 2018.

N. Zander, T. Bog, S. Kollmannsberger, D. Schillinger, and E. Rank. Multi-level hp-adaptivity: high-order mesh adaptivity without the difficulties of constraining hanging nodes. *Comput Mech*, 55: 499–517, 2015. doi: https://doi.org/10.1007/s00466-014-1118-x.

N. Zander, T. Bog, M. Elhaddad, F. Frischmann, S. Kollmannsberger, and E. Rank. The multi-level hp-method for three-dimensional problems: Dynamically changing high-order mesh refinement with arbitrary hanging nodes. *Computer Methods in Applied Mechanics and Engineering*, 310:252–277, 2016a. ISSN 0045-7825. doi: https://doi.org/10.1016/j.cma.2016.07.007. URL https://www.sciencedirect.com/science/article/pii/S0045782516307289.

N. Zander, T. Bog, M. Elhaddad, F. Frischmann, S. Kollmannsberger, and E. Rank. The multi-level hp-method for three-dimensional problems: Dynamically changing high-order mesh refinement with arbitrary hanging nodes. *Computer Methods in Applied Mechanics and Engineering*, 310:252–277, 2016b.

K. Zeng, D. Pal, H. J. Gong, N. Patil, and B. Stucker. Comparison of 3dsim thermal modelling of selective laser melting using new dynamic meshing method to ansys. *Materials Science and Technology*, 31(8):945–956, 2015. doi: 10.1179/1743284714Y.0000000703. URL https://doi.org/10.1179/1743284714Y.0000000703.

X. Zeng, G. Scovazzi, N. Abboud, O. ColomÃ©s, and S. Rossi. A dynamic variational multiscale method for viscoelasticity using linear tetrahedral elements: A dynamic vms approach for viscoelasticity. *International Journal for Numerical Methods in Engineering*, 112, 05 2017. doi: 10.1002/nme.5591.

Y. Zhang, Q. Chen, G. Guillemot, C. A. Gandin, and M. Bellet. Numerical modelling of fluid and solid thermomechanics in additive manufacturing by powder-bed fusion: Continuum and level set formulation applied to track- and part-scale simulations. *Comptes Rendus Mecanique*, 09 2018a. doi: 10.1016/j.crme.2018.08.008.

Y. Zhang, G. Guillemot, M. Bernacki, and M. Bellet. Macroscopic thermal finite element modeling of additive metal manufacturing by selective laser melting process. *Computer Methods in Applied Mechanics and Engineering*, 331:514–535, 2018b. ISSN 0045-7825. doi: https://doi.org/10.1016/j.cma.2017.12.003. URL https://www.sciencedirect.com/science/article/pii/S0045782517307545.

H. Zhou and M. F. Randolph. Computational techniques and shear band development for cylindrical and spherical penetrometers in strain-softening clay. *International Journal of Geomechanics*, 7(4):287–295, 2007. doi: 10.1061/(ASCE)1532-3641(2007)7:4(287).

X. K. Zhu and Y. J. Chao. Numerical simulation of transient temperature and residual stresses in friction stir welding of 304l stainless steel. *Journal of Materials Processing Technology*, 146:263–272, 02 2004. doi: 10.1016/j.jmatprotec.2003.10.025.

O. C. Zienkiewicz. Displacement and equilibrium models in finite element method by b. fraejis de veubeke, chapter 9, pages 145-197 of stress analysis, edited by o. c. zienkiewicz and g. s. holister, published by john wiley & sons. *International Journal for Numerical Methods in Engineering*, 52(3):287–342, 1965. doi: https://doi.org/10.1002/nme.339.

O. C. Zienkiewicz and R. L. Taylor. *The Finite Element Method*. Butterworth-Heinemann, Oxford, UK, 2000.

O. C. Zienkiewicz and J. Z. Zhu. A simple error estimator and adaptive procedure for practical engineerng analysis. *International Journal for Numerical Methods in Engineering*, 24(2):337–357, 1987. doi: https://doi.org/10.1002/nme.1620240206. URL https://onlinelibrary.wiley.com/doi/abs/10.1002/nme.1620240206.

O. C. Zienkiewicz and J. Z. Zhu. The superconvergent patch recovery and a posteriori error estimates. part 1: The recovery technique. *International Journal for Numerical Methods in Engineering*, 33(7):1331–1364, 1992a. doi: https://doi.org/10.1002/nme.1620330702. URL https://onlinelibrary.wiley.com/doi/abs/10.1002/nme.1620330702.

O. C. Zienkiewicz and J. Z. Zhu. The superconvergent patch recovery and a posteriori error estimates. part 2: Error estimates and adaptivity. *International Journal for Numerical Methods in Engineering*, 33(7):1365–1382, 1992b. doi: https://doi.org/10.1002/nme.1620330703. URL https://onlinelibrary.wiley.com/doi/abs/10.1002/nme.1620330703.

O. C. Zienkiewicz, R. L. Taylor, and J. M. Too. Reduced integration technique in general analysis of plates and shells. *International Journal for Numerical Methods in Engineering*, 3(2):275–290, 1971. doi: https://doi.org/10.1002/nme.1620030211. URL https://onlinelibrary.wiley.com/doi/abs/10.1002/nme.1620030211.

O. C. Zienkiewicz, P. C. Jain, and E. Onìate. Flow of solids during forming and extrusion: Some aspects of numerical solutions. *International Journal of Solids and Structures*, 14(1):15–38, 1978. ISSN 0020-7683. doi: https://doi.org/10.1016/0020-7683(78)90062-8. URL https://www.sciencedirect.com/science/article/pii/0020768378900628.

O. C. Zienkiewicz, J. Z. Zhu, and N. G. Gong. Effective and practical h–p-version adaptive analysis procedures for the finite element method. *International journal for numerical methods in engineering*, 28(4):879–891, 1989.

Part II

APPENDIX

This part contains all cientific contributions supporting this Thesis. In addition, the participations in national and international conferences are listed.

A

PUBLISHED ARTICLES

A.1 Paper 1

Title: An Adaptive Finite Element Strategy for numerical simulation of Additive Manufacturing processes.

Authors:

- **J. Baiges**: Associate Professor of Continuum Mechanics and Structural analysis at the Universitat Politècnica de Catalunya (Technical University of Catalonia BarcelonaTech). Affiliated Scientist at the International Center for Numerical Methods in Engineering (CIMNE).
- **M. Chiumenti**: Full Professor of Continuum Mechanics and Structural analysis at the Universitat Politècnica de Catalunya (Technical University of Catalonia BarcelonaTech). Affiliated Scientist at the International Center for Numerical Methods in Engineering (CIMNE).
- **C. A. Moreira**: PhD Candidate in Civil Engineering in UPC BarcelonaTech and International Center for Numerical Methods in Engineering (CIMNE).
- **M. Cervera**: Full Professor of Continuum Mechanics and Structural analysis at the Universitat Politècnica de Catalunya (Technical University of Catalonia BarcelonaTech). Affiliated Scientist at the International Center for Numerical Methods in Engineering (CIMNE).
- **R. Codina**: Full Professor of Continuum Mechanics and Structural analysis at the Universitat Politècnica de Catalunya (Technical University of Catalonia BarcelonaTech). Affiliated Scientist at the International Center for Numerical Methods in Engineering (CIMNE).

Additive Manufacturing
Editor-in-Chief: R. Wicker
ISSN: 2214-8604
Elsevier Editors
https://doi.org/10.1016/j.addma.2020.101650
Link to Publisher

Additive Manufacturing 37 (2021) 101650

Contents lists available at ScienceDirect

Additive Manufacturing

journal homepage: www.elsevier.com/locate/addma

An adaptive Finite Element strategy for the numerical simulation of additive manufacturing processes

Joan Baiges [a], Michele Chiumenti [a,b], Carlos A. Moreira [a,b], Miguel Cervera [a,b], Ramon Codina [a,b]

[a] Universitat Politécnica de Catalunya, Jordi Girona 1-3, Edifici C1, 08034 Barcelona, Spain
[b] Centre Internacional de Métodes Numérics a l'Enginyeria (CIMNE), Edifici C1, Campus Nord UPC C/ Gran Capitá S/N, 08034 Barcelona, Spain

ARTICLE INFO

Keywords:
Finite Element
adaptive refinement
additive manufacturing
numerical simulation

ABSTRACT

In this work an adaptive Finite Element strategy to deal with the numerical simulation of Additive Manufacturing (AM) processes is presented. The Selective Laser Melting (SLM) is chosen as the reference technology because of its great diffusion in the industrial manufacturing chain, although the proposed methodology can be applied to the numerical simulation of all types of AM. An octree-based mesh adaptivity approach is adopted allowing for the use of much finer meshes within the processing zone, the so called Thermo-Mechanically Affected Zone (TMAZ), if compared to the rest of the computational domain. Although the adaptive meshing is vital to keep controlled the computational resources through the entire simulation of the fabrication process, the accuracy of the results can be compromised by the coarsening strategy, and particularly when simulating the SLM process, where the mesh size can vary from microns (TMAZ) to centimetres (close to the build-plate). This loss of accuracy can spoil the original efforts in refining the mesh in the process zone. Therefore a strategy to compensate for information loss in the adaptive refinement simulation of additive manufacturing processes is developed. The main idea is to add two correction terms which compensate for the loss of accuracy in the coarsening process of the mesh in the already manufactured regions. The proposed correction terms can be interpreted as a Variational Multiscale enhancement on the adaptive mesh. This allows one to successfully simulate the additive manufacturing process by using an adaptively coarsened mesh, with results which have an accuracy very similar to the one of a uniformly refined mesh simulation, at a fraction of the computational cost. Numerical examples illustrate the performance of the proposed strategy.

1. Introduction

The numerical simulation of Additive Manufacturing (AM) processes has been capturing the interest of the scientific community during the last years. Many efforts have been done to reproduce the fabrication process in a way as faithful as possible to the industrial practice. We refer to *high fidelity* analysis when the objective is to simulate the actual scanning sequence (laser Electron Beam (EB) melting processes) or the metal deposition pattern (wire melting or blown-powder processes). Following this concept, fully coupled thermo-mechanical analysis are conducted on an evolving (growing) computational domain which closely follows the building process.Most of the original works on AM simulation make use of the numerical framework used for the welding or multi-pass welding analysis, adopting very similar numerical strategies to solve the thermal/coupled thermo-mechanical problem [10,13]. These strategies have been applied to validate additive manufacturing numerical simulation using experimental data [16,17,37], including stress and deformation evaluation [32–34]. A review of the residual stresses can be found in [8] and the influence of the how scanning strategies affect the residual stresses are subject of [12,40]. While the constitutive models used for the characterization of the material behavior have demonstrated to be suitable for the AM analysis, the numerical strategy has shown its limitations when trying to afford simulations on components of industrial interest. This problem is more and more evident when moving the focus from Wire Arc Additive Manufacturing (WAAM), where the thickness of the deposited layer is within the range of 1–3 mm, to Selective Laser Melting (SLM), that makes use of a laser source to (selectively) melt powder-bed layers of about 20–60 μm. This is the reason why the numerical simulation of the SLM process is generally addressed using simplified strategies based on the *Inherent Strain* method [11,22,44,48,49]. Hence, the coupled thermo-mechanical process is replaced by a sequence of purely mechanical computations in a layer-by-layer (or even multi-layer) manner. This is physically motivated by the fact that during the recoating

E-mail address: joan.baiges@upc.edu (J. Baiges).

https://doi.org/10.1016/j.addma.2020.101650
Received 17 June 2020; Received in revised form 4 September 2020; Accepted 5 October 2020
Available online 9 October 2020

process, when a new powder-bed is spread, the temperature of the built decreases to reach the value of the build-plate, de-coupling the analysis of the last printed layer from the rest of the built. In the common practice, the Thermo-Mechanically Affected Zone (TMAZ) penetrates only 100–150 μm (just few layers) through the substrate (or the more recent printed layers). Hence, the temperature gradients (induced by the laser source), as well as the evolution of the plastic strains (due to the material shrinkage), affect the last few printed layers, only. A second simplification hypothesis consists of assuming a purely elastic stress analysis being the end-user the final responsible of defining or obtaining a suitable Inherent-Strain tensor that characterizes the process in terms of distortions and residual stresses of the manufactured component. The Inherent-Strain tensor can be obtained from experimental data or previous small-scale, non-linear, numerical simulations [9]. This tensor includes both the thermal and the plastic strains defined as a uniform (averaged) distribution over each printed layer. This hypothesis relays on the fact that the melt-pool is very small, if compared with the size of the entire layer, its effects being very localized and almost independent of the boundary conditions. Other approaches to obtain the Inherent Strain tensor are possible, such as the modified version of the Inherent Strain Method is presented for the Direct Energy Deposition (DED) in LENS (Laser Engineered Net Shaping) presented in [28,29] and the extension of this work for lattice support structures in powder bed technology is introduced in [30].

Although the inherent strain method alleviates the computation requirements for the simulation of the SLM process, the huge number of layers necessary to build the final component as well as the mesh size required for the Finite Element (FE) discretization still need very large computational time and memory requirements.

The approach followed in this work consists in combining a FE High Performance Computing (HPC) framework together with dynamic mesh adaptation, which mitigates the computational effort by refining the mesh at the TMAZ while coarsening it anywhere else. An octree-based coarsening strategy is adopted (see Fig. 1). The main idea of octree strategies is to hierarchically refine/coarsen elements, which allows the refinement process to be efficient and relatively simple to parallelize [18,36,39,41]. The octree method allows for a fast coarsening of the mesh while minimizing the data-transfer between meshes. It also demonstrates to be suitable for its parallelization in MPI-based HPC environments. The enhancement provided by AMR and parallelism for the solution of AM processes can be found in several works.

Ref. [20] uses a coarsening algorithm to reduce the computational cost. The algorithm keeps a fine mesh on the two layers below the deposition area and merges the elements below this region maintaining at least 1 fine layer below the deposition. Plastic strains and hardening variables are interpolated to the new Gauss points. [38] proposes an adaptive re-meshing to minimize the number of nodes to predict distortions and residual stresses in the simulation of LPBF where the layers being solved are kept with a fine mesh and a coarse mesh at the inactive and previous solved layers. [26] uses dynamically changing meshes based on a combination of hp-finite elements and the finite cell method to treat state and field variables to reduce the number of nodes on the simulation to save computational resources.

In [21] a thermo-mechanical LPBF is validated by comparing predicted and measured distortions. The work is based on a multi-scale approach and uses mesh adaptivity to reduce mesh density according to a pre-activation remeshing scheme. The authors refer to the adaptivity as one of the sources of error between the observed results of model-experiment. [27] addresses several coarsening strategies using Hex8 elements with smooth transitions between coarse and fine mesh regions. The authors compare the coarsening strategies with static mesh results validated experimentally comparing temperature field, distortions and residual stresses in a thin wall structure. A common strategy is to apply a dynamic mesh with a refined area near the heat source in LPBF and compare the adaptive solution with a fix uniform mesh for the thermal problem [25,50]. The work of [42] compares the performance of the thermo-mechanical solution using the monolithic and adiabatic [2] approaches using AMR to refine and coarsen structured meshes where required.

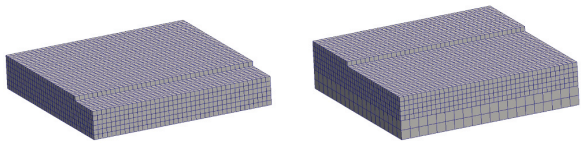

Fig. 1. AM process simulation: Initial uniform mesh (left); mesh coarsening far from the TMAZ (right).

Nevertheless, by using intensive adaptive refinement for the AM processes, one of the main concerns is the loss of information in the data-transfer when switching from a fine mesh (TMAZ) to a coarser one. This information loss can lead to a reduction of accuracy spoiling the final results.

In this work a strategy to compensate for information loss in the adaptive refinement simulation of AM processes is presented. The main idea is to add two correction terms to the boundary value problem defined for the coarser mesh to preserve the results obtained in the finer mesh just before the coarsening procedure. The proposed methodology can be understood as a Variational Multiscale approach [23], in which the model for the subscales arising from finer discretizations is exactly known. The method is derived from the approaches presented in [5,6], where coarsening correction terms were applied in order to enhance the performance of reduced order models.

The proposed correction method is applied to the numerical simulation of SLM processes by the *inherent strain* method. Nevertheless, the same methodology can be extended to the high-fidelity analysis of more complex AM processes (e.g. WAAM, DED, etc.) involving thermo-mechanical coupling and elasto-visco-plastic constitutive behavior.

The paper is organized as follows: in Section 2 the FE modeling of the AM process by SLM is presented. Section 3 focuses on the proposed adaptive methodology and the strategy to correct the information loss in the coarsening process. In Section 4 several numerical examples illustrate the performance of the proposed strategy, and finally some conclusions close the work in Section 5.

2. Finite Element modeling of the additive manufacturing process by SLM

The most suitable numerical strategy to tackle the simulation of the SLM process is based on the Inherent Strain approach. This method enables for a fast prediction of the distortions and residual stresses of the fabricated component assuming the general hypotheses widely accepted in Computational Welding Mechanics (CWM) [35,46,47]. In this case, the fully coupled transient thermo-mechanical analysis is replaced by a layer-by-layer (or even multi-layer) sequence of steady-state mechanical analyses. Hence, the original CAD geometry is firstly sliced according to the thickness of the powder-bed and then the FE discretization is generated accordingly. The birth-death FE activation technique is adopted [14,15,17,19,31] to add to the computational domain Ω all the finite elements belonging to each layer (slice) arising from the laser melting process of the powder bed. The analysis follows the two-step sequence of the actual SLM process: (i) recoating and (ii) laser-scanning. From the modeling point of view, the former consists of updating the computational domain by adding all the elements belonging to each new layer. The latter stage performs the stress analysis on the new domain.

In the initial FE discretization $\Omega_h^o = \Omega_h(t=0)$ all the elements are inactive: they do not belong to the computational domain, so that they are neither computed nor assembled into the global system of equations. The time discretization consists of a uniform partition of the analysis period $[0, T]$ into N time intervals, which correspond to the total number

of layers required to complete the whole SLM process. This given, when the first layer is activated, the corresponding stress analysis is performed on Ω_h^1. The whole layer activation sequence follows.

The stress analysis enforces the conservation of the balance of momentum equation within the current active domain Ω_h^{n+1} at time $t^{n+1} \in [0, T]$. We denote as t^{n+1} the current time instant to indicate that an implicit approach for the time integration is used. The corresponding Dirichlet and Neumann boundary conditions are applied on $\Gamma_D^{n+1} = \Gamma_D(t^{n+1})$ and $\Gamma_N^{n+1} = \Gamma_N(t^{n+1})$, respectively, which results in the following set of equations:

$$\begin{aligned} -\nabla\cdot\boldsymbol{\sigma} &= \boldsymbol{b} \quad \text{in } \Omega_h^{n+1}, \\ \boldsymbol{u} &= \bar{\boldsymbol{u}} \quad \text{on } \Gamma_D^{n+1}, \\ \boldsymbol{\sigma}\cdot\boldsymbol{n} &= \bar{\boldsymbol{t}} \quad \text{on } \Gamma_N^{n+1}, \end{aligned} \tag{1}$$

where $\boldsymbol{u}$ is the displacement field, $\boldsymbol{\sigma}$ is the Cauchy stress tensor, $\boldsymbol{b}$ are the external body forces and, $\bar{\boldsymbol{u}}$ and $\bar{\boldsymbol{t}}$ are the prescribed displacements and the prescribed tractions on Γ_D^{n+1} and Γ_N^{n+1}, respectively.

After the finite element discretization, the discrete weak form of (1) at time $t^{n+1} \in [0, T]$ can be written as:

$$\begin{aligned} \int_{\Omega_h^{n+1}} \boldsymbol{\epsilon}(\delta\boldsymbol{v}_h) : \boldsymbol{\sigma}(\boldsymbol{u}_h^{n+1})\, d\Omega &= \int_{\Omega_h^{n+1}} \delta\boldsymbol{v}_h\cdot\boldsymbol{b}\, d\Omega \\ &\quad + \int_{\Gamma_N^{n+1}} \delta\boldsymbol{v}_h\cdot\bar{\boldsymbol{t}}\, d\Gamma \quad \forall \delta\boldsymbol{v}_h \in V_h^{n+1}. \end{aligned} \tag{2}$$

where $\delta\boldsymbol{v}_h$ are the test functions and V_h^{n+1} is the finite element space for the displacements.

The total strain tensor $\boldsymbol{\epsilon}(\boldsymbol{u}) = \frac{1}{2}\left(\nabla\boldsymbol{u} + (\nabla\boldsymbol{u})^T\right) = \nabla^S\boldsymbol{u}$ can be split into the elastic strains, $\boldsymbol{\epsilon}_e$, the visco-plastic strains including phase transformation and creep induced strains, $\boldsymbol{\epsilon}_{vp}$, and the thermal deformation including the shrinkage effect during the phase-change transformation, $\boldsymbol{\epsilon}_{th}$, as:

$$\epsilon = \epsilon_e + \epsilon_{vp} + \epsilon_{th} \tag{3}$$

The constitutive model reads as:

$$\boldsymbol{\sigma} = \mathbb{C} : \boldsymbol{\epsilon}_e = \mathbb{C} : \left(\boldsymbol{\epsilon} - \boldsymbol{\epsilon}_{vp} - \boldsymbol{\epsilon}_{th}\right) \tag{4}$$

where $\mathbb{C}$ is the elastic constitutive tensor. Defining the inherent strain as: $\boldsymbol{\epsilon}_{inh} = \boldsymbol{\epsilon}_{vp} + \boldsymbol{\epsilon}_{th}$, the constitutive equation can be rewritten as:

$$\boldsymbol{\sigma}(\boldsymbol{u}) = \mathbb{C} : (\boldsymbol{\epsilon}(\boldsymbol{u}) - \boldsymbol{\epsilon}_{inh}) \tag{5}$$

Note that the inherent strain tensor is typically obtained either by experimental calibration by matching the actual distortion of representative demonstrators or by a high-fidelity simulation of the moving melt-pool at the TMAZ [24,43,45]. Hence, both the thermal coupling and the plastic analysis are avoided, thus minimizing the computational cost.

Nevertheless, according to the activation process, each new layer is born with an initial displacement field, $\boldsymbol{u}_o$, induced by the movement of the nodes shared with the pre-existing active elements. This means that at the instant of the activation, the newly activated elements inherit an initial strain field $\boldsymbol{\epsilon}(\boldsymbol{u}_o) = \nabla^S\boldsymbol{u}_o$ induced by those initial displacements. If not removed from the computation, this strains transform into a spurious pre-stress field which pollutes the entire solution. Hence, to deal with the AM analysis, the constitutive equation must be corrected as:

$$\boldsymbol{\sigma}(\boldsymbol{u}, \boldsymbol{\epsilon}_{inh}, \boldsymbol{\epsilon}_{act}) = \mathbb{C} : (\boldsymbol{\epsilon}(\boldsymbol{u}) - \boldsymbol{\epsilon}_{inh} - \boldsymbol{\epsilon}_{act}) \tag{6}$$

where $\boldsymbol{\epsilon}_{act} = \nabla^S\boldsymbol{u}_o$ are the so called activation strains.

Fig. 2 illustrates the displacement field caused by the effect of the inherent strains $\boldsymbol{\epsilon}_{inh}$. Displacements are magnified by several orders of magnitude so that they can be appreciated in the figure. Active elements are depicted in red, while inactive elements are depicted in green. The highlighted green element is the element which is going to be activated in the next time step. The element is deformed due to the displacements of the nodes which belong to already activated elements. This initial or activation deformation shall not introduce any stresses in the newly printed material. To compensate for it, the initial or activation strain $\boldsymbol{\epsilon}_{act}$ is introduced.

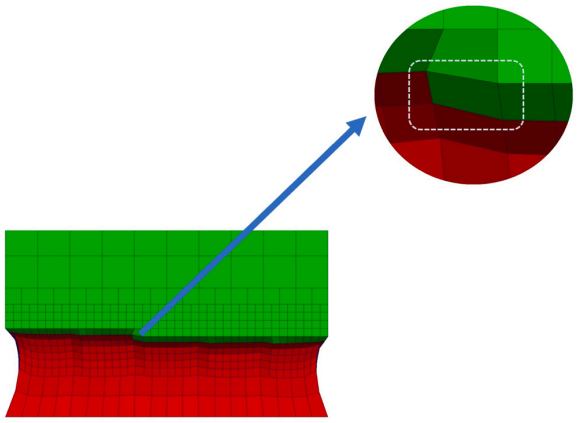

Fig. 2. Displacement field caused by inherent strains.

This given, the weak form of the mechanical problem suitable for AM analysis can be rewritten using the following compact form: find a displacement field $\boldsymbol{u}_h^{n+1}$ such that:

$$B^{n+1}\left(\delta\boldsymbol{v}_h, \boldsymbol{\sigma}(\boldsymbol{u}_h^{n+1}, \epsilon_{act}^{n+1}, \epsilon_{inh}^{n+1})\right) = F^{n+1}(\delta\boldsymbol{v}_h) \quad \forall \delta\boldsymbol{v}_h \in V_h^{n+1}, \tag{7}$$

where

$$\begin{aligned} B^{n+1}\left(\delta\boldsymbol{v}_h, \boldsymbol{\sigma}(\boldsymbol{u}_h^{n+1}, \epsilon_{\text{act}}^{n+1}, \epsilon_{\text{inh}}^{n+1})\right) &:= \int_{\Omega_h^{n+1}} \epsilon(\delta\boldsymbol{v}_h) : \mathbb{C} : \left(\epsilon(\boldsymbol{u}_h^{n+1})\right. \\ &\quad \left. - \epsilon_{\text{act}}^{n+1} - \epsilon_{\text{inh}}^{n+1}\right) d\Omega, \end{aligned} \tag{8}$$

$$F^{n+1}(\delta\boldsymbol{v}_h) := \int_{\Omega_h^{n+1}} \delta\boldsymbol{v}_h\cdot\boldsymbol{b}\, d\Omega + \int_{\Gamma_N^{n+1}} \delta\boldsymbol{v}_h\cdot\bar{\boldsymbol{t}}\, d\Gamma \tag{9}$$

3. Coarsening and correction strategy

3.1. Octree refinement strategy

For the solution of Eq. (7) an adaptive finite element method is used. This is very convenient since it allows to use a fine mesh in the regions where material is being printed and where both large temperature gradients and stress concentrations occur. At the same time it allows to coarsen the mesh once the simulation advances and less precision is required on that area. An octree refinement strategy is used (see our previous works on adaptive methods for computational solid mechanics [3,4,7]). Fig. 1 illustrates the adopted refinement strategy. The simulation departs from a coarse mesh which covers the complete simulation domain over time. The mesh is then refined by subdividing the elements in the areas close to the melt-pool. This can be done for both hexahedral and tetrahedral elements. As the manufacturing process advances, a finer mesh is used in the TMAZ (upper layers), while a mesh coarsening is performed elsewhere. The hierarchical octree refinement strategy results in hanging nodes (see Fig. 3) in the finite element mesh which need to be properly treated [3].

3.2. Adaptive finite element approach

Let us consider an adaptively refined finite element space in the active domain, V_h^{n+1}, and the discrete weak form of the problem given by

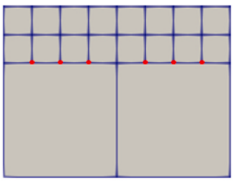

Fig. 3. Hanging nodes (*red*) at the interface between refined and coarse meshes. (For interpretation of the references to color in this figure legend, the reader is referred to the web version of this article.)

Eqs. (7)–(9). Note that the finite element space V_h^{n+1} evolves after the deposition of each new layer following the printing process, as well because of the adaptive refinement and coarsening process. When a new finite element mesh is generated because of the mesh adaptivity process, information from the previous mesh needs to be projected onto the new mesh.

For the displacement field, a nodal projection is used, which means that for already existing nodes the nodal displacement values do not change, and for new nodes, the values are interpolated point to point from the old mesh onto the new one. Therefore, the displacements at t^n in the mesh at t^{n+1} are given by:

$$P_h^{n+1}\left(\boldsymbol{u}_h^n\right), \tag{10}$$

where $P_h^{n+1}(\cdot)$ is the point to point projection onto V_h^{n+1}.

For the historical variables defined at the integration points, such as $\boldsymbol{\epsilon}_{\text{act}}$ and $\boldsymbol{\epsilon}_{\text{inh}}$, the projection process is done element by element, the quantities are transferred through an elementwise L^2 projection, which is denoted by Π_h^{n+1}. Thus:

$$\Pi_h^{n+1}(\epsilon_{\text{act}}^n), \tag{11}$$

$$\Pi_h^{n+1}(\epsilon_{\text{inh}}^n). \tag{12}$$

are the strains $\boldsymbol{\epsilon}_{act}$ and $\boldsymbol{\epsilon}_{inh}$ at t^n in the mesh at t^{n+1}. For each element K^{n+1} of the new mesh the projection is computed solving:

$$\int_{K^{n+1}} \delta\boldsymbol{\gamma}_h : \Pi_h^{n+1}(\epsilon^n) d\Omega = \int_{K^{n+1}} \delta\boldsymbol{\gamma}_h : \epsilon^n d\Omega, \quad \forall \delta\boldsymbol{\gamma}_h \in W_{h,K^{n+1}}$$

where now $\delta\boldsymbol{\gamma}_h$ are the tensorial weight functions and $W_{h,K^{n+1}}$ is the tensorial finite element space of the new mesh restricted to the considered element. Once computed, $\Pi_h^{n+1}(\boldsymbol{\epsilon}^n)$ is interpolated and stored at the new element quadrature points. Note that $\Pi_h^{n+1}(\boldsymbol{\epsilon}^n)$ belongs to the element-wise tensorial finite element space $W_{h,K^{n+1}}$, which is of the same approximation order as the displacement space V_h^{n+1}, whereas $\boldsymbol{\epsilon}^n$ belongs to the strains finite element space, which is typically one approximation order inferior than the displacement space V_h^{n+1}.

3.3. Stress correction terms

During the coarsening step between successive adaptive meshes, part of the information stored in the coarsened region is lost. This is so because of the projection errors associated to P_h^{n+1} and Π_h^{n+1}, and also because in the coarsening process the finite element space changes from V_h^n to V_h^{n+1}. This causes that when straightforwardly computing the stresses which result from the adaptive simulation of the AM process by using inherent and activation strains, it is observed that the obtained results are of poor quality and not in concordance with those obtained with an equivalent fine mesh simulation. This effect is particularly apparent when low order elements with a poor representation of the stress field (namely tetrahedral elements) are used. The obtained stress field if of a much lower quality than the one obtained for coarser non-adaptive meshes.

The reason for this behavior is twofold: on the one hand the activation (or inherent) strains on the fine mesh before coarsening $\boldsymbol{\epsilon}_{\text{act}}^n$ can present heavy element to element jumps, specially if low order elements with a poor gradient representation are used. When coarsened, activation strains result in an L^2 averaged field $\Pi_h^{n+1}(\boldsymbol{\epsilon}_{\text{act}}^n)$ which introduces the appropriate average forces field, but which can result in an inaccurate local strain value. This representation is translated into a poor local solution stress field when the next step of the simulation is performed. Secondly, when mesh coarsening is performed, there will be nodes which were previously free which will become hanging in the new mesh. Displacement values at these nodes will automatically be switched from their free value to an interpolated value from the corresponding parent nodes. This results in important changes in the strain values, which automatically translates into incorrect local stress values on the elements to which these hanging nodes belong.

Due to this, it is necessary to correct the obtained stress values through a stress correction term. Let us define the stress field on the current step $\boldsymbol{\sigma}_h^{n+1}$ straightforwardly computed from the current step variables:

$$\boldsymbol{\sigma}_h^{n+1} = \boldsymbol{\sigma}\left(\boldsymbol{u}_h^{n+1}, \epsilon_{act}^{n+1}, \epsilon_{inh}^{n+1}\right), \tag{13}$$

and the stresses from the previous time step computed on the current step mesh, by using the projected previous step variables, $\hat{\boldsymbol{\sigma}}_h^n$:

$$\hat{\boldsymbol{\sigma}}_h^n = \boldsymbol{\sigma}\left(P_h^{n+1}(\boldsymbol{u}_h^n), \Pi_h^{n+1}(\epsilon_{act}^n), \Pi_h^{n+1}(\epsilon_{inh}^n)\right). \tag{14}$$

Note that both quantities are defined in the mesh at step $n+1$. Recall that due to the nature of activation and inherent strains:

$$\begin{aligned} \epsilon_{act}^{n+1} &= \Pi_h^{n+1}(\epsilon_{act}^n) + \Delta\epsilon_{act}^{n+1}, \\ \epsilon_{inh}^{n+1} &= \Pi_h^{n+1}(\epsilon_{inh}^n) + \Delta\epsilon_{inh}^{n+1}. \end{aligned}$$

The proposed total corrected stress field $\boldsymbol{\sigma}^{n+1}$ is defined as:

$$\boldsymbol{\sigma}^{n+1} = \boldsymbol{\sigma}_h^{n+1} + \tilde{\boldsymbol{\sigma}}^{n+1} \tag{15}$$

with:

$$\tilde{\boldsymbol{\sigma}}^{n+1} = \Pi_h^{n+1}(\boldsymbol{\sigma}^n) - \hat{\boldsymbol{\sigma}}_h^n, \tag{16}$$

where $\tilde{\boldsymbol{\sigma}}^{n+1}$ is the stress correction term. Let us remark the recursive nature of Eqs. (15)–(16), where the total corrected stress field $\boldsymbol{\sigma}^{n+1}$ depends on the projection of the total corrected stress field at the previous step $\Pi_h^{n+1}(\boldsymbol{\sigma}^n)$. At the first step $\tilde{\boldsymbol{\sigma}}^1 = \boldsymbol{0}$ is set. Note also that Eqs. (15)–(16) imply that the total stress at time step $n+1$ can be interpreted as the decomposition into:

$$\boldsymbol{\sigma}^{n+1} = \Pi_h^{n+1}(\boldsymbol{\sigma}^n) + \Delta\boldsymbol{\sigma}^{n+1},$$

where the first term is the contribution of the previous time steps with minimum information loss as a result of the stress correction term, and the second one is the increment in stresses caused by load increments $\Delta\boldsymbol{\epsilon}_{act}^{n+1}$, $\Delta\boldsymbol{\epsilon}_{inh}^{n+1}$ at the current step, with:

$$\Delta\boldsymbol{\sigma}^{n+1} = \boldsymbol{\sigma}_h^{n+1} - \hat{\boldsymbol{\sigma}}_h^n,$$

as defined in Eqs. (13)–(14).

In the first coarsening step, the correction term (16) is just the difference between the projected stress field at the previous time step, and the stress computed in the new mesh with the projected variables from the previous step, namely displacements and inherent and activation strains field. For successive steps, due to the recursive nature of $\tilde{\boldsymbol{\sigma}}$, information on the fine meshes at previous steps is successively transferred throughout the simulation, minimizing information loss.

3.4. Force correction terms

The introduction of the stress correction terms (16) is not enough to prevent information loss during successive coarsening steps. This is so because there is no guarantee that the solution of the finite element problem in the previous mesh is at equilibrium when projected onto the new coarsened mesh. The optimal situation would be to preserve the results obtained through the solution of problem (7) at time step n into the new (coarsened) finite element mesh at time $n+1$. In general this does not happen and thus:

$$\exists \delta \boldsymbol{v}_h \in \hat{V}_h^{n+1} | B^n\left(\delta \boldsymbol{v}_h, \hat{\boldsymbol{\sigma}}_h^n + \widetilde{\boldsymbol{\sigma}}^{n+1}\right) = B^n\left(\delta \boldsymbol{v}_h, \Pi_h^{n+1}(\boldsymbol{\sigma}^n)\right) \neq F^n(\delta \boldsymbol{v}_h). \tag{17}$$

where now $\hat{V}_h^{n+1}$ is the coarsened finite element space at t^{n+1} prior to the new element activation, that is, the space associated to the mesh at $n+1$ but covering only the domain Ω^n, instead of Ω^{n+1}. Due to this, the equilibrium state *attimestepn* on the coarsened mesh $n+1$ is not attained for $P_h^{n+1}(\boldsymbol{u}_h^n)$ but for $\hat{\boldsymbol{u}}_h^n$, the solution to:

$$B^n\left(\delta \boldsymbol{v}_h, \boldsymbol{\sigma}\left(\hat{\boldsymbol{u}}_h^n, \Pi_h^{n+1}(\epsilon_{\text{act}}^n), \Pi_h^{n+1}(\epsilon_{\text{inh}}^n)\right) + \widetilde{\boldsymbol{\sigma}}^{n+1}\right) = F^n(\delta \boldsymbol{v}_h) \quad \forall \delta \boldsymbol{v}_h \in \hat{V}_h^{n+1}. \tag{18}$$

In order to correct this issue, a *force coarsening correction term* is computed which compensates for coarsening information loss. The correction term is defined as:

$$C^{n+1}(\delta \boldsymbol{v}_h, \boldsymbol{u}_h^n, \epsilon_{\text{act}}^n, \epsilon_{\text{inh}}^n) := B^n\left(\delta \boldsymbol{v}_h, \Pi_h^{n+1}(\boldsymbol{\sigma}^n)\right) - F^n(\delta \boldsymbol{v}_h) \quad \delta \boldsymbol{v}_h \in \hat{V}_h^{n+1}. \tag{19}$$

This term corresponds to the forces residual obtained by projecting the solution obtained at time n onto the new mesh at time $n+1$, including the stresses correction term $\widetilde{\boldsymbol{\sigma}}^{n+1}$, in the equilibrium equation. When adding (19) to Eq. (18), the resulting weak form is:

$$\begin{aligned} &B^n\left(\delta \boldsymbol{v}_h, \boldsymbol{\sigma}\left(\hat{\boldsymbol{u}}_h^n, \Pi_h^{n+1}(\epsilon_{\text{act}}^n), \Pi_h^{n+1}(\epsilon_{\text{inh}}^n)\right) + \widetilde{\boldsymbol{\sigma}}^{n+1}\right) \\ &= F^n(\delta \boldsymbol{v}_h) + C^{n+1}(\delta \boldsymbol{v}_h, \boldsymbol{u}_h^n, \epsilon_{\text{act}}^n, \epsilon_{\text{inh}}^n) \quad \forall \delta \boldsymbol{v}_h \in \hat{V}_h^{n+1}. \end{aligned} \tag{20}$$

The solution to (20) is $\hat{\boldsymbol{u}}_h^n = P_h^{n+1}(\boldsymbol{u}_h^n)$. By inserting (19) in the formulation, we successfully compensate for information loss in the coarsening process in the equilibrium equation. Note that this means that the solution at time step $n+1$ can be interpreted as the decomposition into:

$$\boldsymbol{u}_h^{n+1} = P_h^{n+1}(\boldsymbol{u}_h^n) + \Delta \boldsymbol{u}_h^{n+1},$$

where the first term is the contribution of the previous time steps with minimum information loss thanks to the modification of the equilibrium equation, and the second one is the increment in displacements caused by the load increments $\Delta \boldsymbol{\epsilon}_{\text{act}}^{n+1}$, $\Delta \boldsymbol{\epsilon}_{\text{inh}}^{n+1}$ at the current step.

By taking into account (19), the resulting finite element problem at time step $n+1$ is: find a displacement field $\boldsymbol{u}_n^{n+1}$ such that:

$$\begin{aligned} &B^{n+1}(\delta \boldsymbol{v}_h, \boldsymbol{\sigma}(\boldsymbol{u}_h^{n+1}, \epsilon_{\text{act}}^{n+1}, \epsilon_{\text{inh}}^{n+1}) + \widetilde{\boldsymbol{\sigma}}^{n+1}) \\ &= F^{n+1}(\delta \boldsymbol{v}_h) + C^{n+1}(\delta \boldsymbol{v}_h, \boldsymbol{u}_h^n, \epsilon_{\text{act}}^n, \boldsymbol{\epsilon}_{\text{inh}}^n) \quad \forall \delta \boldsymbol{v}_h \in V_h^{n+1}. \end{aligned} \tag{21}$$

3.5. Interpretation as a variational multiscale method

The corrections proposed in Subsections 3.3 and 3.4 can be interpreted as a Variational Multiscale approach (see [23]), in which the value of the displacement and stress subscales is exactly known. Let us decompose the solution at time n into its projection onto V_h^{n+1} and the remaining part referred to as the subscales, $\widetilde{\boldsymbol{u}}^n$. This latter corresponds to the information loss in the projection from V_h^n to V_h^{n+1}. Thus:

$$\boldsymbol{u}_h^n = P_h^{n+1}(\boldsymbol{u}_h^n) + \widetilde{\boldsymbol{u}}^n. \tag{22}$$

Similarly, activation and inherent strains are decomposed into:

$$\begin{aligned} \epsilon_{\text{act}}^n &= \Pi_h^{n+1}(\epsilon_{\text{act}}^n) + \widetilde{\epsilon}_{\text{act}}^n, \\ \epsilon_{\text{inh}}^n &= \Pi_h^{n+1}(\epsilon_{\text{inh}}^n) + \widetilde{\epsilon}_{\text{inh}}^n. \end{aligned} \tag{23}$$

Eq. (16) straightforwardly defines the stress subscales $\widetilde{\boldsymbol{\sigma}}$.

Correction stresses $\widetilde{\boldsymbol{\sigma}}$ and correction forces $C^{n+1}(\delta \boldsymbol{v}_h, \boldsymbol{u}_h^n, \epsilon_{\text{act}}^n, \epsilon_{\text{inh}}^n)$ precisely account for the (otherwise lost) contribution of $\widetilde{\boldsymbol{u}}^n, \widetilde{\boldsymbol{\epsilon}}_{\text{act}}^n, \widetilde{\boldsymbol{\epsilon}}_{\text{inh}}^n$, and $\widetilde{\boldsymbol{\sigma}}$ to the bilinear form. This interpretation gives a variational foundation to the proposed correction terms.

4. Numerical examples

In this section some numerical examples illustrate the performance of the proposed methodology.

The objectives are two-fold: (a) to reduce the computational effort using mesh refinement and, particularly, mesh coarsening, and (b) to minimize the effects induced by the mesh coarsening using the proposed correction terms. Both the CPU-time and the result accuracy using the mesh adaptivity *with* and *without* the correction term are compared to a fixed fine FE mesh used as a reference. These numerical examples do not pretend to present accurate results for the quantities of interest of a particular simulation (the used finite element meshes are possibly too coarse for this), but on the contrary they have been selected because they are illustrative and allow us to show the improvements that can be obtained by using the strategy proposed in this work.

The material and process parameters used in the numerical examples are shown in Table 1 and the building process follows a layer-by-layer activation scheme.

Three test-cases are proposed. The first one adopts a fixed computational domain and it is intended to demonstrate the necessity of the correction term to preserve the solution obtained with the finest mesh used in the adaptive process. The second example shows the virtue of the adaptive technology when a growing computational domain is used as required for the simulation of the AM process. Finally, an industrial component is simulated with the proposed technology to show the speed-up obtained with respect to the use of a fixed mesh while preserving the same accuracy.

To assess the global error of each example, a *relative* L^2 *error* norm of the displacement field is computed at the end of the simulation as:

$$e_{L^2} = \frac{\sqrt{\int_\Omega \left(P_h^{\text{coarse}}(\boldsymbol{u}_h^{\text{fine}}) - \boldsymbol{u}_h^{\text{coarse}}\right) d\Omega}}{\sqrt{\int_\Omega \left(P_h^{\text{coarse}}(\boldsymbol{u}_h^{\text{fine}})\right)^2 d\Omega}} \tag{24}$$

where $P_h^{\text{coarse}}(\boldsymbol{u}_h^{\text{fine}})$ is the projection of the reference (fixed fine mesh) solution and $\boldsymbol{u}_h^{\text{coarse}}$ is the solution obtained with the coarsened mesh both *with* and *without* the correction term.

Remark: Note that the error is computed after point to point projecting the fine solution onto the coarse mesh: this is so because the objective of the methodology is to avoid any spurious displacement due to the coarsening of lower layers to be transferred to the upper layers, where the printing is taking place and which have still not been coarsened. This translates into trying to minimize the difference between the fine and the coarse solutions on the degrees of freedom which have not

Table 1
Simulation parameters.

Parameter	Cantilever Beam	Slender Column	Gear Component
Young's Modulus (E)	100 GPa	100 GPa	100 GPa
Poisson's ratio (ν)	0.3	0.3	0.3
Density (ρ)	4420 kg/m^3	4420 kg/m^3	4420 kg/m^3
Layer thickness (t)	(−)	0.10 mm	1 mm
Refinement height (h_{ref})	3 m	0.5 mm	1 mm
$\epsilon_{inh}^x = \epsilon_{inh}^y$	(−)	-0.67	-0.67
ϵ_{inh}^z	(−)	0.0	0.0

been coarsened, and hence the proposed definition of the relative *L2 error* norm.

The numerical simulations are carried out using the FEMUSS (*Finite Element Method Using Subgrid Scales*) software developed by the authors at the International Center for Numerical Methods in Engineering (CIMNE). The post-processing is done using Paraview [1].

4.1. Cantilever beam

This example demonstrates the necessity of using the proposed correction terms to retain the solution accuracy of the finest mesh used when a coarsening strategy is employed, in a very simple setting. The objective is to observe how, for a single simulation step, information is transferred from a fine to a coarse mesh thanks to the correction terms. As it will be shown, if no coarsening correction terms are used all the information on the solution obtained in the fine mesh is lost when coarsening. On the contrary, if the correction terms are used, optimal projected solutions for both displacements and stresses on the coarse mesh are obtained.

The dimensions of a slender cantilever beam are reported in Fig. 4. The beam is clamped at one end and subjected to its self-weight, only. The reference solution is obtained using a uniform mesh with an element size: $h = 6.25$ mm. The adaptive strategy starts from the same fine mesh. Once the solution is obtained, a coarsening step increases the element size up to 50 mm (see Fig. 5). Next, the simulation is repeated on the new coarse mesh. This is done both for a trilinear hexahedra mesh and for a linear tetrahedra mesh.

Figs. 6 and 7 compare the magnitudes of the vertical displacements for the fine mesh, coarse mesh *without* and coarse mesh *with* the correction terms for the hexahedra and tetrahedra cases respectively. Figs. 8 and 9 do the same comparison for the normal stresses in the main bending direction.

In both the hexa and tetrahedra cases the solution in the coarse mesh achieved *without* the correction terms is too stiff because of the very poor finite element approximation space. This are simply new simulations on the coarse meshes, and they do not take advantage of the information obtained in the first step of the simulation on the fine mesh. Also, the obtained stress fields are poor, this can be clearly observed in the tetrahedra mesh stress plot, where the stress field is constant element to element and presents large jumps between adjacent elements. On the hexahedra elements, the stresses are also discontinuous element to element, but they have a linear component in space, so the effect is not so apparent.

On the contrary, when the correction terms are used, the information on the fine mesh is transferred to the coarser mesh, and the agreement with the reference solution is optimal (for this single step simulation displacements (in the nodes) and stresses (at the integration points) are identical in the fine and the coarse meshes except for projection errors). In the stress field plot, it is worth observing that for linear tetrahedra, stresses are no longer constant element to element thanks to the correction terms.

The global errors are presented in Table 2 where the corresponding *relative* L^2 *error* norms are computed according to equation 24. As expected, the error is null for the coarse mesh if the coarsening correction terms are employed.

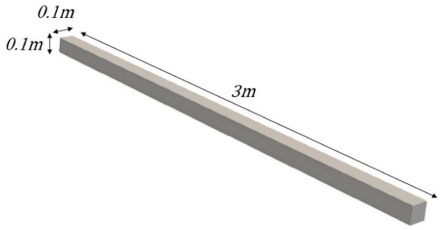

Fig. 4. Cantilever beam: Geometry and dimensions.

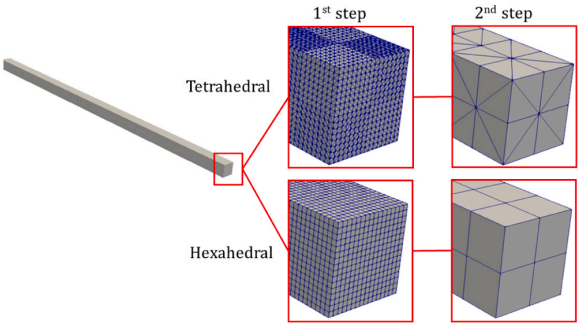

Fig. 5. Cantilever beam: fine (reference) and coarse meshes.

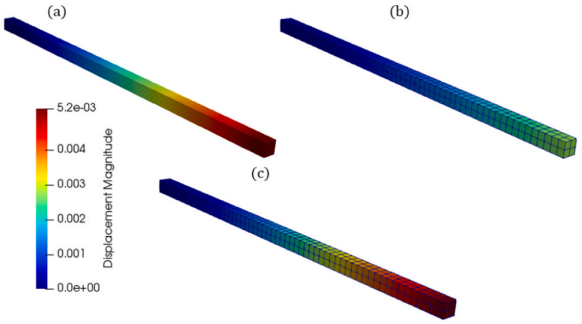

Fig. 6. Cantilever beam: Displacement results for the hexahedral mesh. (a) Fine mesh. (b) Adaptive mesh *without* correction terms. (c) Adaptive mesh *with* correction terms.

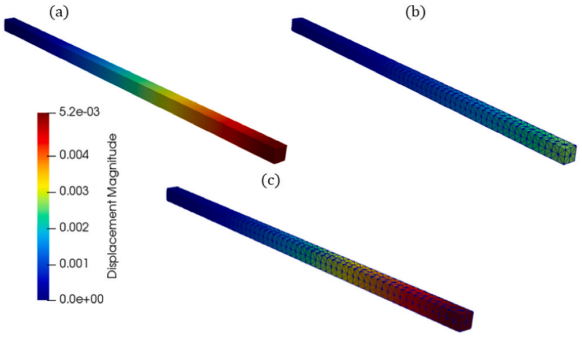

Fig. 7. Cantilever beam: Displacement results for the tetrahedral mesh. (a) Fine mesh. (b) Adaptive mesh *without* correction terms. (c) Adaptive mesh *with* correction terms.

The key point of the methodology is that if a new load increment was now solved on the coarse mesh, the resulting displacement and stress increments would be computed on such current coarse mesh. However, the displacement and stress increments associated to the original load, which were computed on the fine mesh, would not loose the fine mesh accuracy. This is especially important in AM simulations where elements will be concentrated dynamically in the region of the melting-pool (TMAZ).

4.2. Slender column

This example proves the efficiency of the coarsening strategy to

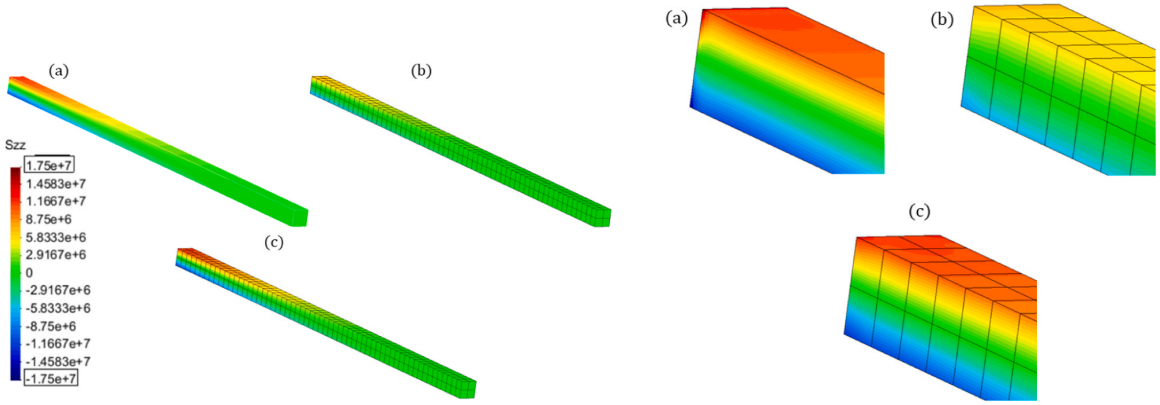

Fig. 8. Cantilever beam: Stress results for the hexahedra mesh. (a) Fine mesh. (b) Adaptive mesh *without* correction terms. (c) Adaptive mesh *with* correction terms.

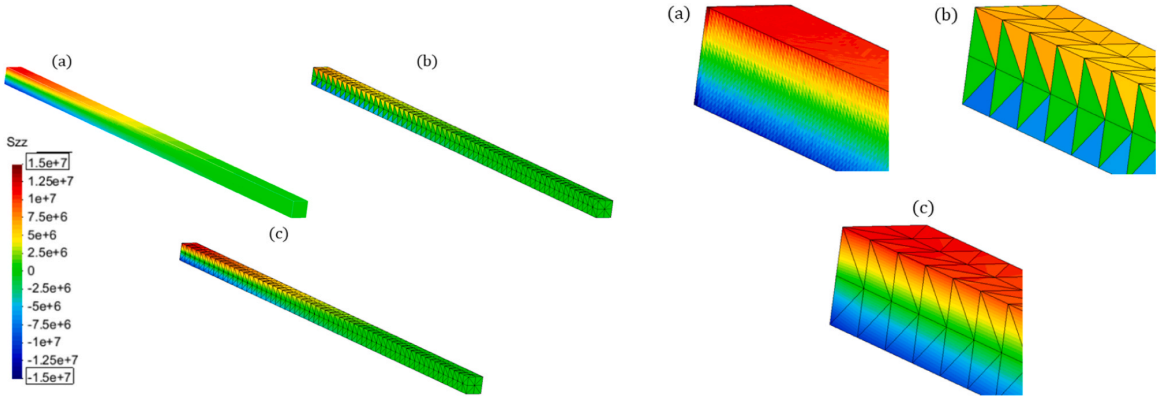

Fig. 9. Cantilever beam: Stress results for the tetrahedra mesh. (a) Fine mesh. (b) Adaptive mesh *without* correction terms. (c) Adaptive mesh *with* correction terms.

Table 2
Cantilever beam: relative global error e_{L^2} norm.

Model	Hexahedra	Tetrahedra
Adaptive mesh *without* correction term	46.9%	50.0%
Adaptive mesh *with* correction term	0%	0%

analyse growing domains as required for the numerical simulation of the AM process. This is particularly necessary when using the layer-by layer activation technique and slender parts.

The selected geometry consists of a 10 mm high column of 1×1 mm^2 square base. A total number of 100 layers are activated in 100 time-steps. Two different solutions are compared in Fig. 10: (a) a uniform mesh characterized by an element size: $h = 0.03125$ mm and, (b) an adaptive mesh having the same element size within the process region and a maximum coarsening up to $h = 0.5$ mm. The finer discretization follows the activation process to maintain the highest resolution in the TMAZ while a coarser mesh is adopted elsewhere.

Fig. 11 shows the evolution of the displacements *with* and *without* the proposed correction term at point P situated at coordinates (0, 0, 1) mm (see Fig. 10). The adaptive solutions are compared to the solution obtained with the fine fixed mesh used as a reference. It is observed that *without* the correction term the cumulative error is between 20% (x and y components) and 40% (z component), while the difference is between 2% (x and y components) and 8% (z component) when using the correction strategy.

Fig. 12 shows the plot of the displacement and stress fields at the end

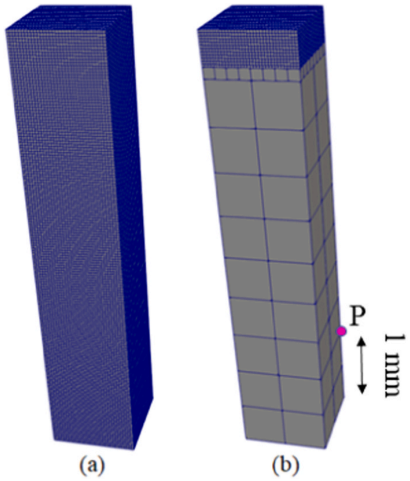

Fig. 10. Slender column: (a) Fixed mesh with hexahedral elements. (b) Adaptive meshing at the end of the simulation and position of point P.

of the simulation for the fixed and adaptive meshes. Regarding displacements, it can be observed that the adaptive solution *with* correction terms ensures that the nodal values are much closer to the solution of the fine mesh during the whole simulation. The improvement is even more

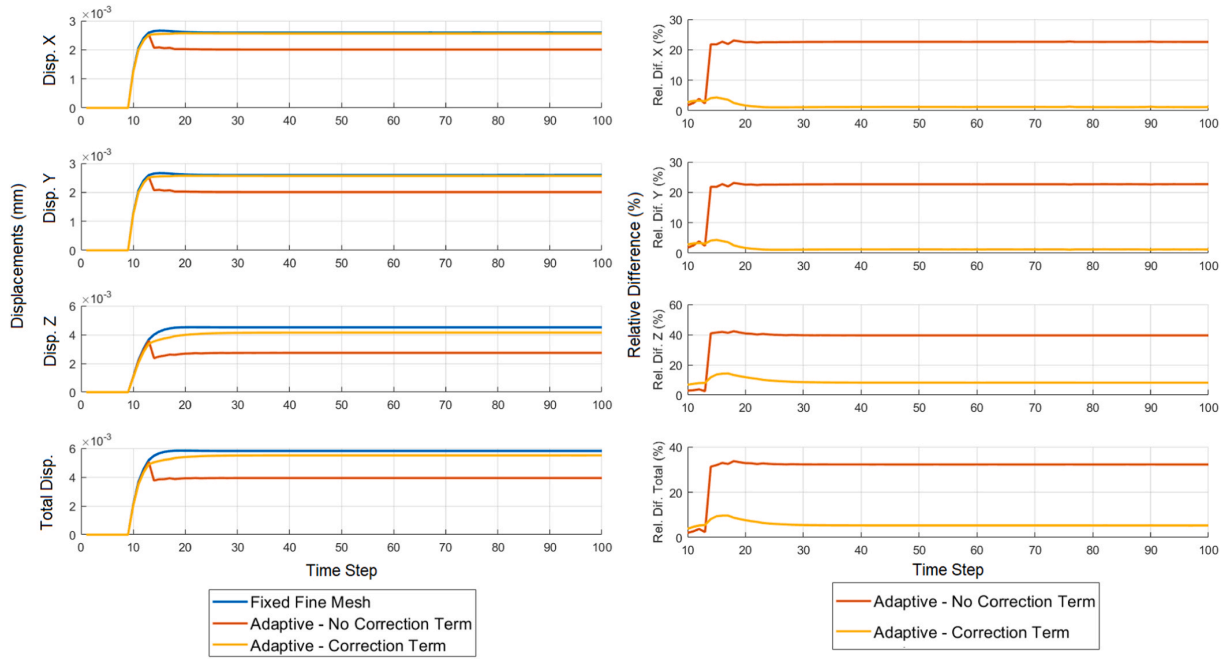

Fig. 11. Slender column: Evolution of the displacements (*left*) and the relative difference vs. the fixed fine mesh (*right*) at point P during the activation process.

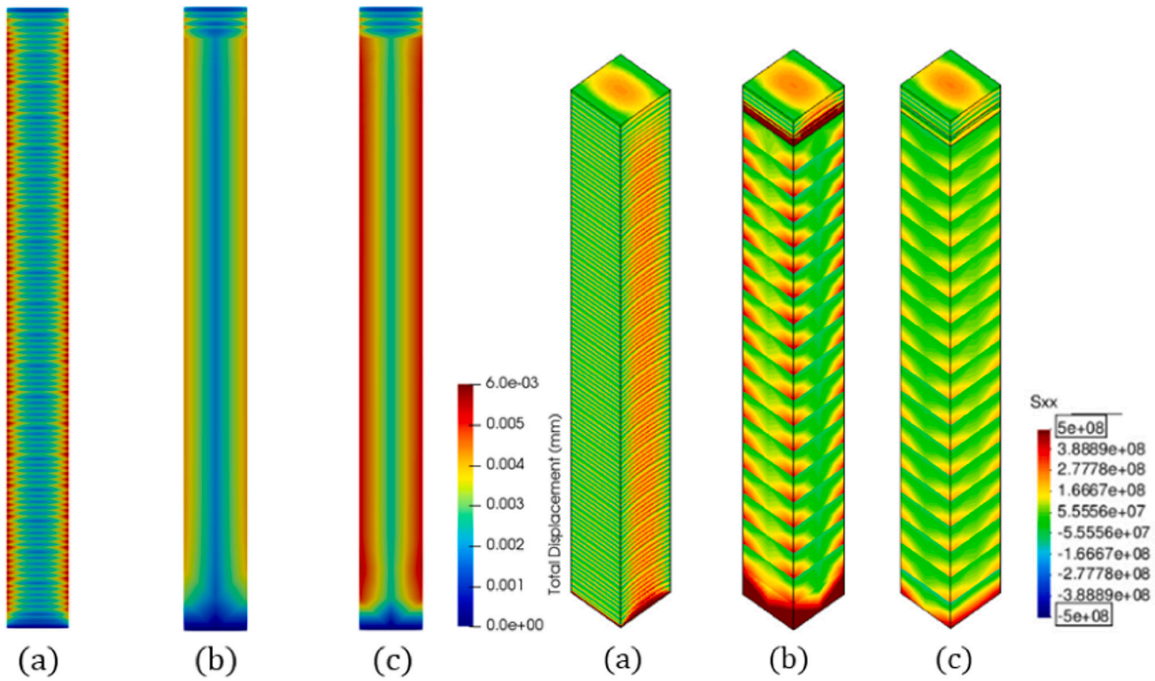

Fig. 12. Slender column: Displacement (left) and stress (right) fields at the end of the simulation. (a) Fine mesh. (b) Adaptive mesh *without* correction terms. (c) Adaptive mesh *with* correction terms.

relevant in the stresses case. A remarkable generalized lack of global accuracy in the stress computation is observed in the adaptive case *without* correction term, with a spurious stress jump in the interface between the fine and coarse mesh areas in the top of the column. This spurious stress jump is caused by the switching of free nodes to hanging nodes in the coarsening process as explained in Section 3.3. The adaptive simulation *with* correction terms, on the contrary, shows a very good agreement with the fine mesh simulation (except for the expected and unavoidable loss of resolution due to extreme coarsening). Fig. 13 compares the CPU-time and the number of active nodes (mesh size)

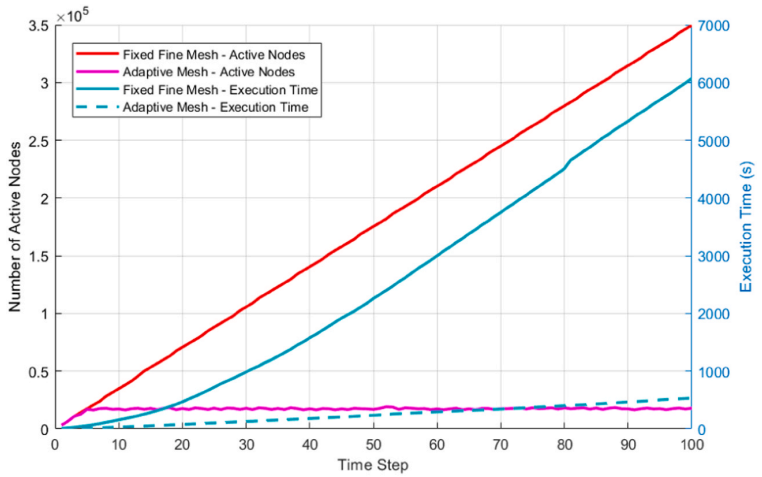

Fig. 13. Slender column: Number of active nodes (*left y-axis*) and execution time (*right y-axis*) comparison between fixed and adaptive meshes.

using the fixed and the adaptive meshes. During the activation of the first 5 layers, the two strategies adopt the same mesh and consequently approximately the same solution time is required. Next, the adaptive strategy is switched on. Thereafter, the mesh size (number of active nodes) of the adaptive mesh is kept almost constant allowing for a reduced CPU-time increment for each new time-step. Contrarily, the fixed mesh requires an increasing amount of resources as the growing process proceeds. Therefore, the use of a fixed mesh is not recommended for the numerical simulation of industrial AM processes and, particularly, when the high-fidelity simulation of the actual layer thickness and the detailed scanning sequence is required.

4.3. Gear component

The last example corresponds to an industrial component: a gear 17 mm high with an outer diameter of 40 mm. The gear is attached to the base-plate, thus the movements of all the nodes belonging to its lower surface are prescribed. The computational domain is discretized by an unstructured tetrahedral mesh. On the one hand, a fixed coarse mesh is generated with an average element size of 0.70 mm and a total number of 880, 384 elements and 169, 316 nodes. On the other hand, a fine mesh (used as the numerical reference) is characterized by an average mesh size of 0.35 mm and a total number of elements 7, 470, 787 and 1, 259, 626 nodes. Finally, the adaptive mesh adopts the same mesh size as the fine mesh within the process zone (defined as the volume enclosed up to a vertical distance h_{ref}) and it is coarsened up to the size of the fixed coarse mesh elsewhere (see Fig. 15). In this case, the average mesh includes about 493, 058 nodes and 2, 743, 781 elements.

The *P* point on the external surface, at 4.3 mm from the base plate, is chosen to record the evolution of the radial displacement on the different meshes used (see Fig. 14). The layer thickness is 1 mm so that 17 time-steps are required to complete the AM process. Note that the layer thickness chosen is the minimal to allow for the use of the fixed fine mesh (adopted as the numerical reference) in a reasonable CPU-time. Fig. 16 shows the total displacement magnitude at the end of the simulation for the four adopted meshes. Fig. 17 shows the difference

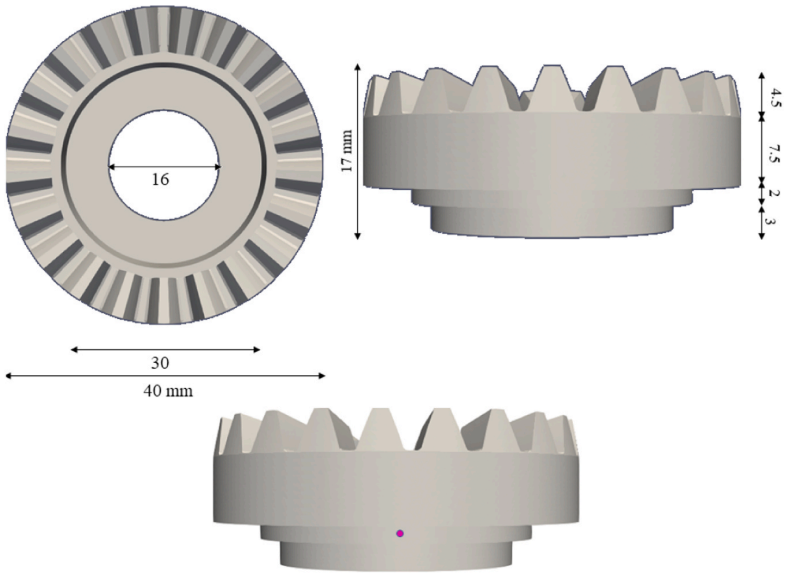

Fig. 14. Gear component: Geometry and position of the reference point *P*.

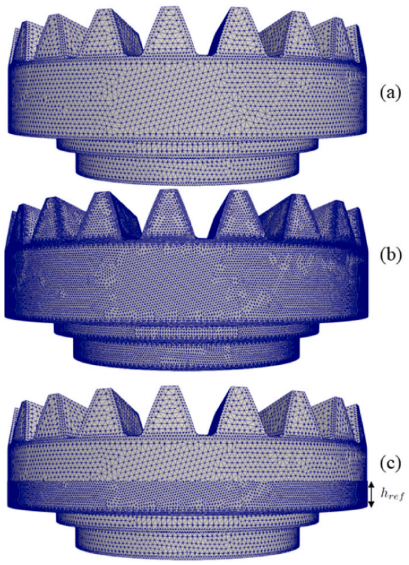

Fig. 15. Gear component: (a) Fixed coarse mesh. (b) Fixed fine mesh. (c) Adaptive mesh.

between such displacement and the displacement on the reference fine mesh. As expected accuracy is better for the adaptive simulation *with* correction terms. Fig. 18(*a*) shows the evolution of the radial displacements at point P using both the fixed fine and coarse meshes and the adaptive solution *with* and *without* the correction term. Fig. 18(*b*) presents the corresponding relative error with respect to the fixed fine mesh. Once again, the agreement of the adaptive solution with the proposed correction with the fine mesh is remarkable. The relative local error is lower than 2.50% while a standard adaptivity without the correction shows a local error of about 14%.

The global error analysis is presented in Fig. 17: the errors are computed as the difference between the reference solution (fixed fine mesh) and the results obtained with the coarse mesh and the adaptive technology, and projected on the coarse mesh for their visualization. Table 3 provides the global relative L^2 error computed according to equation 24: the corrected methodology increases the global accuracy of about 40% with respect to the crude adaptivity and of about 70% with respect to the solution obtained with the fixed coarse mesh.

Fig. 19 shows the Von-Mises stress field at a cut along the central plane of the gear component. The results from the fixed coarse and fine meshes are quite similar. However, the adaptive mesh *without* the correction terms approximates the Von-Mises stress field very poorly. The reason for this is that linear tetrahedral elements are used in this simulation. Due to this, the activation strain field, computed from the gradient of an initial displacement field as defined in Section 2, presents heavy jumps from element to element in the adaptive mesh prior to coarsening. This is illustrated in Fig. 20. When coarsened, the projected activation strain field on the coarse mesh is assigned an averaged value

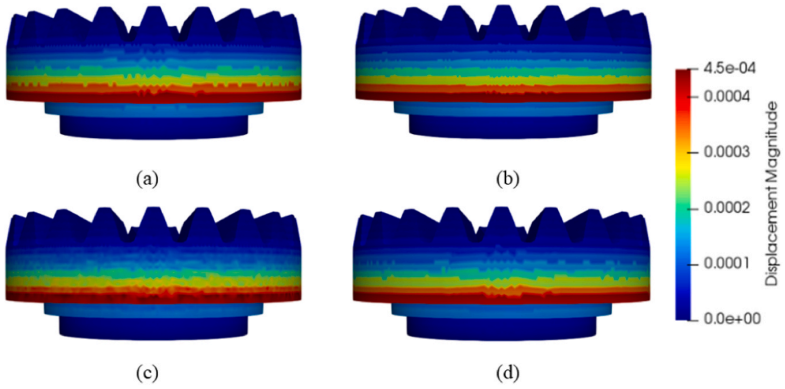

Fig. 16. Gear: Final displacement. (a) Fixed coarse mesh. (b) Fixed Fine mesh. (c) Adaptive mesh *without* correction terms. (d) Adaptive mesh *with* correction terms.

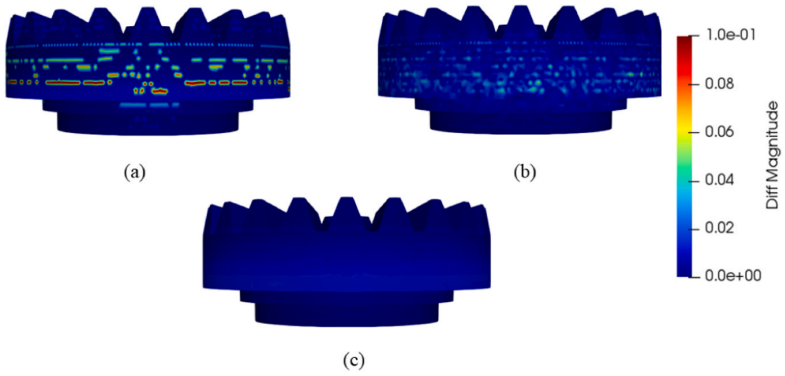

Fig. 17. Gear: Displacement relative difference w.r.t reference mesh projected onto the coarse mesh. (a) Fixed coarse mesh. (b) Adaptive mesh *without* correction terms. (c) Adaptive mesh *with* correction terms.

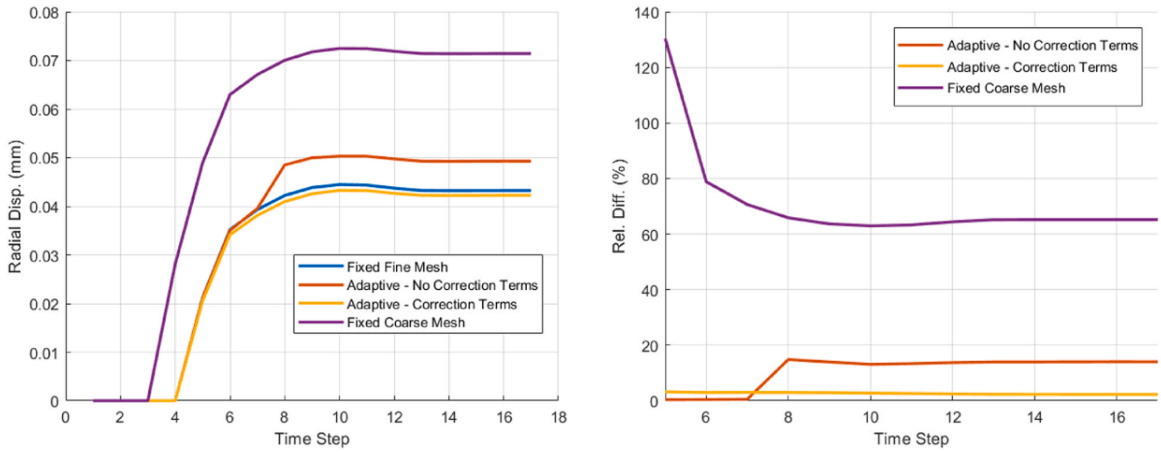

Fig. 18. Gear: evolution of the radial displacement at point P (*left*) and the relative difference with respect to the fixed fine mesh (*right*).

Table 3
Gear: relative global error e_{L^2} norm.

Model	Relative e_{L^2} norm
Fixed coarse mesh	11.9%
Adaptive mesh *without* correction term	5.9%
Adaptive mesh *with* correction term	3.6%

(Fig. 20 (b), (c)). This averaged value is used together with the displacement field in order to compute stresses, and this results in a very poor approximation, as shown in Fig. 19 (c). By using the stress correction terms this phenomenon is corrected, resulting in the stress field presented in Fig. 19 (d), which is pretty much the projection of the fine mesh stress field in Fig. 19 (b) onto the coarsened adaptive mesh.

Fig. 21 shows graphically the computational efficiency of the proposed adaptive technology in terms of CPU-time and maximum memory consumed during the simulation. In terms of solution time a speed-up of 2.25 with respect to the fixed fine solution is obtained. This speed-up can be increased by reducing the size of the moving fine mesh which is following the TMAZ. In the actual process the heat penetration is of about 2–3 layer thickness. Therefore, the mesh refinement can be reduced to this size, only. Finally, observe that the computational cost due to the evaluation of the correction term is negligible allowing for its use for any mesh discretization.

5. Conclusions

In this work an adaptive FE strategy to deal with the numerical simulation of AM processes has been presented. An octree-based mesh adaptivity approach has been adopted allowing for the use of much finer meshes within the processing zone, the TMAZ, if compared to the rest of the computational domain. Although the adaptive meshing is vital to keep the computational resources bounded through the entire simulation of the fabrication process, the accuracy of the results can be compromised by the coarsening strategy. This loss of accuracy can spoil the original efforts in refining the mesh in the process zone. Therefore a strategy to compensate for information loss in the adaptive refinement

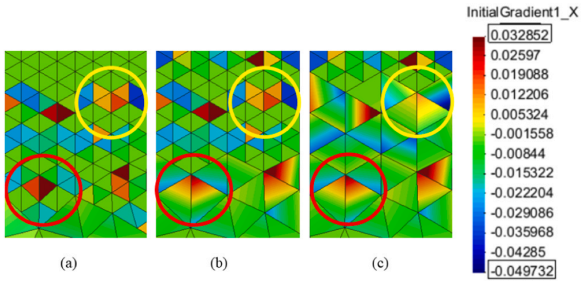

Fig. 20. Evolution of $\epsilon_{\text{inh}} + \epsilon_{\text{act}}$ fields, ϵ^x component, on a tetrahedral mesh through the coarsening process.

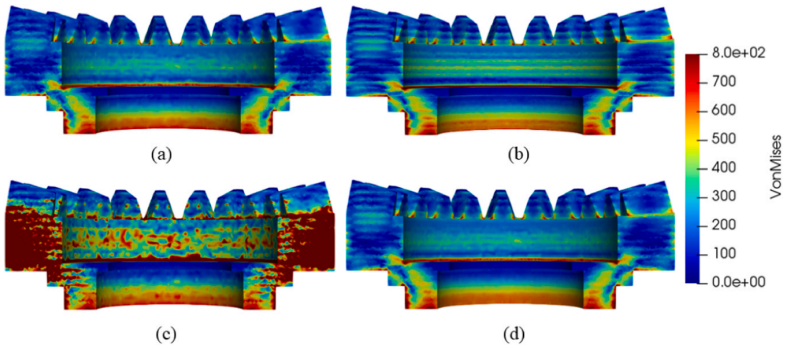

Fig. 19. Gear: Von-Misses stress at a cut along the central plane. (a) Fixed coarse mesh. (b) Fixed Fine mesh. (c) Adaptive mesh *without* correction terms. (c) Adaptive mesh *with* correction terms.

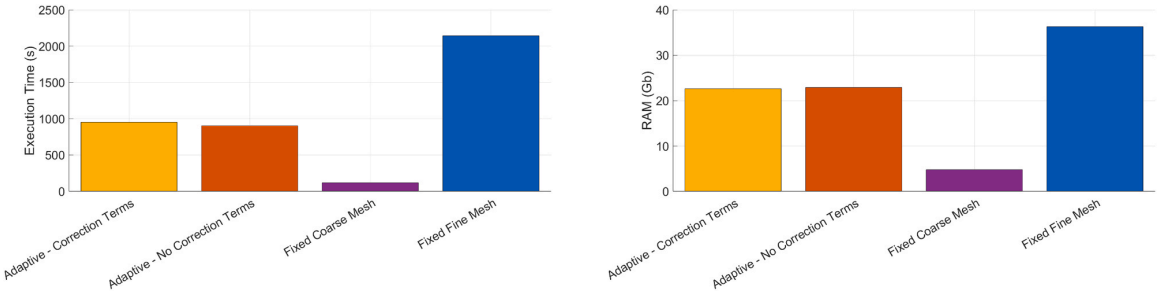

Fig. 21. Gear: Comparison of CPU-time (*left*) and maximum memory consumption (*right*) between adopted models.

simulation of additive manufacturing processes is developed.

The main idea is to add two correction terms which compensate for the loss of accuracy in the coarsening process of the mesh in already manufactured regions. The first term corrects the errors introduced in the stress field by the coarsening process. The second correction term consists of a forcing term introduced in the weak form of the problem which prevents loss of information in the displacement field. This allows to successfully simulate the additive manufacturing process by using an adaptively coarsened mesh, with results which have an accuracy very similar to the one of a uniformly refined mesh simulation, at a fraction of the computational cost. Also, the proposed correction terms can be interpreted as a Variational Multiscale enhancement on the adaptive mesh, which gives a variational foundation to the proposed correction strategy.

The numerical examples show the generality of the proposed methodology, which has been applied to different FE meshes, AM processes, several geometries, and its success in reducing the overall computational cost. The coarsening correction terms have turned out to be key in order to obtain a good accuracy in the simulation.

The ideas presented in this work can be extended to more complex problems such as coupled thermo-mechanical simulations including non-linear behavior like plastic or damage constitutive models. This will be a matter of future work.

Declaration of Competing Interest

The authors declare that they have no known financial interests or personal relationships that could have appeared to influence the work reported in this paper.

Acknowledgments

J. Baiges gratefully acknowledges the support of the Spanish Government through the Ramón y Cajal grant RYC-2015-17367. R. Codina gratefully acknowledges the support received through the ICREA Acadèmia Research Program of the Catalan Government. The financial support from the Spanish Ministry of Economy and Competitiveness, through the Severo Ochoa Programme for Centres of Excellence in R&D (CEX2018-000797-S), is gratefully acknowledged. The authors also acknowledge the financial support provided by the Spanish Ministry of Economy via the ADaMANT project (DPI2017-85998-P): Computational Framework for Additive Manufacturing of Titanium Alloy.

References

[1] J. Ahrens, B. Geveci, C. Law, ParaView: An End-User Tool for Large Data Visualization. Visualization Handbook, Elsevier, 2005.
[2] F. Armero, J.C. Simo, A new unconditionally stable fractional step method for non-linear coupled thermomechanical problems, Int. J. Numer. Methods Eng. 35 (4) (1992) 737–766.
[3] J. Baiges, C. Bayona, Refficientlib: an efficient load-rebalanced adaptive mesh refinement algorithm for high-performance computational physics meshes, SIAM J. Sci. Comput. 39 (2) (2017) 65–95.
[4] J. Baiges, R. Codina, Variational multiscale error estimators for solid mechanics adaptive simulations: an orthogonal subgrid scale approach, Comput. Methods Appl. Mech. Eng. 325 (2017) 37–55.
[5] J. Baiges, R. Codina, I. Castañar, E. Castillo, A finite element reduced-order model based on adaptive mesh refinement and artificial neural networks, Int. J. Numer. Methods Eng. 121 (4) (2020) 588–601.
[6] J. Baiges, R. Codina, S. Idelsohn, Reduced-order subscales for POD models, Comput. Methods Appl. Mech. Eng. 291 (2015) 173–196.
[7] J. Baiges, J. Martínez-Frutos, D. Herrero-Pérez, F. Otero, A. Ferrer, Large-scale stochastic topology optimization using adaptive mesh refinement and coarsening through a two-level parallelization scheme, Comput. Methods Appl. Mech. Eng. 343 (2019) 186–206.
[8] J.L. Bartlett, X. Li, An overview of residual stresses in metal powder bed fusion, Addit. Manuf. 27 (2019) 131–149.
[9] M. Bugatti, Q. Semeraro, Limitations of the inherent strain method in simulating powder bed fusion processes, Addit. Manuf. 23 (2018) 329–346.
[10] M. Cervera, C. Agelet De Saracibar, M. Chiumenti, Thermo-mechanical analysis of industrial solidification processes, Int. J. Numer. Methods Eng. 46 (9) (1999) 1575–1591.
[11] Q. Chen, X. Liang, D. Hayduke, J. Liu, L. Cheng, J. Oskin, R. Whitmore, A. To, inherent strain based multiscale modeling framework for simulating part-scale residual deformation for direct metal laser sintering, Addit. Manuf. 28 (2019) 406–418.
[12] B. Cheng, S. Shrestha, K. Chou, Stress and deformation evaluations of scanning strategy effect in selective laser melting, Addit. Manuf. 12 (2016) 240–251.
[13] M. Chiumenti, C. Agelet de Saracibar, M. Cervera, On the numerical modeling of the thermomechanical contact for metal casting analysis, J. Heat Transf. 130 (6) (2008), 061301.
[14] M. Chiumenti, M. Cervera, N. Dialami, B. Wu, L. Jinwei, C. Agelet de Saracibar, Numerical modeling of the electron beam welding and its experimental validation, Finite Elem. Anal. Des. 121 (2016) 118–133.
[15] M. Chiumenti, M. Cervera, A. Salmi, C.D. Saracibar, N. Dialami, K. Matsui, Finite element modeling of multi-pass welding and shaped metal deposition processes, Comput. Methods Appl. Mech. Eng. 199 (37–40) (2010) 2343–2359.
[16] M. Chiumenti, X. Lin, M. Cervera, W. Lei, Y. Zheng, W. Huang, Numerical simulation and experimental calibration of additive manufacturing by blown powder technology. Part I: thermal analysis, Rapid Prototyp. J. 23 (2) (2017) 448–463.
[17] M. Chiumenti, E. Neiva, E. Salsi, M. Cervera, S. Badia, J. Moya, Z. Chen, C. Lee, C. Davies, Numerical modelling and experimental validation in selective laser melting, Addit. Manuf. 18 (2017) 171–185.
[18] E.R. Denlinger, M. Gouge, J. Irwin, P. Michaleris, Thermomechanical model development and in situ experimental validation of the laser powder-bed fusion process, Addit. Manuf. 16 (2017) 73–80.
[19] E.R. Denlinger, J.C. Heigel, P. Michaleris, Residual stress and distortion modeling of electron beam direct manufacturing Ti-6Al-4V, Proc. Inst. Mech. Eng. Part B J. Eng. Manuf. 229 (10) (2015) 1803–1813.
[20] E.R. Denlinger, J. Irwin, P. Michaleris, Thermomechanical modeling of additive manufacturing large parts, J. Manuf. Sci. Eng. 136 (6) (2014).
[21] M. Gouge, E. Denlinger, J. Irwin, C. Li, P. Michaleris, Experimental validation of thermo-mechanical part-scale modeling for laser powder bed fusion processes, Addit. Manuf. 29 (2019), 100771.
[22] M. Hill, D. Nelson, The inherent strain method for residual stress determination and its application to a long welded joint, ASME-Publ.-PVP 318 (1995) 343–352.
[23] T. Hughes, G. Feijóo, L. Mazzei, J. Quincy, The variational multiscale method-a paradigm for computational mechanics, Comput. Methods Appl. Mech. Eng. 166 (1–2) (1998) 3–24.
[24] T.-S. Jun, A.M. Korsunsky, Evaluation of residual stresses and strains using the eigenstrain reconstruction method, Int. J. Solids Struct. 47 (13) (2010) 1678–1686.
[25] K. Khan, A. De, Modelling of selective laser melting process with adaptive remeshing, Sci. Technol. Weld. Join. 24 (5) (2019) 391–400.
[26] S. Kollmannsberger, A. Özcan, M. Carraturo, N. Zander, E. Rank, A hierarchical computational model for moving thermal loads and phase changes with applications to selective laser melting, Comput. Math. Appl. 75 (5) (2018) 1483–1497.

[27] C. Li, E.R. Denlinger, M.F. Gouge, J.E. Irwin, P. Michaleris, Numerical verification of an octree mesh coarsening strategy for simulating additive manufacturing processes, Addit. Manuf. 30 (2019), 100903.
[28] X. Liang, Q. Chen, L. Cheng, D. Hayduke, A.C. To, Modified inherent strain method for efficient prediction of residual deformation in direct metal laser sintered components, Comput. Mech. 64 (6) (2019) 1719–1733.
[29] X. Liang, L. Cheng, Q. Chen, Q. Yang, A.C. To, A modified method for estimating inherent strains from detailed process simulation for fast residual distortion prediction of single-walled structures fabricated by directed energy deposition, Addit. Manuf. 23 (2018) 471–486.
[30] X. Liang, W. Dong, S. Hinnebusch, Q. Chen, H.T. Tran, J. Lemon, L. Cheng, Z. Zhou, D. Hayduke, A.C. To, Inherent strain homogenization for fast residual deformation simulation of thin-walled lattice support structures built by laser powder bed fusion additive manufacturing, Addit. Manuf. 32 (2020), 101091.
[31] L.-E. Lindgren, A. Lundback, M. Fisk, R. Pederson, J. Andersson, Simulation of additive manufacturing using coupled constitutive and microstructure models, Addit. Manuf. 12 (2016) 144–158 (Special Issue on Modeling and Simulation for Additive Manufacturing).
[32] X. Lu, X. Lin, M. Chiumenti, M. Cervera, Y. Hu, X. Ji, L. Ma, W. Huang, In situ measurements and thermo-mechanical simulation of ti-6al-4v laser solid forming processes, Int. J. Mech. Sci. 153–154 (2019) 119–130.
[33] X. Lu, X. Lin, M. Chiumenti, M. Cervera, Y. Hu, X. Ji, L. Ma, H. Yang, W. Huang, Residual stress and distortion of rectangular and s-shaped ti-6al-4v parts by directed energy deposition: modelling and experimental calibration, Addit. Manuf. 26 (2019) 166–179.
[34] X. Lu, X. Lin, M. Chiumenti, M. Cervera, J. Li, L. Ma, L. Wei, Y. Hu, W. Huang, Finite element analysis and experimental validation of the thermomechanical behavior in laser solid forming of ti-6al-4v, Addit. Manuf. 21 (2018) 30–40.
[35] H. Murakawa, Y. Luo, Y. Ueda, Inherent Strain as an Interface Between Computational Welding Mechanics and its Industrial Application, 1998, pp. 597–619. Book Inst. Mater.
[36] E. Neiva, S. Badia, A.F. Martín, M. Chiumenti, A scalable parallel finite element framework for growing geometries. Application to metal additive manufacturing, Int. J. Numer. Methods Eng. 119 (11) (2019) 1098–1125.
[37] E. Neiva, M. Chiumenti, M. Cervera, E. Salsi, G. Piscopo, S. Badia, A.F. Martín, Z. Chen, C. Lee, C. Davies, Numerical modelling of heat transfer and experimental validation in powder-bed fusion with the virtual domain approximation, Finite Elem. Anal. Des. 168 (2020), 103343.
[38] A. Olleak, Z. Xi, Efficient lpbf process simulation using finite element modeling with adaptive remeshing for distortions and residual stresses prediction, Manuf. Lett. 24 (2020) 140–144.
[39] D. Pal, N. Patil, K.H. Kutty, K. Zeng, A. Moreland, A. Hicks, D. Beeler, B. Stucker, A generalized feed-forward dynamic adaptive mesh refinement and derefinement finite-element framework for metal laser sintering-part II: nonlinear thermal simulations and validations2, J. Manuf. Sci. Eng. 138 (6) (2016), 061003.
[40] L. Parry, I. Ashcroft, R. Wildman, Understanding the effect of laser scan strategy on residual stress in selective laser melting through thermo-mechanical simulation, Addit. Manuf. 12 (2016) 1–15.
[41] N. Patil, D. Pal, H. KhalidRafi, K. Zeng, A. Moreland, A. Hicks, D. Beeler, B. Stucker, A generalized feed forward dynamic adaptive mesh refinement and derefinement finite element framework for metal laser sintering-part I: formulation and algorithm development, J. Manuf. Sci. Eng. 137 (4) (2015), 041001.
[42] D. Riedlbauer, P. Steinmann, J. Mergheim, Thermomechanical finite element simulations of selective electron beam melting processes: performance considerations, Comput. Mech. 54 (2014) 109–122.
[43] I. Setien, M. Chiumenti, S. van der Veen, M.S. Sebastian, F. Garciandía, A. Echeverría, Empirical methodology to determine inherent strains in additive manufacturing, Comput. Math. Appl. 78 (2019) 2282–2295.
[44] T. Terasaki, T. Akiyama, Mechanical behaviour of joints in FSW: residual stress, inherent strain and heat input generated by friction stir welding, Weld. World 47 (2003) 24–31.
[45] Y. Ueda, Y. Kim, A. Umekuni, Measuring theory of three-dimensional residual stresses using a thinly sliced plate perpendicular to welded line, Trans. JWRI 14 (2) (1985) 151–157.
[46] Y. Ueda, H. Murakawa, N. Ma, Welding Deformation and Residual Stress Prevention, Elsevier, 2012.
[47] Y. Ueda, H. Murakawa, K. Nakacho, N. Ma, Establishment of computational welding mechanics, Weld. Surf. Rev. 8 (1) (1997) 265–299.
[48] Y. Ueda, K. Fukuda, Y. Kim, New measuring method of axisymmetric three-dimensional residual stresses using inherent strains as parameters, J. Eng. Mater. Technol. 108 (4) (1986) 328–334.
[49] Y. Ueda, K. Fukuda, K. Nakacho, S. Endo, A new measuring method of residual stresses with the aid of finite element method and reliability of estimated values, Trans. Jpn. Weld. Res. Inst. 4 (2) (1975) 151–157.
[50] K. Zeng, D. Pal, H.J. Gong, N. Patil, B. Stucker, Comparison of 3dsim thermal modelling of selective laser melting using new dynamic meshing method to ansys, Mater. Sci. Technol. 31 (8) (2015) 945–956.

A.2 Paper 2

Title: Stress, strain and dissipation accurate 3-field formulation for inelastic isochoric deformation.

Authors:

- **M. Chiumenti**: Full Professor of Continuum Mechanics and Structural analysis at the Universitat Politècnica de Catalunya (Technical University of Catalonia BarcelonaTech). Affiliated Scientist at the International Center for Numerical Methods in Engineering (CIMNE).
- **M. Cervera**: Full Professor of Continuum Mechanics and Structural analysis at the Universitat Politècnica de Catalunya (Technical University of Catalonia BarcelonaTech). Affiliated Scientist at the International Center for Numerical Methods in Engineering (CIMNE).
- **C. A. Moreira**: PhD Candidate in Civil Engineering in UPC BarcelonaTech and International Center for Numerical Methods in Engineering (CIMNE).
- **G. B. Barbat**: Associate Lecturer of Continuum Mechanics and Structural analysis at the Universitat Politècnica de Catalunya (Technical University of Catalonia BarcelonaTech). Post-doctoral Researcher at the International Center for Numerical Methods in Engineering (CIMNE).

Finite Elements in Analysis and Design
Editor-in-Chief: John E. Dolbow
ISSN: 0168-874X
Elsevier Editors
https://doi.org/10.1016/j.finel.2021.103534
Link to Publisher

Finite Elements in Analysis and Design 192 (2021) 103534

Contents lists available at ScienceDirect

Finite Elements in Analysis and Design

journal homepage: www.elsevier.com/locate/finel

Stress, strain and dissipation accurate 3-field formulation for inelastic isochoric deformation

M. Chiumenti *, M. Cervera, C.A. Moreira, G.B. Barbat

International Center for Numerical Methods in Engineering (CIMNE), Universidad Politécnica de Cataluña (UPC), Edificio C1, Campus Norte, Gran Capitán s/n, 08034, Barcelona, Spain

ARTICLE INFO

Keywords:
Stress accurate
Incompressible limit
Mixed three-field finite element technology
Variational multi scale (VMS) stabilization

ABSTRACT

This work exploits the high accuracy of the mixed 3−field $\mathbf{u}/\mathbf{e}/p$ formulation to address materially non-linear inelastic problems including isochoric deformations.

Motivated by the strain-driven format of several constitutive equations used in FEA, the mixed $\mathbf{u}/\mathbf{s}/p$ formulation is reinterpreted, selecting the deviatoric strains as primary variables, together with the displacements and the pressure field.

The mixed formulation is complemented with several constitutive equations suitable for Solid and Fluid Mechanics.

The convergence rate upon mesh refinement, as well as the enhanced accuracy of the stress and strain fields is proven in several non-linear problems with isochoric deformation in both the elastic and the inelastic ranges. 2*D* and 3*D* problems involving different FE discretizations are solved with *J*2−plasticity, *J*2−damage and Bingham models, all of them including strain localization. Numerical results show that perfectly convergent and mesh-independent results are achieved in terms of peak load, failure mechanism, stress release and energy dissipation. Revealing comparison with the $\mathbf{u}/p$ formulation is also addressed.

1. Introduction

The aim of this work is to exploit the advantages of the mixed displacement/deviatoric-strain/pressure ($\mathbf{u}/\mathbf{e}/p$)3−field formulation for the solution of material non-linear problems in Computational Solids and Fluid Mechanics. The authors have introduced this FE technology in a previous work where enhanced accuracy was proven for both compressible and incompressible elasticity problems [1]. The scope of this work is to solve materially non-linear Stokes problems where a variety of constitutive laws can be adopted for solid and fluid analyses. Within the former setting, elasticity, plasticity or damage constitutive laws are tackled within the infinitesimal strain theory, while the latter is suitable to analyze different rigid-viscoplastic flows such as Bingham, Norton-Hoff, Sheppard-Wright and Carreau, among others.

This flexibility is very appealing to address the numerical simulation of different industrial manufacturing processes including metal forming, forging, extrusion, Friction Stir Welding (FSW), or machining operations, and many others. All these processes are non-linear, present stress concentrations and most of them show strain localization through the formation of shear bands. Moreover, the deviatoric nature of the plastic strains arising from the plasticity models used in metal forming, as well as the intrinsic isochoric nature of the constitutive laws used to characterize the rigid-plastic material flow, require a FE technology able to deal with the incompressibility constraint. Hence, stress accuracy and performance in the incompressible limit are both mandatory requirements that motivate this work.

Popular solutions to tackle the quasi-incompressible limit are: the reduced and selective integration methods [2,3,4,5], the B-bar and F-bar elements [6,7,8,9] and the enhanced assumed strain methods [10,11,12]. Although they cannot be used in the incompressible limit, these approaches have proven to be reliable in quasi-isochoric problems for hexahedral elements but they do not have a straightforward generalization to tetrahedral grids, being the preferred choice for the automatic mesh generation.

Alternatively, the use of mixed displacement/pressure ($\mathbf{u}/p$) or velocity/pressure ($\mathbf{v}/p$) formulations have been proposed to avoid the volumetric locking when approaching the incompressible limit. The use of different stabilization techniques and particularly the Varia-

* Corresponding author.
E-mail address: michele.chiumenti@upc.edu (M. Chiumenti).
URL: http://www.cimne.com (M. Chiumenti).

https://doi.org/10.1016/j.finel.2021.103534
Received 24 May 2020; Received in revised form 30 November 2020; Accepted 1 December 2020
Available online 6 March 2021

tional Multi-Scale (VMS) method allows for the adoption of equal-order piecewise linear interpolations for both displacement (velocity) and pressure, circumventing the *inf-sup* conditions [13,14] for the Stokes and Navier-Stokes problems [15,16,17]. The approach was extended to incompressible elasticity [18,19], elastoplasticity [20,21], elastodynamic problems [22,23,24,25,26] and hyperelastic finite deformation [27,28,29,30]. The Orthogonal Subgrid Scales (OSS) method [15] was presented by the authors to address problems in incompressible elasticity and J2-plasticity, and damage analysis including the strain localization process induced by strain-softening laws [31,32–34,35,36,37].

The stress/strain accuracy can be enhanced by adopting the mixed displacement/stress ($\mathbf{u}/\boldsymbol{\sigma}$) formulation, where both displacements and stresses are used as primary variables in the finite element discretization [38,39,40,41,42,43]. This given, a natural way to access the incompressible limit with stress accuracy consists of splitting the stress tensor into its deviatoric and spherical (volumetric) parts, being the latter the pressure field, p. Hence, when the (deviatoric)-stress tensor, $\mathbf{s}$, together with both the pressure and the displacement fields are taken as primary variables, the mixed 3−field ($\mathbf{u}/\mathbf{s}/p$) formulation arises, as shown in Ref. [1].

Nevertheless, numerous material laws and the corresponding computational algorithms are strain-driven: the strain tensor is the input to the constitutive equations while the stress tensor is the corresponding outcome. This motivates the mixed displacement/strain ($\mathbf{u}/\boldsymbol{\varepsilon}$) formulation. Thus, the same implementation of the constitutive laws used for the standard irreductible (displacements-based) element is suitable for the mixed $\mathbf{u}/\boldsymbol{\varepsilon}$ technology.

The displacement/strain formulation was successfully used to encompass non-linear problems including finite displacements in dynamic problems [44], strain-localization in plasticity [45,46,47,48] and crack propagation using damage models in mode-I [40,49,50] and mixed modes [51,52,53]. However, the strain/displacement formulation is not able to reach the incompressible limit. This is the motivation of the present work: the development of a mixed displacement/(deviatoric)-strains/pressure ($\mathbf{u}/\mathbf{e}/p$) 3−field formulation as accurate as the strain/displacement FE technology but able to treat isochoric deformations.

The outline of the paper is as follows. In Section 2 and Section 3, the framework suitable for solids and fluids is presented. The continuum problem (strong form) is shown in Sections 2.1 and 3.1, respectively. The volumetric/deviatoric split of the stresses and strains as well as the constitutive tensor is described in Section 2.2. Next, the constitutive equations suitable for both computational solid (Section 2.3) and fluid mechanics (Section 3.2) are described. The weak form of the 3−field formulation is detailed in Sections 2.4 and 3.3, respectively. Sections 2.5 and 3.4 deal with the discrete approximation of the problem by the Galerkin method. The Variational Multi-Scale (VMS) approach required when using equal order linear interpolation for all fields is described in Section 2.6. This method allows for circumventing the inf-sup stability condition [14]. Section 4 shows different numerical examples to assess the accuracy and robustness of the proposed formulation.

2. Solid mechanics

2.1. The continuum problem

Let us denote by $\Omega(\mathbf{X}) \in \mathbb{R}^{n_{\text{dim}}}$ an open and bounded *material* domain of n_{dim} dimensions where $\mathbf{X}$ are the coordinates of its *material* points. The boundary $\partial\Omega$ is split into $\partial\Omega_u$ and $\partial\Omega_t$, being $\partial\Omega = \partial\Omega_u \cup \partial\Omega_t$ and $\partial\Omega_u \cap \partial\Omega_t = 0$, such that the prescribed displacements, $\overline{\mathbf{u}}$, are specified on $\partial\Omega_u$ (Dirichlet boundary conditions) and the prescribed tractions, $\overline{\mathbf{t}}$, are applied on $\partial\Omega_t$ (Neumann boundary conditions).

The continuum mechanical problem is defined by the following 3 equations:

$$\nabla \cdot \boldsymbol{\sigma} + \mathbf{b} = \mathbf{0} \tag{1}$$

$$\boldsymbol{\sigma} - \mathbb{C} : \boldsymbol{\varepsilon} = \mathbf{0} \tag{2}$$

$$\boldsymbol{\varepsilon} - \nabla^s \mathbf{u} = \mathbf{0} \tag{3}$$

where the unknowns are the displacement $\mathbf{u}(\mathbf{X})$, the Cauchy stresses $\boldsymbol{\sigma}(\mathbf{X})$ and the strain field $\boldsymbol{\varepsilon}(\mathbf{X})$, respectively. The first one is the *balance of momentum (equilibrium) equation*, the second is the *constitutive equation* and the last one is the *kinematic equation* (in the hypothesis of infinitesimal strains), and where $\mathbf{b}$ are the external loads per unit of volume and $\mathbb{C}$ is a generic 4th order (secant) constitutive tensor.

Replacing the strains from Eq. (3) into the constitutive Eq. (2) and substituting the resulting stresses into Eq. (1), the result is *Navier*'s equation:

$$\nabla \cdot \left(\mathbb{C} : \nabla^s \mathbf{u}\right) + \mathbf{b} = \mathbf{0} \tag{4}$$

which is written in terms of the displacement field only, being the strains and the stresses:

$$\boldsymbol{\varepsilon}(\mathbf{u}) = \nabla^s \mathbf{u} \tag{5}$$

$$\boldsymbol{\sigma}(\mathbf{u}) = \mathbb{C} : \boldsymbol{\varepsilon}(\mathbf{u}) \tag{6}$$

Alternatively, the mixed $\boldsymbol{\sigma}/\boldsymbol{u}$ formulation uses both stresses and displacements as master fields:

$$\nabla \cdot \boldsymbol{\sigma} + \mathbf{b} = \mathbf{0} \tag{7}$$

$$\boldsymbol{\sigma} - \mathbb{C} : \nabla^s \mathbf{u} = \mathbf{0} \tag{8}$$

obtained by substituting Eq. (3) into Eq. (2).

Nevertheless, the constitutive equations, as used in FEM, are generally strain-driven, hence it is convenient to keep the strains as one of the independent variables, together with the displacement field, as:

$$\nabla \cdot (\mathbb{C} : \boldsymbol{\varepsilon}) + \mathbf{b} = \mathbf{0} \tag{9}$$

$$\boldsymbol{\varepsilon} - \nabla^s \mathbf{u} = \mathbf{0} \tag{10}$$

The result is the mixed $\boldsymbol{\varepsilon}/\boldsymbol{u}$ formulation, where the constitutive Eq. (2) has been plugged into the balance Eq. (1) while Eq. (10) enforces the kinematic constraint.

2.2. The volumetric/deviatoric split

Most of the constitutive equations can be split into their volumetric and deviatoric components by assuming a volumetric/deviatoric split of the free energy potential. This split implies that: (i) the volumetric deformation (volume change) is governed by the pressure field, only; (ii) the distortions are induced by the deviatoric part of the stress field. Hence, the two deformation modes are uncoupled.

Let us define the rank−4 volumetric and deviatoric projection tensors, $\mathbb{V}$ and $\mathbb{P}$, as follows:

$$\mathbb{V} = \frac{1}{3}(\mathbf{I} \otimes \mathbf{I}) \tag{11}$$

$$\mathbb{P} = \mathbb{I} - \frac{1}{3}(\mathbf{I} \otimes \mathbf{I}) \tag{12}$$

$$\mathbb{P} + \mathbb{V} = \mathbb{I} \tag{13}$$

where $\mathbb{I} = \left[\delta_{ij}\delta_{kl}\right]$ and $\mathbf{I} = \left[\delta_{ij}\right]$ are the rank−4 and the rank−2 identity tensors, respectively (δ_{ij} is Kronecker's delta).

The spherical (volumetric) and the deviatoric parts of the stress tensor, $\boldsymbol{\sigma}$, are obtained as:

$$\mathbb{V} : \boldsymbol{\sigma} = \frac{1}{3}(\mathbf{I} \otimes \mathbf{I}) : \ \boldsymbol{\sigma} = p\,\mathbf{I} \tag{14}$$

$$\mathbb{P} : \boldsymbol{\sigma} = \left[\mathbb{I} - \frac{1}{3}(\mathbf{I}\otimes\mathbf{I})\right] : \boldsymbol{\sigma} = \boldsymbol{\sigma} - p\,\mathbf{I} = \mathbf{s} \tag{15}$$

where $p(\boldsymbol{\sigma}) = \frac{1}{3}(\boldsymbol{\sigma} : \mathbf{I}) = \frac{1}{3}\mathrm{tr}(\boldsymbol{\sigma})$ is the *pressure* and $\mathbf{s}$ =dev $(\boldsymbol{\sigma})$ are the deviatoric stresses. This given, the stress tensor can be rebuilt adding both components of the split as:

$$\boldsymbol{\sigma} = p\,\mathbf{I} + \mathbf{s} \tag{16}$$

The same procedure is used to split the strain tensor $\boldsymbol{\varepsilon}$, as:

$$\mathbb{V} : \boldsymbol{\varepsilon} = \frac{1}{3}(\mathbf{I}\otimes\mathbf{I}) : \boldsymbol{\varepsilon} = \frac{1}{3}e_{vol}\,\mathbf{I} \tag{17}$$

$$\mathbb{P} : \boldsymbol{\varepsilon} = \left[\mathbb{I} - \frac{1}{3}(\mathbf{I}\otimes\mathbf{I})\right] : \boldsymbol{\varepsilon} = \boldsymbol{\varepsilon} - \frac{1}{3}e_{vol}\,\mathbf{I} = \mathbf{e} \tag{18}$$

where $e_{vol} = \boldsymbol{\varepsilon}\mathbf{:}\,\mathbf{II}$ =tr $(\boldsymbol{\varepsilon})$ and $\mathbf{e} = \mathbb{P} : \boldsymbol{\varepsilon}$ = dev $(\boldsymbol{\varepsilon})$ are the volumetric and deviatoric component of $\boldsymbol{\varepsilon}$, respectively. This tensor is rebuilt as:

$$\boldsymbol{\varepsilon} = \frac{1}{3}\,e_{vol}\,\mathbf{I} + \mathbf{e} \tag{19}$$

In solid mechanics, the constitutive relationship between stresses and strains expressed in secant form is:

$$\boldsymbol{\sigma} = \mathbb{C} : \boldsymbol{\varepsilon} \tag{20}$$

where the constitutive tensor $\mathbb{C}$ is split as:

$$\mathbb{C} = \mathbb{C}^{vol} + \mathbb{C}^{dev} \tag{21}$$

$\mathbb{C}^{vol}$ and $\mathbb{C}^{dev}$ being the *spheric* and the *deviatoric* parts of the tensor, extracted as:

$$\mathbb{C}^{vol} = \mathbb{V} : \mathbb{C} \tag{22}$$

$$\mathbb{C}^{dev} = \mathbb{P} : \mathbb{C} \tag{23}$$

Introducing the split of stresses and strains given by Eqs. (16) and (19) into Eq. (20), the constitutive relationship can be rewritten as:

$$p\,\mathbf{I} + \mathbf{s} = \mathbb{C} : \left(\frac{1}{3}e_{vol}\,\mathbf{I} + \mathbf{e}\right) \tag{24}$$

that is:

$$p = C^{vol}\,e_{vol} \tag{25}$$

$$\mathbf{s} = \mathbb{C}^{dev} : \mathbf{e} \tag{26}$$

which are the volumetric and the deviatoric components of the original constitutive equation (20), being $C^{vol} = \frac{1}{9}\mathbf{I} : \mathbb{C} : \mathbf{I}$.

Note that in the case of *isotropic* materials the constitutive tensor can be written as:

$$\mathbb{C}^{vol} = 3\overline{K}\,\mathbb{V} = \overline{K}\,(\mathbf{I}\otimes\mathbf{I}) \tag{27}$$

$$\mathbb{C}^{dev} = 2\overline{G}\,\mathbb{P} = 2\overline{G}\,\left[\mathbb{I} - \frac{1}{3}(\mathbf{I}\otimes\mathbf{I})\right] \tag{28}$$

where $\overline{K}$ and $\overline{G}$ are the effective *bulk modulus* and the effective *shear modulus* of the material, respectively. Thus, the constitutive equation reduces to:

$$p = \overline{K}\,e_{vol} \tag{29}$$

$$\mathbf{s} = 2\overline{G}\,\mathbf{e} \tag{30}$$

When approaching the incompressible limit, $\overline{K} \to \infty$, it is convenient to write Eq. (29) as:

$$e_{vol} = \frac{p}{\overline{K}} \tag{31}$$

so that, in the limit, Eq. (31) transforms into: $e_{vol} = 0$, or, making use of Eq. (3), as the kinematic constraint:

$$\nabla\cdot\mathbf{u} = 0 \tag{32}$$

Remark 1. *The effective values of $\overline{K}$ and $\overline{G}$ depend on the actual constitutive equations used to characterize the material behavior, as illustrated in the following Section. For isotropic elasticity, these parameters correspond to their elastic counterparts: $\overline{K} = K$ and $\overline{G} = G$.*

2.3. Constitutive modeling

Firstly, the elastic constitutive equation is derived from the strain energy density function (hyperelastic model). Next and following the same procedure, both *J*2-plasticity and *J*2-damage models are detailed including the evolution laws of the corresponding internal variables and the definition of the mechanical dissipation. The latter is used to show the accuracy of the 3-field formulation.

2.3.1. Elasticity

Elasticity is the starting point to introduce the volumetric/deviatoric split as well as the basis for the following elasto-plastic or elasto-damage constitutive models. In particular, *incompressible* elasticity is widely used in different applications such as rubbers, elastomers, biological tissues, etc.

Let us write the strain energy density function, Ψ, as:

$$\Psi = \frac{1}{2}\,\boldsymbol{\varepsilon} : \mathbb{C} : \boldsymbol{\varepsilon} \tag{33}$$

and introducing the split of the strain tensor in Eq. (19), it can be split as:

$$\Psi = \Psi_{vol}(e_{vol}) + \Psi_{dev}(\mathbf{e}) = \frac{1}{2}\,K\,e_{vol}^2 + \frac{1}{2}\,2G\,\mathbf{e} : \mathbf{e} \tag{34}$$

where the bulk modulus $K = \frac{E}{3(1-2\nu)}$ and the shear modulus $G = \frac{E}{2(1+\nu)}$ are defined in terms of Young's modulus and Poisson's ratio, E and ν, respectively.

Applying Coleman's method [54], the rate of mechanical dissipation, $\dot{D}_{mech}$, is defined as:

$$\dot{D}_{mech} = \boldsymbol{\sigma} : \dot{\boldsymbol{\varepsilon}} - \dot{\Psi} \geq 0 \tag{35}$$

and using the split of the stress tensor in Eq. (16), the mechanical dissipation results in:

$$\dot{D}_{mech} = \left(p - \frac{\partial\Psi}{\partial e_{vol}}\right)\,\dot{e}_{vol} + \left(\mathbf{s} - \frac{\partial\Psi}{\partial\mathbf{e}}\right) : \dot{\mathbf{e}} \geq 0 \tag{36}$$

From this, the constitutive equations of the hyperelastic problem are derived as:

$$p = \frac{\partial\Psi}{\partial e_{vol}} = K\,e_{vol} \tag{37}$$

$$\mathbf{s} = \frac{\partial\Psi}{\partial\mathbf{e}} = 2G\,\mathbf{e} \tag{38}$$

and the mechanical dissipation cancels out:

$$\dot{D}_{mech} = 0 \tag{39}$$

2.3.2. J2−plasticity

The main hypothesis of the *J2-elasto-plastic constitutive model* consists of the additive split of the total deviatoric strains, $\mathbf{e}$, into their elastic and plastic counterparts, $\mathbf{e}^e$ and $\mathbf{e}^p$, respectively, as:

$$\mathbf{e} = \mathbf{e}^e + \mathbf{e}^p \tag{40}$$

Hence, the (elastic) strain energy density function, Ψ^e, is written in terms of the (total) volumetric deformation and the elastic deviatoric strains:

$$\Psi^e = \Psi^e_{vol}(e_{vol}) + \Psi^e_{dev}(\mathbf{e}^e) \tag{41}$$

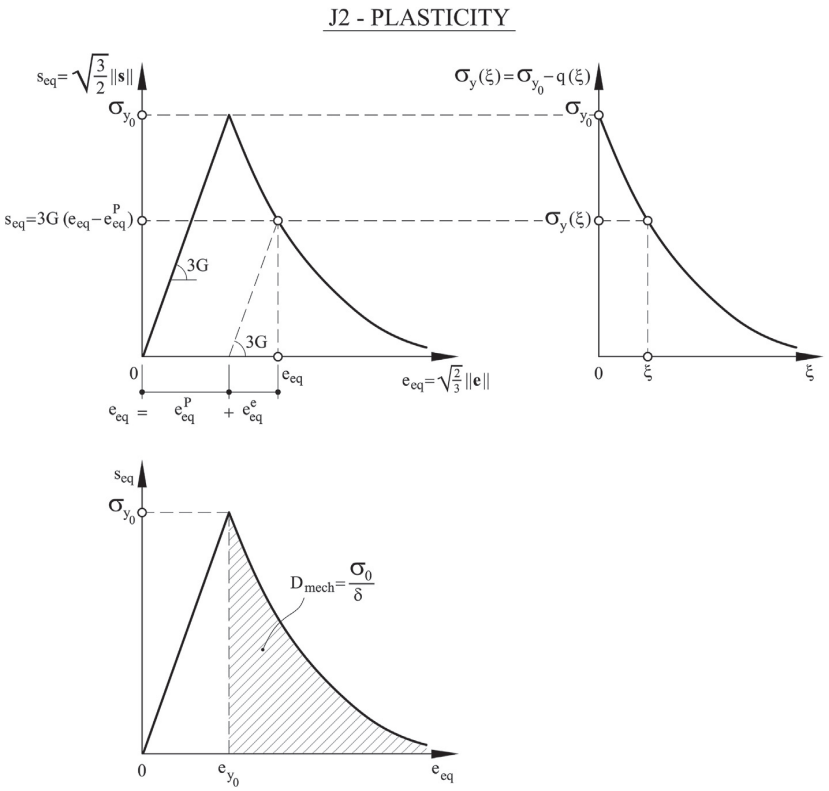

Fig. 1. J2 Elasto-plastic model.

$$= \frac{1}{2}\, K\, e_{vol}^2 + \frac{1}{2}\, 2G\, \mathbf{e}^e : \mathbf{e}^e \tag{42}$$

$$= \frac{1}{2}\, K\, e_{vol}^2 + \frac{1}{2}\, 2G\, \left(\mathbf{e} - \mathbf{e}^p\right) : \left(\mathbf{e} - \mathbf{e}^p\right) \tag{43}$$

Applying Coleman's method [54]:

$$\dot{D}_{mech} = \left(p - \frac{\partial \Psi^e}{\partial e_{vol}}\right)\, \dot{e}_{vol} + \left(\mathbf{s} - \frac{\partial \Psi^e}{\partial \mathbf{e}^e}\right) : \dot{\mathbf{e}}^e + \mathbf{s} : \dot{\mathbf{e}}^p \geq 0 \tag{44}$$

the constitutive equations of the *J2-elasto-plastic constitutive model* are:

$$p = K\, e_{vol} \tag{45}$$

$$\mathbf{s} = 2G\, \mathbf{e}^e = 2G\, \left(\mathbf{e} - \mathbf{e}^p\right) \tag{46}$$

while the mechanical dissipation results in:

$$\dot{D}_{mech} = \mathbf{s} : \dot{\mathbf{e}}^p \geq 0 \tag{47}$$

The evolution of the plastic deformations, $\mathbf{e}^p$, depends on the definition of the yield surface. The von Mises yield function, φ, typically used in isotropic *J2*-plasticity, is defined as:

$$\varphi = s_{eq} - \sigma_y \leqslant 0 \tag{48}$$

where $s_{eq} = \sqrt{\frac{3}{2}}\,\|\mathbf{s}\| = \sqrt{3}\sqrt{J2}$ is the *equivalent* von Mises stress, being *J2* the 2nd invariant of the deviatoric stress tensor. The tensile strength of the material is defined as:

$$\sigma_y = \sigma_{yo} - q\,(\xi) \tag{49}$$

where σ_{yo} is the initial yield stress and $q\,(\xi)$ is the stress-like internal variable, conjugate to the *isotropic hardening/softening* variable ξ, and defined as:

$$q\,(\xi) = -\left(\sigma_\infty - \sigma_{yo}\right)\left[1 - \exp\left(-\delta\xi\right)\right] \tag{50}$$

where σ_∞ is the saturation (ultimate) stress and δ is the coefficient of the saturation hardening/softening law (see Fig. 1).

Remark 2. *The von Mises yield function can be defined by the equivalent format as:*

$$\varphi^* = \|\mathbf{s}\| - R \leqslant 0 \tag{51}$$

where $R = \sqrt{\frac{2}{3}}\sigma_y\,(\xi)$ *is the radius of the cylinder that characterizes the von Mises yield surface* [55].

Let us introduce the rate of plastic work $\dot{W}^p\,(\mathbf{s}, q)$, defined as:

$$\dot{W}^p\,(\mathbf{s}, q) = \mathbf{s} : \dot{\mathbf{e}}^p + q\, \dot{\xi} \tag{52}$$

The evolution laws of both the plastic strains and the isotropic hardening/softening variable are obtained through the principle of maximum (plastic) work [55]. Thus, the functional:

$$F\,(\mathbf{s}, q) = -\dot{W}^p\,(\mathbf{s}, q) + \dot{\gamma}\; \varphi\,(\mathbf{s}, q) \tag{53}$$

is minimized while satisfying the restriction induced by the yield surface:

$$\frac{\partial F\,(\mathbf{s}, q)}{\partial \mathbf{s}} = -\frac{\partial \dot{W}^p\,(\mathbf{s}, q)}{\partial \mathbf{s}} + \dot{\gamma}\; \frac{\partial \varphi\,(\mathbf{s}, q)}{\partial \mathbf{s}} = 0 \tag{54}$$

$$\frac{\partial F\,(\mathbf{s}, q)}{\partial q} = -\frac{\partial \dot{W}^p\,(\mathbf{s}, q)}{\partial q} + \dot{\gamma}\; \frac{\partial \varphi\,(\mathbf{s}, q)}{\partial q} = 0 \tag{55}$$

Hence, the evolution laws result in:

$$\dot{\mathbf{e}}^p = \dot{\gamma}\ \frac{\partial \varphi(\mathbf{s})}{\partial \mathbf{s}} = \sqrt{\frac{3}{2}}\dot{\gamma}\ \mathbf{n} \tag{56}$$

$$\dot{\xi} = \dot{\gamma} \tag{57}$$

where $\dot{\gamma}$ and $\mathbf{n} = \frac{\mathbf{s}}{\|\mathbf{s}\|}$ are the plastic multiplier and the normal to the yield surface, respectively.

The corresponding loading and unloading (Kuhn-Tucker) conditions hold:

$$\dot{\gamma} > 0 \quad \varphi = 0 \quad \text{Plastic loading} \tag{58}$$

$$\dot{\gamma} = 0 \quad \varphi < 0 \quad \text{Elastic unloading} \tag{59}$$

$$\dot{\gamma}\varphi = 0 \tag{60}$$

In plastic loading, the plastic multiplier $\dot{\gamma}$, is obtained through the consistency condition, $\dot{\varphi} = 0$, as:

$$\dot{\varphi}(\mathbf{s}, q) = \frac{\partial \varphi}{\partial \mathbf{s}} : \dot{\mathbf{s}} + \frac{\partial \varphi}{\partial q}\dot{q} = \frac{\partial \varphi}{\partial \mathbf{s}} : 2G\ \left(\dot{\mathbf{e}} - \dot{\mathbf{e}}^p\right) + \frac{\partial \varphi}{\partial q}\frac{dq}{d\xi}\dot{\xi} = 0 \tag{61}$$

Substituting the evolution laws in Eqs. (56) and (57), yields:

$$\dot{\gamma} = \sqrt{\frac{2}{3}}\beta\ (\mathbf{n} : \dot{\mathbf{e}}) \tag{62}$$

and, thereby, the evolution law of the plastic strains can be written as:

$$\dot{\mathbf{e}}^p = \beta\ (\mathbf{n} \otimes \mathbf{n}) : \dot{\mathbf{e}} \tag{63}$$

where $\beta = 3G\ /\left(3G\ + \frac{dq}{d\xi}\right)$ and $\beta = 1$ in the particular case of perfect plasticity.

Note that, from Eqs. (56) and (57), it is also possible to write:

$$\dot{\xi} = \dot{e}^p_{eq} \tag{64}$$

where $e^p_{eq} = \sqrt{\frac{2}{3}}\|\mathbf{e}^p\|$ is the *equivalent* (plastic) strain. Thus, the isotropic hardening/softening variable yields:

$$\xi = \max\left(e^p_{eq}\right) \tag{65}$$

This given, the mechanical dissipation can be rewritten as:

$$\dot{D}_{mech} = \mathbf{s} : \dot{e}^p = s\ \dot{\gamma} = \sigma_y(\xi)\ \dot{\xi} \geq 0 \tag{66}$$

being $s_{eq} = \sigma_y$ in plastic loading ($\varphi = 0,\ Eq.(48)$).

Remark 3. *In the case of strain-softening, the total energy (per unit volume) dissipated during the fracture process, D_{mech}, within the localization band, must fulfill the equation:*

$$D_{mech} = \frac{G_f}{h} \tag{67}$$

where G_f is the Mode-II fracture energy (per unit of surface) and h is the localization bandwidth. The total dissipation, D_{mech}, yields:

$$D_{mech} = \int_0^\infty \dot{D}_{mech}\ dt = \int_0^\infty \sigma_y(\xi)\ d\xi = \frac{\sigma_{yo}}{\delta} \tag{68}$$

being the saturation stress set to $\sigma_\infty = 0$, (see Fig. 1). Thereby, the exponent of the exponential law in Eq. (50), δ, can be expressed as [35]:

$$\delta = \frac{\sigma_{yo}}{G_f}h \tag{69}$$

Remark 4. *Further generalizations considering pressure sensitive elasto-plastic models such as linear Druker-Prager, or orthotropic Hill's plasticity can be also accommodated into this split format.*

2.3.3. J2−damage

Damage models are useful for the analysis of materials that show degradation of both stiffness and strength. In the case of metallic alloys, damage mainly affects the shear stiffness, that is, the deviatoric component of the constitutive equation. Thus, the *J2-isotropic damage model* accounts for the degradation of the mechanical properties of these materials.

The (elastic) strain energy density function reads:

$$\Psi^e = \frac{1}{2}\ K\ e^2_{vol} + \frac{1}{2}\ (1-d)\ 2G\ \mathbf{e} : \mathbf{e} \tag{70}$$

where $0 \leqslant d \leqslant 1$ is the damage index controlling the degradation of the shear modulus. Applying Coleman's method:

$$\dot{D}_{mech} = \left(p - \frac{\partial \Psi^e}{\partial e_{vol}}\right)\ \dot{e}_{vol} + \left(\mathbf{s} - \frac{\partial \Psi^e}{\partial \mathbf{e}}\right) : \dot{\mathbf{e}} - \frac{\partial \Psi^e}{\partial d}\ \dot{d} \geq 0 \tag{71}$$

the constitutive equations of the *J2-isotropic damage constitutive model* are:

$$p = K\ e_{vol} \tag{72}$$

$$\mathbf{s} = (1-d)\ 2G\ \mathbf{e} \tag{73}$$

and the mechanical dissipation is:

$$\dot{D}_{mech} = \left(\frac{1}{2}\ 2G\ \mathbf{e} : \mathbf{e}\right)\ \dot{d} \geq 0 \tag{74}$$

As for $J2-$plasticity, the equivalent stress is defined as: $s_{eq} = \sqrt{\frac{3}{2}}\|\mathbf{s}\|$, while the equivalent strain is $e_{eq} = \sqrt{\frac{2}{3}}\|\mathbf{e}\|$. This given, it is useful to write the relationship between s_{eq} and e_{eq}, as:

$$s_{eq} = (1-d)\ 3G\ e_{eq} \tag{75}$$

and the mechanical dissipation as:

$$\dot{D}_{mech} = \frac{1}{2}\ 3G\ e^2_{eq}\ \dot{d} \geq 0 \tag{76}$$

The $J2-$damage constitutive model adopts the same yield surface defined as for $J2-$plasticity (48) as well as the same exponential law to characterize the evolution of the tensile strength (49), as shown in Fig. 2.

The inelastic work reduces to:

$$\dot{W}^p(q) = q(\xi)\ \dot{\xi} \tag{77}$$

and, according to the principle of maximum dissipation, the functional to be minimized is:

$$F(q) = -\dot{W}^p(q) + \dot{\gamma}\ \varphi(q) \tag{78}$$

and, thereby:

$$\frac{dF(q)}{dq} = -\frac{d\dot{W}^p(q)}{dq} + \dot{\gamma}\ \frac{d\varphi(q)}{dq} = 0 \tag{79}$$

From the above equation, the evolution law for the softening variable, ξ, results in

$$\dot{\xi} = \dot{\gamma} \tag{80}$$

Using the consistency condition, $\dot{\varphi} = 0$, the value of the multiplier turns out:

$$\dot{\gamma} = \dot{e}_{eq} \rightarrow \dot{\xi} = \dot{e}_{eq} \tag{81}$$

The corresponding loading and unloading (Kuhn-Tucker) conditions hold:

$$\dot{\gamma} > 0 \quad \varphi = 0 \quad \text{Loading} \tag{82}$$

$$\dot{\gamma} = 0 \quad \varphi < 0 \quad \text{Unloading} \tag{83}$$

$$\dot{\gamma}\varphi = 0 \tag{84}$$

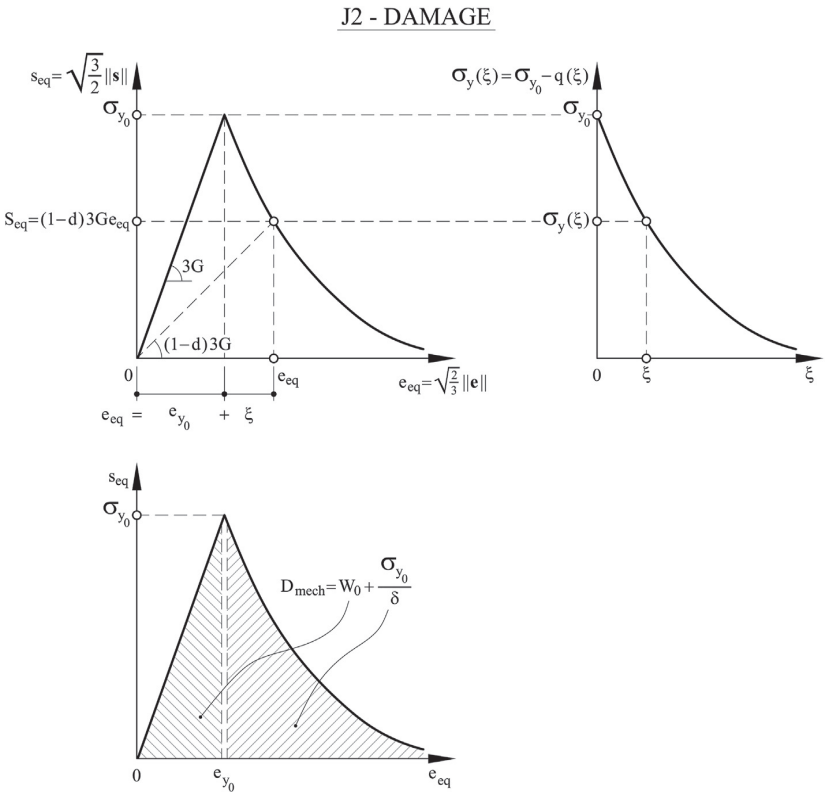

Fig. 2. J2 Elasto-damage model.

Remark 5. *The tensile strength can be expressed using the equivalent definition as:*

$$\sigma_y(\xi) = (1-d)\ 3G\ \left(e_{yo}+\xi\right) \tag{85}$$

where $e_{yo} = \sigma_{yo}/3G$ is the (equivalent) strain at the elastic limit. Consequently, the yield criterion can be rewritten in a more convenient form as:

$$\varphi^* = e_{eq} - \left(e_{yo}+\xi\right) \leqslant 0 \tag{86}$$

and the consistency condition, $\dot{\varphi}^* = 0$, returns the expected result as shown in Eq. (81), and consequently: the softening variable is computed as:

$$\xi = \max\left(e_{eq} - e_{yo}\right) \quad e_{eq} \geq e_{yo} \tag{87}$$

The damage variable evolves once the yield criterion is satisfied: $\varphi = 0$, thus:

$$\begin{cases} s_{eq} = (1-d)\ 3G\ e_{eq} = \sigma_y(\xi) \\ e_{eq} = e_{yo} + \xi \end{cases} \quad \rightarrow \quad d = 1 - \frac{\sigma_y(\xi)}{\sigma_{yo} + 3G\ \xi} \tag{88}$$

where $\sigma_{yo} = 3G\ e_{yo}$.

Remark 6. *The total energy (per unit volume) dissipated during the fracture process is (see Fig. 2):*

$$D_{mech} = \int_0^\infty \dot{D}_{mech}\ dt = W_o^e + \frac{\sigma_{yo}}{\delta} \tag{89}$$

where $W_o^e = \frac{1}{2}\frac{\sigma_{yo}^2}{3G}$ is the modulus of resilience (maximum energy per unit volume that can be absorbed up to the elastic limit without permanent damage). According to Eq. (67), the exponent of the softening law, δ, can be expressed as [56]:

$$\delta = \frac{\sigma_{yo}}{G_f - W_o^e h} h \tag{90}$$

2.4. The 3-field formulation

The mixed $\mathbf{u}/\mathbf{e}/p$ formulation is obtained by applying the volumetric/deviatoric split to the $\mathbf{u}/\boldsymbol{\varepsilon}$ formulation (9 – 10), as:

$$\nabla\cdot\left(\mathbb{C}^{dev} : \mathbf{e}\right) + \nabla p + \mathbf{b} = \mathbf{0} \tag{91}$$

$$\mathbb{P} : \nabla^s\mathbf{u} - \mathbf{e} = \mathbf{0} \tag{92}$$

$$\nabla\cdot\mathbf{u} - \frac{p}{C^{vol}} = 0 \tag{93}$$

where Eq. (91) is the balance of momentum equation in mixed form, including the contributions of the deviatoric stresses and the pressure, $\mathbf{s}(\mathbf{e})$ and p, respectively. Eqs. (92) and (93) are the deviatoric and the volumetric components of the kinematic equation (10).

The *weak* form of the mixed 3−field formulation reads:

$$\int_\Omega \delta\mathbf{u}^T\ \nabla\cdot\left(\mathbb{C}^{dev} : \mathbf{e}\right)\ dV + \int_\Omega \delta\mathbf{u}^T\ \nabla p\ dV + \int_\Omega \delta\mathbf{u}^T\ \mathbf{b}\ dV = 0 \tag{94}$$

$$\int_\Omega \delta\mathbf{e}^T\ \left(\mathbb{P} : \nabla^s\mathbf{u}\right)\ dV - \int_\Omega \delta\mathbf{e}^T\ \mathbf{e}\ dV = 0 \tag{95}$$

$$\int_\Omega \delta p^T\ \left(\nabla\cdot\mathbf{u}\right)\ dV - \int_\Omega \delta p^T\ \frac{p}{C^{vol}}\ dV = 0 \tag{96}$$

where $\delta\mathbf{u}$, $\delta\mathbf{e}$ and δp are the test functions of the displacement, deviatoric strains and the pressure field, respectively. Integrating Eq. (94) by parts and taking $\delta\mathbf{u}=\mathbf{0}$ on $\partial\Omega_u$, the problem is written as:

$$\begin{aligned}&\int_\Omega \left(\nabla^s\delta\mathbf{u}\right)^T\ \left(\mathbb{C}^{dev}:\mathbf{e}\right)\ dV+\int_\Omega\left(\nabla\cdot\delta\mathbf{u}\right)^T\ p\ dV=F\left(\delta\mathbf{u}\right)\\&\int_\Omega \delta\mathbf{e}^T\ \left(\mathbb{P}:\nabla^s\mathbf{u}\right)\ dV-\int_\Omega\delta\mathbf{e}^T\ \mathbf{e}\ dV=0\\&\int_\Omega \delta p^T\ \left(\nabla\cdot\mathbf{u}\right)\ dV-\frac{1}{C^{vol}}\int_\Omega\delta p^T\ p\ dV=0\end{aligned}\tag{97}$$

where $F\left(\delta\mathbf{u}\right)$ is the work of the external loads, defined as:

$$F\left(\delta\mathbf{u}\right)=\int_\Omega\delta\mathbf{u}^T\ \mathbf{b}\ dV+\int_{\partial\Omega_t}\delta\mathbf{u}^T\ \overline{\mathbf{t}}\ dS\tag{98}$$

being $\overline{\mathbf{t}}$ the prescribed tractions on $\partial\Omega_t$ (Neumann's boundary conditions).

Problem (97) involves the first derivatives of $\mathbf{u}$. Hence, the natural space for the continuum displacements is $V=H^1(\Omega)^{n_{\dim}}$. $H^m(\Omega)$ denotes the space of functions whose derivatives (up to order $m\geq 0$) belong to $L^2(\Omega)$. The corresponding variations are defined in $V_0=\{\delta\mathbf{u}(\mathbf{X})\in V\mid\delta\mathbf{u}=\mathbf{0}\ \text{ for }\forall\mathbf{X}\in\partial\Omega_u\}$. The natural space for the deviatoric part of the strain field $\mathbf{e}$, and its variations $\delta\mathbf{e}$, is $S=\left\{\mathbf{e}(\mathbf{X})=\left[e_{ij}(\mathbf{X})\right],\ \ e_{ij}=e_{ji}\in L^2(\Omega)\ \mid tr\left(\mathbf{e}\right)=0\ \text{ for }\forall\mathbf{X}\in\Omega\right\}$. The pressure field p, and its variation δp, belong to space $Q=L^2(\Omega)$.

Other functional settings may be considered by changing the terms integrated by parts. In fact, the formulation that yields optimal stress convergence for equal interpolation for all the unknowns requires more regularity on the stresses. We will not treat this issue in this work (see Ref. [57] for similar ideas in the context of Darcy's problem).

Problem (97) is complemented by Dirichlet's boundary conditions in terms of the prescribed displacements $\mathbf{u}(\mathbf{X})=\overline{\mathbf{u}}$ for $\forall\mathbf{X}\in\partial\Omega_u$.

Remark 7. *To achieve symmetry, the second equation is multiplied by* $\mathbb{C}$*, and because* $\mathbb{C}^{dev}=\mathbb{P}:\mathbb{C}$*, problem (97) reads:*

$$\begin{aligned}&\int_\Omega \left(\nabla^s\delta\mathbf{u}\right)^T\ \left(\mathbb{C}^{dev}:\mathbf{e}\right)\ dV+\int_\Omega\left(\nabla\cdot\delta\mathbf{u}\right)^T\ p\ dV=F\left(\delta\mathbf{u}\right)\\&\int_\Omega \delta\mathbf{e}^T\ \left(\mathbb{C}^{dev}:\nabla^s\mathbf{u}\right)\ dV-\int_\Omega\delta\mathbf{e}^T\ \left(\mathbb{C}:\mathbf{e}\right)\ dV=0\\&\int_\Omega \delta p^T\ \left(\nabla\cdot\mathbf{u}\right)\ dV-\int_\Omega\delta p^T\ \frac{p}{C^{vol}}\ dV=0\end{aligned}\tag{99}$$

2.5. Discrete approximation of the 3-field problem

To obtain the discrete Galerkin Finite Element (FE) approximation of problem (99), the material domain $\Omega(\mathbf{X})$, is discretized into finite elements, $\Omega^{(e)}$, so that: $\Omega=\bigcup_{e=1}^{ne}\Omega^{(e)}$, being *ne*, the total number of elements,

The continuum solution $\left\{\mathbf{u},\quad\mathbf{e},\quad p\right\}\in\mathbb{W}=V\times S\times Q$ is approximated by $\left\{\mathbf{u}_h,\quad\mathbf{e}_h,\quad p_h\right\}$ defined onto the Galerkin FE space: $\mathbb{W}_h=V_h\times S_h\times Q_h$. Thus, the discrete counterpart of the weak form of the 3−field problem is written as:

$$\begin{aligned}&\int_\Omega \left(\nabla^s\delta\mathbf{u}_h\right)^T\ \left(\mathbb{C}^{dev}:\mathbf{e}_h\right)\ dV+\int_\Omega\left(\nabla\cdot\delta\mathbf{u}_h\right)^T\ p_h\ dV=F\left(\delta\mathbf{u}_h\right)\\&\int_\Omega \delta\mathbf{e}_h^T\ \left(\mathbb{C}^{dev}:\nabla^s\mathbf{u}_h\right)\ dV-\int_\Omega\delta\mathbf{e}_h^T\ \left(\mathbb{C}:\mathbf{e}_h\right)\ dV=0\\&\int_\Omega \delta p_h^T\ \left(\nabla\cdot\mathbf{u}_h\right)\ dV-\int_\Omega\delta p_h^T\ \frac{p_h}{C^{vol}}\ dV=0\end{aligned}\tag{100}$$

being $\int_\Omega(\cdot)\ dV=\bigcup_{e=1}^{ne}\int_{\Omega^{(e)}}(\cdot)\ dV$

Denoting by $\mathbf{U}=\left[U_i^A\right]=\left[U_x^A\quad U_y^A\quad U_z^A\right]$, $\mathbf{E}=\left[E_i^A\right]=\left[E_{xx}^A\quad E_{yy}^A\quad E_{zz}^A\quad E_{xy}^A\quad E_{xz}^A\quad E_{yz}^A\right]$ and $\mathbf{P}=\left[P^A\right]$ the nodal values of the master fields, their element-wise approximation is written as:

$$\mathbf{u}_h^{(e)}=\mathbf{N}_u\mathbf{U}=\left[N^A I_{(3x3)_{ij}}U_j^A\right]\tag{101}$$

$$\mathbf{e}_h^{(e)}=\mathbf{N}_e\mathbf{E}=\left[N^A I_{(6x6)_{ij}}E_j^A\right]\tag{102}$$

$$p_h^{(e)}=\mathbf{N}_p\mathbf{P}=\left[N^A P^A\right]\tag{103}$$

where $\mathbf{N}_u=\left[N^A I_{(3x3)_{ij}}\right]$, $\mathbf{N}_e=\left[N^A I_{(6x6)_{ij}}\right]$ and $\mathbf{N}_p=\left[N^A\right]$ are the matrices incorporating the shape functions, N^A, at each node A, adopted for the FE interpolation of all master fields.

The elemental stiffness matrix of the *algebraic form* of problem (100) is:

$$\mathbb{K}_h^{(e)}=\int_{\Omega^{(e)}}\begin{bmatrix}\left[\mathbf{0}\right]&\left[\mathbf{B}^T\mathbf{C}^{dev}\mathbf{N}_e\right]&\left[\mathbf{G}\mathbf{N}_p\right]\\\left[\mathbf{N}_e^T\mathbf{C}^{dev}\mathbf{B}\right]&-\left[\mathbf{N}_e^T\mathbf{C}\mathbf{N}_e\right]&\left[\mathbf{0}\right]\\\left[\mathbf{N}_p^T\mathbf{G}^T\right]&\left[\mathbf{0}\right]&-\frac{1}{C^{vol}}\left[\mathbf{N}_p^T\mathbf{N}_p\right]\end{bmatrix}dV\tag{104}$$

where $\mathbf{G}=\left[G_i^A\right]$ and $\mathbf{G}^T$ stand for the (discrete) gradient and divergence matrices, while $\mathbf{B}=\left[B_{ij}^A\right]$ and $\mathbf{B}^T$ are the (discrete) symmetric gradient and divergence (applied to 2nd order tensors expressed in Voigt's notation). Finally, $\mathbf{C}$ and $\mathbf{C}^{dev}$ are the rank −2 constitutive matrices and its deviatoric part, when both stresses and strains are expressed in Voigt's notation.

2.6. Variational-multi-scale stabilization technique

In this work, continuous *equal order linear interpolation* for all fields is assumed. This choice does not comply with the compatibility limitations stated by the inf-sup stability condition [14]. This can be circumvented by using a *stabilization technique*. The *Variational Multi-Scale* (VMS) method is introduced to stabilize the mixed discrete formulation and allowing for the use of linear interpolations for all master fields.

The basic idea of the VMS method consists of approximating the space $\mathbb{W}$, where the continuum solution belongs to, at two different levels of resolution (scales): a coarse FE space $\mathbb{W}_h$ and a finer one, $\widetilde{\mathbb{W}}$. Hence, the enhanced approximation is defined as:

$$\begin{cases}\mathbf{u}\simeq\mathbf{u}_h+\widetilde{\mathbf{u}}\\\mathbf{e}\simeq\mathbf{e}_h+\widetilde{\mathbf{e}}\\p\simeq p_h+\widetilde{p}\end{cases}\qquad\text{in}\quad\mathbb{W}\simeq\mathbb{W}_h\oplus\widetilde{\mathbb{W}}\tag{105}$$

On the one hand, the coarse scale can be solved using the standard FE interpolation; on the other hand, the sub-grid scale cannot be solved and only its *effect* is accounted for, enhancing the stability of the mixed formulation. According to the original work of Codina [58], the sub-grid approximation is expressed in terms of the residuals of the projected (Galerkin) components of Eqs. (91)–(93) as:

$$\widetilde{\mathbf{u}}=\tau_u\ R_u^h=\tau_u\ \left[\nabla\cdot\left(\mathbb{C}^{dev}:\mathbf{e}_h\right)+\nabla p_h+\mathbf{b}\right]\tag{106}$$

$$\widetilde{\mathbf{e}}=\tau_e\ R_e^h=\tau_e\ \left[\mathbb{P}:\nabla^s\mathbf{u}_h-\mathbf{e}_h\right]\tag{107}$$

$$\widetilde{p}=\tau_p\ R_p^h=\tau_p\ \left[\nabla\cdot\mathbf{u}_h-\frac{p_h}{C^{vol}}\right]\tag{108}$$

where the stabilization parameters [59,1]:

$$\tau_u=c_u\frac{hL}{2\widetilde{C}^{dev}}\tag{109}$$

$$\tau_e = c_e \frac{h}{L} \tag{110}$$

$$\tau_p = c_p \widetilde{C}^{vol} \frac{h}{L} \tag{111}$$

are expressed in terms of the element size h, the characteristic length of the computational domain L, as well as two additional parameters related to the *effective* deviatoric and volumetric stiffness of the material: the *secant* shear modulus, defined as: $2\widetilde{C}^{dev} = \|\mathbf{s}_h\| / \|\mathbf{e}_h\|$, and the *compressibility* modulus, $\widetilde{C}^{vol}$. Coefficients c_u, c_e and c_p are constants to be chosen.

According to Fourier's analysis in Ref. [57], the compressibility modulus can be defined as:

$$\widetilde{C}^{vol} = \left(\frac{c_1}{2\widetilde{C}^{dev}} + \frac{c_2}{C^{vol}} \right)^{-1} \tag{112}$$

where c_1 and c_2 are arbitrary constants.

Remark 8. *In isotropic elasticity, $2\widetilde{C}^{dev} = 2G$, and choosing $c_1 = 1$ and $c_2 = 2/3$, then:*

$$\widetilde{C}^{vol} = \frac{2G}{3}\left(\frac{1+\upsilon}{1-\upsilon}\right) \quad \begin{cases} \upsilon = 0 & \widetilde{C}^{vol} = \dfrac{2G}{3} = K \\ \upsilon = 0.5 & \widetilde{C}^{vol} = 2G \end{cases}$$

The solution of the problem is approximated as:

$$\mathbf{u} \simeq \mathbf{u}_h + \widetilde{\mathbf{u}} = \mathbf{u}_h \; + \; \tau_u \; \left[\nabla \cdot \left(\mathbb{C}^{dev} : \mathbf{e}_h \right) + \nabla p_h + \mathbf{b} \right] \tag{113}$$

$$\mathbf{e} \simeq \mathbf{e}_h + \widetilde{\mathbf{e}} = (1 - \tau_e) \; \mathbf{e}_h + \tau_e \; \left[\mathbb{P} : \nabla^s \mathbf{u}_h \right] \tag{114}$$

$$p \simeq p_h + \widetilde{p} = \left(1 - \frac{\tau_p}{C^{vol}} \right) \; p_h + \tau_p \; \left[\nabla \cdot \mathbf{u}_h \right] \tag{115}$$

Remark 9. *Note that in the incompressible limit $C^{vol} \to \infty$ and $\nabla \cdot \mathbf{u}_h \to 0$; thus, the pressure field: $p \simeq p_h$.*

Introducing the approximate fields (113–115) into the original problem (99), the elemental stiffness matrix of the problem, now including the VMS stabilization, is expressed as:

$$\mathbb{K}^{(e)} = \mathbb{K}_h^{(e)} - \tau_u \, \mathbb{K}_{\tau_u}^{(e)} - \tau_e \, \mathbb{K}_{\tau_e}^{(e)} - \tau_p \, \mathbb{K}_{\tau_p}^{(e)} \tag{116}$$

where there exist 3 different contributions to add stability to the Galerkin problem. The matrix form of these terms is:

$$\mathbb{K}_{\tau_u}^{(e)} = \int_{\Omega^{(e)}} \begin{bmatrix} [\mathbf{0}] & [\mathbf{0}] & [\mathbf{0}] \\ [\mathbf{0}] & \left[\left(\mathbf{C}^{dev}\mathbf{B} \right) \left(\mathbf{C}^{dev}\mathbf{B} \right)^T \right] & \left[\left(\mathbf{C}^{dev}\mathbf{B} \right) \mathbf{G} \right] \\ [\mathbf{0}] & \left[\mathbf{G}^T \left(\mathbf{C}^{dev}\mathbf{B} \right)^T \right] & [\mathbf{G}^T\mathbf{G}] \end{bmatrix} dV \tag{117}$$

$$\mathbb{K}_{\tau_e}^{(e)} = \int_{\Omega^{(e)}} \begin{bmatrix} -\left[\mathbf{B}^T \left(\mathbf{C}^{dev}\mathbf{B} \right) \right] & \left[\left(\mathbf{C}^{dev}\mathbf{B} \right)^T \mathbf{N}_e \right] & [\mathbf{0}] \\ \left[\mathbf{N}_e^T \left(\mathbf{C}^{dev}\mathbf{B} \right) \right] & -\left[\mathbf{N}_e^T \mathbf{C} \mathbf{N}_e \right] & [\mathbf{0}] \\ [\mathbf{0}] & [\mathbf{0}] & [\mathbf{0}] \end{bmatrix} dV \tag{118}$$

$$\mathbb{K}_{\tau_p}^{(e)} = \int_{\Omega^{(e)}} \begin{bmatrix} -\left[\mathbf{G}\mathbf{G}^T \right] & [\mathbf{0}] & \dfrac{1}{C^{vol}} \left[\mathbf{G}\mathbf{N}_p \right] \\ [\mathbf{0}] & [\mathbf{0}] & [\mathbf{0}] \\ \dfrac{1}{C^{vol}} \left[\mathbf{N}_p^T \mathbf{G}^T \right] & [\mathbf{0}] & -\dfrac{1}{\left(C^{vol} \right)^2} \left[\mathbf{N}_p^T \mathbf{N}_p \right] \end{bmatrix} dV \tag{119}$$

Remark 10. *The sub-grid scales are "small" compared to the FE scales and they vanish at a rate equal to one order higher than the FE interpolation degree. For linear elements this means that the sub-grid scales reduce with the square of the element size. Thus, the relative weight of the sub-grid scale can be used as an efficient indicator of the discretization error of a given FE mesh and it can be used as driver for adaptive mesh refinement in linear and nonlinear solid mechanics* [60,61].

3. Fluid mechanics

3.1. The continuum problem

In fluid mechanics, $\Omega(\mathbf{x})$ denotes a *spatial* domain, composed of *spatial points*, $\mathbf{x}$, and $\mathbf{u}(\mathbf{x})$ stands for the *velocity field*.

Eqs. (1)–(3) define the associated mechanical problem when Cauchy's equilibrium equation (1) is assumed in its *steady-state* form. This framework is suitable for laminar flow problems characterized by very low Reynolds numbers (ratio of inertial forces to viscous forces). Thus, it is possible to neglect the inertia forces (convection), compared to the frictional shear forces due to the actual (very high) viscosity values. As shown through the numerical assessment, this is applied in incompressible *rigid-viscoplastic flows*, as typically found in many industrial manufacturing processes, such as extrusion, Friction Stir Welding (FSW) or forging.

On the one hand, the kinematic constraint to enforce the *isochoric* behavior (*incompressibility*) must be satisfied:

$$\nabla \cdot \mathbf{u} = 0 \tag{120}$$

On the other hand, the strain-rate, $\boldsymbol{\epsilon} = \nabla^s \mathbf{u}$, is a fully deviatoric field, thus: $\boldsymbol{\epsilon} \equiv \mathbf{e}$.

The resulting set of equations defining the continuum problem is:

$$\nabla \cdot \mathbf{s} + \nabla p + \mathbf{b} = \mathbf{0} \tag{121}$$

$$\mathbf{e} - \nabla^s \mathbf{u} = \mathbf{0} \tag{122}$$

$$\nabla \cdot \mathbf{u} = 0 \tag{123}$$

3.2. Constitutive modeling

Two different *non-Newtonian* viscous models suitable for the analysis of rigid-viscoplastic flows are presented: Norton-Hoff and Bingham models. Both of them allow for the definition of the constitutive equation as:

$$\mathbf{s} = 2\mu_{eff} \; \mathbf{e} \tag{124}$$

where μ_{eff} is the *effective* viscosity which characterizes the specific viscous law.

In fluid mechanics, the equivalent strain-rate is defined as: $\gamma = \sqrt{2}\,\|\mathbf{e}\|$, being conjugate to the equivalent stress: $\tau = \frac{1}{\sqrt{2}}\,\|\mathbf{s}\| = \sqrt{J_2}$. Consequently, making use of the constitutive Eq. (124), the following equation holds:

$$\tau = \mu_{eff} \; \gamma \tag{125}$$

The mechanical dissipation is computed as:

$$\dot{D}_{mech} = \mathbf{s} : \mathbf{e} = \tau \; \gamma \geq 0 \tag{126}$$

3.2.1. Visco-plastic Norton-Hoff model

The Norton-Hoff model is characterized by an effective viscosity of the form:

$$\mu_{eff} \; (\gamma) = \mu_o \; \gamma^{m-1} \tag{127}$$

being μ_o and m the consistency parameter and the flow index, respectively. Therefore, the Norton-Hoff model is defined by the following *power law*:

$$\tau = \mu_o \; \gamma^m \leftrightarrow \mathbf{s} = 2\mu_o \; \gamma^{m-1} \; \mathbf{e} = 2\mu_{eff} \; \mathbf{e} \tag{128}$$

Note that for $m = 1$ the *Newtonian* behavior is recovered: $\mu_{eff} = \mu_o$, and the corresponding constitutive equation reduces to:

$$\mathbf{s} = 2\mu_o \; \mathbf{e} \tag{129}$$

3.2.2. Regularized Bingham model

The Bingham model characterizes a material that behaves as rigid at low stresses but flows as a viscous fluid under sufficiently high shear stress. The corresponding mathematical model assumes that the fluid starts flowing, with a constant viscosity μ, when the initial shear threshold, τ_{yo}, is overpassed. Thus:

$$\begin{aligned} \gamma &= 0 \quad \text{if} \quad \tau < \tau_{yo} \\ \gamma &= \frac{1}{\mu}\left(\tau - \tau_{yo}\right) \quad \text{if} \quad \tau \geq \tau_{yo} \end{aligned} \tag{130}$$

The rheological model can be written in terms of an effective viscosity, μ_{eff}, defined as:

$$\mu_{eff}\ (\gamma) = \mu + \frac{\tau_{yo}}{\gamma} \tag{131}$$

Note that when $\gamma \to 0$, this ideal rheological model presents a singularity because the effective viscosity, $\mu_{eff}(\gamma) \to \infty$. This aspect is a serious inconvenient from the numerical point of view. Many authors have proposed regularized versions of the Bingham model to remove this singularity [62,63,64]. In this work, the Tanner and Milthorpe model is adopted [64]. Therefore, the actual rigid behavior of the fluid when $\tau < \tau_{yo}$ is replaced by a fictitious viscosity (i.e. a regularization parameter), $\mu_o \gg \mu$, and the following bilinear form turns out:

$$\begin{aligned} \tau &= \mu_o\, \gamma \quad \text{if} \quad \tau < \tau_{yo} \\ \tau &= \left(\mu + \frac{\tau_{yo}}{\gamma}\right)\gamma \quad \text{if} \quad \tau \geq \tau_{yo} \end{aligned} \tag{132}$$

and the effective viscosity results in:

$$\begin{aligned} \mu_{eff}\ (\gamma) &= \mu_o \quad \text{if} \quad \tau < \tau_{yo} \\ \mu_{eff}\ (\gamma) &= \mu + \frac{\tau_{yo}}{\gamma} \quad \text{if} \quad \tau \geq \tau_{yo} \end{aligned} \tag{133}$$

3.3. The 3-field formulation

In this Section, the mixed $\mathbf{u}/\mathbf{e}/p$ problem (see Eqs. (91)–(93)) is particularized for incompressible fluids characterized by their effective viscosity, $\mu_{eff}(\gamma)$, as:

$$2\mu_{eff}\ \nabla\cdot\mathbf{e} + \nabla p + \mathbf{b} = \mathbf{0} \tag{134}$$

$$\nabla^s\mathbf{u} - \mathbf{e} = \mathbf{0} \tag{135}$$

$$\nabla\cdot\mathbf{u} = 0 \tag{136}$$

The corresponding weak form reads:

$$\begin{aligned} &\int_\Omega \left(\nabla^s\delta\mathbf{u}\right)^T\ \left(2\mu_{eff}\ \mathbf{e}\right)\ dV + \int_\Omega \left(\nabla\cdot\delta\mathbf{u}\right)^T\ p\ dV = F(\delta\mathbf{u}) \\ &\int_\Omega \delta\mathbf{e}^T\ \left(2\mu_{eff}\ \nabla^s\mathbf{u}\right)\ dV - \int_\Omega \delta\mathbf{e}^T\ \left(2\mu_{eff}\ \mathbf{e}\right)\ dV = 0 \\ &\int_\Omega \delta p^T\ \left(\nabla\cdot\mathbf{u}\right)\ dV = 0 \end{aligned} \tag{137}$$

where the 2nd equation has been multiplied by $2\mu_{eff}$ to achieve symmetry.

Problem (137) is complemented by Dirichlet's boundary conditions in terms of prescribed velocities, $\overline{\mathbf{u}}$.

3.4. Algebraic form

The elemental stiffness matrix of problem (137) is expressed as:

$$\mathbb{K}^{(e)} = \mathbb{K}_h^{(e)} - \tau_u\ \mathbb{K}_{\tau_u}^{(e)} - \tau_e\ \mathbb{K}_{\tau_e}^{(e)} \tag{138}$$

where the Galerkin term is:

$$\mathbb{K}_h^{(e)} = \int_{\Omega^{(e)}} \begin{bmatrix} [\mathbf{0}] & 2\mu_{eff}\left[\mathbf{B}^T\mathbf{N}_e\right] & \left[\mathbf{G}\mathbf{N}_p\right] \\ 2\mu_{eff}\left[\mathbf{N}_e^T\mathbf{B}\right] & -2\mu_{eff}\left[\mathbf{N}_e^T\mathbf{N}_e\right] & [\mathbf{0}] \\ \left[\mathbf{N}_p^T\mathbf{G}^T\right] & [\mathbf{0}] & [\mathbf{0}] \end{bmatrix} dV \tag{139}$$

and the contributions adding stability to the Galerkin problem are:

$$\mathbb{K}_{\tau_u}^{(e)} = \int_{\Omega^{(e)}} \begin{bmatrix} [\mathbf{0}] & [\mathbf{0}] & [\mathbf{0}] \\ [\mathbf{0}] & \left(2\mu_{eff}\right)^2\left[\mathbf{B}\mathbf{B}^T\right] & 2\mu_{eff}\left[\mathbf{B}\mathbf{G}\right] \\ [\mathbf{0}] & 2\mu_{eff}\left[\mathbf{G}^T\mathbf{B}^T\right] & \left[\mathbf{G}^T\mathbf{G}\right] \end{bmatrix} dV \tag{140}$$

$$\mathbb{K}_{\tau_e}^{(e)} = \int_{\Omega^{(e)}} \begin{bmatrix} -2\mu_{eff}\left[\mathbf{B}^T\mathbf{B}\right] & 2\mu_{eff}\left[\mathbf{B}^T\mathbf{N}_e\right] & [\mathbf{0}] \\ 2\mu_{eff}\left[\mathbf{N}_e^T\mathbf{B}\right] & -2\mu_{eff}\left[\mathbf{N}_e^T\mathbf{N}_e\right] & [\mathbf{0}] \\ [\mathbf{0}] & [\mathbf{0}] & [\mathbf{0}] \end{bmatrix} dV \tag{141}$$

PLEASE

... (142)

Remark 3.1. *Note that in the incompressible limit, the pressure field: $p \simeq p_h$. Therefore, the stabilization terms arising from the pressure sub-scale vanish, see* Eq. (108).

4. Numerical results

In this section, the proposed $\mathbf{u}/\mathbf{e}/p$ formulation is assessed by solving several numerical examples including both solid and fluid analyses. Different constitutive models as introduced in Sections 3 and 4 are adopted for both 2*D* and 3*D*. Different FE discretizations are also tested: triangular, quadrilaterals and hexahedral elements.

The objectives are three-fold: (a) to show the faster convergence rate of the 3−field formulation over other available FE formulations, (b) to demonstrate the enhanced accuracy of the stress and strain fields over the $\mathbf{u}/p$ formulation (used as the reference solution in isochoric problems) and, as a consequence of this, (c) to show mesh bias independence when addressing strain localization problems.

The stabilization coefficients used in all examples are $c_u = 1.0$, $c_p = 1.0$ for both the $\mathbf{u}/p$ and $\mathbf{u}/\mathbf{e}/p$ formulations. The latter requires a third stabilization coefficient: $c_e = 1.0$.

The Newton-Raphson method is adopted to solve the nonlinear system of equations in an incremental and manner. The number of time-steps set for all cases is 400. The convergence norm based on residual forces is 10^{-5}.

The numerical simulations are solved using an enhanced version of the in-house finite element software COMET [65]. The pre and post processing is performed with GiD [66]. Both softwares are developed at the International Center for Numerical Methods in Engineering (CIMNE).

4.1. Convergence test

The first example consists of a benchmark to assess the convergence rate of different finite elements formulations: standard irreducible (based on displacements, only), mixed $\mathbf{u}/p$ FE technology and the proposed mixed 3−field formulation.

The problem consists of a square domain, $\Omega = [0,1]\times[0,1]$ in $\mathbb{R}^2$, with homogeneous boundary conditions.

The exact solution is given in terms of horizontal and vertical displacements, $u(x,y)$ and $v(x,y)$, respectively defined as:

$$u(x,y) = +2x^2y(x-1)^2(y-1)(2y-1) \tag{143}$$

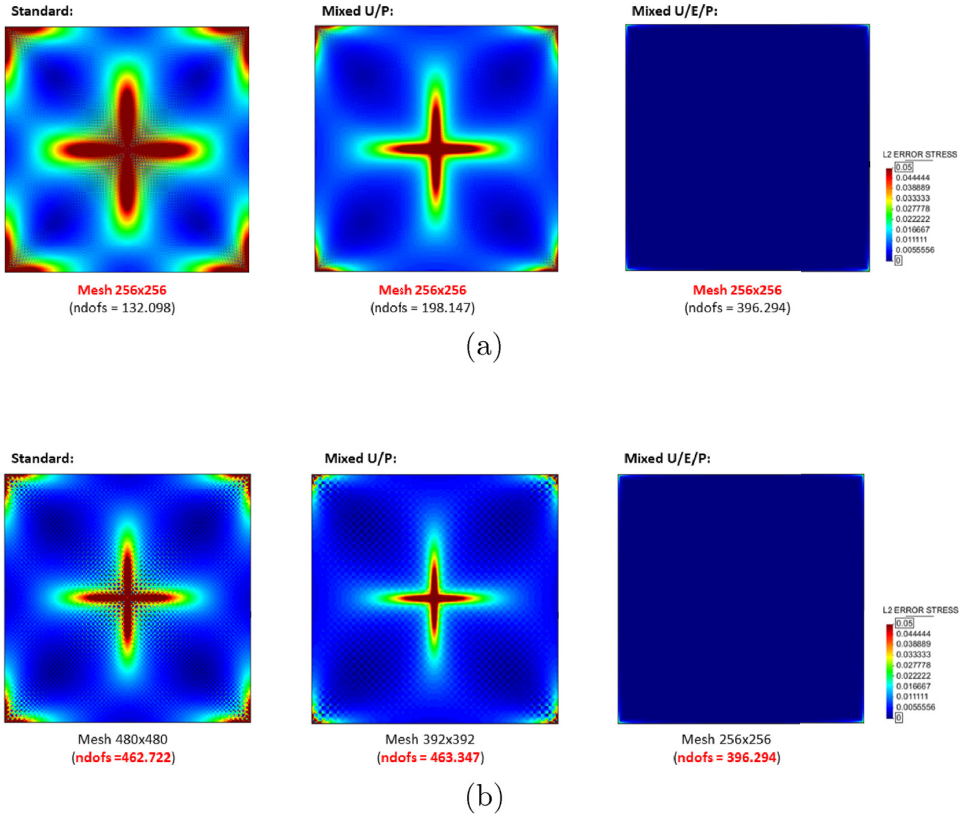

Fig. 3. Local error of the stress field (L2-norm) using: (a) the same mesh; (b) similar number of degrees of freedom.

$$v(x,y) = -2xy^2(x-1)(y-1)^2(2x-1) \tag{144}$$

The corresponding strain field is:

$$\varepsilon_{xx}(x,y) = \frac{\partial u}{\partial x} = +4xy(x-1)(y-1)(2x-1)(2y-1) \tag{145}$$

$$\varepsilon_{yy}(x,y) = \frac{\partial v}{\partial y} = -4xy(x-1)(y-1)(2x-1)(2y-1) \tag{146}$$

$$\begin{aligned}\varepsilon_{xy}(x,y) &= \frac{1}{2}\left(\frac{\partial u}{\partial y} + \frac{\partial v}{\partial x}\right)\\ &= (y-x)(x+y-1)(6x^2y - 6x^2y^2 - x^2\\ &\quad +6xy^2 - 6xy + x - y^2 + y)\end{aligned}$$

Note that $\varepsilon_{xx}(x,y) = -\varepsilon_{yy}(x,y)$ and, in plane strain, $\varepsilon_{zz}(x,y) = 0$. Thus, the problem is isochoric: $e_{vol} = 0$.

Assuming isotropic elasticity, the stresses are

$$\sigma_{xx}(x,y) = (\lambda + 2\mu)\varepsilon_{xx}(x,y) + \lambda\varepsilon_{yy}(x,y) \tag{148}$$

$$\sigma_{yy}(x,y) = \lambda\varepsilon_{xx}(x,y) + (\lambda + 2\mu)\varepsilon_{yy}(x,y) \tag{149}$$

$$\sigma_{xy}(x,y) = 2\mu\varepsilon_{xy}(x,y) \tag{150}$$

where $\lambda = \frac{\nu E}{(1+\nu)(1-2\nu)}$ and $\mu = \frac{E}{2(1+\nu)}$ are the Lamé parameters expressed in terms of the Young modulus, $E = 2,000$MPa and the Poisson ratio, $\nu = 0.3$. The value of Poisson's ratio allows for using standard irreducible elements in the convergence test.

The FE discretization makes use of different structured meshes varying between 4×4 and 480×480 quadrilateral elements.

The *local* $L2$-norm of the stress field error is evaluated at each Gauss point as:

$$\|\boldsymbol{\sigma}\|_{L2}^{local} = \sqrt{\frac{(\sigma_{xx}^c - \sigma_{xx}^a)^2 + (\sigma_{yy}^c - \sigma_{yy}^a)^2 + (\sigma_{xy}^c - \sigma_{xy}^a)^2}{\left(\sigma_{xx}^a\right)^2 + \left(\sigma_{yy}^a\right)^2 + \left(\sigma_{xy}^a\right)^2}} \tag{151}$$

where the super-indexes c and a stand for the computed and analytical values, respectively. The *global* $L2$-norm is evaluated by summing the contributions at all Gauss points.

Fig. 3 depicts the distribution of the local error based on the stress field. Fig. 3(a) compares the 3 FE technologies (standard irreducible, mixed $\mathbf{u}/p$ and the proposed $\mathbf{u}/\mathbf{e}/p$ formulation) adopting the same mesh, while Fig. 3(b) shows the error for a similar number of degrees of freedom. The accuracy of the proposed 3−field formulation is remarkable.

Fig. 4 shows the displacement convergence rate upon mesh size. As expected the 3 FE technologies present the same slope of 2.0. More interesting is the convergence rate of the stress field. The global error is demonstrated in Fig. 5. The accuracy is assessed upon mesh refinement (Fig. 5(a)) and increasing the number of degrees of freedom (Fig. 5(b)). The convergence rate is 1.0 for both the *standard* and the mixed $\mathbf{u}/p$ formulations while the 3−field formulation achieves the expected superior convergence rate slope of 1.5 (see Ref. [58]).

Therefore, to achieve the same accuracy, e.g. 1% of global error, both the irreducible and the $\mathbf{u}/p$ formulations require a mesh size, h, almost 10 times finer ($h \leqslant 0.003$ and $h \leqslant 0.005$, respectively) than for the 3-field FE technology ($h \leqslant 0.04$). A similar result is obtained in

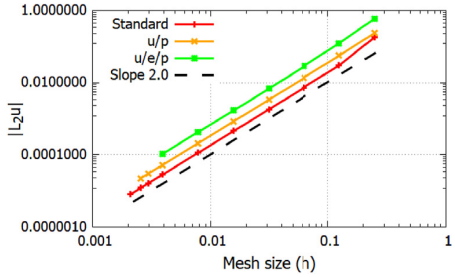

Fig. 4. Convergence rate of the displacement field of the three FE technologies upon mesh refinement.

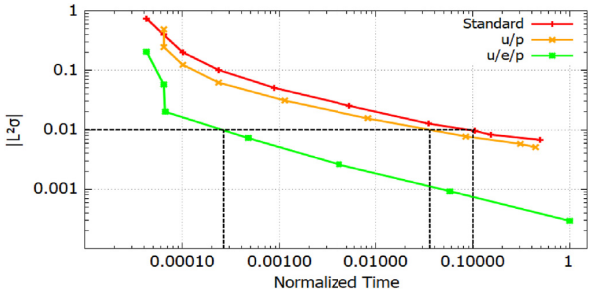

Fig. 6. Convergence rate of the three FE technologies upon normalized cpu-time.

terms of the number of degrees of freedom (*dofs*): to get an error lower than 1%, the $\mathbf{u}/\mathbf{e}/p$ formulation needs 4,292 *dofs*, while the mixed $\mathbf{u}/p$ requires 118,150 *dofs* (27 times more) and the standard irreducible formulation needs 211,300 *dofs* (49 times more if compared to the 3-field and almost 2 times more than the mixed $\mathbf{u}/p$ formulation).

Fig. 6 depicts the *cpu*-time needed by each FE technology to achieve a given global stress accuracy. In particular, to reduce the simulation error below 1%, the $\mathbf{u}/\mathbf{e}/p$ formulation is almost 10 time faster compared to the other technologies: $t_{\mathbf{u}/\mathbf{e}/p} \simeq 2.5 \times 10^{-4} s$, $t_{\mathbf{u}/p} \simeq 5 \times 10^{-3} s$ and $t_{\mathbf{u}} \simeq 3 \times 10^{-3} s$, respectively. The values are normalized with respect to the *cpu*-time needed for the solution of the 256×256 mesh with the 3−field formulation.

4.2. Perforated strip

This example consists of the 2*D* plane-strain analysis of a perforated strip subjected to uniaxial stretching. The axial load is applied through a rigid plate. Because of the double symmetry, only one quarter of the domain (the top right quarter) needs to be discretized. Fig. 7(*a*) depicts the geometry of the problem. The dimensions are relative to the size of the hole: $r = 1m$.

Both *J2-Plasticity* and *J2-Damage* constitutive models are adopted with a strain softening law to favor strain localization. The Young modulus of the material is $E = 10$MPa, the Poisson ratio $\nu = 0.5$ (incompressible elasticity), yield stress $\sigma_y = 10$KPa, and fracture energy $G_f = 400\text{J/m}^2$.

The expected failure mechanism consists of the formation of two symmetric slip-lines exactly at $\theta_{cr} = \pm 45°$ with the horizontal axis [46]. The total amount of energy, W_{mech}, dissipated up to failure is:

$$W_{mech} = \frac{9r}{cos\ \theta_{cr}}\ G_f = 5,091\ J \tag{152}$$

This value is used as the analytical reference to assess the accuracy of the different FE technologies used for the numerical simulation.

Fig. 7(*b*) shows a structured mesh of 10,060 triangular elements and 5,182 nodes, being the average element size: $h = 0.20m$. This FE discretization is used to obtain the numerical *reference*, because this mesh is well-aligned with the direction of the expected slip-line.

Fig. 8 shows the failure mechanism (slip-lines) obtained using the *J*2-plasticity and *J*2-damage models. Note that the strain localization is concentrated in one single element across the thickness of the shear band when the mixed $\mathbf{u}/p$ formulation is adopted (see Fig. 8(*b*) and (*d*)), being the double for the 3−field formulation (see Fig. 8(*a*) and (*c*)). This is because of the different interpolation of the strain field used by the two mixed FE technologies: discontinuous and continuous strains/stresses for the $\mathbf{u}/p$ and $\mathbf{u}/\mathbf{e}/p$ formulations, respectively.

Fig. 9 compares the load vs. displacement curves for all the case-studies. The curves are practically overlapped as demonstrated by the relative errors of the computed mechanical dissipation with respect to the analytical solution, reported in Table 1. Therefore, when the mesh is aligned with the slip-lines both FE technologies predict almost the exact solution.

An unstructured mesh of 7,711 triangular elements and 3,993 nodes with the same average element size, $h = 0.20m$ is analyzed next (see Fig. 7(*c*)). Fig. 10 reports the contour-fills of the *J*2 strains corresponding to the different analyses. All results are qualitatively satisfactory, showing shear bands at $\pm 45°$. Nevertheless, the accuracy of the different FE technologies can be appreciated in Fig. 12 where the load vs. displacement curves are shown. The 3−field formulation demonstrates its accuracy for both the *J*2−plasticity and *J*2−damage constitutive models even if an unstructured FE mesh is used. The curves are overlapped to the reference one with a small error in both cases (see Table 2).

This is not the case for the mixed $\mathbf{u}/p$ formulation. In the case of *J*2−damage, the quantitative error is small but the failure mechanism is not exactly the same, as shown by the corresponding load/displacement curve at the initiation of the shear band. The lack of accuracy is more evident for *J*2−plasticity. In Table 2 an error close to 30% is reported with respect to the reference solution, in terms of mechanical dissipation. This is due to the stress locking shown by the mixed $\mathbf{u}/p$ formulation when dealing with a directional inelastic flow, as the plastic flow in *J*2−plasticity. This is due to the poor performance of low order standard FE for reproducing opening or sliding modes which are not normal

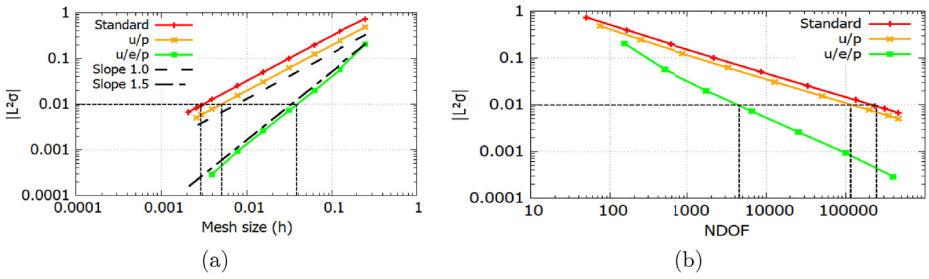

Fig. 5. Convergence rate of the stress field for the three FE technologies: (a) upon mesh refinement; (b) upon number of degrees of freedom.

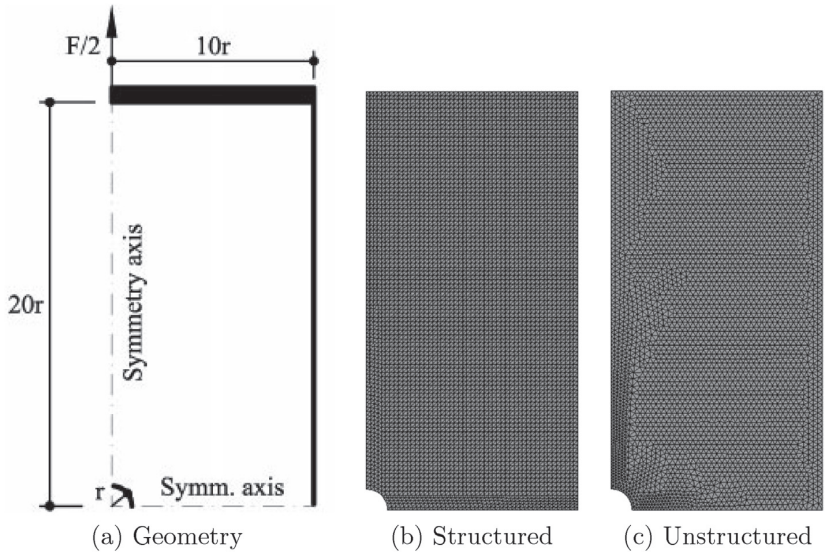

Fig. 7. Perforated strip under uniaxial stretching.

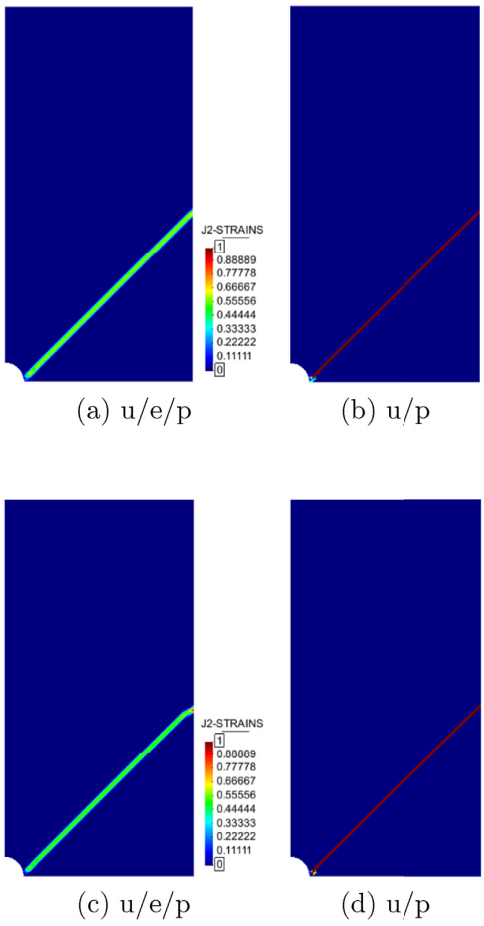

Fig. 8. Perforated strip. Strain localization analysis: reference results for J2-plasticity (a)–(b) and J2 damage (c)–(d).

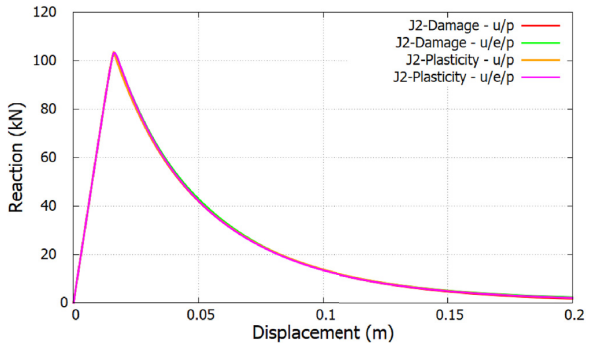

Fig. 9. Perforated strip: load vs. displacement curves. Solution obtained using a structured mesh aligned with the shear band for both J2-plasticity and J2-damage models.

Table 1
Structured mesh: relative errors of the computed mechanical dissipation with respect to the analytical value.

FE Technology	Const. Model	W_{mech} $[J]$	Error $[\%]$
$\mathbf{u}/p$	$J2-$plasticity	4,994	1.91
$\mathbf{u}/p$	$J2-$damage	4,947	2.82
$\mathbf{u}/\mathbf{e}/p$	$J2-$plasticity	4,991	1.96
$\mathbf{u}/\mathbf{e}/p$	$J2-$damage	5,053	0.75

or parallel, respectively, to one of the sides of the element. In Fig. 11, the spurious stresses at the end when the shear band is fully formed can be appreciated. Note that the $\mathbf{u}/\mathbf{e}/p$ formulation performs very well, while stress release does entirely occur for the mixed $\mathbf{u}/p$ formulation in conjunction with incremental $J2-$plasticity (see Fig. 11(b)). For the $\mathbf{u}/p$ formulation in conjunction with $J2-$damage, the spurious strains do not translate into spurious stresses because of the secant format of the constitutive model and scalar damage.

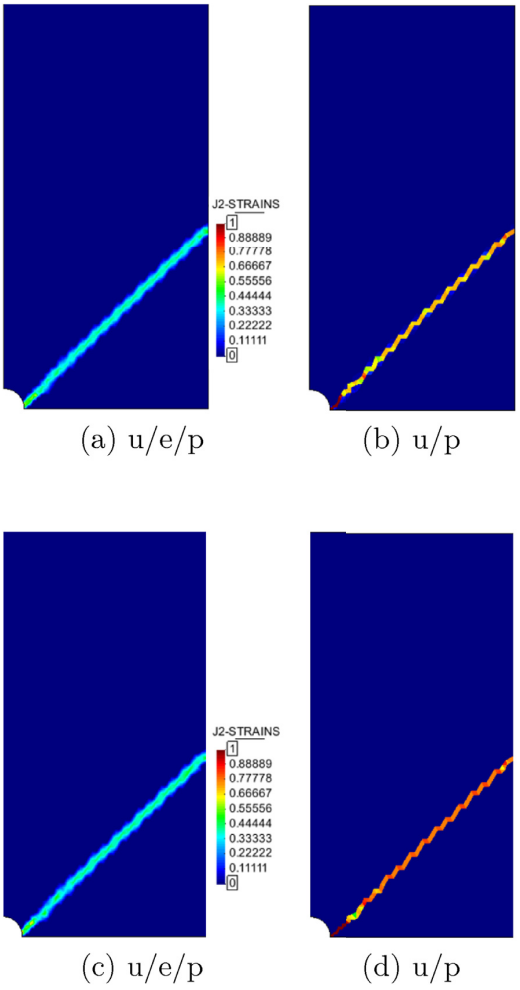

Fig. 10. Perforated strip. Strain localization obtained with the unstructured mesh for J2-plasticity (a)–(b) and J2 damage (c)–(d).

Table 2
Unstructured mesh: relative errors on the computed mechanical dissipation with respect to the analytical value.

FE Technology	Const. Model	W_{mech} $[J]$	Error $[\%]$
$\mathbf{u}/p$	$J2-$plasticity	6,538	28.4
$\mathbf{u}/p$	$J2-$damage	5,416	6.4
$\mathbf{u}/\mathbf{e}/p$	$J2-$plasticity	5,364	5.4
$\mathbf{u}/\mathbf{e}/p$	$J2-$damage	5,280	3.7

4.3. Perforated thin-wall cylinder

As a third example, a thin-wall cylinder, $30m$ height with an outer diameter of $6m$ and a wall thickness of $0.2m$ is addressed. The cylinder has a $0.40 \times 0.40\text{m}^2$ perforation at mid-height and it is subjected to vertical stretching by an imposed vertical displacement, $\delta_z = 0.20m$ applied to the top boundary. Due to the double symmetry of the problem, only one quarter of the domain is considered (see Fig. 13).

A uniform structured FE mesh is generated including 3,749 hexahedral elements and 7,750 nodes (see Fig. 13). This discretization consists of 31,000 *dofs* and 77,500 *dofs* for the $\mathbf{u}/p$ and the $\mathbf{u}/\mathbf{e}/p$ formulations, respectively.

Table 3
Difference between mixed FE formulations and analytical values.

FE Technology	W_{mech} $[J]$	Error $[\%]$	θ_{cr}	Error $[\%]$
$\mathbf{u}/p$	1,222	39.98	32.17°	8.8
$\mathbf{u}/\mathbf{e}/p$	874	0.11	35.05°	0.6

A fully incompressible ($\nu = 0.5$) elasto-$J2$-damage constitutive model is adopted including the same softening law and the same material properties as in the previous problem.

The radial stresses through the wall are null, so that plane stress conditions apply in the problem. A slip-line is expected to start from the perforation, with an angle of $\theta_{cr} = 35.26°$ with respect to the an horizontal plane, to later develop showing a helicoidal shape and causing the failure of the structure [46].

The total amount of energy $W_{mech} = AG_f$, dissipated up to the failure is:

$$W_{mech} = h\left(\frac{\pi\varphi_{mean}/2 - h}{\cos\theta_{cr}}\right) G_f = 873\ J \tag{153}$$

where φ_{mean} is the average diameter of the cylinder and A is the fracture surface, computed by multiplying the thickness of the cylinder by the length of the shear band (see Fig. 14).

Fig. 15 shows the failure mechanism (slip-line) at the end of the strain localization process for the mixed $\mathbf{u}/\mathbf{e}/p$ and the $\mathbf{u}/p$ formulations, respectively. Once again, both results are qualitatively good, being the mixed $\mathbf{u}/p$ solution sharper ($b = h$) than the one obtained by the $3-$field formulation ($b = 2h$), being b the shear bandwidth.

Nevertheless, in Fig. 16, it is possible to appreciate the differences found in the load vs. displacement curves recorded for both analyses. The shear band obtained with the mixed $\mathbf{u}/p$ elements is discontinuous at some instances. Contrarily, the $3-$field formulation is able to generate a well defined solution during the entire analysis (see Fig. 17). The accuracy of the two formulations is also reflected in the load/displacement curves. The energy dissipated by the $3-$field formulation is almost exact, while the mixed $\mathbf{u}/p$ produces an error close to 40%, as shown in Table 3.

Table 3 also shows the value of the critical angle θ_{cr}, that is the slope of the shear band starting at the perforation. Once again, the accuracy of the mixed $\mathbf{u}/\mathbf{e}/p$ formulation is remarkable.

4.4. Elasto-plastic extrusion

Extrusion is a manufacturing process suitable to multifold engineering applications ranging from metal forming processes to the food industry.

The numerical example proposed here consists of a $2:1$ reduction direct extrusion, where a displacement, $\delta_x = 0.10m$ is applied through the piston. Fig. 18 shows the $3D$ geometry of the problem and the corresponding dimensions. Note that due to the double symmetry conditions of the problem, one quarter of the total domain is simulated.

According to Hill's solution [67], two shear bands at $\pm$ 45° and a slip-surface defined by a quarter circumference are expected, once the extrusion mechanism is fully developed as shown in Fig. 19. The mechanical dissipation, $W_{mech} = AG_f$, is computed as:

$$W_{mech} = \left(2 + \frac{\pi}{2}\right) Rd\ G_f = 25.3\ J \tag{154}$$

where the radius of the slip-line is: $R = H\sqrt{2}$, being $H = 0.125m$ and $d = 0.1m$.

An incompressible ($\nu = 0.5$) elasto$-J2-$plastic constitutive model is adopted, including the same softening law and the same material properties as in the previous problems.

A fully structured hexahedral FE mesh is generated, made of 18,227 nodes and 15,600 elements of an average size, $h = 0.01m$ (see Fig. 18). Both mixed $\mathbf{u}/p$ and $\mathbf{u}/\mathbf{e}/p$ formulation are tested and compared.

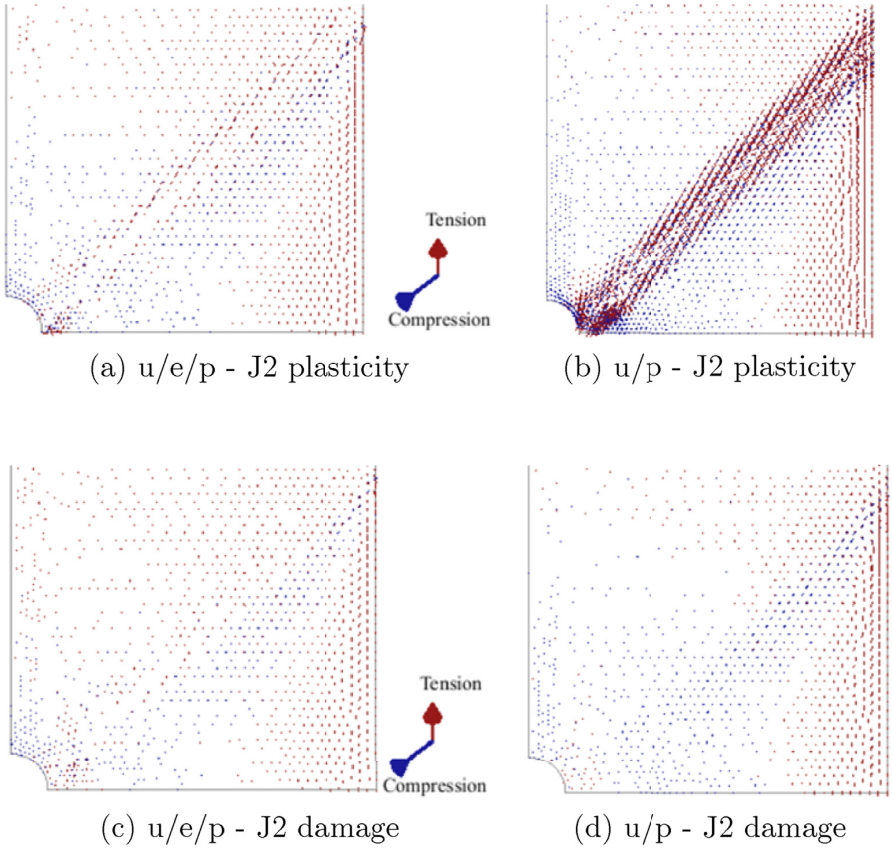

Fig. 11. Residual (principal) stresses at the end of the loading process when the unstructured mesh is used.

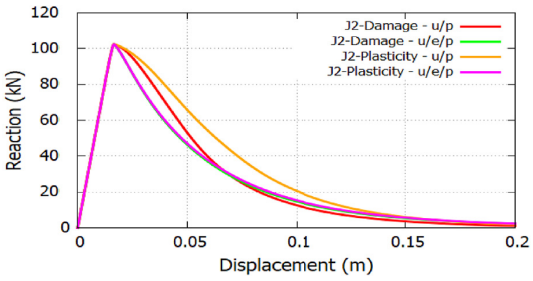

Fig. 12. Perforated strip: load vs. displacement curves. Solution obtained using the unstructured mesh for both J2-plasticity and J2-damage models.

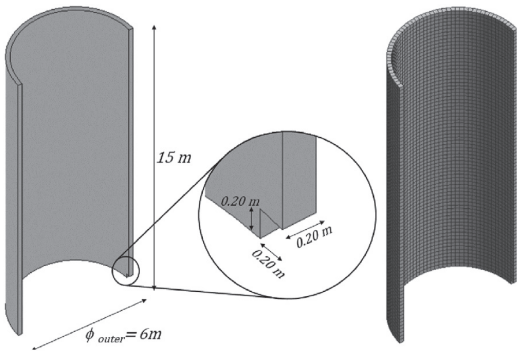

Fig. 13. Perforated thin-wall cylinder: geometry and FE mesh.

Fig. 20 shows the two shear bands as obtained by the mixed $\mathbf{u}/\mathbf{e}/p$ and mixed $\mathbf{u}/p$ formulations. Once again, the accuracy of the solution given by the 3− field analysis is remarkable: the slope of the shear bands is almost exact (46.12°) despite the coarse mesh used (see Table 4). Fig. 21(a) shows the well defined slip surface, less sensitive to the background mesh than for the $\mathbf{u}/p$ formulation (see Fig. 21(b)).

Fig. 22 shows the extrusion force as a function of the imposed displacement at the piston surface. Both FE technologies are able to capture correctly the peak load. Nevertheless, the mechanical dissipation (e.g. heat generated by the plastic deformation) is over-estimated by the $\mathbf{u}/p$ formulation as reported in Table 4.

4.5. Rigid-viscoplastic extrusion

In this example, an extrusion problem is also addressed, but now an Eulerian framework is adopted [68]. A rigid-viscoplastic Bingham model is characterized by an initial shear threshold, $\tau_{yo} = 1,000$Pa. The constitutive model makes use of an initial viscosity (regularization parameter): $\mu_o = 10^6 Pa \cdot s$.

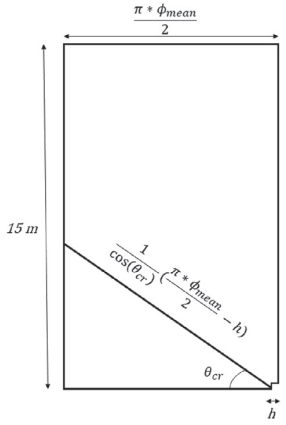

Fig. 14. Perforated thin-wall cylinder: length of the shear band.

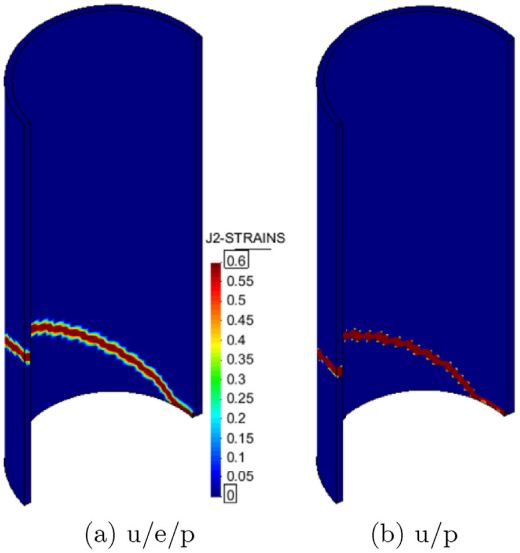

Fig. 15. Perforated thin-wall cylinder. Strain localization analysis: (a) Mixed u/e/p, (b) Mixed u/p formulation.

The analysis consists of a direct extrusion process characterized by a $3:1$ reduction, as shown in Fig. 23. The problem is solved in $2D$ plane-strain conditions and only half of the actual geometry is analyzed because of the existing symmetry conditions.

The FE mesh consists of $2,821$ nodes and $5,340$ triangular elements with an average size of $0.1m$. Both the mixed $\mathbf{u}/p$ and the $\mathbf{u}/\mathbf{e}/p$ formulations are analyzed.

The extrusion pressure, p_{extr}, is given by Ref. [67]:

$$p_{extr} = \frac{4}{3}\left(\frac{\pi}{2} + 1\right)\tau_y = 3,428\ Pa \tag{155}$$

and the expected failure mechanism is shown in Fig. 24.

Fig. 25 shows the streamlines and the yield region, once the extrusion mechanism is fully developed. The agreement with the analytical result is remarkable. A smoother solution is achieved with the 3−field formulation (Fig. 25(a)), although the $\mathbf{u}/p$ formulation also achieves good definition in this very fine mesh. The value of the extrusion pressure predicted by both FE technologies is almost exact (see Table 5). Note that this value follows from the failure mechanism and the flow stress.

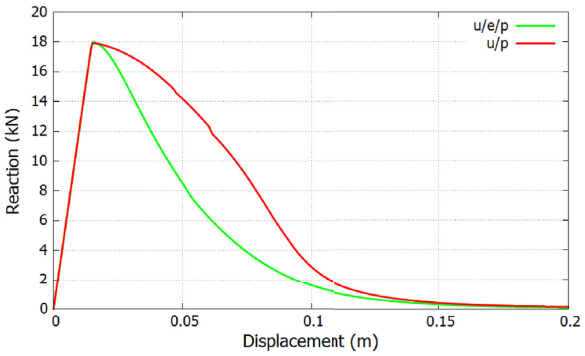

Fig. 16. Perforated thin-wall cylinder: load vs. displacement curves.

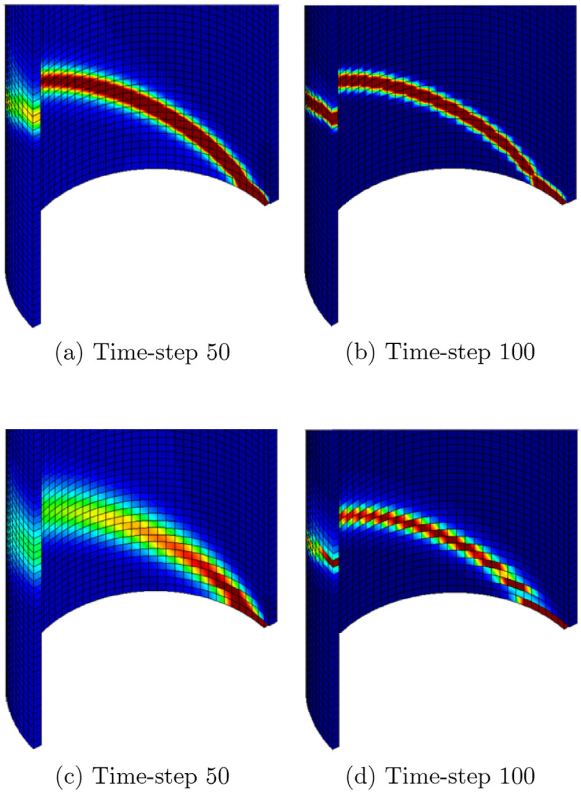

Fig. 17. Strain localization at different time-steps: u/e/p formulation in (a)–(b) and u/p formulation in (c)–(d).

Table 4
Elasto-plastic extrusion: relative errors of both the mechanical dissipation and the shear-band angles with respect to the analytical values.

FE Technology	W_{mech} $[J]$	Error $[\%]$	θ_{cr}	Error $[\%]$
$\mathbf{u}/p$	47.7	88.54	48.6°	8.00
$\mathbf{u}/\mathbf{e}/p$	27.3	7.91	46.12°	2.49

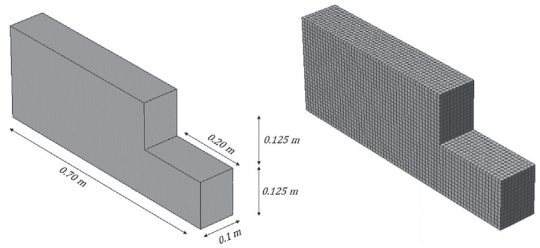

Fig. 18. Elasto-plastic extrusion: geometry and FE mesh.

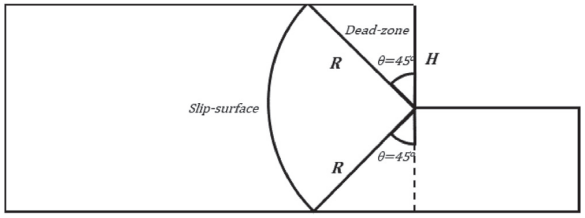

Fig. 19. Elasto-plastic extrusion with 2:1 reduction.

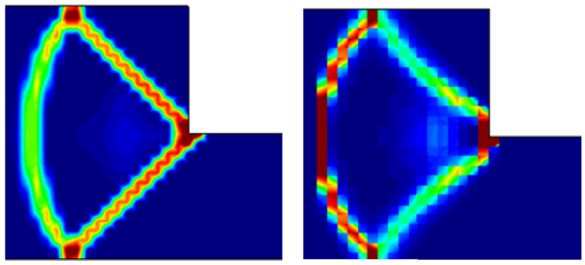

(a) u/e/p (b) u/p

Fig. 20. Elasto-plastic extrusion: shear bands obtained through the numerical simulations.

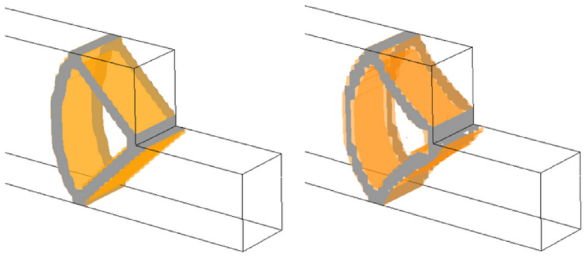

(a) u/e/p (b) u/p

Fig. 21. Elasto-plastic extrusion: slip-surface and shear bands obtained through the numerical simulations.

5. Concluding remarks

This paper exploits the accuracy of the proposed 3−field formulation to tackle highly non-linear problems including isochoric elastic (incompressible elasticity) and inelastic deformations while, at the same time, achieving a remarkable degree of accuracy of both the stress and the strain fields and, ensuingly, the mechanical work and the dissipated energy.

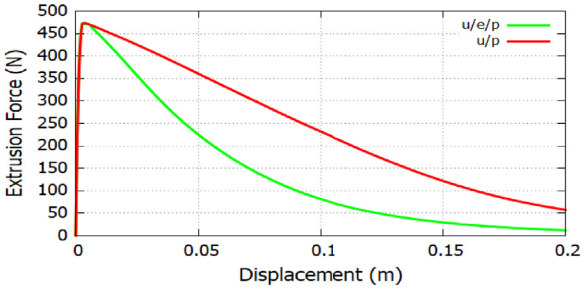

Fig. 22. Elasto-plastic extrusion: Force vs Displacement curve.

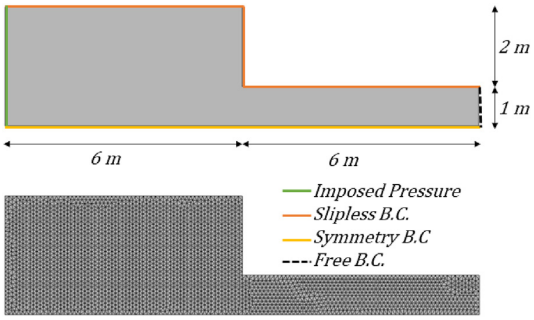

Fig. 23. Rigid-viscoplastic extrusion: Problem setting and FE mesh.

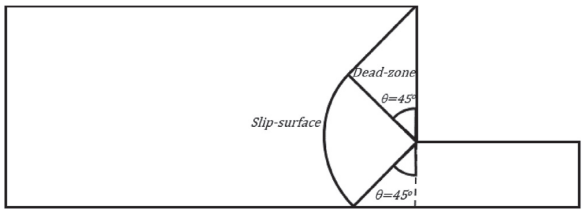

Fig. 24. Expected slip-lines during the extrusion process.

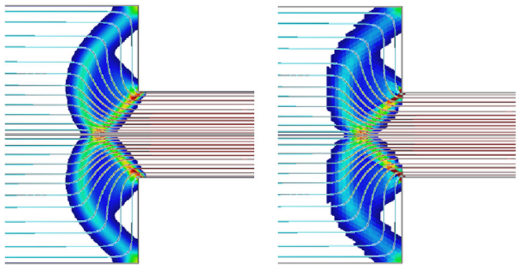

(a) u/e/p (b) u/p

Fig. 25. Rigid-viscoplastic extrusion: Streamlines and yield region.

The mixed $\mathbf{u}/\mathbf{e}/p$ formulation is developed, being suitable for several constitutive equations in Solid Mechanics (e.g. $J2$−plasticity, Drucker-Prager, $J2$−damage, etc..) and Fluid Dynamics (e.g. non-Newtonian rigid-viscoplastic flows).

The proposed 3−field formulation is convergent upon mesh refinement with a convergence rate higher than the well-known mixed $\mathbf{u}/p$

Table 5
Extrusion pressure: relative errors with respect to the analytical value.

FE Technology	Extrusion pressure $[Pa]$	Error $[\%]$
$\mathbf{u}/p$	3,410.9	0.50
$\mathbf{u}/\mathbf{e}/p$	3,408.4	0.58

formulation. Regarding efficiency, for a given accuracy, faster convergence is attained in terms of mesh refinement, degrees of freedom and cpu-time.

Several strongly non-linear problems including strain localization and the formation of shear bands are solved in 2*D* and 3*D* using triangular and quadrilateral meshes to demonstrate that the obtained solutions are free of any volumetric or shear locking.

The remarkable degree of accuracy makes the proposed mixed $\mathbf{u}/\mathbf{e}/p$ formulation very appealing for the solution of engineering problems including many industrial manufacturing processes (e.g. extrusion, forging, Additive Manufacturing, Friction Stir Welding, among others).

Declaration of competing interest

The authors declare that they have no known competing financial interests or personal relationships that could have appeared to influence the work reported in this paper.

Acknowledgments

The financial support from the Spanish Ministry of Economy and Competitiveness, through the *Severo Ochoa Programme for Centres of Excellence in R&D* (CEX2018-000797-S), is gratefully acknowledged.

The authors also acknowledge the financial support provided by the Spanish Ministry of Economy via the *ADaMANT* project (DPI2017-85998-P): Computational Framework for Additive Manufacturing of Titanium Alloy, as well as the support provided by the Spanish Ministry of Education to Mr. Gabriel Barbat via the *FPU* program.

References

[1] M. Chiumenti, M. Cervera, R. Codina, A mixed three-field FE formulation for stress accurate analysis including the incompressible limit, Comput. Methods Appl. Mech. Eng. 283 (2015) 1095–1116, https://doi.org/10.1016/j.cma.2014.08.004.
[2] T.J.R. Hughes, Equivalence of finite elements for nearly incompressible elasticity, Trans. ASME, J. Appl. Mech. 44 (1) (1977) 181–183.
[3] T.J.R. Hughes, The Finite Element Method: Linear Static and Dynamic Finite Element Analysis, Prentice-Hall, Englewood Cliffs, New Jersey, 1987.
[4] T.J.R. Hughes, Generalization of selective integration procedure to anisotropic and nonlinear media, Internat. J. Numer. Methods Engrg. 15 (1) (1980) 1413–1418.
[5] D.S. Malkus, T.J.R. Hughes, Mixed finite element methods - reduced and selective integration techniques: a unification of concepts, Comput, Methods Appl. Mech. Engrg. 15 (1) (1978) 68–81.
[6] E.A. de Souza Neto, D. Peric, M. Dutko, D.R.J. Owen, Design of simple low order finite elements for large strain analysis of nearly incompressible solids, Int. J. Solid Struct. 33 (20–22) (1996) 3277–3296.
[7] E.A. de Souza Neto, F.M. Andrade Pires, D.R.J. Owen, F-bar-based linear triangles and tetrahedra for finite strain analysis of nearly incompressible solids. Part I: formulation and benchmarking, Internat. J. Numer. Methods Engrg. 62 (3) (2005) 353–383.
[8] Y. Onishi, R. Iida, K. Amaya and, F-bar aided edge-based smoothed finite element method using tetrahedral elements for finite deformation analysis of nearly incompressible solids, Internat. J. Numer. Methods Engrg. 109 (11) (2017) 1582–1606.
[9] L. de Vivo, F. Marotti de Sciarra, The B-bar method and the limitation principles, Int. J. Solid Struct. 36 (34) (1999) 5177–5206.
[10] E.A. de Souza Neto, D. Peric, G.C. Huang, D.R.J. Owen, Remarks on the stability of enhanced strain elements in finite elasticity and elastoplasticity, Commun. Numer. Methods Eng. 11 (11) (1995) 951–961.
[11] A. Krischok, C. Linder, On the enhancement of low-order mixed finite element methods for the large deformation analysis of diffusion in solids, Internat. J. Numer. Methods Engrg. 106 (4) (2016) 278–297.
[12] J.C. Simo, M.S. Rifai, A class of mixed assumed strain methods and the method of incompatible modes, Internat. J. Numer. Methods Engrg. 29 (8) (1990) 1595–1638.
[13] I. Babuška, Error-bounds for finite element method, Numer. Math. 16 (4) (1971) 322–333.
[14] F. Brezzi, M. Fortin, first ed., Mixed and Hybrid Finite Element Methods, vol. 15, Springer, New York, 1991. Springer Series in Computational Mathematics.
[15] R. Codina, Stabilization of incompressibility and convection through orthogonal sub-scales in finite element methods, Comput. Methods Appl. Mech. Eng. 190 (2000) 1579–1599.
[16] L.P. Franca, T.J.R. Hughes, Two classes of mixed finite element methods, Comput. Methods Appl. Mech. Eng. 69 (1) (1988) 89–129.
[17] T.J.R. Hughes, L.P. Franca, M. Balestra, A new finite element formulation for computational fluid dynamics: V. Circumventing the Babuška-Brezzi condition: a stable Petrov–Galerkin formulation of the Stokes problem accommodating equal-order interpolations, Comput. Methods Appl. Mech. Eng. 59 (1) (1986) 85–99.
[18] L.P. Franca, T.J.R. Hughes, A.F.D. Loula, I. Miranda, A new family of stable elements for nearly incompressible elasticity based on a mixed Petrov-Galerkin finite element formulation, Numer. Math. 53 (1988) 123–141.
[19] T.J.R. Hughes, L.P. Franca, A new finite element formulation for computational fluid dynamics: VII. The Stokes problem with various well-posed boundary conditions: symmetric formulations that converge for all velocity/pressure spaces, Comput. Methods Appl. Mech. Eng. 65 (1) (1987) 85–96.
[20] A.M. Maniatty, Y. Liu, O. Klaas, M.S. Shephard, Stabilized finite element method for viscoplastic flow: formulation and a simple progressive solution strategy, Comput. Methods Appl. Mech. Eng. 190 (35–36) (2001) 4609–4625.
[21] A.M. Maniatty, Y. Liu, Stabilized finite element method for viscoplastic flow: formulation with state variable evolution, Internat. J. Numer. Methods Engrg. 56 (2) (2003) 185–209.
[22] J. Liu, A.L. Marsden, A unified continuum and variational multiscale formulation for fluids, solids, and fluid–structure interaction, Comput. Methods Appl. Mech. Eng. 337 (2018) 549–597.
[23] S. Rossi, N. Abboud, G. Scovazzi, Implicit finite incompressible elastodynamics with linear finite elements: a stabilized method in rate form, Comput. Methods Appl. Mech. Eng. 311 (2016) 208–249.
[24] G. Scovazzi, B. Carnes, X. Zeng, S. Rossi, A simple, stable, and accurate linear tetrahedral finite element for transient, nearly, and fully incompressible solid dynamics: a dynamic variational multiscale approach, Int. J. Numer. Methods Eng. 106 (2016) 799–839.
[25] G. Scovazzi, T. Song, X. Zeng, A velocity/stress mixed stabilized nodal finite element for elastodynamics: analysis and computations with strongly and weakly enforced boundary conditions, Comput. Methods Appl. Mech. Eng. 325 (2017) 532–576.
[26] X. Zeng, G. Scovazzi, N. Abboud, O. Colomés, S. Rossi, A dynamic variational multiscale method for viscoelasticity using linear tetrahedral elements, Int. J. Numer. Methods Eng. 112 (2017) 1951–2003.
[27] J. Bonet, A.J. Gil, R. Ortigosa, A computational framework for polyconvex large strain elasticity, Comput. Methods Appl. Mech. Eng. 283 (2015) 1061–1094.
[28] A.M. Maniatty, Y. Liu, O. Klaas, M.S. Shephard, Higher order stabilized finite element method for hyperelastic finite deformation, Comput. Methods Appl. Mech. Eng. 191 (13–14) (2002) 1491–1503.
[29] A. Masud, T.J. Truster, A framework for residual-based stabilization of incompressible finite elasticity: stabilized formulations and methods for linear triangles and tetrahedra, Comput. Methods Appl. Mech. Eng. 267 (2013) 359–399.
[30] J. Schröder, P. Wriggers, D. Balzania, A new mixed finite element based on different approximations of the minors of deformation tensors, Comput. Methods Appl. Mech. Eng. 200 (2011) 49–52.
[31] C. Agelet de Saracibar, M. Chiumenti, Q. Valverde, M. Cervera, On the orthogonal subgrid scale pressure stabilization of small and finite deformation J2 plasticity, Comput. Methods Appl. Mech. Eng. 195 (2006) 1224–1251.
[32] M. Cervera, M. Chiumenti, Q. Valverde, C. Agelet de Saracibar, Mixed linear/linear simplicial elements for incompressible elasticity and plasticity, Comput. Methods Appl. Mech. Eng. 192 (2003) 5249–5263.
[33] M. Cervera, M. Chiumenti, C. Agelet de Saracibar, Softening, localization and stabilization: capture of discontinuous solutions in J2 plasticity, Int. J. Num. Anal. Meth. Geomechanics 28 (2004) 373–393.
[34] M. Cervera, M. Chiumenti, C. Agelet de Saracibar, Shear band localization via local J_2 continuum damage mechanics, Comput. Methods Appl. Mech. Eng. 193 (2004) 849–880.
[35] M. Cervera, M. Chiumenti, Size effect and localization in J_2 plasticity, Int. J. Solid Struct. 46 (2009) 3301–3312.
[36] M. Chiumenti, Q. Valverde, C. Agelet de Saracibar, M. Cervera, A stabilized formulation for incompressible elasticity using linear displacement and pressure interpolations, Comput. Methods Appl. Mech. Eng. 191 (2002) 5253–5264.
[37] M. Chiumenti, Q. Valverde, C. Agelet de Saracibar, M. Cervera, A stabilized formulation for incompressible plasticity using linear triangles and tetrahedra, Int. J. Plast. 20 (2004) 1487–1504.
[38] J. Bonet, A.J. Burton, A simple average nodal pressure tetrahedral element for incompressible and nearly incompressible dynamic explicit applications, Commun. Numer. Methods Eng. 14 (5) (1998) 437–449.
[39] J. Bonet, H. Marriott, O. Hassan, Stability and comparison of different linear tetrahedral formulations for nearly incompressible explicit dynamic applications, Internat. J. Numer. Methods Engrg. 50 (1) (2001) 119–133.
[40] M. Cervera, M. Chiumenti, R. Codina, Mixed stabilized finite element methods in nonlinear solid mechanics. Part I: formulation, Comput. Methods Appl. Mech. Eng. 199 (2010) 2559–2570.

[41] C.R. Dohrmann, M.W. Heinstein, J. Jung, S.W. Key, W.R. Witkowski, Node-based uniform strain elements for three-node triangular and four-node tetrahedral meshes, Internat. J. Numer. Methods Engrg. 47 (9) (2000) 1549–1568.
[42] M.W. Gee, C.R. Dohrmann, S.W. Key, W.A. Wall, A uniform nodal strain tetrahedron with isochoric stabilization, Internat. J. Numer. Methods Engrg. 78 (4) (2009) 429–443.
[43] M.A. Puso, J. Solberg, A stabilized nodally integrated tetrahedral, Internat. J. Numer. Methods Engrg. 67 (6) (2006) 841–867.
[44] N. Lafontaine, R. Rossi, M. Cervera, M. Chiumenti, Explicit mixed strain-displacement finite element for dynamic geometrically non-linear solid mechanics, Comput. Mech. 55 (2015) 543–559.
[45] L. Benedetti, M. Cervera, M. Chiumenti, Stress-accurate mixed FEM for soil failure under shallow foundations involving strain localization in plasticity, Comput. Geotech. 64 (2015) 32–47, https://doi.org/10.1016/j.compgeo.2014.10.004.
[46] M. Cervera, M. Chiumenti, L. Benedetti, Codina, Mixed stabilized finite element methods in nonlinear solid mechanics. Part III: compressible and incompressible plasticity, Comput. Methods Appl. Mech. Eng. 285 (2015) 752–775, https://doi.org/10.1016/j.cma.2014.11.040.
[47] M. Cervera, N. Lafontaine, R. Rossi, M. Chiumenti, Explicit mixed strain-displacement finite elements for compressible and quasi-incompressible elasticity and plasticity, Comput. Mech. 58 (3) (2016) 511–532, https://doi.org/10.1007/s00466-016-1305-z.
[48] N. Lafontaine, R. Rossi, M. Cervera, Chiumenti, Formulación mixta estabilizada explícita de elementos finitos para sólidos compresibles y quasi-incompresibles, Rev. Int. Métodos Numéricos Cálculo Diseño Ing. (2015) 169.
[49] M. Cervera, M. Chiumenti, R. Codina, Mixed stabilized finite element methods in nonlinear solid mechanics. Part II: strain localization, Comput. Methods Appl. Mech. Eng. 199 (2010) 2571–2589.
[50] M. Cervera, M. Chiumenti, Codina, Mesh objective modeling of cracks using continuous linear strain and displacement interpolations, Int. J. Numer. Methods Eng. 87 (2011) 962–987, https://doi.org/10.1002/nme.3148.
[51] L. Benedetti, M. Cervera, M. Chiumenti, High-fidelity prediction of crack formation in 2D and 3D pullout tests, Comput. Struct. 172 (2016) 93–109, https://doi.org/10.1016/j.compstruc.2016.05.001.
[52] L. Benedetti, M. Cervera, M. Chiumenti, 3D numerical modelling of twisting cracks under bending and torsion of skew notched beams, Eng. Fract. Mech. 176 (2017) 235–256, https://doi.org/10.1016/j.engfracmech.2017.03.025.
[53] M. Cervera, G.B. Barbat, M. Chiumenti, Finite element modeling of quasi-brittle cracks in 2D and 3D with enhanced strain accuracy, Comput. Mech. 60 (2017) 767–796, https://doi.org/10.1007/s00466-017-1438-8.
[54] B.D. Coleman, W. Noll, The thermodynamics of elastic materials with heat conduction and viscosity, Arch Ration Mech 13 (1) (1963) 167–178.
[55] J.C. Simo, T.J.R. Hughes, Computational Inelasticity, Springer-Verlag New York, 1998, ISBN: 978-0-387-97520-7.
[56] M. Cervera, M. Chiumenti, Smeared crack approach: back to the original track, Int. J. Numer. Anal. Methods GeoMech. 30 (12) (2006) 1173–1199.
[57] S. Badia, R. Codina, Unified stabilized finite element formulations for the Stokes and the Darcy problems, SIAM J. Numer. Anal. 17 (2009) 309–330.
[58] R. Codina, Finite element approximation of the three field formulation of the Stokes problem using arbitrary interpolations, SIAM J. Numer. Anal. 47 (2009) 699–718.
[59] E. Castillo, R. Codina, Variational multi-scale stabilized formulations for the stationary three-field incompressible viscoelastic flow problem, Comput. Methods Appl. Mech. Eng. 279 (2014) 579–605.
[60] J. Baiges, R. Codina, Variational Multiscale error estimators for solid mechanics adaptive simulations: an Orthogonal Subgrid Scale approach, Comput. Methods Appl. Mech. Eng. 325 (2017) 37–55.
[61] C. Bayona, R. Codina, J. Baiges, Variational Multiscale error estimators for the adaptive mesh refinement of compressible flow, Comput. Methods Appl. Mech. Eng. 337 (2018) 501–526, https://doi.org/10.1016/j.cma.2018.03.010.
[62] D.D. dos Santos, S. Frey, M.F. Naccache, P.R. de Souza Mendes, Numerical approximations for flow of viscoplastic fluids in a lid-driven cavity, J. Non-Newtonian Fluid Mech. 166 (12–13) (2011) 667–679.
[63] T.C. Papanastasiou, Flows of materials with yield, J. Rheol. 31 (1987) 385–404.
[64] R.I. Tanner, J.F. Milthorpe, Numerical simulation of the flow of fluids with yield stresses, in: C. Taylor, J.A. Johnson, W.R. Smith (Eds.), Proceedings of the Third International Conference on Numerical Methods in Laminar and Turbulent Flow, 1983, pp. 680–690. Swansea, UK.
[65] M. Cervera, C. Agelet de Saracibar, M. Chiumenti, COMET: COupled MEchanical and Thermal Analysis. Data Input Manual, 2002. Technical report IT-308, htpp://www.cimne.upc.es Version 5.0.
[66] A. Coll, R. Ribó, M. Pasenau, E. Escolano, J.Suit Perez, A. Melendo, A. Monros, J. Gárate, GiD v.13 Reference Manual, 2016. CIMNE htpp://www.gidhome.com.
[67] R. Hill, The Mathematical Theory of Plasticity, Oxford University Press, 1950.
[68] E. Moreno, A. Larese, M. Cervera, Modeling of Bingham and Herschel-Bulkley flows with mixed stabilized P1/P1 finite elements using orthogonal subgrid scales, J. Non-Newtonian Fluid Mech. 228 (2016) 1–16, https://doi.org/10.1016/j.jnnfm.2015.12.005.

A.3 Paper 3

Title: Accurate thermal-induced structural failure analysis under incompressible conditions.

Authors:

- **C. A. Moreira**: PhD Candidate in Civil Engineering in UPC BarcelonaTech and International Center for Numerical Methods in Engineering (CIMNE).
- **G. B. Barbat**: Associate Lecturer of Continuum Mechanics and Structural analysis at the Universitat Politècnica de Catalunya (Technical University of Catalonia BarcelonaTech). Post-doctoral Researcher at the International Center for Numerical Methods in Engineering (CIMNE).
- **M. Cervera**: Full Professor of Continuum Mechanics and Structural analysis at the Universitat Politècnica de Catalunya (Technical University of Catalonia BarcelonaTech). Affiliated Scientist at the International Center for Numerical Methods in Engineering (CIMNE).
- **M. Chiumenti**: Full Professor of Continuum Mechanics and Structural analysis at the Universitat Politècnica de Catalunya (Technical University of Catalonia BarcelonaTech). Affiliated Scientist at the International Center for Numerical Methods in Engineering (CIMNE).

Engineering Structures
Editor-in-Chief: S. J. Dyke
ISSN: 0141-0296
Elsevier Editors
https://doi.org/10.1016/j.engstruct.2022.114213
Link to Publisher

Engineering Structures 261 (2022) 114213

Contents lists available at ScienceDirect

Engineering Structures

journal homepage: www.elsevier.com/locate/engstruct

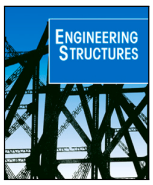

Accurate thermal-induced structural failure analysis under incompressible conditions

Carlos A. Moreira *, Gabriel B. Barbat, Miguel Cervera, Michele Chiumenti

International Center for Numerical Methods in Engineering (CIMNE), Technical University of Catalonia, Edificio C1, Campus Norte, Gran Capitán s/n, 08034 Barcelona, Spain

A B S T R A C T

In this work, the performance of the mixed 3-field *displacement/deviatoric-strain/pressure* ($\mathbf{u}/\mathbf{e}/p$) finite element is examined for nonlinear thermo-mechanical structural applications under incompressible behavior. The proposed FE model increases the solution accuracy in terms of strains and stresses, guaranteeing mesh-objective results in nonlinear analyses. Structural failure is modelled with J2-plasticity and J2-damage constitutive laws, introducing the isochoric behavior, typical of metals, in the material response. The solution of the coupled thermal and mechanical problems follows a staggered scheme and temperature dependent material properties are introduced to study the effect of the thermal coupling in the mechanical problem. This FE approach is applicable with any interpolation basis: triangles, quadrilaterals, tetrahedras, hexahedras and prisms.

A set of numerical benchmark problems is proposed to examine the influence of the enhanced accuracy of the proposed model in thermally-induced structural failure analyses in incompressible conditions. The study includes the comparison of the $\mathbf{u}/\mathbf{e}/p$ and $\mathbf{u}/p$ FE formulations, where the effect of the thermal coupling in the problem is investigated. The superior performance of the 3-field formulation with regard to the evaluation of collapse mechanisms, failure loads, mechanical dissipation and numerical stability in incompressible situations is shown.

1. Introduction

Isochoric behavior in solid mechanics can be found in situations with incompressible elasticity, such as rubber-like materials, or undrained saturated porous media; also, in nonlinear constitutive laws with isochoric flow, such as plasticity models using the Von Mises yield criterion typical for metals. In the latter case, the standard displacement-based formulation [1] fails to solve these incompressible situations, resulting in an almost completely locked solution, due to numerical difficulties caused by the volumetric constraints and spurious pressure oscillations [2–4].

To avoid or reduce the volumetric locking in these situations, several numerical strategies have been proposed in the literature. These are based on the use of mixed formulations [5–11], enhanced assumed strains methods [3,4,12–14], nodal pressure and strain averaging [15–19]; and reduced and selective integration [20–22]. Within the mixed approaches, the displacement/pressure ($\mathbf{u}/p$) FE has become a widespread method to solve incompressibility both in solid and fluid mechanics.

Recently, the authors have proposed the use of the mixed stress/displacement ($\boldsymbol{\sigma}/\mathbf{u}$) and strain/displacement ($\boldsymbol{\epsilon}/\mathbf{u}$) finite element formulations to increase the accuracy of the computed solution in terms of stresses and strains [23–32]. This increase in the precision of the calculations has proven to be crucial to obtain mesh objective results in structural failure problems [24,28,29]. In nonlinear applications, the $\boldsymbol{\epsilon}/\mathbf{u}$ FE is preferred over the $\boldsymbol{\sigma}/\mathbf{u}$ because it allows to readily implement and adopt the constitutive laws usually considered in solid mechanics, which are defined in strain-driven format.

In view of this, the 3-field displacements/deviatoric-stress/pressure $\mathbf{u}/\mathbf{s}/p$ and the displacement/deviatoric-strain/pressure $\mathbf{u}/\mathbf{e}/p$ FEs have been proposed to address incompressible problems with enhanced accuracy compared to the mixed displacement/pressure $\mathbf{u}/p$ FEs commonly adopted in isochoric problems [33–36]. These three methods require the constitutive equation split into its volumetric and deviatoric components.

Alternatively, the use of an $\boldsymbol{\epsilon}$/B-bar method has been proposed, showing a better accuracy with respect to the standard B-bar approach also commonly adopted to solve nearly incompressible problems [10,20–22]. These strategies present the advantage of not requiring the split of the constitutive equation in volumetric and deviatoric parts. Notwithstanding, this approach is unfit for the elastic incompressible limit ($\nu = 0.5$) and can be used only in the near incompressible limit. Also, they present the limitation of being restricted to quadrilaterals and hexahedral elements.

* Corresponding author.
E-mail addresses: carlos.augusto.moreira.filho@upc.edu (C.A. Moreira), gabriel.barbat@upc.edu (G.B. Barbat), miguel.cervera@upc.edu (M. Cervera), michele.chiumenti@upc.edu (M. Chiumenti).

https://doi.org/10.1016/j.engstruct.2022.114213
Received 20 December 2021; Received in revised form 18 March 2022; Accepted 27 March 2022
Available online 30 April 2022

Table 1
FE and their applicability.

	Standard ($\mathbf{u}$)	B-bar	$\mathbf{u}/p$	$\boldsymbol{\sigma}/u$	$\boldsymbol{\epsilon}/\mathbf{u}$	$\boldsymbol{\epsilon}$/B-bar	$\mathbf{u}/\mathbf{s}/p$	$\mathbf{u}/\mathbf{e}/p$
References	[1]	[20–22]	[5–11]	[28]	[23–27,29–31]	[10]	[34]	[33,35]
Incompressibility	✘	✓*	✓	✘	✘	✓*	✓	✓
Strain-driven constitutive laws	✓	✓	✓	✘	✓	✓	✘	✓
Avoids the split of constitutive equations	✓	✓	✘	✓	✓	✓	✘	✘
Higher stress/strain accuracy	✘	✘	✘	✓	✓	✓	✓	✓
General interpolation basis (triangles, quadrilaterals, tetrahedras, hexahedras, prisms)	✓	✘	✓	✓	✓	✘	✓	✓

Table 1 summarizes the advantages and disadvantages of these alternative formulations. The superscript (*) in the B-bar and $\boldsymbol{\epsilon}$/B-bar methods indicates that they are not apt for fully incompressible problems and are used for near incompressibility only.

In our previous work [35] it was shown that, when considering incompressibility, the mixed displacement/deviatoric-strain/pressure $\mathbf{u}/\mathbf{e}/p$ formulation allows for a better evaluation of stresses, strains and mechanical dissipation than the mixed displacement/pressure $\mathbf{u}/p$ element and that a spurious overestimation of the mechanical dissipation in nonlinear analyses takes place with the $\mathbf{u}/p$ FE.

Mixed finite elements have been extensively used to solve problems involving softening behavior in damage and plasticity, strain localization and size-effect [27–29,32,37–41], but few studies, so far, have been conducted considering non-isothermal behavior [42–45].

Saloustros et al. (2021) [10] detail the advantages of using mixed solid elements to address typical plate, beam and shell problems; among them: this approach does not require additional kinematical hypotheses (planar sections; shear stress and warping through the thickness); does not pose compatibility problems between different elements used by the structural model; can easily accommodate construction details (e.g., web-perforated steel beams, layered elements, element-stiffeners); does not require rotational degrees of freedom and awkward boundary condition alternatives (e.g., “soft” and “hard” supports). In the specific case of thermal loading, no additional assumptions need to be made about the through thickness temperature distribution.

Alternatively, the Carrera Unified Formulation (CUF) [46] has been applied to solve different multifield problems in multilayered structures using beam, plates and shell elements. The CUF has been used with thermal loads [47], thermo-elastic coupling [48,49], piezoelectric structures [50,51] and a complete multifield formulation has been proposed [52,53].

The interest in solving coupled thermo-mechanical problems arises from engineering applications where temperature-dependency of the mechanical properties is relevant as, for instance, on the fire analysis of structures, manufacturing processes (casting, welding, additive manufacturing, etc.), aerospace industry, turbines and high-speed civil transport industry [54]. Specifically, in structural failure problems, the presence of an external heat source and/or the mechanical dissipation that takes place during the process may produce an increase in the temperature field that significantly influences the observed nonlinear behavior of the material.

For these reasons, this work focuses on the accurate analysis of thermally-coupled structural failure under isochoric conditions. The computation of the coupled thermal and mechanical problems is made following a staggered approach. The mixed $\mathbf{u}/\mathbf{e}/p$ FE formulation is employed to solve the mechanical problem, with the aim of increasing the accuracy of the computed stresses, strains and mechanical dissipation and to obtain mesh-objective results. Structural failure is modelled using J2-damage and J2-plasticity constitutive laws, introducing an incompressible behavior in the material nonlinear response. The thermal problem is solved using an implicit Euler method and temperature-dependent material properties are considered in the analysis. A comparison of the performance of the 3-field formulation with the $\mathbf{u}/p$ element is introduced to assess the advantages of the proposed model.

The objectives of this paper are: (1) to extend the mixed $\mathbf{u}/\mathbf{e}/p$ formulation to address the incompressible limit and isochoric constitutive laws in thermo-mechanical applications; (2) to investigate the influence of temperature-dependent parameters in thermo-mechanical failure; (3) to assess the enhanced accuracy of the 3-field ($\mathbf{u}/\mathbf{e}/p$) over the mixed $\mathbf{u}/p$ in thermo-mechanical analyses.

Therefore, the paper is organized as follows. Section 2 addresses the mixed $\mathbf{u}/\mathbf{e}/p$ strong and weak forms, as well as the resulting FE formulation. In Section 3 the coupling between the thermal and mechanical problems is introduced. In Section 4 the constitutive models adopted in the numerical examples, isotropic J2-damage and J2-plasticity, are summarized. In Section 5 several numerical simulations are presented to compare the performance and accuracy of the 3-field formulation with respect to the $\mathbf{u}/p$ FE in thermo-mechanical problems. Finally, Section 6 presents the concluding remarks.

2. Mixed 3-field ($\mathbf{u}/\mathbf{e}/p$) mechanical problem

2.1. Volumetric/deviatoric split

Using Voigt’s notation, in 3D, the displacement $\mathbf{u} = (u, v, w)^T$ is a vector of 3 components and the stress $\boldsymbol{\sigma} = (\sigma_x, \sigma_y, \sigma_z, \tau_{xy}, \tau_{yz}, \tau_{xz})^T$ and the strain $\boldsymbol{\epsilon} = (\epsilon_x, \epsilon_y, \epsilon_z, \epsilon_{xy}, \epsilon_{yz}, \epsilon_{xz})^T$ are vectors of 6 components.

The constitutive equation relates the stress vector σ and the strain vector $\boldsymbol{\epsilon}$

$$\boldsymbol{\sigma} = \mathbf{C}\boldsymbol{\epsilon} \tag{1}$$

where $\mathbf{C}$ is the fourth-order secant constitutive tensor expressed in Voigt’s notation as a 6×6 matrix. In this work, the nonlinear mechanical behavior is introduced through the adoption of the J2-damage and J2-plasticity constitutive laws, presented in Section 4. These establish the nonlinear relation between stresses and strains followed by the material and define the corresponding secant constitutive matrix $\mathbf{C}$.

Herein, the volumetric/deviatoric split of the stresses and strains is introduced, respectively as:

$$\boldsymbol{\sigma} = p\mathbf{I} + \mathbf{s} \tag{2}$$

$$\boldsymbol{\epsilon} = \frac{1}{3} e_{vol}\mathbf{I} + \mathbf{e} \tag{3}$$

where $\mathbf{I} = (1, 1, 1, 0, 0, 0)^T$ is the second-order identity tensor in Voigt’s notation, p is the pressure, which is a scalar, and $\mathbf{s}$ is the deviatoric-stress vector

$$p = \frac{1}{3}(\sigma_x + \sigma_y + \sigma_z) \tag{4}$$

$$\mathbf{s} = (\sigma_x - p, \sigma_y - p, \sigma_z - p, \tau_{xy}, \tau_{yz}, \tau_{xz})^T \tag{5}$$

also, e_{vol} is the volumetric strain (scalar), and $\mathbf{e}$ is the deviatoric-strain vector, defined as

$$e_{vol} = (\epsilon_x + \epsilon_y + \epsilon_z) = \mathbf{G}^T\mathbf{u} \tag{6}$$

$$\mathbf{e} = (\varepsilon_x - \frac{1}{3}e_{vol}, \varepsilon_y - \frac{1}{3}e_{vol}, \varepsilon_z - \frac{1}{3}e_{vol}, \varepsilon_{xy}, \varepsilon_{yz}, \varepsilon_{xz})^T \tag{7}$$

e_{vol} can be computed as the divergence of the displacements $\mathbf{u}$ where $\mathbf{G} = (\partial_x, \partial_y, \partial_z)^T$ is the gradient operator and $\mathbf{G}^T$ is the adjoint divergence operator.

The volumetric/deviatoric split is also applied to the constitutive relationship:

$$p = C^{vol} e_{vol} \tag{8}$$

$$\mathbf{s} = \mathbf{C}^{dev}\mathbf{e} \tag{9}$$

where C^{vol} is defined as $C^{vol} = \frac{1}{9}\mathbf{I}^T\mathbf{C}\mathbf{I}$ and $\mathbf{C}^{dev}$ is the deviatoric secant constitutive matrix.

Note that

$$\mathbf{s} = \mathbf{C}^{dev}\boldsymbol{\varepsilon} \tag{10}$$

Let $\mathbf{J}$ be the fourth-order identity tensor, expressed following Voigt's notation as a 6×6 identity matrix

$$\mathbf{J} = \begin{bmatrix} 1 & 0 & 0 & 0 & 0 & 0 \\ 0 & 1 & 0 & 0 & 0 & 0 \\ 0 & 0 & 1 & 0 & 0 & 0 \\ 0 & 0 & 0 & 1 & 0 & 0 \\ 0 & 0 & 0 & 0 & 1 & 0 \\ 0 & 0 & 0 & 0 & 0 & 1 \end{bmatrix} \tag{11}$$

and the volumetric and deviatoric fourth-order operators, $\mathbf{V}$ and $\mathbf{Y}$, respectively, are introduced in Voigt's notation as

$$\mathbf{V} = \frac{1}{3}\mathbf{I}\mathbf{I}^T = \frac{1}{3}\begin{bmatrix} 1 & 1 & 1 & 0 & 0 & 0 \\ 1 & 1 & 1 & 0 & 0 & 0 \\ 1 & 1 & 1 & 0 & 0 & 0 \\ 0 & 0 & 0 & 0 & 0 & 0 \\ 0 & 0 & 0 & 0 & 0 & 0 \\ 0 & 0 & 0 & 0 & 0 & 0 \end{bmatrix} \tag{12}$$

$$\mathbf{Y} = \mathbf{J} - \mathbf{V} = \frac{1}{3}\begin{bmatrix} 2 & -1 & -1 & 0 & 0 & 0 \\ -1 & 2 & -1 & 0 & 0 & 0 \\ -1 & -1 & 2 & 0 & 0 & 0 \\ 0 & 0 & 0 & 3 & 0 & 0 \\ 0 & 0 & 0 & 0 & 3 & 0 \\ 0 & 0 & 0 & 0 & 0 & 3 \end{bmatrix} \tag{13}$$

For the case of isotropic materials, C^{vol} and $\mathbf{C}^{dev}$ in Eqs. (8) and (9) can be written as

$$C^{vol} = K \tag{14}$$

$$\mathbf{C}^{dev} = \mathbf{Y}\mathbf{C} = 2G\mathbf{Y} \tag{15}$$

where K is the secant bulk modulus and G is the secant shear modulus.

This leads to the following constitutive relationships:

$$p = Ke_{vol} \tag{16}$$

$$\mathbf{s} = 2G\mathbf{e} \tag{17}$$

2.2. Strong form

The strong form of the nonlinear solid mechanics problem is written in terms of the displacement $\mathbf{u}$, deviatoric-strain $\mathbf{e}$, and pressure p fields. The displacement $\mathbf{u}$ and the total strains $\boldsymbol{\varepsilon}$ are related through the compatibility equation

$$\boldsymbol{\varepsilon} = \mathbf{S}\mathbf{u} \tag{18}$$

where $\mathbf{S}$ is the differential symmetric gradient operator

$$\mathbf{S} = \begin{bmatrix} \partial_x & 0 & 0 & \partial_y & 0 & \partial_z \\ 0 & \partial_y & 0 & \partial_x & \partial_z & 0 \\ 0 & 0 & \partial_z & 0 & \partial_y & \partial_x \end{bmatrix}^T \tag{19}$$

Equilibrium between the stress vector $\boldsymbol{\sigma}$ and the body forces $\mathbf{f} = (f_x, f_y, f_z)^T$ is defined by the Cauchy equation

$$\mathbf{S}^T\boldsymbol{\sigma} + \mathbf{f} = \mathbf{0} \tag{20}$$

where $\mathbf{S}^T$ is the differential divergence operator, adjoint to the $\mathbf{S}$ in Eq. (18).

Introducing the split of the strains, Eqs. (3) and (6), in Eq. (18), leads to

$$\mathbf{e} = \mathbf{S}\mathbf{u} - \frac{1}{3}\mathbf{I}\underbrace{(\mathbf{G}^T\mathbf{u})}_{e_{vol}} = \mathbf{W}\mathbf{u} \tag{21}$$

where $\mathbf{W}$ is the operator defined as

$$\mathbf{W} = \mathbf{S} - \frac{1}{3}\mathbf{I}\mathbf{G}^T = \frac{1}{3}\begin{bmatrix} 2\partial_x & -\partial_x & -\partial_x & 3\partial_y & 0 & 3\partial_z \\ -\partial_y & 2\partial_y & -\partial_y & 3\partial_x & 3\partial_z & 0 \\ -\partial_z & -\partial_z & 2\partial_z & 0 & 3\partial_y & 3\partial_x \end{bmatrix}^T \tag{22}$$

Note that $\mathbf{W} = \mathbf{Y}\mathbf{S}$.

Next, introducing Eqs. (2) and (9) in Eq. (20), where the identity $\mathbf{S}^T\mathbf{I} = \mathbf{G}$ is used, and Eq. (6) in Eq. (8), the continuous strong form of the mixed $\mathbf{u}/\mathbf{e}/p$ formulation is

$$\begin{aligned} \mathbf{S}^T(\mathbf{C}^{dev}\mathbf{e}) + \mathbf{G}p + \mathbf{f} &= \mathbf{0} \\ \mathbf{W}\mathbf{u} - \mathbf{e} &= \mathbf{0} \\ \mathbf{G}^T\mathbf{u} - \frac{p}{C^{vol}} &= 0 \end{aligned} \tag{23}$$

together with the prescribed mechanical boundary conditions. The boundary Γ can be split according to the Dirichlet and Newman conditions imposed, respectively as Γ_u and Γ_t, such that $\Gamma = \Gamma_u \cup \Gamma_t$ and $\Gamma_u \cap \Gamma_t = \varnothing$.

It is assumed herein that the prescribed displacements vanish on the boundary Γ_u

$$\mathbf{u} = \mathbf{0} \text{ in } \Gamma_u \tag{24}$$

In addition, the prescribed traction on the boundary Γ_t are

$$\mathbf{t} = \bar{\mathbf{t}} \text{ in } \Gamma_t \tag{25}$$

2.3. Weak form

The variational form of the problem in Eqs. (23) is then obtained as follows.

Firstly, Eq. (23)a is premultiplied by an arbitrary virtual displacement $\delta\mathbf{u}$ and integrated over the spatial domain:

$$\int_\Omega \delta\mathbf{u}^T[\mathbf{S}^T(\mathbf{C}^{dev}\mathbf{e})]d\Omega + \int_\Omega \delta\mathbf{u}^T[\mathbf{G}p]d\Omega + \int_\Omega \delta\mathbf{u}^T\mathbf{f}d\Omega = \mathbf{0} \qquad \forall\delta\mathbf{u} \tag{26}$$

The virtual displacement $\delta\mathbf{u}$ also conforms with the boundary conditions, so that $\delta\mathbf{u} = \mathbf{0}$ in Γ_u. Then, the Divergence Theorem is applied to the first and second terms of Eq. (26) and the boundary term is split $\Gamma = \Gamma_u \cup \Gamma_t$. The Dirichlet boundary terms vanish ($\delta\mathbf{u} = \mathbf{0}$) and, considering that $\mathbf{S}^T\mathbf{I} = \mathbf{G}$, the variational form of Eq. (26) becomes

$$\begin{aligned} \int_\Omega (\mathbf{S}\delta\mathbf{u})^T(\mathbf{C}^{dev}\mathbf{e})d\Omega + \int_\Omega (\mathbf{S}\delta\mathbf{u})^T(p\mathbf{I})d\Omega &= \int_\Omega \delta\mathbf{u}^T\mathbf{f}d\Omega + \int_{\Gamma_t} \delta\mathbf{u}^T\bar{\mathbf{t}}d\Gamma \\ &= W(\delta\mathbf{u}) \quad \forall\delta\mathbf{u} \end{aligned} \tag{27}$$

Eq. (27) is equivalent to the Principle of Virtual Work, as the right hand side term, noted $W(\delta\mathbf{u})$, is the virtual work done by the traction $\bar{\mathbf{t}}$ and body forces $\mathbf{f}$ while the left hand side constitutes the virtual work of the internal forces.

Secondly, Eq. (23)b is premultiplied by $\mathbf{C}^{dev}$ to obtain a symmetric problem and then premultiplied by an arbitrary virtual deviatoric-strain vector $\delta\mathbf{e}$ and integrated over the spatial domain

$$\int_\Omega \delta\mathbf{e}^T[\mathbf{C}^{dev}(\underbrace{\mathbf{Y}\mathbf{S}}_{=\mathbf{W}}\mathbf{u})]d\Omega - \int_\Omega \delta\mathbf{e}^T(\mathbf{C}^{dev}\mathbf{e})d\Omega = \mathbf{0} \qquad \forall\delta\mathbf{e} \tag{28}$$

Note that $\mathbf{C}^{dev}\mathbf{Y} = \mathbf{C}^{dev}$.

Thirdly, Eq. (23)*c* is premultiplied by an arbitrary virtual pressure vector δp and integrated over the spatial domain

$$\int_\Omega \delta p^T(\mathbf{G}^T\mathbf{u})d\Omega - \int_\Omega \delta p^T \frac{p}{C^{vol}} d\Omega = 0 \qquad \forall \delta p \tag{29}$$

The resulting variational form of the 3-field formulation is:

$$\begin{aligned} \textstyle\int_\Omega (\mathbf{S}\delta\mathbf{u})^T(\mathbf{C}^{dev}\mathbf{e})d\Omega + \int_\Omega (\mathbf{S}\delta\mathbf{u})^T(p\mathbf{I})d\Omega = W(\delta\mathbf{u}) \quad & \forall \delta\mathbf{u} \\ \textstyle\int_\Omega \delta\mathbf{e}^T[\mathbf{C}^{dev}(\mathbf{S}\mathbf{u})]d\Omega - \int_\Omega \delta\mathbf{e}^T(\mathbf{C}^{dev}\mathbf{e})d\Omega = \mathbf{0} \quad & \forall \delta\mathbf{e} \\ \textstyle\int_\Omega \delta p^T(\mathbf{G}^T\mathbf{u})d\Omega - \int_\Omega \delta p^T \frac{p}{C^{vol}} d\Omega = 0 \quad & \forall \delta p \end{aligned} \tag{30}$$

The solution to the mixed problem is: find the unknowns $\mathbf{u}$, $\mathbf{e}$ and p that verify the system of Eqs. (30) and comply with the boundary condition $\mathbf{u} = \mathbf{0}$ on Γ_u given the arbitrary virtual displacement $\delta\mathbf{u}$, which also vanishes on Γ_u and the arbitrary virtual deviatoric-strain and pressure $\delta\mathbf{e}$ and δp, respectively.

2.4. FE approximation

The continuous domain of the problem is discretized in a FE partition such that $\Omega = \cup\Omega_e$, and discrete FE approximations of the displacements $\mathbf{u}$, the deviatoric-strains $\mathbf{e}$ and the pressure p are taken, such that

$$\begin{aligned} \mathbf{u} &\doteq \hat{\mathbf{u}} = \mathbf{N}_u\mathbf{U} \\ \mathbf{e} &\doteq \hat{\mathbf{e}} = \mathbf{N}_e\mathbf{E} \\ p &\doteq \hat{p} = \mathbf{N}_p\mathbf{P} \end{aligned} \tag{31}$$

where $\mathbf{U}$, $\mathbf{E}$ and $\mathbf{P}$ are vectors comprising the values of the displacements, deviatoric-strains and pressures at the nodes of the finite element mesh. $\mathbf{N}_u$, $\mathbf{N}_e$ and $\mathbf{N}_p$ are the matrices containing the interpolation functions adopted in the FE approximation.

In the Galerkin method, the same approximation is taken for the discrete virtual displacements, virtual deviatoric-strains and virtual pressure, so that

$$\begin{aligned} \delta\mathbf{u} &\doteq \delta\hat{\mathbf{u}} = \mathbf{N}_u\delta\mathbf{U} \\ \delta\mathbf{e} &\doteq \delta\hat{\mathbf{e}} = \mathbf{N}_e\delta\mathbf{E} \\ \delta p &\doteq \delta\hat{p} = \mathbf{N}_p\delta\mathbf{P} \end{aligned} \tag{32}$$

Introducing these approximations, the system of Eqs. (30) becomes:

$$\begin{aligned} \textstyle\int_\Omega \underbrace{(\mathbf{S}\mathbf{N}_u\delta\mathbf{U})^T}_{=\delta\mathbf{U}^T\mathbf{B}_u^T}(\mathbf{C}^{dev}\mathbf{N}_e\mathbf{E})d\Omega + \int_\Omega (\mathbf{S}\mathbf{N}_u\delta\mathbf{U})^T(\mathbf{N}_p\mathbf{P}\mathbf{I})d\Omega = \hat{W}(\delta\mathbf{U}) \quad & \forall\delta\mathbf{U} \\ \textstyle\int_\Omega \delta\mathbf{E}^T\mathbf{N}_e^T[\mathbf{C}^{dev}\underbrace{(\mathbf{S}\mathbf{N}_u\mathbf{U})}_{=\mathbf{B}_u\mathbf{U}}]d\Omega - \int_\Omega \delta\mathbf{E}^T\mathbf{N}_e^T(\mathbf{C}^{dev}\mathbf{N}_e\mathbf{E})d\Omega = \mathbf{0} \quad & \forall\delta\mathbf{E} \\ \textstyle\int_\Omega \delta\mathbf{P}^T\mathbf{N}_p^T(\mathbf{G}^T\mathbf{N}_u\mathbf{U})d\Omega - \int_\Omega^T \delta\mathbf{P}^T\mathbf{N}_p^T\frac{\mathbf{N}_p\mathbf{P}}{C^{vol}}d\Omega = 0 \quad & \forall\delta\mathbf{P} \end{aligned} \tag{33}$$

where $\mathbf{B}_u = \mathbf{S}\mathbf{N}_u$ is the discrete strain–displacement matrix.

In Eq. (33)*a* $\hat{W}(\delta\mathbf{U})$ is the work done by the traction $\bar{\mathbf{t}}$ and body forces $\mathbf{f}$ defined as

$$\hat{W}(\delta\mathbf{U}) = \int_\Omega \delta\mathbf{U}^T\mathbf{N}_u^T\mathbf{f}d\Omega + \int_{\Gamma_t} \delta\mathbf{U}^T\mathbf{N}_u^T\bar{\mathbf{t}}d\Gamma \tag{34}$$

Note that the equality $\mathbf{G} = \mathbf{S}^T\mathbf{I}$ can be used again in the second term in Eq. (33)*a*

$$\int_\Omega (\mathbf{S}\mathbf{N}_u\delta\mathbf{U})^T(\mathbf{N}_p\mathbf{P}\mathbf{I})d\Omega = \int_\Omega \delta\mathbf{U}^T\mathbf{N}_u^T\mathbf{S}^T\mathbf{I}\mathbf{N}_p\mathbf{P}d\Omega = \int_\Omega \delta\mathbf{U}^T\mathbf{N}_u^T\mathbf{G}\mathbf{N}_p\mathbf{P}d\Omega \tag{35}$$

This shows that the resulting problem is symmetric.

The virtual displacement $\delta\mathbf{U}$, virtual deviatoric-strain $\delta\mathbf{E}$ and virtual pressure $\delta\mathbf{P}$ are arbitrary nodal vectors. Therefore, the system of Eqs. (33) can be written in matrix form as

$$\begin{bmatrix} \mathbf{0} & \mathbf{K}_{UE} & \mathbf{K}_{UP} \\ (\mathbf{K}_{UE})^T & -\mathbf{M}_{EE} & \mathbf{0} \\ (\mathbf{K}_{UP})^T & \mathbf{0} & -\mathbf{M}_{PP} \end{bmatrix} \begin{bmatrix} \mathbf{U} \\ \mathbf{E} \\ \mathbf{P} \end{bmatrix} = \begin{bmatrix} \mathbf{F} \\ \mathbf{0} \\ \mathbf{0} \end{bmatrix} \tag{36}$$

where $[\mathbf{U}\,\mathbf{E}\,\mathbf{P}]^T$ is the array of nodal values of displacements, deviatoric-strains and pressure and

$$\mathbf{M}_{EE} = \int_\Omega \mathbf{N}_e^T\mathbf{C}^{dev}\mathbf{N}_e d\Omega \tag{37}$$

$$\mathbf{M}_{PP} = \int_\Omega \mathbf{N}_p^T\frac{1}{C^{vol}}\mathbf{N}_p d\Omega \tag{38}$$

$$\mathbf{K}_{UE} = \int_\Omega \mathbf{B}_u^T\mathbf{C}^{dev}\mathbf{N}_e d\Omega \tag{39}$$

$$\mathbf{K}_{UP} = \int_\Omega \mathbf{N}_u^T\mathbf{G}\mathbf{N}_p d\Omega \tag{40}$$

and

$$\mathbf{F} = \int_\Omega \mathbf{N}_u^T\mathbf{f}d\Omega + \int_{\Gamma_t} \mathbf{N}_u^T\bar{\mathbf{t}}d\Gamma \tag{41}$$

2.5. Variational multi-scale stabilization

A crucial issue for mixed methods is stability. In order to ensure this, the mixed interpolation adopted needs to satisfy the Inf–Sup condition. However, stable combinations of interpolation spaces are problem dependent, difficult to formulate and, often, rather exotic [6,55–58].

A common strategy when using mixed FEs is to adopt equal order interpolation functions for all the proposed fields. This approach is preferred because it is far simpler to formulate and implement. However, equal order interpolation does not comply with the Inf–Sup condition [59,60] and requires the use of a stabilization method. Techniques based on the Variational Multi-Scale method (VMS) [61–63] have been used to this end. They consist on the numerical enrichment of the FE fields adding a fine scale refinement to the FE solution, which provides the discrete problem with the necessary stability. Within the VMS approach, Codina introduced the Orthogonal Subgrid-Scales (OSS) in which the fine scales are chosen orthogonal to the FE space [64–66].

The VMS technique has been successfully applied to stabilize the following mixed formulations using equal order linear approximations for all fields: displacement/pressure ($\mathbf{u}/p$); stress/displacement ($\boldsymbol{\sigma}/\mathbf{u}$); strain/displacement ($\boldsymbol{\epsilon}/\mathbf{u}$); displacement/deviatoric-stress/pressure ($\mathbf{u}/\mathbf{s}/p$); as well as the displacement/deviatoric-strain/pressure ($\mathbf{u}/\mathbf{e}/p$) FEs [25,28,29,34,67–70].

In this work, equal order linear interpolation functions are used for all unknown fields. A Variational Multiscale Stabilization procedure is adopted to circumvent the strictness of the Inf–Sup condition. The stabilization procedure modifies the discrete variational form within the framework of the VMS methods [5,62,63,65].

The idea of the VMS approach is to enhance the FE approximation of the continuous solution by adding to the discrete fields $\mathbf{u}_h$, $\mathbf{e}_h$, and p_h (from the FE space) a term $\tilde{\mathbf{u}}$, $\tilde{\mathbf{e}}$, and $\tilde{p}$ approximating the finer sub-grid scale that cannot be captured at the FE scale:

$$\begin{aligned} \mathbf{u} &\doteq \hat{\mathbf{u}} = \mathbf{u}_h + \tilde{\mathbf{u}} \\ \mathbf{e} &\doteq \hat{\mathbf{e}} = \mathbf{e}_h + \tilde{\mathbf{e}} \\ p &\doteq \hat{p} = p_h + \tilde{p} \end{aligned} \tag{42}$$

The Appendix details the derivation of the discrete stabilized formulation for the $\mathbf{u}/\mathbf{e}/p$ FEs.

The resulting stabilized FE system of equations is shown as Eq. (43) in Box I where $[\mathbf{U}\,\mathbf{E}\,\mathbf{P}]^T$ is the array of nodal values of displacements, deviatoric-strains and pressure and

$$\mathbf{K}_{UU}^{\mathbf{e}} = \int_\Omega \mathbf{B}_u^T\mathbf{C}^{dev}\mathbf{B}_u d\Omega \tag{44}$$

$$\mathbf{K}_{UU}^{p} = \int_\Omega \mathbf{N}_u^T\mathbf{G}\mathbf{G}^T\mathbf{N}_u d\Omega \tag{45}$$

$$\mathbf{K}_{EE} = \int_\Omega (\mathbf{N}_e^T\mathbf{S}\mathbf{C}^{dev})(\mathbf{C}^{dev}\mathbf{S}^T\mathbf{N}_e)d\Omega \tag{46}$$

$$\mathbf{K}_{PP} = \int_\Omega \mathbf{N}_p^T\mathbf{G}^T\mathbf{G}\mathbf{N}_p d\Omega \tag{47}$$

$$\begin{bmatrix} \tau_e \mathbf{K}^{\mathbf{e}}_{UU} + \tau_p \mathbf{K}^{p}_{UU} & (1-\tau_e)\mathbf{K}_{UE} & (1-\frac{\tau_p}{C^{vol}})\mathbf{K}_{UP} \\ (1-\tau_e)(\mathbf{K}_{UE})^T & -(1-\tau_e)\mathbf{M}_{EE} - \tau_u \mathbf{K}_{EE} & -\tau_u \mathbf{K}_{EP} \\ (1-\frac{\tau_p}{C^{vol}})(\mathbf{K}_{UP})^T & -\tau_u (\mathbf{K}_{EP})^T & -(1-\frac{\tau_p}{C^{vol}})\mathbf{M}_{PP} - \tau_u \mathbf{K}_{PP} \end{bmatrix} \begin{bmatrix} \mathbf{U} \\ \mathbf{E} \\ \mathbf{P} \end{bmatrix} = \begin{bmatrix} \mathbf{F} \\ \mathbf{0} \\ \mathbf{0} \end{bmatrix} \tag{43}$$

Box I.

$$\mathbf{K}_{EP} = \int_{\Omega} (\mathbf{N}_e^T \mathbf{S} \mathbf{C}^{dev})(\mathbf{G}\mathbf{N}_p) d\Omega \tag{48}$$

Note that the problem is symmetric and that for a converged solution (when $h \to 0$), the stabilization terms vanish. For non-converged situations these terms depend on the residual value of the system of equations. Varying the stabilization parameters τ_u, τ_e and τ_p produces slightly different results for a given FE mesh; however, the residual-based nature ensures the uniqueness of the solution upon mesh convergence. In linear problems, the optimal convergence rate is achieved using the stabilization parameters defined in Eq. (A.4) of the Appendix, which decrease on mesh refinement [71].

Finally, some remarks regarding the implementation of the formulation in FE codes are given.

Note that the $\mathbf{K}_{EE}$ and $\mathbf{K}_{EP}$ sub-matrices in Eqs. (46) and (48) can be rewritten as

$$\mathbf{K}_{EE} = \int_{\Omega} (\mathbf{B}_e \mathbf{C}^{dev})(\mathbf{C}^{dev} \mathbf{B}_e^T) d\Omega \tag{49}$$

$$\mathbf{K}_{EP} = \int_{\Omega} (\mathbf{B}_e \mathbf{C}^{dev})(\mathbf{G}\mathbf{N}_p) d\Omega \tag{50}$$

where $\mathbf{B}_e^{(i)}$ is a submatrix with an analogous structure to $\mathbf{B}_u^{(i)}$, defined for each node (i) of a given element as

$$\mathbf{B}_e^{(i)} = \mathbf{N}_e^{(i)^T} \mathbf{S} = \begin{bmatrix} \partial_x N_e^{(i)} & 0 & 0 & \partial_y N_e^{(i)} & 0 & \partial_z N_e^{(i)} \\ 0 & \partial_y N_e^{(i)} & 0 & \partial_x N_e^{(i)} & \partial_z N_e^{(i)} & 0 \\ 0 & 0 & \partial_z N_e^{(i)} & 0 & \partial_y N_e^{(i)} & \partial_x N_e^{(i)} \end{bmatrix}^T \tag{51}$$

In this work, where the same interpolation functions are used for both the displacement and the deviatoric-strain, $\mathbf{B}_e$ and $\mathbf{B}_u$ are the same.

Note also that when using the same interpolation functions for both the displacement and the pressure, the submatrix $\mathbf{N}_u^T \mathbf{G}$ is equal to the submatrix $\mathbf{G}\mathbf{N}_p$. Specifically, it can be observed that, for each node (i) of a given element:

$$\mathbf{N}_u^{(i)^T} \mathbf{G} = (\partial_x N_u^{(i)} \partial_y N_u^{(i)} \partial_z N_u^{(i)})^T \tag{52}$$

$$\mathbf{G}\mathbf{N}_p^{(i)} = (\partial_x N_p^{(i)} \partial_y N_p^{(i)} \partial_z N_p^{(i)})^T \tag{53}$$

3. Thermal problem and thermo-mechanical coupling

3.1. Strong form

The strong form of the thermal problem is written in terms of the temperature T as the energy balance equation

$$\rho c \dot{T} = -\nabla \cdot \mathbf{q} + \dot{R} + \dot{\mathcal{D}}_{mech} \; on \; \Omega \tag{54}$$

where $\dot{T}$ is the temperature time derivative, $\rho = \rho(T)$ is the temperature-dependent material density, $c = c(T)$ is the temperature-dependent specific heat capacity of the material, $\dot{R}$ represents the heat source that may be present in the problem and $\dot{\mathcal{D}}_{mech}$ is the rate of mechanical dissipation that takes place in the body, dependent on the constitutive model employed. Here, the heat flux, $\mathbf{q}$, is computed according to the Fourier law

$$\mathbf{q} = -k \nabla T \tag{55}$$

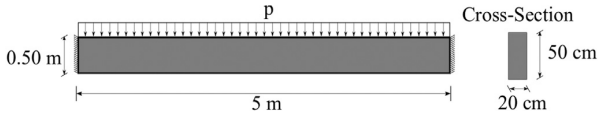

Fig. 1. Double clamped rectangular beam: Problem setting.

with $k = k(T)$ being the thermal conductivity of the material, also temperature-dependent. The left-hand side of Eq. (54) is the enthalpy rate where the heat capacity is $C = C(T) = \rho(T)c(T)$.

Introducing Eq. (55) in (54), the strong form becomes

$$C\dot{T} - \nabla \cdot (k \nabla T) = \dot{R} + \dot{\mathcal{D}}_{mech} \quad on \; \Omega \tag{56}$$

together with the prescribed thermal boundary conditions.

3.2. Weak form

Introducing δT as a virtual temperature field and integrating Eq. (56) over the domain Ω, the weak form of the energy balance is written as

$$\int_{\Omega} (\delta T C \dot{T}) d\Omega + \int_{\Omega} (k \nabla \delta T \cdot \nabla T) d\Omega = \int_{\Omega} [\delta T (\dot{R} + \dot{\mathcal{D}}_{mech})] d\Omega + \int_{\Gamma_q} (\delta T \bar{q}) d\Gamma \tag{57}$$

where the divergence theorem has been applied to the second term. The domain is closed by a smooth boundary Γ, such that $\Gamma = \Gamma_T \cup \Gamma_q$ and $\Gamma_T \cap \Gamma_q = \oslash$, where Γ_T and Γ_q are the boundaries with prescribed temperatures and fluxes respectively. It is assumed that the prescribed temperatures vanish at the boundary Γ_T. The prescribed heat fluxes in the boundary Γ_q are noted $\bar{q}$.

The initial conditions are defined in terms of the initial temperature field at $t = 0$, where $T(t = 0) = T_0$.

3.3. FE approximation

Similarly to the mechanical problem, the domain Ω is discretized in a FE partition such that $\Omega = \cup \Omega_e$, with the temperature and virtual temperature fields approximated according to the Galerkin method

$$\begin{aligned} T &\doteq \hat{T} = \mathbf{N}_T \mathbf{T} \\ \delta T &\doteq \delta \hat{T} = \mathbf{N}_T \delta \mathbf{T} \end{aligned} \tag{58}$$

where $\mathbf{T}$ and $\delta \mathbf{T}$ are the finite element nodal temperature and virtual temperature vectors, respectively, and $\mathbf{N}_T$ is the matrix containing the interpolation function adopted.

Introducing the FE discrete approximations into the continuous weak form of Eq. (57), results in

$$\begin{aligned} &\int_{\Omega} \delta \mathbf{T}^T \mathbf{N}_T^T C \mathbf{N}_T \dot{\mathbf{T}} d\Omega + \int_{\Omega} \delta \mathbf{T}^T \mathbf{N}_T^T \mathbf{G}^T k \mathbf{G}\mathbf{N}_T \mathbf{T} d\Omega \\ &= \int_{\Omega} \delta \mathbf{T}^T \mathbf{N}_T^T (\dot{R} + \dot{\mathcal{D}}_{mech}) d\Omega + \int_{\Gamma_q} (\delta \mathbf{T}^T \mathbf{N}_T^T \bar{q}) d\Gamma \; \forall \delta \mathbf{T} \end{aligned} \tag{59}$$

and the choice of the virtual field is arbitrary, thus the Galerkin approximation of Eq. (59) is

$$\int_{\Omega} \mathbf{N}_T^T C \mathbf{N}_T d\Omega \dot{\mathbf{T}} + \int_{\Omega} \mathbf{B}_T^T k \mathbf{B}_T d\Omega \mathbf{T} = \int_{\Omega} \mathbf{N}_T^T (\dot{R} + \dot{\mathcal{D}}_{mech}) d\Omega + \int_{\Gamma_q} (\mathbf{N}_T^T \bar{q}) d\Gamma$$

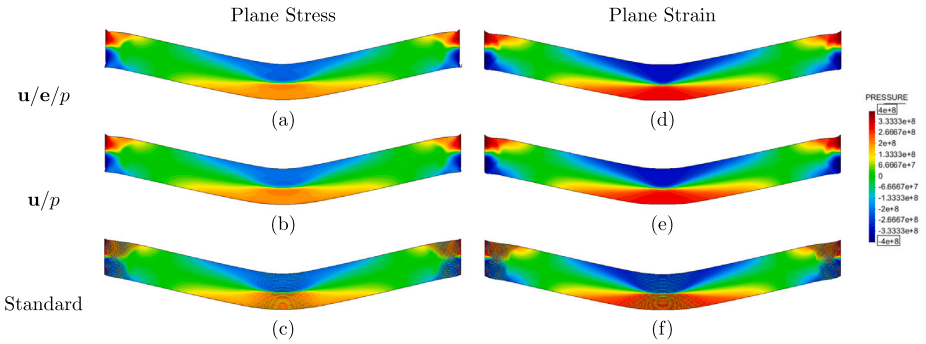

Fig. 2. Double clamped rectangular beam: Pressure in [Pa]. Plane-stress (*a*)–(*c*). Plane-strain (*d*)–(*f*).

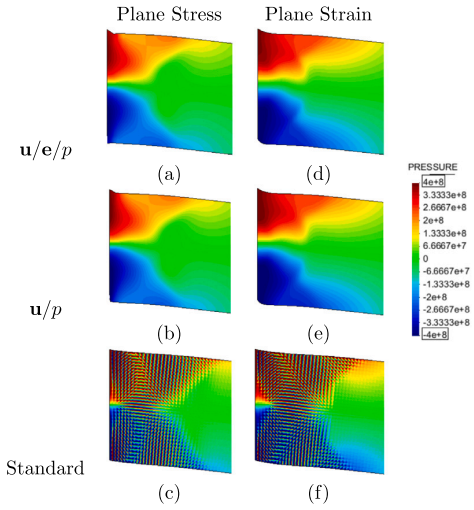

Fig. 3. Double clamped rectangular beam: Pressure in [Pa] at the left support. Plane-stress (*a*)–(*c*). Plane-strain (*d*)–(*f*).

(60)

with $\mathbf{B}_T = \mathbf{G}\mathbf{N}_T$.

3.4. Thermo-mechanical coupling

The coupled thermo-mechanical problem considered in this work is established in strong form by Eqs. (23) and (56). The corresponding discrete weak form of the problem being numerically computed is determined by Eqs. (43) and (60).

The time integration scheme adopted in Refs. [72–75] is considered to solve the discrete problem in time. The two sub-problems, mechanical and thermal, are solved sequentially following a staggered incremental procedure. When the mechanical dissipation is much lower than the energy input from the heat source, the thermo-mechanical coupling is weak, and a staggered solution of the thermal and the mechanical sub-problems is preferred instead of a monolithic approach.

For every time increment $\Delta t = t_{n+1} - t_n$ between time steps t_n and t_{n+1}, to obtain the solution at time t_{n+1}, first the mechanical sub-problem is calculated with all the state variables of the solution known at time instant t_n. This results in an intermediate solution, which is then used as a starting point to compute the thermal problem. According to the considerations in Ref. [74], the proposed algorithm does not need an iterative loop over the two sub-problems within the same time-step to ensure the convergence of the solution.

Due to the nonlinearity of the mechanical sub-problem, which includes J2-damage and J2-plasticity constitutive laws, an iterative Picard algorithm is introduced for its solution. Also, temperature-dependent mechanical properties are introduced, which are determined at t_{n+1} using the temperature computed at t_n.

As the thermal sub-problem in Eq. (60) involves the time derivatives of the temperature, an implicit Euler scheme is adopted for its solution. Temperature-dependent thermal properties are introduced as well, making the problem nonlinear. However, the resulting thermal sub-problem is solved in an incrementally linear manner. For this, material properties are also computed at time step t_{n+1} using the temperature field obtained at t_n.

For additional details on the thermo-mechanical coupling, Refs. [72–75] are recommended.

4. Constitutive laws

The mixed $\mathbf{u}/\mathbf{e}/p$ formulation requires the split of the constitutive law into the volumetric and deviatoric parts as shown in Eqs. (8) and (9). This section introduces the J2-damage and J2-plasticity laws used in this work to model the nonlinear material behavior in structural failure problems. The damage and yield surfaces of both models are described by the *Von Mises* criterion. Both models are comprehensibly described in Ref. [35]. For additional details on the constitutive laws, Ref. [35] is recommended.

4.1. J2-damage

In this section, the J2-damage model is presented. An isotropic damage model is considered for the deviatoric secant constitutive matrix $\mathbf{C}^{dev}$

$$\mathbf{C}^{dev} = (1 - d_s)\mathbf{C}_0^{dev} \tag{61}$$

where $\mathbf{C}_0^{dev}$ is the initial elastic deviatoric constitutive matrix and d_s is a damage variable modeling the degradation of the material, which ranges $0 \leqslant d_s \leqslant 1$.

The effective deviatoric-stress $\bar{\mathbf{s}}$ is defined as $\bar{\mathbf{s}} = \mathbf{C}_0^{dev}\mathbf{e}$ and the corresponding equivalent effective deviatoric-stress τ is

$$\tau = \sqrt{\frac{3}{2}}\,\|\bar{\mathbf{s}}\| = \sqrt{\frac{3}{2}}\left[\bar{\mathbf{s}}^T\bar{\mathbf{s}}\right]^{1/2} \tag{62}$$

The damage criterion, $\mathcal{F}_d$, is

$$\mathcal{F}_d = \tau - r(\bar{\mathbf{s}}) \leqslant 0 \tag{63}$$

where r is the current damage threshold. Its initial value is the tensile strength of the material, $r_0 = \sigma_y$. According to the Kuhn–Tucker optimality and consistency conditions, the value of the damage threshold at time t is explicitly updated as

$$r(\bar{\mathbf{s}}) = \max(r_0, \max \tau(\hat{t})) \qquad \hat{t} \in [0, t] \tag{64}$$

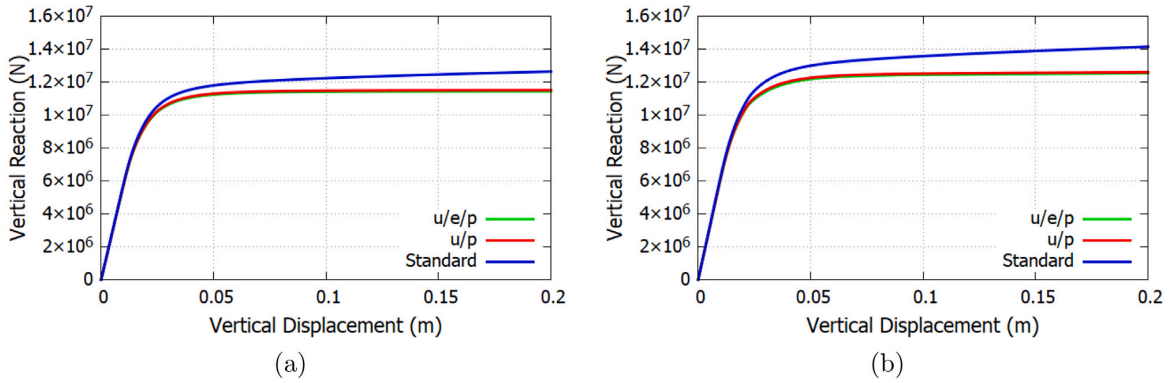

Fig. 4. Double clamped rectangular beam: Vertical reaction (*half*) vs vertical displacement. (*a*) Plane-stress. (*b*) Plane-strain.

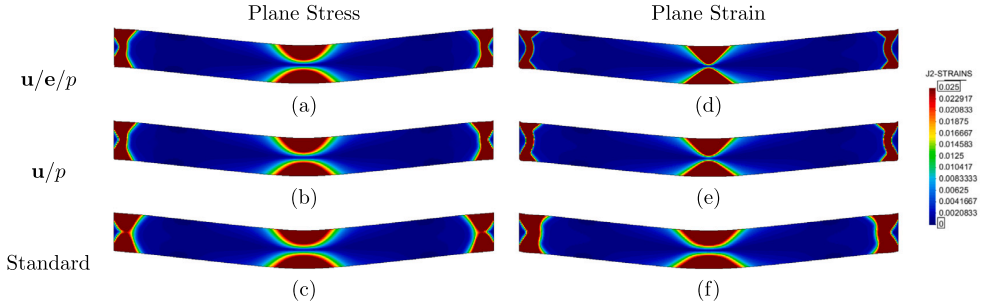

Fig. 5. Double clamped rectangular beam: J2-strains. Plane-stress (*a*)–(*c*). Plane-strain (*d*)–(*f*).

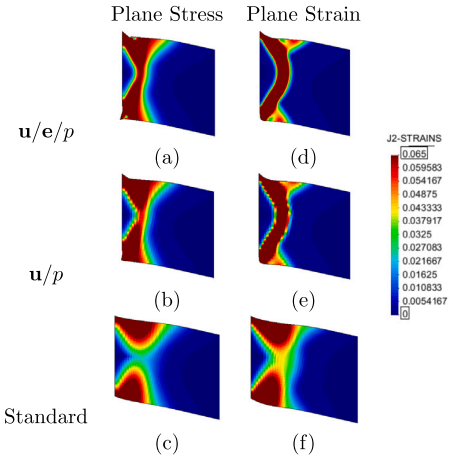

Fig. 6. Double clamped rectangular beam: J2-strains detail at the left support. Plane-stress (*a*)–(*c*). Plane-strain (*d*)–(*f*).

The evolution of the internal damage variable is defined by

$$d_s = d_s(r) = 1 - \frac{r_0}{r}\exp\left(-2H_S\left(\frac{\langle r - r_0\rangle}{r_0}\right)\right) \tag{65}$$

where H_S is a positive softening parameter controlling the rate of material degradation and $\langle\cdot\rangle$ are the Macaulay brackets such that $\langle x\rangle = x$ if $x \geqslant 0$, $\langle x\rangle = 0$ if $x < 0$.

The mechanical dissipation $\dot{\mathcal{D}}_{mech}$ for this constitutive law is

$$\dot{\mathcal{D}}_{mech} = \psi_0 \dot{d}_s = \frac{1}{2}\mathbf{e}^T \mathbf{C}_0^{dev}\mathbf{e}\dot{d}_s \geq \mathbf{0} \tag{66}$$

where $\psi_0 = \frac{1}{2}\mathbf{e}^T\mathbf{C}_0^{dev}\mathbf{e}$ is the initial elastic strain energy density per unit of volume of the undamaged material and $\dot{d}_s$ is the derivative of the damage d_s with respect to time.

The total dissipation along the process is [35]

$$\mathcal{D}_{mech} = \int_{t=0}^{t=\infty}\dot{\mathcal{D}}_{mech}dt = \int_0^{\infty}\frac{1}{2}\mathbf{e}^T\mathbf{C}_0^{dev}\mathbf{e}\dot{d}_s dt = W_0^e + \frac{W_0^e}{H_S} \tag{67}$$

where W_0^e is the maximum energy per unit volume that can be absorbed up to the elastic limit without permanent damage. For the case of isotropic materials, $W_0^e = \frac{1}{2}\frac{(\sigma_y)^2}{3G_0}$, G_0 being the initial elastic shear modulus. The previous expression of $\mathcal{D}_{mech}$ can be related to the fracture energy $\mathcal{G}_f$ as [76,77]

$$\mathcal{D}_{mech} = \frac{\mathcal{G}_f}{b} \tag{68}$$

where b is the bandwidth of the strain localization, which is equal to $2h$ for the 3-field element, h being the FE size. This results in

$$H_S = \frac{\bar{H}_S b}{1 - \bar{H}_S b} \tag{69}$$

$$\bar{H}_S = \frac{(\sigma_y)^2}{6G_0\mathcal{G}_f} \tag{70}$$

Eqs. (64)–(66) guarantee the irreversible nature and the positiveness of the dissipation.

4.2. J2-plasticity

Herein, the J2-plasticity model is presented. The deviatoric plastic strains $\mathbf{e}^p$ are introduced as

$$\mathbf{s} = \mathbf{C}_0^{dev}\mathbf{e}^e = \mathbf{C}_0^{dev}(\mathbf{e} - \mathbf{e}^p) \tag{71}$$

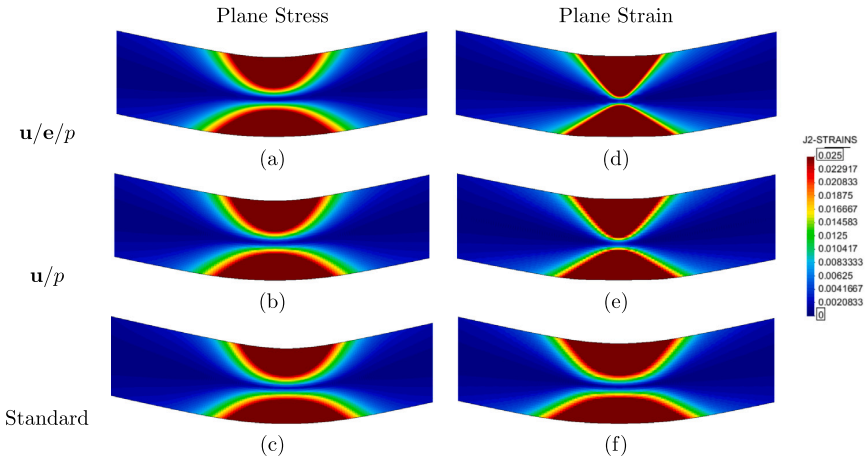

Fig. 7. Double clamped rectangular beam: J2-strains detail at the center of the beam. Plane-stress (*a*)–(*c*). Plane-strain (*d*)–(*f*).

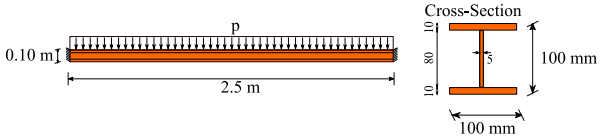

Fig. 8. Double clamped I-shaped beam: Problem setting.

where $\mathbf{C}_0^{dev}$ is the deviatoric part of the elastic constitutive matrix and $\mathbf{e}^e$ are the deviatoric elastic strains computed as

$$\mathbf{e}^e = \mathbf{e} - \mathbf{e}^p \tag{72}$$

The constitutive equation can be rewritten in terms of the secant deviatoric constitutive matrix

$$\mathbf{s} = \left[\mathbf{C}_0^{dev} - \frac{(\mathbf{C}_0^{dev}\mathbf{e}^p)(\mathbf{C}_0^{dev}\mathbf{e}^p)^T}{\mathbf{e}^T\mathbf{C}_0^{dev}\mathbf{e}^p}\right]\mathbf{e} = \mathbf{C}^{dev}\mathbf{e} \tag{73}$$

where $\mathbf{C}^{dev}$ is the deviatoric part of the secant nonlinear constitutive tensor, which is symmetric by construction.

Taking into account that, for an isotropic material, $\mathbf{C}_0^{dev} = 2G_0\mathbf{Y}$, that $\mathbf{e} = \mathbf{Ye}$ and that $\mathbf{e}^p$ is also purely deviatoric i.e. $\mathbf{e}^p = \mathbf{Ye}^p$, Eq. (73) can be simplified to

$$\mathbf{s} = 2G_0\left[\mathbf{J} - \frac{\mathbf{e}^p(\mathbf{e}^p)^T}{\mathbf{e}^T\mathbf{e}^p}\right]\mathbf{e} \tag{74}$$

Using the equivalent deviatoric-stress, τ, defined in Eq. (62), the plastic yield surface, $\mathcal{F}_p$, is defined as

$$\mathcal{F}_p = \tau - r_p(q) \leqslant 0 \tag{75}$$

where $r_p(q)$ are the admissible deviatoric-stresses, and q is a stress-like internal variable that controls the *softening* of the model. The deviatoric stress threshold is

$$r_p(q) = \sigma_y - q(\xi) \tag{76}$$

where σ_y is the initial uniaxial stress threshold, ξ is the equivalent plastic strain and $q(\xi)$ is the softening function, that in this work is exponential:

$$\xi = \sqrt{\frac{2}{3}}\,\|\mathbf{e}^p\| \tag{77}$$

$$q(\xi) = \sigma_y \exp\left(\frac{-2H}{\sigma_y}\xi\right) \qquad \text{for } 0 \leqslant \xi \leqslant \infty \tag{78}$$

where H is the softening parameter.

The plastic evolution laws are

$$\dot{\mathbf{e}}^p = \dot{\lambda}\mathbf{n} \tag{79}$$

$$\dot{\xi} = \dot{\lambda}\sqrt{\frac{2}{3}} \tag{80}$$

where $\dot{\lambda}$ is the plastic multiplier determined by the Kuhn–Tucker optimality and consistency conditions and $\mathbf{n}$ is the normal to the yield surface, defined by

$$\mathbf{n} = \frac{\partial \mathcal{F}_p}{\partial \mathbf{s}} = \frac{\mathbf{s}}{\|\mathbf{s}\|} \tag{81}$$

The rate of plastic work is $\dot{\mathcal{D}}_{mech} = \mathbf{s} : \dot{\mathbf{e}}^p$ and the total deviatoric plastic work along the softening process is

$$\mathcal{D}_{mech} = \int_{t=0}^{t=\infty} \dot{\mathcal{D}}_{mech}dt = \int_0^\infty q(\xi)d\xi = \frac{\sigma_y^2}{2H} \tag{82}$$

Also, the dissipated energy in a softening process can be related to the fracture energy $\mathcal{G}_f$ as

$$\mathcal{D}_{mech} = \frac{\mathcal{G}_f}{b} = \frac{\mathcal{G}_f}{2h} \tag{83}$$

where b is the bandwidth of the strain localization, that in this work is $2h$ for the 3-field element, h being the mesh size.

Finally, the softening parameter H can be computed using Eq. (82) and (83) as

$$H = \frac{\sigma_y^2}{2\mathcal{G}_f}b = 2h\bar{H} \tag{84}$$

$$\bar{H} = \frac{\sigma_y^2}{2\mathcal{G}_f} \tag{85}$$

The parameter H depends on the mesh resolution h and the material properties.

5. Numerical simulations

In this section, the enhanced accuracy and the mesh independence of the mixed $\mathbf{u}/\mathbf{e}/p$ formulation are assessed in isothermal (Section 5.1) and non-isothermal (Sections 5.2–5.5) failure problems. Temperature-dependent properties are considered. The simulations include the J2-damage and J2-plasticity constitutive models, introducing the isochoric behavior into the problem; thus the requirement of using a FE approach such as $\mathbf{u}/\mathbf{e}/p$, capable of resolving incompressible conditions. Several FE discretizations (triangular, quadrilaterals and hexahedral elements) are used to show the generality of the formulation.

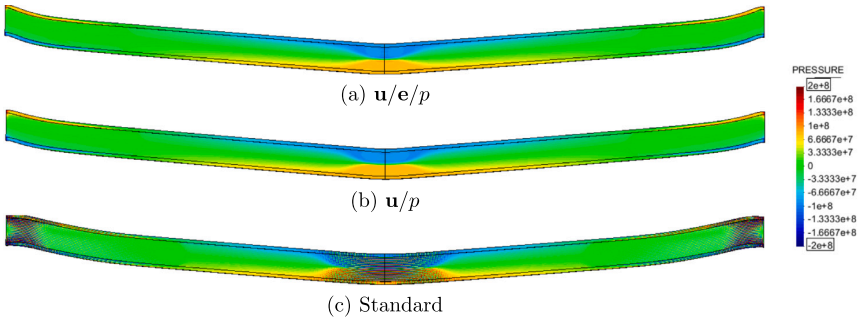

Fig. 9. Double clamped I-shaped beam: Pressure in [Pa].

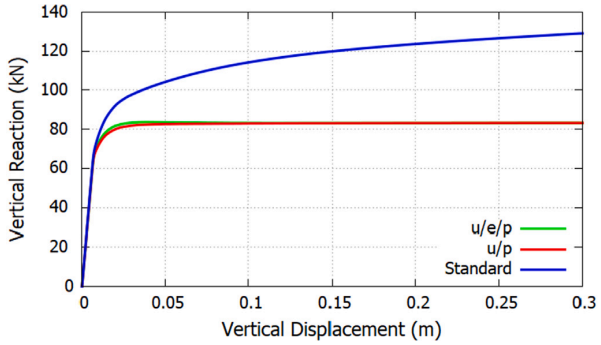

Fig. 10. Double clamped I-shaped beam: Vertical reaction (*half*) vs vertical displacement.

The nonlinear problem is solved incrementally in a (pseudo) time step-by-step manner; at each step a staggered scheme is used for the mechanical and the thermal problems. An iterative Picard algorithm is employed in the mechanical problem. A convergence based on the norm of the residuals of Eqs. (43) with a tolerance of 10^{-5} is adopted at each time step. The thermal problem is solved in a linear incremental manner and an implicit backward Euler scheme is adopted for its resolution.

The mixed $\mathbf{u}/\mathbf{e}/p$ formulation is compared with the $\mathbf{u}/p$ FE in terms of result accuracy, collapse mechanism prediction and numerical stability. The approximations adopted are *Q1Q1* and *P1P1* for $\mathbf{u}/p$ and *Q1Q1Q1* and *P1P1P1* for $\mathbf{u}/\mathbf{e}/p$ in the mechanical simulation and *Q1* and *P1* for the thermal field, depending on the FE discretization.

The stabilization constants defined in Eq. (A.4) of the Appendix are taken as $L_0 = 1.0$, $c_u = 1.0$, $c_p = 0.0$ and $c_e = 0.1$ for both the $\mathbf{u}/p$ and $\mathbf{u}/\mathbf{e}/p$ formulations.

An enhanced version of the finite element code COMET (see [78]), developed by the authors, is used to solve the numerical simulations. The pre and post process is done with GiD, a software developed at the International Center for Numerical Methods in Engineering (CIMNE) [79]. Paraview [80] is used for post processing as well.

5.1. Double clamped beam

5.1.1. Rectangular beam

In this section the development of plastic hinges is studied in a clamped–clamped beam in plane-stress and plane-strain conditions. In the present examination, the performance of the standard, $\mathbf{u}/p$ and $\mathbf{u}/\mathbf{e}/p$ FE formulations are investigated when used in conjunction with an isochoric (incompressible) nonlinear constitutive model. The numerical simulations compare their solution in an isothermal setting. The geometry and loading conditions of the beam are shown in Fig. 1.

The collapse mechanism predicted from the limit analysis of the beam consists in the formation of two plastic hinges at the clamped ends and, ultimately, of a third plastic hinge at the center of the beam.

The constitutive model adopted is elasto-perfect J2-Plasticity with a Young's modulus of $E = 200$ [GPa], Poisson's ratio of $\nu = 0.3$ and an uniaxial yield stress threshold of $\sigma_y = 500$ [MPa]. For the plane-stress assumption, where the transversal stress is $\sigma_z = 0$, the theoretical ultimate distributed load is $p_u = 4000$ [kN/m] and the vertical reaction in each end is 10,000 [kN]. For the plane-strain case, the influence of $\sigma_z \neq 0$ reflects on the perceived yield threshold, $\bar{\sigma}_y \geq \sigma_y$ [81], which, in the case of the Von Mises criterion, is given by

$$\bar{\sigma}_y = \frac{\sigma_y}{\sqrt{1 - \nu + \nu^2}}$$

so, the corresponding plane-strain condition ultimate load is $p_u = 4500$ [kN/m] resulting in a vertical reaction of 11,250 [kN] in each end.

A structured quadrilateral mesh is adopted and, due to the symmetry of the problem, half of the domain is considered, with a total of 5494 elements and a FE size of $h = 0.015$ [m]. An arc-length strategy is used in the simulations, controlling the displacement at the top midpoint.

Fig. 2 shows the pressure computed in plane-stress and plane-strain conditions for the standard, $\mathbf{u}/p$ and $\mathbf{u}/\mathbf{e}/p$ FEs. The standard element presents spurious oscillations of the pressure field while the mixed formulations provide a smooth (correct) solution. Fig. 3 shows the detail of the pressure at the left support where the poor performance of the standard element is noticeable.

Fig. 4 shows the vertical reaction of one clamped end *versus* the vertical displacement of the mid-span. In this simulation without material softening, the two mixed FE formulations coincide while the standard formulation presents a spurious hardening behavior due to the volumetric locking that takes place in the computed solution. This shows the inability of the standard FE formulation in reproducing nonlinear isochoric behavior such as J2-plasticity.

Fig. 5 shows the J2-strains for the three FEs formulations. It can be seen that the plastic hinges at the clamped ends form an arch that connects the top and bottom faces of the beam. Close to the clamped end, a region with no strain localization that extends towards the center of the beam can be observed. The support and central hinges are detailed in Figs. 6 and 7, respectively.

The numerical results in terms of load capacity in Fig. 4 for plane-stress are higher than the theoretical results derived from the plastic limit analysis. This is because of the assumption that the plastic hinge develops exactly at the clamped face of the beam, which limit analysis translates into assuming that the effective span coincides with the geometric span. Fig. 5 shows that this is not the case; a dead-region is formed, which decreases the value of the effective span length, considered to be the distance from hinge to hinge, and increases the ultimate load. In the plane stress case, the maximum vertical reaction in $\mathbf{u}/\mathbf{e}/p$ is 11,440 [kN], for the $\mathbf{u}/p$ is 11,510 [kN] and for the standard

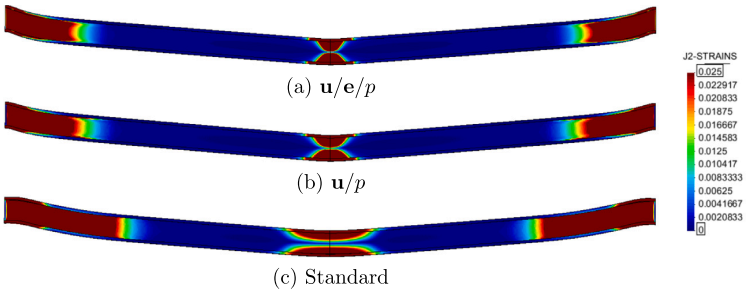

Fig. 11. Double clamped I-shaped beam: J2-strains.

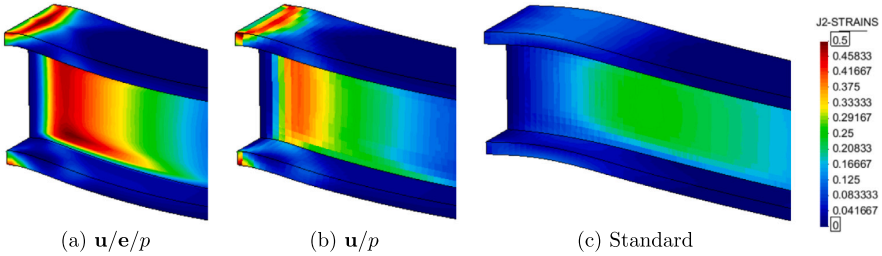

Fig. 12. Double clamped I-shaped beam: J2-strains detail at the left clamped-end.

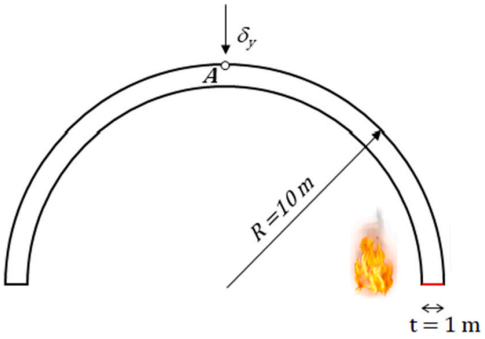

Fig. 13. Semicircular arch: Problem setting.

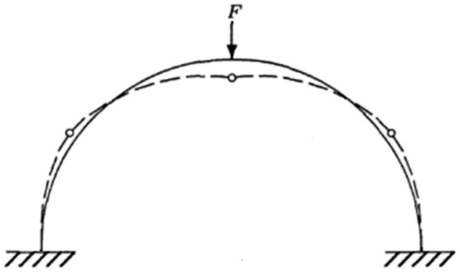

Fig. 14. Semicircular arch: Collapse mechanism in an isothermal setting in dashed line. *Source:* Adapted from [81].

formulation is 12,640 [kN] at $\delta_y = 0.20$ [m]; the theoretical one when adopting a reduced effective span of $L_{eff} = 4.52$ [m], as observed in the numerical solution, is 11,060 [kN].

5.1.2. I-shaped beam

In the following, the numerical simulation of the formation of plastic hinges is considered in an I-shaped beam. The goal of this section is to analyze the phenomenon in a 3D geometry, where the cross section of the beam does not have constant width.

Fig. 8 shows the geometry and boundary conditions of this case. The analysis is performed using elasto-perfect J2-plasticity, with a Young modulus $E = 200$ [GPa], Poisson's ratio of $\nu = 0.3$ and an uniaxial yield stress threshold $\sigma_y = 245$ [MPa]. Considering the geometrical span length $L = 2.5$ [m], as shown in Fig. 8, the theoretical ultimate load of the beam is $p = 61.47$ [kN/m]. This results in a vertical reaction on each end of $R = 76.8$ [kN].

Due to symmetry, half of the problem is considered. The simulation is performed using an arc-length strategy controlling the vertical displacement at the beam top midpoint. The domain is discretized using a structured mesh of hexahedral elements of size $h = 5 \cdot 10^{-3}$ [m], with a total of 25,000 elements. At one end the beam is clamped and at the mid-span symmetry conditions are applied.

Fig. 9 shows the pressure for the three FEs, where it can be seen that the solution obtained by the standard formulation suffers from spurious oscillations. Fig. 10 shows the evolution of the vertical reaction at the left clamped end with the vertical displacement at the mid-span. In this simulation without material softening, both mixed formulations reach similar final bearing capacities, with the $\mathbf{u}/\mathbf{e}/p$ value being 83.1 [kN] and the $\mathbf{u}/p$ value 83.4 [kN], while the standard FE produces a much stiffer solution due to the volumetric locking originated by the incapability of the standard element to address the material isochoric (incompressible) behavior.

Fig. 11 presents the J2-strains for the three formulations where a slightly different strain distribution on the web is observed between

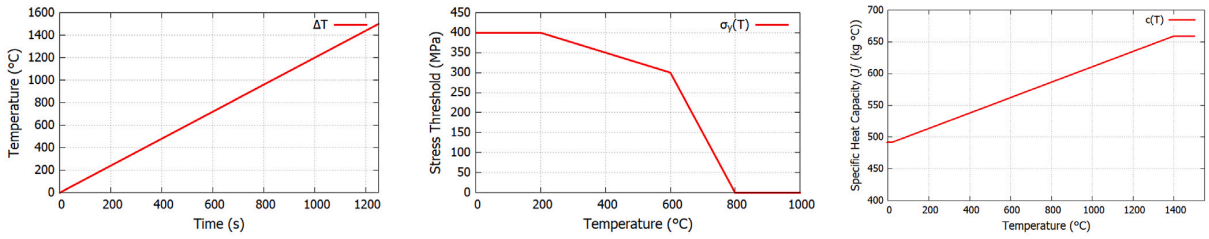

Fig. 15. Semicircular arch: (*a*) Heat source increment over time. Evolution of the (*b*) stress threshold and (*c*) specific heat capacity with temperature.

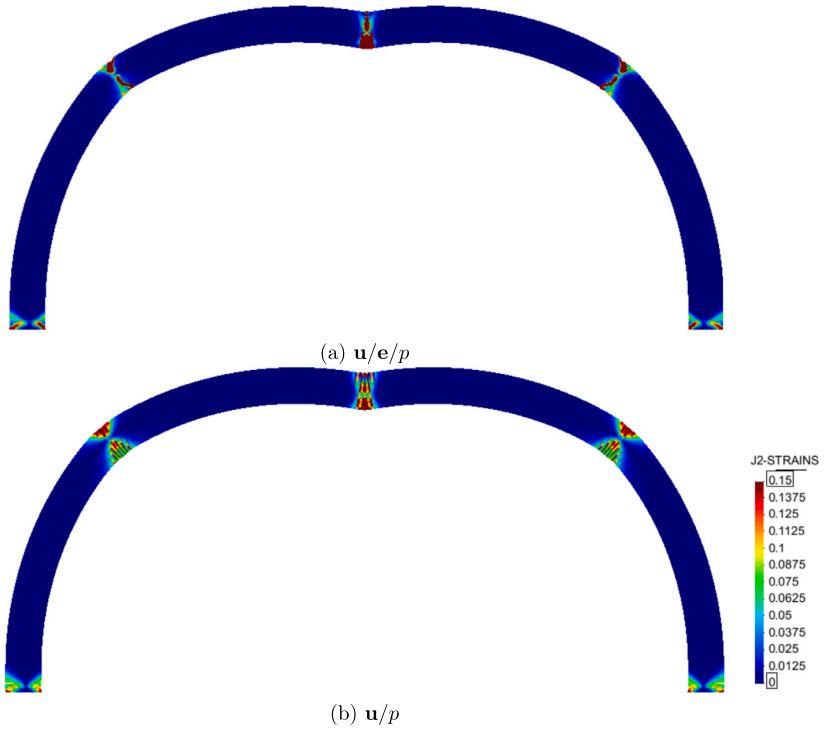

Fig. 16. Semicircular arch: Reference model (isothermal) failure mechanism for $\delta_y = 1.6\,[\text{m}]$.

the mixed formulations. The J2-strains for the $\mathbf{u}/p$ element are more uniform throughout the web height. Fig. 12 provides a zoom at the clamped end for a total displacement of $|\delta| = 0.30\,[\text{m}]$. The $\mathbf{u}/p$ formulation has a lower accuracy in terms of strains and is not able to capture the distribution observed in the 3-field solution. The standard formulation presents a much broader area where the J2-strains develop, Fig. 11, but the J2-strains magnitude are much smaller than the mixed formulations values, Fig. 12, due to the volumetric locking of the standard element.

It can be seen in Fig. 12 how also in this case a dead region where no localization occurs develops next to the clamped face of the beam. This reduces the effective span length of the beam to $L_{eff} = 2.45\,[\text{m}]$. The resulting ultimate load is $p = 64\,[\text{kN/m}]$, and the expected vertical reaction at each beam end (half vertical reaction) is $R = 80\,[\text{kN}]$. The load capacities observed in Fig. 10 when using the $\mathbf{u}/p$ and $\mathbf{u}/\mathbf{e}/p$ FEs agree with these values.

5.2. Semicircular arch

In the next simulation, a semicircular arch in plane-stress conditions is considered with temperature-dependent material properties. A heat source is placed at one end of the arch, weakening the bearing capacity. The aim of this example is to assess the difference in the failure mechanisms provided by the 3-field and $\mathbf{u}/p$ solutions.

The arch is clamped in both ends and has an outer radius $R = 10\,[\text{m}]$, a thickness $t = 1.0\,[\text{m}]$, a width $\omega = 0.5\,[\text{m}]$ and is subjected to a vertical displacement $\delta_y = 2.5\,[\text{m}]$ downwards with a heat source placed on the right clamping (see Fig. 13). Fig. 13 shows the point A chosen to measure the evolution of the temperature.

An isothermal reference case is also considered to assess the influence of the temperature on the failure mechanism. The structure, if not subjected to temperature effects, fails with the formation of symmetrical hinges [81] as presented in Fig. 14.

The constitutive model adopted is the isotropic J2-Damage and the material properties are described in Table 2. The heat load is described

Table 2
Semicircular arch: Material properties.

Property	Value
Young's Modulus [GPa]	200
Fracture Energy [MJ/m^2]	60
Density [kg/m^3]	7800
Thermal Conductivity [W/(m °C)]	45
Thermal Expansion coefficient [m/(m °C)]	$12 \cdot 10^{-6}$

in Fig. 15(*a*). The yield stress threshold, σ_y, and the specific heat capacity, c, vary in function of the temperature, see Fig. 15(*b*) and (*c*). These evolution functions of the material temperature-dependency are taken based on the behavior reported for steel in Ref. [82].

A structured quadrilateral mesh with 16 elements through the thickness is adopted, resulting in a total of 8000 elements with an average size of $h = 0.0625$ [m].

Fig. 16 shows the failure mechanism for the isothermal case, comparable to the expected behavior in Fig. 14. Fig. 17 details the evolution of the intermediate plastic hinge in four different time steps. The lack of accuracy of the $\mathbf{u}/p$ formulation introduces stress locking, precludes the achievement of a localized solution and exhibits the banding phenomenon in Fig. 17*c* (*right*), in contrast to the $\mathbf{u}/\mathbf{e}/p$ result. This increases the mechanical dissipation 32.2% for the $\mathbf{u}/p$ element compared to the 3-field solution, as can also be seen in the reaction vs displacement plot in Fig. 18(*a*). This also produces an overestimation of the failure load by $\mathbf{u}/p$ of 2.29% with respect to the $\mathbf{u}/\mathbf{e}/p$, as can be appreciated in Fig. 18(*a*).

Fig. 19 shows the unsymmetrical failure mechanism induced by the heat source positioned at the right hand side base for the mixed $\mathbf{u}/\mathbf{e}/p$ and the mixed $\mathbf{u}/p$. The right base of the arch loses strength at a faster rate which produces the unsymmetrical failure mechanism. Although both solutions are unsymmetrical, a large difference is observed between both collapse mechanisms. The $\mathbf{u}/\mathbf{e}/p$ element yields a sliding mechanism, due to the loss of strength at the arch base, while the $\mathbf{u}/p$ displays a stiffer solution, resulting from the stress locking observed at the hinges.

Fig. 18 presents the vertical reaction vs displacement plot for the $\mathbf{u}/p$ and $\mathbf{u}/\mathbf{e}/p$ formulations (recall that the reference case is isothermal) and the temperature evolution at point A. The differences between the 3-field and the $\mathbf{u}/p$ solutions are caused by the formation of a different failure mechanism and the over dissipation exhibited by the $\mathbf{u}/p$, both originated from the poor evaluation of the stress/strain field. Note also that the resulting bearing capacities are different: $55,396\,kN$ for the $\mathbf{u}/p$ and $53,720\,kN$ for the $\mathbf{u}/\mathbf{e}/p$, a 3.12% difference. The heat increase at the base barely affects the peak load value with respect to the isothermal case, but the resulting nonlinear structural response is greatly modified. The measured temperature increase at point A, presented in Fig. 18(*b*), depends on the mechanical dissipation and captures the instant when the localization occurs, when the peak value is attained. The hinge is formed sooner in the $\mathbf{u}/\mathbf{e}/p$ solution, denoting that the $\mathbf{u}/p$ has a stiffer behavior and delays the localization process.

5.3. Temperature induced failure - 3D frame

The following example is a 3D frame subjected to self-weight. The structural failure is induced by an incremental heat source placed on the right portion of the beam–column connection, shown in Fig. 20 and defined in Fig. 21(*a*). The frame has a total height of 3 [m] with a free span of 4.8 [m]. The heat-affected area is a portion of the beam with 1.2 [m] in length from the right beam–column connection. The beam and column cross-sections are presented in Fig. 20.

The constitutive model is perfect J2-Plasticity, Young's modulus is $E = 200$ [GPa], the material density is $\rho = 7800$ [kg/m^3] and the thermal expansion coefficient is $\alpha = 12 \cdot 10^{-6}$ [m/(m °C)]. The yield stress threshold, σ_y, the specific heat capacity, c, and the thermal conductivity, k, are temperature dependent, as shown in Fig. 21 (*b*)–(*d*). The evolution laws are taken based on the behavior reported in Ref. [82]. The simulation is performed with a time step of 20 [s] in a total of 10,000 [s] and a structured hexahedral mesh with element size $h = 0.025$ [m] (39,936 elements in total).

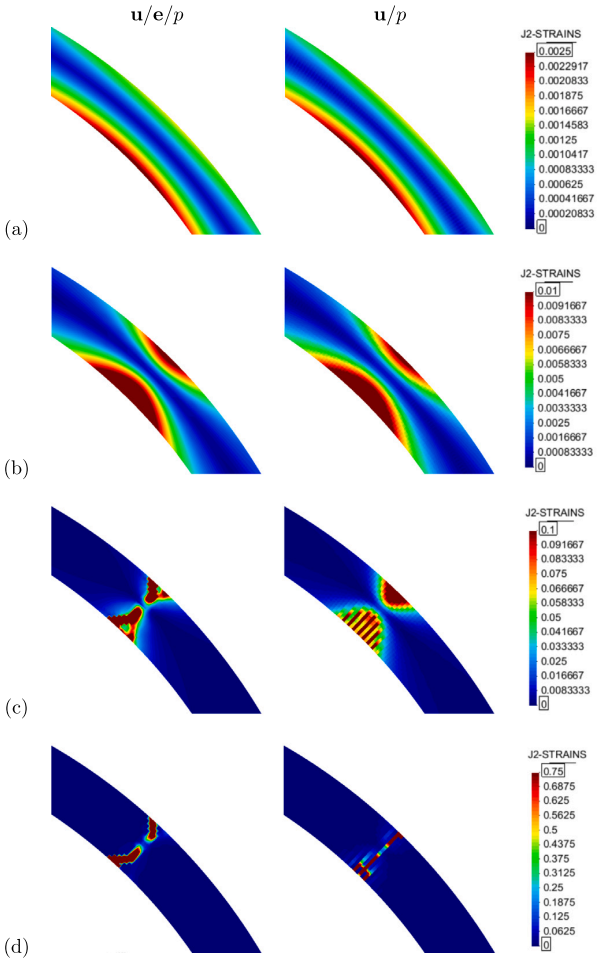

Fig. 17. Semicircular arch: Reference model (isothermal) detail of the development of the intermediate plastic hinge. (*a*) $\delta_y = 0.10$ [m]. (*b*) $\delta_y = 0.30$ [m]. (*c*) $\delta_y = 1.20$ [m]. (*d*) $\delta_y = 2.5$ [m].

Fig. 22 shows the evolution of the vertical reaction at each column. On the one hand, the $\mathbf{u}/p$ simulation stops at 3880 [s], when the temperature in the heated region reaches 796 °C, due to the degradation of the strength of the beam in the heated zone. On the other hand, the $\mathbf{u}/\mathbf{e}/p$ formulation manages to conclude the analysis successfully.

Figs. 23(*a*)–(*b*) shows the J2-strains developed by the mixed $\mathbf{u}/p$ and $\mathbf{u}/\mathbf{e}/p$ formulations a few time-steps before the mixed $\mathbf{u}/p$ formulation fails. This is caused by the lack of local convergence of the $\mathbf{u}/p$ formulation, which induces a premature shear mechanism at the heated beam–column connection, observed in the following time-step in Fig. 23(*c*)–(*d*). On the other hand, this does not happen in the enhanced accuracy mixed $\mathbf{u}/\mathbf{e}/p$ formulation and the analysis follows on until the final time-step $t = 10,000$ [s].

5.4. The Prandtl Punch test

The Prandtl Punch test consists of a rigid punch pressed into a semi-infinite domain in plane-strain conditions. The geometry considered is

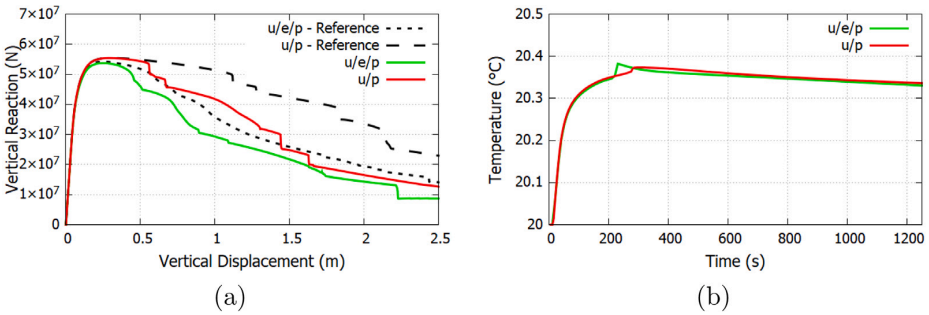

Fig. 18. Semicircular arch: (*a*) Reaction vs displacement curves and (*b*) temperature evolution over time at point *A*.

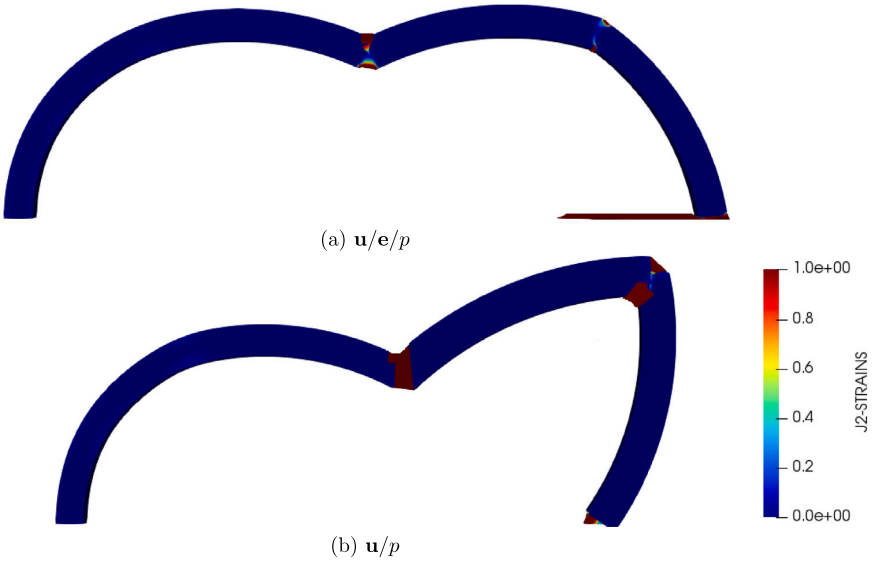

Fig. 19. Semicircular arch: Failure mechanism with heated base for $\delta_y = 2.50\,[\mathrm{m}]$.

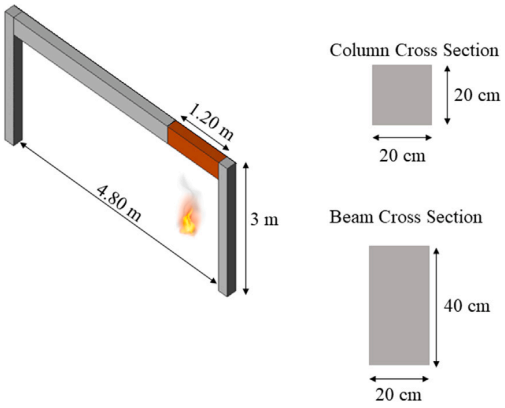

Fig. 20. 3D frame with heat source at the right quarter portion of the beam–column connection: Problem setting.

a 4 [m] × 2 [m] ($x \times y$) region with a rigid punch of size 1.0 [m] centered at the top portion of the domain (see Fig. 24). Due to the symmetry of the problem only half of the domain is considered.

Also, in this section, artificial properties are considered, to better demonstrate the capacities of both mixed FE formulations. The constitutive model is J2-Damage with a high value for the fracture energy ($G_f \longrightarrow \infty$). The material properties are Young's Modulus, $E = 10\,[\mathrm{MPa}]$, density, $\rho = 7800\,[\mathrm{kg/m^3}]$, Poisson's ratio $\nu = 0.5$ (incompressible elastic behavior), specific heat capacity, $c = 5{\cdot}10^{-5}\,[\mathrm{J/(kg\,°C)}]$, and the evolution of the yield-threshold with respect to the temperature is shown in Fig. 25. Two simulations, one with null thermal conductivity and one including an external heat source, are performed in this section. In this problem with elastic incompressible behavior, the pressure stabilization constant is set to $c_p = 0.1$.

Computations are conducted using a 14,608 unstructured triangular element mesh in the first case and a 6400 quadrilateral element discretization in the second one, with the element size being $h = 0.025$ [m] in both meshes. A downward vertical displacement of $\delta_y = 0.20$ [m] is applied to the rigid punch area in 500 [s] (500 steps).

The failure mechanism in an isothermal setting is shown in Fig. 26 with critical angles of $\theta = \pm 45°$ from the edge of the punch with the horizontal plane. The analytical peak load (yield load), q, for the rigid

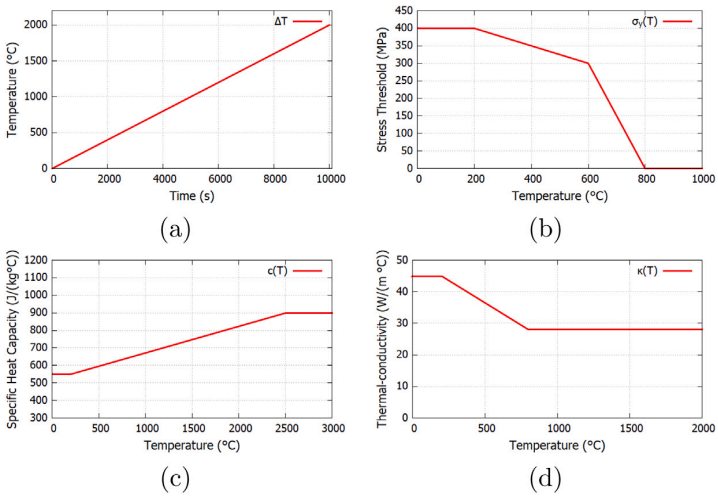

Fig. 21. 3D frame: (*a*) Heat source increment over time. (*b*) Uniaxial stress threshold, (*c*) Specific heat capacity, (*d*) Thermal conductivity, evolution with the temperature.

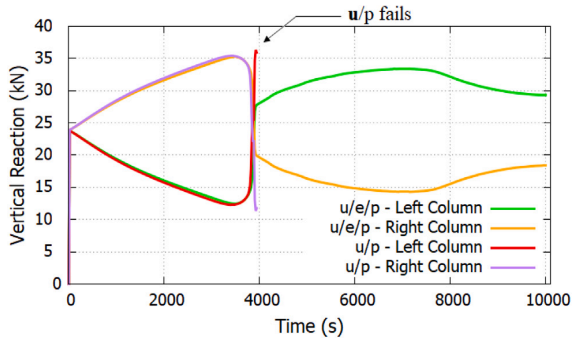

Fig. 22. 3D frame: Evolution curves of the bearing capacity of the columns.

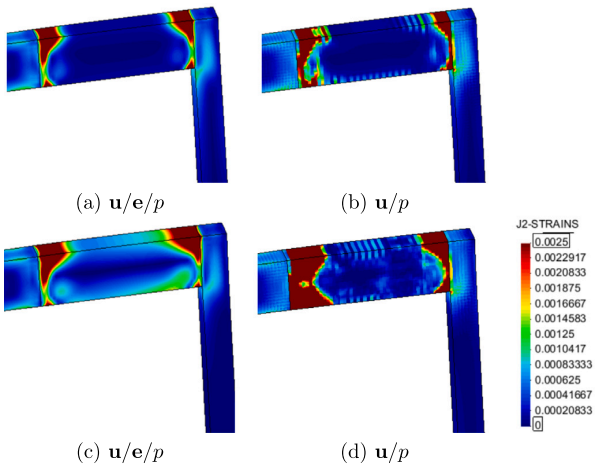

Fig. 23. 3D frame: J2-strains at the beam–column connection (*a*)–(*b*) at the time step $t = 3820$ s and (*c*)–(*d*) at time step $t = 3880$ s, before the $\mathbf{u}/p$ solution fails.

punch in an isothermal setting is given by [83]:

$$q = 4a\left(1 + \frac{\pi}{2}\right)\tau_{ps}$$

Table 3
Prandtl's Punch test: Peak load relative errors for the half-domain in an isothermal setting at 20 °C.

	Peak load [N]	Error [%]
$\mathbf{u}/\mathbf{e}/p$	15,257	2.79
$\mathbf{u}/p$	15,264	2.84

where τ_{ps} is the yield stress threshold in pure shear, defined as a function the uniaxial yield stress threshold, σ_y, as $\tau_{ps} = \frac{\sigma_y}{\sqrt{3}}$ and $2a$ is the width of the punch ($2a = 1$ [m]). For a stress threshold $\sigma_y(20\ °C) = 10$ [kPa], the peak load for the half-domain is $q_{1/2} = 14,842.5$ [N/m].

Table 3 presents the peak load for the isothermal setting of the half-domain computed by both FE formulations.

5.4.1. Case 1: Numerical simulation with null thermal conductivity

The objective of this simulation is to illustrate a case where the temperature increase is produced exclusively by the mechanical dissipation. The thermal conductivity is set to *zero* to emulate null thermal inertia. In this way, mechanical dissipation increases the temperature locally, without thermal conduction. Point *A*, shown in Fig. 24, is chosen to evaluate the evolution of the J2-stresses and the temperature, presented in Fig. 27. The $\mathbf{u}/p$ element produces a higher mechanical dissipation [35], resulting in a higher temperature increase, Fig. 27*a*, affecting the computed yield threshold and reducing the J2-stresses observed at point *A*, Fig. 27*b*.

In the isothermal setting, both mixed formulations reach the yield threshold value, $\sigma_y(20\ °C) = 10$ [kPa], for point *A*. On the other hand, the peak J2-stress values reached in the non-isothermal analysis are $\sigma_y = 9.51$ [kPa] and $\sigma_y = 8.94$ [kPa] for the mixed 3-field and $\mathbf{u}/p$ formulations, respectively. The J2-stresses decrease until they reach the final value of $\sigma_y = 6.95$ [kPa] and $\sigma_y = 6.65$ [kPa] for the 3-field and $\mathbf{u}/p$, respectively.

Fig. 28 shows snapshots of the failure mechanism (*a–b* — near the peak load; *c–d* at the final step) for both formulations. Although the failure mechanisms in both cases are similar, the $\mathbf{u}/p$ formulation shows some mesh sensitivity and presents a vertical slip line that does not develop in the 3-field.

5.4.2. Case 2: Numerical simulation with an external heat source

The following case introduces an external heat source in the problem and the thermal conductivity of the domain is set to $2.5 \cdot 10^{-3}$ [W/(m°C)]. The resulting effects on the failure mechanism,

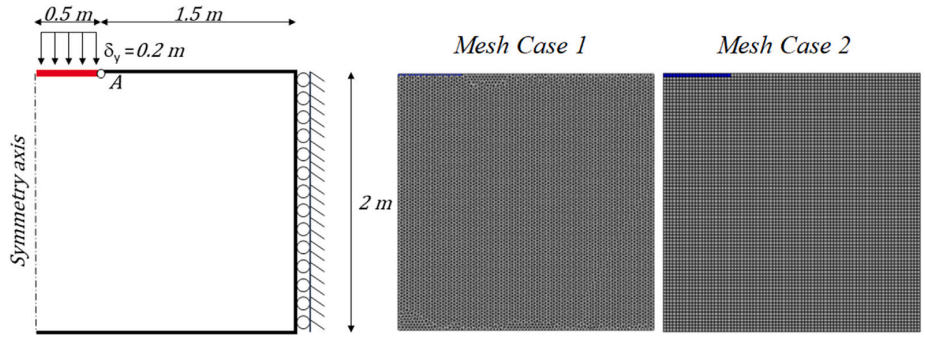

Fig. 24. Prandtl's Punch test: General problem setting and meshes.

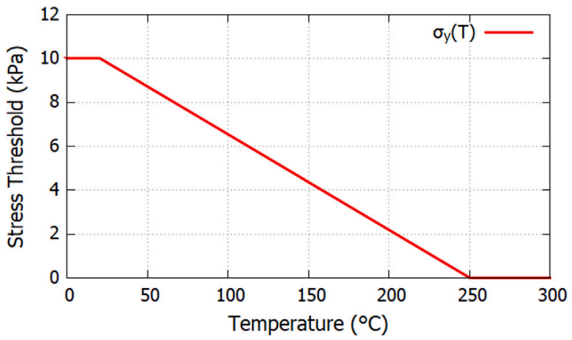

Fig. 25. Prandtl's Punch test: Temperature-dependency of the uniaxial stress threshold.

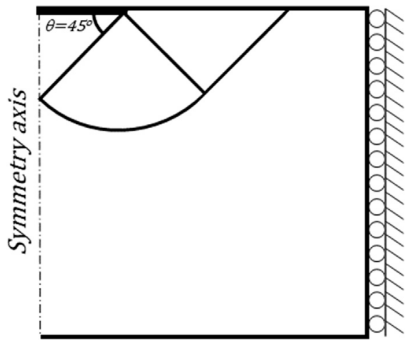

Fig. 26. Prandtl's Punch test: Collapse mechanism in an isothermal setting.

peak load and bearing capacity are explored. The heat source is positioned in the rigid punching area at a constant temperature of 150 [°C].

Fig. 29 shows snapshots of the failure mechanism (*a–b* — near the peak load; *c–d* — at the final step) for both formulations. The increase of temperature in the rigid footing area changes the failure mechanism with respect to the isothermal case, altering its depth, which eventually emerges closer to the heated area. Note that, due to the effect of temperature, the failure mechanism does no longer present a critical angle θ of 45°. Fig. 30(*a*) shows the difference in terms of strains between the computations of both formulations at the end of the simulation. Note that the difference is computed as $[\mathbf{u}/\mathbf{e}/p - \mathbf{u}/p]$, where *blue* values mean that the $\mathbf{u}/p$ solution has higher strains and *red* values otherwise. This represents the superposition of the $\mathbf{u}/p$ and $\mathbf{u}/\mathbf{e}/p$ mechanisms in *blue* and *red*, respectively. It can be seen how the two formulations do not produce the same results due to the poor precision of the $\mathbf{u}/p$ element. Fig. 30(*b*) shows the reaction vs displacement curves, where the effect of the thermal softening induced by the temperature-dependency of the yield stresses, as defined in Fig. 25, can be observed for both formulations. The reference curves are obtained from simulations without a temperature-dependent yield threshold. The higher peak-load observed in the 3-field is a consequence of the broader confined region below the rigid footing compared to the $\mathbf{u}/p$ formulation.

Table 4
Prandtl's Punch test — case 2: Difference between isothermal and non-isothermal critical angles on the slip-line and computed peak-load in the non-isothermal case.

Case	$\Delta\theta$	q [N]
$\mathbf{u}/p$	−13.24°	10,472
$\mathbf{u}/\mathbf{e}/p$	−7.69°	11,070

Table 4 shows the change in the critical angles with respect to the reference case ($\theta = 45°$) caused by the increase of temperature on the rigid footing. It also presents the reduced peak loads which are to be compared to the isothermal simulation results presented in Table 3.

Note that the 3-field formulation is able to produce the original Prandtl collapse mechanism (a slip-line), while the mixed $\mathbf{u}/p$ introduces a vertical punching line to the slip-line mechanism in both sets analyzed.

5.5. Singly perforated thin-walled cylinder

The next example is a thin-walled cylinder 0.6 [m] × 3 [m] × 0.02 [m] (*outer diameter* × *height* × *thickness*) with a perforation of 0.04 [m] × 0.04 [m] × 0.02 [m] (*width* × *height* × *thickness*) subjected to vertical stretching. The cylinder is heated at the perforation, as shown in Fig. 31, in an area of dimensions 0.12 [m] × 0.12 [m] × 0.02 [m] (*width* × *height* × *thickness*). The heat load is described in Fig. 32(*a*).

The constitutive model adopted is the J2-Damage with softening and the material properties are presented in Table 5. One fourth of the domain is considered due to the double symmetry of the problem (see Fig. 31).

As shown in Fig. 31, the perforated cylinder is in a state of plane stress, as the normal stress through the thickness is null. An imposed vertical displacement of $\delta_z = 0.20$ [m] is applied at the top boundary.

The yield stress threshold, σ_y, is temperature-dependent as shown in Fig. 32(*b*), following the observations in Ref. [82].

Fig. 31 presents the cylinder geometry and the structured mesh of hexahedral finite elements of size $h = 0.02$ [m] employed in the simulation, resulting in a total of 3749 elements.

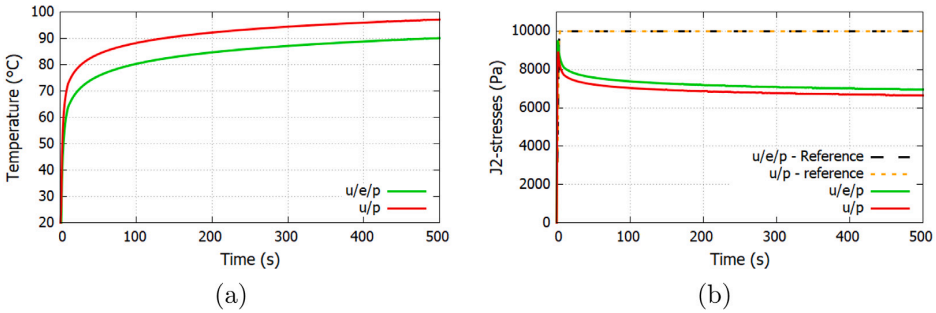

Fig. 27. Prandtl's Punch test — case 1: (*a*) Comparative evolution of the temperature and (*b*) J2-stresses at point *A*.

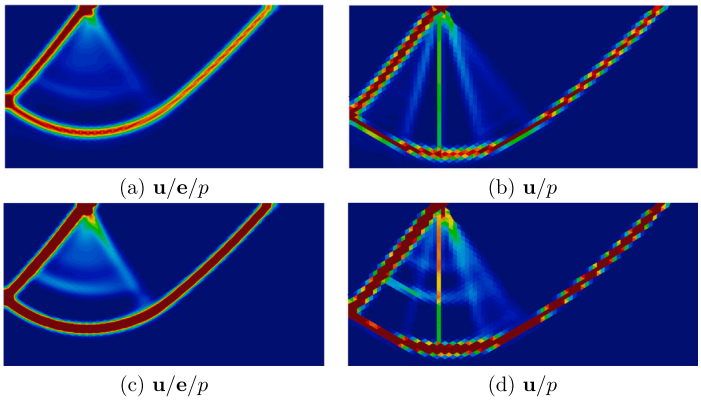

Fig. 28. Prandtl's Punch test — case 1: Collapse mechanisms (*a*)–(*b*) at $d_y = 0.02\,[\mathrm{m}]$ and (*c*)–(*d*) at $d_y = 0.20\,[\mathrm{m}]$.

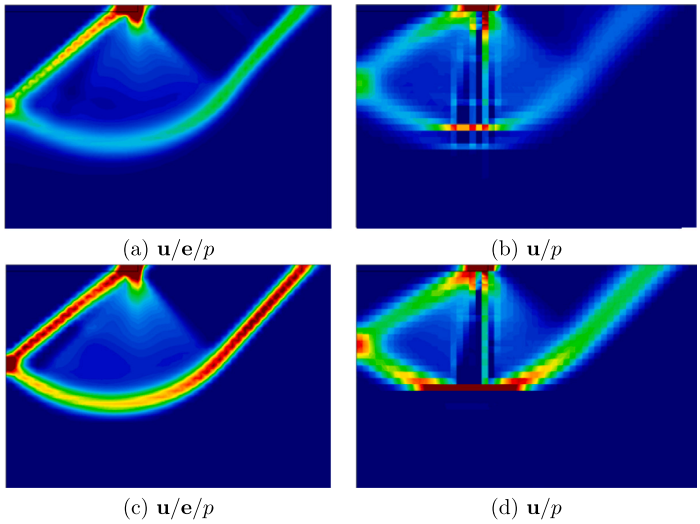

Fig. 29. Prandtl's Punch test — case 2: Collapse mechanisms (*a*)–(*b*) at $d_y = 0.02\,[\mathrm{m}]$ and (*c*)–(*d*) at $d_y = 0.20\,[\mathrm{m}]$.

Fig. 33 shows the load vs displacement curves of the singly perforated thin-walled cylinder computed for both formulations. It can be observed that the peak loads computed with both formulations are in good agreement in this case. However, an important difference on the mechanical dissipation can be appreciated in the analysis. This is caused by the poor evaluation of the stress field in the $\mathbf{u}/p$ formulation, which, as shown in Ref. [35] specially pollutes the computations in the nonlinear range. Conversely, the enhanced precision of the 3-field formulation allows to increase the accuracy of the discrete solution in

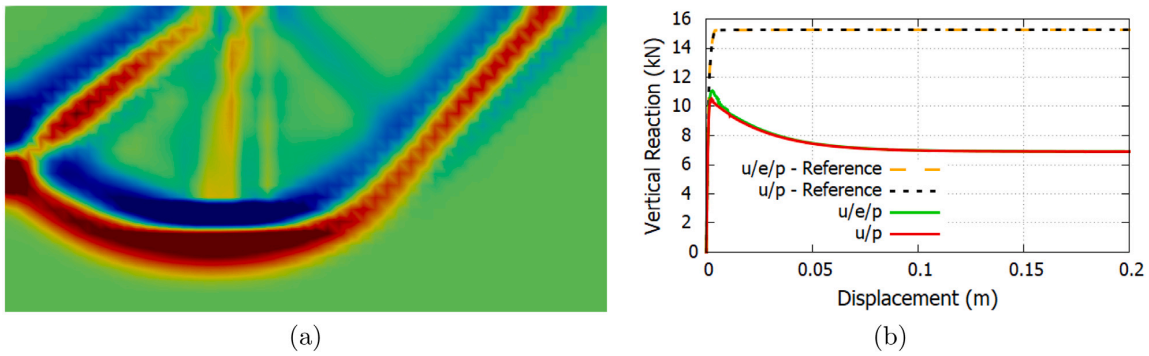

Fig. 30. Prandtl's Punch test — case 2: (*a*) Superimposed collapse mechanisms at $d_y = 0.20$ [m]. In *red* the $\mathbf{u}/\mathbf{e}/p$ solution and the $\mathbf{u}/p$ in *blue*; (*b*) Reaction vs displacement curves. (For interpretation of the references to colour in this figure legend, the reader is referred to the web version of this article.)

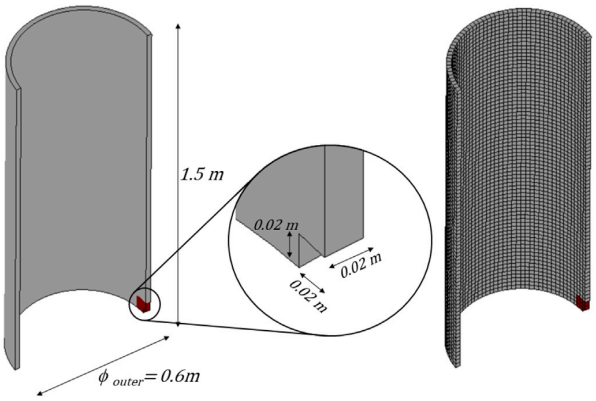

Fig. 31. Singly perforated thin-walled cylinder: Problem setting. Heated area in red. (For interpretation of the references to colour in this figure legend, the reader is referred to the web version of this article.)

Table 5
Singly perforated thin-walled cylinder: Material properties.

Property	Value
Young's Modulus [GPa]	200
Fracture Energy [MJ/m^2]	20
Density [kg/m^3]	7800
Thermal Conductivity [W/(m °C)]	45
Specific Heat Capacity [J/(kg °C)]	500

terms of stress and produces more reliable results, which is particularly crucial in nonlinear problems [35].

Fig. 34 shows the J2-strains at the mid-simulation, Fig. 34(*a*)–(*b*), and at the end of the simulation, Fig. 34(*c*)–(*d*). The difference in the evaluation of the stress field by both formulations produces the contrast observed in Fig. 34. The banding phenomenon, reported in Section 5.2 and in the work [27], is again observed in Fig. 34 for the $\mathbf{u}/p$ formulation when softening behavior is introduced, this time in a thermo-mechanical analysis, while the 3-field solution is correctly localizing in a continuous shear band. Fig. 35 exhibits the principal stress vectors for the same time-steps. There it can be seen the stress-locking phenomenon taking place in the $\mathbf{u}/p$ formulation, where stresses spuriously concentrate in the region of the shear band.

Fig. 36 shows the computed temperature field with both formulations at the time step $t = 750$ [s]. It can be seen that the temperature is higher in the area where the crack develops in the $\mathbf{u}/p$ solution as a result of the higher dissipation of this FE formulation. This evidences the over-dissipation due to stress locking, noticed in Figs. 33 and 35, that takes place in the $\mathbf{u}/p$ formulation due to lack of stress accuracy.

6. Conclusions

In this work, the numerical simulation of thermally-induced structural failure under incompressible conditions is addressed. For this, an enhanced accuracy $\mathbf{u}/\mathbf{e}/p$ formulation is employed and its performance is assessed against the classical $\mathbf{u}/p$ formulation. J2-damage and J2-plasticity nonlinear constitutive laws are introduced to represent the degradation of the isochoric material. Thermal coupling is introduced in the model following a staggered procedure.

The computation of several nonlinear benchmark applications is performed, including strain localization, plasticity and softening behavior. Temperature-dependent material properties are introduced and the influence of the temperature in structural failure is examined with respect to reference isothermal analyses.

It is observed that:

- The standard displacement-based FE formulation from solid mechanics cannot be used to compute problems including incompressible nonlinear constitutive behavior such as the Von Mises yield criterion.
- The 3-field and $\mathbf{u}/p$ FE formulations are both able of considering the elastic incompressibility and the isochoric deformations of the J2-plasticity and J2-damage constitutive models.
- The proposed 3-field FE has a much better performance compared with the $\mathbf{u}/p$ FE in terms of failure mechanisms, bearing capacity, mechanical dissipations, solution stability and is free of stress locking. These aspects are a consequence of the enhanced accuracy of the stress/strain fields considered. Correspondingly, the results computed with the $\mathbf{u}/p$ formulation present serious numerical difficulties in nonlinear applications.
- No spurious mesh dependency can be appreciated in the solutions computed with the $\mathbf{u}/\mathbf{e}/p$ element.
- The proposed method is able to solve incompressible problems using different FE meshes including triangles, quadrilaterals, hexahedra, etc.
- The model reproduces the theoretical load carrying capacity of the numerical benchmarks with accuracy.
- The coupling of the mixed 3-field FE for mechanical problems with the thermal problem is successful and many of the strong points of the 3-field formulation are inherited in thermo-mechanical applications.

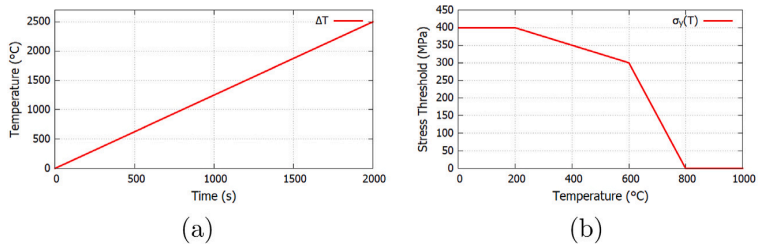

Fig. 32. Singly perforated thin-walled cylinder: (*a*) Temperature increase curve applied on the perforation and (*b*) the uniaxial yield stress threshold evolution with the temperature.

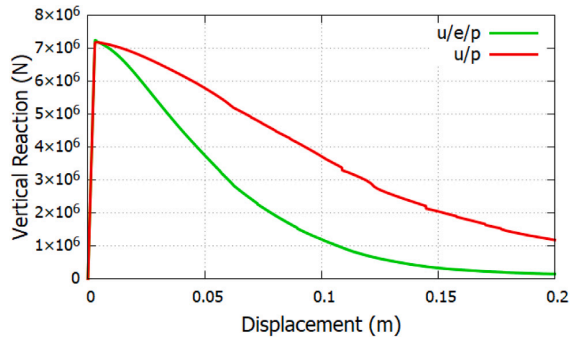

Fig. 33. Singly perforated thin-walled cylinder: Load vs displacement curve.

CRediT authorship contribution statement

Carlos A. Moreira: Formal analysis, Writing – original draft. **Gabriel B. Barbat:** Formal analysis, Writing – original draft. **Miguel Cervera:** Conceptualization, Writing – review & editing, Supervision. **Michele Chiumenti:** Writing – review & editing, Supervision.

Declaration of competing interest

The authors declare that they have no known competing financial interests or personal relationships that could have appeared to influence the work reported in this paper.

Acknowledgments

The authors gratefully acknowledge the financial support from the Spanish Ministry of Economy and Competitiveness, through the Severo Ochoa Programme for Centres of Excellence in R&D (CEX2018-000797-S).

This work has been supported by the European Union's horizon 2020 research and innovation programme (H2020-DT-2019-1 No. 872570) under the KYKLOS 4.0 Project (An Advanced Circular and Agile Manufacturing Ecosystem based on rapid reconfigurable manufacturing process and individualized consumer preferences) and by the Ministry of Science, Innovation and Universities (MCIU), Spain via: the PriMuS project (Printing pattern based and MultiScale enhanced performance analysis of advanced Additive Manufacturing components, ref. num. PID2020-115575RB-I00).

Appendix

The discrete virtual displacements, virtual deviatoric-strains and virtual pressure are approximated as:

$$\begin{aligned}\delta\mathbf{u} &\doteq \delta\hat{\mathbf{u}} = \delta\mathbf{u}_h + \delta\tilde{\mathbf{u}}\\ \delta\mathbf{e} &\doteq \delta\hat{\mathbf{e}} = \delta\mathbf{e}_h + \delta\tilde{\mathbf{e}}\\ \delta p &\doteq \delta\hat{p} = \delta p_h + \delta\tilde{p}\end{aligned} \tag{A.1}$$

Introducing these approximations and the ones in Eq. (42) into the continuous weak form in Eq. (30) and separating the FE and sub-grid scale terms results in the following system of equations:

$$\begin{aligned}
&\int_\Omega [\mathbf{S}\delta\mathbf{u}_h]^T(\mathbf{C}^{dev}\mathbf{e}_h)d\Omega + \int_\Omega [\mathbf{S}\delta\mathbf{u}_h]^T(\mathbf{C}^{dev}\tilde{\mathbf{e}})d\Omega \\
&+ \int_\Omega [\mathbf{S}\delta\mathbf{u}_h]^T(p_h\mathbf{I})d\Omega + \qquad\qquad \forall\delta\mathbf{u}_h \quad (a)\\
&+ \int_\Omega [\mathbf{S}\delta\mathbf{u}_h]^T(\bar{p}\mathbf{I})d\Omega = W(\delta\mathbf{u}_h)\\
&\int_\Omega \delta\mathbf{e}_h^T[\mathbf{C}^{dev}\mathbf{S}\mathbf{u}_h]d\Omega + \int_\Omega \delta\mathbf{e}_h^T[\mathbf{C}^{dev}\mathbf{S}\tilde{\mathbf{u}}]d\Omega + \\
&- \int_\Omega \delta\mathbf{e}_h^T\mathbf{C}^{dev}\mathbf{e}_h d\Omega - \int_\Omega \delta\mathbf{e}_h^T\mathbf{C}^{dev}\tilde{\mathbf{e}}d\Omega = \mathbf{0} \qquad \forall\delta\mathbf{e}_h \quad (b)\\
&\int_\Omega \delta p_h^T(\mathbf{G}^T\mathbf{u}_h)d\Omega + \int_\Omega \delta p_h^T(\mathbf{G}^T\tilde{\mathbf{u}})d\Omega - \int_\Omega \delta p_h^T\tfrac{p_h}{C^{vol}}d\Omega \\
&- \int_\Omega \delta p_h^T\tfrac{\bar{p}}{C^{vol}}d\Omega = 0 \qquad\qquad \forall\delta p_h \quad (c)\\
&\int_\Omega [\mathbf{S}\delta\tilde{\mathbf{u}}]^T(\mathbf{C}^{dev}\mathbf{e}_h)d\Omega + \int_\Omega [\mathbf{S}\delta\tilde{\mathbf{u}}]^T(\mathbf{C}^{dev}\tilde{\mathbf{e}})d\Omega \\
&+ \int_\Omega [\mathbf{S}\delta\tilde{\mathbf{u}}]^T(p_h\mathbf{I})d\Omega + \qquad\qquad \forall\delta\tilde{\mathbf{u}} \quad (d)\\
&+ \int_\Omega [\mathbf{S}\delta\tilde{\mathbf{u}}]^T(\bar{p}\mathbf{I})d\Omega = W(\delta\tilde{\mathbf{u}})\\
&\int_\Omega \delta\tilde{\mathbf{e}}^T[\mathbf{C}^{dev}\mathbf{S}\mathbf{u}_h]d\Omega + \int_\Omega \delta\tilde{\mathbf{e}}^T[\mathbf{C}^{dev}\mathbf{S}\tilde{\mathbf{u}}]d\Omega + \\
&- \int_\Omega \delta\tilde{\mathbf{e}}^T\mathbf{C}^{dev}\mathbf{e}_h d\Omega - \int_\Omega^T \delta\tilde{\mathbf{e}}^T\mathbf{C}^{dev}\tilde{\mathbf{e}}d\Omega = \mathbf{0} \qquad \forall\delta\tilde{\mathbf{e}} \quad (e)\\
&\int_\Omega \delta\tilde{p}^T(\mathbf{G}^T\mathbf{u}_h)d\Omega + \int_\Omega \delta\tilde{p}^T(\mathbf{G}^T\tilde{\mathbf{u}})d\Omega - \int_\Omega \delta\tilde{p}^T\tfrac{p_h}{C^{vol}}d\Omega \\
&- \int_\Omega \delta\tilde{p}^T\tfrac{\bar{p}}{C^{vol}}d\Omega = 0 \qquad\qquad \forall\delta\tilde{p} \quad (f)
\end{aligned} \tag{A.2}$$

The system formed by the sub-grid scale Eqs. (A.2)*d*, (A.2)*e* and (A.2)*f* admits the following solution, corresponding to the residual based sub-grid approach,

$$\begin{aligned}\tilde{\mathbf{u}} &= \tau_u[\mathbf{S}^T(\mathbf{C}^{dev}\mathbf{e}_h) + \mathbf{G}p_h + \mathbf{f}]\\ \tilde{\mathbf{e}} &= \tau_e[\mathbf{W}\mathbf{u}_h - \mathbf{e}_h]\\ \tilde{p} &= \tau_p[\mathbf{G}^T\mathbf{u}_h - \tfrac{p_h}{C^{vol}}]\end{aligned} \tag{A.3}$$

where the stabilization parameters τ_u, τ_e and τ_p are chosen to obtain optimum convergence rates upon mesh refinement [71,84] as:

$$\begin{aligned}\tau_u &= \tfrac{c_u h L_0}{2\tilde{C}^{dev}}\\ \tau_e &= c_e\tfrac{h}{L_0}\\ \tau_p &= c_p\tilde{C}^{vol}\tfrac{h}{L_0}\end{aligned} \tag{A.4}$$

where L_0 is a characteristic length of the problem, c_u, c_e and c_p are arbitrary stabilization constants, h is the FE size and $\tilde{C}^{dev}$ is the secant shear modulus defined as

$$\tilde{C}^{dev} = \frac{\|\mathbf{s}_h\|}{2\|\mathbf{e}_h\|} \tag{A.5}$$

and $\tilde{C}^{vol}$ is the compressibility modulus obtained according to a Fourier analysis in [84] and defined as:

$$\tilde{C}^{vol} = \left(\frac{c_1}{2\tilde{G}} + \frac{c_2}{\tilde{K}}\right)^{-1} \tag{A.6}$$

where $\tilde{G}$ and $\tilde{K}$ are the *effective secant shear modulus* and *effective bulk modulus*, respectively. Choosing the constants $c_1 = 1$ and $c_2 = \frac{2}{3}$, and rewriting $\tilde{C}^{vol}$ in terms of $\tilde{G}$ leads to

$$\tilde{C}^{vol} = \frac{2}{3}\tilde{G}\left(\frac{1+\nu}{1-\nu}\right) \tag{A.7}$$

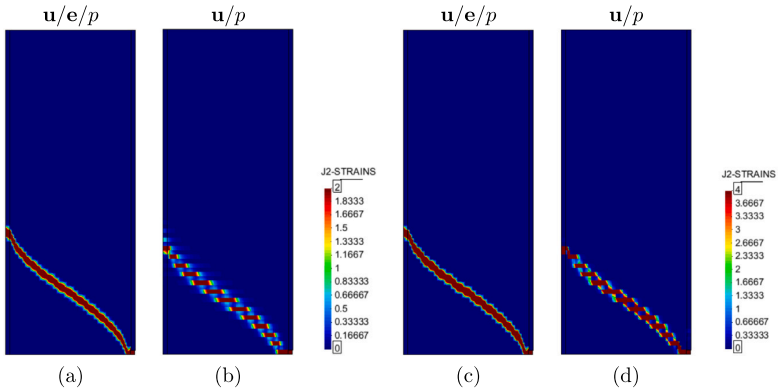

Fig. 34. Singly perforated thin-walled cylinder: J2-strains (*a*)–(*b*) at the mid-simulation and (*c*)–(*d*) at the final time step.

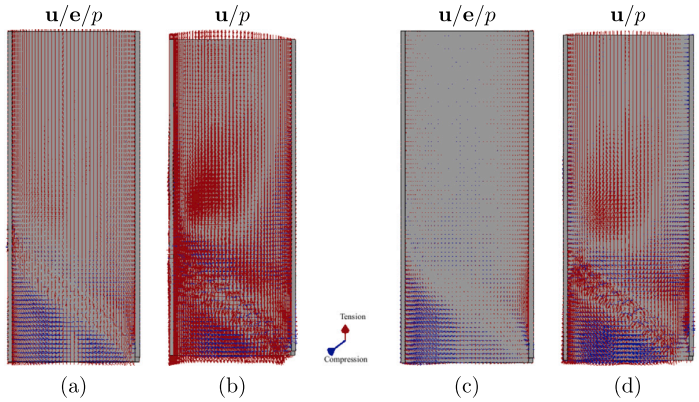

Fig. 35. Singly perforated thin-walled cylinder: Principal stresses vectors (*a*)–(*b*) at the mid-simulation and (*c*)–(*d*) at the final time step.

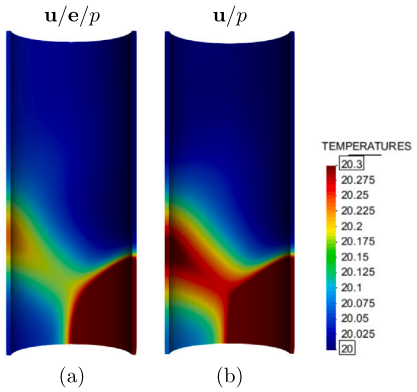

Fig. 36. Singly perforated thin-walled cylinder: Temperature field in [°C] computed with both formulations at the time step $t = 750$ [s].

Then $\bar{\mathbf{u}}$, $\bar{\mathbf{e}}$ and $\bar{p}$ of Eq. (A.3) are introduced into the remaining equations (A.2)*a*, (A.2)*b* and (A.2)*c* to stabilize the discrete FE problem. Note that the stabilization terms in Eq. (A.3) tend to zero upon convergence as they correspond to the residual of the strong form of the problem.

With some manipulation, the stabilized weak form of the problem results in:

$$
\begin{aligned}
&(1-\tau_e)\int_\Omega [\mathbf{S}\delta\mathbf{u}_h]^T(\mathbf{C}^{dev}\mathbf{e}_h)d\Omega + \tau_e\int_\Omega [\mathbf{S}\delta\mathbf{u}_h]^T(\mathbf{C}^{dev}\mathbf{S}\mathbf{u}_h)d\Omega \\
&+(1-\tfrac{\tau_p}{C^{vol}})\int_\Omega [\mathbf{S}\delta\mathbf{u}_h]^T(p_h\mathbf{I})d\Omega \qquad \forall\delta\mathbf{u}_h \\
&+\tau_p\int_\Omega [\mathbf{S}\delta\mathbf{u}_h]^T(\mathbf{G}^T\mathbf{u}_h\mathbf{I})d\Omega = W(\delta\mathbf{u}_h) \\
&(1-\tau_e)\int_\Omega \delta\mathbf{e}_h^T[\mathbf{C}^{dev}\mathbf{S}\mathbf{u}_h]d\Omega \\
&-\tau_u\int_\Omega(\delta\mathbf{e}_h^T\mathbf{S}\mathbf{C}^{dev})(\mathbf{C}^{dev}\mathbf{S}^T\mathbf{e}_h)d\Omega+ \qquad \forall\delta\mathbf{e}_h \\
&-\tau_u\int_\Omega(\delta\mathbf{e}_h^T\mathbf{S})[\mathbf{C}^{dev}\mathbf{G}p_h]d\Omega \\
&-(1-\tau_e)\int_\Omega \delta\mathbf{e}_h^T\mathbf{C}^{dev}\mathbf{e}_h d\Omega = \mathbf{0} \\
&(1-\tfrac{\tau_p}{C^{vol}})\int_\Omega \delta p_h^T(\mathbf{G}^T\mathbf{u}_h)d\Omega - \tau_u\int_\Omega(\delta p_h^T\mathbf{G}^T)(\mathbf{C}^{dev}\mathbf{S}^T\mathbf{e}_h)d\Omega \\
&-\tau_u\int_\Omega(\delta p_h^T\mathbf{G}^T)(\mathbf{G}p_h)d\Omega+ \qquad \forall\delta p_h \\
&-(1-\tfrac{\tau_p}{C^{vol}})\int_\Omega \delta p_h^T\tfrac{p_h}{C^{vol}}d\Omega = 0
\end{aligned}
\tag{A.8}
$$

where the divergence theorem has been applied to the second and third terms of Eq. (A.8)*b* and (A.8)*c*. Note that in this process, the boundary terms of the sub-grid scales are neglected with respect to the other terms. In addition, the body forces, $\mathbf{f}$, are considered constant inside each element.

Next, the FE discrete form of the problem is obtained by substituting $\mathbf{u}_h$, $\mathbf{e}_h$ and p_h (and $\delta\mathbf{u}_h$, $\delta\mathbf{e}_h$, δp_h) by their FE discrete approximations:

$$
\begin{aligned}
&(1-\tau_e)\int_\Omega(\delta\mathbf{U}^T\underbrace{\mathbf{N}_u^T\mathbf{S}^T}_{=\mathbf{B}_u^T})(\mathbf{C}^{dev}\mathbf{N}_e\mathbf{E})d\Omega\\
&+\tau_e\int_\Omega(\delta\mathbf{U}^T\underbrace{\mathbf{N}_u^T\mathbf{S}^T}_{=\mathbf{B}_u^T})(\mathbf{C}^{dev}\underbrace{\mathbf{S}\mathbf{N}_u}_{=\mathbf{B}_u}\mathbf{U})d\Omega+ \qquad \forall\delta\mathbf{U}\\
&+(1-\tfrac{\tau_p}{C^{vol}})\int_\Omega\delta\mathbf{U}^T\mathbf{N}_u^T\mathbf{G}\mathbf{N}_p\mathbf{P}d\Omega\\
&+\tau_p\int_\Omega\delta\mathbf{U}^T\mathbf{N}_u^T\underbrace{\mathbf{S}^T\mathbf{I}}_{=\mathbf{G}}\mathbf{G}^T\mathbf{N}_u\mathbf{U}d\Omega=\quad\hat{W}(\delta\mathbf{U})\\
&(1-\tau_e)\int_\Omega\delta\mathbf{E}^T\mathbf{N}_e^T[\mathbf{C}^{dev}(\underbrace{\mathbf{S}\mathbf{N}_u}_{=\mathbf{B}_u}\mathbf{U})]d\Omega\\
&-\tau_u\int_\Omega(\delta\mathbf{E}^T\mathbf{N}_e^T\mathbf{S}\mathbf{C}^{dev})(\mathbf{C}^{dev}\mathbf{S}^T\mathbf{N}_e\mathbf{E})d\Omega \qquad \forall\delta\mathbf{E}\\
&-\tau_u\int_\Omega(\delta\mathbf{E}^T\mathbf{N}_e^T\mathbf{S})[\mathbf{C}^{dev}(\mathbf{G}\mathbf{N}_p\mathbf{P})]d\Omega\\
&-(1-\tau_e)\int_\Omega\delta\mathbf{E}^T\mathbf{N}_e^T\mathbf{C}^{dev}\mathbf{N}_e\mathbf{E}d\Omega=\mathbf{0}\\
&(1-\tfrac{\tau_p}{C^{vol}})\int_\Omega\delta\mathbf{P}^T\mathbf{N}_p^T(\mathbf{G}^T\mathbf{N}_u\mathbf{U})d\Omega\\
&-\tau_u\int_\Omega(\delta\mathbf{P}^T\mathbf{N}_p^T\mathbf{G}^T)(\mathbf{C}^{dev}\mathbf{S}^T\mathbf{N}_e\mathbf{E})d\Omega+ \qquad \forall\delta\mathbf{P}\\
&-\tau_u\int_\Omega(\delta\mathbf{P}^T\mathbf{N}_p^T\mathbf{G}^T)(\mathbf{G}\mathbf{N}_p\mathbf{P})d\Omega\\
&-(1-\tfrac{\tau_p}{C^{vol}})\int_\Omega\delta\mathbf{P}^T\mathbf{N}_p^T\tfrac{\mathbf{N}_p\mathbf{P}}{C^{vol}}d\Omega=0
\end{aligned}
\tag{A.9}
$$

with

$$
\hat{W}(\delta\mathbf{U})=\int_\Omega\delta\mathbf{U}^T\mathbf{N}_u^T\mathbf{f}d\Omega+\int_{\Gamma_t}\delta\mathbf{U}^T\mathbf{N}_u^T\bar{\mathbf{t}}d\Gamma \tag{A.10}
$$

Once again, the virtual displacement $\delta\mathbf{U}$, virtual deviatoric-strain $\delta\mathbf{E}$ and virtual pressure $\delta\mathbf{P}$ nodal vectors that appear in the system of Eqs. (A.9) are arbitrary, leading to the stabilized system of Eqs. (43).

References

[1] Zienkiewicz OC, Taylor LR, Zhu ZJ. The finite element method: Its basis and fundamentals. 6th ed. Butterworth-Heinemann; 2005.

[2] Miehe C. Aspects of the formulation and finite element implementation of large strain isotropic elasticity. Internat J Numer Methods Engrg 1994;37:1981–2004.

[3] Simo JC, Taylor RL, Pister KS. Variational and projection methods for the volume constraint in finite deformation elasto-plasticity. Comput Methods Appl Mech Engrg 1985;51:177–208.

[4] Simo JC, Rifai MS. A class of mixed assumed strain methods and the method of incompatible modes. Internat J Numer Methods Engrg 1990;29:1595–638.

[5] Agelet de Saracibar C, Chiumenti M, Valverde Q, Cervera M. On the orthogonal subgrid scale pressure stabilization of finite deformation J2 plasticity. Comput Methods Appl Mech Engrg 2006;195:1224–51.

[6] Arnold DN, Brezzi F, Fortin M. A stable finite element for the Stokes equations. Calcolo 1984;21:337–44.

[7] Arnold DN, Winther R. Mixed finite elements for elasticity. Numer Math 2002;92:401–19.

[8] Chama A, Reddy DB. New stable mixed finite element approximations for problems in linear elasticity. Comput Methods Appl Mech Engrg 2013;256:211–23.

[9] Malkus DS, Hughes TJR. Mixed finite element methods - reduced and selective integration techniques: A unification of concepts. Comput Methods Appl Mech Engrg 1978;15:63–81.

[10] Saloustros S, Cervera M, Kim S, Chiumenti M. Accurate and locking-free analysis of beams, plates and shells using solid elements. Comput Mech 2021. http://dx.doi.org/10.1007/s00466-020-01969-0.

[11] Cervera M, Chiumenti M, Di Capua D. Benchmarking on bifurcation and localization in J2 plasticity for plane stress and plane strain conditions. Comput Methods Appl Mech Engrg 2012;241–244:206–24.

[12] Baiocchi C, Brezzi F, Franca L. Virtual bubbles and Galerkin/least-squares type methods (Ga.L.S.). Comput Methods Appl Mech Engrg 1993;105:125–41.

[13] Kasper EP, Taylor RL. A mixed-enhanced strain method. I: Geometrically linear problems. II: Geometrically nonlinear problems. Comput Struct 2000;75:237–50, 251–260.

[14] Reddy BD, Simo JC. Stability and convergence of a class of enhanced assumed strain methods. SIAM J Numer Anal 1995;32:1705–28.

[15] Bonet J, Burton AJ. A simple average nodal pressure tetrahedral element for incompressible and nearly incompressible dynamic explicit applications. Commun Numer Methods Eng 1998;1(4):437–49.

[16] Bonet J, Marriot H, Hassan O. An averaged nodal deformation gradient linear tetrahedral element for large strain explicit dynamic applications. Commun Numer Methods Eng 2001;17:551–61.

[17] Bonet J, Marriot H, Hassan O. Stability and comparison of different linear tetrahedral formulations for nearly incompressible explicit dynamic applications. Internat J Numer Methods Engrg 2001;50:119–33.

[18] Dohrmann CR, Heinstein MW, Jung J, Key SW, Witkowsky WR. Node-based uniform strain elements for three-node triangular and four-node tetrahedral meshes. Internat J Numer Methods Engrg 2000;47:1549–68.

[19] de Souza Neto EA, Pires FMA, Owen DRJ. F-bar-based linear triangles and tetrahedra for finite strain analysis of nearly incompressible solids. Part I: Formulation and benchmarking. Internat J Numer Methods Engrg 2005;62:353–83.

[20] Hughes TJ. Generalization of selective integration procedures to anisotropic and nonlinear media. Internat J Numer Methods Engrg 1980;15(9):1413–8. http://dx.doi.org/10.1002/nme.1620150914.

[21] Nagtegaal JC, Parks DM, Rice JR. On numerically accurate finite element solutions in the fully plastic range. Comput Methods Appl Mech Engrg 1974;4(2):153–77. http://dx.doi.org/10.1016/0045-7825(74)90032-2.

[22] Sloan SW, Randolph MF. Numerical prediction of collapse loads using finite element methods. Int J Numer Anal Methods Geomech 1982;6(1):47–76. http://dx.doi.org/10.1002/nag.1610060105.

[23] Barbat GB, Cervera M, Chiumenti M. Appraisement of planar, bending and twisting cracks in 3D with isotropic and orthotropic damage models. Int J Fract 2018;210(1–2):45–79. http://dx.doi.org/10.1007/s10704-018-0261-3.

[24] Barbat GB, Cervera M, Chiumenti M. Structural size effect: Experimental, theoretical and accurate computational assessment. Eng Struct 2020;213:110555. http://dx.doi.org/10.1016/j.engstruct.2020.110555.

[25] Cervera M, Barbat GB, Chiumenti M. Finite element modelling of quasi-brittle cracks in 2D and 3D with enhanced strain accuracy. Comput Mech 2017;60(5):767–96. http://dx.doi.org/10.1007/s00466-017-1438-8.

[26] Cervera M, Barbat GB, Chiumenti M. Architecture of a multi-crack model with full closing, reopening and sliding capabilities. Comput Mech 2020;65:1593–620. http://dx.doi.org/10.1007/s00466-020-01836-y.

[27] Cervera M, Chiumenti M, Benedetti L, Codina R. Mixed stabilized finite element methods in nonlinear solid mechanics. Part III: Compressible and incompressible plasticity. Comput Methods Appl Mech Engrg 2015;285:752–75.

[28] Cervera M, Chiumenti M, Codina R. Mixed stabilized finite element methods in nonlinear solid mechanics. Part I: Formulation. Comput Methods Appl Mech Engrg 2010;199:2559–70.

[29] Cervera M, Chiumenti M, Codina R. Mixed stabilized finite element methods in nonlinear solid mechanics. Part II: Strain localization. Comput Methods Appl Mech Engrg 2010;199:2571–89.

[30] Cervera M, Chiumenti M, Codina R. Mesh objective modeling of cracks using continuous linear strain and displacement interpolations. Internat J Numer Methods Engrg 2011;87(10):962–87.

[31] Vlachakis G, Cervera M, Barbat GB, Saloustros S. Out-of-plane seismic response and failure mechanism of masonry structures using finite elements with enhanced strain accuracy. Eng Fail Anal 2019;97:534–55. http://dx.doi.org/10.1016/j.engfailanal.2019.01.017.

[32] Cervera M, Barbat GB, Chiumenti M, Wu J-Y. A comparative review of xfem, mixed fem and phase-field models for quasi-brittle cracking. Arch Computat Methods Eng 2022;29:1009–83. http://dx.doi.org/10.1007/s11831-021-09604-8.

[33] Castañar I, Baiges J, Codina R, Venghaus H. Topological derivative-based topology optimization of incompressible structures using mixed formulations. Comput Methods Appl Mech Engrg 2022;390:114438. http://dx.doi.org/10.1016/j.cma.2021.114438.

[34] Chiumenti M, Cervera M, Codina R. A mixed three-field FE formulation for stress accurate analysis including the incompressible limit. Comput Methods Appl Mech Engrg 2015;283:1095–116.

[35] Chiumenti M, Cervera M, Moreira CA, Barbat GB. Stress, strain and dissipation accurate 3-field formulation for inelastic isochoric deformation. Finite Elem Anal Des 2021;192:103534. http://dx.doi.org/10.1016/j.finel.2021.103534.

[36] Castañar I, Baiges J, Codina R. A stabilized mixed finite element approximation for incompressible finite strain solid dynamics using a total lagrangian formulation. Computer Methods in Applied Mechanics and Engineering 2020;368:113164. http://dx.doi.org/10.1016/j.cma.2020.113164.

[37] Cervera M, Chiumenti M. Size effect and localization in J_2 plasticity. Int J Solids Struct 2009;46:3301–12.

[38] Cervera M, Chiumenti M, Agelet de Saracibar C. Softening, localization and stabilization: Capture of discontinuous solutions in J2 plasticity. Int J Numer Anal Methods Geomech 2004;28:373–93.

[39] Cervera M, Chiumenti M, Agelet de Saracibar C. Shear band localization via local J_2 continuum damage mechanics. Comput Methods Appl Mech Engrg 2004;193:849–80.

[40] Chiumenti M, Valverde Q, Agelet de Saracibar C, Cervera M. A stabilized formulation for incompressible plasticity using linear triangles and tetrahedra. Int J Plast 2004;20:1487–504.

[41] Pastor M, Li T, Liu X, Zienkiewicz OC. Stabilized low-order finite elements for failure and localization problems in undrained soils and foundations. Comput Methods Appl Mech Engrg 1999;174:219–34.

[42] Bary B, Ranc G, Durand S, Carpentier O. A coupled thermo-hydro-mechanical-damage model for concrete subjected to moderate temperatures. Int J Heat Mass Transfer 2008;51:2847–62. http://dx.doi.org/10.1016/j.ijheatmasstransfer.2007.09.021.

[43] Li G, Cinefra M, Carrera E. Coupled thermo-mechanical finite element models with node-dependent kinematics for multi-layered shell structures. Int J Mech Sci 2020;171:105379. http://dx.doi.org/10.1016/j.ijmecsci.2019.105379.

[44] Sanavia L, Pesavento F, Schrefler BA. Finite element analysis of non-isothermal multiphase geomaterials with application to strain localization simulation. Comput Mech 2006;37:331. http://dx.doi.org/10.1007/s00466-005-0673-6.

[45] Wang K, Song X. Strain localization in non-isothermal unsaturated porous media considering material heterogeneity with stabilized mixed finite elements. Comput Methods Appl Mech Engrg 2020;359:112770. http://dx.doi.org/10.1016/j.cma.2019.112770.

[46] Carrera E, Cinefra M, Petrolo M, Zappino E. Finite element analysis of structures through unified formulation. In: Finite element analysis of structures through unified formulation. 2014, http://dx.doi.org/10.1002/9781118536643.

[47] Carrera E. Temperature profile influence on layered plates response considering classical and advanced theories. AIAA J 2002;40:1885–96. http://dx.doi.org/10.2514/2.1868.

[48] Carrera E. Transverse normal strain effect on thermal stress analysis of Homogeneous and layered plates. AIAA J 2005;43:2232–42. http://dx.doi.org/10.2514/1.11230.

[49] Robaldo A, Carrera E, Benjeddou A. Unified formulation for finite element thermoelastic analysis of multilayered anisotropic composite plates. J Therm Stresses 2005;28:1031–65. http://dx.doi.org/10.1080/01495730590964963.

[50] Carrera E, Boscolo M, Robaldo A. Hierarchic multilayered plate elements for coupled multifield problems of piezoelectric adaptive structures: Formulation and numerical assessment. Arch Comput Methods Eng 2007;14:383–430. http://dx.doi.org/10.1007/s11831-007-9012-8.

[51] Robaldo A, Carrera E, Benjeddou A. A unified formulation for finite element analysis of piezoelectric plates. Comput Struct 2006;84:1494–505. http://dx.doi.org/10.1016/j.compstruc.2006.01.029.

[52] Carrera E, Brischetto S, Nali P. Variational statements and computational models for MultiField problems and multilayered structures. Mech Adv Mater Struct 2008;15:182–98. http://dx.doi.org/10.1080/15376490801907657.

[53] Carrera E, Brischetto S, Fagiano C, Nali P. Mixed multilayered plate elements for coupled magneto-electro-elastic analysis. Multidiscip Model Mater Struct 2009;5:251–6. http://dx.doi.org/10.1163/157361109789017050.

[54] Carrera E, Fazzolari FA, Cinefra M. Thermal stress analysis of composite beams, plates and shells: Computational modelling and applications. Academic Press; 2015, p. 440.

[55] Gavagnin C, Sanavia L, De Lorenzis L. Stabilized mixed formulation for phase-field computation of deviatoric fracture in elastic and poroelastic materials. Comput Mech 2020;65:1447–65. http://dx.doi.org/10.1007/s00466-020-01829-x.

[56] Jha B, Juanes R. A locally conservative finite element framework for the simulation of coupled flow and reservoir geomechanics. Acta Geotech 2007;2:139–53. http://dx.doi.org/10.1007/s11440-007-0033-0.

[57] Lewis R, Schrefler B. Finite element method in the deformation and consolidation of porous media. New York: Wiley; 1998.

[58] White JA, Borja I. Stabilized low-order finite elements for coupled solid-deformation/fluid-diffusion and their application to fault zone transients. Comput Methods Appl Mech Engrg 2008;197:4353–66. http://dx.doi.org/10.1016/j.cma.2008.05.015.

[59] Babuska I. Error-bounds for finite element method. Numer Math 1971;16:322–33.

[60] Brezzi F, Fortin M. Mixed and hybrid finite element methods. New York: Springer; 1991.

[61] Codina R, Badia S, Baiges J, Principe J. Variational multiscale methods in computational fluid dynamics. In: Encyclopedia of computational mechanics. John Wiley & Sons, Ltd.; 2017, p. 1–28.

[62] Hughes TJR. Multiscale phenomena: Green's function, Dirichlet-to Neumann formulation, subgrid scale models, bubbles and the origins of stabilized formulations. Comput Methods Appl Mech Engrg 1995;127:387–401.

[63] Hughes TJR, Feijoó GR, L. Mazzei, Quincy JB. The variational multiscale method-a paradigm for computational mechanics, echanics. Comput Methods Appl Mech Engrg 1998;166:3–28.

[64] Badia S, Codina R. Stabilized continuous and discontinuous Galerkin techniques for Darcy flow. Comput Methods Appl Mech Engrg 2010;199:1654–67.

[65] Codina R. Stabilization of incompressibility and convection through orthogonal sub-scales in finite element methods. Comput Methods Appl Mech Engrg 2000;190:1579–99.

[66] Codina R. Finite element approximation of the three field formulation of the Stokes problem using arbitrary interpolations. SIAM J Numer Anal 2009;47:699–718.

[67] Cervera M, Chiumenti M, Valverde Q, Agelet de Saracibar C. Mixed linear/linear simplicial elements for incompressible elasticity and plasticity. Comput Methods Appl Mech Engrg 2003;192:5249–63.

[68] Chiumenti M, Valverde Q, Agelet de Saracibar C, Cervera M. A stabilized formulation for incompressible elasticity using linear displacement and pressure interpolations. Comput Methods Appl Mech Engrg 2002;191:5253–64.

[69] Codina R, Blasco J. Stabilized finite element method for transient Navier–Stokes equations based on pressure gradient projection. Comput Methods Appl Mech Engrg 2000;182:287–300.

[70] Codina R. Stabilized finite element approximation of transient incompressible flows using orthogonal subscales. Comput Methods Appl Mech Engrg 2002;191:4295–321.

[71] Castillo E, Codina R. Variational multi-scale stabilized formulations for the stationary three-field incompressible viscoelastic flow problem. Comput Methods Appl Mech Engrg 2014;279:579–605.

[72] Agelet De Saracibar C, Cervera M, Chiumenti M. On the formulation of coupled thermoplastic problems with phase-change. Int J Plast 1999;15(1):1–34.

[73] Agelet de Saracibar C, Cervera M, Chiumenti M. On the constitutive modeling of coupled thermomechanical phase-change problems. Int J Plast 2001;17(12):1565–622.

[74] Chiumenti M, Cervera M, Agelet de Saracibar C, Dialami N. Numerical modeling of friction stir welding processes. Comput Method Appl Mech Engrg 2013;254:353–69.

[75] Dialami N. Cervera M, Chiumenti M, Agelet de Saracibar C. Local–global strategy for the prediction of residual stresses in FSW processes. Int J Adv Manuf Technol 2017;88(3099):9–3111. http://dx.doi.org/10.1007/s00170-016-9016-3.

[76] Bazant ZP, Oh BH. Crack band theory for fracture of concrete. Mater Struct 1983;16:155–77.

[77] Pietruszczak S, Mroz Z. Finite element analysis of deformation of strain-softening materials. Internat J Numer Methods Engrg 1981;17:327–34.

[78] Cervera M, Agelet de Saracibar C, Chiumenti M. COMET: Coupled mechanical and thermal analysis. Data input manual, version 5.0. Technical report IT-308, 2002, http://www.cimne.upc.es.

[79] GiD v13 Reference Manual, Coll A, Ribó R, Pasenau M, Escolano E, Perez J Suit. CIMNE. CIMNE; 2016.

[80] Ahrens J, Geveci B, Law C. Paraview: An end-user tool for large data visualization, visualization handbook. Elsevier; 2005.

[81] Lubliner J. Plasticity theory. In: Dover books on engineering. Dover Publications; 2008.

[82] Bhatti Ayjwat A, Barsoum Zuheir, Murakawa Hidekazu, Barsoum Imad. Influence of thermo-mechanical material properties of different steel grades on welding residual stresses and angular distortion. Mater Des 2014;65:878–89. http://dx.doi.org/10.1016/j.matdes.2014.10.019.

[83] Hill R. The mathematical theory of plasticity. Oxford University Press; 1950.

[84] Badia S, Codina R. Unified stabilized finite element formulations for the Stokes and the Darcy problems. SIAM J Numer Anal 2009;17:309–30.

A.4 Paper 4

Title: A multi-criteria *h*-adaptive finite-element framework for industrial part-scale thermal analysis in additive manufacturing processes.

Authors:

- **C. A. Moreira**: PhD Candidate in Civil Engineering in UPC BarcelonaTech and International Center for Numerical Methods in Engineering (CIMNE).
- **M. A. Caicedo**: Assistant Professor of Continuum Mechanics and Structural analysis at the Universitat Politècnica de Catalunya (Technical University of Catalonia BarcelonaTech).
- **M. Cervera**: Full Professor of Continuum Mechanics and Structural analysis at the Universitat Politècnica de Catalunya (Technical University of Catalonia BarcelonaTech). Affiliated Scientist at the International Center for Numerical Methods in Engineering (CIMNE).
- **M. Chiumenti**: Full Professor of Continuum Mechanics and Structural analysis at the Universitat Politècnica de Catalunya (Technical University of Catalonia BarcelonaTech). Affiliated Scientist at the International Center for Numerical Methods in Engineering (CIMNE).
- **J. Baiges**: Associate Professor of Continuum Mechanics and Structural analysis at the Universitat Politècnica de Catalunya (Technical University of Catalonia BarcelonaTech). Affiliated Scientist at the International Center for Numerical Methods in Engineering (CIMNE).

Engineering with Computers
Editor-in-Chief: Jessica Zhang
ISSN: 0177-0667
Springer Nature Editors
https://doi.org/10.1007/s00366-022-01655-0
Link to Publisher

Engineering with Computers
https://doi.org/10.1007/s00366-022-01655-0

ORIGINAL ARTICLE

A multi-criteria *h*-adaptive finite-element framework for industrial part-scale thermal analysis in additive manufacturing processes

Carlos A. Moreira[1,2] · **Manuel A. Caicedo**[2,3] · **Miguel Cervera**[1,2] · **Michele Chiumenti**[1,2] · **Joan Baiges**[1]

Received: 27 December 2021 / Accepted: 29 March 2022

Abstract
This work presents an *h*-adaptive finite-element (FE) strategy to address the numerical simulation of additive manufacturing (AM) of large-scale parts. The wire-arc additive manufacturing is chosen as the demonstrative technology for its manufacturing capabilities suitable for industrial purposes. The scanning path and processing parameters of the simulation are provided via a RS-274 (GCode) file, being the same as the one delivered to the AM machine. The approach is suitable for industrial applications and can be applied to other AM processes. To identify the location in the FE mesh of the heat affected zone (HAZ), a collision detection algorithm based on the separating axis theorem is used. The mesh is continuously adapted to guarantee the necessary mesh resolution to capture the phenomena inside and outside the HAZ. To do so, a multi-criteria adaptive mesh refinement and coarsening (AMR) strategy is used. The AMR includes a geometrical criterion to guarantee the FE size within the HAZ, and a Zienkiewicz–Zhu-based a-posteriori error estimator to guarantee the solution accuracy elsewhere. Thus, the number of active FEs is controlled and mesh manipulation by the end-user is avoided. Numerical simulations comparing the *h*-adaptive strategy with the (reference) fixed fine meshes are performed to prove the computational cost efficiency and the solution accuracy.

Keywords Finite elements · Multi-criteria adaptive mesh refinement · Additive manufacturing · GCode-based simulation · Hierarchical octree-based meshes

1 Introduction

Meeting the demands of new design strategies in terms of optimality and functionality of many industrially relevant settings involves the use of suitable additive manufacturing (AM) techniques. When complex geometries are generated via shape optimization analysis, or provided by a multi-scale analysis, where specific micro-scale is required to fulfill certain functionalities (e.g., weight reduction, thermal conduction or noise isolation) [30, 42, 51, 56], traditional manufacturing processes often fail to meet the design requirements. Therefore, the use of AM manufacturing techniques to fabricate such geometries is preferred.

Powder-based AM technologies, as selective laser melting (SLM), electron beam melting (EBM) and selective laser sintering (SLS), produce very thin layers, ranging from 25 to 100 (μm), while wire feeding technologies, for instance Wire-Arc additive manufacturing (WAAM), and direct energy deposition (DED) technologies, such as laser engineered net shaping (LENS) and electron beam freeform fabrication (EBF^3), provide layer thickness in the range of 1000–5000 (μm). Although the former produce a final product of higher quality [6], they are limited by the actual dimension of the AM chamber. Therefore, WAAM or DED technologies are suitable when dealing with large-size components (where the height can range from tens of centimeters to meters) due their capacity to print thicker layers.

✉ Carlos A. Moreira
camoreira@cimne.upc.edu

1 Department of Civil and Environmental Engineering (DECA), Barcelona School of Civil Engineering (ETSECCPB), Universitat Politècnica de Catalunya (UPC), Edificio C1, Campus Norte, Gran Capitán s/n, 08034 Barcelona, Spain

2 International Center for Numerical Methods in Engineering (CIMNE), Edificio C1, Campus Norte, Gran Capitán s/n, 08034 Barcelona, Spain

3 Department of Strength of Materials and Structural Engineering (RMEE), Barcelona East School of Engineering (EEBE), Universitat Politècnica de Catalunya (UPC), Av. Eduard Maristany 16, 08019 Barcelona, Spain

Published online: 07 June 2022

Together with the evolution of AM techniques, appropriate CAD tools have been developed to bridge the gap between designers and the manufacturing process, playing a crucial role in the design to production pipeline. Once the computer aided design (CAD) geometry has been prepared, the resulting STereoLithography (STL) mesh is sliced to produce the scanning sequence for each layer [52, 53]. Two formats are commonly used: the common layer interface (CLI) [18] and the RS-274 (GCode). CLI contains only the geometry of the scanning path, while the GCode also includes a series of machine tools commands.

Nowadays, the calibration of the AM process parameters is a trial and error process, and experiments are costly. Therefore, a major effort is being put into the development of efficient and accurate finite-element (FE) frameworks for the simulation of AM processes. In addition, from the numerical point of view, complex geometries require several hundreds of scanning tracks to conform the geometry to be read from the CLI/GCode files. As a consequence, a large number of FEs need to be used to describe the computational domain, resulting in a high computational cost [39]. The part-scale meshing step is challenging when complex geometries are involved. Standard solutions adopt an initial FE mesh to accurately describe the geometry resulting in huge FE meshes and large pre-process data files.

Because of this, computational models have been restricted to validation, using simple geometries (e.g., thin-walled structures, cuboids, beams, bridges) with a reduced mesh size [15, 29, 35, 50]. However, to assess the quality and performance of the printed part, high-fidelity (HF) simulations are mandatory to optimize the process parameters. For instance, the accurate prediction of the thermal history is necessary to analyze the metallurgical evolution at the micro-scale [31, 32, 38]. In this context, the sizes of the FEs and the laser-spot must be comparable [19]; for industrial-sized components, this specification implies a dense FE mesh at the heat affected zone (HAZ).

From the computational point of view, problems involving growing domains require a strict control on the evolution of the active FEs and the proper load balancing among processors is crucial. Recently, a scanwise refinement scheme based on the laser position with a fix refinement distance ahead and behind from the HAZ has been proposed by [46, 47] to reduce the computational cost. This approach proposes a refined volume exclusively based on the geometrical entities.

Alternatively, a multi-scale approach is performed by [28] using dynamic adaptive mesh refinement and coarsening (AMR) technique to reduce the computational cost. The simulation is split into the part-scale and the small-scale models. In the part-scale model, pre-activation adaptivity is applied to coarsen the FEs inside the current layer group prior to their activation, but it requires an initial fine mesh to describe the geometry. A multi-level method using *hp*-AMR combined with the finite cell method have been applied by [48] demanding more costly FE approximations.

Other more elaborated approaches use unfitted boundary strategies to properly describe complex geometries, some of them exhibiting the well known small-cut cell problem that yields ill-conditioned systems [7, 9, 13, 14, 43, 45, 48]. In addition, integrating cut FEs may require extra computational cost, stability issues and is not easy to implement [4, 10, 20, 41]. This motivated the shifted-boundary method (SBM) and shifted-interface method (SIM), both substitute the initial domain by a surrogate domain, where the Dirichlet boundary conditions are replaced by equivalent Neumann boundary conditions in a surrogate domain. The challenges in the former approach are the computation and stability of the Neumann conditions for the surrogate domain and also the presence of edges and corners might induce numerical instability and requires a mapping strategy [5, 41]. The latter approach makes use of the ideas of SBM, but requires the use of mixed formulations to deal with the jumps in the primal variable and its fluxes [34].

A scalable parallel AM framework is provided in [44] using a geometry criterion based on the Separating Axis Theorem (SAT). The criterion adopted transforms the HAZ into a cuboid and apply the SAT to check if the FEs intersect or not the HAZ [24, 27]. All the FEs intersecting the HAZ cuboid are refined and the accuracy elsewhere is achieved by the imposition of the 2:1 ratio, i.e., both coarse and fine FEs must fullfil the following relation: $h_c = 2 \times h_f$, where h_c and h_f denote the representative sizes for the coarse and fine FEs, respectively.

To sum-up the main difficulties encountered in the mentioned approaches for simulating the AM process for complex geometries are: (1) the usage of fixed fine meshes is unfeasible to simulate industrial-scale components; (2) some AMR strategies are purely based on geometric parameters without including an error-estimator based on the accuracy of the temperature of the problem; (3) the necessity of using fine meshes to accurately reproduce the boundaries of the domain; (4) the use of complex and costly techniques to integrate cut FEs in embedded approaches; and (5) the imposition of a 2:1 balance scheme is not optimal to keep the number of FEs controlled.

To overcome such difficulties, the AM pipeline for simulating large scale industrial components presented in this article includes the following features:

(a) The geometry is defined by using CLI/GCode formats, both widely used in industrial applications. The geometry information is described by a sequence of straight lines, namely, hatches. The laser path describing the

geometry is the common link between the two formats. The GCode offers additional features for each hatch, such as laser speed, power source and cooling pauses. This enhances the flexibility of the simulation, allowing to modify the process parameters (i.e., scanning speed, power input, feeding rate, waiting time) as delivered to the AM machine.

(b) The AMR strategy allows to keep the number of FEs under control throughout the simulation while having a very fine mesh resolution at the HAZ. Simultaneously, the SAT [24, 27, 44] is performed to find the intersection of the HAZ with a background mesh, and refine the intersecting FEs until the desired refinement level has been reached. In addition, to guarantee the proper use of resources, the proposed strategy periodically performs a load re-balancing process to provide a similar amount of FEs per process in parallel computing.

(c) The solution accuracy is guaranteed by an a-posteriori error estimator criterion, on the current state of variables along the simulation. Based on a Based on a Zienkiewicz–Zhu (ZZ) error estimator, the temperature gradient at the super-convergent points of the FE is computed and projected back to the nodes, where the nodal error must be evaluated by the L_2 projection (see. e. g [57–59]).

The objective of this paper is to present a robust parallel *h*-adaptive FE framework applied to the thermal analysis of AM processes.

The outline of this paper is as follows. Section 2 introduces the external heat source and the boundary conditions for the WAAM thermal model. Section 3 describes the spatial and time discretizations. In Sect. 4, the main ingredients of the AM pipeline are described. Section 4.1 describes the GCode input-data format. In Sect. 4.2, some aspects about the AMR strategy are detailed. In Sect. 4.3, all the criteria used to generate the coarsening and refinement flags to adapt the mesh are described. Section 5 provides a set of numerical examples comparing the multi-criteria AMR, the layer-wise AMR and the uniform fixed fine meshes. Finally, in Sect. 6, some relevant conclusions are presented.

2 The thermal model

2.1 The continuum problem: strong and weak forms

Let Ω be a growing open bounded domain in $\mathbb{R}^3$ with the boundary Γ. The strong form of the balance of energy equation is given by

$$\dot{H} = -\nabla \cdot \boldsymbol{q} + \dot{r}, \tag{1}$$

where $\dot{H}$, $\dot{r}$ and $\boldsymbol{q}$ are the rate of enthalpy, rate of heat source and the heat-flux per unit volume, respectively. The heat flux, $\boldsymbol{q}$, is defined through Fourier's law as

$$\boldsymbol{q} = -k\nabla T, \tag{2}$$

where T is the temperature field and k is the (temperature dependent) thermal-conductivity.

The phase-change process is generally much faster than the thermal diffusion due to the concentrated laser beam at the HAZ, being its global influence negligible [18], because melting and solidification occur within the same time interval. Thus, the enthalpy rate can be simply written as

$$\dot{H} = C\dot{T}, \tag{3}$$

where C is the (temperature dependent) heat capacity. Introducing Eqs. (2, 3) in Eq. (1), yields

$$C\dot{T} - \nabla \cdot (k\nabla T) = \dot{r} \text{ in } \Omega, \tag{4}$$

After applying the divergence theorem to the second term and introducing the test functions $\delta\eta$, compatible with the Dirichlet boundary conditions, the weak form of Eq. (4) is given by

$$\begin{aligned} &\int_\Omega [(C\dot{T})\delta\eta]\mathrm{d}\Omega + \int_\Omega [k\nabla T \cdot \nabla\delta\eta]\mathrm{d}\Omega \\ &= \int_\Omega [\dot{r}\delta\eta]\mathrm{d}\Omega - \int_\Gamma [(q_{\text{cond}} + q_{\text{rad}} + q_{\text{conv}})\delta\eta]\mathrm{d}\Gamma, \end{aligned} \tag{5}$$

The first integral of the right-hand side of Eq. (5) is the external work of the thermal loads and the second integral is related to the heat losses. Thus, q_{cond} is the heat loss because of the heat conduction between the substrate and the printed component, q_{rad} is the radiation flux through the environment, and q_{conv} is the equivalent heat flux by convection [18, 36].

The solution to the AM thermal problem consists in finding $T(t) \in H^1(\Omega(t))$ in $(t_\text{i}, t_\text{f}]$, that satisfies Eq. (5) subjected to the initial conditions $T(\boldsymbol{x}, t_\text{i}) = T_0(\boldsymbol{x})$, where t_i and t_f are the initial and final time of the AM process, and the following appropriate boundary conditions.

2.2 The external heat source

In the context of AM simulations, the external heat source is generated by the power input (e.g., electric arc, laser beam or electron beam) while following the pre-defined scanning path. To properly track the heat source during the material deposition process, two methodologies are widely used. The first one represents the power input as a Gaussian/double-ellipsoid density distribution [17, 26, 28, 49], while the

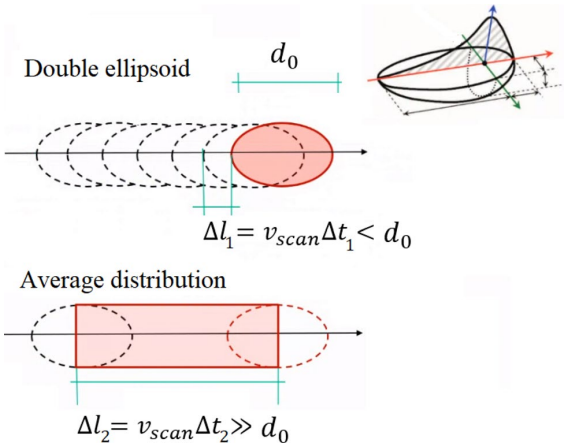

Fig. 1 Power distributions and their corresponding HAZ

second one consider an average value of the power uniformly distributed in the HAZ [33, 37, 40]. In what follows, we will consider the latter approach suitable for part-scale analyses and validated with several numerical and experimental tests [18, 19]. Figure 1 shows the power distribution as a function of the length-scale, Δl_1, for the double-ellipsoid distribution, and Δl_2, for the average distribution, where v_{scan} is the laser scanning speed, Δt_1 and Δt_2 are the time increment for the double-ellipsoid and average approaches, respectively, and d_0 the spot size.

2.3 Boundary conditions

The boundary of the domain, Γ, is subjected to the following two heat loss mechanisms: (1) heat transfer by conduction at the contact surface between the substrate and the component and (2) heat transfer by radiation and convection through the surfaces in contact with the environment. Therefore, the boundary Γ is split into two regions, namely: the substrate-component boundary, Γ_s, and the environment boundary, Γ_e.

The temperature T_s is the temperature at the interface between substrate and component on Γ_s, thus

$$T\,|_{\Gamma_s} = T_s, \tag{6}$$

Heat conduction: The heat loss by conduction between the substrate and component is given by Newton's law [23] as

$$q_{\text{cond}} = h_{\text{cond}}(T - T_s), \text{ on } \Gamma_s, \tag{7}$$

where h_{cond} is the HTC by conduction.

Environment heat loss: The heat loss through the environment is a combination of both convection and radiation heat transfer, expressed by Newton's law as

$$q_{\text{conv}} = h_{\text{conv}}(T - T_e), \text{ on } \Gamma_e, \tag{8}$$

$$q_{\text{rad}} = h_{\text{rad}}(T - T_e), \text{ on } \Gamma_e, \tag{9}$$

where h_{conv} and h_{rad} are the HTCs associated to the convection and radiation, respectively, and T_e is the environment temperature. The HTC for the radiation [19] can be expressed as

$$h_{\text{rad}} = \sigma\varsigma(T^3 + T^2T_e + TT_e^2 + T_e^3), \tag{10}$$

where σ is the Stefan–Boltzmann constant and ς is the emissivity parameter of the radiating surface.

3 The discrete problem

AM processes involve growing-in-time domains. As a consequence, an initial discrete domain, referred to as $\Omega(t_0)$, is taken as point of departure to be continuously adapted along the simulation. This initial discrete domain depends on many factors, among them, the AM technology and the chamber, where the piece is printed, specific for every printing machine. We consider this initial discrete domain $\Omega(t_0)$ containing the bounding box of the component (domain where the piece is printed), including the substrate domain, where the piece is supported during the printing process, see Fig. 2. This split allows to handle complex mesh patterns generated by the AMR process in the component part, while no adaptivity processes in the substrate domain are performed along the simulation.

To obtain the required mesh density at the HAZ, the initial mesh is subjected to several AMR cycles according to geometrical criteria. Essentially, the initial bounding box is adapted to obtain a proper discretization to capture the temperature dissipation in the melt-pool, see Sect. 4.3.1. Once the mesh has been generated, the FEs are progressively activated following the laser path, as explained later in Sect. 4.1.

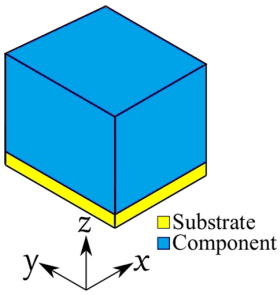

Fig. 2 In blue, the bounding box level zero FE for the component part and, in yellow, the level zero FE for the substrate part (Color figure online)

3.1 Spatial discretization

Consider the AM process defined in the time interval $(0, T]$, divided into N time steps with $t \in (0, T]$. For a given time step, where the increment of time is defined as $(\Delta t = t^{n+1} - t^n)$, the laser beam activates a set of FEs as determined by the scanning path.

Thus, at time step t^{n+1} the domain is decomposed into its active and inactive parts. The active part is defined as a FE partition $\Omega_{\text{act}} \subseteq (\Omega_a^{n+1} \cup \Omega_a^n)$, where Ω_a^{n+1} and Ω_a^n, are the sets of activated FEs at t^{n+1} and t^n, respectively. The inactive domain is defined as $\Omega_{\text{ina}} \subseteq (\Omega_i^{n+1} \cup \hat{\Omega}_i^{n+1})$, where Ω_i^{n+1} is the domain of inactive FEs and $\hat{\Omega}_i^{n+1}$ the domain of inactive FEs that share nodes with Ω_{act}. Figure 3 shows an example of this classification of FEs at time t^{n+1}, for a given scanning path in an arbitrary layer.

The domain Ω_{act} is built as the union of FEs intersected by the scanning path. To determine how the domain Ω_{act} evolves along the simulation, the path-length increment per time-step, Δl, is user-defined as an input argument. The strategy will activate all the FEs intersected by the laser path, until the increment of laser path reaches the value Δl, see Fig. 4a. Vertical movements are considered when the laser changes its position from one layer to the next one.

Similar to the classification of FEs, the nodes are also classified according to their status (active/inactive) and their geometric position in the component part. An active node belongs to the component and it is located either at the surface or in the interior of the component. Nodes are classified in the following three sets: (1) ξ^{skin} contains all nodes belonging to the surface of the active portion of the component (i.e., they belong simultaneously to Ω_{act} and $\hat{\Omega}_i^{n+1}$), (2) ξ^{int} is the set of active nodes in the interior of the component (i. e. they belong to Ω_{act}), (3) ξ^{ina} is the set of nodes belonging to inactive FEs (Ω_i^{n+1}). Figure 4b shows an example of all sets.

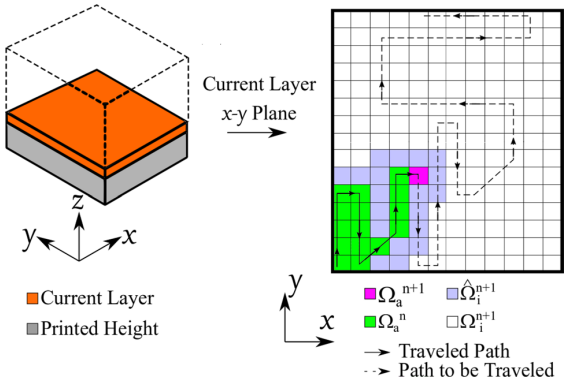

Fig. 3 FEs classification at t^{n+1} according to the scanning path activation

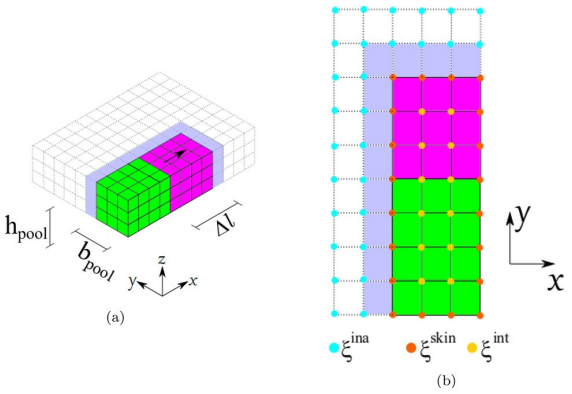

Fig. 4 **a** FEs activation process: green FEs are the elements activated in the previous time-steps. Purple FEs elements are activated within the current time-step; the volume of the purple domain corresponds to V_{HAZ}^{n+1}. **b** Classification of nodes (Color figure online)

The volume activated between the initial and final position during the time-step, $\Delta t = t^{n+1} - t^n$, defines the HAZ as

$$V_{\text{HAZ}}^{n+1} = \sum_{e=1}^{n_e} V^{(e)}|_{e \in \text{HAZ}}, \tag{11}$$

where V_{HAZ}^{n+1}, $V^{(e)}$ and n_e are the discrete volume of the HAZ, the volume of each FE and number of activated FEs inside the HAZ, respectively. The average heat density distribution per unit of volume is computed as

$$\dot{r} = \frac{\eta W}{V_{\text{HAZ}}^{n+1}}, \tag{12}$$

where η denotes the efficiency of the heat absorption and W the total power input.

3.2 Time integration

The implicit backward Euler method is used to advance in time [1, 2, 16, 22]. The time-increment is set automatically according to the metal deposition speed, v_{dep}, and the re-coating speed, v_{rec}, which may vary from hatch to hatch. The deposition speed determines the time-increment when the laser is on (Δt_{on}), while the re-coating speed allows the computation of the time-increment for the laser to be re-positioned for the next hatch, allowing previous printed hatches to experience cooling effects, while the laser is off (Δt_{off}); for example, when a given layer is totally printed, and the laser beam is moved to the next one. In some cases,

additional re-positioning tasks may be performed, and the re-positioning time must be accounted for.

For both laser status, the time-increment, for a constant (user-defined) Δl, is computed as

$$\Delta t_{\text{on}} = \frac{\Delta l}{v_{\text{dep}}}, \tag{13}$$

$$\Delta t_{\text{off}} = \frac{\Delta l}{v_{\text{rec}}}, \tag{14}$$

In some cases, the over-heating of the laser require pauses during the manufacturing process. When a given pause is scheduled, the time evolves within a number of time-steps defined by the user, n_{pause}. Then, the time-increment is computed as

$$\Delta t_{\text{pause}} = \frac{t_{\text{pause}}}{n_{\text{pause}}}, \tag{15}$$

where no deposition occurs and the laser is set as off, allowing the component to cool down.

4 AM via hierarchical octree-based adaptive meshes

In this section, a hierarchical octree-based adaptive FE mesh strategy for AM is described. Its objective is to ease the tasks performed by the user, avoiding cumbersome geometry manipulation, and providing a user-friendly environment to tackle complex geometries. The approach enables to eliminate both the user interaction and the need for initial fine meshes to describe complex geometries. As an example, Fig. 5a shows a section cut of a complex geometry embedded in the initial bounding box and surrounded by inactive elements; Fig. 5b shows a top view of the component and the FEs mesh around it, Fig. 5c, d shows the evolution of the mesh following the HAZ for two different times.

The first step to start the AM simulation consists of computing the maximum length increment per time-step, Δl, the minimum mesh size (the maximum level of refinement) to describe the HAZ and the maximum mesh size allowed (coarsest level) away from the HAZ. The path data and process parameters are read from the GCode. The number of steps of the simulation is computed dividing the total distance of the scanning path by Δl. This given, an initial uniform refinement (Cartesian Voxelization) is performed. Next, the thermal problem is solved and the error estimators based on the temperature field and the corresponding array of coarsening and refinement flags are also computed. Then, the AMR performs the mesh refinement and data transfer. Next, the FEs activation strategy generates the new computational domain for the next time step.

In large-scale simulations, the use of more than one CPU is required. In this context, once the variables of the problem have been projected to the new mesh and all nodes and related data are redistributed among tasks to balance the load per CPU and guarantee the proper memory usage. Algorithm 1 presents the implementation aspects of the adaptive AM simulation pipeline.

Algorithm 1: Time-stepping and FEs activation in parallel AMR simulation for AM processes.

```
Read input data and generate the initial background mesh (uniformly refined octree)
Compute array of time-steps based on the deposition Δl defined by the user.
current_time_step ← 1
Initialize welding path.
Activate the FEs for the first step with deposition.
while current_time_step≤ num_time_steps do
    Solve thermal problem
    Compute error estimators based on the temperature field.
    Compute array of coarsening and refinement flags f_t.
    current_time_step ← current_time_step+ 1
    if current_time_step≤ num_time_steps then
        Compute the array of coarsening and refinement flags based on the geometry of the welding path f_g.
        Generate the final array of coarsening and refinement flags f.
        Adapt the background mesh Ω_h^b.
        Transfer variables to the new mesh.
        Activation of FEs to build the updated domain.
        Redistribute mesh and migrate variables among tasks.
        Generate postprocess.
```

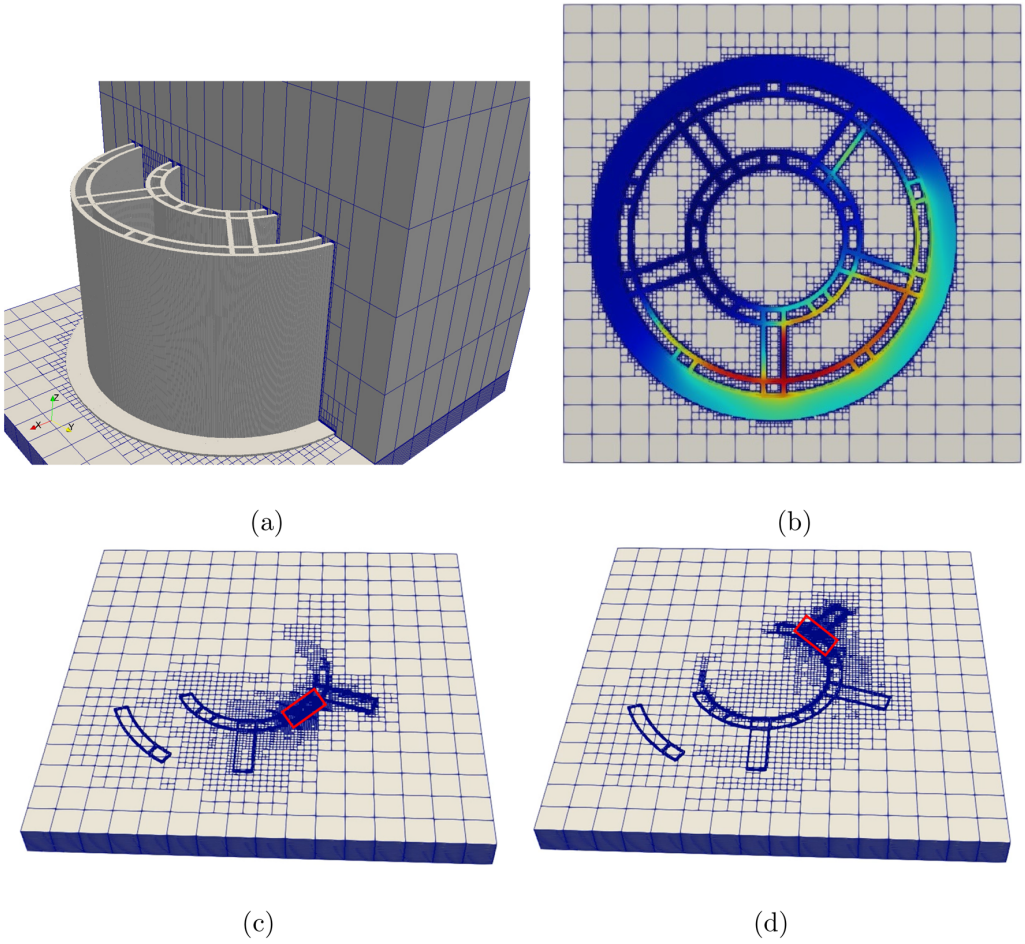

Fig. 5 Spatial discretization. **a** Section cut of the component embedded in the inactive domain. **b** Top view from the component and the surrounding FEs mesh. **c**, **d** Evolution of the FEs mesh following the HAZ bounding box at two different times

In Sect. 4.1, some basic features of the input data containing the scanning path geometry in GCode format are described. In Sect. 4.2, some aspects of the AMR techniques applied to hierarchical octree-based meshes are presented. Finally, in Sect. 4.3, the multi-criteria used to adapt the mesh size are outlined.

4.1 Input data: the GCode format

GCode is a format broadly used in industrial machine tooling. The advantage of using the GCode format relies on the fact that it can include additional data related to the processing parameters, such as the power input, time pauses, depositing and re-coating speeds, useful to inform the machine and the simulation too.

Regarding the GCode commands: `G1`/`G0` correspond to movement commands, where `G0` is a fast straight movement (with no deposition), and `G1` is a straight line movement with material feeding. Command `E` provides the information of the deposition process, where the attached value corresponds to the material feeding; if this value is different from zero, the laser is depositing new material in this segment, otherwise the laser is moving without deposition. Command `F` refers to the laser speed (in (mm/min)). The coordinates defined in a given command line corresponds to the final (x, y) coordinates of the hatch, while the initial coordinate of the hatch are defined in the previous command line. The power source can be changed along the AM process using the command `G108` and introducing the P (power source) followed by `S` (of set) and the value of the new power source in $[W]$. In some cases, pauses are required

during the printing process. This time interval can be set by `G4` followed by `S` and the value of the pause in [s]. In this format, the layer thickness is defined by the difference between two consecutive z-coordinates.

As an example, Fig. 6 shows a code snippet describing a laser beam path in GCode format, and Table 1 shows the list of representative properties stored by hatch.

Although the GCode format is most used due to its flexibility, there are other formats also supported by the present framework. This is the case of the CLI format, which only provides the geometry of the scanning path; process parameters need to be input separately.

4.2 Adaptive mesh coarsening and refinement

In this section, a brief description of the adaptivity strategy used is given; interested readers may find further details in reference [11].

The hierarchy of refinement levels is defined by an octree parental structure, where zero level FEs are parents to the one level (this way, one level FEs are children of the zero level FEs), and the one level FEs are parent to two level FEs. Figure 7 shows the hierarchical tree of parental relations of the FEs.

The refinement strategy produces a non-conforming mesh with hanging nodes. The treatment of hanging nodes adopted in this work is detailed in [12], and summarized herein; interested readers may find other hanging nodes

```
;Generated with Cura_SteamEngine 4.4.1
;LAYER_COUNT:247
;LAYER:0
G108 P S2000 ;Set laser power
G0 F3600 X163.281 Y128.413 Z0.2 ;Repositioning hatch speed 3600 mm/min
G1 F1800 X163.542 Y125.695 E0.03424 ;Depositing hatch 1800 mm/min
G1 X163.967 Y122.663 E0.07264 ;Depositing hatch 1800 mm/min
G1 X164.643 Y119.722 E0.11048 ;Depositing hatch 1800 mm/min
G108 P S1000 ;Set laser power
G1 X165.578 Y116.833 E0.14856 ;Depositing hatch 1800 mm/min
G1 X166.736 Y114.088 ;Recoating hatch 1800 mm/min
G1 X168.169 Y111.382 E0.22432 ;Depositing hatch 1800 mm/min
G1 X169.785 Y108.875 ;Recoating hatch 1800 mm/min
G1 X171.621 Y106.508 E0.29929 ;Depositing hatch 1800 mm/min
G1 X173.702 Y104.26 ;Recoating hatch 1800 mm/min
G4 S90 ;Set pause 90s
G1 X175.924 Y102.243 Z0.4 ;Repositioning hatch 1800 mm/min
G1 F2000 X178.3 Y100.436 E0.41277 ;Depositing hatch 2000 mm/min
```

Fig. 6 Code snippet in GCode format containing an example of laser beam path

Table 1 List of the process parameters provided by the GCode

Code	Command	Units
`G0/G1`	Hatch movement	mm
`F`	Update speed	mm/min
`G4`	Introduce time pause	s
`G108`	Update laser power	Watts
`E`	Extruding material	mm

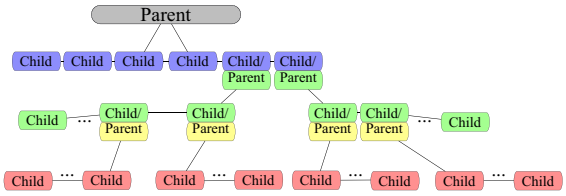

Fig. 7 FEs hierarchy following the color scheme in Fig. 9

treatment techniques in [8, 9, 21, 43, 54, 55]. The modified test/shape function is written as

$$\phi_p^*(\boldsymbol{x}) = \phi_p(\boldsymbol{x}) + \sum_{i=1}^{n_{\text{child}}} (\phi_p(\boldsymbol{x_i})\phi_{c_i}(\boldsymbol{x})), \tag{16}$$

where the modified parent test/shape function, ϕ_p^*, is written in terms of the original (parents) shape/test function, ϕ_p, and the children shape/test function, ϕ_{c_i}, according to the spatial location of the child, where $\boldsymbol{x_i}$ is the ith hanging child position, and n_{child} is the number of children FEs.

The straight-forward application of the parent/child hanging node constraint may lead to scenarios, where a child node is active and contributes to an inactive parent, causing a singular system. To avoid this situation, the algorithm checks if the parent node is active or inactive. Figure 8 shows the change on the hanging/parent nodes classification in $t = t^n$, Fig. 8a, and in $t = t^{n+1}$, Fig. 8b.

Let the zero level mesh (bounding box) be the initial mesh for the AMR strategy. The strategy requires an array of coarsening and refinement flags, $\mathbf{f}$, to perform the adaptivity process according to an established criterion, this being performed in an iterative procedure until the mesh does not require further adaptivity or once the maximum number of adaptivity cycles is reached. The multi-criteria strategy to mark the FEs is described in Sect. 4.3.

When mesh refinement is required, an isotropic octree division of each parent FEs into two new FEs in each direction is performed. Thus, each FEs is divided into 8 new FEs in one cycle. Figure 9 shows an initial mesh (just one

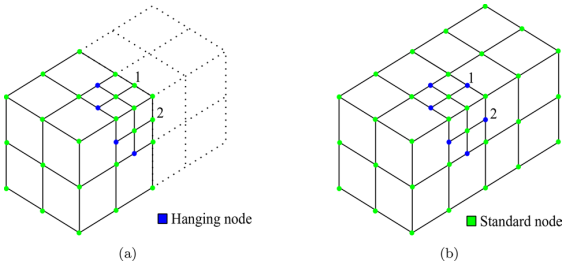

Fig. 8 Nodal hanging/parent classification. **a** $t = t^n$. **b** $t = t^{n+1}$

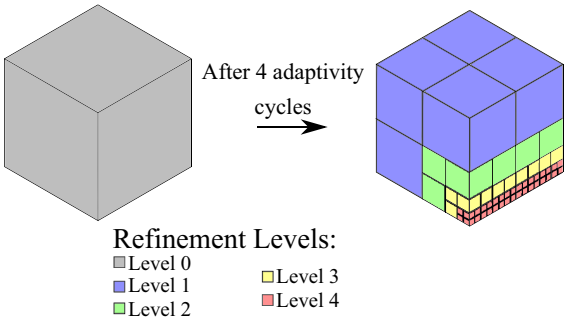

Fig. 9 Illustration of the refinement levels after 4 adaptivity cycles

FEs, the bounding box corresponding to the component part) subjected to 4 adaptivity cycles. The figure at the right hand side denotes the color pattern of each refinement level after four AMR cycles.

4.3 Multi-criteria AMR

This AMR strategy is developed in such a way that different adaptivity criteria can be used in the same simulation. This design takes advantage of the Object-Oriented programming, where a set of objects provide an array of coarsening and refinement flags, $\mathbf{f}$, to be compared to obtain the most critical scenario.

The criteria used to adapt the mesh are described in the following. In Sect. 4.3.1, a geometrical criterion based on the intersection of the FEs mesh with the bounding box of the HAZ is presented. In Sect. 4.3.2, a criterion based on a-posteriori error estimators of the temperature is presented. Each criterion performs a search of FEs to mark them as: to refine (1), to do nothing (0) or to coarsen (−1). The outcome of this process is an array that contains the coarsening and refinement flags for all FEs. This array is sent to the library in charge of performing the AMR process [11], where all related data structures are also updated.

For the temperature field, a point-to-point projection is used. This procedure is straightforward for nested octree-based meshes; temperature at the hanging nodes is interpolated from the corresponding parent elements.

4.3.1 Geometry-based adaptivity

The geometric criterion consists in a search algorithm, where an oriented reference volume intersects the FEs of the background mesh Ω_h^b. The oriented volume (OV) is a fictitious prism, containing the HAZ at t^{n+1}, being immersed in Ω_h^b. The dimensions of the prism are: the hatch length, the melt-pool width, b_{pool}, and the HAZ height including the current layer thickness and the laser penetration (melt-pool depth), h_{pool}.

The intersection between the OV and the FEs rely on the separating axis theorem/hyperplane separating theorem (SAT/HST) [24, 27, 44] which states that a pair of convex polytopes, formed by E edges and F faces each, intersect if they overlap at least in one of their projections onto their $E^2 + 2F$ planes. When both polytopes are box-shaped, i. e. they contain parallel faces and edges, the number of planes to be tested is considerably reduced. Thus, $E = 3$ and $F = 3$, resulting in only 15 testing planes. In case of using tetrahedra, the number of testing planes is increased to 44 ($E = 6$ and $F = 4$).

In practice, this test compares the projected distance of the pair of polytopes centers, s, with their projected half-sides, r_{OV} and r_{FE}, onto the normal direction of the test plane, $\mathbf{n}_{\text{tp}}$. If $s > r_{\text{OV}} + r_{\text{FE}}$, the plane is a separating plane, hence the polytopes do not overlap. If the test finds a separating plane, no further checks are required, and both OV and FEs do not intersect; otherwise a new test plane should be verified. The method chooses as testing planes, 3 independent planes describing the OV, 3 independent planes describing the FEs of the Ω_h^b, and the 9 cross-product between them. Figure 10 presents a visual description of this method.

If the OV and the FEs overlap, then the tested FEs belongs to Ω_a^{n+1}, and is marked as to be refined ($f_i = 1$). If a separating axis is detected, and the tested FEs does not belong to $\hat{\Omega}_i^{n+1}$, this FEs $\in (\Omega_a^n \cup \Omega_i^{n+1})$ is marked as to be coarsened ($f_i = -1$), see Fig. 3. The case where the FEs $\in \hat{\Omega}_i^{n+1}$, then it is marked as to do nothing ($f_i = 0$), to prevent it from being

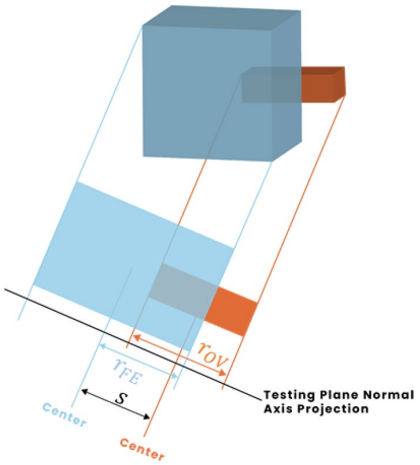

Fig. 10 Graphical interpretation of the SAT: in orange, the OV and in blue the target FEs taken from the background mesh. r_{OV} and r_{FE} denote the projection of the half-sides of the FEs and the OV onto the testing plane normal vector, respectively. In addition, s denotes the projection of the distance between their geometrical centers

coarsened; this preserves the geometry of the growing-in-time domain.

The number of adaptivity cycles depends on the accuracy desired to represent the OV. The refinement level per FEs, referred to as Lev(FEs), is computed and compared with the minimum, $Y_{\min}$, and maximum, $Y_{\max}$, respectively. Then, the corresponding coarsening and refinement flag for the ith FEs, f_i, is determined as follows

$$\begin{aligned} \text{Lev(FEs)} < Y_{\min} &\rightarrow f_i = 1 \\ \text{FEs} \in (\Omega_a^n \cup \Omega_i^{n+1}) \wedge \text{Lev(FEs)} > Y_{\min} &\rightarrow f_i = -1 \\ \text{FEs} \in (\Omega_a^{n+1}) \wedge \text{Lev(FEs)} < Y_{\max} &\rightarrow f_i = 1 \\ \text{FEs} \in \hat{\Omega}_i^{n+1} &\rightarrow f_i = 0 \end{aligned}$$

In consequence, the number of computations required is bounded by the difference between the maximum and minimum refinement levels [44]. Figure 11 shows a 2D example, the OV inside Ω_h^b and the final mesh using the SAT test after computing 5 adaptivity cycles with and without the 2:1 balance between FEs.

Alternatively, another geometry-based strategy is the layer-wise AMR, which consists of keeping refinement in the latest set of layers from the current deposition layer to a fix distance down in the building direction. Therefore, the finest mesh size is preserved for the latest layers to avoid continuous remeshing, thus minimizing the data transfer and CPU time.

4.3.2 A-posteriori error-estimators adaptivity

To avoid that the coarsening process near the OV affects the accuracy of the solution, an a-posteriori error-estimator is used [57]. This section presents the gradient-based approach adopted in this work.

The discretization error, $\mathbf{e}$, for a given discrete solution can be computed as

$$\mathbf{e} = \nabla T - \nabla T_h, \tag{17}$$

where ∇T and ∇T_h correspond to the temperature gradient obtained with analytical (exact) and the discrete FE solutions, respectively. However, exact solutions are only known in very simple cases. Thus, Zienkiewicz et al. [58, 59] present a methodology to obtain an accurate error-estimate when the exact solution is not available. The authors show that there exist a set of super-convergent points within the FE discretization, where the solution can be used as reference value when computing the error estimator. These values are a-posteriori computed at the FE super-convergent points and projected to the FE nodes. Thus, Eq. (17) is modified as

$$\bar{\mathbf{e}} = P(\nabla \bar{T}) - \nabla T_h, \tag{18}$$

where $\bar{\mathbf{e}}$ is the discrete error estimator for the gradient of temperature, $\nabla \bar{T}$ is the gradient of the temperature computed at the super-convergent points, $P(\cdot)$ is a projection operator that projects $\nabla \bar{T}$ onto the nodes of the FE mesh, and ∇T_h is the gradient of temperature computed with the FE solution.

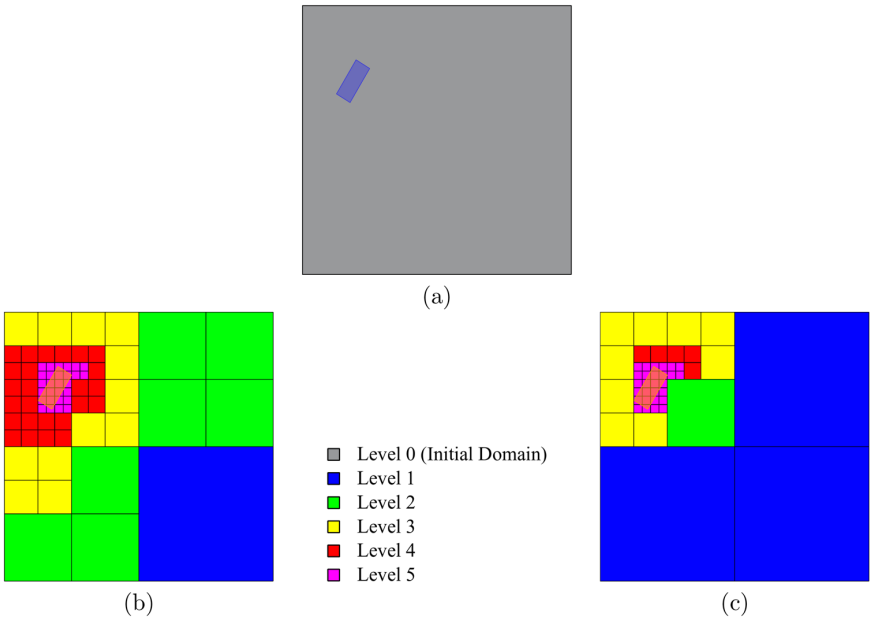

Fig. 11 **a** OV embedded into the initial domain; final mesh after 5 adaptivity cycles, **b** with 2:1 balance; **c** without 2:1 balance

As a matter of example, in the standard hexahedra tri-linear FE, the super-convergent point is the barycenter of the FE.

Finally, the L_2-norm of the $\bar{\mathbf{e}}$ for the ith FE, $\mathbf{e}_i$, is computed and compared with the minimum and maximum admissible errors, as follows

$$\begin{aligned} \mathbf{e}_i < \mathbf{e}_{\min} &\rightarrow f_i = -1 \\ \mathbf{e}_i \geq \mathbf{e}_{\max} &\rightarrow f_i = 1 \\ \mathbf{e}_{\min} \leq \mathbf{e}_i < \mathbf{e}_{\max} &\rightarrow f_i = 0 \end{aligned}$$

5 Numerical examples

In the examples presented in this section, the WAAM thermal problem is simulated. Nevertheless, the multi-criteria approach is technology independent and can be adapted to other AM processes.

The objective of the presented numerical examples is to demonstrate the suitability of the multi-criteria approach to industrial part-scale simulations with regard to the computational cost-efficiency and accuracy. Figure 12 shows the temperature dependent properties of the Ti6Al4V titanium-alloy used in all the numerical simulations.

The Cartesian adaptive FE meshes are obtained from an uniform Cartesian Voxelization of the initial Bounding Box, which include the part geometry. The minimum and maximum $\mathbf{e}_{L_2}$ threshold are 10^{-4} and 10^{-3}, respectively. The fixed fine FE meshes are obtained to match the FE size of the maximum refinement level of the adaptive mesh, which corresponds to the resolution inside the HAZ.

To assess the global error of the multi-criteria approach with respect to the fine mesh solution, a relative L_2 error norm of the temperature field is computed at the end of the simulation as

$$e_{L_2} = \frac{\sqrt{\int \left(P_h^{\text{coarse}}(\boldsymbol{u}_h^{\text{fine}}) - \boldsymbol{u}_h^{\text{coarse}}\right)_\Omega^2 \mathrm{d}\Omega}}{\int \left(P_h^{\text{coarse}}(\boldsymbol{u}_h^{\text{fine}})\right)_\Omega \mathrm{d}\Omega}, \tag{19}$$

where $P_h^{\text{coarse}}(\boldsymbol{u}_h^{\text{fine}})$ is the point to point projection of the reference (fixed fine mesh) solution onto the adaptive mesh and $\boldsymbol{u}_h^{\text{coarse}}$ is the solution obtained with the adaptive refined mesh.

The performance and numerical accuracy among the multi-criteria AMR and different mesh strategies are assessed and compared. Section 5.1 compares the multi-criteria AMR with a reference fix fine mesh and the AMR using only the geometric criterion. In Sect. 5.2, the multi-criteria AMR is used and the results are compared with experimental data and with the layer-wise strategy. Finally, Sect. 5.3 simulates a complex geometry modelled automatically from the GCode provided.

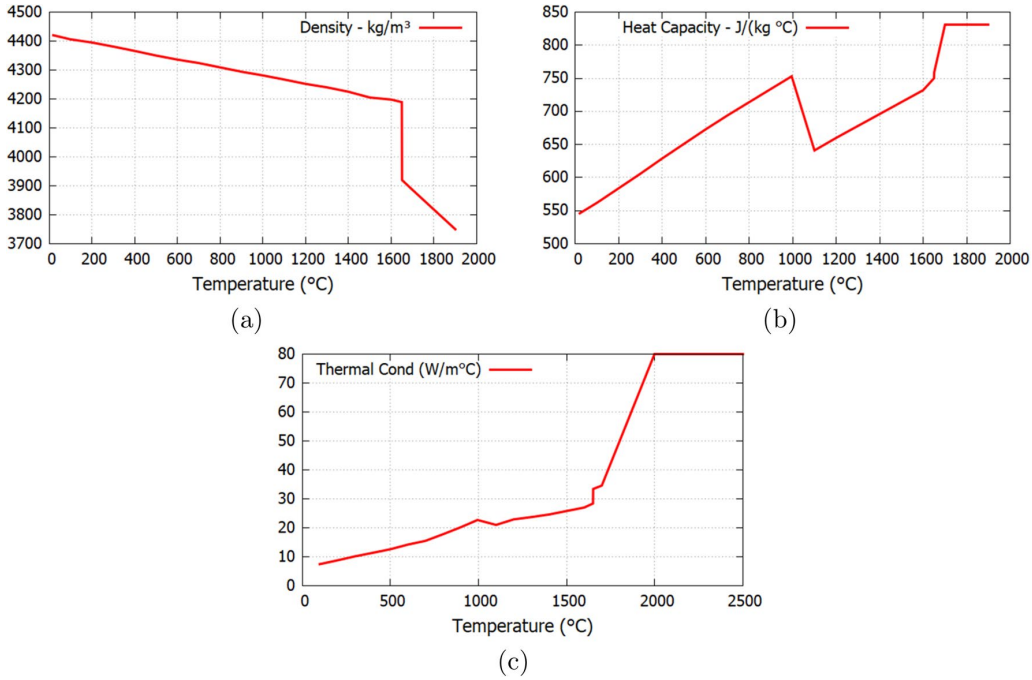

Fig. 12 Temperature dependent properties for the Ti6Al4V. **a** Density; **b** heat capacity; **c** thermal conductivity

The numerical simulations are carried out using the in-house software FEMUSS (Finite-Element Method Using Sub-grid Scales) developed at the International Center for Numerical Methods in Engineering (CIMNE). All the computations are performed in a distributed-memory environment using an Intel i7-10700 @2.9GHz with 16 CPU's (8 cores and 2 threads-per-core) and 32 GB RAM memory. The thermal-problem is solved using the bi-conjugated gradient solver together with the Additive Schwarz Method. The post-processing is done using Paraview [3].

5.1 Printing of a cube

In this section, the 3D printing of a cube of side $a = 100$ (mm) is simulated to study the accuracy and computational efficiency of the proposed multi-criteria AMR. To compare the solution of the approach, the numerical results obtained with the fixed fine mesh are compared to the AMR using only the geometric criterion. The bottom corner of the cube is chosen to compare the local accuracy of the AMR strategies with respect to the fixed fine mesh.

The domain has been discretized into hexahedral FEs, a total of 7 uniform AMR cycles are performed to obtain a proper discretization to capture the phenomena in the HAZ (this discretization corresponds to $2^7 = 128$ FEs per side). In this case, the FE representative size inside the HAZ is $h = 0.78125$ (mm). This mesh contains a total of 2,097,152 hexahedral FEs.

Figure 13 shows the fixed fine mesh, and the AMR using the multi-criteria and the geometric criterion, respectively. The difference of both AMR solutions compared to the fixed fine mesh is remarkable; also, the influence of the a-posteriori criterion can be appreciated when compared to the purely geometry-based AMR (see Fig. 15).

The convective flow inside the melt-pool is considered by increasing of the thermal conductivity above the melting temperature [25]. The heat loss by radiation and convection are considered at all external surfaces and the environment temperature is set to 20 (°C). The radiation emissivity is $\varsigma = 0.7$. The HTC for convection increases linearly from $h_{\text{conv}}(20\,^{\circ}\text{C}) = 10\,(\text{W}/(\text{m}^2 \cdot {}^{\circ}\text{C}))$ to $h_{\text{conv}}(1000\,^{\circ}\text{C}) = 100\,(\text{W}/(\text{m}^2 \cdot {}^{\circ}\text{C}))$.

The cube is built in a sequence of 16 layers, where the power source is $W = 5$ (kW) with a heat absorption efficiency of $\eta = 0.75$. The simulation accuracy depends on the melt-pool deposition process which is set to $\Delta l = 12.5$ (mm), defining the length of the melt-pool, and its base and height $b_{\text{pool}} = h_{\text{pool}} = 12.5$ (mm). In this experiment, a constant speed for both, deposition and re-coating is considered, $v_{\text{rec}} = v_{\text{dep}} = 3600$ (mm/min).

Figure 14 shows the evolution of the number of active FEs for the length-scale adopted in the simulation in total of 2087 time-steps and the dashed lines are the average number of active FEs of the AMR simulations. Figure 14a shows the evolution of the three strategies; the difference in the final number of active FEs of the fixed fine mesh compared to the AMR strategies is remarkable. Figure 14b shows the initial 200 time-steps, where the number of active FEs of the fixed fine mesh develops at a much faster rate than the AMR strategies. Figure 14c shows that the AMR strategies increase the number of active FEs initially and stabilize around a much smaller value than the fixed fine mesh, keeping the size of the problem controlled throughout the simulation. The multi-criteria approach has an average number of active FEs of 10,500, almost twice the size of the purely geometric criterion (5400 average active FEs). This reduction represents 1.00% and 0.51% of the average total number of active FEs of the fixed fine mesh at the end of the simulation for the multi-criteria AMR and the geometry-based AMR, respectively.

The real-time run for the fixed fine mesh case is 7 (h) 24 (min). The computational time reduction for the multi-criteria AMR and the purely geometric AMR are 88.57% and 91.21%, respectively. Table 2 shows the time spent by each module.

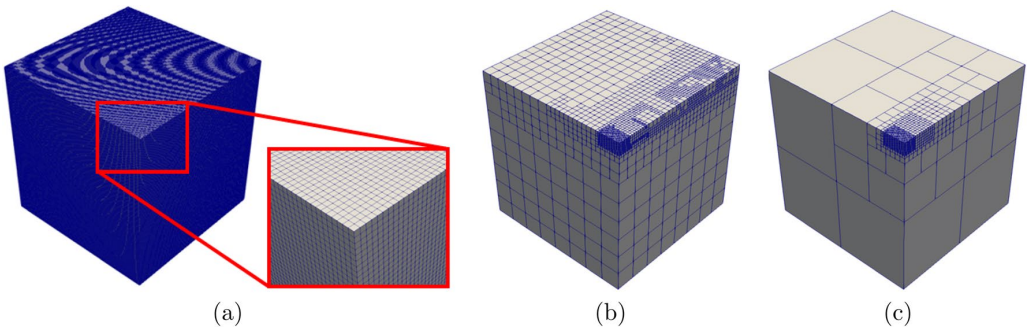

Fig. 13 Cube: final meshes. **a** Fixed mesh; **b** multi-criteria AMR; **c** geometric AMR criterion

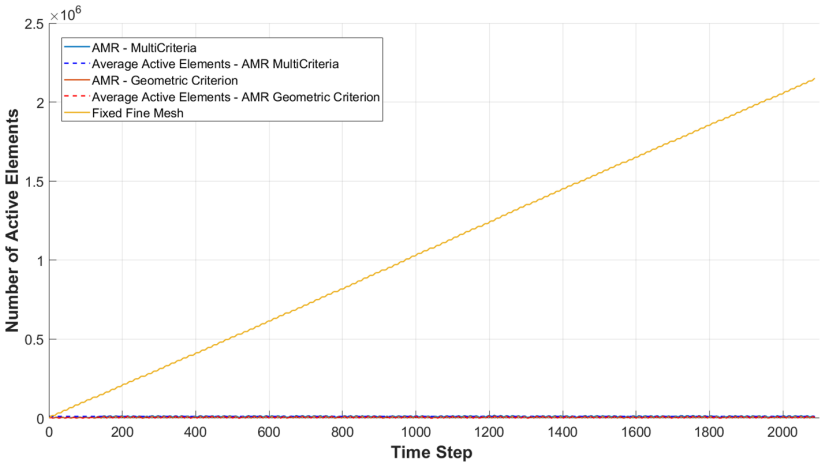

(a)

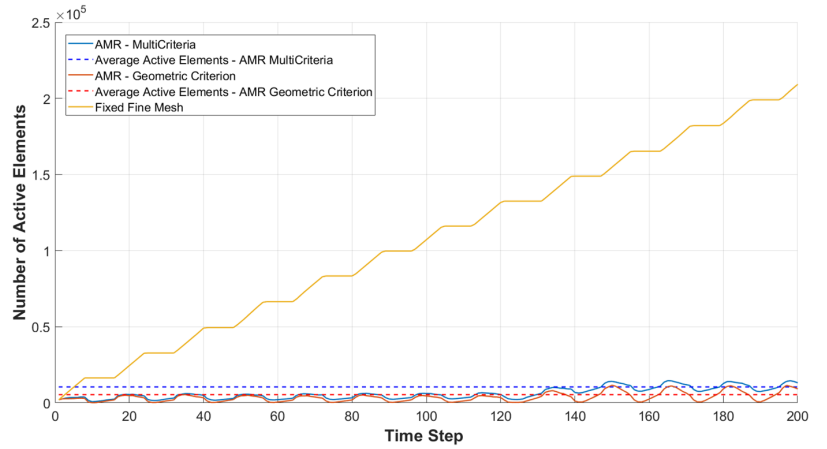

(b)

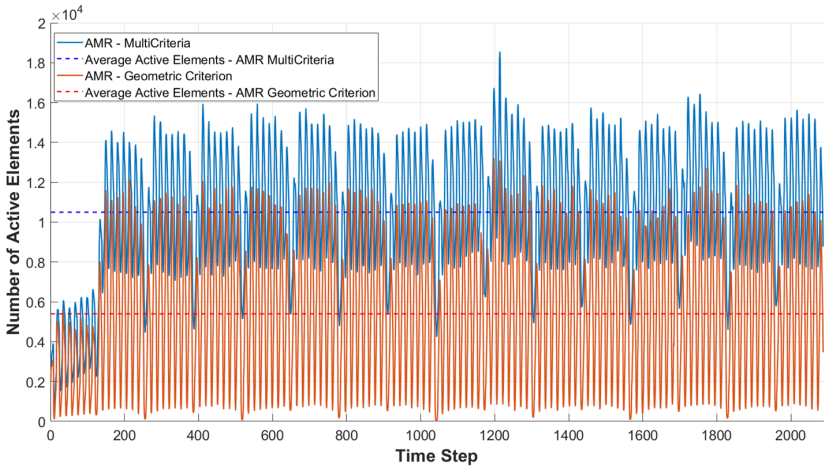

(c)

Fig. 14 Cube: **a** evolution of the number of active FEs per time step; **b** zoom on the evolution of active FEs for the initial 200 time-steps; **c** detail of the evolution of active FEs for the AMR strategies

Table 2 Details on the real-time consumption for each module

Module	Fixed fine mesh (h:min)	Multi-criteria AMR (h:min)	Geometric-criterion AMR (h:min)
`Thermal`	7:04	0:23	0:18
`Meshing`	0:00	0:16	0:13
`Element activation`	0:20	0:11	0:07

Figure 15 shows the evolution of the temperature at the bottom corner of the cube to assess the local accuracy of both AMR strategies. In the case of the thermal problem, the accuracy is enhanced by the a-posteriori error estimate at a computational cost around 3% higher than the purely geometric AMR for this example.

Figure 16 shows the relative difference of the temperature field of the AMR strategies with respect to the fixed fine mesh at the end of the simulation. The local maximum relative differences observed are 2.47% and 21.33% for the multi-criteria AMR and the purely geometric AMR, respectively. Applying Eq. (19), the global error computed for the multi-criteria AMR and the geometric-based AMR are 0.81% and 6.71%, respectively.

5.2 Printing of a thin-wall

In the next example, the computational cost and accuracy of the multi-criteria AMR and the layer-wise AMR are compared with the experimental data obtained from the printing of a thin-walled component using the WAAM process.

In the experimental setting, a thin wall is built upon the deposition of 18 layers of thickness $t = 4.5$ (mm). Figure 17 shows the geometry of the thin wall and the substrate. The metal deposition goes from the initial to the final position with a constant speed of 100 (mm/min) and after concluding the current layer, the re-coating velocity is 514 (mm/min). In this experiment, two scenarios have been considered: a cooling interval between layers of (I) 5 min:21 s and (II) 10 min:21 s (see Fig. 18).

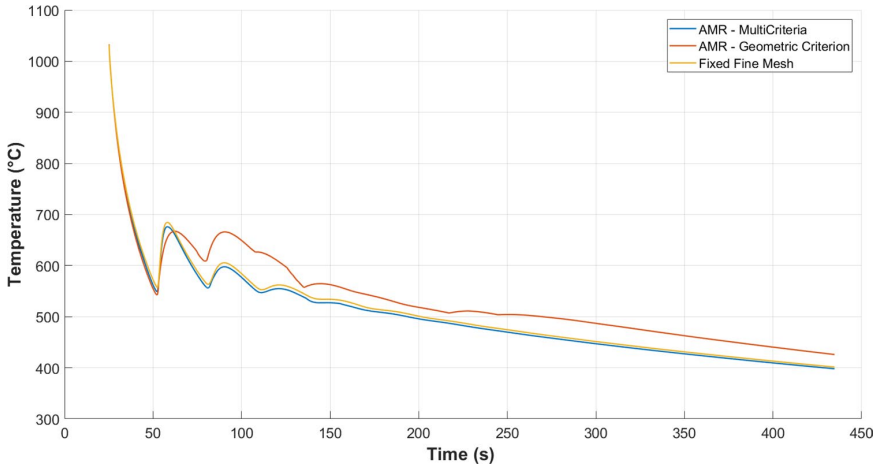

Fig. 15 Cube: temperature evolution of the cube bottom corner

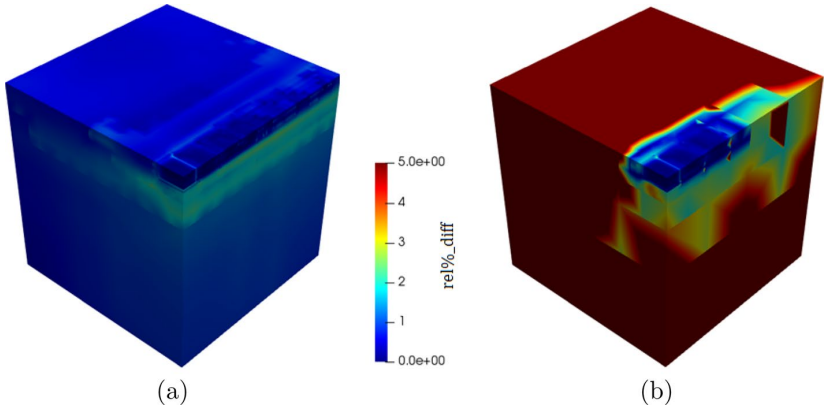

Fig. 16 Cube: relative percentual difference of the temperature field of the **a** multi-criteria AMR and **b** geometric-based AMR, with respect to the fixed fine mesh

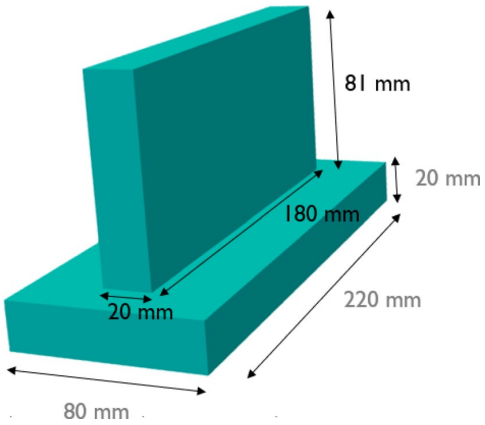

Fig. 17 Thin-wall: geometry

The GCode provides a variable value for the power source for the first 3 layers and thereafter the power is kept constant for the remaining 15 layers. Table 3 shows the power source, while the heat absorption efficiency is set to a value of $\eta = 0.75$.

The chamber temperature, measured in-situ, is 17 (°C) and a radiation emissivity of $\varsigma = 0.7$ is considered. The HTC for convection is taken as $h_{\text{conv}} = 10$ (W/(m^2 · °C)). To consider the contact of the bottom surface of the substrate with the stainless steel work-bench, the conduction HTC value is set to $h_{\text{cond}} = 100$ (W/(m^2 · °C)). The time-stepping is defined by a fix movement of the heat source of $\Delta l = 10.0$ (mm), the melt-pool base, $b_{\text{pool}} = 20.0$ (mm), and the height (layer thickness and HAZ penetration), $h_{\text{pool}} = 9.0$ (mm).

The initial mesh consists of two bounding boxes: one to include the thin-wall and one for the substrate. The dimensions of the initial bounding box for the thin-wall and for the substrate are $220 \times 80 \times 81$ (mm^3) and $220 \times 80 \times 20$ (mm^3), respectively. The maximum and minimum adaptivity level considered in this case is 8 and 4, respectively. In addition, an alternative AMR strategy is forced to keep the finest mesh throughout the last 3 layers, while the mesh below it is coarsened to the minimum refinement level chosen. Figure 19 shows the initial mesh and the different adaptive meshes for each strategy at an intermediate time step.

Table 3 Thin-wall: laser power per layer

	Laser power (W)
Layer 1	$P + 1045.6$
Layer 2	$P + 522.0$
Layer 3	$P + 196.8$
Layer 4–18	P

The thermo-couples are positioned 5 (mm) from the thin-wall deposition starting point, at the top of the currently deposited layer. The temperature is measured 21 (s) prior to the deposition of the next layer. Figure 20 shows the temperature evolution of the two AMR strategies compared to the experimental data at the measurement points of each layer for the two idle time scenarios. The temperature evolution from the layer-wise AMR and the multi-criteria AMR show good agreement with the experimental results. The average errors associated to the 5 (min) and 10 (min) curves are 4.8% and 4.4%, respectively. The small width of the thin-wall makes the positioning of the thermocouples difficult in the experimental setting. Regarding the 5 (min) test, the thermo-couple was misplaced in the initial three layers and the data is not available.

The real-time run for the layer-wise AMR case is 10 (h) 34 (min), and the multi-criteria AMR yields a computational time reduction of 87.37%. The saving in time is a consequence of the reduced number of FEs required by the multi-criteria AMR strategy (see Fig. 21).

The peak value of active FEs on the initial steps of the simulation is due to the layer-wise strategy, refining the substrate with a very dense FEs mesh. The peak number of active FEs is 8,804,331 for the layer-wise AMR and 526,541 for the multi-criteria AMR. After the refinement height of the layer-wise strategy leaves the substrate (around time step 200) the effect on the substrate is reduced and the number of active FEs remains almost constant. For the layer-wise strategy, the average number of active FEs is 1,166,199, being highly influenced by the initial steps, whereas the multi-criteria strategy average number is 90.81% lower, being

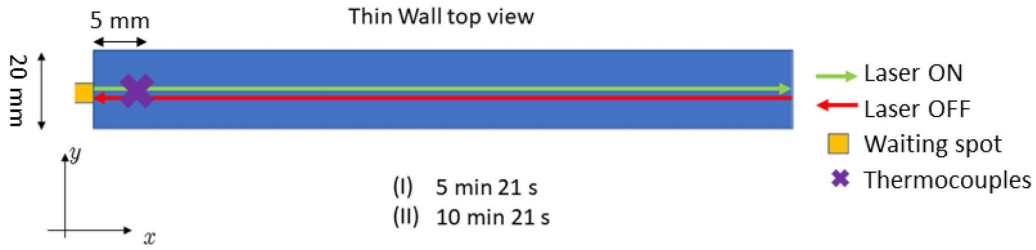

Fig. 18 Thin-wall: laser path for a generic layer and the waiting time for the two scenarios

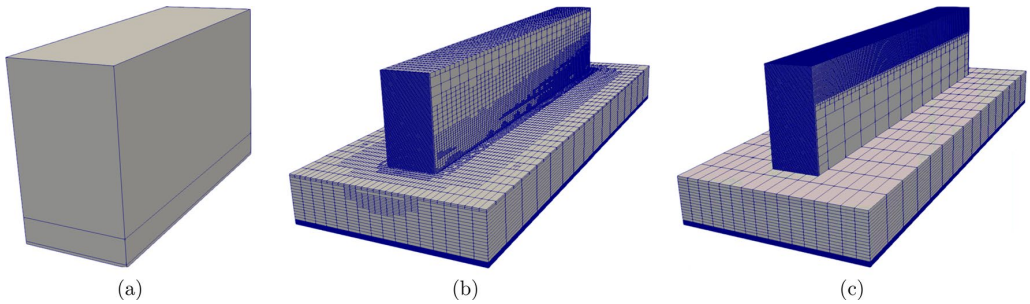

Fig. 19 Thin-wall: **a** initial FE mesh; **b** multi-criteria AMR; **c** layer-wise AMR

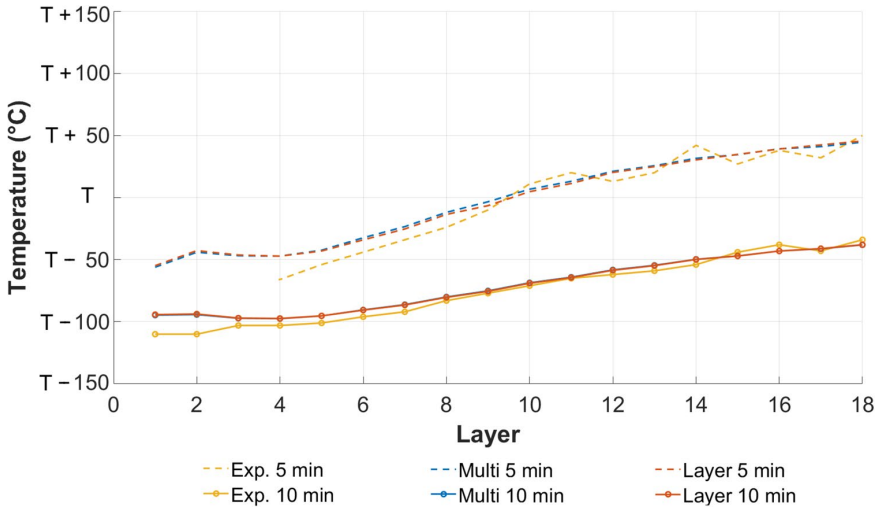

Fig. 20 Thin-wall: comparison of the experimental results vs. numerical results of the AMR strategies

close to the time reduction in the simulation obtained by the multi-criteria.

The requirement of the layer-wise AMR strategy of having 3 adapted layers below the current deposition height is far from optimal when the manufacturing process is capable of depositing thick layers of material, compromising the computational cost due to the large number of active FEs. Even when the refinement height is no longer affecting the substrate this strategy presents almost 5 times the number of active FEs compared to the ones obtained with the multi-criteria approach. Another shortcoming of the layer-wise approach is that the mesh remains constant during pauses, whereas the multi-criteria AMR reduces the number of FEs based on the data provided by the cooling process, avoiding excessive coarsening that may affect the accuracy of the model.

5.3 Printing of an optimized door handle

In the next example, a complex geometry taking from a topological optimization analysis, is analyzed using both the fixed fine mesh and the multi-criteria AMR.

Due to the complex geometry of the door handle, the structure walls are very thin and hollow, in consequence a balance between computational saving time using mesh coarsening techniques and a proper description of the shape must be guaranteed.

The goal of this example is to compare the performance of the fixed fine mesh and the multi-criteria AMR in a scenario, where the coarsening speed-up benefits are constrained by the complexity of the geometry.

The printed component geometry is obtained from the STereoLithography file and converted to a GCode file using

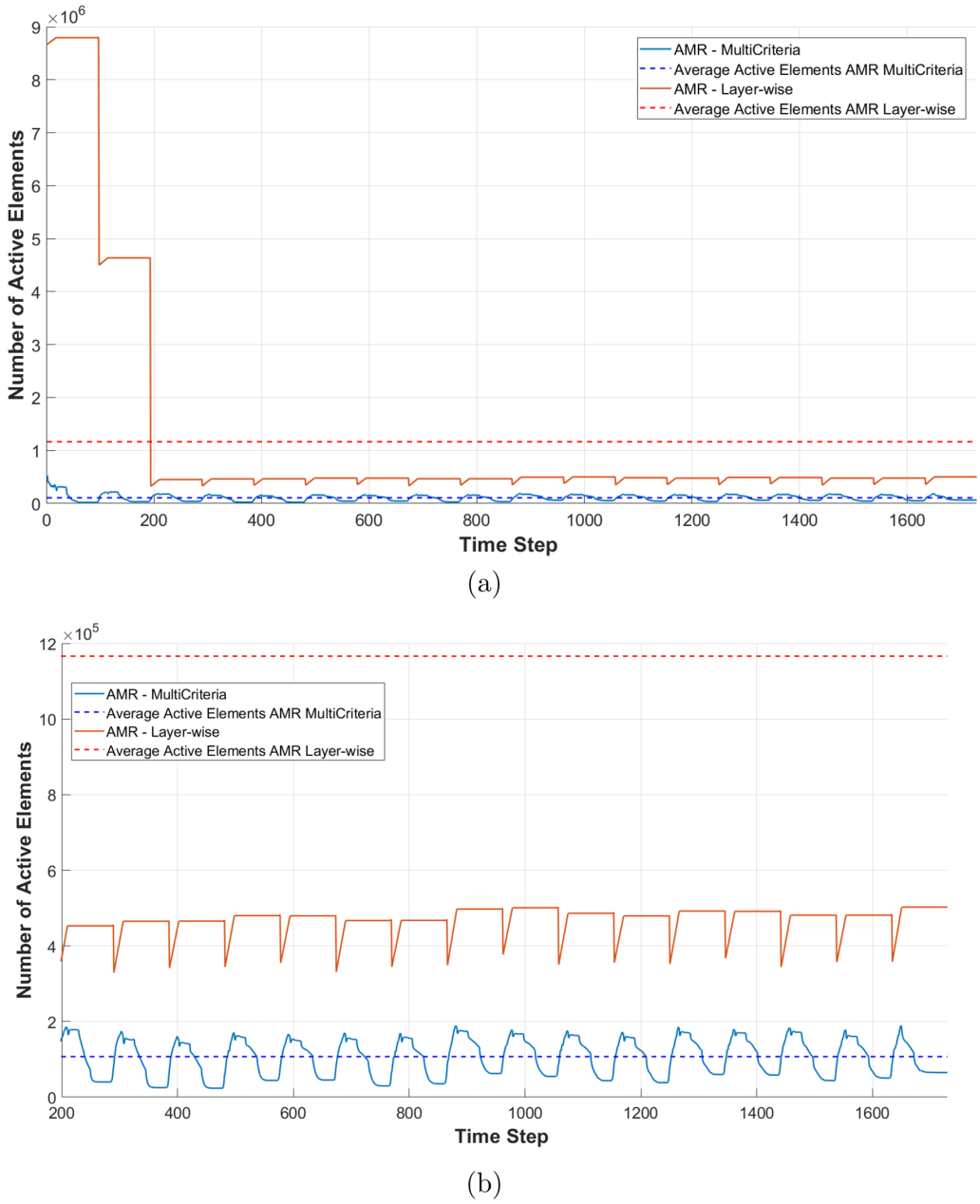

Fig. 21 Thin-wall: **a** evolution of the number of active FEs per time step; **b** detail from time-step 200 to the end of simulation for the 10 (min) waiting time case

the open-source software CURA. Hence, no user manipulation is required and the mesh resolution depends on the maximum refinement level adopted for the geometric-based AMR criterion.

Figure 22 shows the door handle geometry and the points P1 and P2, of coordinates (37.73, 101.48, 2.99) (mm) and (120.0, 117.31, 52.02) (mm) are chosen to measure the temperature evolution for both FE meshes.

The discrete domain is built departing from a bounding box of dimensions $180 \times 135 \times 70$ (mm^3) being generated with the data provided by a GCode file. The minimum and maximum refinement levels adopted are 4 and

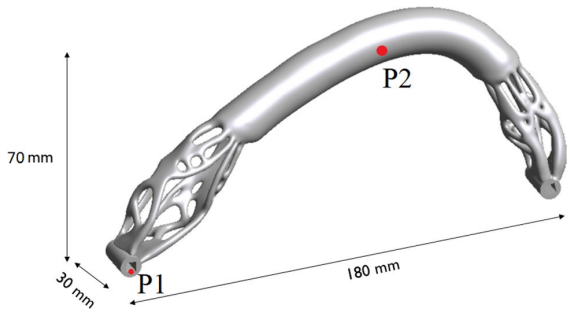

Fig. 22 Door handle: **a** geometry; **b** position of the points P1 and P2

9, respectively. The fixed fine mesh model has a total of 1,644,511 active FEs.

The environment temperature is 20 (°C) and a radiation emissivity of $\varsigma = 0.7$ is considered. The HTC by convection is fix to a constant value $h_{\text{conv}} = 10$ (W/(m$^2 \cdot$ °C)). In this case, we considered the laser movement defining the time-marching scheme is $\Delta l = 800.0$ (mm), the melt-pool base and height are $b_{\text{pool}} = 500.0$ (μm) and $h_{\text{pool}} = 100.0$ (μm), respectively.

Figure 23 shows the evolution of the component building and the inactive background mesh required. Figure 24 shows a cross section of the door handle for both FE models; note that the difference between the finest and the coarsest FEs in the multi-criteria AMR is of 2 refinement levels.

Figure 25 shows the evolution and the average number of the active FE. Ideally, the AMR strategy exhibits a fluctuation of the number of active FEs around a constant threshold, as observed in previous examples using simpler geometries. In this case, the complexity of the geometry of the hollowed thin-walled door-handle induces a geometric constraint to the coarsening technique inhibiting higher coarsening capabilities. For the fixed fine mesh, the average number of active FEs is 764,923, whereas the multi-criteria strategy average is 57.89% lower (322,099 active FEs). The real-time run for the fixed fine mesh case is 14 (h) 6 (min) obtaining a time reduction of 29.91% when the multi-criteria AMR is used.

Figure 26 shows the temperature evolution at points P1 and P2, showing the agreement between the two strategies. Figure 27 graphically shows the relative percentual difference of the temperature field of the multi-criteria AMR

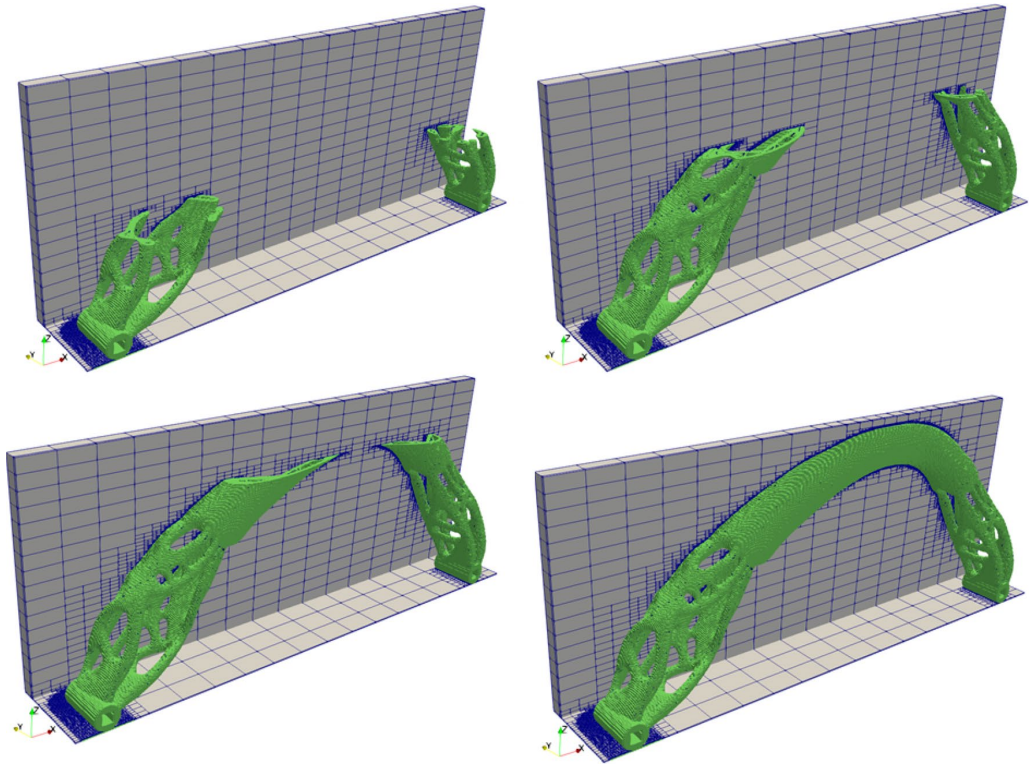

Fig. 23 Evolution of the background FE mesh during the building process

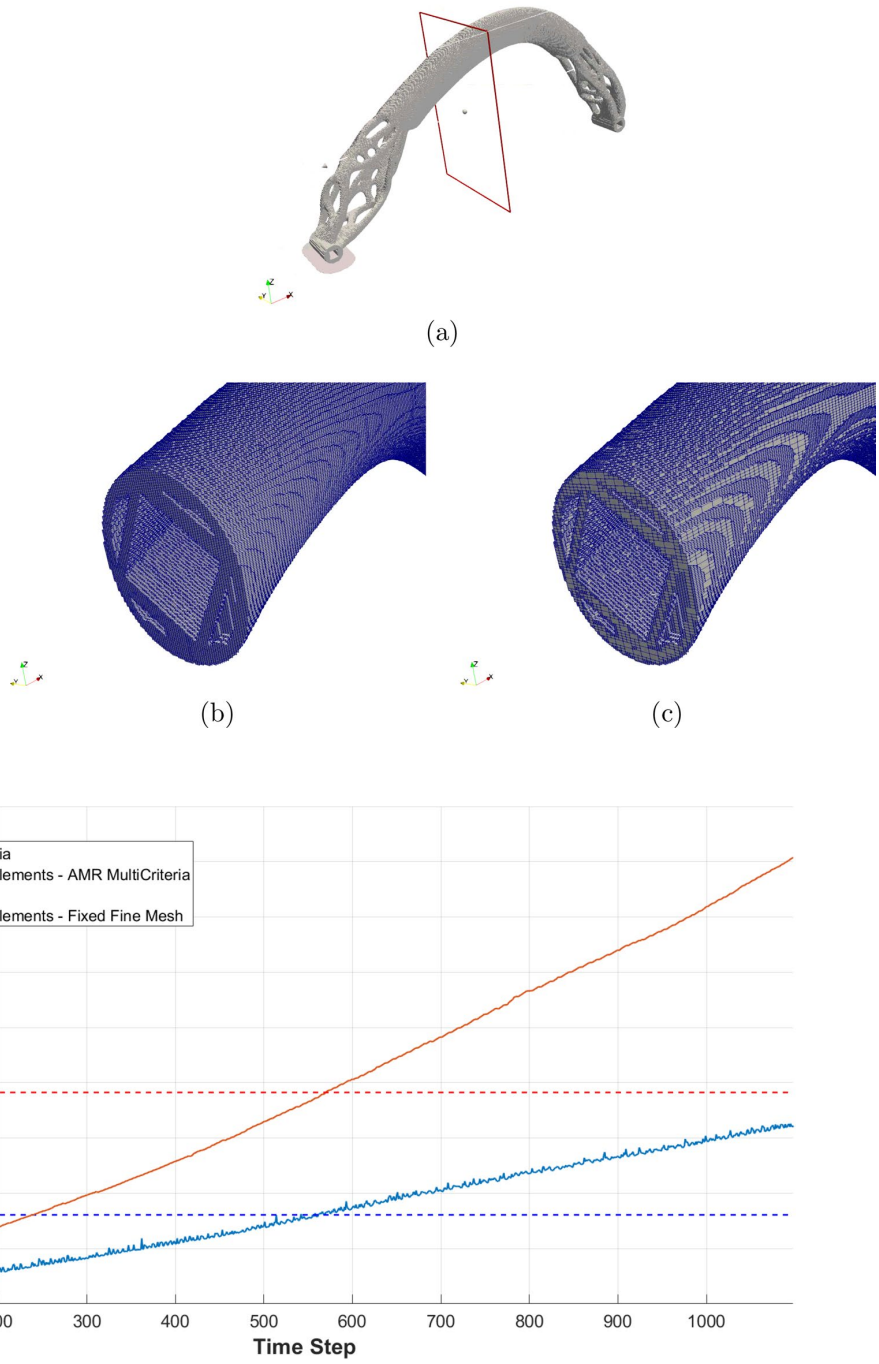

Fig. 24 Door handle: **a** position of the section cut; **b** fixed fine mesh; **c** multi-criteria AMR mesh

Fig. 25 Door handle: evolution of the number of active FEs per time step

strategy with respect to the fixed fine mesh at the end of the simulation, where the maximum relative difference observed is 1.81%. The global error obtained by applying Eq. (19) is 0.28%. The strategy produces very accurate results at a fraction of the computational cost, even when coarsening is restricted by geometric constraints due to the complexity of the component.

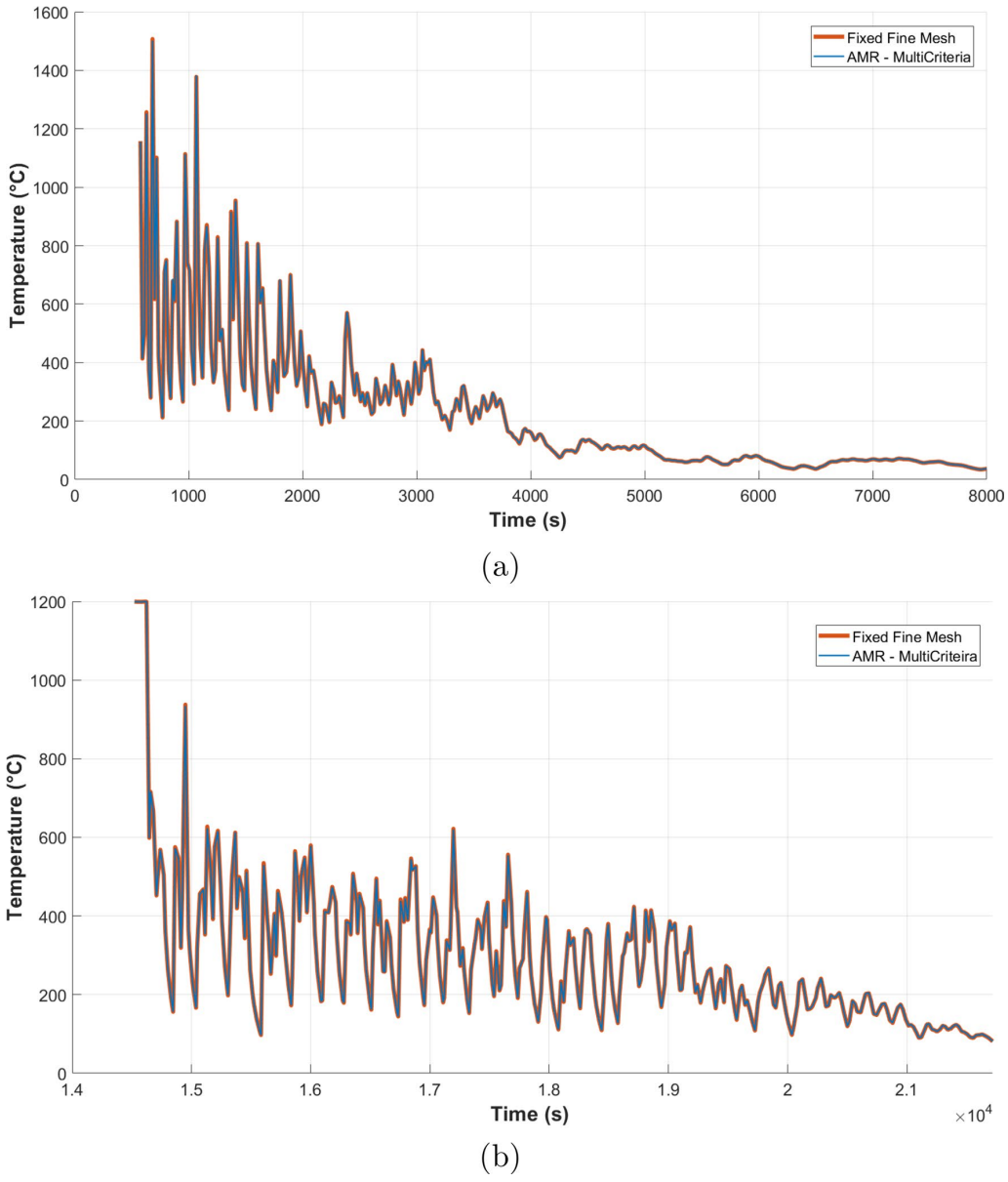

Fig. 26 Door handle: temperature curves evolution of points **a** P1 and **b** P2 for both models

6 Conclusions

In this work, a robust parallel *h*-adaptive framework to simulate AM processes focusing on industrial part-scale simulation is presented. The motivation arises from the necessity of the industry to take advantage of the capabilities of AM simulation to produce complex optimized solutions to enhance the performance of industrial components. In this sense, the use of the GCode file to define the geometry of the components is crucial, because it is a flexible format, where the process parameters may be introduced and changed throughout the simulation. The use of the GCode removes both CAD cleaning and meshing operations, very challenging when dealing with complex geometries. Therefore, the proposed strategy allows for a user-friendly environment for industrial part-scale analyses.

The scalability of the industrial use of AM processes depends on the reduction of the printing time for large-scale

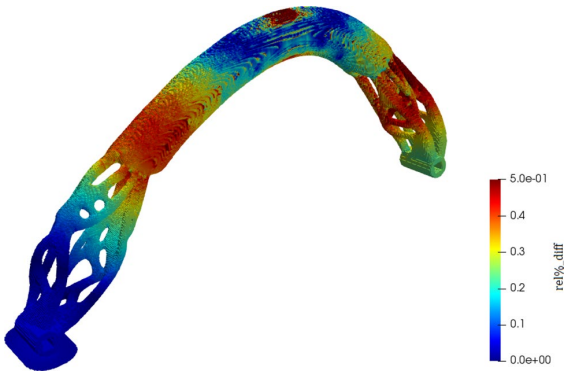

Fig. 27 Door handle: relative percentual difference of the temperature field of the multi-criteria AMR with respect to the fixed fine mesh

components. The success on the numerical simulation depends on its capability to reduce the overall simulation time without loss of accuracy. For this reason, the multi-criteria approach has a geometrical-based criterion to identify the current position of the laser, creating a maximum refined area at the vicinity of the HAZ by means of the separating-axis theorem. All FEs belonging to the HAZ are activated on the current time-step and the geometric resolution depends on the user-defined maximum level of refinement. The boundaries of the domain are represented by a fitted FE mesh, which does not require cut FE integration schemes. The accuracy is assured by the a-posteriori error estimate based on the temperature gradients, avoiding the imposition of a 2:1 balance scheme.

The numerical examples show compelling results in terms of computational cost reduction and accuracy compared to alternative approaches to simulate AM processes. The multi-criteria approach is easy to implement and can be applied to several others AM processes.

The AMR strategy presented herein is now being developed into a thermo-mechanical setting. To make it applicable for industrial needs, a ROM of the thermo-mechanical problem may be incorporated to speed-up the computational model.

Acknowledgements The financial support from the Spanish Ministry of Economy and Competitiveness, through the Severo Ochoa Programme for Centres of Excellence in R&D (CEX2018-000797-S), is gratefully acknowledged. This work has been supported by the European Union's horizon 2020 research and innovation programme (H2020-DT-2019-1 no. 872570) under the KYKLOS 4.0 Project (An Advanced Circular and Agile Manufacturing Ecosystem based on rapid reconfigurable manufacturing process and individualized consumer preferences) and by the Ministry of Science, Innovation and Universities (MCIU) via: the PriMuS project (Printing pattern based and MultiScale enhanced performance analysis of advanced Additive Manufacturing components, ref. num. PID2020-115575RB-I00). J. Baiges gratefully acknowledges the support of the Spanish Government through the Ramón y Cajal Grant RYC-2015-17367.

Funding Open Access funding provided thanks to the CRUE-CSIC agreement with Springer Nature.

References

1. Agelet de Saracibar C, Cervera M, Chiumenti M (1999) On the formulation of coupled thermoplastic problems with phase-change. Int J Plast 15(1):1–34
2. Agelet de Saracibar C, Cervera M, Chiumenti M (2001) On the constitutive modeling of coupled thermomechanical phase-change problems. Int J Plast 17(12):1565–1622
3. Ahrens J, Geveci B, Law C (2005) ParaView: an end-user tool for large data visualization. Visualization handbook. Elsevier, New York
4. Annavarapu C, Hautefeuille M, Dolbow JE (2012) A robust nitsche's formulation for interface problems. Comput Methods Appl Mech Eng 225–228:44–54
5. Atallah NM, Canuto C, Scovazzi G (2021) Analysis of the shifted boundary method for the poisson problem in general domains. ArXiv:2006.00872
6. Babuska TF, Krick BA, Susan DF, Kustas AB (2021) Comparison of powder bed fusion and directed energy deposition for tailoring mechanical properties of traditionally brittle alloys. Manuf Lett 28:30–34
7. Badia S, Caicedo MA, Martín AF, Principe J (2021) A robust and scalable unfitted adaptive finite element framework for nonlinear solid mechanics. Comput Methods Appl Mech Eng 386:114093
8. Badia S, Martín AF, Neiva E, Verdugo F (2020) A generic finite element framework on parallel tree-based adaptive meshes. SIAM J Sci Comput 42(6):C436–C468
9. Badia S, Martín AF, Neiva E, Verdugo F (2021) The aggregated unfitted finite element method on parallel tree-based adaptive meshes. SIAM J Sci Comput 43(3):C203–C234
10. Badia S, Verdugo F, Martín AF (2018) The aggregated unfitted finite element method for elliptic problems. Comput Methods Appl Mech Eng 336:533–553
11. Baiges J, Bayona C (2017) Refficientlib: an efficient load-rebalanced adaptive mesh refinement algorithm for high-performance computational physics meshes. SIAM J Sci Comput 39(2):65–95
12. Baiges J, Codina R, Pont A, Castillo E (2017) An adaptive fixed-mesh ale method for free surface flows. Comput Methods Appl Mech Eng 313:159–188
13. Carraturo M, Jomo J, Kollmannsberger S, Reali A, Auricchio F, Rank E (2020) Modeling and experimental validation of an immersed thermo-mechanical part-scale analysis for laser powder bed fusion processes. Addit Manuf 36:101498

14. Carraturo M, Kollmannsberger S, Reali A, Auricchio F, Rank E (2021) An immersed boundary approach for residual stress evaluation in selective laser melting processes. Addit Manuf 46:102077
15. Cheng B, Shrestha S, Chou K (2016) Stress and deformation evaluations of scanning strategy effect in selective laser melting. Addit Manuf 12:240–251
16. Chiumenti M, Cervera M, Agelet de Saracibar C, Dialami N (2013) Numerical modeling of friction stir welding processes. Comput Methods Appl Mech Eng 254:353–369
17. Chiumenti M, Cervera M, Dialami N, Wu B, Li J, Agelet de Saracibar C (2016) Numerical modeling of the electron beam welding and its experimental validation. Finite Elem Anal Des 121:118–133
18. Chiumenti M, Lin X, Cervera M, Lei W, Zheng Y, Huang W (2017) Numerical simulation and experimental calibration of additive manufacturing by blown powder technology. Part i: thermal analysis. Rapid Prototyp J 23(2):448–463
19. Chiumenti M, Neiva E, Salsi E, Cervera M, Badia S, Moya J, Chen Z, Lee C, Davies C (2017) Numerical modelling and experimental validation in selective laser melting. Addit Manuf 18:171–185
20. de Prenter F, Verhoosel C, van Zwieten G, van Brummelen E (2017) Condition number analysis and preconditioning of the finite cell method. Comput Methods Appl Mech Eng 316:297–327 (**Special Issue on Isogeometric Analysis: Progress and Challenges**)
21. Di Stolfo P, Schröder A, Zander N, Kollmannsberger S (2016) An easy treatment of hanging nodes in hp-finite elements. Finite Elem Anal Des 121:101–117
22. Dialami N, Cervera M, Chiumenti M, Agelet de Saracibar C (2017) Numerical modeling of friction stir welding processes. Int J Adv Manuf Technol 88:3099–3111
23. Dialami N, Chiumenti M, Cervera M, Agelet de Saracibar C (2013) An apropos kinematic framework for the numerical modeling of friction stir welding. Comput Struct 117:48–57
24. Eberly D (2002) Dynamic collision detection using oriented bounding boxes. Geometric tools Inc, Cadott
25. Fallah V, Alimardani M, Corbin SF, Khajepour A (2011) Temporal development of melt-pool morphology and clad geometry in laser powder deposition. Comput Mater Sci 50(7):2124–2134
26. Goldak J, Chakravarti A, Bibby M (1984) A new finite element model for welding heat sources. Metall Trans B 15:299–305
27. Gottschalk S, Manocha D, Lin MC (2000) Collision queries using oriented bounding boxes. PhD thesis, University of North Carolina at Chapel Hill
28. Gouge M, Denlinger E, Irwin J, Li C, Michaleris P (2019) Experimental validation of thermo-mechanical part-scale modeling for laser powder bed fusion processes. Addit Manuf 29:100771
29. Hackenhaar W, Mazzaferro JA, Montevecchi F, Campatelli G (2020) An experimental-numerical study of active cooling in wire arc additive manufacturing. J Manuf Process 52:58–65
30. Junk S, Klerch B, Nasdala L, Hochberg U (2018) Topology optimization for additive manufacturing using a component of a humanoid robot. Procedia CIRP 70:102–107 (**28th CIRP Design Conference 2018, 23--25 May 2018. Nantes, France**)
31. Kelly S, Kampe S (2004) Microstructural evolution in laser-deposited multilayer ti-6al-4v builds: part i. Microstructural characterization. Metall Mater Trans A 35:1861–1867
32. Kobryn P, Semiatin S (2003) Microstructure and texture evolution during solidification processing of ti-6al-4v. J Mater Process Technol 135(2–3):330–339
33. Li C, Fu C, Guo Y, Fang F (2016) A multiscale modeling approach for fast prediction of part distortion in selective laser melting. J Mater Process Technol 229:703–712
34. Li K, Atallah NM, Main GA, Scovazzi G (2020) The shifted interface method: a flexible approach to embedded interface computations. Int J Numer Methods Eng 121(3):492–518
35. Lu X, Lin X, Chiumenti M, Cervera M, Hu Y, Ji X, Ma L, Huang W (2019) In situ measurements and thermo-mechanical simulation of ti-6al-4v laser solid forming processes. Int J Mech Sci 153–154:119–130
36. Lu X, Lin X, Chiumenti M, Cervera M, Hu Y, Ji X, Ma L, Yang H, Huang W (2019) Residual stress and distortion of rectangular and s-shaped ti-6al-4v parts by directed energy deposition: modelling and experimental calibration. Addit Manuf 26:166–179
37. Lu X, Lin X, Chiumenti M, Cervera M, Li J, Ma L, Wei L, Hu Y, Huang W (2018) Finite element analysis and experimental validation of the thermomechanical behavior in laser solid forming of ti-6al-4v. Addit Manuf 21:30–40
38. Lu X, Zhang G, Li J, Cervera M, Chiumenti M, Chen J, Lin X, Huang W (2021) Simulation-assisted investigation on the formation of layer bands and the microstructural evolution in directed energy deposition of Ti6Al4V blocks. Virtual Phys Prototyping 16(4):387–403
39. Luo Z, Zhao Y (2018) A survey of finite element analysis of temperature and thermal stress fields in powder bed fusion additive manufacturing. Addit Manuf 21:318–332
40. Ma L, Bin H (2007) Temperature and stress analysis and simulation in fractal scanning-based laser sintering. Int J Adv Manuf Technol 34:898–903
41. Main A, Scovazzi G (2018) The shifted boundary method for embedded domain computations. Part i: Poisson and stokes problems. J Comput Phys 372:972–995
42. Malekipour E, Tovar A, El-Mounayri H (2018) Heat conduction and geometry topology optimization of support structure in laser-based additive manufacturing, vol 10. pp 17–27 (2018)
43. Neiva E, Badia S (2021) Robust and scalable h-adaptive aggregated unfitted finite elements for interface elliptic problems. Comput Methods Appl Mech Eng 380:113769
44. Neiva E, Badia S, Martín AF, Chiumenti M (2019) A scalable parallel finite element framework for growing geometries application to metal additive manufacturing. Int J Numer Methods Eng 119(11):1098–1125
45. Neiva E, Chiumenti M, Cervera M, Salsi E, Piscopo G, Badia S, Martín AF, Chen Z, Lee C, Davies C (2020) Numerical modelling of heat transfer and experimental validation in powder-bed fusion with the virtual domain approximation. Finite Elem Anal Des 168:103343
46. Olleak A, Xi Z (2020) Scan-wise adaptive remeshing for efficient lpbf process simulation: the thermal problem. Manuf Lett 23:75–78
47. Olleak A, Xi Z (2020) A scan-wise adaptive remeshing framework for thermal simulation of the selective laser melting process. Int J Adv Manuf Technol 107:573–584
48. Ozcan A, Kollmannsberger S, Jomo J, Rank E (2019) Residual stresses in metal deposition modeling: discretizations of higher order. Comput Math Appl 78(7):2247–2266 (**Simulation for Additive Manufacturing**)
49. Ren J, Liu J, Yin J (2010) Simulation of transient temperature field in the selective laser sintering process of w/ni powder mixture. In: International conference on computer and computing technologies in agriculture. pp 494–503
50. Serdeczny MP, Comminal R, Pedersen DB, Spangenberg J (2018) Experimental validation of a numerical model for the strand shape in material extrusion additive manufacturing. Addit Manuf 24:145–153
51. Setaki F, Tenpierik M, Turrin M, van Timmeren A (2014) Acoustic absorbers by additive manufacturing. Build Environ 72:188–200
52. Singh S, Ramakrishna S, Singh R (2017) Material issues in additive manufacturing: a review. J Manuf Process 25:185–200
53. Wong KV, Hernandez A (2012) A review of additive manufacturing. ISRN mechanical engineering

54. Zander N, Bog T, Elhaddad M, Frischmann F, Kollmannsberger S, Rank E (2016) The multi-level hp-method for three-dimensional problems: dynamically changing high-order mesh refinement with arbitrary hanging nodes. Comput Methods Appl Mech Eng 310:252–277
55. Zander N, Bog T, Kollmannsberger S, Schillinger D, Rank E (2015) Multi-level hp-adaptivity: high-order mesh adaptivity without the difficulties of constraining hanging nodes. Comput Mech 55:499–517
56. Zhu J, Zhou H, Wang C, Zhou L, Yuan S, Zhang W (2021) A review of topology optimization for additive manufacturing: status and challenges. Chin J Aeronaut 34(1):91–110
57. Zienkiewicz OC, Zhu JZ (1987) A simple error estimator and adaptive procedure for practical engineering analysis. Int J Numer Methods Eng 24(2):337–357
58. Zienkiewicz OC, Zhu JZ (1992) The superconvergent patch recovery and a posteriori error estimates. Part 1: the recovery technique. Int J Numer Methods Eng 33(7):1331–1364
59. Zienkiewicz OC, Zhu JZ (1992) The superconvergent patch recovery and a posteriori error estimates. Part 2: error estimates and adaptivity. Int J Numer Methods Eng 33(7):1365–1382

B

PRESENTATIONS IN INTERNATIONAL CONFERENCES

During the development of the Thesis, the partial advances and results have been presented in several national and international specialized conferences. The list of attended conferences are:

- **G.B. Barbat, C.A. Moreira, M. Cervera and M. Chiumenti** Modelling of incompressible damage with an enhanced-accuracy mixed thermo-mechanical formulation, VIII International Conference on Coupled Problems in Science and Engineering, Sitges, Spain. June 2019.
- **C.A. Moreira, G.B. Barbat, M. Chiumenti and M. Cervera** Mixed FE formulation for modelling incompressible damage with thermo-mechanical coupling, XV International Conference on Computational Plasticity. Fundamentals and Applications, Barcelona, Spain. September 2019.
- **M. Chiumenti, M. Cervera, C.A. Moreira and G.B. Barbat** On the mixed three-field formulation for strain localization problems encompassing the incompressible limit, International Conference on Plasticity, Damage and Fracture 2020 (ICPDF 20), Rivera Maya, Mexico. January 2020.
- **M. Chiumenti, J. Baiges, M. Cervera, R. Codina, M. Caicedo, C.A. Moreira and J.M. Martinez** HPC framework for the thermo-mechanical simulation of DED Additive Manufacturing processes, Simulation for Additive Manufacturing (SimAM-2021), Glasgow, United Kingdom. September 2021.
- **C.A. Moreira, J. Baiges, M. Cervera, M.A. Caicedo and M. Chiumenti** An automatic octree mesh generation based on laser activation path for the metal deposition process in Additive Manufacturing, XVI International Conference on Computational Plasticity. Fundamentals and Applications, Barcelona, Spain. September 2021.
- **J. Baiges, M. Chiumenti, C.A. Moreira, M. Cervera and R. Codina** An adaptive finite element strategy for numerical simulation of Additive Manufacturing processes, XVI International Conference on Computational Plasticity. Fundamentals and Applications, Barcelona, Spain. September 2021.

Colophon

This document was typeset using the typographical `classicthesis` style developed by André Miede. The package uses Hermann Zapf's *Palatino* and *Euler* type faces (Type 1 PostScript fonts *URW Palladio L* and *FPL*) are used. The style was inspired by Robert Bringhurst's seminal book on typography "*The Elements of Typographic Style*".